September 23, 2014

A validated approach to modeling collapse of steel structures

V. V. Saykin
Northeastern University

J. Song
Seoul National University, Korea

J. F. Hajjar
Northeastern University

Report No. NEU-CEE-2014-02

Northeastern University was founded in 1898, as a private research university. Northeastern University is a leader in worldwide experiential learning, urban engagement, and interdisciplinary research that meets global and societal needs. Department of Civil and Environmental Engineering has over 100 years of history and tradition in research, teaching and service to the community, making important contributions to the development of our civil infrastructure and the environment, both nationally and internationally.

Contact:
Department of Civil & Environmental Engineering
400 Snell Engineering Center
Northeastern University
360 Huntington Avenue
Boston, MA 02115
(617) 373-2444
(617) 373-4419 (fax)

The authors thank D. Deniz, T. Nguyen, A. Kanvinde, Mr. C. Smith, E. V. Livingston, S. I. Jassam, J. Moradei, S. D. Earl, and D. P. Gray for their contributions to this research. This material is based upon work supported by the National Science Foundation under Grant No. CMMI-1000666, Northeastern University, and the University of Illinois at Urbana-Champaign. This work used the Extreme Science and Engineering Discovery Environment (XSEDE), which is supported by National Science Foundation grant number OCI-1053575. Any opinions, findings and conclusions or recommendations expressed in this material are those of the authors and do not necessarily reflect the views of the National Science Foundation

Northeastern University

Boston, Massachusetts

September 2014

Abstract

A civil engineering structure is faced with many hazardous conditions such as blasts, earthquakes, hurricanes, tornadoes, floods, and fires during its lifetime. Even though structures are designed for credible events that can happen during a lifetime of the structure, extreme events do happen and cause catastrophic failures. Understanding the causes and effects of structural collapse is now at the core of critical areas of national need. One factor that makes studying structural collapse difficult is the lack of full-scale structural collapse experimental test results against which researchers could validate their proposed collapse modeling approaches. The goal of this work is the creation of an element deletion strategy based on fracture models for use in validated prediction of collapse of steel structures. The current work reviews the state-of-the-art of finite element deletion strategies for use in collapse modeling of structures. It is shown that current approaches to element deletion in collapse modeling do not take into account stress triaxiality in vulnerable areas of the structure, which is important for proper fracture and element deletion modeling. The report then reviews triaxiality and its role in fracture prediction. It is shown that fracture in ductile materials is a function of triaxiality. It is also shown that, depending on the triaxiality range, different fracture mechanisms are active and should be accounted for. An approach using semi-empirical fracture models as a function of triaxiality are employed. The models to determine fracture initiation, softening and subsequent finite element deletion are outlined. This procedure allows for stress-displacement softening at an integration point of a finite element in order to subsequently remove the element. This approach avoids abrupt changes in the stress that would create dynamic

instabilities, thus making the results more reliable and accurate. The calibration and validation of these models are shown. The calibration is performed using a particle swarm optimization algorithm to establish accurate parameters when calibrated to circumferentially notched tensile coupons. It is shown that consistent, accurate predictions are attained using the chosen models. The variation of triaxiality in steel material during plastic hardening and softening is reported. The range of triaxiality in steel structures undergoing collapse is investigated in detail and the accuracy of the chosen finite element deletion approaches is discussed. This is done through validation of different structural components and structural frames undergoing severe fracture and collapse.

Table of Contents

List of Figures

List of Tables

1 Introduction

1.1 Background and Motivation

A civil engineering structure may be faced with many hazardous conditions such as blasts, earthquakes, hurricanes, tornadoes, floods, and fires during its lifetime. Even though structures are designed for credible events that can happen during their lifetime , extreme events can happen that may cause catastrophic failures.. In recent years such events as the collapse of Wedbush Building due to a construction accident (Mercury News 2013), and the structural collapses during the 1994 Northridge (Cooper et al. 1994) and 1995 Kobe earthquakes (Miyazaki et al. 2013) have highlighted the limitation of knowledge and understanding of structural behavior of steel structures undergoing collapse (Khandelwal 2008; Szyniszewski et al. 2012).

Most collapse happens due to fracture in significant structural members. Fracture in steel structures has gained growing attention after the 1994 Northridge earthquake and the 1995 Hyogoken-Nanbu earthquake in Kobe (Kuwamura 2003). More than 100 moment frames in Kobe and its surrounding areas were reported to sustain severe cracks or fracture at beam-to-column connections, about 30 buildings among which partially or totally collapsed (Kuwamura et al. 1997).

Understanding the causes and effects of structural collapse is now at the core of critical areas of national need. One factor that makes studying structural collapse difficult is the lack of full-scale structural collapse experimental results against which researchers can validate their

proposed collapse modeling approaches. Current collapse models of steel structures typically use a constant critical strain approach to model fracture in steel members (Khandelwal et al. 2009; Sadek et al. 2010; Szyniszewski et al. 2012). The constant critical strain approach simplifies the fracture initiation process to a single value of critical strain while ignoring ductile fracture's dependence on stress triaxiality. A lack of an alternative accurate and validated structural collapse models limits the options for design against disproportionate collapse.

1.2 Project Overview

To advance the modeling of collapse of steel structures, this research was initiated to create an integrated platform for validated prediction of collapse of steel structures. The overall project was subdivided into three parts: (1) the development of a stochastic model to predict the collapse limit-state; (2) the formulation of a macromodel for collapse of steel structures; and (3) the development of a finite element model able to accurately model collapse. The stochastic model aims to properly quantify the bias and uncertainty of macromodel predictions and develop factors to predict collapse capacity and demand for use in performance-based design and collapse assessment. To facilitate this, a macromodel is formulated by developing special fracture elements with the ability to account for softening and subsequent element deletion to model fracture. The macromodel was to be validated against finite element models.

The third part includes the development of an approach for finite element analysis to account for nonlinear dynamic processes such as contact, inelastic behavior, large deformations, softening, and element deletion. The primary focus is on implementing micromechanical fracture models to account for fracture of steel elements during collapse by modeling element

softening and deletion to represent material separation. These models are to be calibrated and validated through a comprehensive set of experimental results, ranging from coupon tests through to complete structures subjected to collapse.

1.3 Objectives and Outline

The objective of this work is to develop a strategy to model fracture initiation, propagation and softening, and eventual finite element deletion within the context of finite element modeling to be used in predicting collapse behavior of steel structures. This is done by using fracture semi-empirical models which include the influence of stress triaxiality on fracture initiation, softening, and element deletion. Previous studies in progressive collapse of steel structures relied on the use of constant critical strain criteria for element deletion which does not take into account the effect of triaxiality on fracture (Khandelwal et al. 2009). In addition, depending on the level of triaxiality, different fracture initiation mechanisms are active and are accounted for in this study by two micromechanical models: the Void Growth Model (VGM) and the Bao-Wierzbicki Model (Rice et al. 1969; Bao et al. 2004). Together this accounts for a complete triaxiality range that civil engineering structures are likely to encounter, providing a robust and accurate approach for collapse analysis of steel structures. The softening and finite element deletion is modeled through the use of Hillerborg Model (Hillerborg et al. 1976). Using these three models to model fracture in finite element simulation of collapse of steel structures is then calibrated and validated through a comprehensive set of experiments. This approach improves on the current constant critical strain method that is commonly used in the following ways: it captures fracture's dependence on triaxiality, it considers the history of triaxiality in an

element, and it alleviates dynamic instabilities by deleting an element when the stress and stiffness are degraded to zero (Hillerborg et al. 1976; Khandelwal et al. 2005; Wierzbicki et al. 2005; Szyniszewski et al. 2012). As finite elements are deleted, the fracture propagates through the critical structural element. This causes the loss of load carrying capacity in structural elements and propagates collapse. This work describes this approach and highlights its advantages and shortcomings.

Chapter 2 of this work describes the current state-of-the-art related to the deletion of finite elements to simulate disassociation of material as part of collapse of structures. The main focus of the chapter is on the benefits and shortcomings of the constant critical strain approach to finite element deletion. The chapter also summarizes the Gurson model, including its advantages and disadvantages. The Gurson Model has been used for modeling collapse of steel structures (Khandelwal et al. 2005).

Chapter 3 describes the influence of triaxiality on fracture initiation and propagation in metals. The chapter summarizes the three stages of ductile fracture: micro-void nucleation, growth, and coalescence, and how each stage is affected by triaxiality. An overview is then presented of ductile fracture as a function of triaxiality. This includes a discussion of a fracture cut-off limit, how different fracture mechanisms are active at different triaxiality ranges, and a discussion on the effect of triaxiality on fracture in steel structures. The chapter finishes with a discussion of other important parameters that effect fracture in ductile metals.

Chapter 4 describes the Void Growth Model (VGM) and Bao-Wierzbicki (B-W) model. The chapter covers their formulations and how the models are applied in finite element software.

In addition, it describes the Hillerborg model by which softening is modeled by progressively degrading the element stress and stiffness.

Chapter 5 describes the calibration process for finite element deletion in modeling collapse of steel structures. The chapter summarizes the parameters of the calibration simulations such as the material model, the geometric nonlinearity, and the contact model used, and discusses the specimens used for calibration and their boundary and loading conditions. It then summarizes the Particle Swarm Optimization method used for calibrating the parameters of the fracture models, the error function used, and the results attained. The variations of fracture critical parameters that are related to the three calibrated models, VGM-BW, VGM, and Constant Strain. A relationship between the Charpy V-Notch (CVN) Impact test and the fracture models is described.

Chapter 6 describes the validations that were performed by comparison of the simulation results and the experimental results. The validation set ranges in complexity from simple tensile coupon specimens to multi-story steel frames subjected to complete collapse. A comparison of the constant critical strain, VGM, and B-W models of fracture initiation and their influence on the global behavior of steel structures undergoing collapse are discussed.

Chapter 7 summarizes this work and provides conclusions and recommendations. It discusses the advantages and disadvantages of the proposed finite element deletion in modeling collapse of steel structures. It then provides recommendations on choosing the appropriate finite element deletion model and on future work in collapse modeling.

Through robust validation, the developed collapse model provides a platform to assess the collapse capacity of steel structures, with more accuracy than current constant critical strain approaches.

2 Background

This chapter summarizes the current methods related to finite element deletion in simulating disassociation of material while modeling collapse of steel structures.

2.1 Constant Critical Strain at Fracture

To model collapse of steel structures, one needs to account for complex material and geometrical nonlinearities, contact, and finite element softening and subsequent deletion. Finite element elimination has been often used to facilitate disassociation of materials during structural collapse (Khandelwal et al. 2005; Khandelwal et al. 2009; Sadek et al. 2010; Szyniszewski et al. 2012). This enables modeling of structures undergoing large deformations, fracturing to complete separation, and precipitating dynamic impact loading on other elements through contact modeling (Alashker et al. 2011). A challenge to accurately model collapse of steel structures has been in accounting efficiently and comprehensively for fracture mechanics through finite element deletion.

The constant critical strain approach is commonly used to identify the initiation of fracture in metals (Sadek et al. 2010). In this approach, a critical equivalent plastic strain at fracture is specified at an integration point of a element. Upon reaching this equivalent plastic strain at an integration point of the finite element, the element is suddenly removed (Khandelwal et al. 2008). Figure 2.1 illustrates the general concept. The constant critical strain approach is used most often in modeling collapse of steel structures because of its practicality, ease of use, and a lack of complexity. However, this may create an oversimplified model for a complex fracture

process that occurs during collapse of steel structures. This means that the calibrated critical strain may be valid only for a situation that has similar boundary conditions, geometrical configuration, and loading history as the experimental setup that was used for calibration. For all other cases it will typically either over or underpredict the results.

Figure 2.2 shows that the critical strain is indifferent to triaxiality, while the true theoretical fracture strain is highly dependent on triaxiality (Rice et al. 1969; Wierzbicki et al. 2005). This approach should only be used were triaxiality range is small and does not change during loading from the calibration range. Traditionally the critical strain value is calibrated from a tensile test of an unnotched specimen, which is represented by a peak value of true fracture strain in Figure 2.2. However, this value often overpredicts the capacity of a material in most other triaxiality regions, leading to a less accurate approximation of most other loading conditions (Wierzbicki et al. 2005). Most of the time, the critical strain value is treated as an adjustable parameter to achieve the best correlation between experimental results and simulations (Wierzbicki et al. 2005; Khandelwal et al. 2008; Szyniszewski 2009), but this makes the approach less flexible for broad use (Wierzbicki et al. 2005; Sadek et al. 2010).

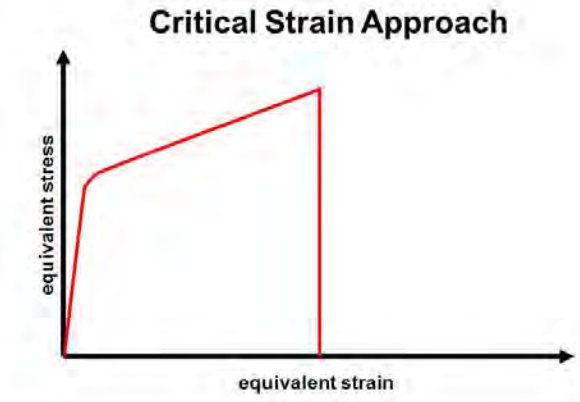

Figure 2.1: Critical strain approach to finite element elimination

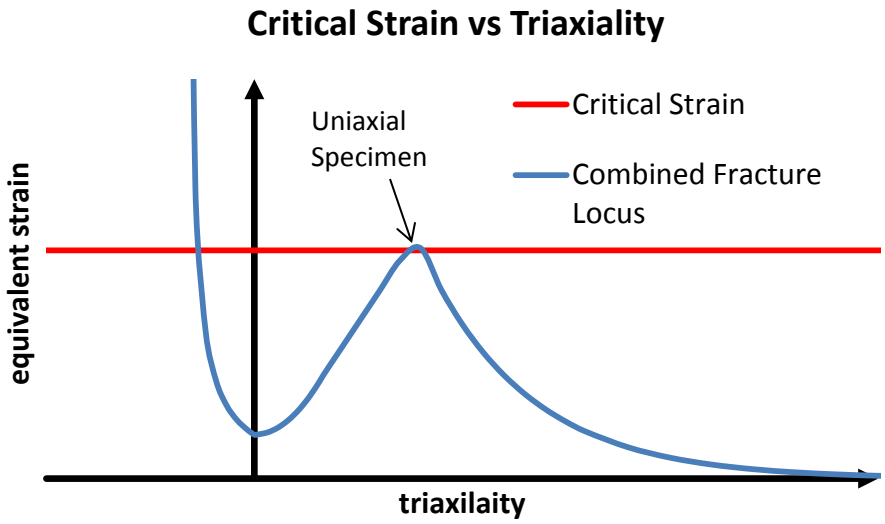

Figure 2.2: Critical strain versus triaxiality (Wierzbicki et al. 2005)

Khandelwal et al. (2005) initially used a constant value of 0.2 for the critical equivalent plastic strain to precipitate deletion of fully integrated shell finite elements. Khandelwal et al. (2008) then extended this approach and used it in conjunction with beam elements. Khandelwal et al. (2008) used different critical strain values depending on the element, beam connection type, and beam depth, varying from 0.03 to 0.095. These values were arrived at by comparing the results from macromodel finite element analyses with simulation results from continuum finite element analysis that employed the Gurson Model for element softening and deletion (Khandelwal et al. 2007). This approach was later used to perform progressive collapse studies on steel structures (Khandelwal 2008; Khandelwal et al. 2009).

Subsequently, Main et al. (2009) studied several prototype steel moment-frame buildings to assess their vulnerability to progressive collapse using the constant critical strain approach so as to quantify and compare the relative robustness of different structural systems. The authors used the macromodel approach developed by Khandelwal et al. (2008) in which a combination

of beam and discrete spring elements are used to represent the nonlinear behavior and failure of the various connections in each building through the critical strain approach.

A dynamic energy based method for progressive collapse analysis was proposed using the constant critical strain approach as an element deletion criteria (Szyniszewski 2009). The main conclusion was that if a collapsing structure is capable of attaining a stable energy state through absorption of gravitational energy, then collapse will be arrested. Otherwise, if a deficit in energy dissipation develops, the unabsorbed portion of released gravitational energy is converted into kinetic energy and collapse propagates from a stable state to an unstable state until total failure occurs (Szyniszewski 2009). This same conclusion was reached in a later study that employed the same constant critical strain approach (Szyniszewski et al. 2012). The authors used typical stress-strain relationships and a value of critical equivalent plastic strain of 0.2. In addition, the Szyniszewski (2010) used the same constant critical strain approach to study the effect of random imperfections on progressive collapse.

Sadek et al. (2010) conducted an experimental and computational study to investigate the behavior of steel moment connections under scenarios in which a column is removed due to an extreme event. A series of sub-assemblages were tested by applying vertical axial compression to a column that lacked support at its bottom end and that was connected on either side to girders using either welded unreinforced flange-bolted web (WUF-B) or reduced beam section (RBS) moment connections. The girders were also connected to supporting columns at their far ends by using the WUF-B and RBS connection, respectively. The testing continued until fracture occurred at the connection ends and significant load-carrying capacity of the connections was

lost. Sadek et al. (2010) then performed a computational study of the experimental results. In their simulations, they used a piecewise linear plasticity model with constant equivalent plastic strain to failure for continuum, shell, and beam elements. These elements were deleted upon reaching the failure strain simulating fracture. Dependent on the material type, type of element formulation, and mesh density (Sadek et al. 2010). For this reason, Sadek et al. (2010) accounted for these dependences by performing iterative finite element analyses of the material tensile coupon tests and adjusting the failure strain until quantitative agreement of the measured and calculated engineering stress-strain behavior in the softening region was reached. Due to the mesh dependency of the approach, Sadek et al. (2010) used the same mesh density in the calibration and sub-assemblage finite element simulations. It was also concluded that coarser meshes require the use of smaller values of the failure strain to achieve consistent results. The calibrated failure strains were validated through simulation of the material tensile coupon testing. This approach was also employed for modeling fracture of high strength bolts by calibrating to a double shear test. This is the only case found in the literature of using the critical strain approach to model shear loading induced fracture.

The constant critical strain approach to model finite element deletion in progressive collapse studies of steel structures was also employed by several researchers (Alashker et al. 2010; Alashker et al. 2011; Li et al. 2011; Li et al. 2012; Jamshidi et al. 2013; Li et al. 2013). In some of this prior research, the value of the critical strain at fracture is based upon steel tensile coupon experimental results. In these prior studies, element deletion typically occurs suddenly when the critical strain values are reached.

2.2 Gurson Model

An alternative approach to modeling fracture in collapse of steel structures was used by Khandelwal et al. (2007) through employing a Gurson Model (Gurson 1975) to simulate softening leading to finite element deletion. The Gurson Model is a porous plasticity model that defines the inelastic flow of the porous metal on the basis of a potential function that characterizes the porosity in terms of a single state variable, the relative density (Gurson 1975; ABAQUS 2011). The advantage of the Gurson Model over the constant critical strain approach is that it captures the variation of fracture strain in the high triaxiality region by accounting for micro-void nucleation, growth and coalescence. In addition, Gurson Model allows for stress and stiffness softening and finite element deletion which alleviates the dynamic instability that is prevalent with the constant critical strain approach. The disadvantage of the Gurson Model is the difficulty calibrating the nonphysical parameters of the model. The calibration and validation of the parameters of the Gurson Model were outlined in Khandelwal et al. (2007). The calibrated parameters varied with element size to reduce computational cost. The authors modified the nucleation strain to accommodate larger element sizes used in subassemblage simulations. In addition, the Gurson model was used in conjunction with shell elements that cannot capture triaxial effects.

2.3 Summary

Several studies have been performed on collapse of steel structures using the constant critical strain approach, in which element deletion generally occurs when a critical value of equivalent plastic strain is reached at any integration point of an element. Preliminary studies have shown

that an alternative approach that includes material softening leading to finite element deletion has the potential to yield better results (Bao et al. 2004; Wierzbicki et al. 2005; Khandelwal et al. 2009; Sadek et al. 2010). The approach should be firmly grounded in micromechanical fracture models that can account for different state of stress and strain, coupled with stress softening to delete a finite element.

3 Triaxiality and Fracture Initiation

3.1 Introduction

Stress triaxiality, referred to as triaxiality hereafter, is addressed in relation to the existence of tensile stress in the directions other than the primary stress direction. Triaxiality of a differential element of material may be viewed as a measure of the constraint surrounding the element, thus influencing the ability of the material to exhibit plastic flow (Schafer et al. 2000). It represents a ratio of the state of stress that the material experiences at a certain location and time to the stress that contributes to yielding (Ojdrovic et al. 2004). Triaxiality is defined as a ratio of mean stress to equivalent stress. It is given by the equation:

$$T = \frac{\sigma_m}{\bar{\sigma}} = \frac{(\sigma_1 + \sigma_2 + \sigma_3)/3}{\sqrt{1/2[(\sigma_1 - \sigma_2)^2 + (\sigma_2 - \sigma_3)^2 + (\sigma_3 - \sigma_1)^2]}} \tag{3.1}$$

where σ_m and $\bar{\sigma}$ are mean stress and equivalent stress, respectively. The variables σ_1, σ_2, and σ_3 represent the three principal stresses. Here, the equivalent stress is taken as the von Mises stress, related directly to maximum distortional strain energy. Von Mises stress thus predicts yielding solely based on the shear distortion of the material and is independent of hydrostatic stress under which the material expands or shrinks with no angular distortion.

The triaxiality may be visualized in principal stress space as the slope of the stress vector relative to the pi-plane (Smith, C. M. 2013). According to Equation (3.1), the hydrostatic stress triaxiality is infinite since the equivalent stress equals 0. This means that if the material is subjected to hydrostatic stress, it is assumed to be completely prevented from having plastic

flow. This is a key concept for the proposed work related to fracture mechanics for ductile metals. In addition, triaxiality is negative under compression and positive under tension. Hence, a positive triaxiality causes voids present in a ductile material to grow, while a negative triaxiality causes voids in a ductile material to shrink (Arndt et al. 1997). Triaxiality depends on the difference between principal stresses and represents the material's constraint to plastic flow.

3.2 Triaxiality in Fracture of Ductile Metals

Triaxiality has been shown to be an important component contributing to fracture in ductile metals (Wierzbicki et al. 2005). While plasticity models often treat yielding of ductile metals independently of hydrostatic stress, fracture initiation is often seen to be dependent on hydrostatic stress (McClintock, F. A. 1968; Rice et al. 1969; Atkins 1996; Bao et al. 2005). The concept of ductile fracture is based on micro-void nucleation (Schluter et al. 1996), growth (McClintock, F. A. 1968; Rice et al. 1969; Kanvinde et al. 2004; Bao et al. 2005), and coalescence (Geltmacher et al. 1996), which are all based on triaxiality. In addition, studies have shown that ductile fracture in metals is path dependent (Bao et al. 2005; Wierzbicki et al. 2005; Smith, C. M. 2013). As such, a level of triaxiality must be assumed implicitly if not explicitly.

3.2.1 Nucleation

There are several criteria put forward to describe the process of void nucleation, including critical stress and critical strain (Arndt et al. 1997). The underlying concept of these criteria is that once a critical stress is exceeded at the interface of an inclusion, debonding of the particle occurs, and if the stress is exceeded at the center of the inclusion, cracking of the particle

occurs, causing void nucleation. In addition, for structural steel, void nucleation has been shown experimentally to occur immediately after plastification (Arndt et al. 1997). Structural metals that experience plastic flow are thus considered to have voids nucleated at inclusions; therefore, in finite element analysis, it is commonly assumed that voids nucleate at an equivalent plastic strain of 0 (Argon et al. 1975). This is a reasonable assumption even though voids nucleate throughout the loading process (Le Roy et al. 1981; Thomason 1985).

3.2.2 Void Growth

Void growth starts when a void nucleation strain is achieved and ends when a void coalescence strain is achieved. Cylindrical and spherical void growth models were first proposed by McClintock, F. A. (1968) and Rice et al. (1969), respectively. The fundamental conclusion that they arrived at is that void growth in ductile metals depends exponentially on triaxiality. It was later confirmed analytically and experimentally that crack formation is governed mainly by triaxiality and equivalent strain (Arndt et al. 1997; Bao 2005). Depending on the level of triaxiality, the voids could grow symmetrically in high triaxiality regions and elongated in low triaxiality regions (Smith, C. M. 2013). It has been reported that material typically does not lose strength during this period of void growth, likely due to material hardening, and that upon reaching a critical void size, it does not cause immediate strength degradation but instead causes material softening (Kuwamura et al. 1997).

3.2.3 Coalescence

When voids in a ductile material grow to a critical size, it has been shown that void coalescence occurs (Thomason 1985). Strain localization in the inter-void ligament immediately precedes

void coalescence, which leads to a net-section based softening of the material (Smith, C. M. 2013). This stage represents the initiation of a macrocrack. As this softening occurs with small volume of the material, the available elastic strain energy is sufficient to quickly drive coalescence (Smith, C. M. 2013). As voids continue to coalesce, the crack propagates. The higher the stress triaxiality the lower is the void volume at fracture initiation (Arndt et al. 1997). As triaxiality increases, it causes an increase in the tensile and shear stresses between two smaller voids, causing them to merge into a larger singular one. Both tensile and shear stresses promote the coalescence of voids by either an increasing nucleation of secondary voids, by a higher local void growth rate, or by the shear fracture of the ligament between both voids (Arndt et al. 1997).

3.2.4 General Effect of Triaxiality on Ductile Fracture

Through the definition of triaxiality seen in Equation (3.1, triaxiality is zero when the material is in a state of pure shear. For uniaxial loading in a tensile coupon, triaxiality is approximately 0.33; for biaxial tension this value is 0.67; for notched bars, this value can vary from approximately 0.33 to 1.59 (Schafer et al. 2000). Negative triaxiality can be achieved either in upsetting, or compression, tests or by applying hydrostatic pressure to a notched specimen. Upsetting tests consist of cylinders subjected to compressive force. In the upsetting tests, the crack will occur in the equatorial region or the centerline of the cylinder on the outer surface of the specimens and not at the center of the specimen, as it does with tensile coupons. In addition, it was shown experimentally and analytically that fracture cannot occur below triaxiality of –1/3 (Bao et al. 2005).

It should also be noted that effects of specimen size result from material inhomogeneity. However, since structural steel is fairly homogeneous, the calibration of ductile fracture models for steel should be valid for a wide range of full-scale structures (Bao 2005).

Different fracture mechanisms are active at different triaxiality ranges in ductile metals and the transition zone between them is not clearly defined or understood (Bao et al. 2005). The first mechanism, described above, is ductile fracture based on micro-void nucleation, growth, and coalescence mechanism and is the fundamental cause of void based fractures, which occur for a range of high triaxiality. The second mechanism causes a fracture surface that is relatively flat, where no clear voids are observed, occurring in negative and low positive triaxiality ranges (Hooputra et al. 2004; Bao et al. 2005). This mechanism is less well understood and is referred to as shear fracture. Figure 3.1 shows how shear and ductile fracture mechanisms affect the equivalent fracture strain as a function of triaxiality. The behavior of shear fracture in a positive triaxiality range has been shown to be metal type dependent (Bao et al. 2005). Triaxiality range from 0 to about 0.4 is referred to as transition zone from shear to ductile fracture. It has been reported that some aluminum (Al2024-T351) and steel (AISI 4340) materials have an increasing equivalent plastic strain to fracture with an increase in triaxiality in the transition zone, which is shown by the second shear fracture curve in Figure 3.1 while materials like copper (OFHC) and other aluminums (1100-0) have a decreasing equivalent plastic strain to fracture with increase in triaxiality in this region, shown by the first shear fracture curve (Bao et al. 2005). The fracture in the transition zone may see fracture develop as a combination of shear fracture and ductile fracture mechanisms. Most likely, some combination of fracture occurs in which it initiates due

to void nucleation and growth, and changing then to shear fracture mechanism (Bao et al. 2004).

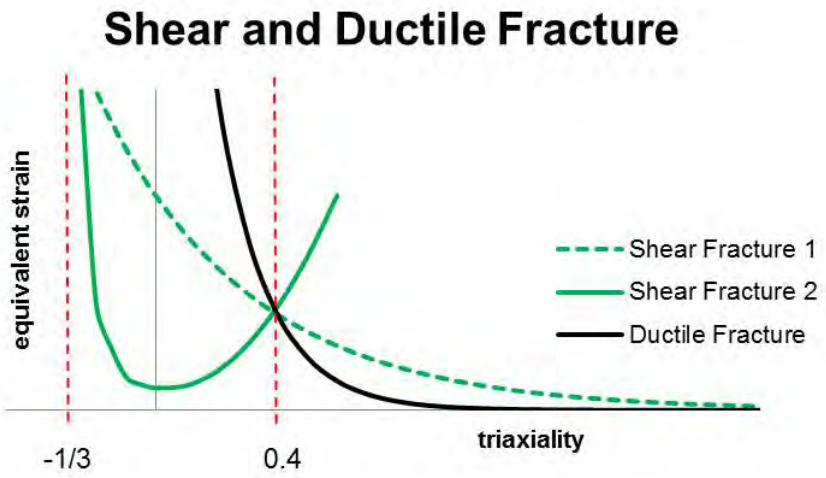

Figure 3.1: General curves for shear and ductile fracture mechanisms (Bao et al. 2005)

3.3 Other Parameters that Influence Ductile Fracture

Several studies have found that the void growth approach based on triaxiality does not accurately predict fracture strain at low values of stress triaxiality (Koplik et al. 1988; Barsoum et al. 2007). It has been shown that that the Lode angle variable that is the normalized third invariant of the deviatoric stress tensor has a distinct influence on fracture strain (Kofiani et al. 2013). Lode angle is defined as the angle within a deviatoric plane (a plane orthogonal to the hydrostatic axis) between a deviatoric principal stress axis and the stress vector (Smith, C. M. 2013). Using the deviatoric stress tensor (J_2 and J_3) the Lode angle may be calculated directly according to the following equation:

$$\cos(3\theta) = \frac{3\sqrt{3}J_3}{2J_2^{3/2}} \tag{3.2}$$

Lode angle is important in differentiating between the axisymmetric and plane strain stress state conditions. For structural steel A572 Grade 50, it has been shown that the fracture strain for plane strain condition is approximately 50% greater than for an axisymmetric stress state (Smith, C. M. 2013). Smith, C. M. (2013) later concluded that structural steel material in high triaxiality region for an axisymmetric stress state will have lower fracture ductility than under plane strain conditions. This relationship is opposite to what others have found for other metals (Bao et al. 2004; Bai et al. 2008; Coppola et al. 2009). This strongly suggests that the Lode angle effect should be studied and calibrated for each metal individually and cannot be generalized.

It was shown experimentally that the Lode angle's influence on ductile fracture initiation becomes weak in the high range of triaxiality (Hancock et al. 1983; Bai et al. 2008). This was shown true for some metals like DH36 steel, which had almost identical fracture strain at high triaxiality for different Lode angles. In addition, the Lode angle changes throughout loading, which affects the calibration of the fracture loci especially for ductile metals, causing significant differences between calibration process that utilized initial triaxiality of the specimen with the one that utilized the average triaxiality of the specimen throughout loading (Bai et al. 2009).

The Lode angle is an important parameter for fracture prediction, especially under low values of triaxiality. However, there is currently a significant disadvantage to including Lode angle as a parameter in one's fracture initiation model. This is due to the fact that so far no conclusive

experimental results show the shape of the Lode angle dependence function because insufficient tests have been conducted to test the material under a constant hydrostatic pressure (Xue et al. 2008). In addition, one cannot assume a uniform effect of the Lode angle on fracture strain with different triaxiality (Bai et al. 2008). Researchers have found both positive (Bai et al. 2008) and negative (Coppola et al. 2009) effects of the Lode angle on ductility and have modeled the transition between the axisymmetric and plane strain condition as quadratic (Bao et al. 2004), cubic (Bai et al. 2008), and elliptical (Coppola et al. 2009). There is a lack of consensus on the functional form of the Lode angle, or even its underlying mechanism and the magnitude of the influence (Smith, C. M. 2013).

In collapse modeling of steel structures the models used for fracture initiation should be accurate and robust enough to capture the global behavior and easy to use and understand to find wide acceptance amongst structural engineers. Since the effect of the Lode angle on ductile fracture is not well understood and there is a serious lack of experimental tests to accurately determine its effect, the fracture initiation model to be used in finite element elimination strategy in collapse modeling of steel structures currently should not include the Lode angle as a parameter.

4 Fracture Models and Element Deletion

4.1 Fracture Models for use in Collapse Modeling of Steel Structures

Fracture in steel structures has gained growing attention after the 1994 Northridge earthquake and the 1995 Hyogoken-Nanbu earthquake in Kobe (Kuwamura 2003). More than 100 moment frames in Kobe and its surrounding areas were reported to sustain severe cracks or ductile fractures at beam-to-column connections, and approximately 30 buildings partially or totally collapsed (Kuwamura et al. 1997). It was found that fracture initiated primarily in the heat affected zone (HAZ) of the welded connections and propagated in the base metal (Kuwamura et al. 2003). On the other hand, fracture initiation was observed in the fusion zones of the deposited metals of moment resisting connections in the Northridge earthquake and was primarily due to the low notch toughness of the weld metal (Lu et al. 2000; Kuwamura et al. 2003). This was also shown in large-scale testing (Kuwamura et al. 1997). The Northridge fractures were referred to as brittle fractures, but (Schafer et al. 2000; Kuwamura et al. 2003) indicate that these were triggered by ductile fracture initiation after undergoing significant plastic strain. However, ductile fracture initiation was not reported to precede brittle cleavage fracture in some cases (Kaufmann et al. 1995).

Fracture initiation in T-stub connections as a function of triaxiality was studied by Ojdrovic et al. (2004) as a representation of a beam flange welded to a column flange of a welded moment connection. This work showed that as the load increased, the triaxiality was slightly relieved through the thickness of the flange, except at the bottom of the weld, where triaxiality was the

largest and continued to increase. They concluded that fracture initiation occurred at locations of highest triaxiality and maximum principal stress, and that higher stress triaxiality allows a higher maximum principal stress to be sustained prior to fracture. However, a moment connection would see significantly higher stresses than a small-scale tension test and thus will likely yield fractures due to the high triaxiality demands.

According to Schafer et al. (2000), welded steel moment frame connections undergo a complex multi-axial state of stress that leads to high levels of stress triaxiality. Triaxiality has been discussed in the literature as a probable cause of the poor performance of moment connections (Blodgett 1995; Yang et al. 1995; SAC Joint Venture 1996). Some of the benefits of using micromechanical fracture models based on triaxiality in the study of fracture in steel structures over traditional linear elastic fracture mechanics is that they are able to account for issues such as strength mismatch at the interfaces of welds and parent material that causes stress concentrations (Schafer et al. 2000).

Traditional linear elastic-plastic crack-tip fracture mechanics has been used successfully to improve structural steel component design to delay the onset of brittle fracture (Smith, C. M. 2013). The use of the J-integral and the stress intensity factor K_{IC}, can accurately predict fracture initiation at initial flaws with high triaxiality, but they rely on an assumed correspondence between far-field stresses and strains and the condition at the crack tip (Anderson 2005). Through these methods, structural steel connections were improved by becoming more ductile and increasing the strain capacity. However, the large scale plasticity of improved steel connections accompanying fracture violates the assumptions of traditional

fracture mechanics. On the other hand, local micromechanical fracture models overcome these limitations because they are applied directly to continuum element, small volume, experiencing a certain stress and strain state. Hence, there is no need to make the far-field stress and strain assumptions with local micromechanical fracture models. The success of these micromechanical fracture models has been demonstrated under many different stress and strain conditions. For this study, micromechanical fracture initiation models are used in concert with a finite element deletion for collapse modeling of steel structures. However, the constant critical strain approach is still the method of choice to model fracture of structural steel components.

The constant critical strain approach for element deletion is based on a critical equivalent plastic strain being reached. The equivalent plastic strain at the point of fracture initiation at the critical location in tensile specimens is taken as a measure of ductility, but it is dependent on the state of stress, which is related to the shape of specimen, and varies for different geometries, making it potentially too restrictive to serve as a sole fracture initiation criterion (Bao 2005). In addition, it was observed that for the same material, different uniaxially-loaded specimens gave different strains values at failure based on the amount of confinement the specimen provided at the critical location (Clausing 1970). This was confirmed by (Mirza et al. 1996), who reported that equivalent plastic strain at fracture initiation is strongly dependent on the level of triaxiality, even though the dependence varied for different materials. It has also been observed that strain is not constant across the cross-section at material locations where fracture occurs, and large differences in triaxiality and equivalent plastic strain at fracture were found between solutions that considered Constant Strain and those that did not (Alves et al.

1999). Therefore, the constant critical strain approach has limitations especially in complex fracture development in steel structures during collapse. Different micromechanical fracture initiation models have thus been investigated that are based on the history of triaxiality during loading for collapse modeling of steel structures. (Wierzbicki et al. 2005) describes seven fracture initiation models, including their calibration procedures. Additional summaries of different fracture models may be found in (Atkins 1997) and (McClintock, F. 2003). After conducting a review of available fracture initiation models, it was decided to use the Void Growth Model (VGM) developed by Rice et al. (1969) in higher triaxiality regions and the hybrid of VGM and Bao-Wierzbicki Model (VGM-BW) to account for lower and negative triaxiality region. The softening and finite element deletion is modeled through the use of Hillerborg Model which is implemented in the VGM and VGM-BW models (Hillerborg et al. 1976). These models are accurate and robust enough for collapse modeling of steel structures and simple enough to utilize.

4.1.1 Void Growth Model

The VGM was developed by (Rice et al. 1969) for high triaxiality regions. The model is based on the ductile fracture assumptions: void nucleation, growth, and coalescence described above. Rice and Tracey analyzed the growth of spherical void with radius R_v in a rigid-plastic continuum with no strain hardening. It was concluded that equivalent plastic strain to fracture was an exponential function of triaxiality. A triaxiality of greater than 3 would cause the voids to grow in the oblate shape while triaxiality of less than 1 would cause the voids to grow asymmetrically. To account for hardening behavior (D'Escatha et al. 1979) replaced the yield

stress by effective von Mises stress which gave the following equation for the growth of a spherical void in a plastic continuum with strain hardening:

$$\frac{dR_v}{R_v} = 0.283e^{1.5T}d\bar{\varepsilon}^{pl} \tag{4.1}$$

where:

- T – triaxiality
- $\bar{\varepsilon}^{pl}$ – equivalent plastic strain
- $d\bar{\varepsilon}^{pl}$ – incremental form of equivalent plastic strain

Rice et al. (1969) noted that the axial elongation of a void is independent of the average volume expansion leading to the approximation that the failure state can be quantified effectively using the void volume fracture. To find the total void growth during a plastic loading excursion, Equation (**4.1**) is integrated, leading to the VGM criterion given by

$$\int_0^{\bar{\varepsilon}_f^{pl}} \frac{d\bar{\varepsilon}^{pl}}{\eta e^{-\beta T}} = 1 \tag{4.2}$$

The equivalent plastic strain at fracture initiation is given by

$$\bar{\varepsilon}_{FI}^{pl}(T) = \eta e^{-\beta T} \tag{4.3}$$

where:

- $\bar{\varepsilon}_{FI}^{pl}(T)$– critical equivalent plastic strain at fracture initiation
- β – material property constant
- η – material capacity constant
- $\bar{\varepsilon}^{pl} = \int_0^t \sqrt{\frac{2}{3}\,\dot{\varepsilon}^{pl}:\dot{\varepsilon}^{pl}}\,dt$

Despite many different suggestions to improve the VGM criteria such as the one by (Huang 1991) with improved results, the exponential Equation (4.3) remained the standard basis for most modern fracture models (Smith, Chris M. et al. 2013). The reason for this is that it is very accurate in high-triaxiality regions. However, it is not applicable for lower triaxiality regions.

4.1.2 Bao-Wierzbicki Fracture Model

To account for lower triaxiality regions, parts of the Bao-Wierzbicki criterion (Bao et al. 2004) will be utilized in this work. Bao et al. (2004) proposed a piecewise fracture initiation (B-W) model that accounts for a complete range of triaxiality. The main contribution is a general methodology for constructing the fracture locus for any ductile material (Bao et al. 2004). After performing experimental tests and numerical simulations, the equivalent strain to fracture versus triaxiality was plotted. The fracture initiation point was determined by a significant load drop in the force-displacement responses for tensile and shear tests and by observance of fracture on the surface of the equatorial area of the upsetting tests. Since triaxiality was not constant throughout deformation, an average triaxiality was used to define the value of equivalent plastic strain to fracture. It was shown that there are three distinct branches in this relationship with possible slope discontinuities in the transition regions. For the negative triaxiality region, fracture was governed by a shear mode of failure; for the large positive triaxiality region, fracture was governed by void growth; and a combination of shear and void growth governed the lower positive triaxiality region (Bao et al. 2004).

The full criterion is given by Equation (4.4 (Bao et al. 2004). It accounts for a fracture cut-off at a triaxiality of -1/3. The B-W model is designed to capture separate fracture mechanisms of void

growth in the higher triaxiality regions and shear fracture in the negative triaxiality region. This is done by having piecewise relationship between the equivalent plastic strain and triaxiality, reflecting the fracture mechanism active at the specific triaxiality ranges. However, the most significant benefit of B-W model is that its parameters can be calibrated from basic material test data.

$$\bar{\varepsilon}_{FI}^{pl}(T) = \begin{bmatrix} \infty \\ C_1/(1+3T) \\ C_1 + (C_2 - C_1)(T/T_o)^2 \\ C_2\,T/T_o \end{bmatrix} \begin{matrix} T \le -1/3 \\ -1/3 < T \le 0 \\ 0 < T \le T_o \\ T_o \le T \end{matrix} \tag{4.4}$$

where:

- $C_1 - \bar{\varepsilon}_{FI}^{pl}$ at $T = 0$
- $C_2 - \bar{\varepsilon}_{\mathrm{FI}}^{\mathrm{pl}}$ at $T_o = 1/3$

$C_1 = C_2(\frac{\sqrt{3}}{2})^{1/m}$ where m is the hardening exponent of a power law for isotropic strain hardening $\sigma = K_p\varepsilon^m$. C_2 may be calculated from the reduction of area A_R of a uniaxial, axisymmetric tensile specimen by $C_2 = -ln(1 - A_R)$, which is also designated as the ductility of the material.

The Bao-Wierzbicki criterion is a compromise between accuracy and practicality. To improve this criterion, it will be combined with the VGM criterion at higher triaxiality regions, giving the following equivalent plastic strain for fracture initiation:

$$\bar{\varepsilon}_{FI}^{pl}(T) = \begin{bmatrix} \infty \\ C_1/(1+3T) \\ C_1 + (C_2 - C_1)(T/T_o)^2 \\ \eta e^{-\beta T} \end{bmatrix} \begin{matrix} T \le -1/3 \\ -1/3 < T \le 0 \\ 0 < T \le T_o \\ T_o \le T \end{matrix} \tag{4.5}$$

This criterion completely covers all triaxiality ranges and in this work is used in the ABAQUS/Explicit finite element software (ABAQUS 2011) to model fracture initiation in finite element deletion.

4.2 Implementation of Fracture Initiation and Damage Models in Finite Element Software

Plastic irreversible damage is often accumulated in arbitrary loading paths of steel material; therefore, plastic deformation history should be accounted for in determining fracture initiation (Xue et al. 2008; Yu et al. 2010). In addition, throughout a loading regime, triaxiality is not constant at a critical location. Therefore, to account for fracture initiation with more consistent accuracy, both equivalent plastic strain and triaxiality should be accounted. In this research, the Void Growth Model (VGM), Bao-Wierzbicki and a damage model, referred to as the Hillerborg Model hereafter, all implemented in the ABAQUS/Explicit finite element software (ABAQUS 2011), are used to account for fracture initiation in a finite element and the subsequent deletion of the element after material softening. This approach is used in conjunction with a von Mises yield surface with associated plastic flow and isotropic hardening behavior. An updated Lagrangian geometrical nonlinear element formulation that includes large strains is also used (ABAQUS 2011). Elements are formulated in the current configuration using current nodal positions. Elastic unloading is assumed. The fracture initiation is governed by Equation (4.6), derived from an original equation by (Rice et al. 1969).

$$\int \frac{d\bar{\varepsilon}^{pl}}{\bar{\varepsilon}_{FI}^{pl}(T)} = 1 \tag{4.6}$$

where:

- $\bar{\varepsilon}_{\mathrm{FI}}^{\mathrm{pl}}(\mathrm{T})$ – critical equivalent plastic strain at fracture initiation given by Equation (4.5

A fundamental assumption of this equation is that the critical equivalent plastic strain is a function of stress triaxiality based on ductile fracture mechanisms explained in the previous Section 3.2. The criteria for fracture initiation is met when the integral of the ratio of the equivalent plastic strain to the critical equivalent plastic strain as a function of triaxiality equals 1 at an integration point of the finite element (Hooputra et al. 2004). For calibration and validation, triaxiality as defined in Equation (3.1, equivalent plastic strain, and other stress-strain related properties are calculated at the integration points of the finite element.

4.2.1 Softening and Element Deletion

The value of the integral in Equation (4.6) increases at each time increment of an analysis as a function of increasing plastic deformation. Upon reaching 1, the fracture initiation criteria is met, which allows for softening to take place (ABAQUS 2011). Void coalescence in a finite element is then represented by softening of an element. Softening of the element is modeled through the Hillerborg Model (Hillerborg et al. 1976). The damage manifests itself through softening of the yield surface and degradation of elasticity modeled by Equation (4.7) and Equation (4.8), respectively. During softening, spatial mesh dependency is introduced based on strain localization, which causes dissipated energy to decrease as the mesh is refined (Hillerborg

et al. 1976; Ehlers 2010; ABAQUS 2011). A stress-displacement relationship has thus been proposed in the literature to mitigate localization (Hillerborg et al. 1976). This is achieved through defining a material parameter that describes the energy required to open a unit area of crack, G_f. The fracture energy is then given by Equation (4.9).

$$\bar{\sigma}_S = (1 - D) * \bar{\sigma}_{NS} \tag{4.7}$$

$$E_s = (1 - D) * E \tag{4.8}$$

$$G_f = \int_{\bar{\varepsilon}_0^{pl}}^{\bar{\varepsilon}_f^{pl}} L\, \bar{\sigma}_y d\bar{\varepsilon}^{pl} = \int_0^{\bar{u}_f^{pl}} \bar{\sigma}_y d\bar{u}^{pl} \tag{4.9}$$

where:

- $\bar{\sigma}_S$ – equivalent stress with softening accounted for
- $\bar{\sigma}_{NS}$ – equivalent stress with no softening being modeled
- D– damage variable
- E_s – elastic modulus modified to account for softening
- E – elastic modulus
- G_f – fracture energy
- $\bar{\varepsilon}_{FI}^{pl}$ – equivalent plastic strain at fracture initiation
- $\bar{\varepsilon}_f^{pl}$, $\bar{u}_f^{pl}$ – equivalent plastic strain, displacement at element deletion, respectively
- L – characteristic length
- σ_y – yield stress

The characteristic length, *L*, depends on the element geometry and formulation (ABAQUS 2011). The equivalent plastic displacement is a fracture work conjugate to the yield stress after the onset of softening. Before fracture initiation, $\bar{u}^{pl}$ equals 0, and after fracture initiation $\bar{u}^{pl} = \int L d\bar{\varepsilon}^{pl}$. The relationship between the equivalent plastic displacement and the damage parameter, *D,* was chosen to be linear in this work after performing numerous simulations and

comparing the softening behavior of the simulations to the behavior seen in corresponding experiments. The damage variable, *D*, is defined by Equation (4.10). The critical equivalent plastic displacement at which *D* equals 1 has to be provided. In this work, when this value is reached at an integration point of an element, the element is deleted. By allowing for monotonically decreasing stress and stiffness during softening, this approach, in addition to mitigating spatial mesh dependency, allows for minimizing spurious transient effects of dynamic instabilities upon element deletion that may cause inaccuracy of the results. This is due to the fact that element stiffness and stress are brought to zero through a linear relationship defined by Equations (4.7), (4.8), and (4.10) thus avoiding abrupt changes in element stiffness and stress and the resulting transient dynamic response.

$$D = \frac{\bar{u}^{pl}}{\bar{u}_f^{pl}} \tag{4.10}$$

Figure 4.1 shows the Hillerborg model, where the damage parameter, *D*, equals 0 at fracture initiation and it increases monotonically to 1 through Equation (4.10) when the element is finally deleted. The $\bar{\sigma}_{FI}$ and $\bar{\varepsilon}_{FI}^{pl}$ variables are the equivalent stress and equivalent plastic strain at fracture initiation. The $\bar{\sigma}_{NS}$ is the equivalent stress with no softening being modeled, and $\bar{\varepsilon}_f^{pl}$ is the equivalent plastic strain at failure.

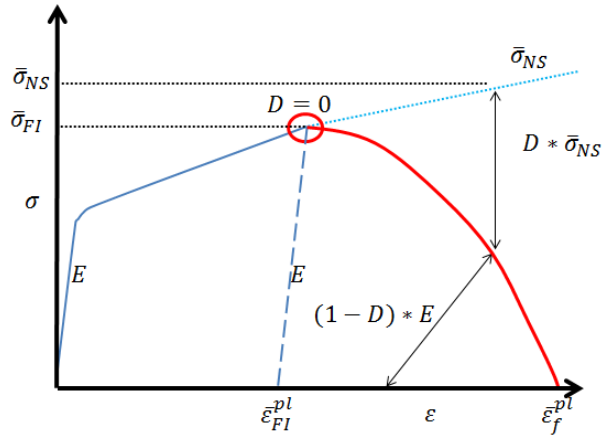

Figure 4.1: Hillerborg model relation of equivalent stress versus equivalent strain at an integration point of an element (ABAQUS 2011)

5 Calibration of Element Deletion Strategy

The chapter summarizes the calibration strategies for element deletion for collapse modeling of steel structures.

5.1 General Considerations for Calibration

The current micromechanical models for fracture initiation, including the VGM and B-W models, and for softening, including the Hillerborg Model, are local fracture models and are dependent on the current stress and strain tensors and the stress and strain histories. As discussed in Chapter 4, the VGM model describes the exponential relationship between equivalent plastic strain at fracture initiation for a high triaxiality range. It has two parameters, η and β, that determine this relationship. The variable η describes mathematically the critical equivalent plastic strain at zero triaxiality, a state of pure shear, which also represents the value of y-intercept when plotting triaxiality (abscissa) versus equivalent plastic strain (ordinate). This parameter could be viewed as the material's fracture capacity (Kanvinde et al. 2004). The parameter β describes the behavior or the relationship of critical equivalent plastic strain to triaxiality. Together these parameters are sufficient to describe the fracture initiation strain as a function of triaxiality at higher triaxiality range (Smith, C. M. 2013). However, this model potentially overestimates the critical strain in lower and negative triaxiality ranges (Myers et al. 2009). To account for lower and negative triaxiality range, the Bao-Wierzbicki Model is used, as discussed in Chapter 4. This model has two parameters, C_1 and C_2, that can be determined from another variable, m, that needs to be calibrated. The

variable C_2 represents the ductility of the material, or the critical equivalent plastic strain at fracture initiation of a tensile coupon specimen, which has a triaxiality of approximately 1/3. This parameter could be determined from Equation (4.4), presented earlier, or from experimental data directly. In the original calibration by (Lee et al. 2004), the triaxiality was treated as an average value over the deformation history and specimen thickness, and in particular the value of triaxiality for C_2 was calibrated at a value greater than 1/3. However, in this study a value of 1/3 is used as an approximation of the triaxiality at the center of the uniaxial tensile specimen (Yu et al. 2010). The variable C_1 represents the critical equivalent plastic strain at fracture initiation for a state of pure shear, i.e., zero triaxiality. This may be determined from shear experimental test setups, yet these tests are not available for structural steels used today in construction. To overcome this limitation, Equation (4.4 is used to determine the value of C_1, which is based on the hypothesis of a maximum shear stress fracture condition from a calibrated parameter *m* described below (Yu et al. 2010). However, Equation (4.4) is based on average triaxiality values, even though triaxiality varied significantly throughout the original experiments. Figure 5.1 shows the location of all the VGM and Bao-Wierzbicki model parameters in a plot of triaxiality versus equivalent plastic strain and Figure 5.2 shows the fracture locus of the combined VGM and Bao-Wierzbicki models.

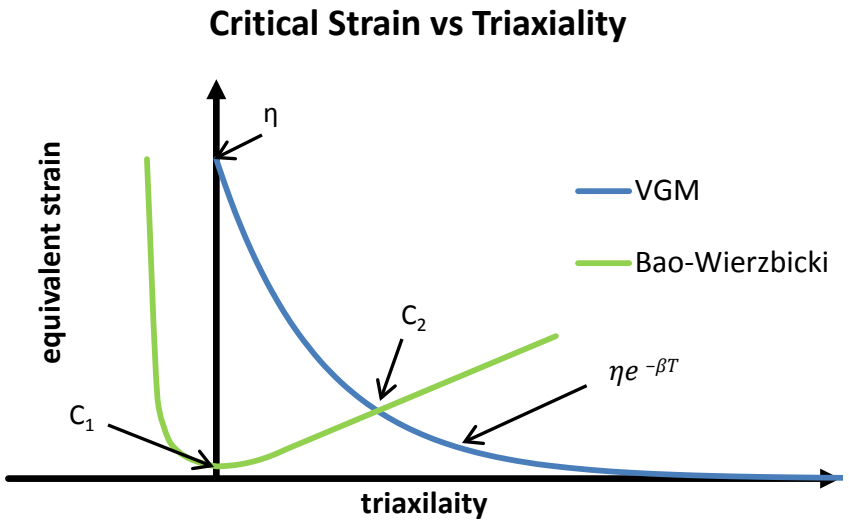

Figure 5.1: Location of the VGM and Bao-Wierzbicki Model parameters on the fracture locus

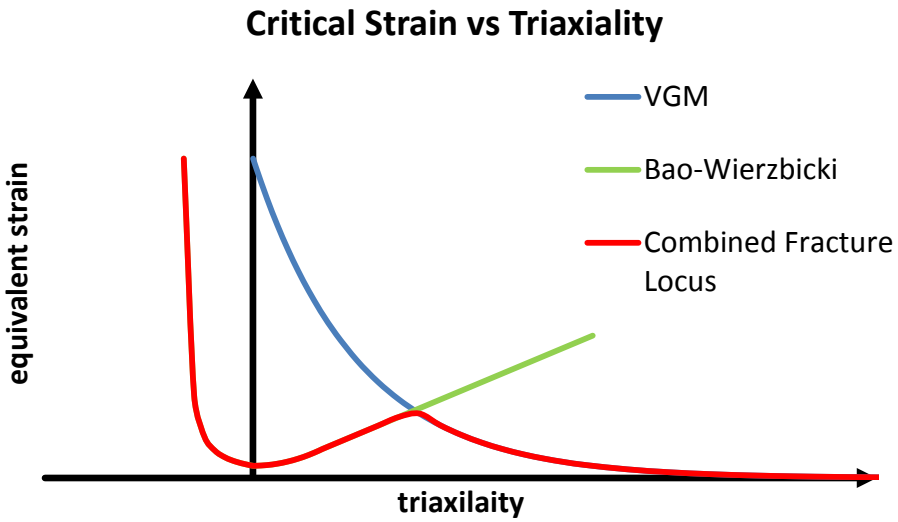

Figure 5.2: Fracture locus of combined VGM and B-W fracture models

Material softening is modeled through the use of Hillerborg Model which characterizes softening as progressive degradation of material's stress and stiffness (ABAQUS 2011), as discussed in Chapter 4. For this model, the equivalent plastic displacement variable, $\bar{u}_f^{pl}$, which determines the value of equivalent plastic displacement at element deletion and is the primary parameter to be calibrated, could be viewed as signifying the average distance between voids

in the real material. It has been shown in previous studies that once voids in the material reach a certain size or the distance between the voids is such that void instability and coalescence occurs, the fracture between the voids is governed by elastic energy (ABAQUS 2011; Smith, C. M. 2013). However, the value of, $\bar{u}_f^{pl}$, which could be looked as the characteristic length of the material, is difficult to determine experimentally (Kanvinde et al. 2004). This is mainly due to the fact that the fractured surface of a specimen will have void nucleation, growth, and coalescence all at the same time. In addition, it is difficult to measure the distances between all of the visible voids since there are so many of them across the thickness of the specimen (Kanvinde et al. 2004). Through the calibration of these variables, the Bao-Wierzbicki and the VGM models are able to account for the complete range and history of triaxiality in determining fracture initiation, while Hillerborg Model captures the void coalescence through an average representation of voids' characteristic length of the material. This is important since even in a circumferentially notched tensile coupon specimen, triaxiality varies widely from element to element and throughout the loading process.

In this work, a Particle Swarm Optimization (PSO) algorithm is used to calibrate fracture initiation and propagation parameters in a finite element through comparison to force-displacement relationship of test specimens which would account for the above described issues.

5.1.1 Accounting for Local Stress-Strain Variation through Global Parameters

The four parameters, $C_1,\ \eta, \beta$ and $\bar{u}_f^{pl}$, that need to be calibrated are functions of local stress-strain tensors that are determined at element integration points. In the past, to determine the

fracture initiation locus, equivalent plastic strain at fracture initiation versus average values of triaxiality plotted at location of fracture were used (Bao et al. 2004; Wierzbicki et al. 2005; Smith, C. M. 2013). To determine the equivalent plastic strain at fracture initiation, the history of equivalent plastic strain was monitored in a finite element simulation of the experimental test specimen at the location of observed fracture. The value of equivalent plastic strain at the displacement that caused fracture in the experiment was taken as the equivalent plastic strain at fracture initiation. In addition, combining this critical equivalent plastic strain with the average triaxiality of the specimen at the center of the specimen or observed fracture location provided a point on the fracture locus. The fracture locus was completed by using specimens and experimental setups with different average triaxiality values (Bao et al. 2004). This approach has yielded good results but could be improved by directly including the history of triaxiality and properly accounting for stress-strain values of the material during softening. However, this approach requires experimental specimens with different values of triaxiality that remains approximately constant throughout loading. This is currently not available for structural steel metals (Smith, C. M. 2013).

The value of triaxiality at the integration point of an element typically varies significantly from element to element through the thickness of the specimen and throughout the loading process, especially during softening. Using an average value of triaxiality throughout the specimen during the loading process adds inaccuracies to the fracture prediction (Smith, C. M. 2013). This is related to the issue of determining a fracture initiation point from experimental data. Fracture initiation happens at a specific point in the material while other parts of the material do not show signs of fracture at that time (Kanvinde et al. 2004). In addition, the location of

fracture initiation is very hard to determine since most of the time it happens inside the specimen and cannot be observed (Kanvinde et al. 2004). Some have used the value of displacement in an experimental force-displacement curve at which degradation of force begins as a value of fracture initiation (Bao et al. 2004; Kanvinde et al. 2004; Wierzbicki et al. 2005). This usually works well for circumferentially notched tensile coupons, but not for other experimental setups like upsetting tests or shear tests (Bao et al. 2004). This approach is also more subjective, since most of the time there is no exact point on the experimental force-displacement curve that signifies fracture initiation, but rather the transition from force hardening to softening is gradual. Therefore, in order to calibrate the models effectively one has to account for all of the variations in stress and strain tensors throughout the loading. However, this is only possible if experimental test data is available for comparison with simulation results at different triaxiality levels. This is very difficult to attain since experimental test setups that can maintain a constant or semi-constant low or negative triaxiality throughout loading are in development stages and much research is still required (Kofiani et al. 2013; Smith, Chris M. et al. 2013). Therefore, for the low and negative triaxiality range, the Bao-Wierzbicki model provides an analytical method for determining C_1 and C_2 parameters from experimental data of a standard tensile coupon specimen (Bao et al. 2004). This method, described by Equation (4.4), allows for the possibility of determining the fracture locus in the low and negative triaxiality range without actually having experimental results in those triaxiality ranges, through the assumptions discussed above, On the other hand, if experimental data is available in the low triaxiality ranges, then one can perform a rigorous calibration by fitting the force-displacement finite element simulation results to the experimental test results

directly. Hence, if the experimental data is available then there is no need for manually determining the fracture initiation point in the force-displacement curve from the experimental results or monitoring the location of fracture initiation because the fracture initiation and softening models used in the finite element simulation could capture all of this on element-by-element basis. The quality of the fit of the calibration would then be decided by a force-displacement curve from the finite element simulation that matches the experimental force-displacement curve, making this approach to calibration completely automatic and capturing all of the stress and strain tensor variations. In summary, two approaches to calibration exist: (1) if experimental test data is available then one could calibrate the fracture models to the force-displacement experimental curves directly, and (2) if experimental data is not available then one has to make significant assumptions when fracture initiates and calibrate analytically.

5.2 Specimens Selection for Calibration

The experimental test results that are usually available for assessing the ductile fracture toughness of structural steel material are circumferentially notched tensile (CNT) coupon specimens. For welded connections, the most common experimental configuration is a lapped specimen. The triaxiality inside the CNT coupon specimens usually falls in the high triaxiality range (i.e. triaxiality greater than 0.3). This makes the CNTs the preferred test specimens for calibrating fracture micromechanical models like the VGM since highly triaxial stress states are the most susceptible to fracture and represent the majority of conditions within structural engineering where ductile fracture is observed (Smith, C. M. 2013).

The most common experimental setup for studying ductile fracture as a function of triaxiality is to test a circumferentially notched tensile coupon (CNT) specimen as shown in Figure 5.3. CNT specimens are traditionally used to investigate ductile fracture under a high triaxiality axisymmetric stress state (Smith, C. M. 2013). A CNT specimen does not have predefined discrete flaws, such as cracks, which makes them a viable experiment for assessing fracture initiation as a function of triaxiality. In these tests, the triaxiality is varied by changing the radius of the notch. However, the average triaxiality does not vary significantly during loading of the specimen (Smith, C. M. 2013). As the notch radius decreases, the triaxiality of the specimen increases and fracture initiation tends to move closer to the surface of the notch since the maximum triaxiality occurs closer to the surface of the notch (Kuwamura et al. 1997; Schafer et al. 2000). As the notch radius increases, the triaxiality at the notch surface of the specimen decreases and the maximum triaxiality and fracture initiation tend to occur at the center of the specimen (Ojdrovic et al. 2004). The variation of equivalent strain across the notch is not large (Bao 2005). If a notch of zero radius is made, then theoretically the specimen will experience infinite triaxiality and immediate fracture will occur upon loading. This is a fundamental prediction seen in the models proposed by McClintock, F. A. (1968) and Rice et al. (1969). In addition, Inglis (1997) discussed similar concepts when he derived stress concentration effects of flaws on fracture by analyzing elliptical holes in flat plates. For example, Inglis (1997) showed in Equation (5.1 that a zero radius of the notch or hole creates infinite stress concentration:

$$\sigma_A = 2\sigma\sqrt{\frac{a}{\rho}} \tag{5.1}$$

where σ_A is the concentrated stress value at the tip of the hole, σ is the stress applied to the plate boundaries, a is the hole dimension, and ρ is the radius of curvature of the elliptical hole. In addition, it has been shown that the crack initiation strain tends to decrease with the notch sharpness or increase in triaxiality, and that the strain at which maximum stress occurs is independent of triaxiality, which corresponds to metal plasticity being independent of hydrostatic stress (Kuwamura et al. 1997). Other important observations that were made by (Kuwamura et al. 1997) are that the peak value of stress triaxiality decreases with an increase of notch radius, and that triaxiality decreases with elevated strain.

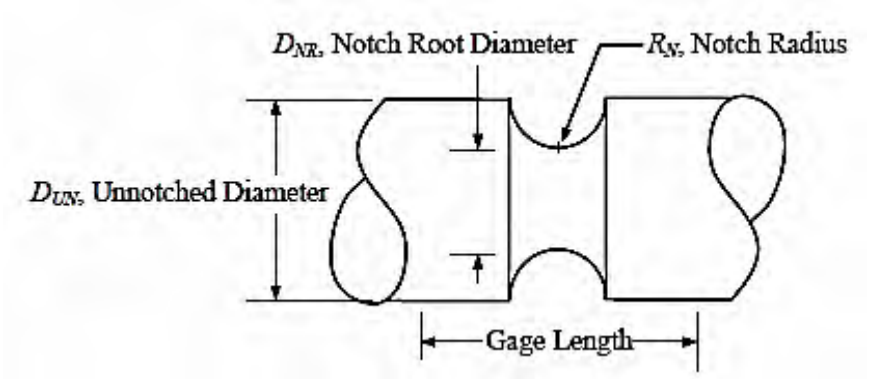

Figure 5.3: Circumferential tensile coupon specimen (Myers et al. 2009)

Another important experimental setup that is used to study fracture initiation is a thin sheet under uniaxial tension (Anderson 2005). Sometimes notches are cut into these sheets. In these experiments, necking occurs before fracture and needs to be considered in the fracture prediction (Bao 2005). It has been observed that a plane strain zone develops at the center region of the gauge section. This zone exhibits high stress and strain and represents the most likely place of fracture to occur (Anderson 2005). In addition, this experimental setup is suitable for specimens extracted from weld material due to the fact that they can account for weld heterogeneous microstructures and irregular shapes by varying the loading direction to the

weldment (Anderson 2005). This experimental setup is suited for testing weldments in metal plates welded directly to each other representing complete or partial penetration groove weld connections or metal plates welded lapped on each other, such as fillet weld connections. Ultimate strength of fillet welds is dependent on the strength of the weld and the direction of loading due to its heterogeneous microstructure (Miazga et al. 1989). For this reason, fillet welds are tested by varying the direction of loading to the weldment. A typical lapped specimen with transverse fillet welds is shown in Figure 5.4. The lapped specimens have variation of triaxiality through the thickness of the specimen with the higher value being in the middle of the specimen due to plane strain condition and the lower triaxiality at the edges of the specimen (Anderson 2005).

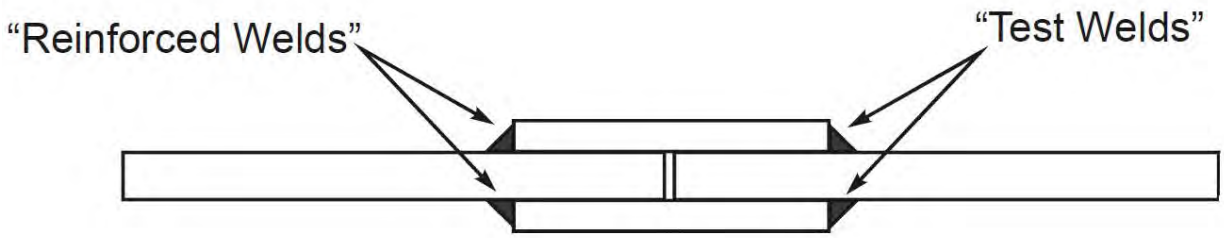

Figure 5.4: Typical side view of transverse lapped specimen (Ng et al. 2002)

5.2.1 Effective Boundary Conditions

In this work, the CNT and lapped specimens are used to calibrate the VGM model parameters. Since the chosen damage models use local values of stress and strain to determine the fracture criteria it is advantageous to use solid elements for calibration of the fracture parameters in CNT simulations to document their variations through the specimen thickness. To alleviate the computational expense of using solid elements to model CNTs a small study was performed to

see if using a one-eighth sized model with appropriate boundary conditions at the lines of symmetry would give similar results as a full-sized solid model.

The two sets of models in this study were different only in implementation of boundary conditions. The models were created in ABAQUS/Explicit using 8-node hexahedral elements with first-order interpolation for the displacement shape functions and reduced integration. Plasticity was modeled with a von Mises yield surface with associated plastic flow and isotropic hardening behavior. The inputs into the plasticity model were from the original papers of the experimental tests. Throughout this work, ABAQUS/Explicit uses a conditionally stable Central Difference algorithm with an automatic time step size calculation. Damping is not defined in the finite element models used throughout this work. A mass density of $7.345*10^{-7}$ $kip*s^2/in^4$ (which equals the density of steel, 490 lb/ft^3, divided by the acceleration of gravity, 32.174 ft/s^2, with units converted accordingly) was used in all of the finite element simulations. An updated Lagrangian geometrical nonlinear element formulation that includes large strains is also used (ABAQUS 2011). Elements are formulated in the current configuration using current nodal positions. The nominal flow property used for each of the steels is a piece-wise linear fit to the measured true stress-strain curve obtained from the experimental test results (Ng et al. 2002; Kanvinde et al. 2004). The mesh of the finite element models used in these and subsequent simulations was typically refined to have a maximum element size of 0.02 inches to account for different boundary conditions at critical locations such as notches in CNTs. The maximum element size is 0.04 inches elsewhere

For the purposes of comparison, both sets of models simulate CNT specimens with notch radii of 0.06, 0.125, and 0.25 inches, the gauge length of 1 inch, notch root diameter of 0.25 inches, and unnotched diameter of 0.5 inches. The material for both of the model sets is A572 Grade 50 steel taken from a plate section. The fracture and plasticity model inputs are identical. Figure 5.5 shows the boundary conditions of the two models in addition to a contour plot of the von Mises stress in ksi for a specimen with notch radius of 0.125 inches. For the full-sized model the loading was simulated in displacement control by specifying a displacement versus time relationship for the y-surface at the top of the model. The bottom part of the model was fixed by specifying zero displacement in the three primary directions defined at the bottom y-surface. For the one-eighth sized model, three symmetry boundary conditions were implemented on the x-, y- and z-surfaces. The symmetry condition specified zero displacement in the direction normal to the surface. The loading was simulated in the same way as in the full-sized model. From Figure 5.5, it can be seen that the stress distribution is virtually the same for both models, including fracture initiation and softening. In addition, Figure 5.6, Figure 5.7, and Figure 5.8 show similar results from the full and one-eighth sized models for experimental specimens CNT-KanA572-P-A.

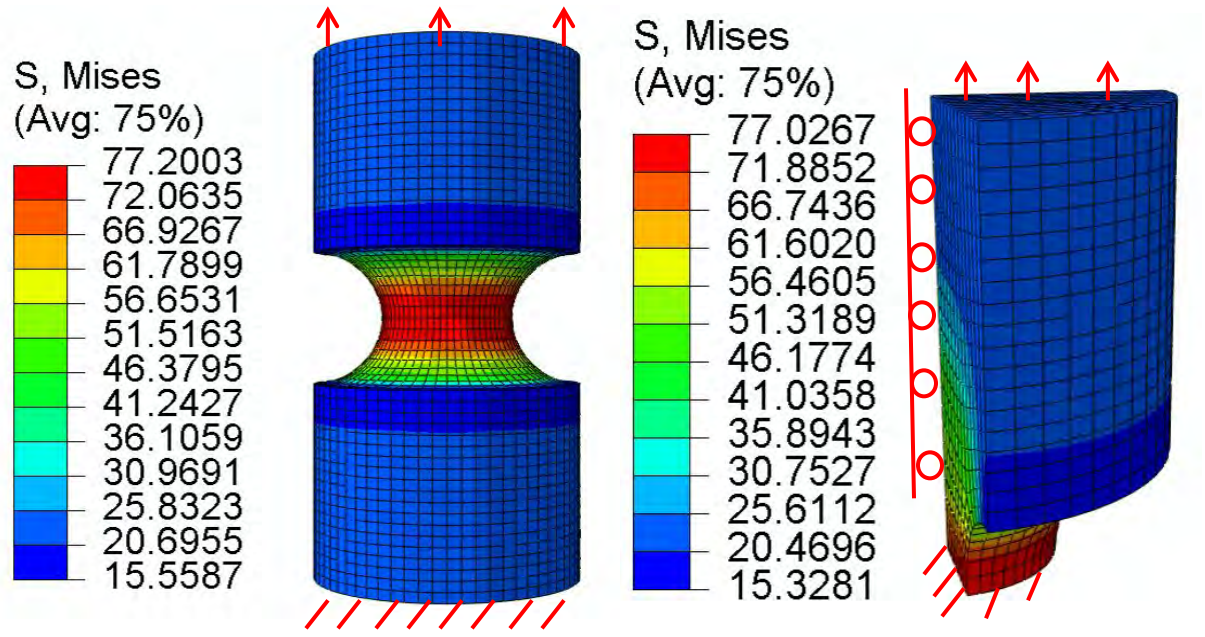

Figure 5.5: Boundary conditions for the full and one-eighth sized model during loading; contours signify the value of von Mises stress in ksi

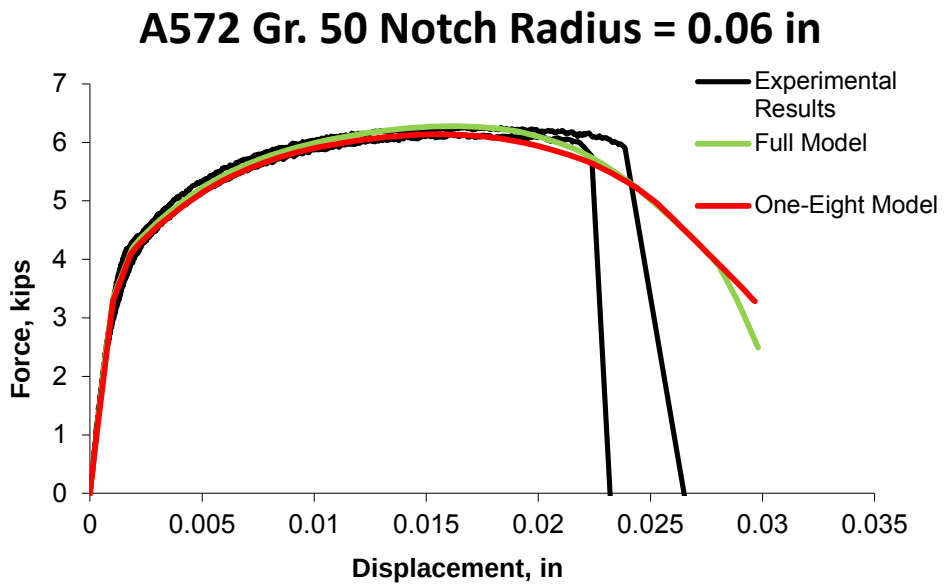

Figure 5.6: Comparison of full and one-eighth sized models for A572 Grade 50 steel CNT taken from a plate with notch radius of 0.06 inches (CNT-KanA572-P-4-5)

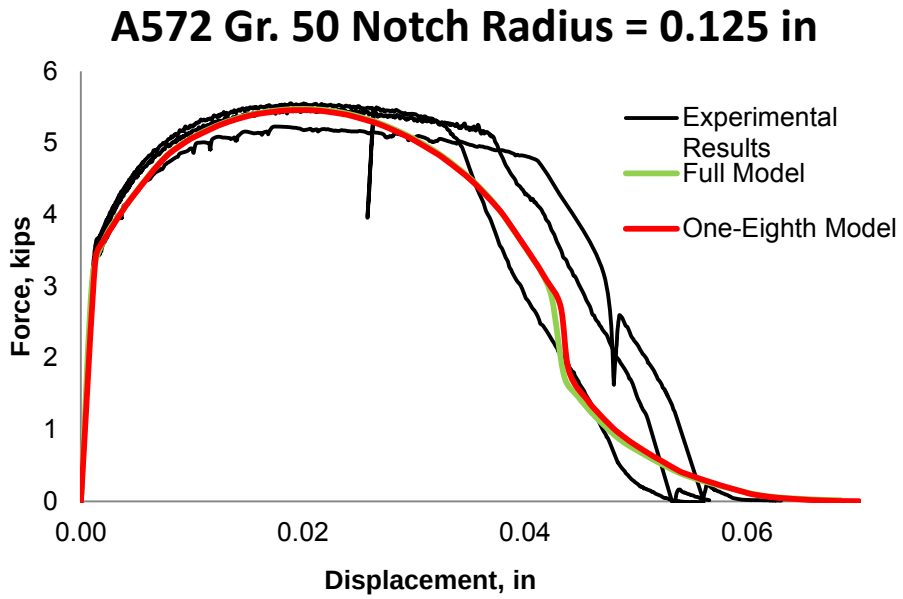

Figure 5.7: Comparison of full and one-eighth sized models for A572 Grade 50 steel CNT taken from a plate with notch radius of 0.125 inches (CNT-KanA572-P-1-3)

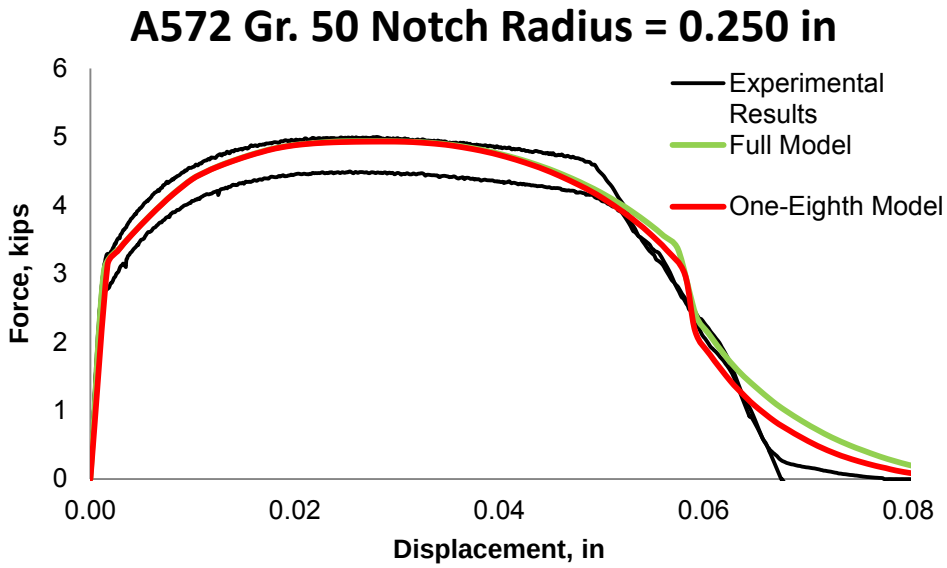

Figure 5.8: Comparison of full and one-eighth sized models for A572 Grade 50 steel CNT taken from a plate with notch radius of 0.25 inches (CNT-KanA572-P-6-7)

Since the force-displacement curves and the stress contours are very similar between the full and one-eighth sized models, it is concluded that one-eighth sized model can be used for calibration purposes in place of the full-sized model, including fracture initiation and softening.

5.3 Calibration of the Void Growth Model

As discussed earlier, the key parameters that control fracture at a macro scale are the current components of stress and strain tensors and their histories. These components are available in Abaqus/Explicit, which allows the implementation of micromechanical fracture models to model material separation during collapse of steel structures.

It is well known that triaxiality varies throughout the thickness of the specimen and throughout the loading. This is complicated further by the fact that plastic strain induces necking, which increases the stress triaxiality, counteracting the effect of the superimposed pressure (Smith, C. M. 2013). In addition, to recover the state of stress and strain at fracture a comparison of the initial and final cross section of the fracture surface is commonly used. This approach makes the assumption of a uniform stress field at the center of the neck and the limited accuracy of measurements at the sharp neck, but is a good approximate measurement of material ductility.

To avoid these assumptions, for the calibration of VGM parameters for structural steel and structural weld material, detailed finite element models of the circumferential notched tensile (CNT) coupon and tensile lapped specimens are created, respectively, in ABAQUS/Explicit using 8 node hexahedral elements with first-order interpolation for the displacement shape functions and reduced integration. Plasticity in the analyses was modeled with a von Mises yield surface with associated plastic flow and isotropic hardening behavior. An updated Lagrangian

geometrical nonlinear element formulation that includes large strains is also used (ABAQUS 2011). Elements are formulated in the current configuration using current nodal positions. Contact was modeled using a balanced master-slave contact pair formulation that uses sophisticated algorithms for tracking the motions of the surfaces (ABAQUS 2011). Contact constraints are enforced through a kinematic contact algorithm (ABAQUS 2011). The nominal flow property used for each of the steels is a piece-wise linear fit to the measured true stress-strain curve obtained from the experimental test results (Ng et al. 2002; Kanvinde et al. 2004). Each steel material was calibrated to experimental test results from CNTs with different root notch sizes through the use of a Particle Swarm Optimization (PSO) algorithm. This allows for calibration of fracture initiation for a particular material across a range of triaxiality. Triaxiality is varied in the various CNT experiments by the root notch size, which ranged from 0.06 to 0.25 inches; the smaller the notch radii, the larger the triaxiality if the root diameter is kept constant. In addition, this approach captures the variation of triaxiality through deformation loading. A one-eighth model was created using appropriate symmetrical boundary conditions to simulate CNT specimens. Typical experimental and simulation setups are shown in Figure 5.9.

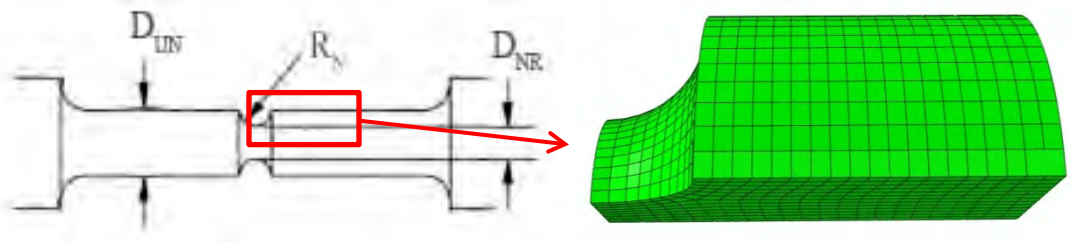

Figure 5.9: CNT typical experimental setup (left) and an eighth-symmetrical simulation model (right)

The weld material was divided into two categories for calibration purposes, which included weld material with and without specified hardness to cover the variability of the weld material. These materials were calibrated to tensile lapped specimens with varying orientation of the weld as compared to the loading direction. To better calibrate to weld heterogeneity and different triaxiality ranges, three loading directions relative to the weld orientations were simulated and compared to experimental test results: transverse, 45 degree, and longitudinal. A typical test setups and simulation models are shown in Figure 5.10, Figure 5.11, and Figure 5.12. To account for different shapes of the weld an average shape was used (Ng et al. 2002). A quarter symmetric models were created using appropriate symmetrical boundary conditions to simulate the transverse and longitudinal specimens and a half-symmetrical model was used to simulate the specimen with a weld orientation at 45 degrees to the loading directions.

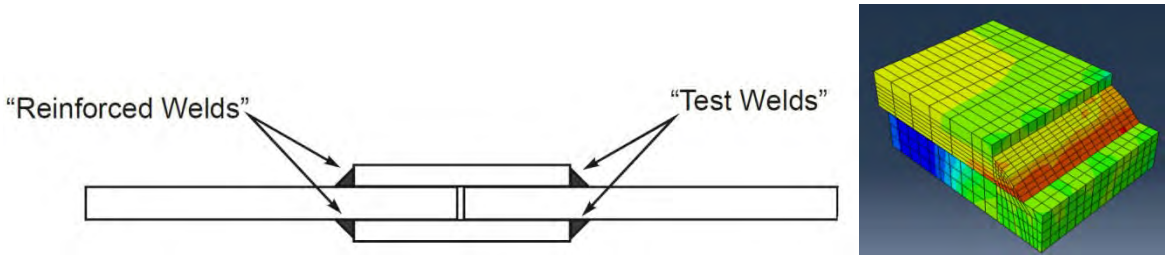

Figure 5.10: Transverse lapped tensile specimen experimental setup (left) and a quarter-symmetrical simulation model (right) (Ng et al. 2002)

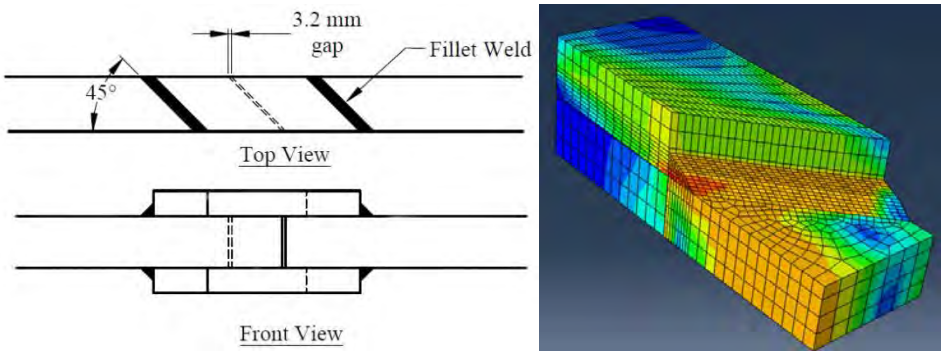

Figure 5.11: 45 Degree lapped tensile specimen experimental setup (left) and a half-symmetrical simulation model (right) (Deng et al. 2006)

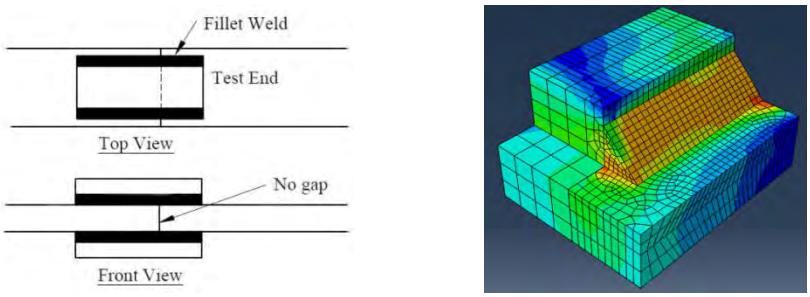

Figure 5.12: Longitudinal lapped tensile specimen experimental setup (Deng et al. 2006) (left) and a quarter-symmetrical simulation model (right)

The parameters that need to be calibrated for this approach are η, the material capacity, β, the material parameter, and $\overline{u}_f^{pl}$ the critical equivalent plastic displacement; these parameters are seen in Equations (4.5 and (4.10). The mesh of the finite element models was typically refined to have a maximum element size of 0.02 inches to account for different boundary conditions at critical locations such as notches in CNTs. The maximum element size is 0.04 inches elsewhere. Table 5.1 outlines the nomenclature used in this work to identify experimental test results.

Table 5.1: Example of nomenclature used to identify experimental test results

Test Nomenclature	Type	Author	Material Type	Material Source	Test Number or Average
TC-KanA572-P-A	TC	Kanvinde	A572 Gr. 50	Plate	A
CNT-MyeA992-W-L-1	CNT	Myers	A992	W-L	1
TC-MyeE70-T6-W-T-A	TC	Myers	E70-T6	W-T	A
TC-MyeA36-B-A	TC	Myers	A36	Bar	A
RBS-SadA992-W-1	RBS	NIST	A992	RBS-W	1
Brace-YurA36-W-1	B-F	Yura	A36	W	1
LPT-NgE70-T4-P-A	LPT	Ng	E70-T4	Weld	A

LPT (LP45, LPL) : Lapped Plates; Transverse, 45 Degrees, or Longitudinal Loading direction
TC : Tensile Coupon Specimen
W-L : Taken from a W-Section in the longitudinal axis
W-T : Taken from a W-Section in a transverse direction to the longitudinal axis
RBS-W : Web of W-section in the RBS connection
Col-F : Flange of a W-Section Column
A : Average test results
CNT: Circumferentially Notched Tensile Coupon

5.3.1 Particle Swarm Optimization

To achieve best fit calibration of the simulation results to experimental test results for the VGM model, a Particle Swarm Optimization (PSO) algorithm was employed. The PSO is an evolutionary computation technique inspired by the social behavior of bird flocking and fish schooling. PSO is a computational method that optimizes a problem by iteratively improving the position of a group, called a swarm, of candidate solutions, called particles, in the parameter space with regards to a given measure of quality, such as a target value of an error quantity (Kennedy 1997). The PSO formulates the problem in the established optimization theory framework that requires the definition of an error function, and an automated algorithm that minimizes that error function through a set of parameters (Kennedy 2010). This is all based on the fact that PSO uses the swarm intelligence concept, which is a property of a system, whereby the collective behaviors of unsophisticated agents that are interacting locally with their environment create coherent global functional patterns (Del Valle et al. 2008). The PSO accounts for (1) Social Concepts: evaluation, comparison, and imitation of others allows for adaptation to the environment and determine the optimal behavior; (2) Swarm Intelligence Principles: including Proximity Principle (space and time computations), Quality Principle (response to quality factors in the environment), Diverse Response Principle (members of the population do not commit activity along excessively narrow channels, Stability Principle (the population does not change every time the environment does), and Adaptability Principle (the population should be able to change its behavior when needed; and (3) Computational Characteristics: a paradigm for implementing adaptive systems through softening parameterization of logical operators that updates individual particles in parallel has the new

value of the particle depend only on the previous values, and performs all updates according to the same rules (Del Valle et al. 2008). This approach avoids the traditional manual trial and error approach, where the parameters are varied manually until the force-displacement curves from simulations and experiments match well. Manual optimization is made difficult by the fact that at large strains, global response and local continuum fields are very sensitive to minor variations in material parameters especially when modeling fracture (Smith, Chris M. et al. 2013). In addition, due to the fact that at large strains stress and strain homogeneity is violated due to some form of localization such as necking, for calibration the fracture parameters should be calibrated by fitting the global force-displacement curve rather than stress-strain curve. In addition, the structural finite element optimization problem is characterized by the high-dimensionality of the search space in addition to computational expense and the granularity of the objective function (Smith, C. M. 2013). It has been shown that PSO is able to adequately account for the specifics of structural finite element optimization problems (Smith, Chris M. et al. 2013). The PSO algorithm requires the definition of an objective or error function that determines the quality of the fit between the experimental and computational results. This approach tries to minimize the objective function which is defined in the force-displacement space by running a nonlinear finite element simulation which generates load-displacement curve for a given design point, which is a candidate parameter set for the VGM fracture model.

PSO creates an array of proposed values for the parameters that will be used for optimization called particle positions and runs a series of simulations. Initially the particle swarm is spread out across the possible solution space according to uniform random distribution. The columns of this array are called iterations and the rows are called particles and the value of each of the

three parameters that are being calibrated located in each input of this array is called a particle position. PSO compares the simulation results with the experimental test or other established results and provides a resulting error value for that particular particle position. PSO then uses this error value to assess the quality of the parameters chosen and determines if the error achieved is smaller than the global best error (Smith, Chris M. et al. 2013). For this work, the error value is calculated by Equation (5.2. This error value has two attributes: (1) it reflects a perfect fit corresponding to zero error values, and (2) it avoids bias towards specific errors or specimens because it captures the area under the force-displacement curve (Smith, Chris M. et al. 2013). This equation allows the error function to account for the size of the specimen; therefore, larger specimens will not give larger error values due to normalization of the error. In adition, the area under the force-displacement curve helps this error value to minimize the significance of any deviations in the force-displacement curve from the overall trend.

$$err = \frac{\Delta E}{E_{ex}} \tag{5.2}$$

where:

- E – energy or the area under force-displacement curve
- ΔE – the difference between the total energy of simulation and experimental results
- E_{ex} – the total energy of the experimental (or other established) results

Each particle is present throughout the history of the analysis and moves around the search space with a calculated “velocity”. The PSO updates the calibrating parameters through updating the velocity using Equation (5.3 and the particle position using Equation (5.4 for each of the particle parameters for the next iteration. Each particle travels in the general direction of the global and personal best known locations (Smith, Chris M. et al. 2013). To avoid all

particles traveling directly to the best know point so that they could explore the neighborhood around the current optimum solution, additional random perturbation are used (Smith, Chris M. et al. 2013). To obtain the quickest convergence to the optimal solution it has been recommended by Smith, Chris M. et al. (2013) to use 5 particles with 15 iterations and inertial function of 1.5, with 0.55 for acceleration constants.

$$v_i(k+1) = \varphi(k)v_i(k) + \alpha_1\gamma_{1i}\big(p_i - x_i(k)\big) + \alpha_2\gamma_{2i}(G - x_i(k)) \tag{5.3}$$

$$x_i(k+1) = x_i(k) + v_i(k+1) \tag{5.4}$$

where:

- *i* – particle index
- *k* – discrete time index
- *v* – velocity of ith particle
- *x* – position of the ith particle
- *p* – best position found by the ith particle (personal best)
- *G* – best position found by swarm (global best, best of personal bests)
- *γ*1,2 – random numbers on the interval [0,1] applied to ith particle
- ϕ – Inertia function = 1.5
- α1,2 – Acceleration constants 0.55

For each simulation, an error value from Equation (5.2 for a set of parameters is compared to the global best parametrical set that has the lowest error value. If it is smaller than the global best, it keeps the values of the parameters as the optimal ones. PSO goes through this process for each particle position and iteration. This process continues until satisfactory results are obtained, which are defined by the lowest error value for all of the runs. For a detailed flow chart of PSO algorithm used for calibration, see Appendix A. For example, material A572 Grade 50 taken from a flange of a W-Section has experimental test results for 6 specimens shown in Table 5.2. Three specimens have a notch radius of 0.126 inches and the other three 0.059

inches. Two finite element simulations, one for specimens with notch radius of 0.126 inches and one for 0.059 inches, are required to calibrate this particular material. The energy which is the area under the force-displacement curve is determined for all of the experimental test results and simulation results. A difference of energy between the simulation result and each corresponding experimental results is determined for two simulations. These differences are normalized by the division of corresponding experimental test result energy. These normalized differences are averaged for the two types of specimens. Then an average is determined between the two type of specimens. This average is the error value defined by Equation (5.2 for this particular material. This is illustrated by Figure 5.13.

Using this approach, the calibrated VGM parameters per structural steel material, their material parameters, and associated information about the original experimental tests are provided in Table 5.2 and Table 5.4. In these tables, D_{UN} is the unnotched root diameter, D_N is the diameter at the notch, R_N is the radius of the notch, and Δ_f is the displacement at which fracture initiation occurred in the experimental test. The calibrated welds with associated information are provided in Table 5.3. Measured properties as shown in these tables are used throughout these simulations. Details of the stress-strain curves used in simulations throughout this work are provided in Appendix C. Figure 5.14 to Figure 5.33 show calibration results for different structural steels taken from different structural components. Figure 5.34 to Figure 5.44 show calibration results for different structural welds with and without specified hardness.

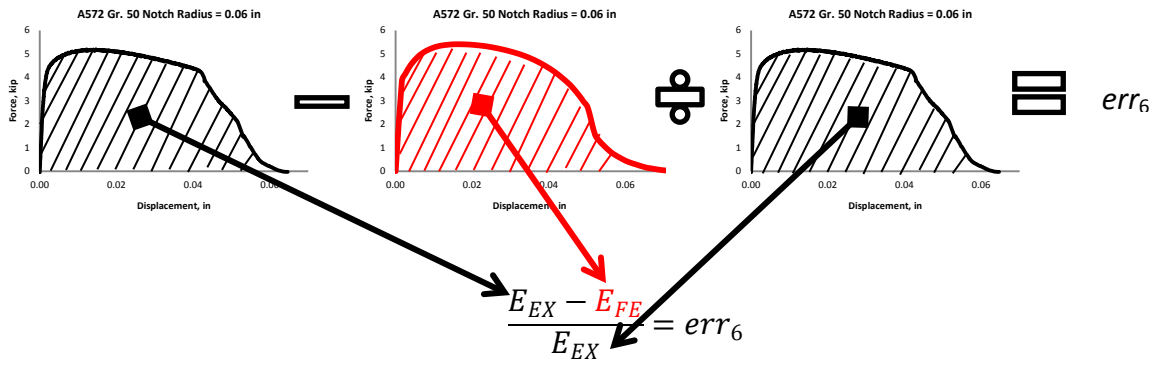

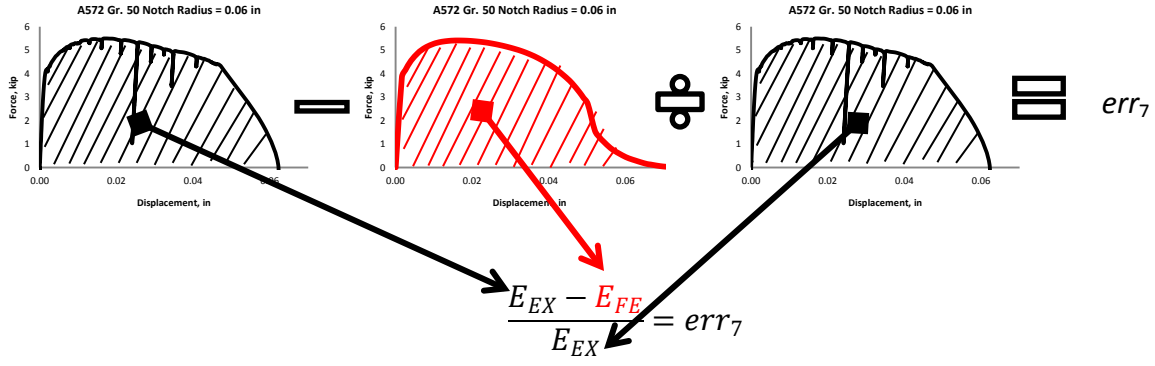

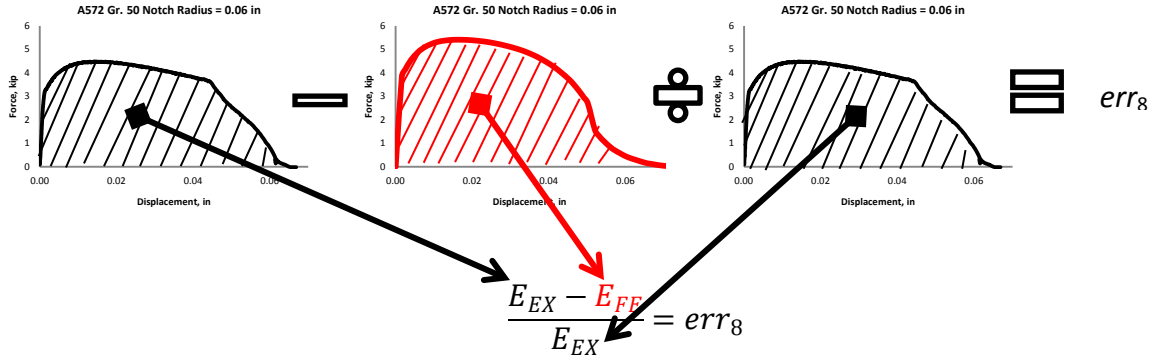

$$Error\ for\ specimen\ with\ notch\ radius\ of\ 0.059\ inches, \frac{err_6 + err_7 + err_8}{3} = err_{0.059}$$

$$Similar\ for\ notch\ radius\ of\ 0.125\ inches, \frac{err_1 + err_2 + err_3}{3} = err_{0.125}$$

$$Error\ for\ the\ material, \frac{err_{0.059} + err_{0.125}}{2} = err_{\mathrm{CNT-KanA572-W-L-A}} = 0.086$$

Figure 5.13: Error calculation for CNT-KanA572-W-L-A, the simulations used an η, β, and $\bar{u}_f^{pl}$ of 1.80, 1.56, and 0.0056 respectively

Table 5.2: Calibration of the structural steels commonly used in North America ranging from low yield to high yield including bridge steel

							Parameters			
Test	D_{UN} *(in)*	D_N *(in)*	R_N *(in)*	σ_y *(ksi)*	σ_u *(ksi)*	Δ_f *(in)*	η	β	$\bar{u}_f^{pl}$	**Error**
CNT-MyeA36-B-1	0.500	0.248	0.126	50	74	0.067	1.65	1.63	0.0046	0.116
CNT-MyeA36-B-2	0.496	0.252	0.126			0.067				
CNT-MyeA36-B-3	0.500	0.252	0.126			0.067				
CNT-MyeA36-B-4	0.496	0.252	0.126			0.066				
CNT-MyeA36-B-5	0.496	0.248	0.063			0.050				
CNT-MyeA36-B-6	0.496	0.248	0.063			0.051				
CNT-MyeA36-B-7	0.492	0.248	0.063			0.051				
CNT-MyeA36-B-8	0.500	0.252	0.063			0.051				
CNT-MyeA992-W-L-1	0.496	0.244	0.067	54	114	0.037	1.00	2.04	0.0041	0.091
CNT-MyeA992-W-L-2	0.496	0.244	0.067			0.039				
CNT-MyeA992-W-L-3	0.496	0.248	0.067			0.038				
CNT-MyeA992-W-T-1	0.689	0.244	0.067	54	114	0.025	1.91	1.85	0.0001	0.102
CNT-MyeA992-W-T-2	0.685	0.244	0.067			0.026				
CNT-MyeA992-W-T-3	0.685	0.244	0.067			0.020				
CNT-KanA572-W-L-1	0.500	0.252	0.126	61	72	0.056	1.80	1.56	0.0056	0.086
CNT-KanA572-W-L-2	0.500	0.252	0.126			0.074				
CNT-KanA572-W-L-3	0.500	0.252	0.126			0.074				
CNT-KanA572-W-L-6	0.500	0.252	0.059			0.044				
CNT-KanA572-W-L-7	0.500	0.252	0.059			0.042				
CNT-KanA572-W-L-8	0.500	0.252	0.059			0.047				
CNT-KanA572-P-1	0.500	0.252	0.126	56	85	0.041	0.95	2.46	0.0053	0.124
CNT-KanA572-P-2	0.500	0.252	0.126			0.033				
CNT-KanA572-P-3	0.500	0.252	0.126			0.037				
CNT-KanA572-P-4	0.500	0.252	0.059			0.022				
CNT-KanA572-P-5	0.500	0.252	0.059			0.024				
CNT-KanA572-P-6	0.500	0.252	0.252			0.049				
CNT-KanA572-P-7	0.500	0.252	0.252			0.050				
CNT-KanA514-P-1	0.500	0.252	0.126	116	124	0.028	1.85	1.75	0.0028	0.128
CNT-KanA514-P-2	0.500	0.252	0.126			0.027				
CNT-KanA514-P-3	0.500	0.252	0.059			0.016				
CNT-KanA514-P-4	0.500	0.252	0.059			0.013				
CNT-KanA514-P-5	0.500	0.252	0.252			0.053				
CNT-KanA514-P-6	0.500	0.252	0.252			0.039				
CNT-KanHPS70W-P-1	0.500	0.252	0.126	85	101	0.066	4.45	2.66	0.0102	0.120
CNT-KanHPS70W-P-2	0.500	0.252	0.126			0.055				
CNT-KanHPS70W-P-3	0.500	0.252	0.059			0.034				
CNT-KanHPS70W-P-4	0.500	0.252	0.059			0.033				
									Average Error =	**0.109**
									Standard Deviation =	**0.015**

Table 5.3: Calibration of structural welds

Test	Hardness Specified	Weld Type	Test Type	Weld Size	Parameters			Error
					η	β	$\overline{u}_f^{pl}$	
LPT-NgE70-T4-P-6.4T4	N	FCAW	Transverse	0.25 in				
LPT-NgE70-T4-P-6.4T5	N	FCAW	Transverse	0.25 in				
LPT-NgE70-T4-P-6.4T6	N	FCAW	Transverse	0.25 in				
LPT-NgE70-T4-P-6.4T8	N	FCAW	Transverse	0.25 in				
LPT-NgE70-T4-P-6.4T9	N	FCAW	Transverse	0.25 in				
LPT-NgE70-T4-P-6.4T10	N	FCAW	Transverse	0.25 in				
LPT-NgE70-T4-P-12.7T21	N	FCAW	Transverse	0.50 in				
LPT-NgE70-T4-P-12.7T22	N	FCAW	Transverse	0.50 in				
LPT-NgE70-T4-P-12.7T23	N	FCAW	Transverse	0.50 in				
LPT-NgE70-T4-P-12.7T24	N	FCAW	Transverse	0.50 in				
LPT-NgE70-T7-P-6.4T11	N	FCAW	Transverse	0.25 in				
LPT-NgE70-T7-P-6.4T12	N	FCAW	Transverse	0.25 in	0.56	4.48	0.0072	0.362
LPT-NgE70-T7-P-6.4T13	N	FCAW	Transverse	0.25 in				
LPT-NgE70-T7-P-6.4T14	N	FCAW	Transverse	0.25 in				
LPT-NgE70-T7-P-6.4T15	N	FCAW	Transverse	0.25 in				
LPT-NgE70-T7-P-12.7T25	N	FCAW	Transverse	0.50 in				
LPT-NgE70-T7-P-12.7T26	N	FCAW	Transverse	0.50 in				
LPT-NgE70-T7-P-12.7T27	N	FCAW	Transverse	0.50 in				
LPT-NgE70-T7-P-12.7T28	N	FCAW	Transverse	0.50 in				
LP45-DenE70-T4-P-12.7F1	N	FCAW	45 Deg.	0.50 in				
LPL-DenE70-T4-P-12.7L1	N	FCAW	Longitudinal	0.50 in				
LP45-DenE70-T7-P-12.7F2	N	FCAW	45 Deg.	0.50 in				
LPL-DenE70-T7-P-12.7L2	N	FCAW	Longitudinal	0.50 in				
LPT-NgE70T-7K2-P-6.4T16	Y	FCAW	Transverse	0.25 in				
LPT-NgE70T-7K2-P-6.4T17	Y	FCAW	Transverse	0.25 in				
LPT-NgE70T-7K2-P-12.7T29	Y	FCAW	Transverse	0.50 in				
LPT-NgE70T-7K2-P-12.7T30	Y	FCAW	Transverse	0.50 in				
LPT-NgE70T-8K6-P-6.4T18	Y	FCAW	Transverse	0.25 in				
LPT-NgE70T-8K6-P-6.4T19	Y	FCAW	Transverse	0.25 in	4.03	3.63	0.0016	0.321
LPT-NgE70T-8K6-P-12.7T31	Y	FCAW	Transverse	0.50 in				
LPT-NgE70T-8K6-P-12.7T32	Y	FCAW	Transverse	0.50 in				
LP45-DenE70T-8K6-P-12.7F3	Y	FCAW	45 Deg.	0.50 in				
LPL-DenE70T-8K6-P-12.7L3	Y	FCAW	Longitudinal	0.50 in				
							Average % Error =	**0.342**
							Standard Deviation =	**0.021**

Table 5.4: Calibration of structural steels commonly used in Japan

Test	D_{UN} (in)	D_N (in)	R_N (in)	σ_y (ksi)	σ_u (ksi)	Δ_f (in)	Parameters η	Parameters β	Parameters $\bar{u}_f^{pl}$	Error
CNT-KanSN490B-P-1	0.500	0.252	0.126	47.6	75	0.061	1.00	0.83	0.0055	0.064
CNT-KanSN490B-P-2	0.500	0.252	0.126			0.064				
CNT-KanSN490B-P-3	0.500	0.252	0.059			0.043				
CNT-KanSN490B-P-4	0.500	0.252	0.059			0.049				
CNT-KanSM490YBTM-P-1	0.500	0.252	0.126	59.9	75	0.092	1.31	0.69	0.0055	0.084
CNT-KanSM490YBTM-P-2	0.500	0.252	0.126			0.092				
CNT-KanSM490YBTM-P-3	0.500	0.252	0.059			0.060				
CNT-KanSM490YBTM-P-4	0.500	0.252	0.059			0.056				
CNT-KanSN490B-W-L-1	0.500	0.252	0.126	49.1	69.0	0.089	1.19	0.77	0.0075	0.084
CNT-KanSN490B-W-L-2	0.500	0.252	0.126			0.091				
CNT-KanSN490B-W-L-3	0.500	0.252	0.059			0.051				
CNT-KanSN490B-W-L-4	0.500	0.252	0.059			0.055				
									Average Error =	0.077
									Standard Deviation =	0.010

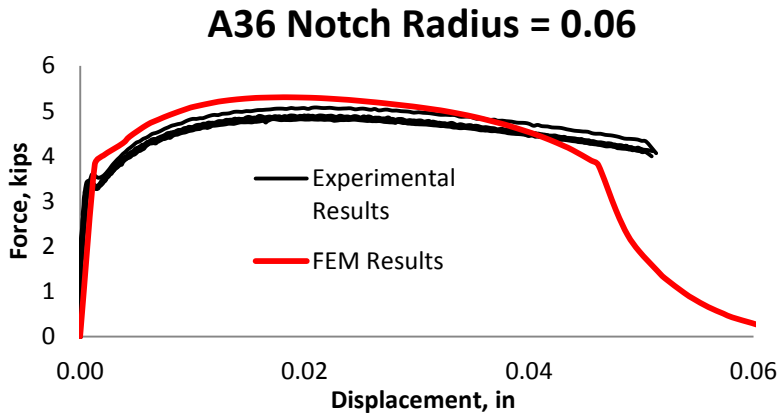

Figure 5.14: Calibration results for CNT-MyeA36-B-5 to CNT-MyeA36-B-8 with notch radius of 0.06 inches and an error value of 0.116

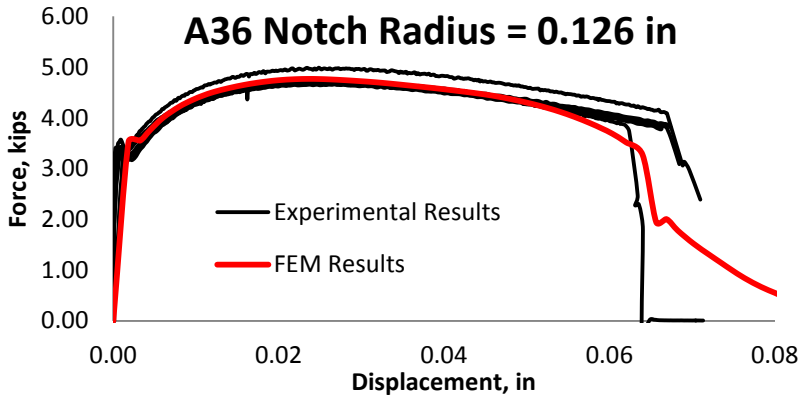

Figure 5.15: Calibration results for CNT-MyeA36-B-1 to CNT-MyeA36-B-4 with notch radius of 0.126 inches and an error value of 0.116

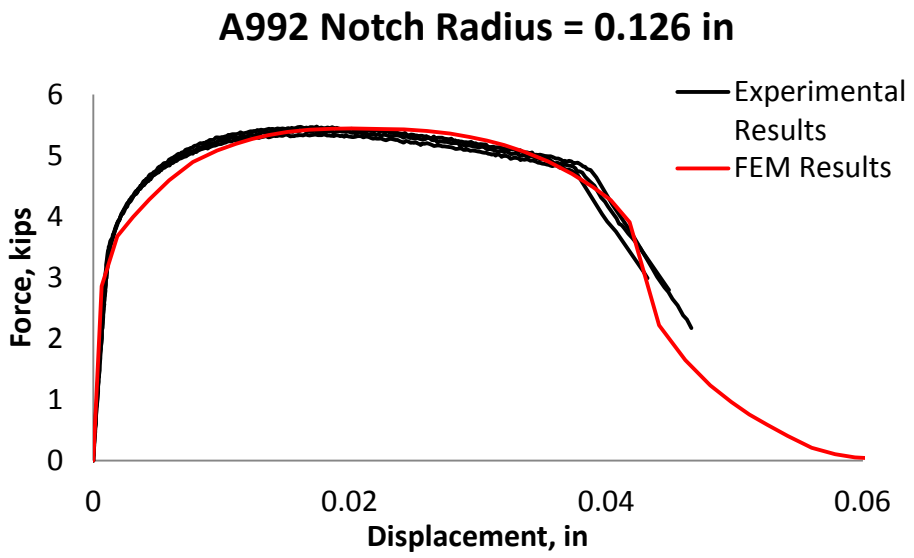

Figure 5.16: Calibration results for CNT-MyeA992-W-L-1 to CNT-MyeA992-W-L-3 with notch radius of 0.126 inches and an error value of 0.091

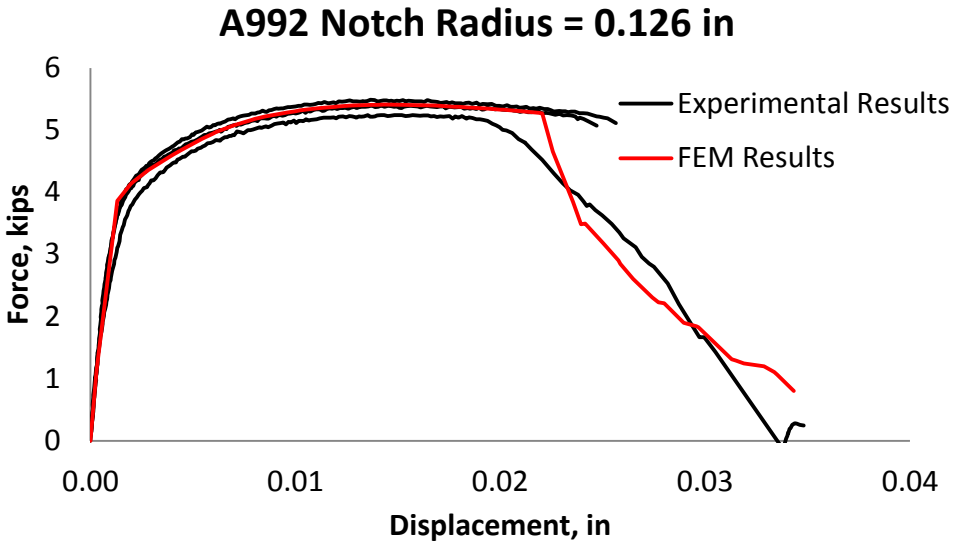

Figure 5.17: Calibration results for CNT-MyeA992-W-T-1 to CNT-MyeA992-W-T-3 with notch radius of 0.126 inches and an error value of 0.102

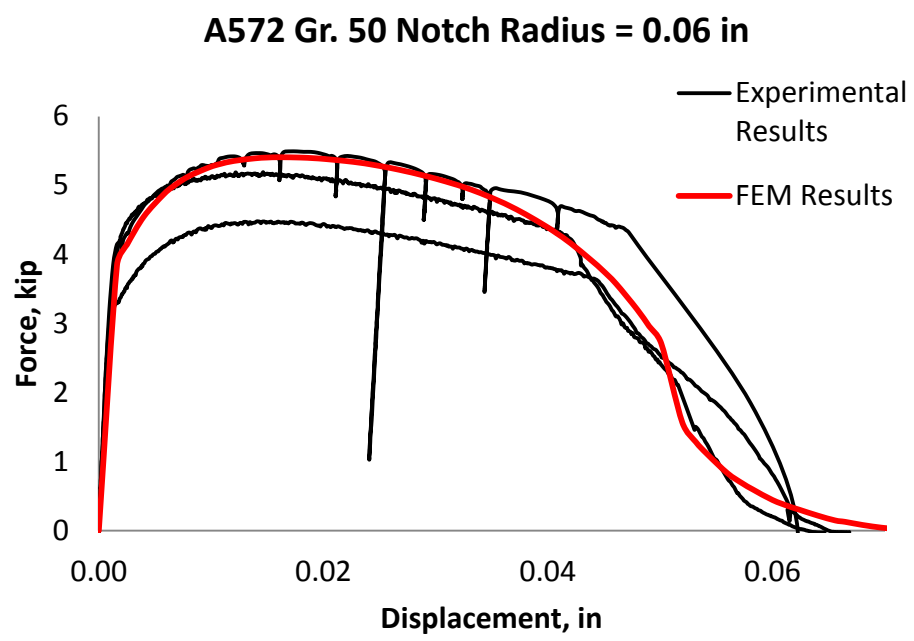

Figure 5.18: Calibration results for CNT-KanA572-W-L-6 to CNT-KanA572-W-L-8 with notch radius of 0.06 inches and an error value of 0.086

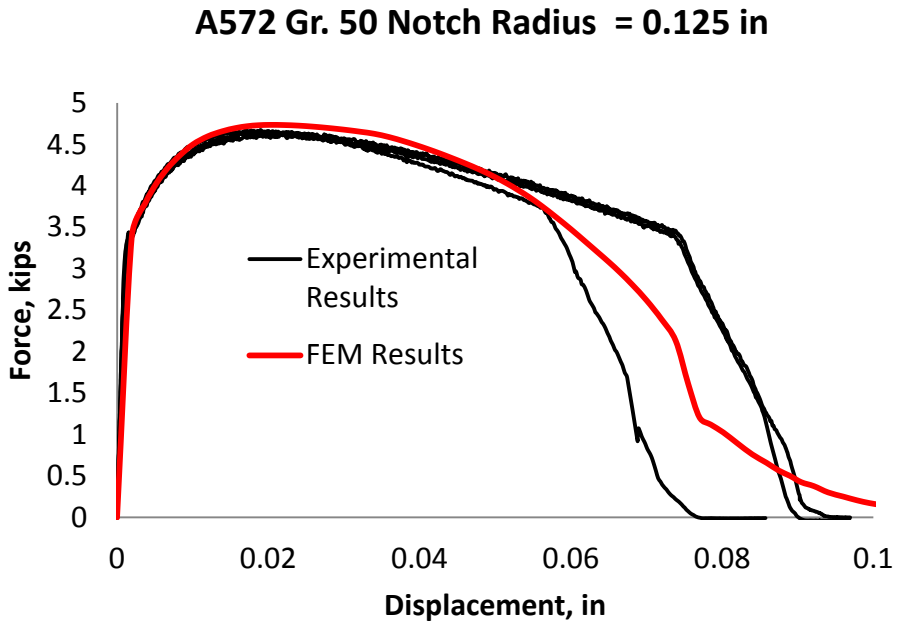

Figure 5.19: Calibration results for CNT-KanA572-W-L-1 to CNT-KanA572-W-L-3 with notch radius of 0.126 inches and an error value of 0.086

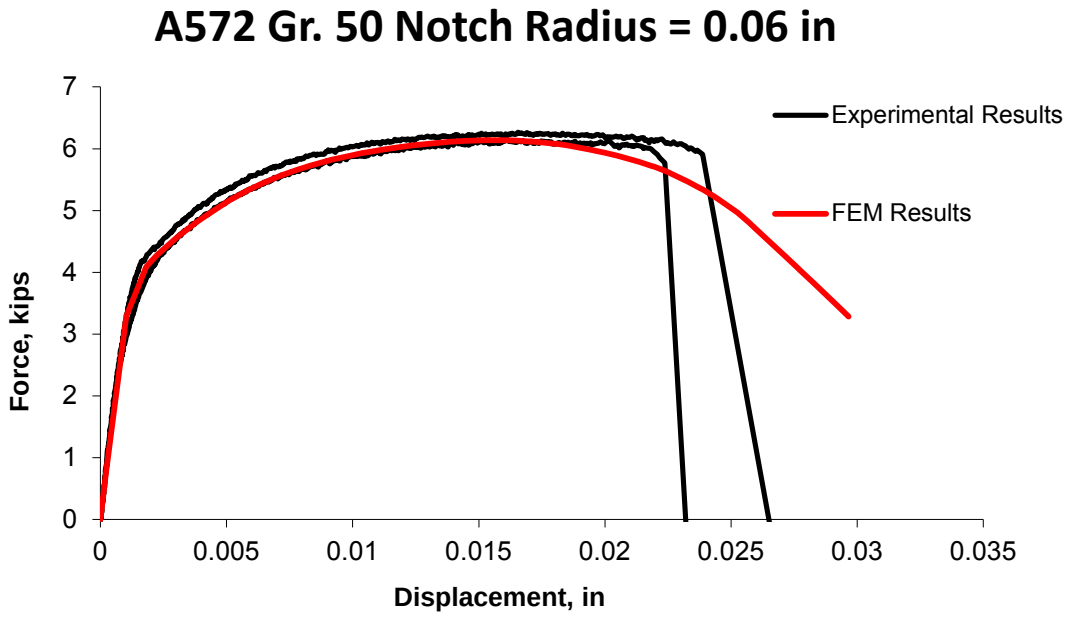

Figure 5.20: Calibration results for CNT-KanA572-P-4 to CNT-KanA572-P-5 with notch radius of 0.06 inches and an error value of 0.124

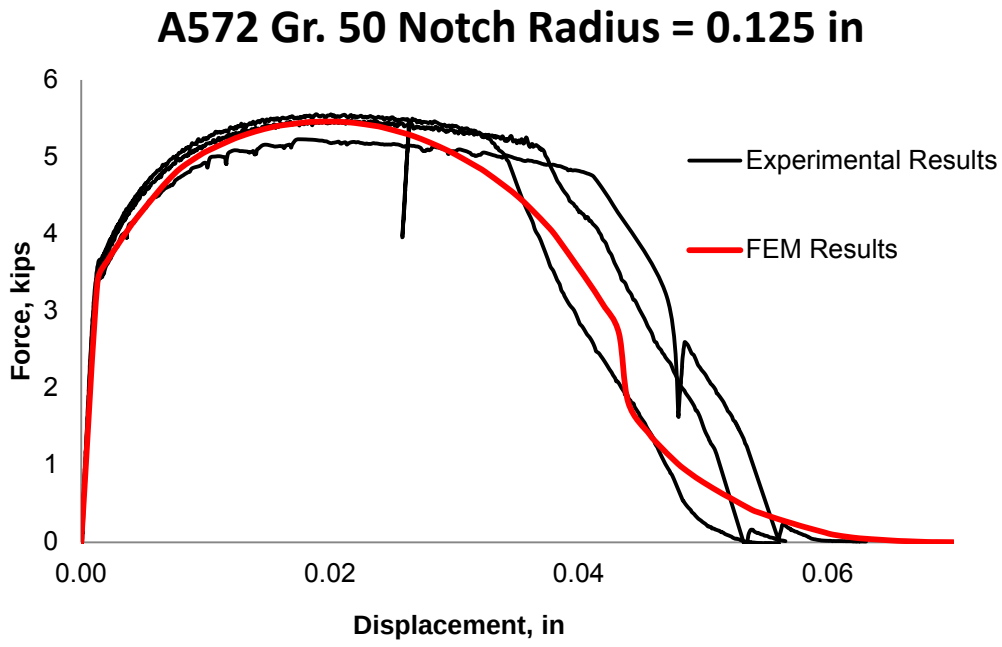

Figure 5.21: Calibration results for CNT-KanA572-P-1 to CNT-KanA572-P-3 with notch radius of 0.125 inches and an error value of 0.124

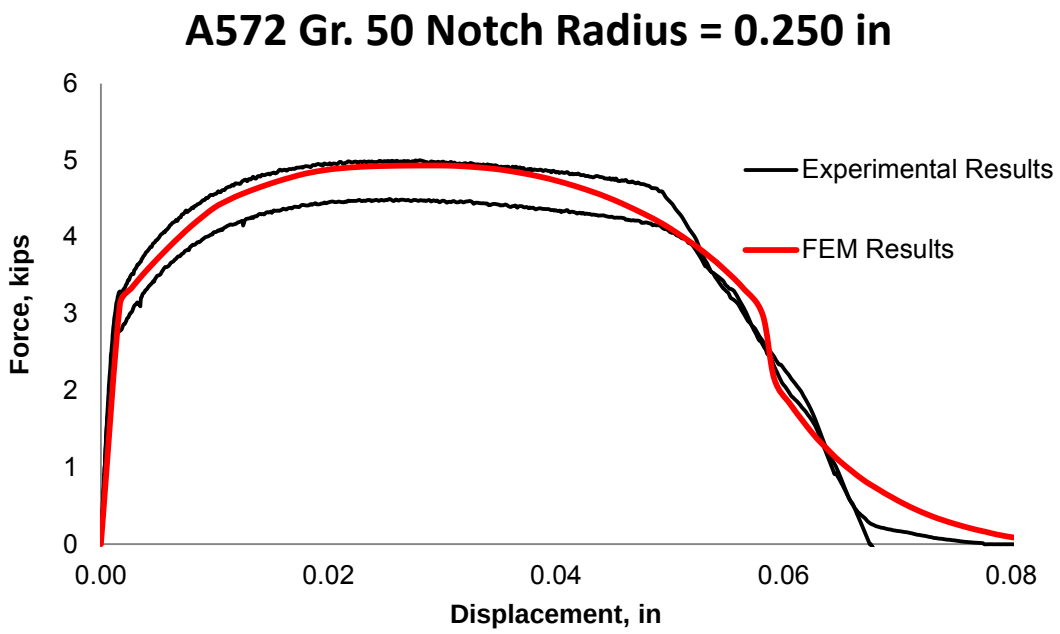

Figure 5.22: Calibration results for CNT-KanA572-P-6 to CNT-KanA572-P-7 with notch radius of 0.250 inches and an error value of 0.124

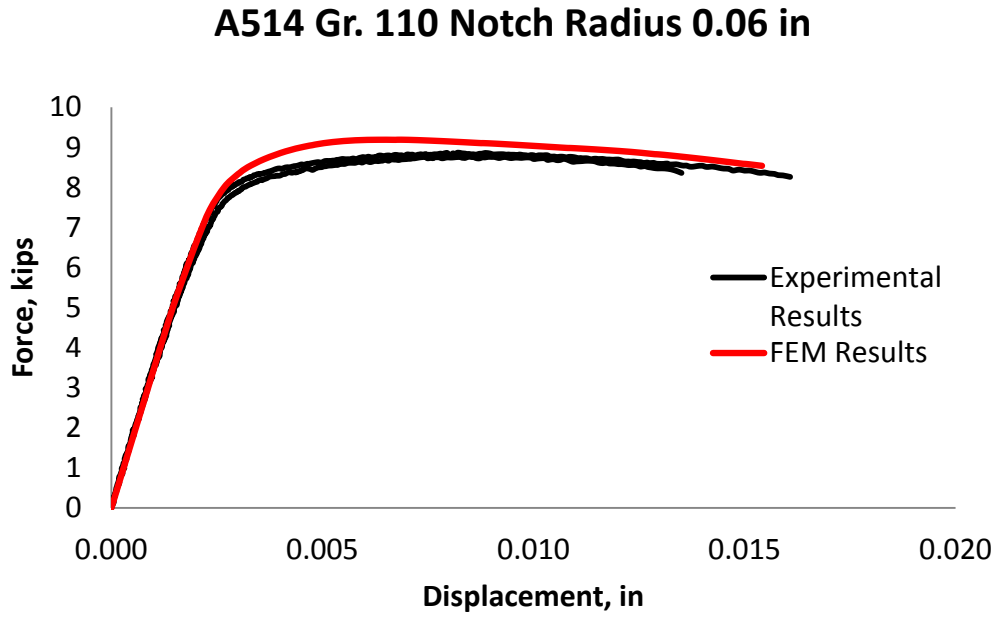

Figure 5.23: Calibration results for CNT-KanA514-P-3 to CNT-KanA514-P-4 with notch radius of 0.06 inches and an error value of 0.128

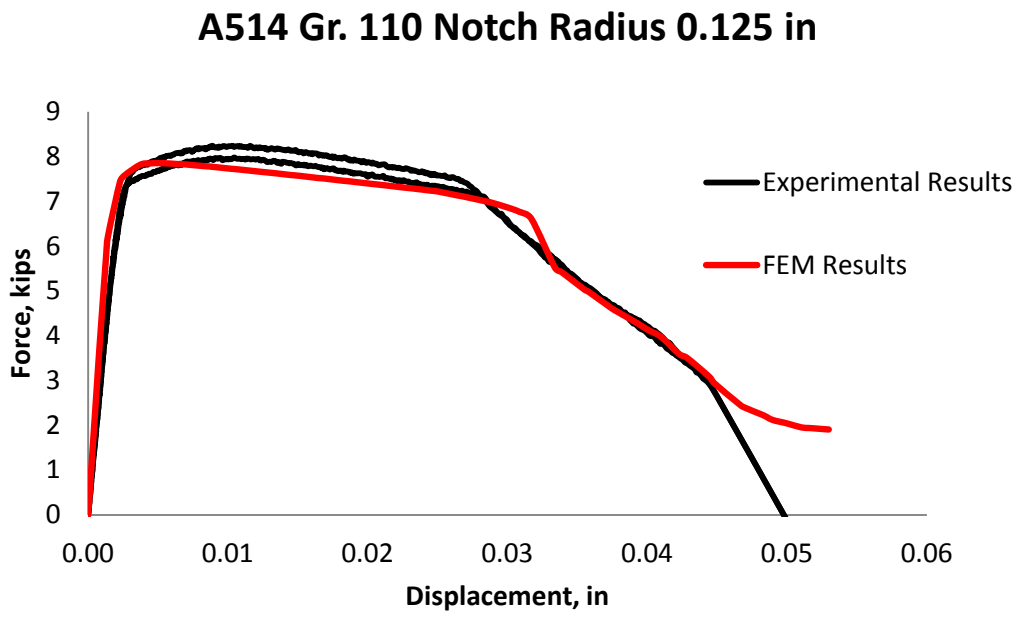

Figure 5.24: Calibration results for CNT-KanA514-P-1 to CNT-KanA514-P-2 with notch radius of 0.125 inches and an error value of 0.128

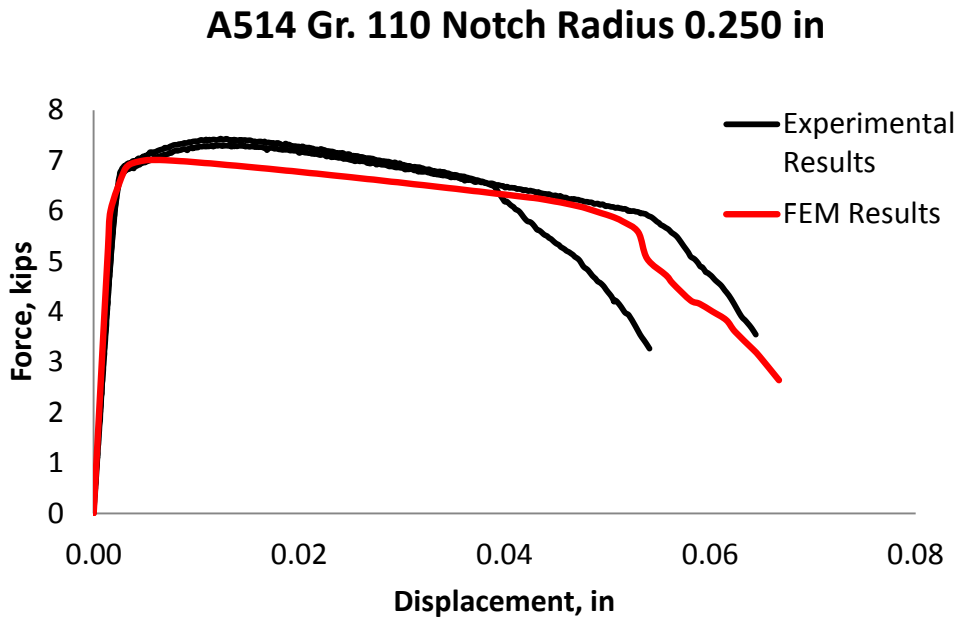

Figure 5.25: Calibration results for CNT-KanA514-P-5 to CNT-KanA514-P-6 with notch radius of 0.250 inches and an error value of 0.128

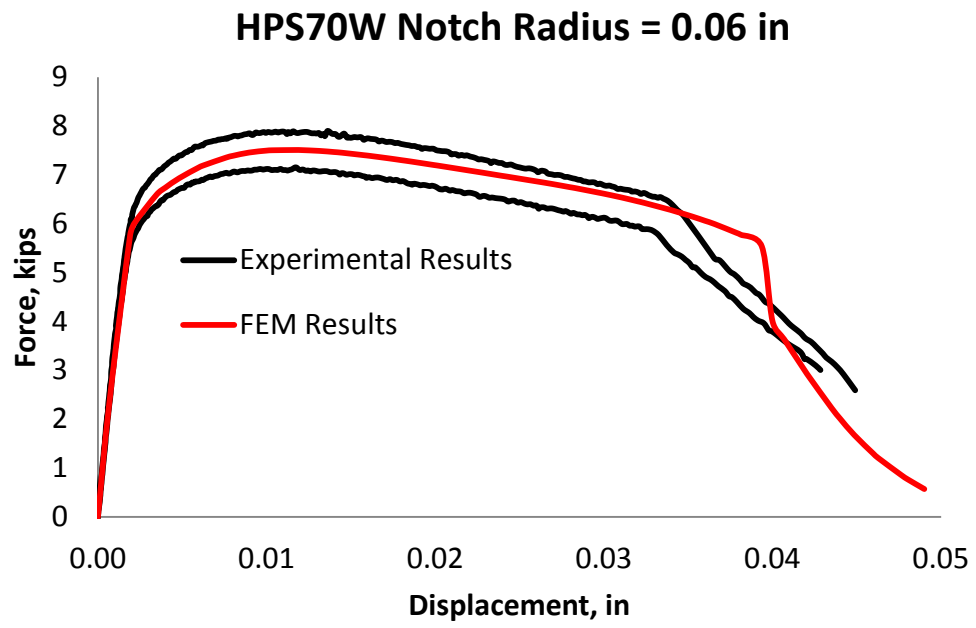

Figure 5.26: Calibration results for CNT-KanHPS70W-P-3 to CNT-KanHPS70W-P-4 with notch radius of 0.06 inches and an error value of 0.120

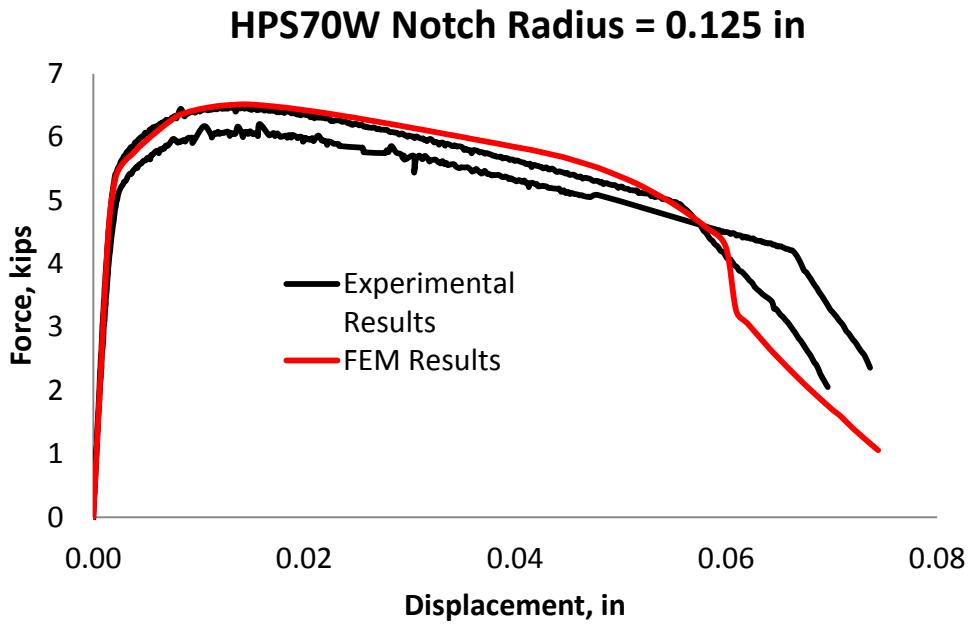

Figure 5.27: Calibration results for CNT-KanHPS70W-P-1 to CNT-KanHPS70W-P-2 with notch radius of 0.125 inches and an error value of 0.120

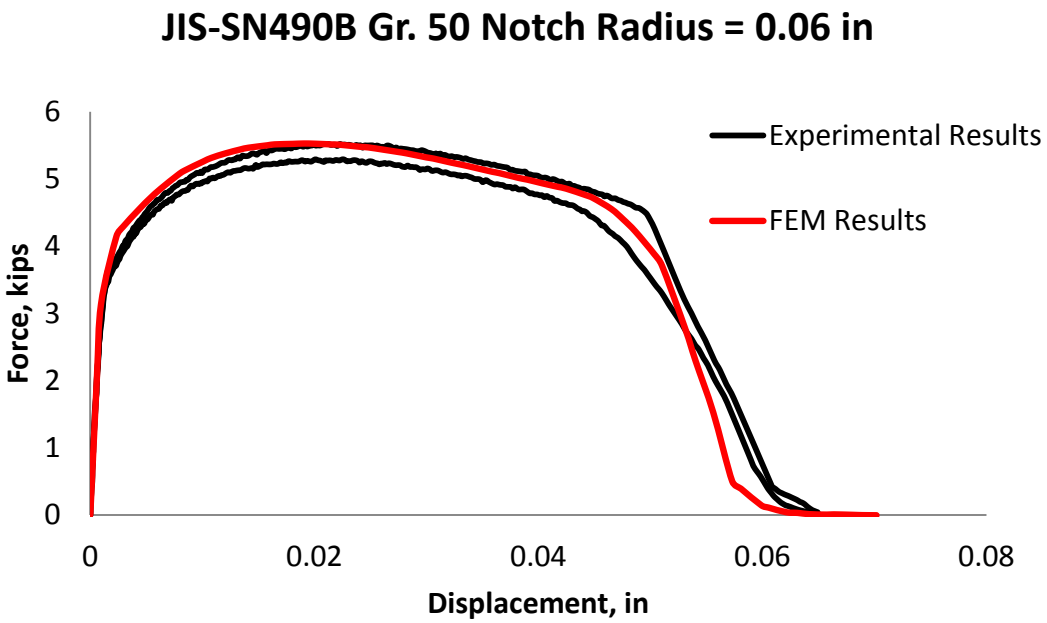

Figure 5.28: Calibration results for CNT-KanSN490B-P-3 to CNT-KanSN490B-P-4 with notch radius of 0.06 inches and an error value of 0.064

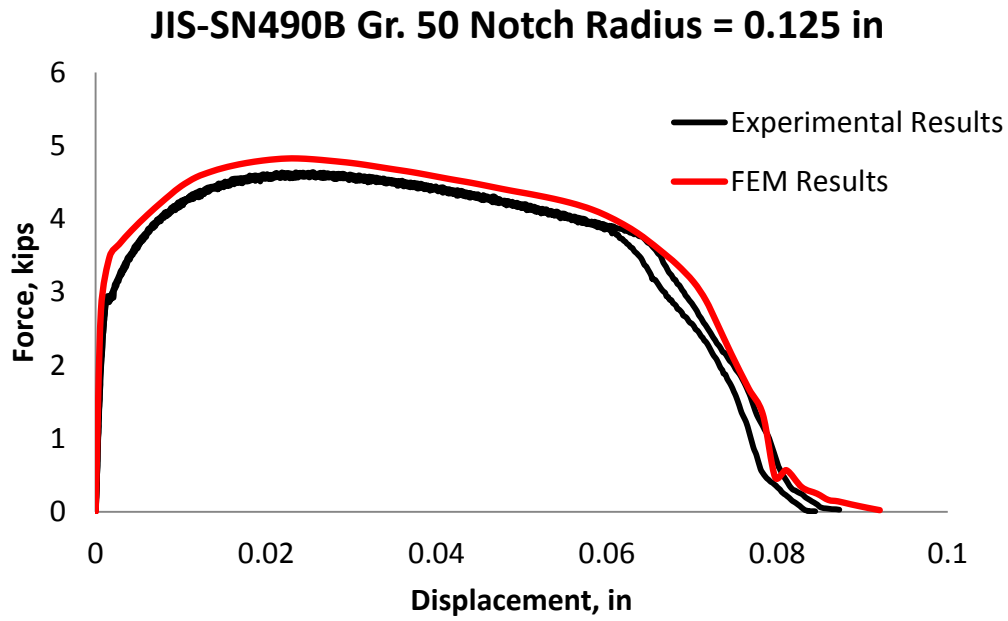

Figure 5.29: Calibration results for CNT-KanSN490B-P-1 to CNT-KanSN490B-P-1 with notch radius of 0.125 and an error value of 0.064

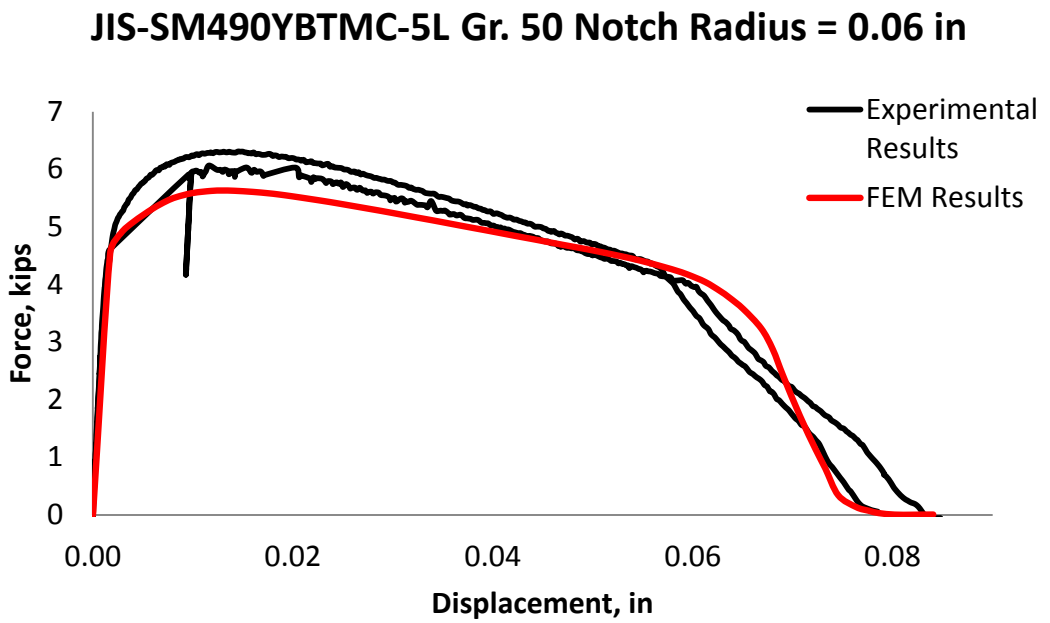

Figure 5.30: Calibration results for CNT-KanSM490YBTM-P-3 to CNT-KanSM490YBTM-P-4 with notch radius of 0.06 and an error value of 0.084

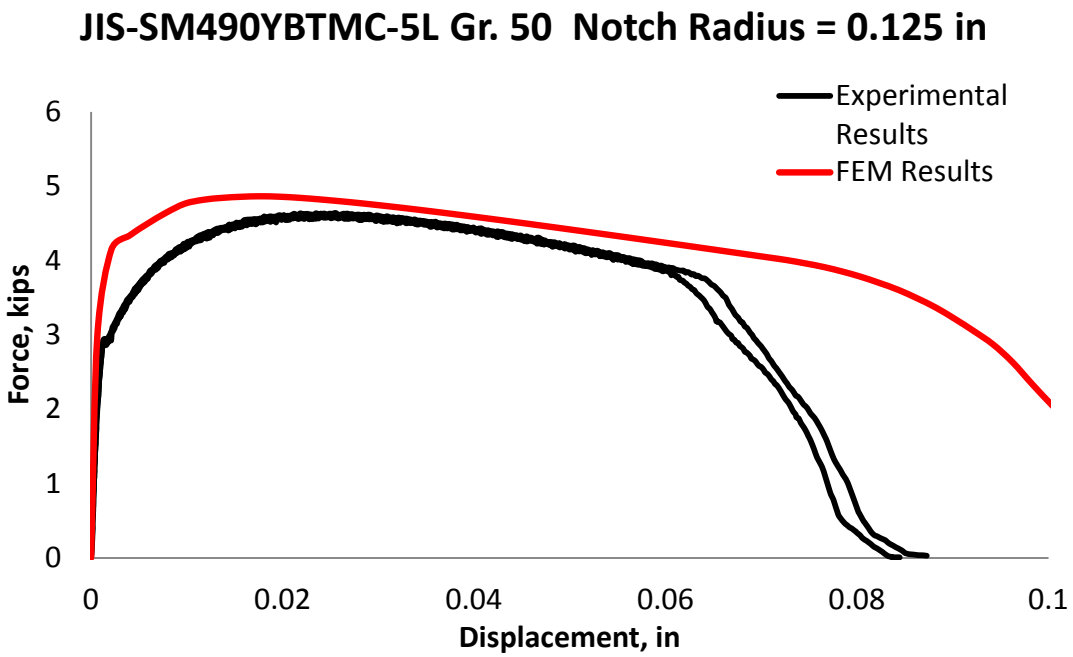

Figure 5.31: Calibration results for CNT-KanSM490YBTM-P-1 to CNT-KanSM490YBTM-P-2 with notch radius of 0.125 and an error value of 0.084

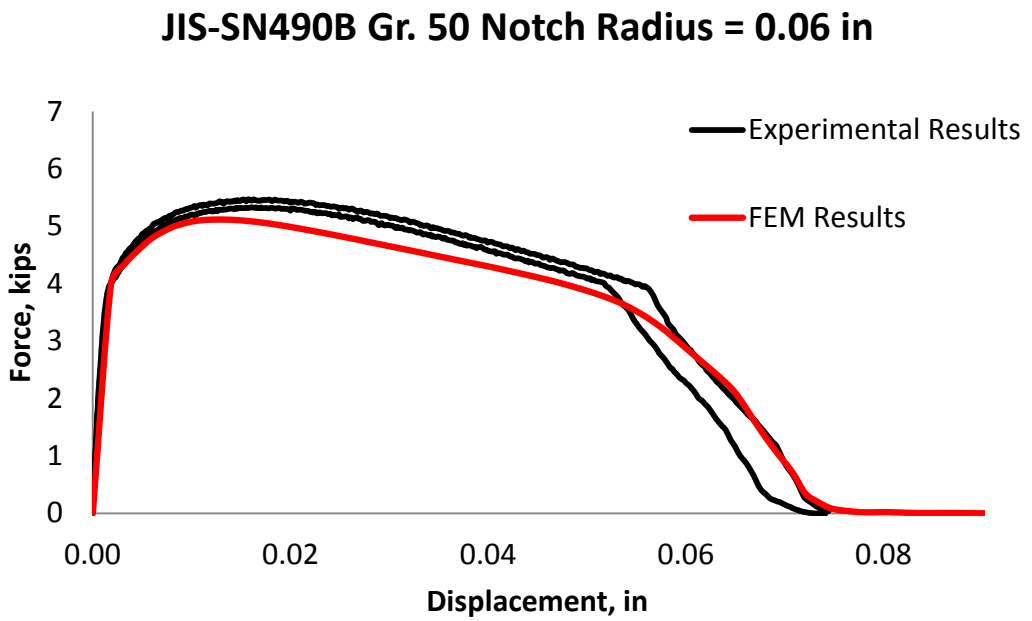

Figure 5.32: Calibration results for CNT-KanSN490B-W-L-3 to CNT-KanSN490B-W-L-4 with notch radius of 0.06 and an error value of 0.084

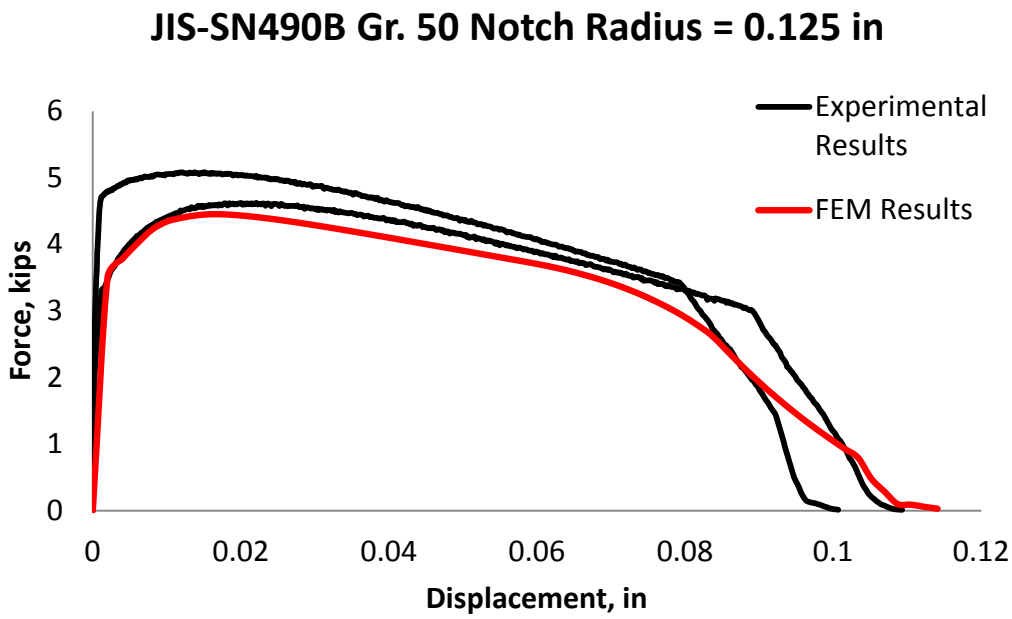

Figure 5.33: Calibration results for CNT-KanSN490B-W-L-1 to CNT-KanSN490B-W-L-2 with notch radius of 0.125 and an error value of 0.084

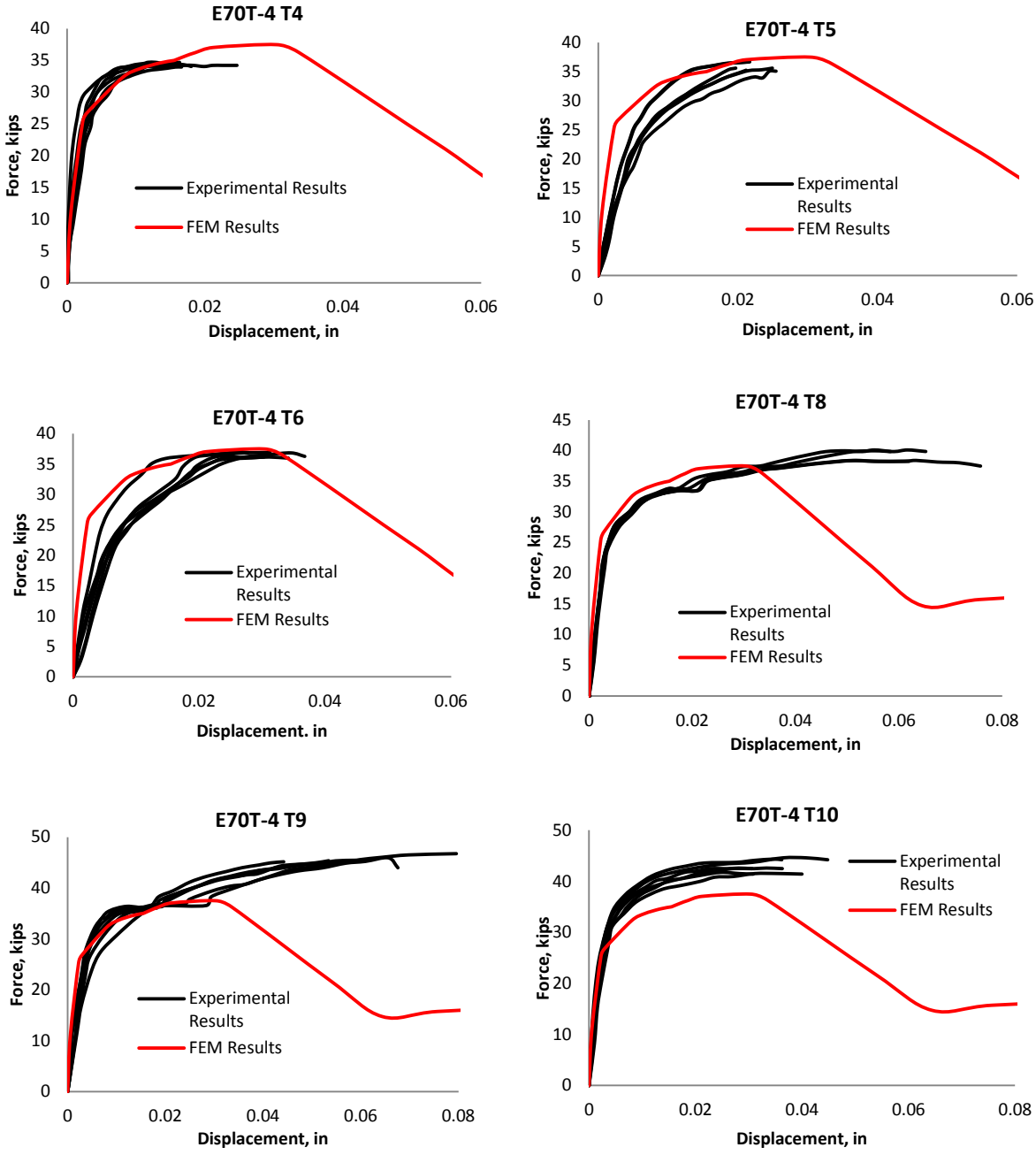

Figure 5.34: Calibration results of LPT-NgE70-T4-P-6.4A using transversely lapped specimen with 0.25 inches thick weld size and with an error of 0.362

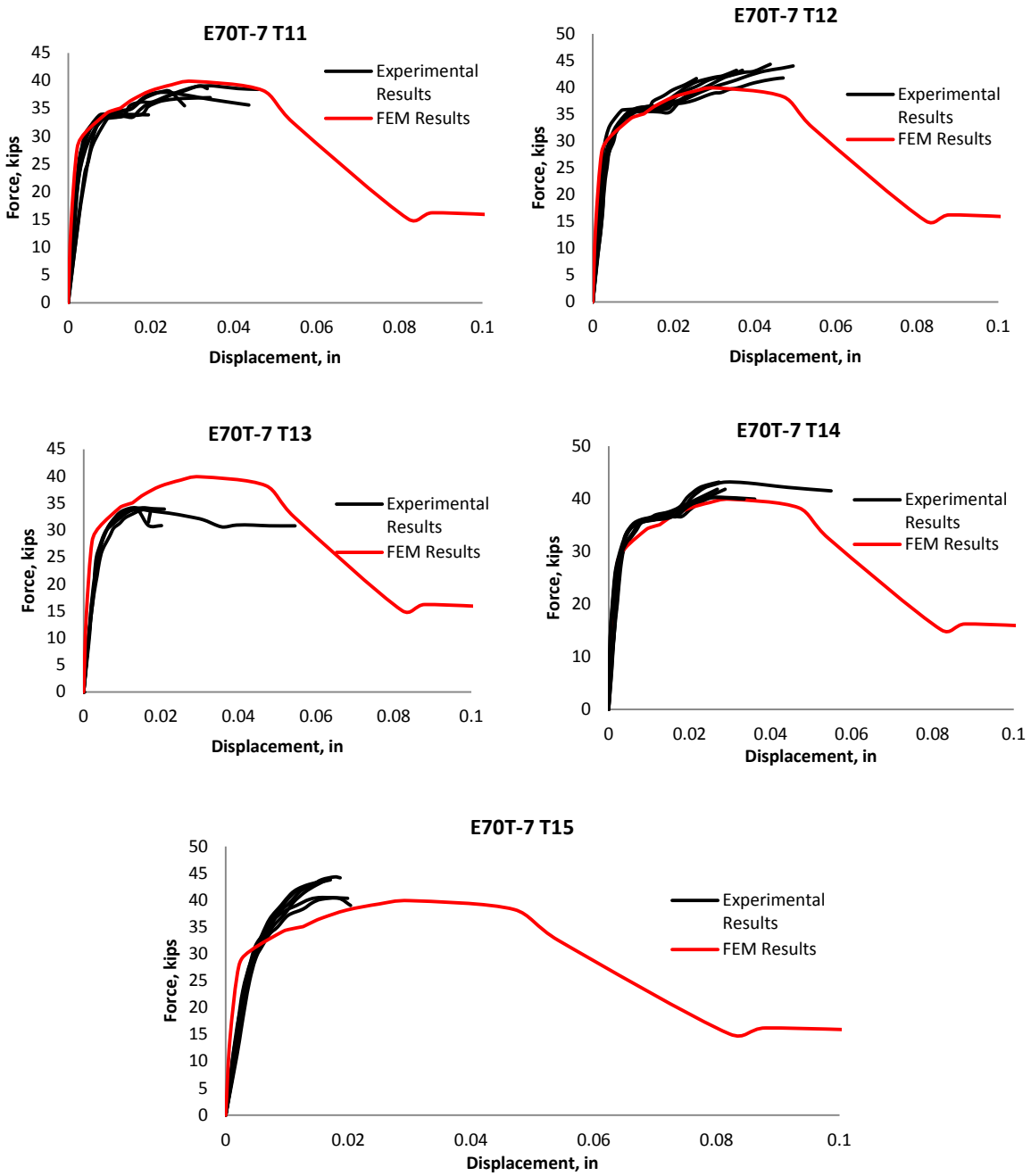

Figure 5.35: Calibration results of LPT-NgE70-T7-P-6.4A using transversely lapped specimen with 0.25 inches thick weld size and with an error of 0.362

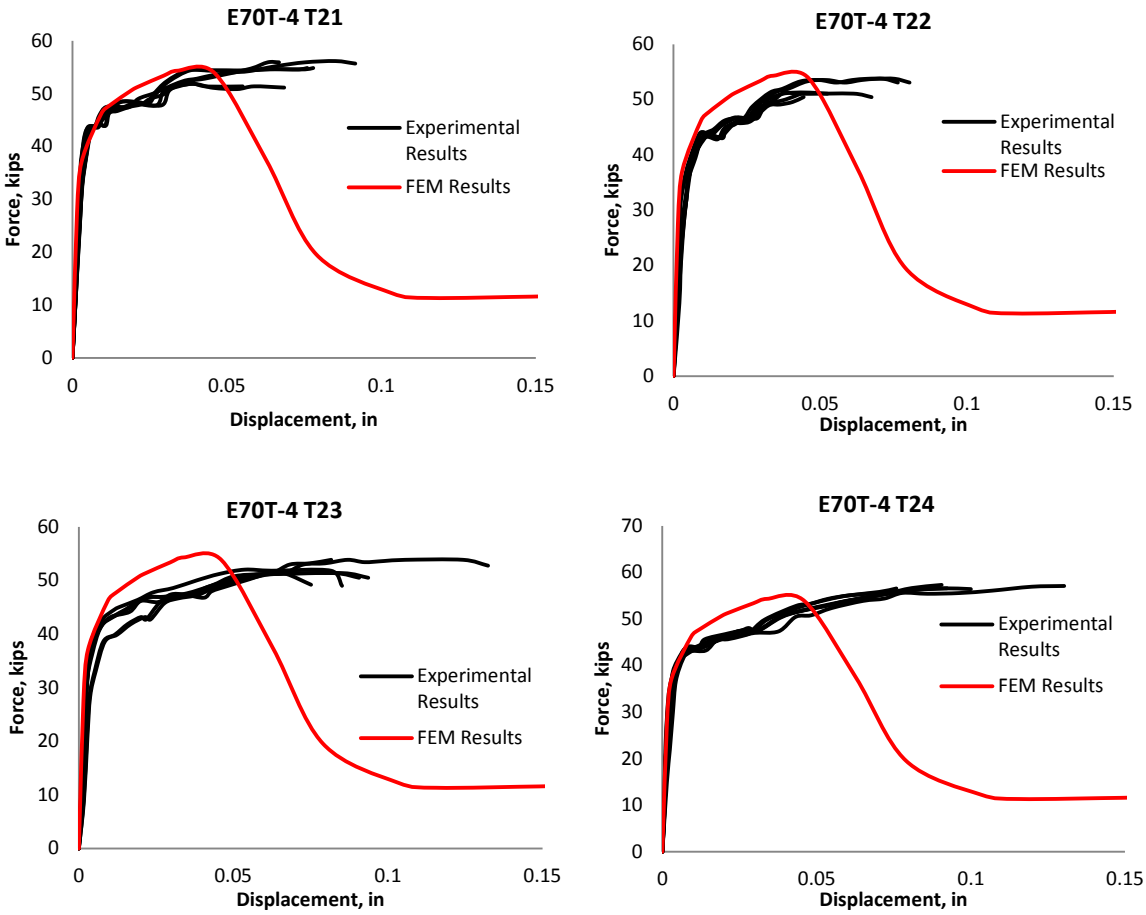

Figure 5.36: Calibration results of LPT-NgE70-T4-P-12.7A using transversely lapped specimen with 0.50 inches thick weld size and with an error of 0.362

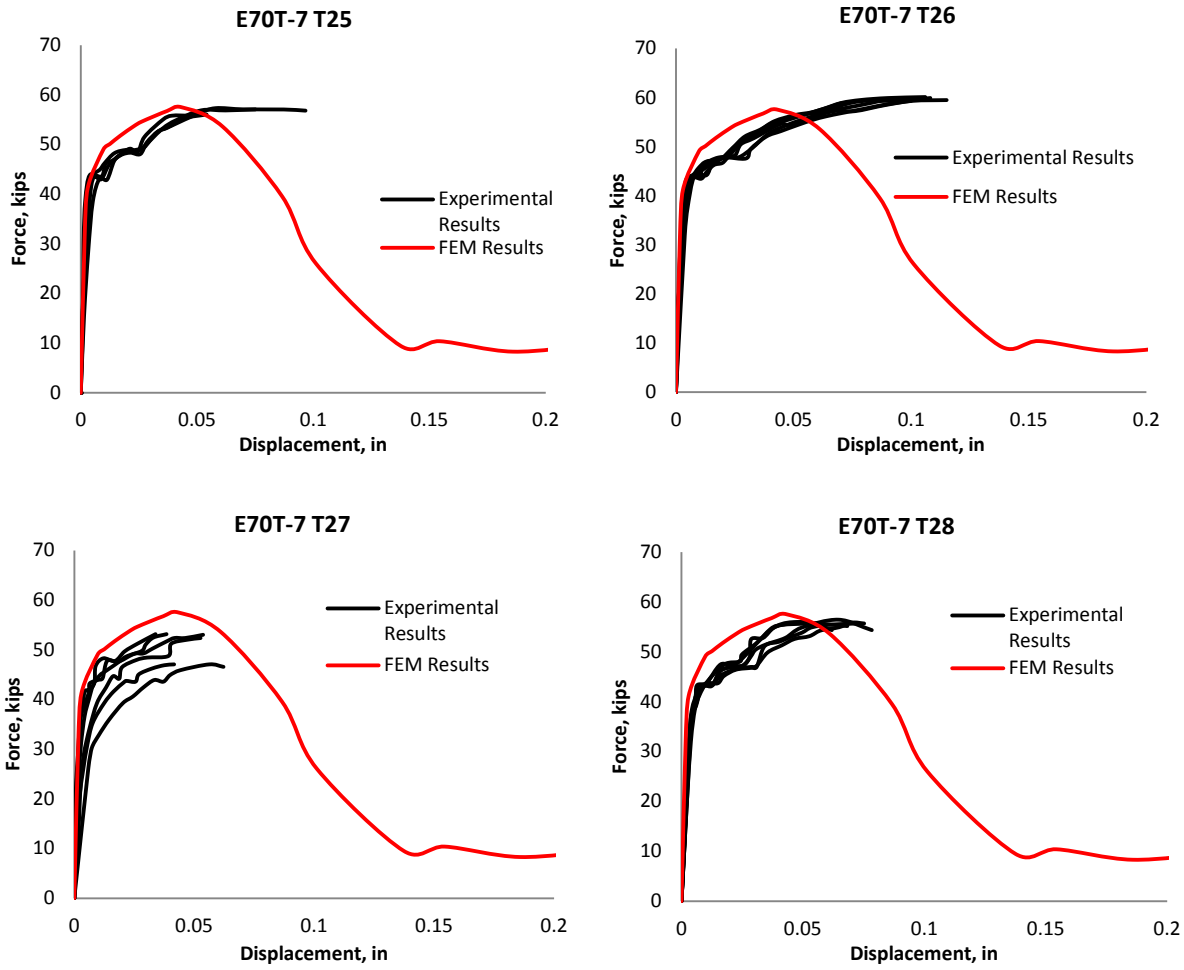

Figure 5.37: Calibration results of LPT-NgE70-T7-P-12.7A using transversely lapped specimen with 0.50 inches thick weld size and with an error of 0.362

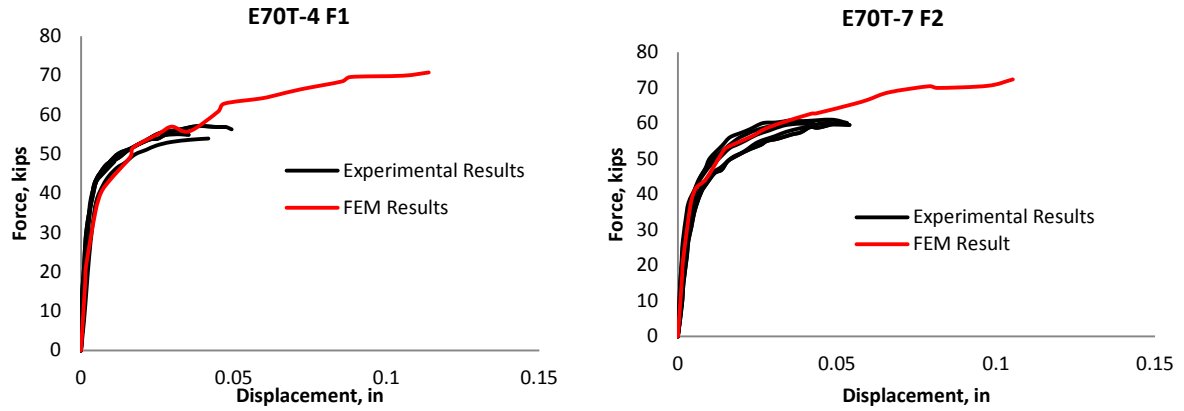

Figure 5.38: Calibration results of LP45-DenE70-T4-P-12.7F1 (left) and LP45-DenE70-T7-P-12.7F2 (right) for a 45 degree lapped specimen with 0.50 inches thick weld size and with an error of 0.362

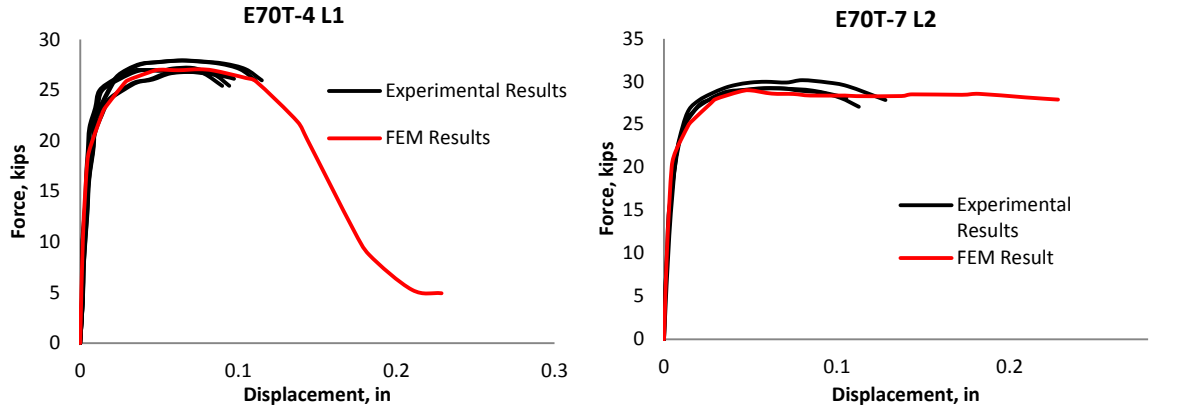

Figure 5.39: Calibration results of LPL-DenE70-T4-P-12.7L1 (left) and LPL-DenE70-T7-P-12.7L2 (right) for a longitudinally lapped specimen with 0.50 inches thick weld size and with an error of 0.362

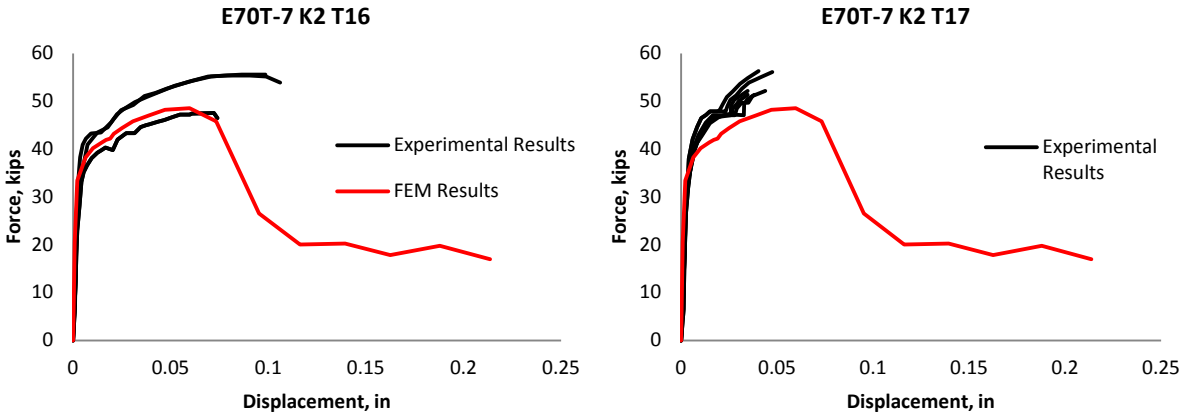

Figure 5.40: Calibration results of LPT-NgE70T-7K2-P-6.4A for a transversely lapped specimen with 0.50 inches thick weld size and with an error of 0.321

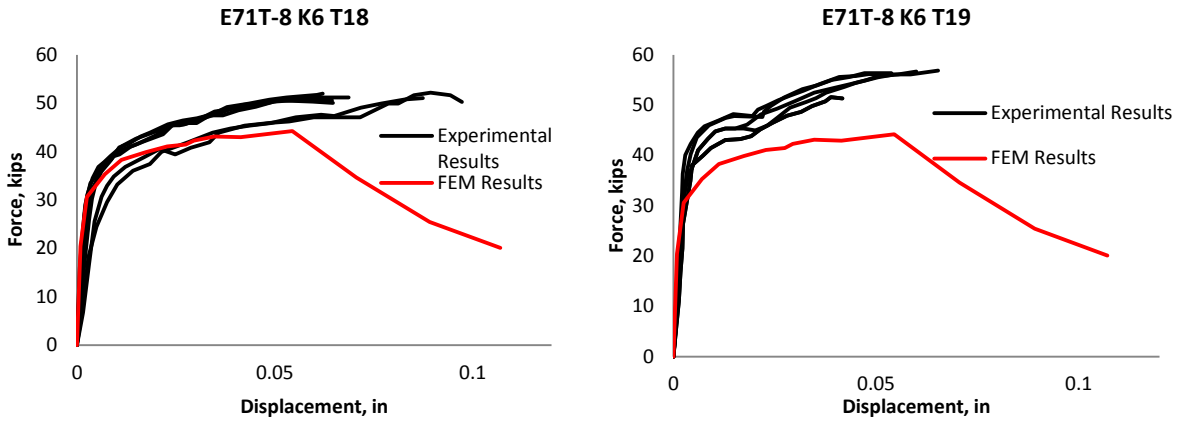

Figure 5.41: Calibration results of LPT-NgE70T-8K6-P-6.4A for a transversely lapped specimen with 0.25 inches thick weld size and with an error of 0.321

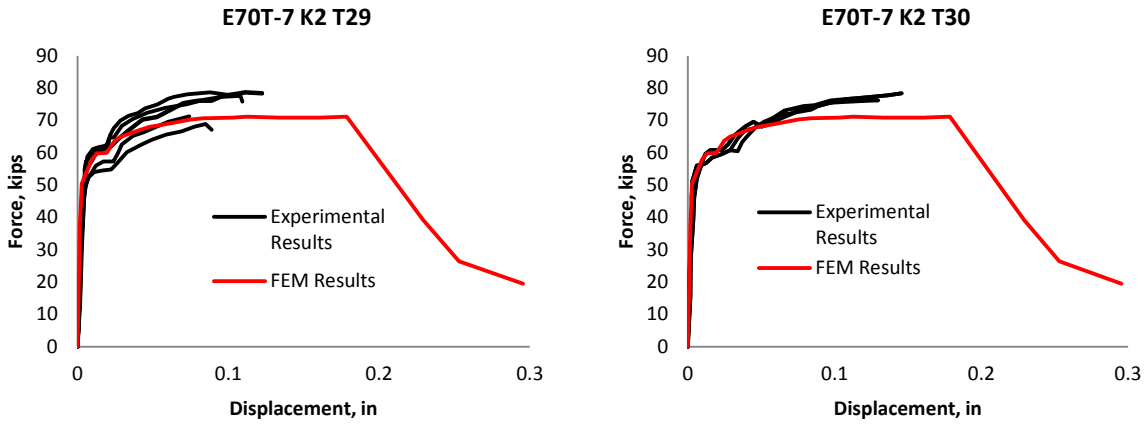

Figure 5.42: Calibration results of LPT-NgE70T-7K2-P-12.7A for a transversely lapped specimen with 0.50 inches thick weld size and with an error of 0.321

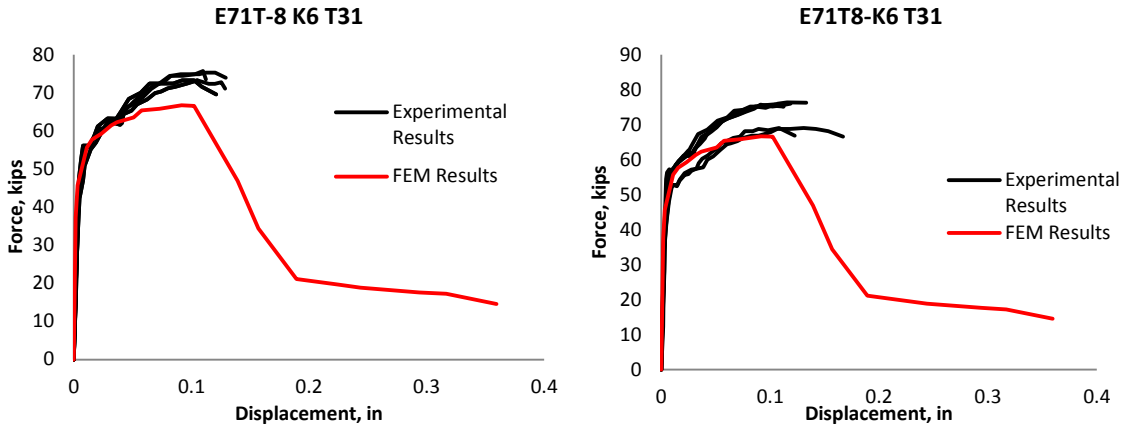

Figure 5.43: Calibration results of LPT-NgE70T-8K6-P-12.7A for a transversely lapped specimen with 0.50 inches thick weld size and with an error of 0.321

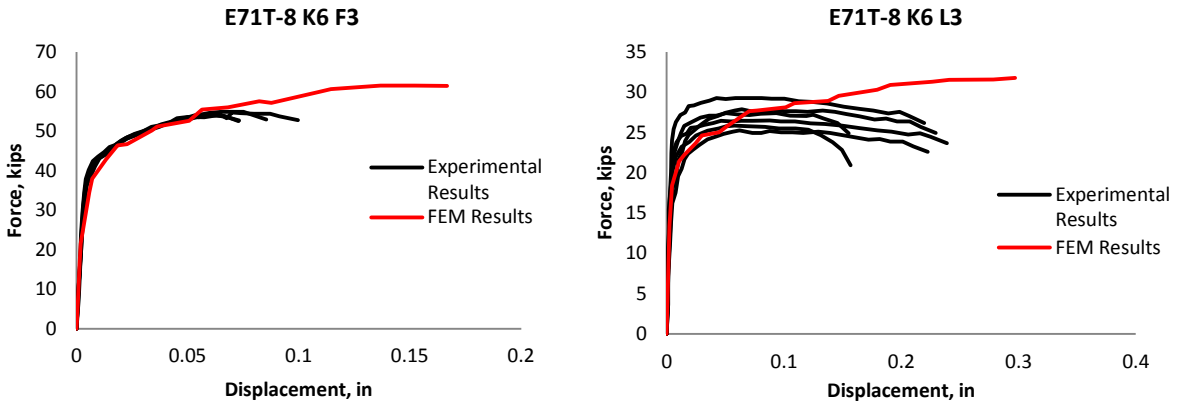

Figure 5.44: Calibration results of LP45-DenE70T-8K6-P-12.7F3 (left) and LPL-DenE70T-8K6-P-12.7L3 (right) lapped specimen with 0.50 inches thick weld size and with an error of 0.321

5.4 Calibration of Bao-Wierzbicki Model

This study is also focused on the calibration of the Bao–Wierzbicki criterion for low and negative triaxiality regions because it covers the fracture modes in those regions. Furthermore, the Bao–Wierzbicki model parameter can be calibrated from basic material test data for industrial applications (Yu et al. 2010). For low and negative triaxiality range Bao-Wierzbicki model provides analytical method for calibrating *m* parameter from which one could calculate C_1 and C_2 parameters from experimental data of a standard tensile coupon specimen (Bao et al. 2004). This method described by Equation (4.4 allows for the possibility to determine the fracture locus in low and negative triaxiality range without having experimental test results in those triaxiality ranges, making this model a good compromise between accuracy and practicality.

The parameters C_1 and C_2 represent the value of equivalent plastic strain at fracture initiation at 0 and 1/3 triaxiality. The parameter $C_2$is determined by Equation (5.5. If the true strain value after initiation of necking was determined by the reduction of area, A_R, then one can take that value of strain at fracture initiation for C_2. The variable C_2 represents the ductility of the material or the critical equivalent plastic strain at fracture initiation of a tensile coupon specimen, which has an assumed triaxiality of 1/3. As discussed earlier, in the original calibration by (Lee et al. 2004), the triaxiality was treated as an average over deformation history, and in particular the value of triaxiality for C_2 was calibrated at a value of triaxiality greater than 1/3. However, in this study a value of 1/3 is used as an approximation of the triaxiality at the center of the uniaxial tensile specimen (Yu et al. 2010).

$$C_2 = -\ln(1 - A_R) \tag{5.5}$$

Parameter C_1 is determined by Equation (5.6. In this equation m is the hardening exponent of a power law for isotropic strain hardening which needs to be calibrated. The variable C_1 represents the critical equivalent plastic strain at fracture initiation for state of pure shear, zero triaxiality. Equation (5.6 is based on the hypothesis of a maximum shear stress fracture condition (Yu et al. 2010).

$$C_1 = C_2\left(\frac{\sqrt{3}}{2}\right)^{1/m} \tag{5.6}$$

The value of *m* was determined by fitting a power law type regression to an isotropic strain hardening curves for a particular material. The power law for isotropic strain hardening is given by Equation (5.7.

$$\sigma = K_p \varepsilon^m \tag{5.7}$$

The values of C_1 and C_2 and associated parameters are provided in Table 5.5 for the experiments used in this work to calculate these values. To achieve this calibration, the isotropic strain hardening plasticity curve and true strain at fracture were ascertained from dogbone tensile coupons specimens exhibiting a broad range of material characteristics for structural steel. This stress-strain plasticity curve is then fitted with regression analysis of a power law type given by Equation (5.7 to determine the value of the exponent *m* through least squares regression, where C_1 and C_2 are given by Equations (5.5 and (5.6. Examples of this approach are shown in Figure 5.45.

Table 5.5: The calibration of Bao-Wierzbicki model parameters

Author	Test	True Strain at Fracture	Hardening Exp.		Fit	B-W Coef.	
			K_p	m	R^2	C_2	C_1
Kanvinde	TC-KanA572-P-A	0.1740	164.43	0.2401	0.9672	0.17398	0.0956
Kanvinde	TC-KanA572-W-L-A	0.2257	119.25	0.1791	0.9972	0.22572	0.1011
Kanvinde	TC-KanA514-P-A	0.1268	132.58	0.0241	0.7419	0.12684	0.0003
Kanvinde	TC-KanHPS70W-P-A	0.2139	131.72	0.0865	0.9527	0.21388	0.0405
Kanvinde	TC-KanSN490B-P-A	0.2652	140.15	0.2373	0.9875	0.26518	0.1446
Kanvinde	TC-KanSM490YBTM-P-A	0.2550	122.5	0.1708	0.9868	0.25496	0.1098
Kanvinde	TC-KanSN490B-W-L-A	0.2371	121.62	0.1945	0.9976	0.23709	0.1132
Myers	TC-MyeA992-W-L-A	0.2485	128.52	0.1793	0.9982	0.24853	0.1114
Myers	TC-MyeA992-W-T-A	0.2485	128.52	0.1793	0.9982	0.24853	0.1114
Myers	TC-MyeA36-B-A	0.1793	135.51	0.2356	0.9937	0.17930	0.0974
Myers	TC-MyeE70-T6-W-T-A	0.1822	110.33	0.0826	0.9519	0.18220	0.0319
Myers	TC-MyeE70-T6-W-L-A	0.1823	113.3	0.0892	0.9598	0.18225	0.0363
NIST Sadek	TC-SadA992-W-W-A	0.1851	121.79	0.1458	0.9985	0.18510	0.0690
NIST Sadek	TC-SadA992-Col-F-A	0.2329	117.07	0.1804	0.9939	0.23286	0.1049
Ng	TC-NgE70-T4-P-A	0.1820	139.52	0.1674	0.9959	0.18197	0.0771
Ng	TC-NgE70-T7-P-A	0.1701	141.11	0.1175	0.9559	0.17008	0.0500
NIST Sadek	Bolt-SadA490-B-A	0.2000	168.93	0.1149	0.9656	0.20000	0.0572

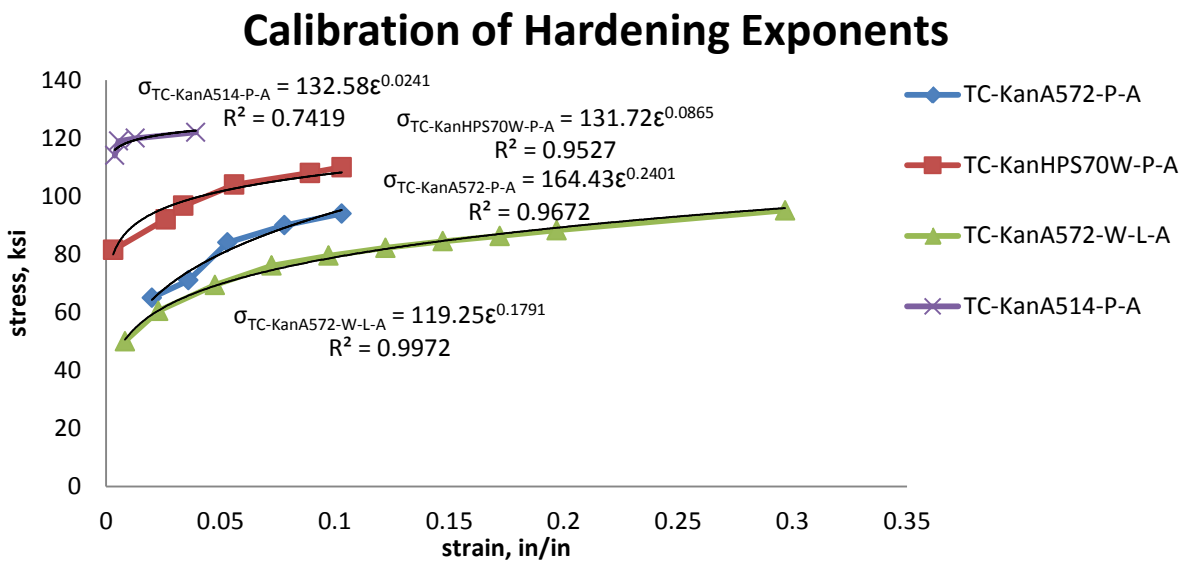

Figure 5.45: Calibration of the hardening exponent of a power law for isotropic strain hardening for use in determining C_1

5.5 Variation of Fracture Critical Parameters During Simulations

The variation of triaxiality and related fracture parameters during loading and its effect on fracture is documented in circumferentially notched tensile specimens in this section. The development and evolution of stress triaxiality and important model components at critical locations are important to document to better understand fracture in steel structures. This documentation comes from the eighth-sized simulations of CNTs using appropriate boundary conditions described above. Figure 5.46 shows the location of each of the elements through the thickness of the CNT for each of the subsequent plots. The elements are numbered 1 through 9 with 1 being at the center of the specimen and 9 being on the surface of the notch. In this section, the results for A572 Grade 50 specimens CNT-KanA572-P-1 till CNT-KanA572-P-7 are

shown and discussed. However, the general trends shown here are found in other structural steel specimens. The results for other CNTs are shown in Appendix B.

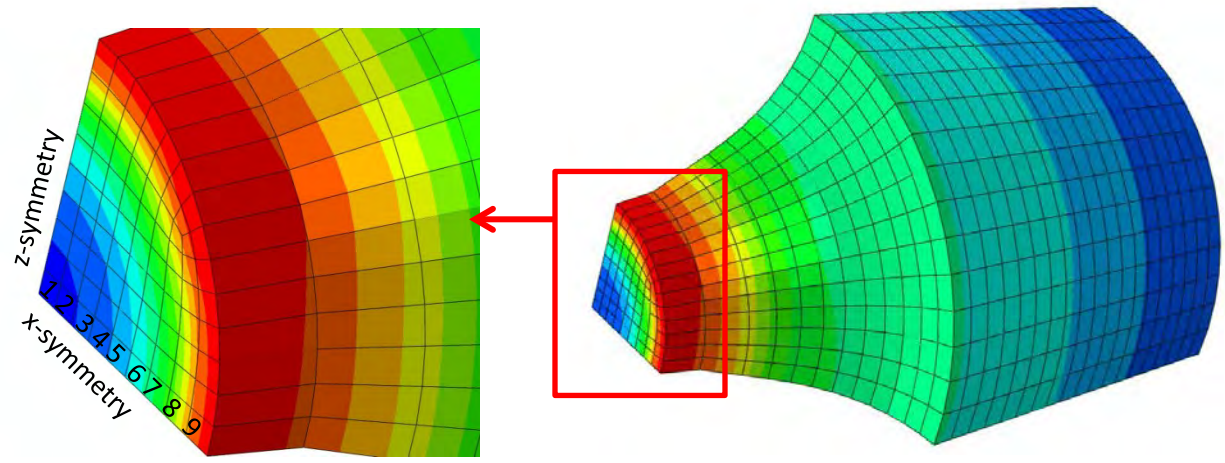

Figure 5.46: Location of each element through the thickness of the CNT specimen. The specimen is shown during loading with countors representing von Mises stress

The variation of triaxiality as the specimens are being loaded for elements laid out through the thickness of the specimen is shown in Figure 5.47, Figure 5.48, and Figure 5.49. Several observations could be made about the variation of triaxiality through thickness of the CNT specimen. The first observation is that the overall or average triaxiality that an element experiences declines as a function of the distance away from the center of a CNT specimen. This confirms the general conclusion reached in the literature about triaxiality in CNT specimens (Anderson 2005). The material on the outer surface has less constraint to plastic flow than elements at the center, which experience more of a plain strain condition, while elements on the outer surface experience more of a plane stress condition (Anderson 2005). This should allow for more deformation capacity for the outer material. This variation of triaxiality across the specimen thickness also calls into question the assumption of average triaxiality across specimen surface which is commonly used to determine the fracture locus (Bao et al. 2004;

Wierzbicki et al. 2005). However, for each element, it can be seen that triaxiality does not vary much throughout the loading until it reaches softening. This means that an average value of triaxiality per element can be used for calibration of fracture initiation models. Another important observation is that softening of stress and stiffness dramatically increases triaxiality in an element for all elements through the thickness of the specimen, except for the outermost ones. This signifies that the elements on the outer surface can successfully yield plastically during extreme loading while elements at the center behave in a more brittle manner by not yielding as much, thereby drastically increasing triaxiality. The reason for the dramatic increase in triaxiality in specimens with notch radius of 0.125 inches and 0.25 inches while for specimen with notch radius of 0.06 inches, the triaxiality increase is more moderate is due to the smaller notch affecting the boundary condition of the specimen by creating a higher concentration of triaxiality in the specimen.

Since the fracture locus is defined in the equivalent plastic strain and triaxiality space it is important to understand the variation of equivalent plastic strain across the CNT specimen thickness in addition to triaxiality. The variation of equivalent plastic strain during loading of the CNT specimens for elements laid out across the thickness of the specimen are shown in Figure 5.50, Figure 5.51, and Figure 5.52. There are clearly visible trends shown in these plots. The elements on the outer surface attain greater strain values than those that are at the center. In addition, as one moves from the center of the specimen, the strain value reached increases. However, the difference is not significant for elements at the center, but it is significant for the outer elements. For the notch radius of 0.125 inches and 0.25 inches the difference of equivalent plastic strain between elements is not significant while the material hardens in

plastic deformation. This is not the case for the specimen with a notch radius of 0.06 inches. In this specimen there is noticeable difference in equivalent plastic strain between elements during plastic hardening and it intensifies even more during softening. In addition, the slope of equivalent plastic strain against displacement is different for each specimen, but is similar for elements in a specimen except for the element on the outer surface of the notch. These differences are probably associated with different triaxiality experienced by elements in different specimens.

Since fracture locus is defined in this work in equivalent plastic strain and triaxiality space, it is also advantageous to study how each element is affected by the chosen fracture initiation criteria of VGM. This variation is shown in Figure 5.53, Figure 5.54, and Figure 5.55. In these plots, the vertical axis was chosen span from 0 to 0.80 for the equivalent plastic strain value and the horizontal axis was chosen to span from 0.2 to 1.4 for the triaxiality value to focus on the important element behavior. In addition, for all elements when they are deleted, the triaxiality value goes to zero; this is not plotted here to avoid cluttering the plot. For each element, the curve is thus plotted until the last data point before zero triaxiality. Several observations are possible from Figure 5.53, Figure 5.54, and Figure 5.55. As was shown in previous plots, after initiation of softening there is a tendency to dramatically increase triaxiality and this tendency becomes stronger as one moves from the outer surface to the center of the specimen. The softening does not necessarily occur when the element's equivalent plastic strain reaches the VGM criteria because Equation (4.6 takes into account the deformation histories illustrated by these plots. However, for elements numbered 1 to 5, there is at first a decrease of triaxiality with an increase in equivalent plastic strain and then an increase of triaxiality with increasing

deformation before softening initiation. Elements numbered 6 to 9 have a more constant level of triaxiality with deformation before softening initiation. It could also be observed that as the notch radius decreases of the CNT specimen the overall triaxiality range increases. In addition, as the notch radius increases the curves for each element across the specimen thickness are more spread out and the elements closer to the center tend to have similar triaxiality variation.

Fracture initiation is defined by Equation (4.6 and it accounts for the history of equivalent plastic strain with loading. This integral is calculated for each element in finite element simulations and determines when to initiate softening. The value of this fracture initiation integral is shown in Figure 5.56, Figure 5.57, and Figure 5.58. It can be seen that the slope or the change with displacement of this integral increases as a function of the distance from the outer surface to the center of a CNT specimen. This signifies that the material in the center of the specimen will initiate softening sooner than the material on the outer surface. This conforms to the conclusions reached in the literature that fracture is almost always initiated at the center of a CNT specimen (Kuwamura et al. 1997; Anderson 2005; Wierzbicki et al. 2005; Smith, C. M. 2013). In addition, it can be seen from these figures that as the notch size increases for the specimen there tends to be a greater difference between the curve of the inner and outer elements. This signifies that the larger notch radius allows for more use of the material on the surface of the notch than smaller notch sizes by increasing the relative amount of deformation the material on the surface can achieve to those in the center. The plateau at a value of the VGM integral of 1.0 signifies that the criteria for softening initiation has been met and stress and stiffness degradation is in progress, as described by Equations (4.7 through (4.10.

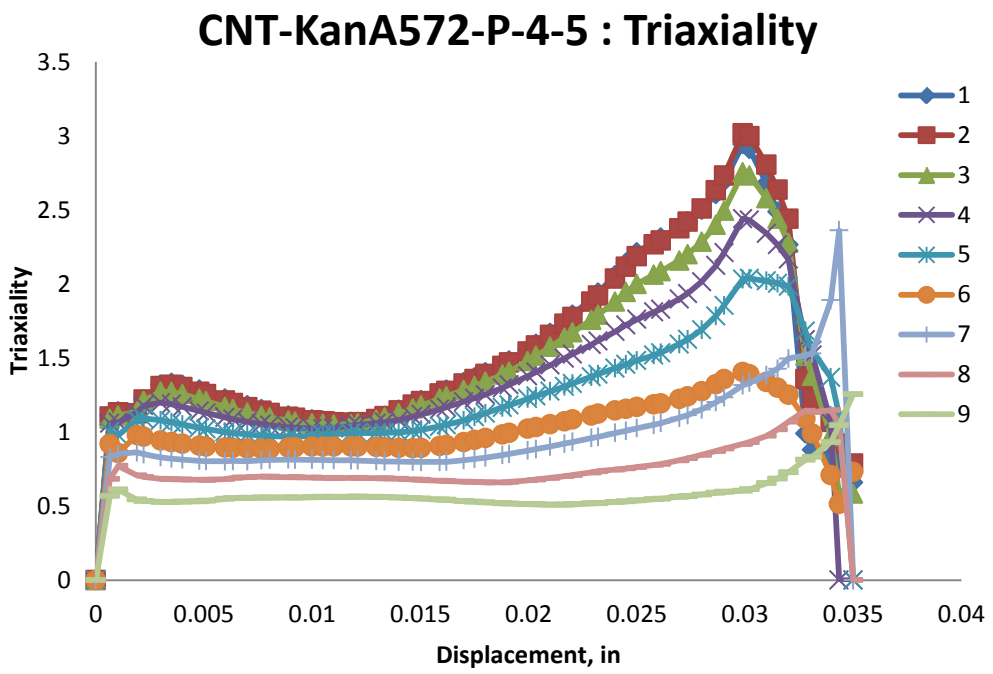

Figure 5.47: Variation of triaxiality with displacement for different elements laid out through the thickness of simulation of CNT-KanA572-P-4 and CNT-KanA572-P-5 specimens

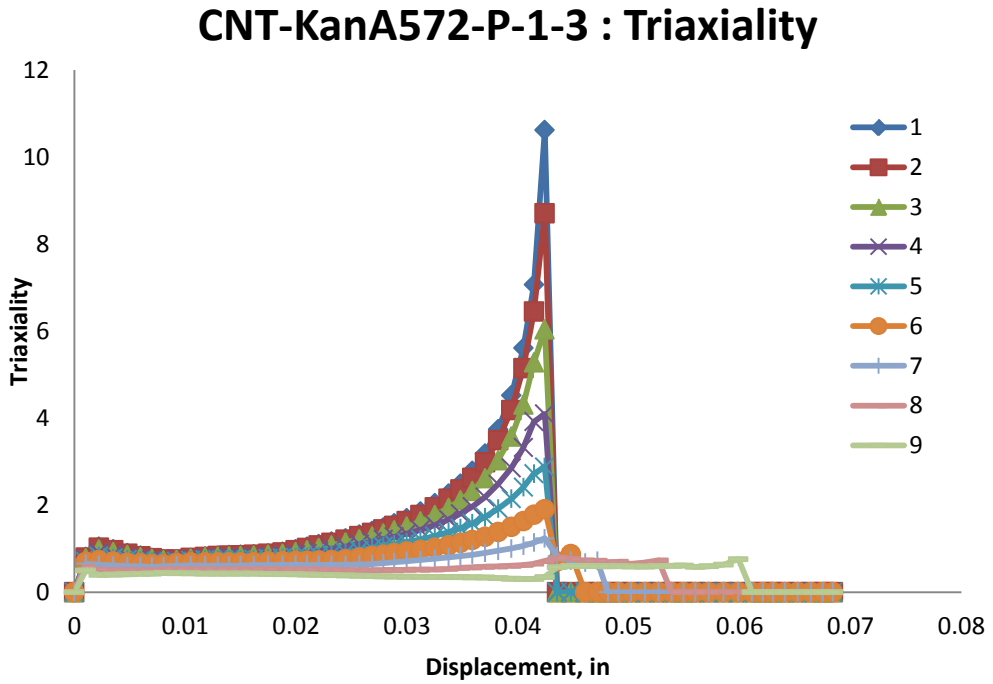

Figure 5.48: Variation of triaxiality with displacement for different elements laid out through the thickness of simulation of CNT-KanA572-P-1 to CNT-KanA572-P-3 specimen

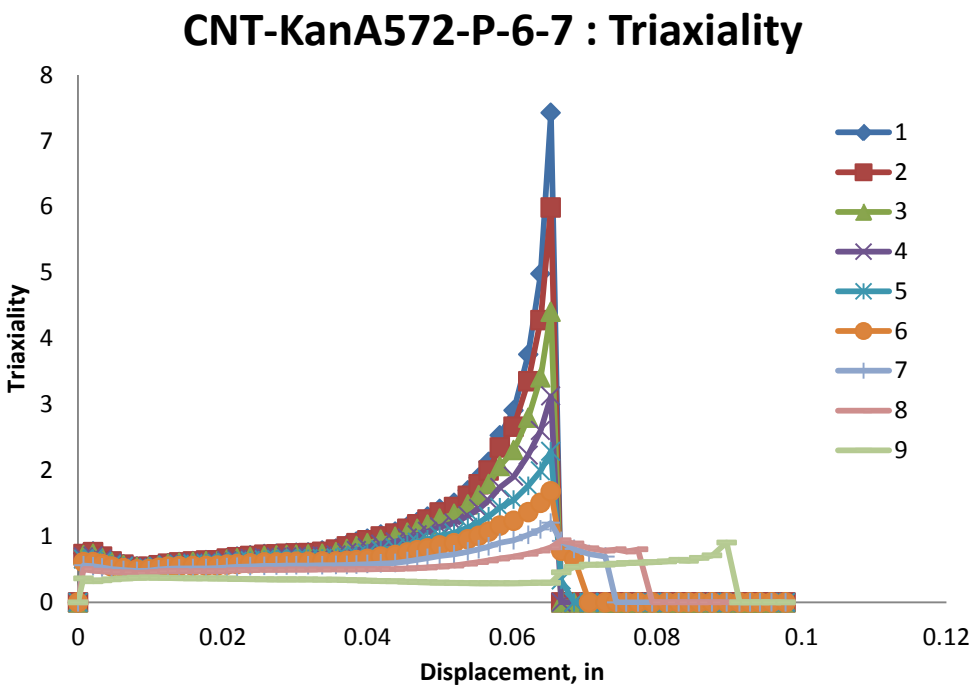

Figure 5.49: Variation of triaxiality with displacement for different elements laid out through the thickness of simulation of CNT-KanA572-P-6 and CNT-KanA572-P-7 specimens

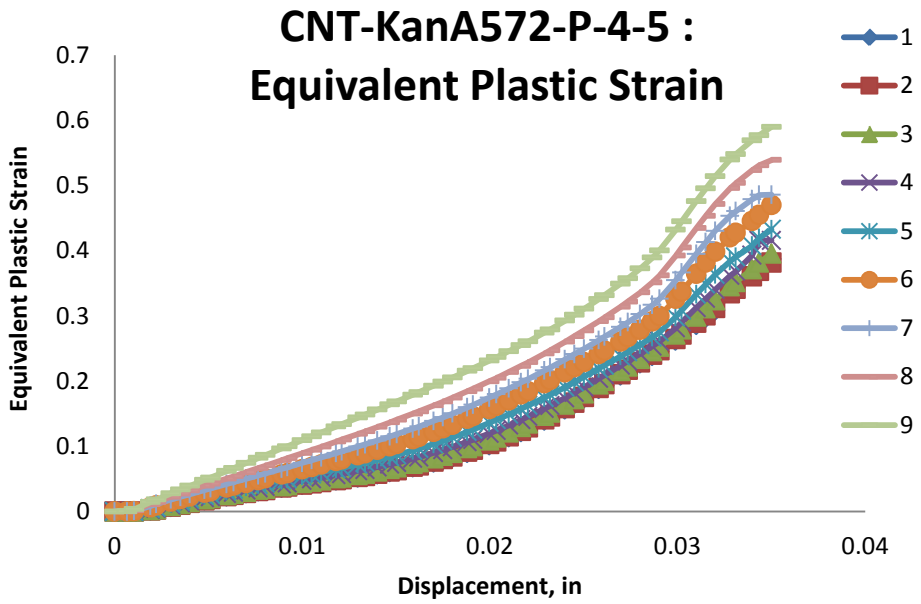

Figure 5.50: Variation of equivalent plastic strain with displacement for different elements laid out through the thickness of simulation of CNT-KanA572-P-4 and CNT-KanA572-P-5 specimens

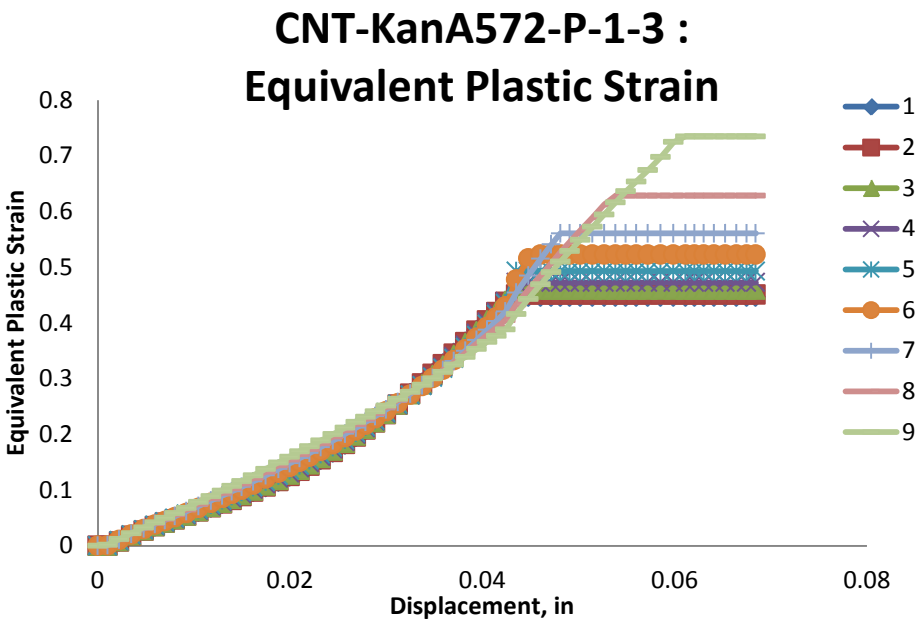

Figure 5.51: Variation of equivalent plastic strain with displacement for different elements laid out through the thickness of simulation of CNT-KanA572-P-1 to CNT-KanA572-P-3 specimens

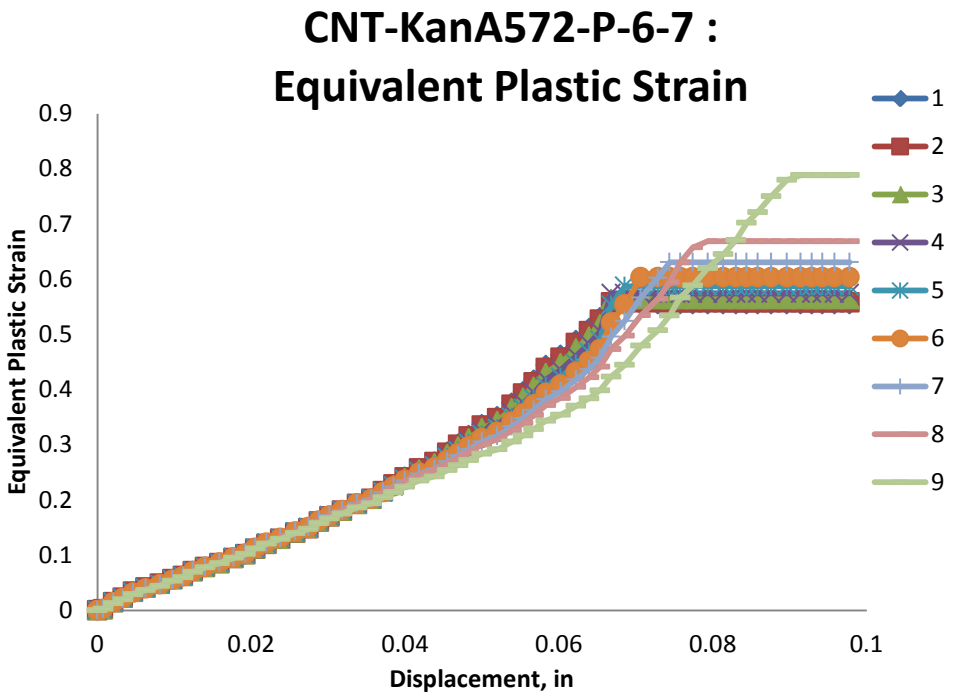

Figure 5.52: Variation of equivalent plastic strain with displacement for different elements laid out through the thickness of simulation of CNT-KanA572-P-6 and CNT-KanA572-P-7 specimens

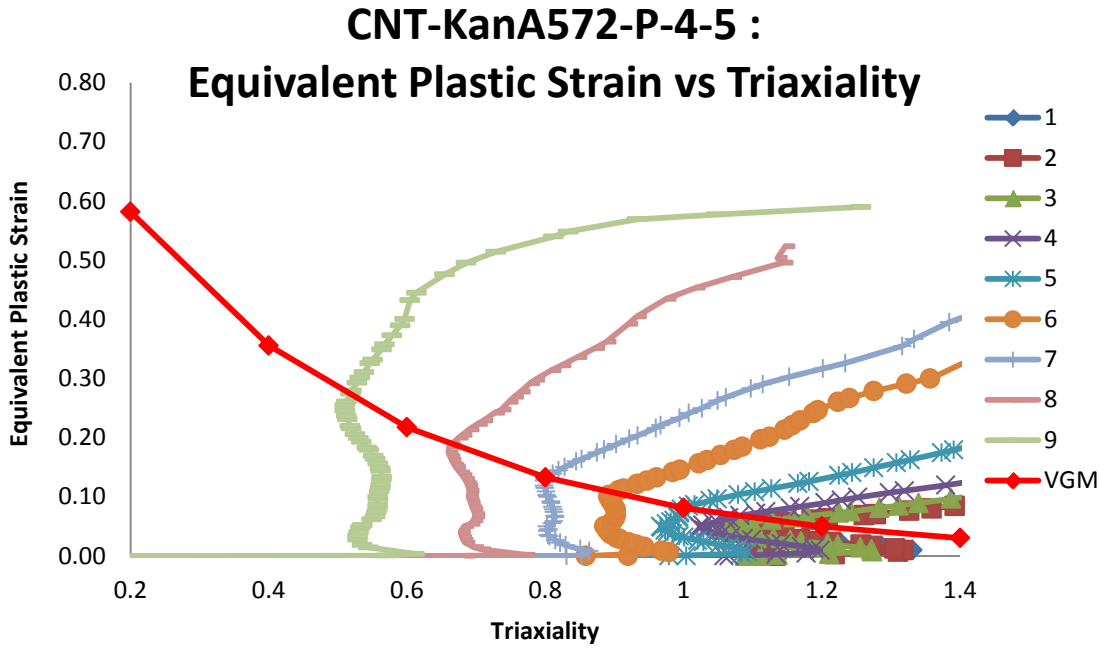

Figure 5.53: Variation of equivalent plastic strain versus triaxiality for different elements laid out through the thickness of simulation of CNT-KanA572-P-4 and CNT-KanA572-P-5 specimens

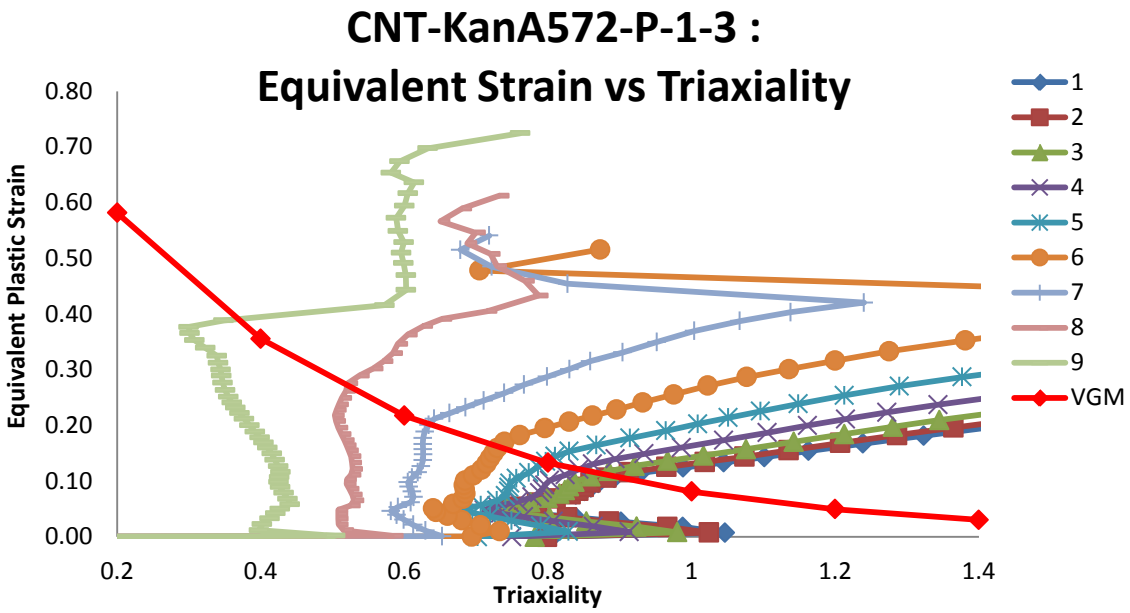

Figure 5.54: Variation of equivalent plastic strain versus triaxiality for different elements laid out through the thickness of simulation of CNT-KanA572-P-1 to CNT-KanA572-P-3 specimens

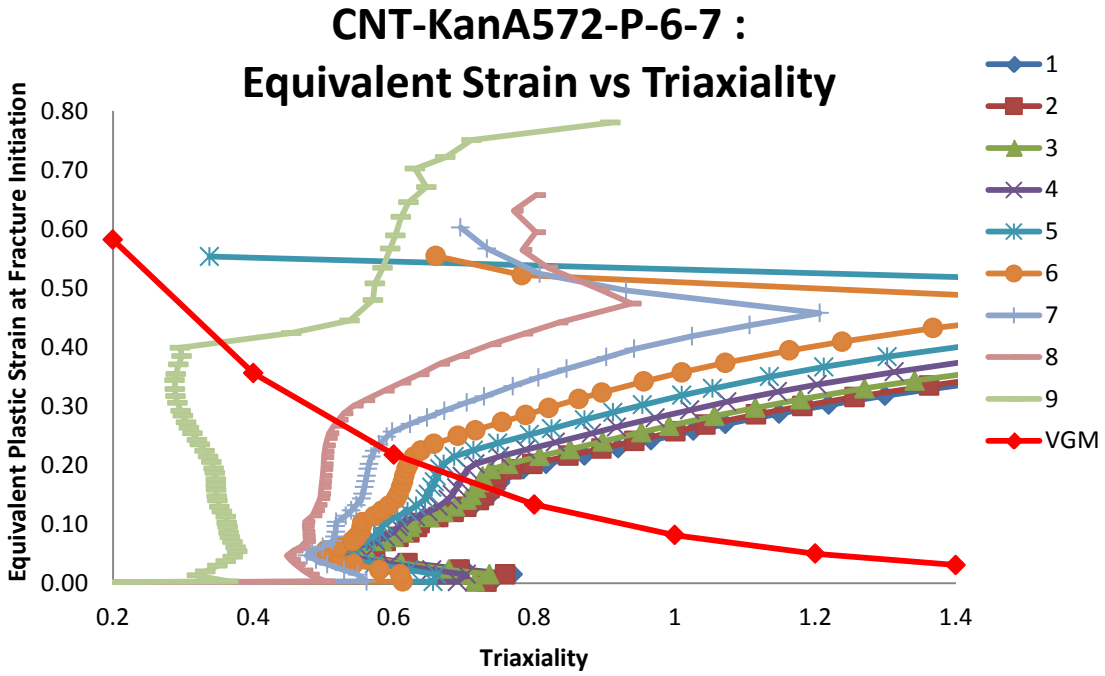

Figure 5.55: Variation of equivalent plastic strain versus triaxiality for different elements laid out through the thickness of simulation of CNT-KanA572-P-6 and CNT-KanA572-P-7 specimens

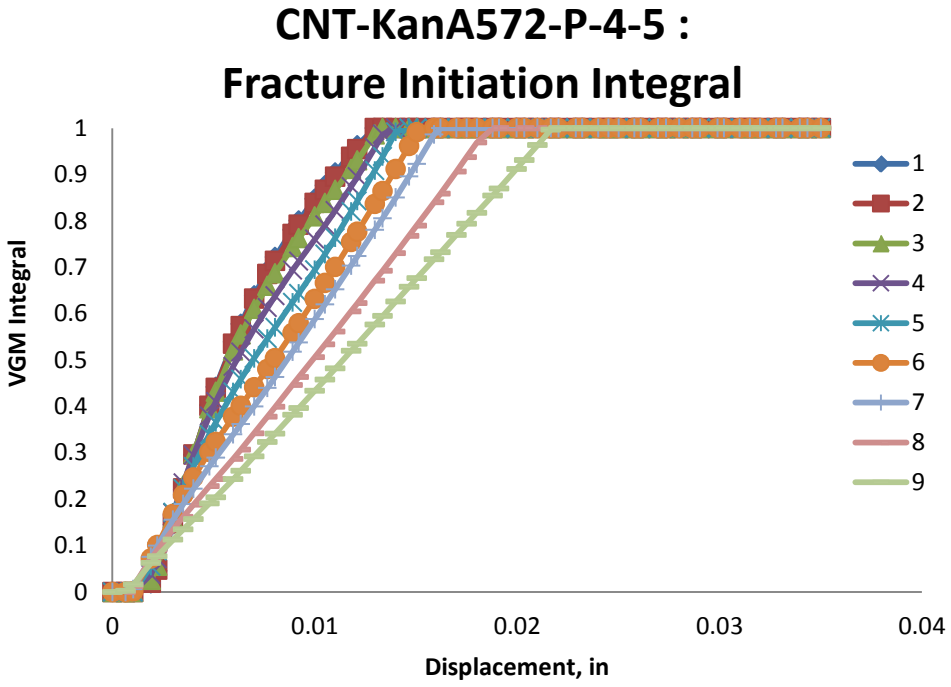

Figure 5.56: Value of fracture initiation integral for different elements laid out through the thickness of simulation of CNT-KanA572-P-4 and CNT-KanA572-P-5 specimens

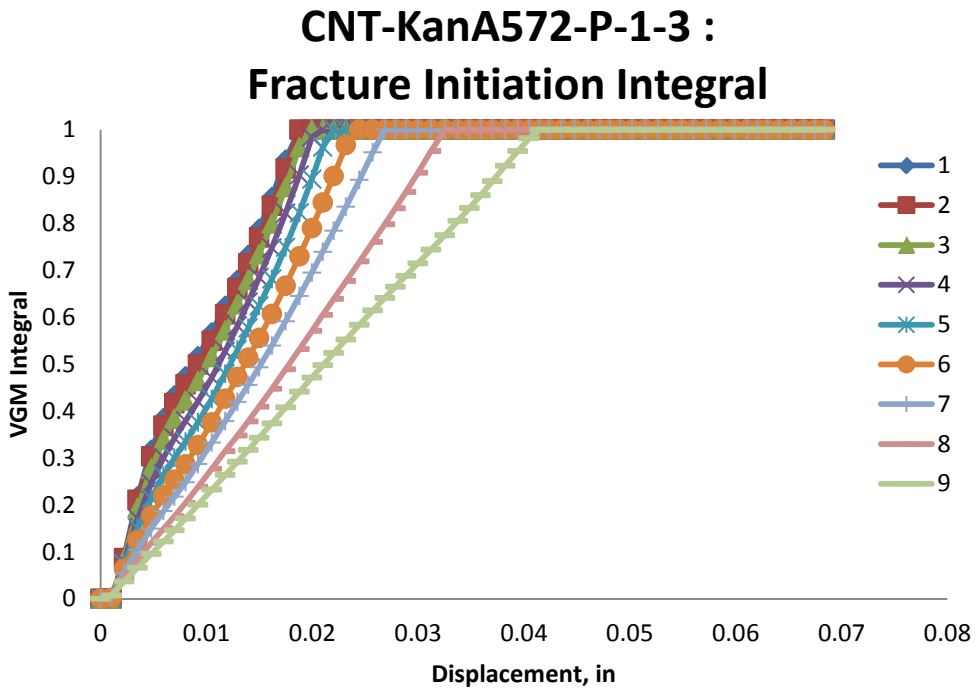

Figure 5.57: Value of fracture initiation integral for different elements laid out through the thickness of simulation of CNT-KanA572-P-1 to CNT-KanA572-P-3 specimens

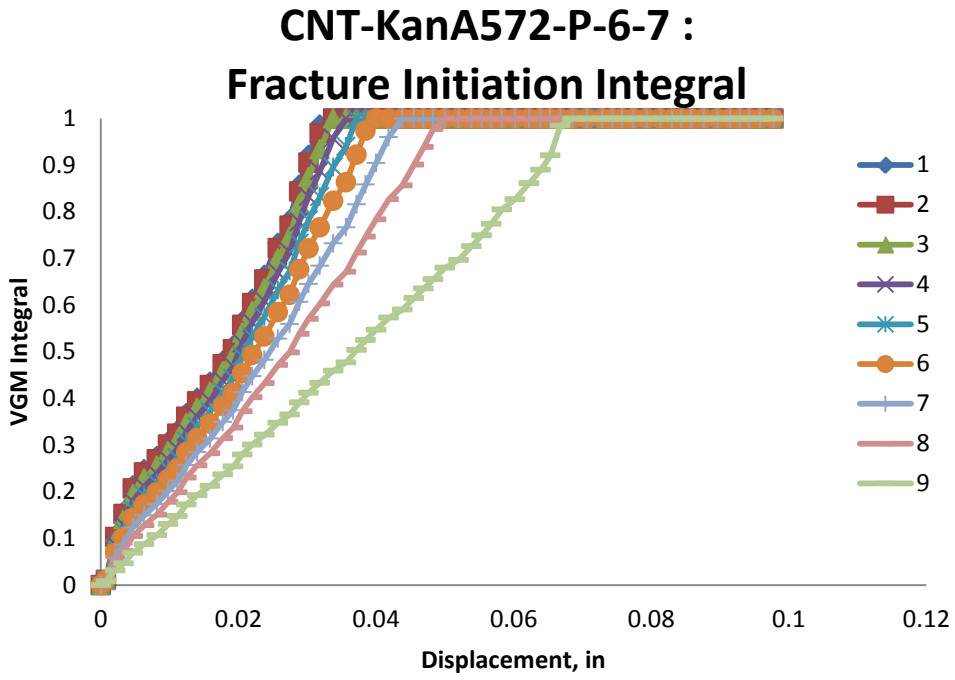

Figure 5.58: Value of fracture initiation integral for different elements laid out through the thickness of simulation of CNT-KanA572-P-6 and CNT-KanA572-P-7 specimens

Triaxiality is defined in Equation (3.1 as a ratio of mean stress to von Mises stress and is the main variable to determine the fracture initiation in ductile metals. For this reason, variation of von Mises stress with displacement is plotted in Figure 5.59, Figure 5.60, and Figure 5.61 for different elements across the thickness of the CNT specimen. It can be observed that the von Mises stress decreases and the displacement at fracture initiation and element deletion also decreases as a function of the distance from the outer surface of the specimen to the inner core, with an exception for the specimen with notch radius of 0.06 inches. For notch radii of 0.125 and 0.250 inches, all elements reach the yield stress at approximately the same displacement, but for the specimen with a notch radius of 0.06 inches, the element on the outer surface reaches the yield stress at a lower displacement than the ones at the center of the specimen. This is most likely related to the sharp notch radius that creates high triaxiality at the surface, forcing higher stress demand on the surface material than on the material at the center of the specimen. In addition, the area under the curve, signifying energy, dramatically increases as a function of the distance from the center of the specimen to the surface. The variation of mean stress versus displacement for finite elements located across the specimen thickness is plotted in Figure 5.62, Figure 5.63, and Figure 5.64. The variation of mean stress is opposite to that of von Mises stress. For mean stress, the elements on the surface of the specimen experienced lower stress levels than those at the center, with a gradual change in between. In addition, elements in the center experienced a higher growth rate of mean stress versus displacement, while the mean stress of the elements on the surface remained constant throughout the loading with a spike right before softening. In addition, the elements on the surface experienced a more gradual softening than those at the center. For a notch radius of

0.06 inches, all of the curves converged at the same displacement value for zero stress level, while for other specimens the outer elements achieved greater displacement.

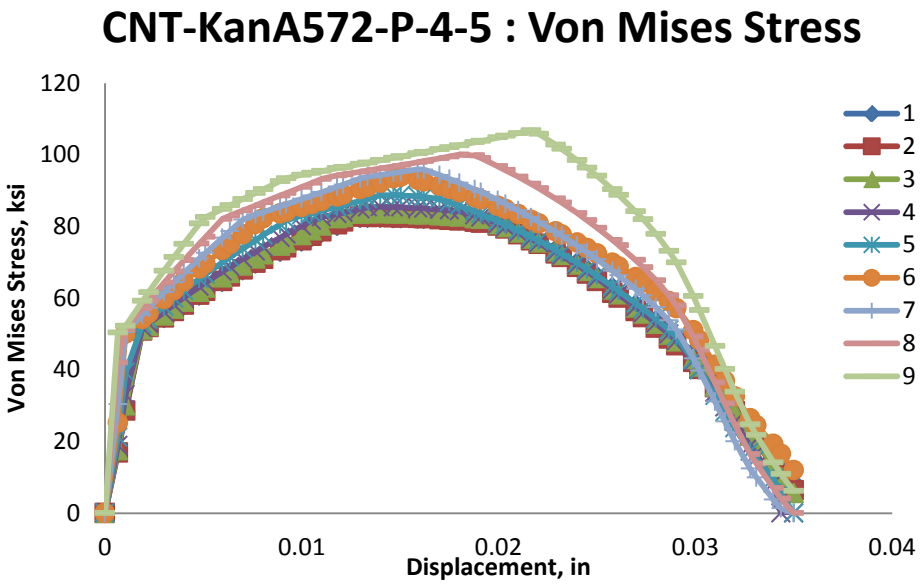

Figure 5.59: Variation of von Mises stress versus displacement for different elements laid out through the thickness of simulation of CNT-KanA572-P-4 and CNT-KanA572-P-5 specimens

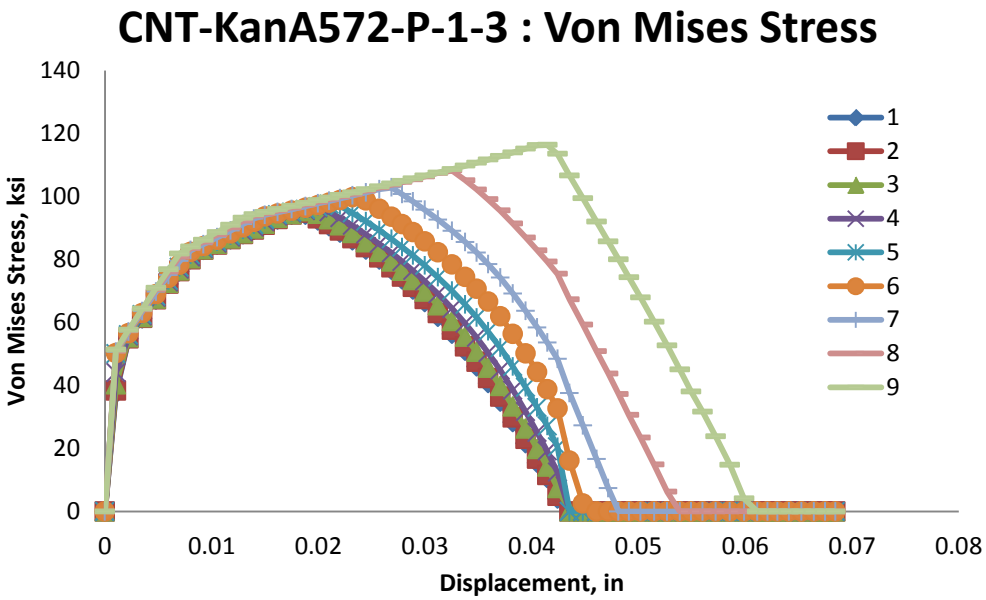

Figure 5.60: Variation of von Mises stress versus displacement for different elements laid out through the thickness of simulation of CNT-KanA572-P-1 to CNT-KanA572-P-3 specimens

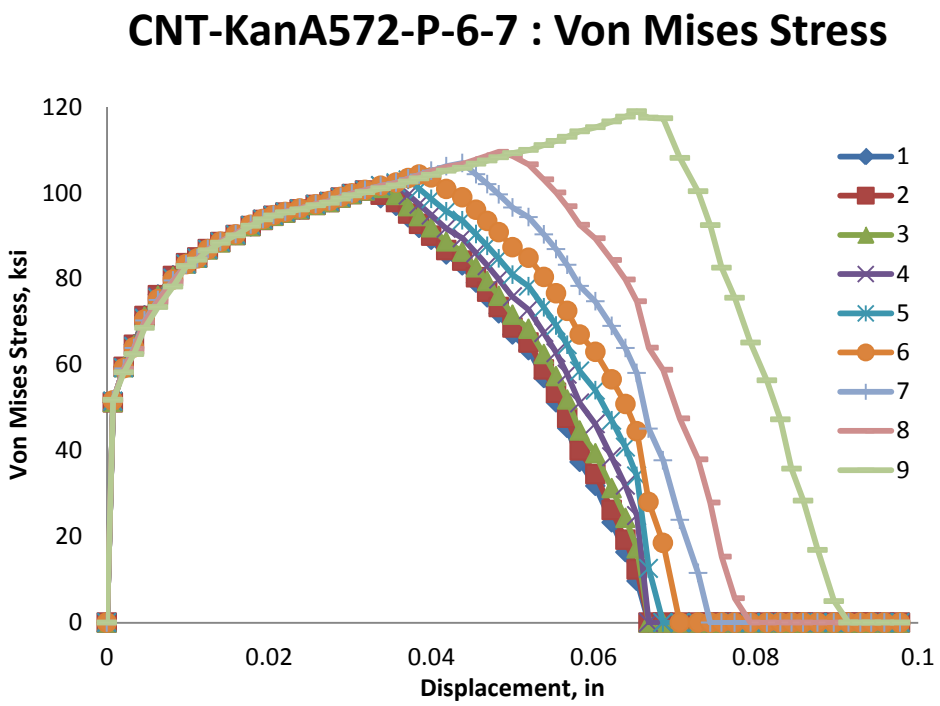

Figure 5.61: Variation of von Mises stress versus displacement for different elements laid out through the thickness of simulation of CNT-KanA572-P-6 and CNT-KanA572-P-7 specimens

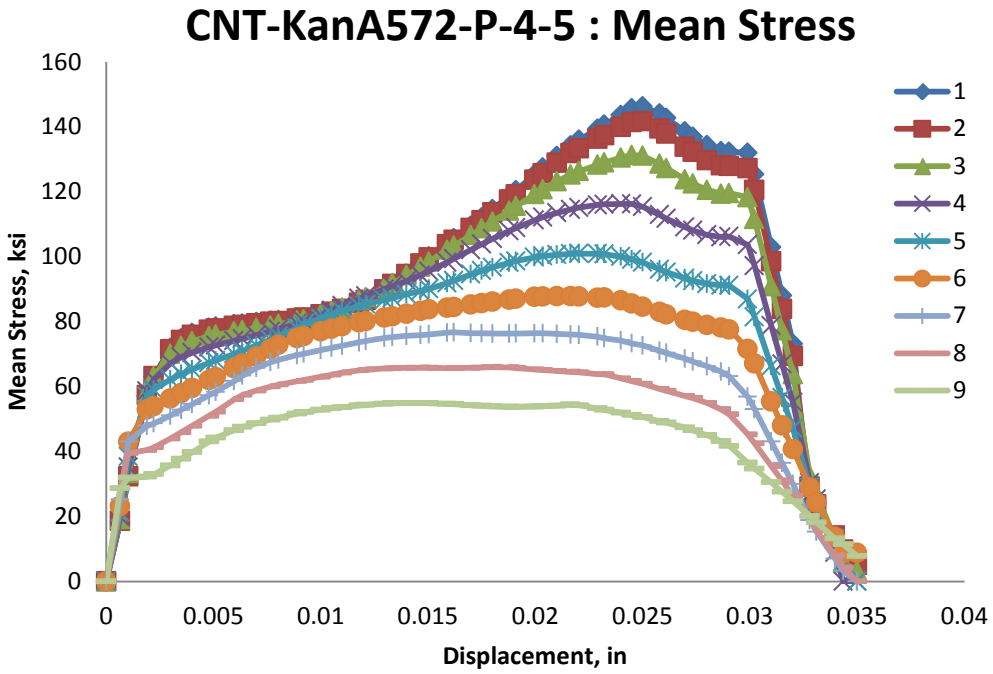

Figure 5.62: Variation of mean stress versus displacement for different elements laid out through the thickness of simulation of CNT-KanA572-P-4 and CNT-KanA572-P-5 specimens

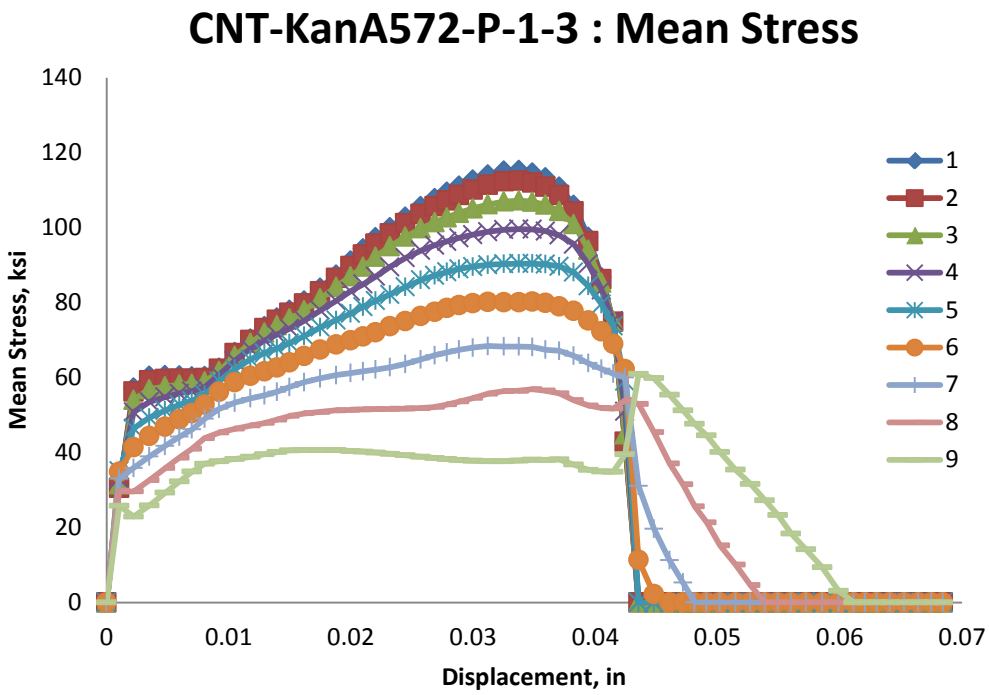

Figure 5.63: Variation of mean stress versus displacement for different elements laid out through the thickness of simulation of CNT-KanA572-P-1 to CNT-KanA572-P-3 specimens

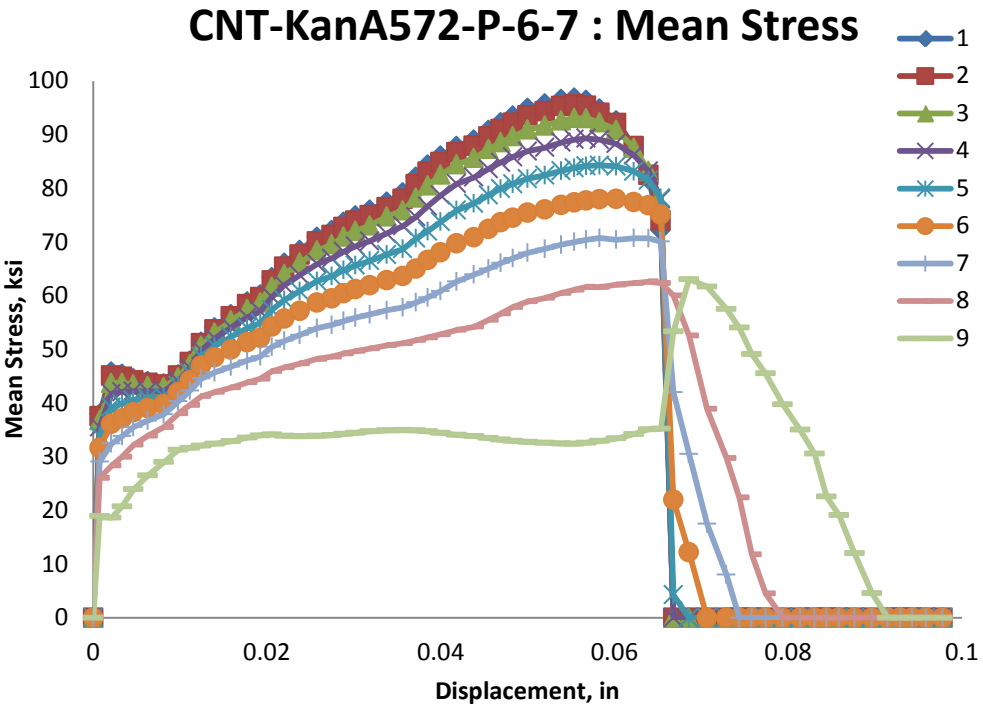

Figure 5.64: Variation of mean stress versus displacement for different elements laid out through the thickness of simulation of CNT-KanA572-P-6 and CNT-KanA572-P-7 specimens

Figure 5.65, Figure 5.66, and Figure 5.67 show the equivalent von Mises stress versus equivalent plastic strain plots for elements across the thickness of the specimens. In these plots it can be seen that the specified material property for isotropic plastic hardening with von Mises yield stress was observed, since all of the elements start plastification at the same von Mises stress and follow the same hardening curve. The specified linear relationship between equivalent plastic displacement and the damage variable could also be seen in that softening is defined by a linear curve. The slope of the softening curve for all of the elements in all of the specimens is also similar. It is worth while noting that all of the curves in specimens with notch radius of 0.125 and 0.25 inches reached zero stress, signifying that they were deleted, while this is not the case for specimen with notch radius of 0.06 inches because the simulation did not displace the specimen far enough. In addition, it is interesting that the elements at the center of the specimen and on the outer surface were not deleted in this simulation. Figure 5.65, Figure 5.66, and Figure 5.67 clearly show that the elements on the surface of the specimens exhibit much larger strain energy using the same material model than those at the center. This behavior is significant, with elements on the surface achieving strain energy almost as twice as large as those at the center. In addition, the larger the notch radius of the specimen, the larger overall von Mises stress, equivalent plastic strain, and strain energy is achieved. This all signifies that triaxiality plays a critical role in the stress-strain excursions of the material. As triaxiality increases, the excursions of the material defined by equivalent plastic stress, strain, and strain energy decreases, which signifies that structural detailing is very important in avoiding fracture and in effective use of the material.

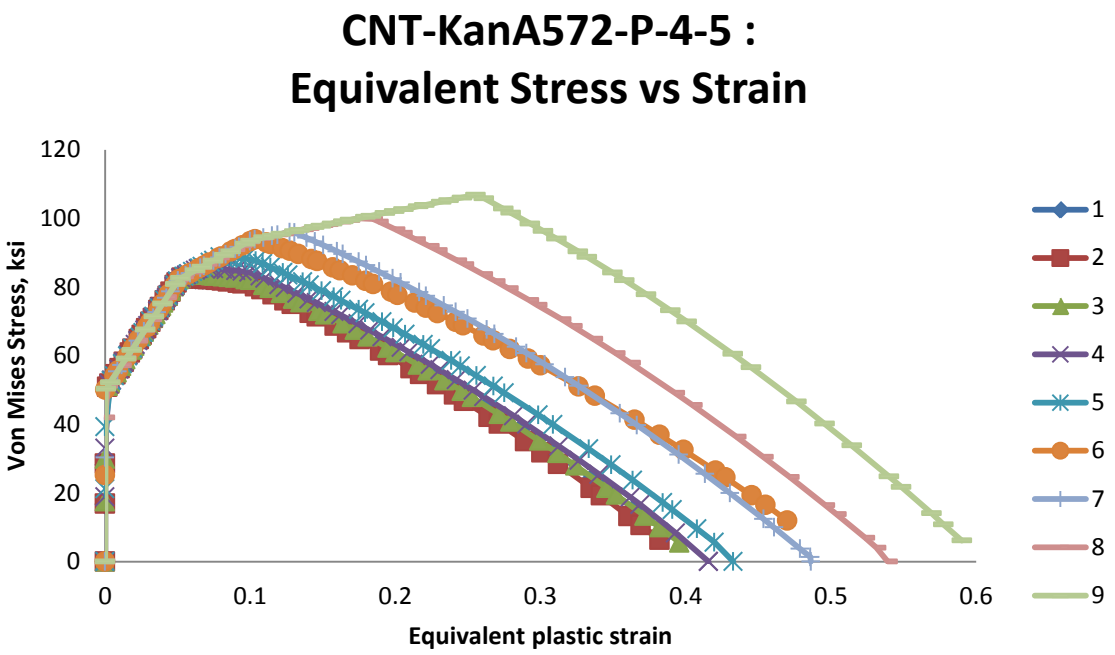

Figure 5.65: Variation of von Mises stress versus equivalent plastic strain for different elements laid out through the thickness of simulation of CNT-KanA572-P-4 and CNT-KanA572-P-5 specimens

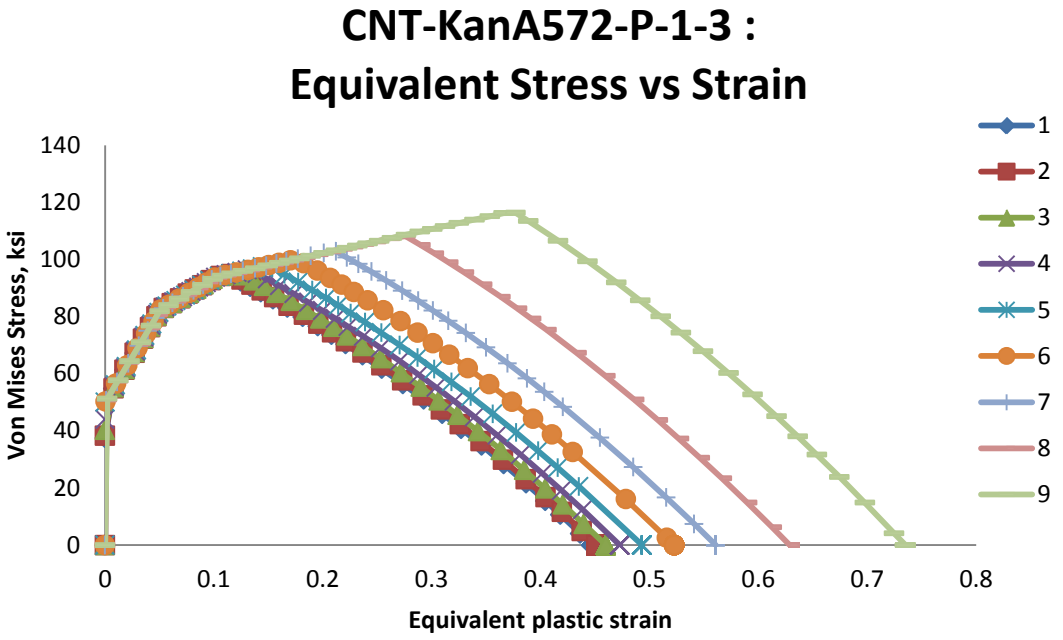

Figure 5.66: Variation of von Mises stress versus equivalent plastic strain for different elements laid out through the thickness of simulation of CNT-KanA572-P-1 to CNT-KanA572-P-3 specimens

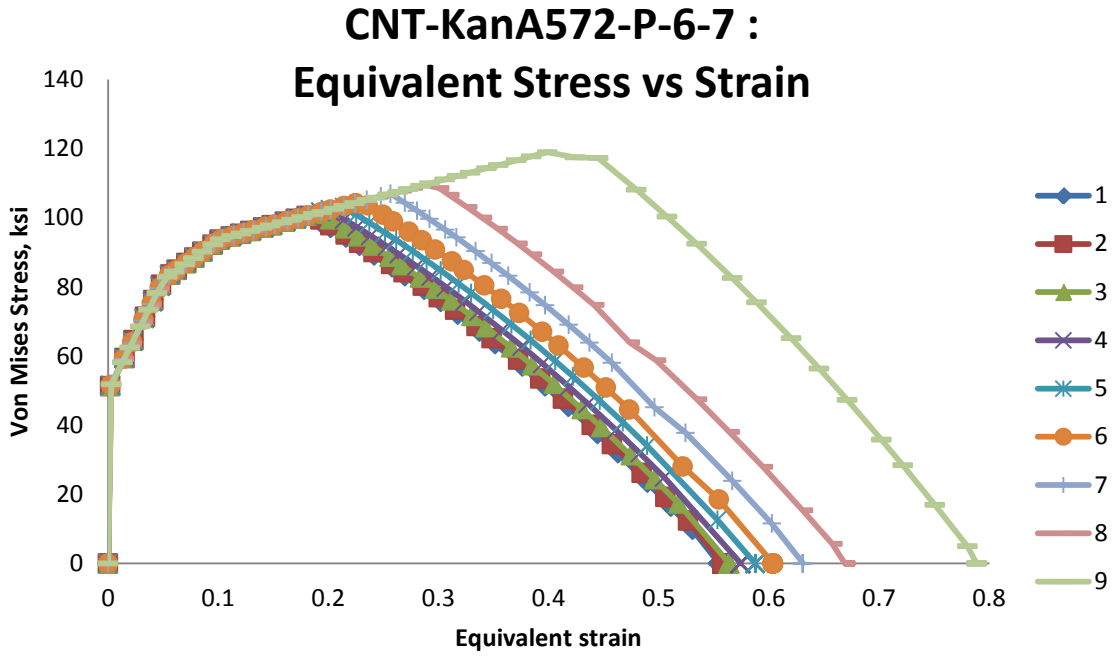

Figure 5.67: Variation of von Mises stress versus equivalent plastic strain for different elements laid out through the thickness of simulation of CNT-KanA572-P-6 and CNT-KanA572-P-7 specimens

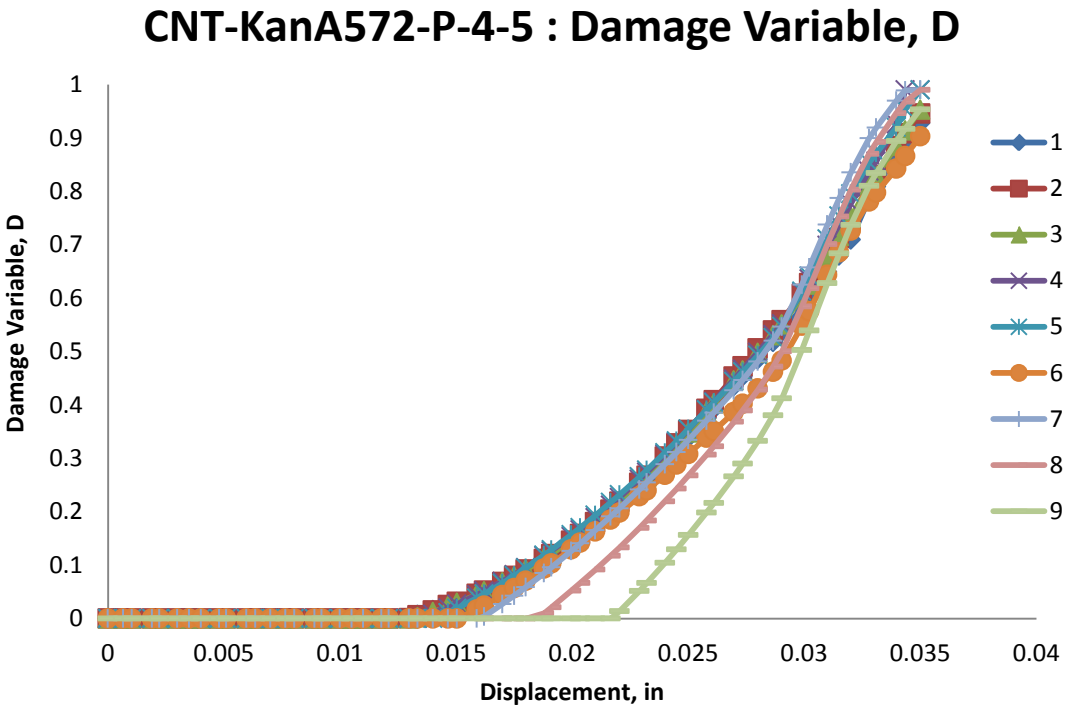

Figure 5.68: Variation of damage variable with displacement for different elements laid out through the thickness of simulation of CNT-KanA572-P-4 and CNT-KanA572-P-5 specimens

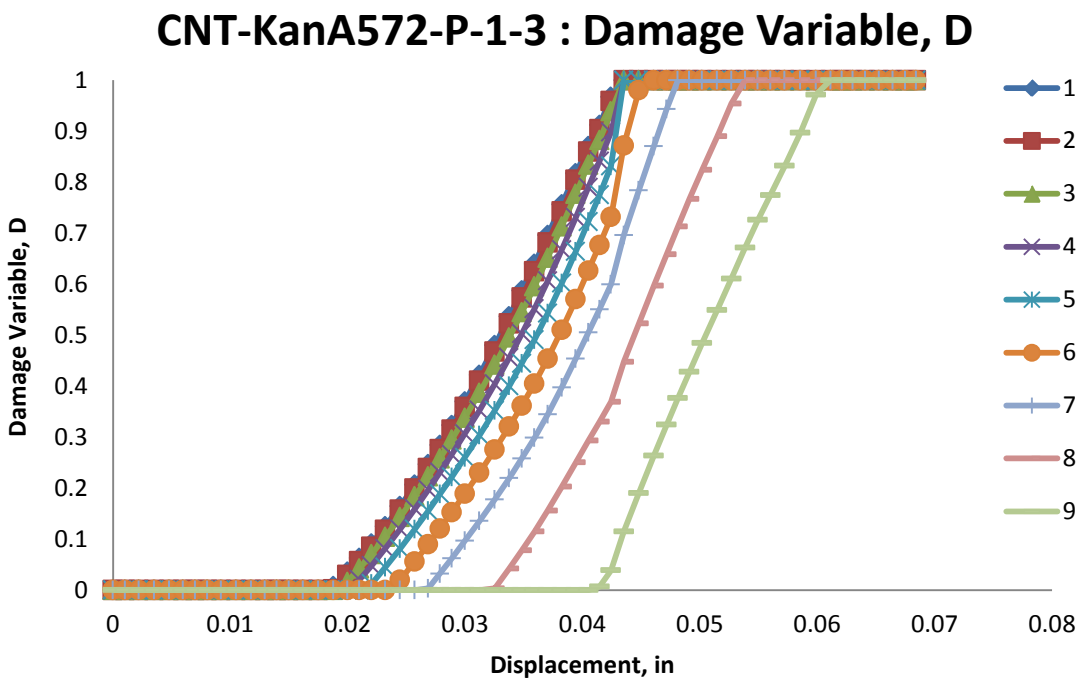

Figure 5.69: Variation of damage variable with displacement for different elements laid out through the thickness of simulation of CNT-KanA572-P-1 to CNT-KanA572-P-3 specimens

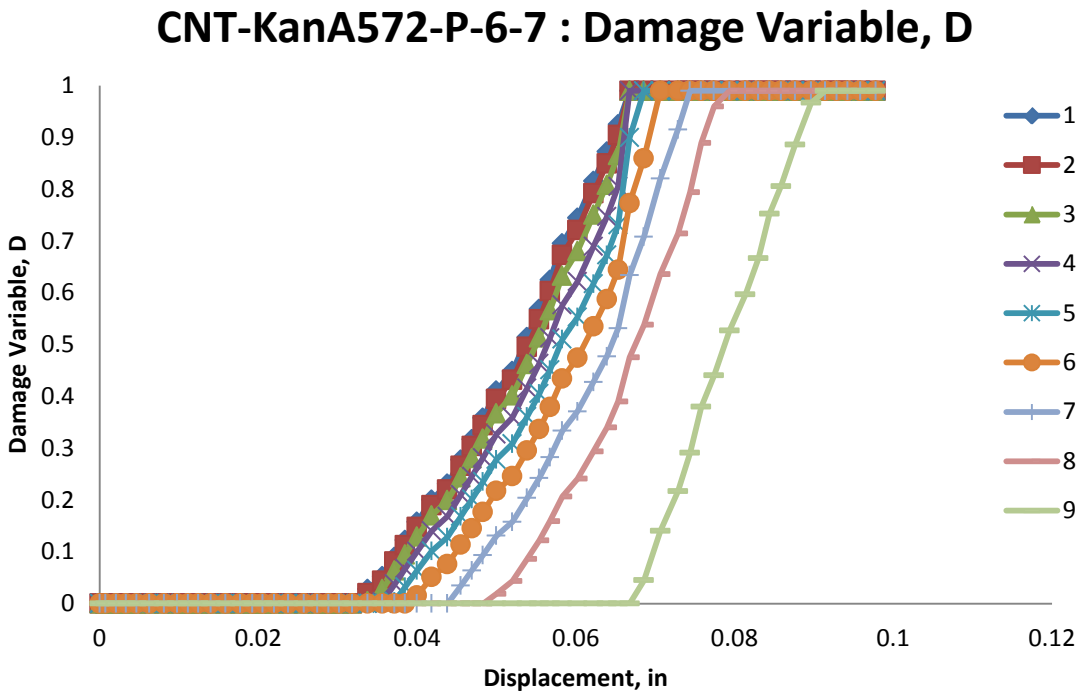

Figure 5.70: Variation of damage variable with displacement for different elements laid out through the thickness of simulation of CNT-KanA572-P-6 and CNT-KanA572-P-7 specimens

Since softening is modeled through the use of a damage variable, this damage variable is plotted for finite elements across specimen thickness in Figure 5.68, Figure 5.69, and Figure 5.70. The plateau at the top of these plots for a damage variable value of 1.0 signifies that the element has lost all of its stress and stiffness and is removed from simulation. The slope of the curves are very similar for the two specimens with larger notch sizes, while the specimen with notch size of 0.06 inches has a varying slope throughout loading. In addition for this specimen there is small distinction between the curve of each of the elements while in the specimens with larger notch radius this distinction is quiet visible. In addition, as one moves from the center of the specimen outwards the distance in displacement value between the curves grows. This signifies that fracture for these specimens starts at the center and propagates outward, with the speed of fracture propagation slowing down as it moves outward. This is due to the fact that the outward element provides more resistance and ductility due to its lower triaxiality, as seen in Figure 5.66 and Figure 5.67.

5.6 Relationship between Fracture Initiation Models and Charpy V-Notch Values

The Charpy impact test is a standardized method of determining the energy absorption of a material during fracture at high strain rate (Standard 2009). This test is also known as the Charpy V-notch test. This absorbed energy is a measure of material's notch toughness and provides information on temperature-dependent ductile-brittle transition (Standard 2009). The tests itself consists of a pendulum of known mass and length that is dropped from a known height to impact a notched specimen of a certain material. The energy is inferred by comparing the difference in the height of hammer before and after the impact (e Meyers et al. 2009). The

advantage of this test is that it is inexpensive, easy to prepare, and quick to perform. A main disadvantage is that results are only comparative (Kurishita et al. 1993). In addition, the notch and specimen dimensions all affect the results (Kurishita et al. 1993). This test could be used to force either a brittle or ductile fracture in a material. This could be done by varying the temperature at which to impact the material. In addition, to determine what actual fracture mechanism occurred in the material, an inspection of the fracture surface may be performed (e Meyers et al. 2009). If the specimen fractured in a flat plane, the fracture was brittle. On the other hand, if the specimen fractured with jagged edges or shear lips, then ductile fracture was the main fracture mechanism. In most cases, the actual fracture shows signs of both mechanisms (e Meyers et al. 2009).

Kanvinde et al. (2004) compared the absorbed energy from the Chapry V-notch impact tests with the η value of the VGM model, with β having a constant value of 1.5. The test followed an ASTM E3 standard to determine the temperature transition curve and the upper shelf energy value for structural steel metal, where the upper shelf value usually references the energy at high enough temperature to induce ductile fracture. Kanvinde et al. (2004) performed a correction for the high dynamic strain rate in order to compare to the fracture parameters of the VGM at near static loading. This is done by relating temperature shift to the yield stress of the material. It was concluded by Kanvinde et al. (2004) that Japanese structural steels usually have higher toughness then their American counterparts. In addition, it was found that specimens taken from wide flange had higher values than those taken from plate sections for the same metal. It was found that correlation between the absorbed energy values and the η value of the VGM model very strong, with a R^2 value of 0.93. Kanvinde et al. (2004) propose a

formula for determining the η value from the results of the CVN test. It must be stated that the values of the VGM parameters were calibrated manually in this study.

In this section, the CVN values from (Kanvinde et al. 2004) will be used to study the relationship between the absorbed energy of the CVN tests to the calibrated fracture initiation parameters that were calibrated using the PSO algorithm, for VGM, and analytically, for B-W model. Table 5.6 shows the absorbed energy values from (Kanvinde et al. 2004) and the calibrated values of VGM and B-W parameters. Figure 5.71 to Figure 5.75 show the correlation between the fracture parameters and the CVN. No strong correlation is found. For the VGM parameter η and B-W parameter $C_{1,}$ which represent the equivalent plastic strain at zero triaxiality, insignificant correlation was found to CVN. This makes sense, since CVN specimens experience very high constraints, therefore a high triaxiality region, while η and C_1 are defined at 0 triaxiality. More in depth studies need to be performed since (Kanvinde et al. 2004) found very high correlation between CVN and η. However, the VGM parameter β and B-W parameter C_2 had the highest correlation of 0.61 and 0.52, respectively, which is consistent with the fact that β and C_2 are responsible for determine the critical equivalent plastic strain value at higher triaxiality regions. The critical equivalent plastic displacement value used for softening did not have significant correlation with CVN.

Table 5.6: Charpy V-Notch absorbed energy values and the parameters of the VGM and B-W models for different steels

Structural Steel	CVN (ft-lb)	VGM parameters			B-W parameters	
		η	β	$\bar{u}_f^{pl}$	C_2	C_1
A572-Gr. 50 from W-section	188	1.79727	1.56285	0.00557	0.22572	0.10111
A572-Gr. 50 from plate	108	0.95115	2.45906	0.00534	0.17398	0.09557
A514 Gr. 110	107	1.84821	1.74697	0.00276	0.12684	0.00032
HPS70W	206	1.28924	1.13975	0.00364	0.21388	0.04055
JIS-SN490B Gr. 50	156	1.00291	0.82713	0.00782	0.26518	0.14464
JIS-SM490YBTMC-5L Gr. 50	246	1.46909	0.83743	0.00827	0.25496	0.10983
JIS-SN490B Gr. 50 from W-section	242	1.36101	0.78515	0.00828	0.23709	0.11317

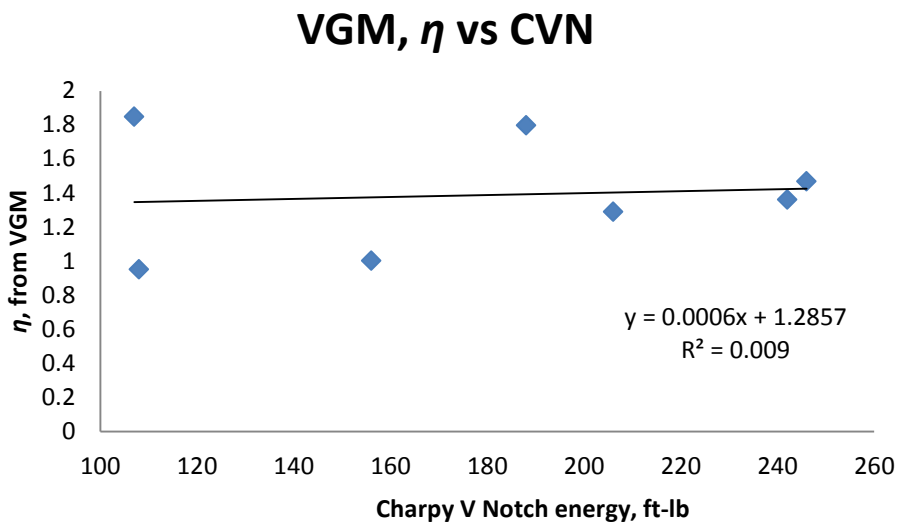

Figure 5.71: Correlation between VGM parameter, η and CVN

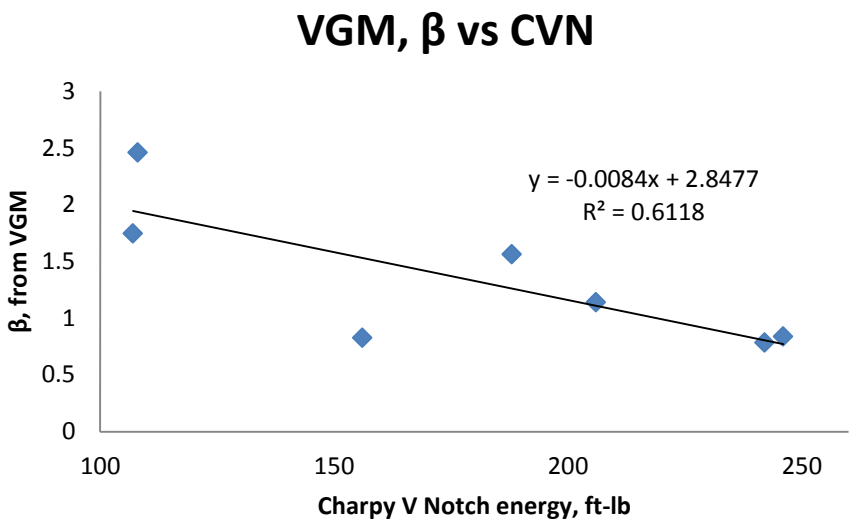

Figure 5.72: Correlation between VGM parameter, β and CVN

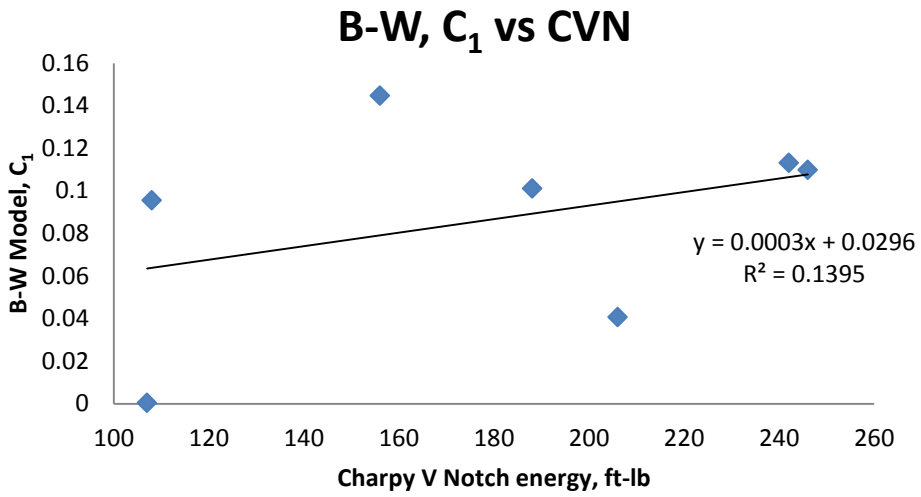

Figure 5.73: Correlation between B-W model parameter, C_1 and CVN

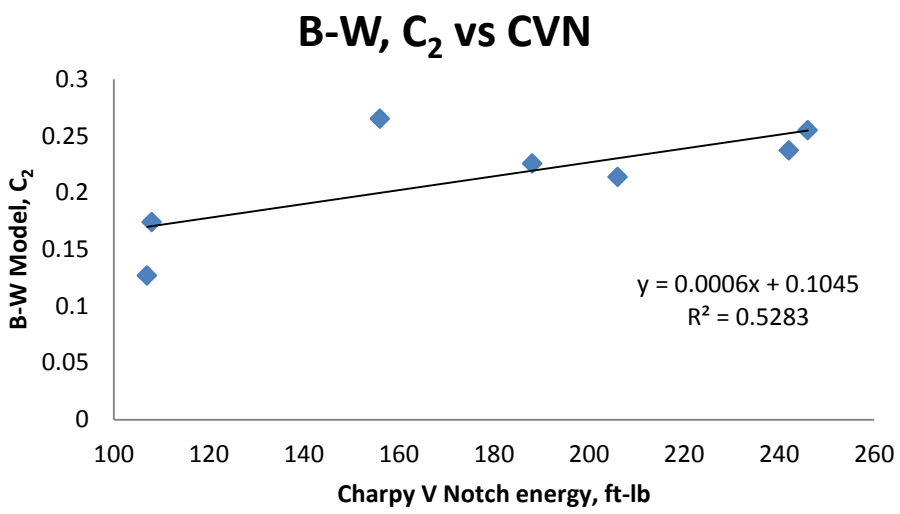

Figure 5.74: Correlation between B-W model parameter, C_2 and CVN

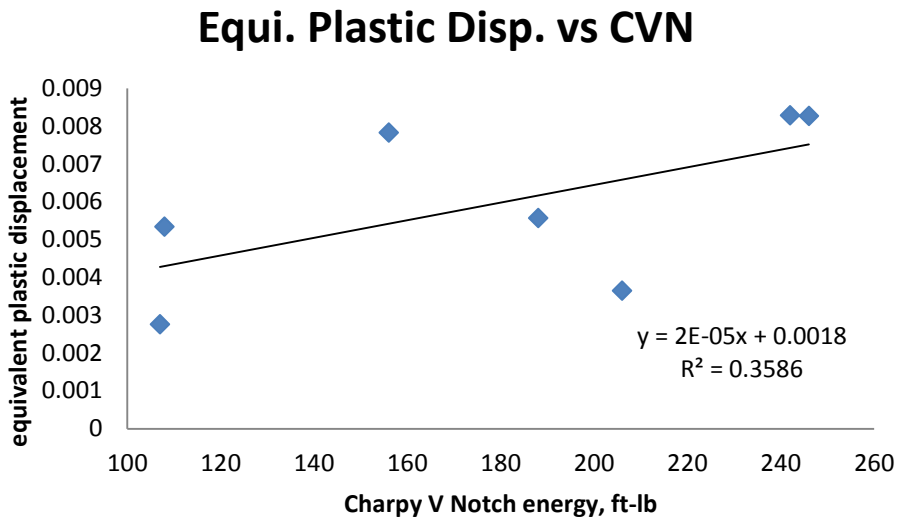

Figure 5.75: Correlation between a softening parameter, $\bar{u}_f^{pl}$ and CVN

5.7 Summary

The current fracture semi-empirical models of fracture initiation, VGM and B-W models, and of softening, Hillerborg Model, are local fracture models and are dependent on the current stress

and strain tensors and their histories. This chapter describes the calibration of the VGM and B-W model parameters through the use of PSO and analytically, respectively. The variation of fracture initiation and propagation parameters through the thickness of a CNT specimen is discussed. In addition, a comparison between the VGM and B-W parameters and Charpy V-notch experiments is made. The calibrated parameters will now be validated through comparison to a comprehensive set of experimental test results ranging from simple coupon specimens to multi-story steel frames subjected to collapse.

6 Validation

In this chapter the validation of the approach for collapse modeling outlined in this research is summarized. After the parameters of the B-W, VGM, and Hillerborg models were calibrated for particular structural steels analytically and based on the use of CNT and tensile lapped specimens, they are validated through comparison with a broad array of experimental test results of steel structures, ranging in complexity from tensile coupons to moment-resisting beam-to-column connections and compared to the current state-of-the-art for finite element deletion in collapse modeling of steel structures, the Constant Strain approach (CS). It is of interest to examine if using calibrated parameters of these fracture micromechanical models would yield an accurate and better prediction of the behavior of steel structures subjected to progressive collapse than the CS approach. The following validations are done through comparison to experimental test results for finite element model simulations that used VGM and B-W criteria (VGM-BW), only VGM criteria, and a constant critical strain (CS) criteria that uses a critical strain value of 0.2 and does not model softening to match previous simulated results in progressive collapse literature (Szyniszewski et al. 2012). The accuracy of the validation results is decided through comparison of the experimental and simulation force-displacement results and if the models were able to properly capture the fracture initiation location and propagation direction seen in the experimental testing. This will show if fracture in steel structures undergoing collapse is dictated by triaxiality and if negative and low triaxiality regions are important, since both the VGM and B-W models are dependent on triaxiality, but the constant critical strain approach is not. The list of validation simulations is provided in

Table 6.1, along with the measured properties used in those simulations. Details of the stress-strain curves used for the simulations are provided in Appendix C. The calibrated parameters were validated in ABAQUS software using an 8 node hexahedral elements with first-order interpolation and reduced integration (i.e., comparable modeling assumptions as were stated for the calibration studies). An updated Lagrangian geometrical nonlinear element formulation that includes large strains is also used (ABAQUS 2011). Contact was modeled using a balanced master-slave contact pair formulation that uses sophisticated tracking algorithms for tracking the motions of the surfaces (ABAQUS 2011). Contact constraints are enforced through a kinematic contact algorithm (ABAQUS 2011). For each particular steel, the plasticity model was identical to the one used in calibration. Throughout this work, ABAQUS/Explicit uses a conditionally stable Central Difference algorithm with an automatic time step size calculation. Damping is not defined in the finite element models used throughout this work. A mass density of $7.345*10^{-7}$ kip*s^2/in^4 was used in all of the finite element simulations.For each validation, a table is provided which shows the exact data point inputs into the plasticity, fracture initiation, and softening models by referencing Chapter 5 and Appendix C specimens. The mesh of the finite element models varied from simulation to simulation but met certain criteria. For each simulation, the mesh size was determined to be adequate to account properly for the experimental boundary conditions and strain gradients when a finer mesh of finite elements gave similar results. In addition, a critical structural part was meshed with at least two elements through its thickness to account for flexure.

For each simulation of an experimental test setup, finite element contour plots are shown below with von Mises stress plotted in ksi units, and force-displacement plots are shown with

force measured in kips and displacement in inches. For each of the validation simulations a plot showing a force-displacement curve for the experimental test result, and simulation results of VGM-BW, VGM, and CS simulations are shown in black, light blue, red, and light green colors, respectively. In addition, as in Section 5.5, a variation of the fracture parameters used for fracture initiation and propagation modeling is shown with 3 curves representing the parameters at three different locations (i.e., three different elements) for each of the three finite element deletion strategies. For each strategy the three curves vary in color from lightest to darkest tone of each strategy's respective color. The curves are numbered 1 through 3 with 1 for the lighter shade and 3 for the darker shade. The curve numbers represent the location of the element in a specimen, with 1 usually being at the center and 3 on the outer surface of the specimen. Element locations are also shown in respective figures to clarify the element locations. In addition, for the three finite element deletion strategies, the three chosen elements for fracture parameter plots are usually the same so a comparison may be made. In addition, the error value used to compare simulation results with experimental test results given by Equation (5.2 is provided for each simulation. Overall, the VGM simulations had a mean error, defined by Equation (5.2, of 0.184 and error standard deviation of 0.092, the VGM-BW simulations had a mean error of 0.214 and error standard deviation of 0.104, and the CS simulations had a mean error of 0.405 and error standard deviation of 0.237. In addition, the VGM model better predicted fracture location and propagation direction than VGM-BW and CS with VGM-BW having sometimes fractures that were considered non-physical and CS rarely capturing the fracture behavior properly.

Table 6.1: Results of validation studies

					Error Value		
Test	**Material Type**	**σ_y (ksi)**	**σ_u (ksi)**	**Δ_f (in)**	**CS**	**VGM**	**VGM-BW**
CNT-MyeA36-B-9	A36	50	74	0.038	0.694	0.204	0.237
CNT-MyeA36-B-10				0.043			
CNT-MyeA36-B-11				0.042			
CNT-MyeA36-B-12				0.041			
CNT-MyeA36-B-13	A36	50	74	0.021	0.643	0.278	0.200
CNT-MyeA36-B-14				0.024			
CNT-MyeA36-B-15				0.024			
CNT-MyeA36-B-16				0.023			
CNT-MyeA36-B-17	A36	50	74	0.036	0.787	0.189	0.263
CNT-MyeA36-B-18				0.036			
CNT-MyeA36-B-19				0.037			
CNT-MyeA36-B-20	A36	50	74	0.020	0.750	0.215	0.195
CNT-MyeA36-B-21				0.025			
CNT-MyeA36-B-22				0.025			
CNT-MyeA36-B-23				0.031			
BH-KanA572-P-1	A572-Gr. 50	56	85	0.140	0.545	0.159	0.294
BH-KanHPS70W-P-1	HPS70W	85	101	0.148	0.669	0.151	0.374
BH-KanHPS70W-P-2	HPS70W	85	101	0.138			
DB-KanA572-P-1	A572-Gr. 50	56	85	0.246	0.466	0.102	0.250
DB-KanHPS70W-P-1	HPS70W	85	101	0.203	0.219	0.158	0.119
DB-KanHPS70W-P-2	HPS70W	85	101	0.216			
CT-KanA572-P-1	A572-Gr. 50	56	85	0.109	0.106	0.108	0.108
CT-KanA572-P-2	A572-Gr. 50	56	85	0.120			
CT-KanA572-P-3	A572-Gr. 50	56	85	0.105			
CT-KanA572-W-1	A572-Gr. 50	61	72	0.422	0.346	0.024	0.065
CT-KanA572-W-2	A572-Gr. 50	61	72	0.409			
CT-KanA572-W-3	A572-Gr. 50	61	72	0.404			
CT-KanA572-W-4	A572-Gr. 50	61	72	0.351	0.521	0.502	0.502
CT-KanA572-W-5	A572-Gr. 50	61	72	0.228			
CT-KanA572-W-6	A572-Gr. 50	61	72	0.450			
CT-KanHPS70W-P-1	HPS70W	85	101	0.13	0.188	0.181	0.176
CT-KanHPS70W-P-2	HPS70W	85	101	0.28			
CT-KanHPS70W-P-3	HPS70W	85	101	0.207			
3PB-KanA572-W-1	A572-Gr. 50	61	72	0.122	0.117	0.115	0.115
3PB-KanA572-W-2	A572-Gr. 50	61	72	0.163			
DAC-BirG40.21-W-1	CSA G40.21-44W	53	79	1.020	0.270	0.270	0.270
MRC-RenA572-W-14-1	A572-Gr. 50	61	72	2.103	0.788	0.106	0.101
MRC-RenA572-W-14-2	A572-Gr. 50	61	72	1.641	0.378	0.166	0.162
MRC-RenA572-W-14-3	A572-Gr. 50	61	72	3.031	0.144	0.312	0.312
MRC-RenA572-W-14-4	A572-Gr. 50	61	72	3.351	0.626	0.159	0.152
WUFB-SadA992-W-1	A992	54	114	31.70	0.381	0.248	0.343
RBS-SadA992-W-1	A992	54	114	18.40	0.511	0.208	0.333
Portal-SchA7-W-1	A36	50	74	9.22	0.189	0.189	0.189
Brace-YurA36-W-1	A36	50	74	3.279	0.106	0.106	0.106
Brace-YurA36-W-2	A36	50	74	3.30	0.126	0.126	0.126
Brace-YurA36-W-3	A36	50	74	2.91	0.147	0.147	0.147
				Average Error =	**0.405**	**0.184**	**0.214**
				Standard Deviation =	**0.237**	**0.092**	**0.104**

6.1 Circumferentially Notched Specimen

Structural steel of type A36 was validated through comparison to CNTs with different notched radius and notch root diameters than specimens used for calibration of the VGM model. This enforced a different triaxiality range throughout the loading for validation specimens than for calibration ones. It was of interest to see if the calibrated VGM fracture locus would be accurate outside the calibrated range and if VGM-BW and CS models can capture fracture behavior in these specimens. The exact plasticity and fracture model inputs are shown in Table 6.2. Validation force-displacement results can be seen in Figure 6.1 to Figure 6.4. The results show that the calibrated fracture locus was able to capture the fracture behavior well in a different triaxiality range for VGM strategy but not for the VGM-BW and CS. In all of the four figures the Constant Strain approach significantly underestimated the equivalent fracture strain resulting in inaccurate results. In addition, in Figure 6.2, Figure 6.3, and Figure 6.4, the CS shows significant vibration in these explicit dynamic analyses after complete separation of the specimen due to the fracture initiation requirement being reached at the same time through the entire specimen thickness, no significant softening being implemented, and the simulations not have damping defined. These results highlight the issue of using a CS strategy, which can induce significant dynamic instabilities during collapse modeling forcing significant error into models' prediction. On the other hand, the VGM-BW and VGM, which model softening through the Hillerborg Model, do not show any signs of dynamic instability for these specimens.

Table 6.2: Plasticity and fracture model inputs for CNT-MyeA36-B-A specimens

		Fracture Model Input		
Test	**Plasticity Model Input**	**VGM**	**VGM-BW**	**CS**
CNT-MyeA36-B-9-12	CNT-MyeA36-B-A	CNT-MyeA36-B-A	TC-MyeA36-B-A	0.2
CNT-MyeA36-B-13-16	CNT-MyeA36-B-A	CNT-MyeA36-B-A	TC-MyeA36-B-A	0.2
CNT-MyeA36-B-17-19	CNT-MyeA36-B-A	CNT-MyeA36-B-A	TC-MyeA36-B-A	0.2
CNT-MyeA36-B-20-23	CNT-MyeA36-B-A	CNT-MyeA36-B-A	TC-MyeA36-B-A	0.2

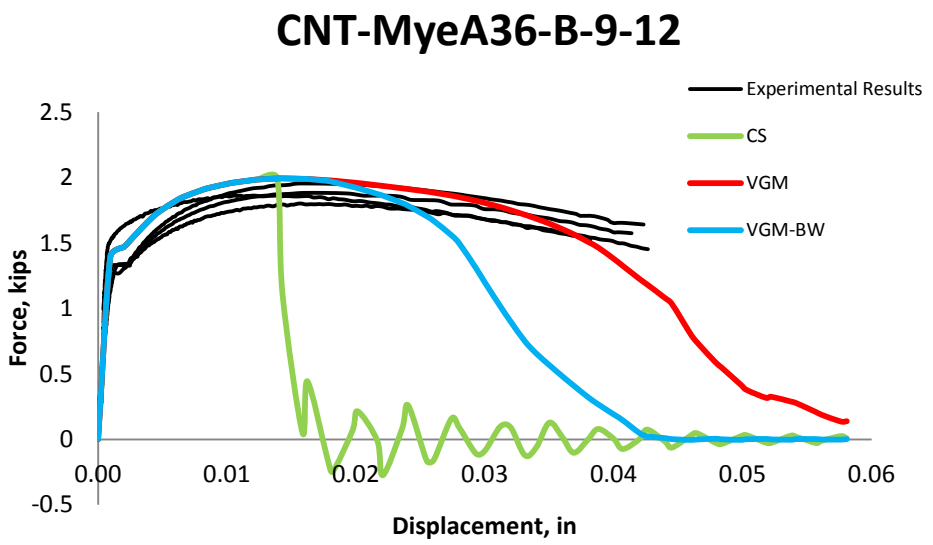

Figure 6.1: Validation results of CNT-MyeA36-B-9-12

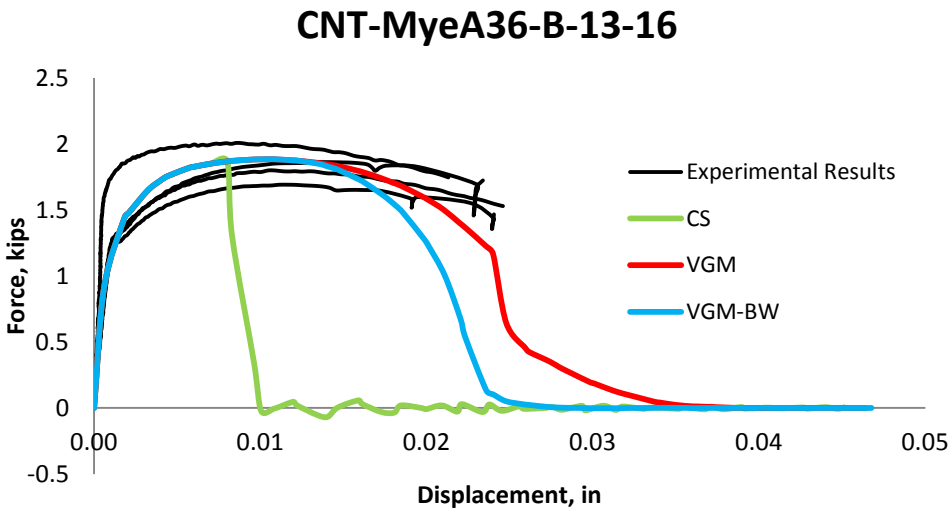

Figure 6.2: Validation results of CNT-MyeA36-B-13-16

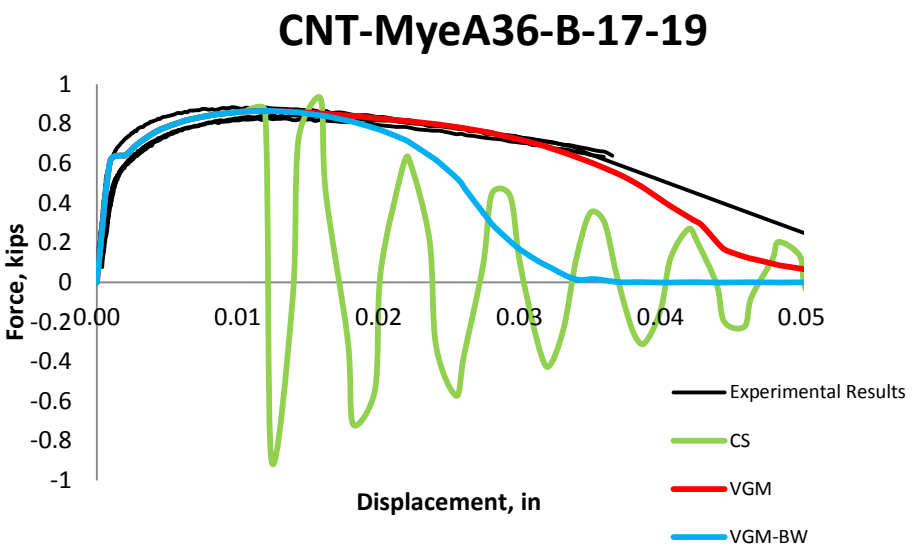

Figure 6.3: Validation results of CNT-MyeA36-B-17-19

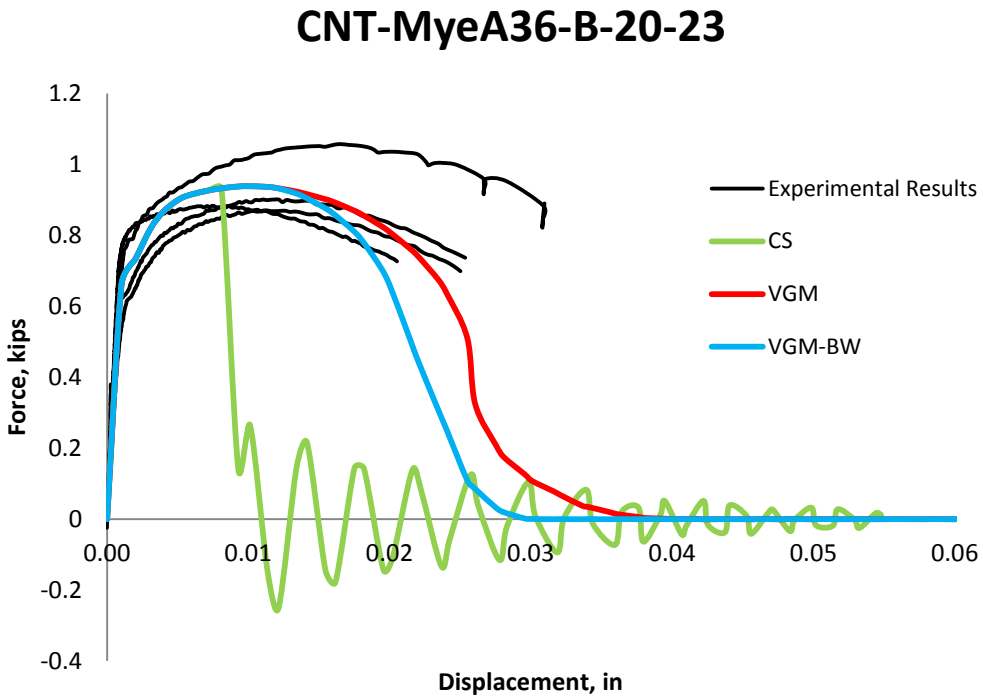

Figure 6.4: Validation results of CNT-MyeA36-B-20-23

For a more in depth investigation of the reasons why each strategy performed the way it did, Figure 6.6 to Figure 6.37 show the variation of triaxiality, equivalent plastic strain, von Mises

and mean stress, the value of fracture initiation integral, and damage variable. The exact elements for which the parameters are plotted are shown in Figure 6.5. Figure 6.6, Figure 6.7, Figure 6.8, and Figure 6.9 show that for a particular element in the CNT specimens the triaxiality varied similarly for the three strategies up to a certain displacement at which softening initiated. The general trend observed in the calibration of the CNT specimens of triaxiality decreasing from the center to the outer surface is also seen in these figures, again confirming the results reported in the literature (Anderson 2005). It is also seen that triaxiality is constant after an initial bump, which is probably due to plastic deformation of the material. In addition, softening greatly increases the triaxiality of the element at the center of specimen, but not for the outer most elements. This is true for the VGM simulations and sometimes for the VGM-BW approach. This usually occurs at a very high strain value and since the CS and to lesser extent VGM-BW failed prematurely this trend is not as strong in these simulations.

The variation of equivalent plastic strain during loading of the four specimens for the three elements across the thickness of the specimen is shown in Figure 6.10 through Figure 6.13. It is seen that elements on the outer surface achieve greater equivalent plastic strain value than those in the center except for the CS simulation where the maximum strain value is always 0.2. It is interesting to note that the elements on the outer surface have greater strain at a certain overall displacement than the inner elements. This shows that while more deformation is occurring on the surface fracture occurs at the center where there is more confinement against plastic flow. The slope of equivalent plastic strain to displacement is usually the same amongst the three finite element deletion strategies until the elements begins to soften, after which it follows its own path.

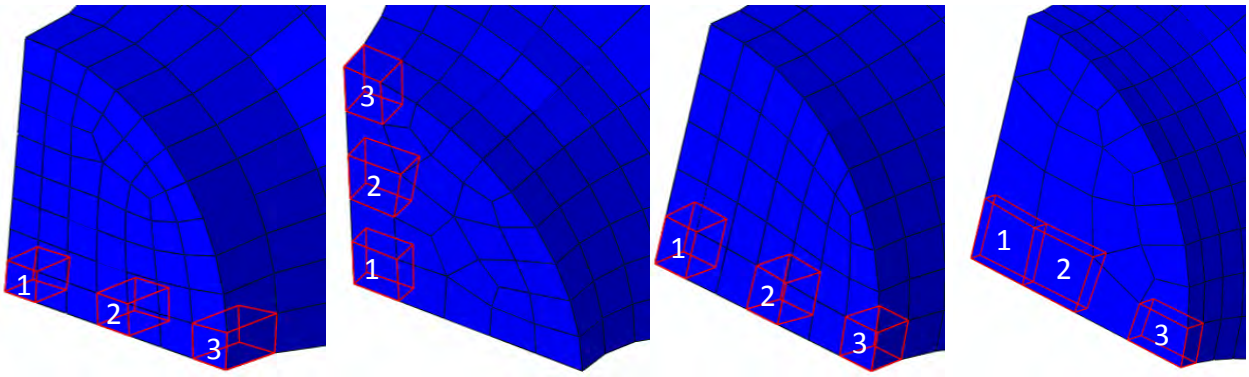

Figure 6.5: Shows the location of the elements for which fracture parameters are plotted below. From left to right CNT-MyeA36-B-9-12, CNT-MyeA36-B-13-16, CNT-MyeA36-B-17-19, and CNT-MyeA36-B-20-23

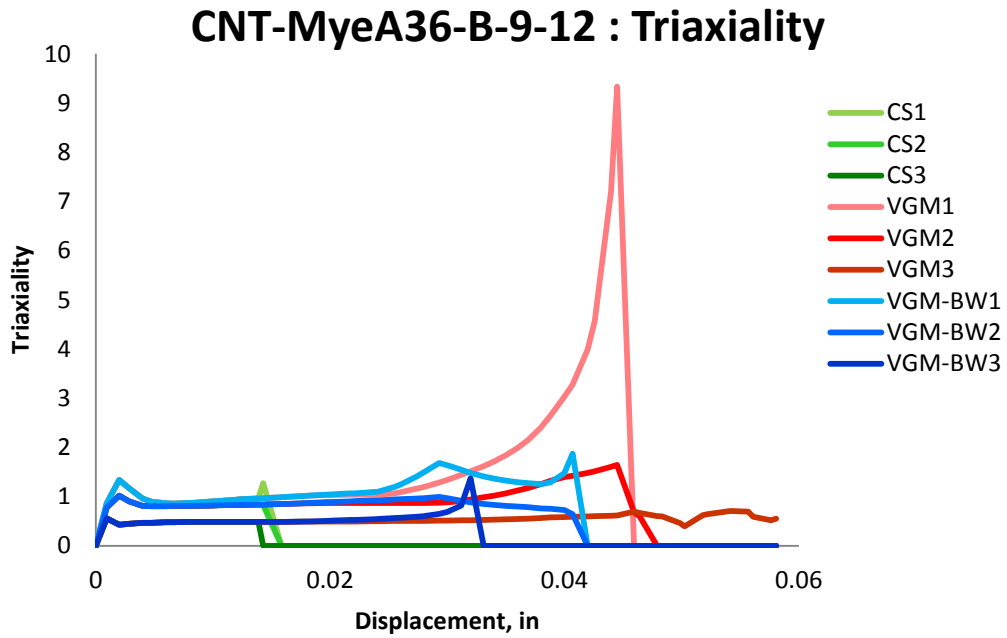

Figure 6.6: Variation of triaxiality with displacement for different elements laid out through the thickness of simulation of CNT-MyeA36-B-9-12 specimens for the three finite element deletion strategies

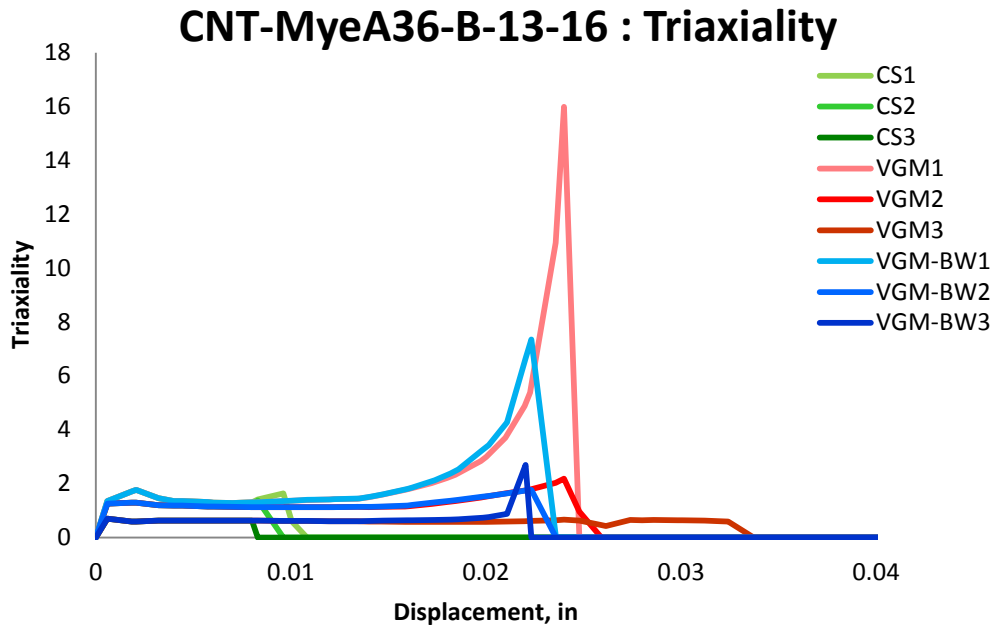

Figure 6.7: Variation of triaxiality with displacement for different elements laid out through the thickness of simulation of CNT-MyeA36-B-13-16 specimen for the three finite element deletion strategies

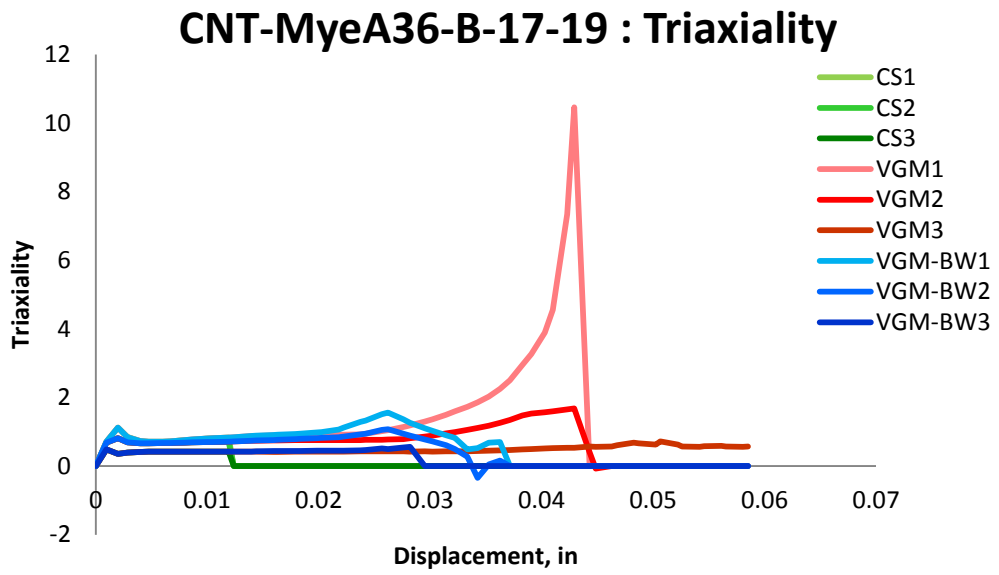

Figure 6.8: Variation of triaxiality with displacement for different elements laid out through the thickness of simulation of C NT-MyeA36-B-17-19 specimen for the three finite element deletion strategies

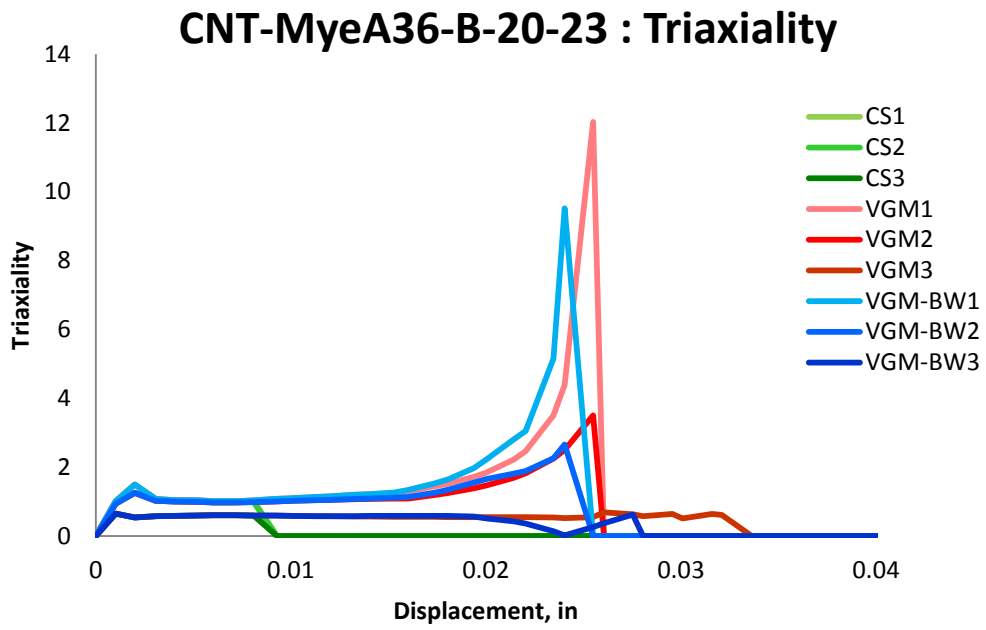

Figure 6.9: Variation of triaxiality with displacement for different elements laid out through the thickness of simulation of CNT-MyeA36-B-20-23 specimen for the three finite element deletion strategies

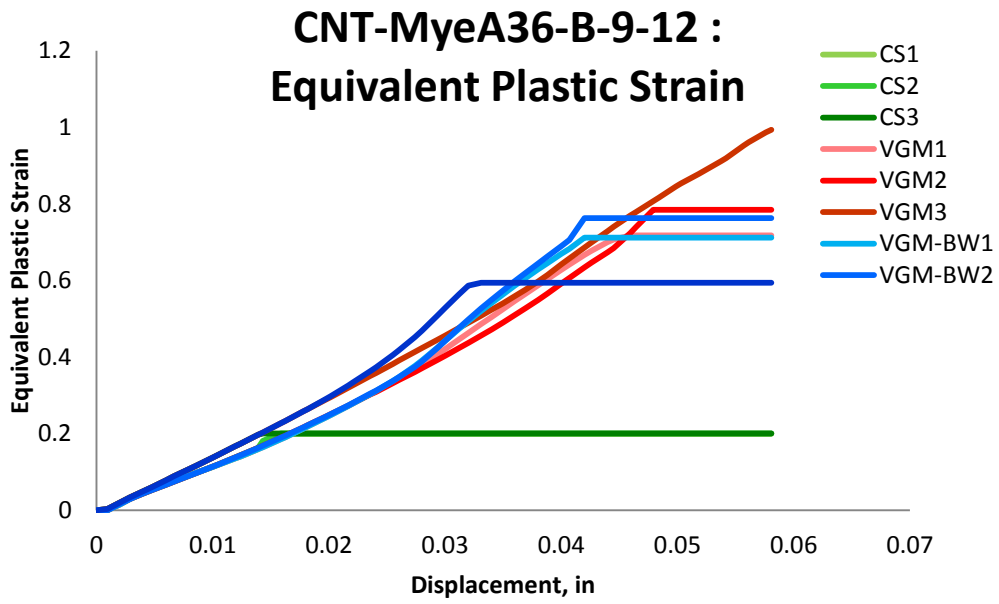

Figure 6.10: Variation of equivalent plastic strain with displacement for different elements laid out through the thickness of simulation of CNT-MyeA36-B-9-12 specimens for the three finite element deletion strategies

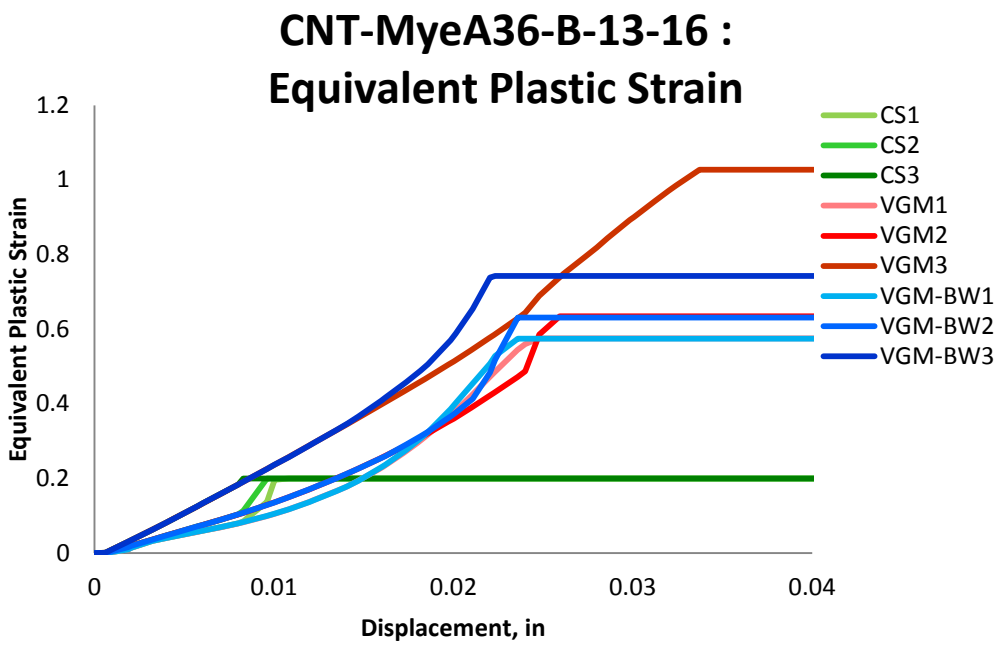

Figure 6.11: Variation of equivalent plastic strain with displacement for different elements laid out through the thickness of simulation of CNT-MyeA36-B-13-16 specimen for the three finite element deletion strategies

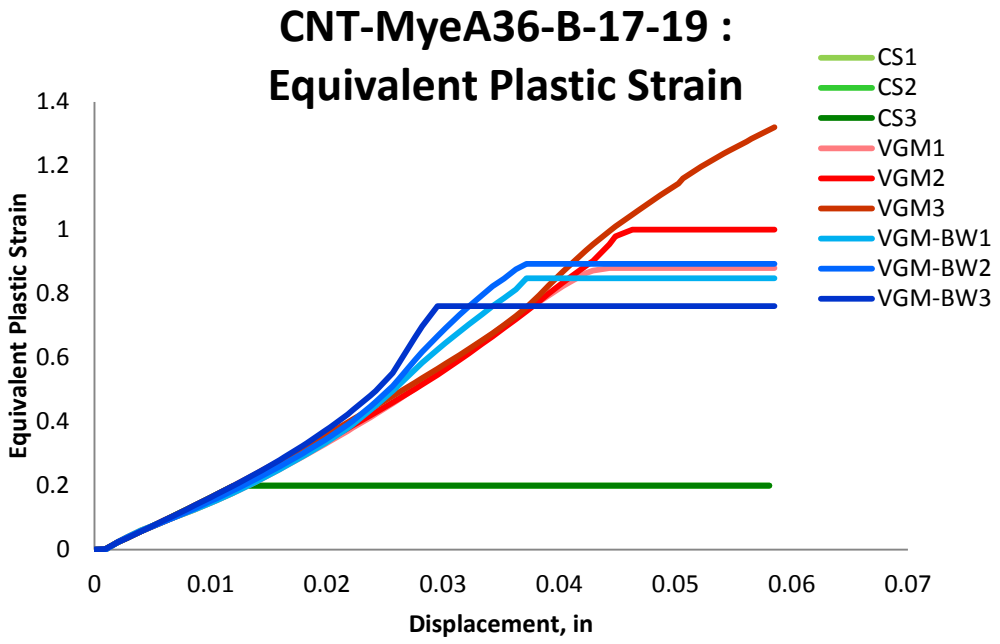

Figure 6.12: Variation of equivalent plastic strain with displacement for different elements laid out through the thickness of simulation of CNT-MyeA36-B-17-19 specimen for the three finite element deletion strategies

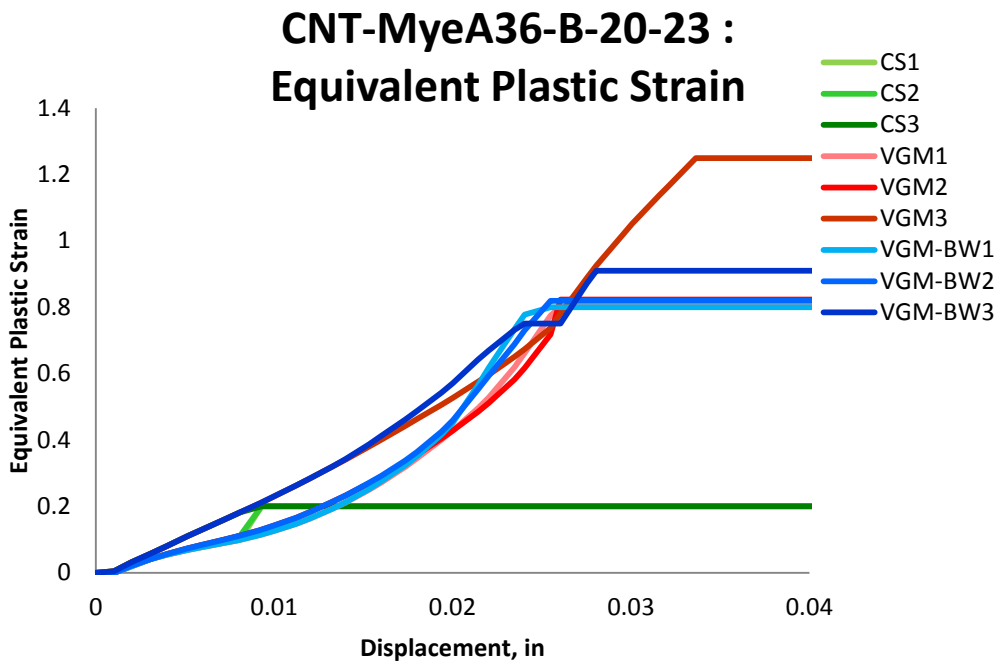

Figure 6.13: Variation of equivalent plastic strain with displacement for different elements laid out through the thickness of simulation of CNT-MyeA36-B-20-23 specimen for the three finite element deletion strategies

Fracture locus, defined in equivalent plastic strain and triaxiality space, is plotted in Figure 6.14 to Figure 6.17. In these plots, the triaxiality value goes to zero for any element that is deleted; however, this is not plotted in these figures to avoid cluttering the plot. Thus, for each element, the curve is plotted until the last data point before zero triaxiality. This approach to plotting in the fracture locus plane is repeated for all of the other simulations in this work. After initiation of softening there is a tendency to dramatically increase triaxiality for the inner elements, but the outer element does not seem to be affected by this. The equivalent plastic strain for the outer element continues to have a near vertical slope throughout the entire loading excursion and is not affected by softening. In general, the equivalent plastic strain in these specimens follows a similar path as it did in the calibration of CNT specimens. There is a significant difference in the triaxiality range of the outer element throughout the loading and the other

two inner elements that are active in a higher triaxiality range than the outer element. In addition, the outer element is affected by the B-W criteria, while the inner elements are not. Therefore, the difference in force-displacement curves between the VGM-BW and VGM strategies is mainly concentrated in the outer elements. In addition, these figures also highlight just by how much the CS strategy underestimates the fracture capacity of this material. This is primarily due to the fact that the triaxiality range of these chosen finite elements is such that the equivalent plastic strain to fracture initiation is much greater for VGM and B-W models than for CS, by as much as a factor of 3.

Fracture initiation, defined by Equation (4.6) accounts for the history of equivalent plastic strain with loading. This integral is calculated at the Gauss point for each finite element and determines when to initiate softening. The value of this fracture initiation integral is shown in Figure 6.18 to Figure 6.21. It can be seen that as one moves from the outer surface of the CNT to the center of the specimen, the slope or the change with time step of this integral increases for the VGM strategy but not for the VGM-BW and CS strategies. In fact, the CS approach has an opposite trend and VGM-BW does not seem to have an apparent trend. In addition, the VGM simulations confirm the conclusion reached in the literature that fracture in CNT specimens is almost always initiated at the center of the specimen. However, the CS and VGM-BW simulations have the fracture start from the outside. This is the same for all of the four specimens.

The variation of von Mises Stress across the thickness of the specimens is plotted in Figure 6.22 to Figure 6.25. For the specimens with overall higher triaxiality range for the chosen finite

elements, the variation of von Mises Stress throughout the loading excursions is noticeably different than in specimens with lower overall triaxiality range. In VGM simulation the stress in the outer elements is higher than in the inner elements. The softening of stress in the VGM simulation has a pattern of outer elements reaching a higher stress value at a higher displacement value. This is not the case for the CS and VGM-BW simulations. No apparent trend or pattern is observable in those methods. While the stress-displacement path for the two inner elements is somewhat similar between the VGM and VGM-BW models, there is a significant difference between the finite element deletion strategies for the outer element. This is due to the fact that at high triaxiality for the inner elements the fracture initiation criteria is met by the VGM criteria for the VGM and VGB-BW simulations but for the lower triaxiality the VGM and B-W models give a different value for critical equivalent plastic strain at fracture initiation. The variation of mean stress versus displacement for finite elements located across the specimen thickness is plotted in Figure 6.26 to Figure 6.29. For mean stress the elements on the surface of the specimen experienced lower stress levels than those at the center, for all of the three finite element deletion strategies. As in other CNT specimens, the elements in the center experienced a higher growth rate of mean stress versus displacement. In addition, the mean stress of the inner elements converged at the same displacement value to zero stress level, while the outer elements achieved greater displacement in VGM simulation, which is the opposite to that of VGM-BW simulation. This signifies that the two inner elements fractured at the same displacement value which may point to a sudden fracture propagation.

Figure 6.30 to Figure 6.33 show the equivalent stress versus strain plots for elements across the thickness of the specimens. In these plots it can be seen that the specified material input for

the isotropic hardening model was adhered to since all of the elements start plastification at the same von Mises stress and follow the same hardening curve. The specified linear relationship between equivalent plastic displacement and the damage variable could also be seen in that softening is defined by a linear curve. The slope of the softening curve for all of the elements in all of the specimens is also the same except for the CS simulations, which had no softening modeled. From these figures it is clearly shown that for the VGM simulations the elements on the surface of the specimens exhibit much larger strain energy using the same material model than those at the center. However, for the VGM-BW, no apparent trend is observable, and CS simulations immediate failure for all of the three elements.

The damage variable is plotted in Figure 6.34 to Figure 6.37. The plateau at the top of these plots for damage variable value of 1 signifies that the element has lost all of its stress and stiffness, and is removed from simulation. For CS simulations, the three elements across the specimen thickness follow almost exactly the same path. This causes dynamic instabilities because all of the elements across the thickness of the specimen fail at once without any softening to redistribute stress. Even though the two inner elements for VGM and VGM-BW model are governed by higher triaxiality of the VGM criteria, their respective curves diverge from one another after a certain point in the loading excursion. This is due to stress redistribution that is happening during the softening of the elements with outer element contributing more to resisting loading in VGM simulation than in VGM-BW simulation.

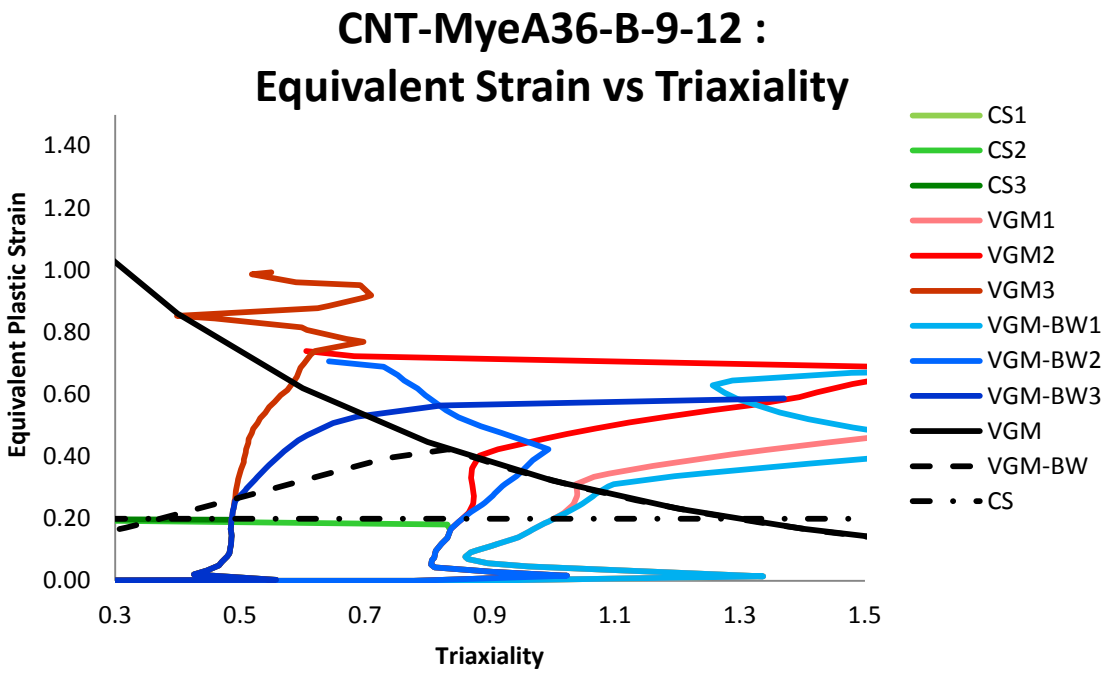

Figure 6.14: Variation of equivalent plastic strain with triaxiality for different elements laid out through the thickness of simulation of CNT-MyeA36-B-9-12 specimens for the three finite element deletion strategies

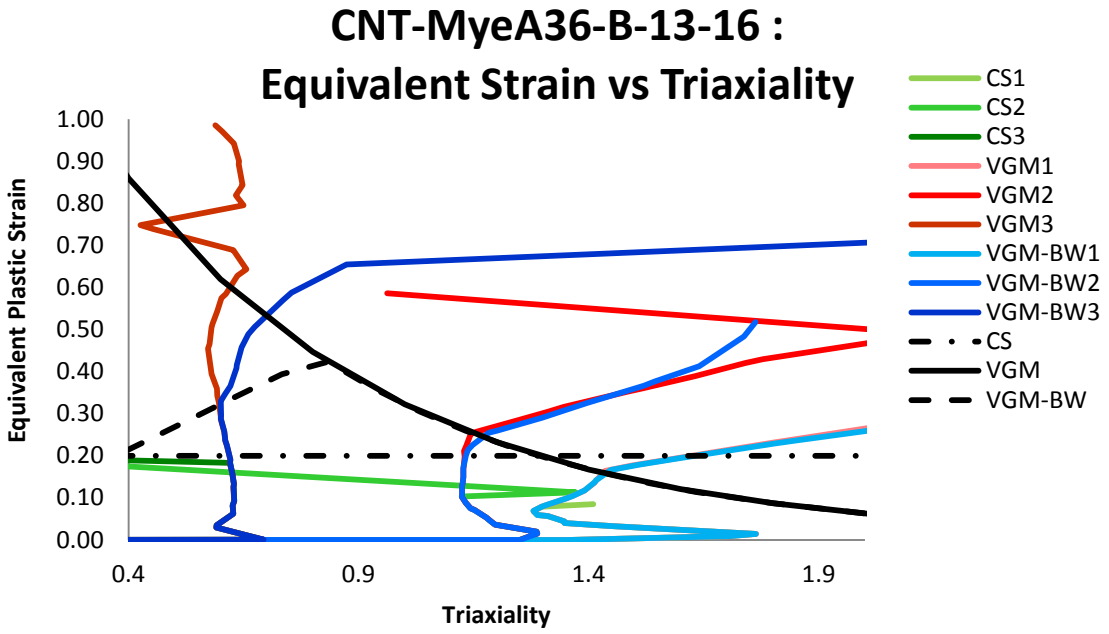

Figure 6.15: Variation of equivalent plastic strain with triaxiality for different elements laid out through the thickness of simulation of CNT-MyeA36-B-13-16 specimen for the three finite element deletion strategies

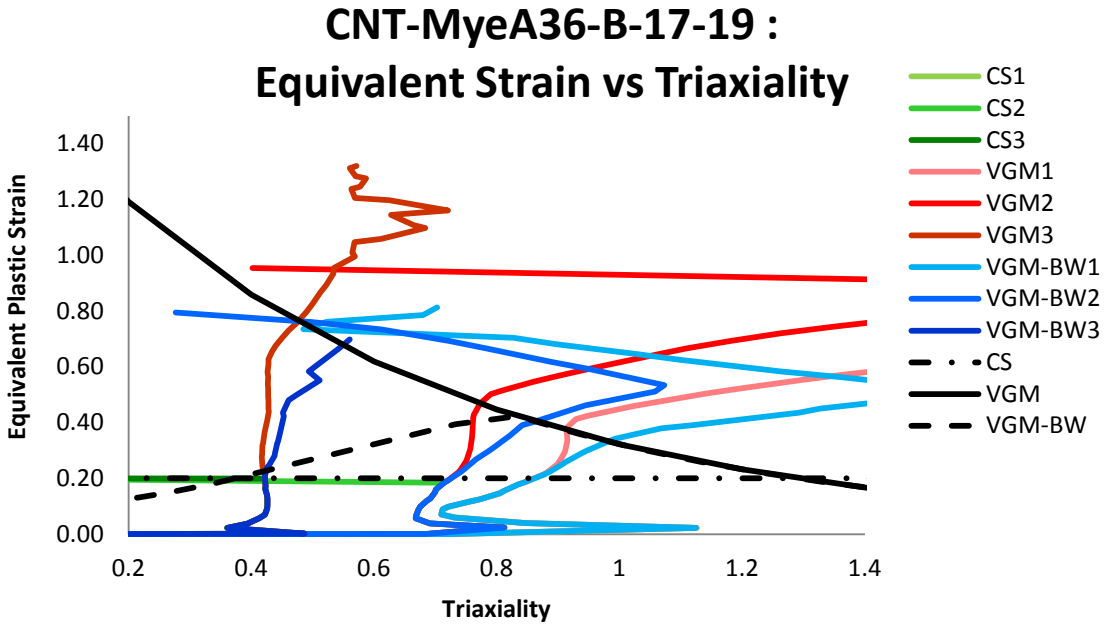

Figure 6.16: Variation of equivalent plastic strain with triaxiality for different elements laid out through the thickness of simulation of CNT-MyeA36-B-17-19 specimen for the three finite element deletion strategies

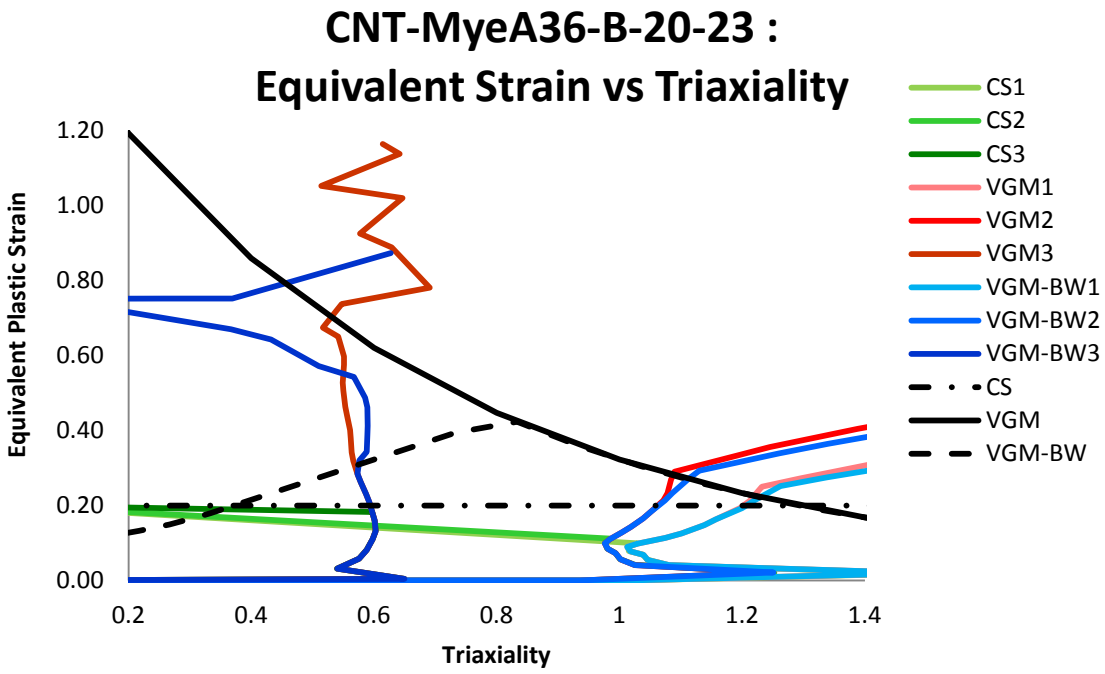

Figure 6.17: Variation of equivalent plastic strain with triaxiality for different elements laid out through the thickness of simulation of CNT-MyeA36-B-20-23 specimen for the three finite element deletion strategies

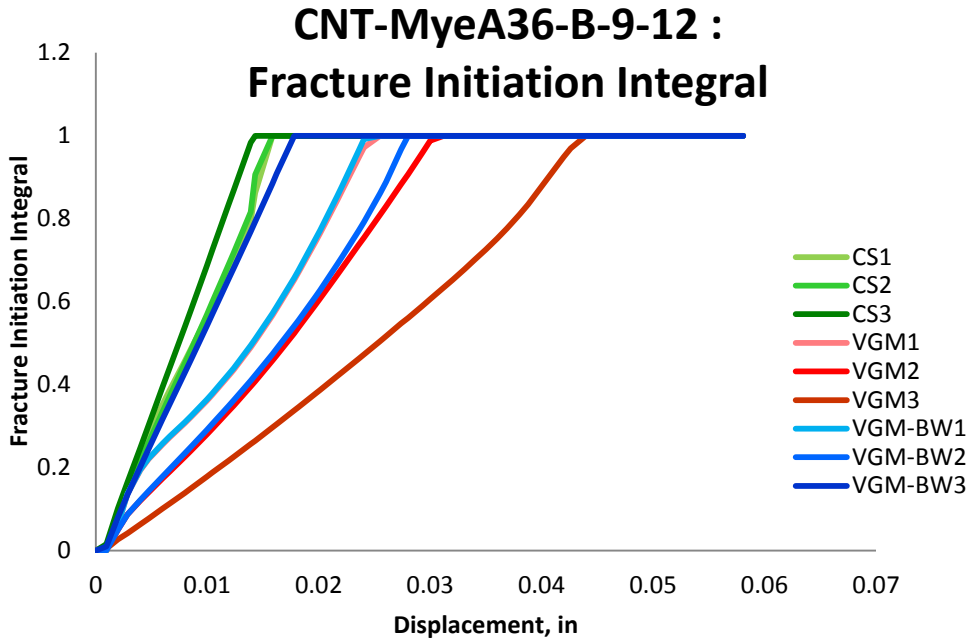

Figure 6.18: Variation of fracture initiation integral value with displacement for different elements laid out through the thickness of simulation of CNT-MyeA36-B-9-12 specimens for the three finite element deletion strategies

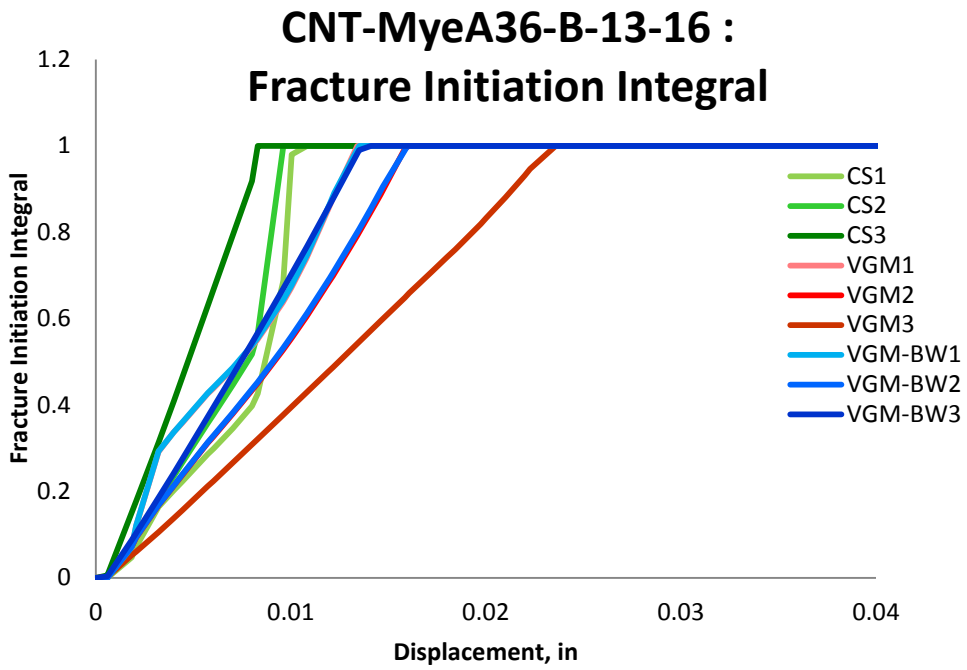

Figure 6.19: Variation of fracture initiaiton integral value with displacement for different elements laid out through the thickness of simulation of CNT-MyeA36-B-13-16 specimen for the three finite element deletion strategies

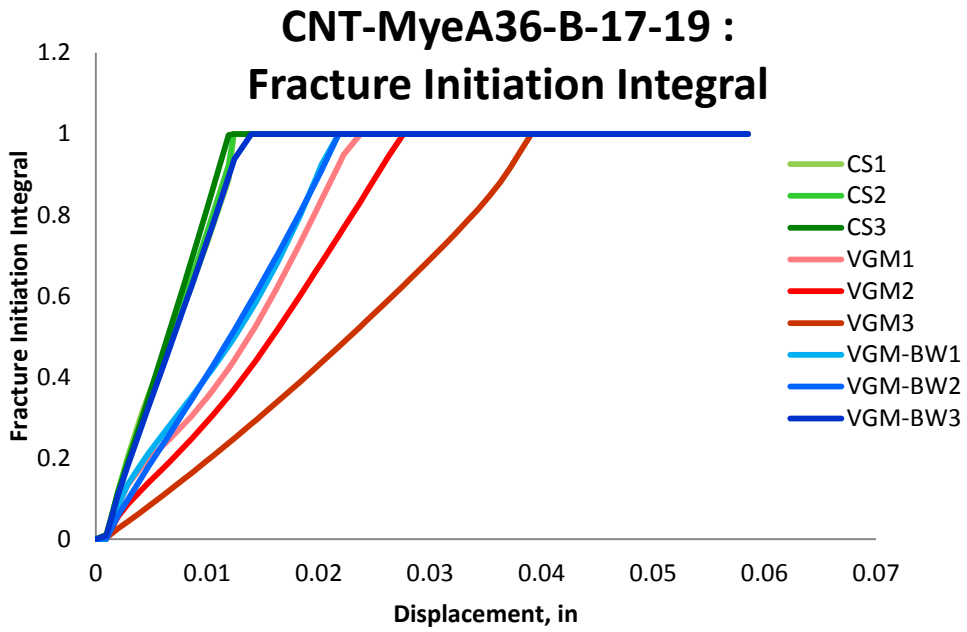

Figure 6.20: Variation of fracture initiation integral with displacement for different elements laid out through the thickness of simulation of CNT-MyeA36-B-17-19 specimen for the three finite element deletion strategies

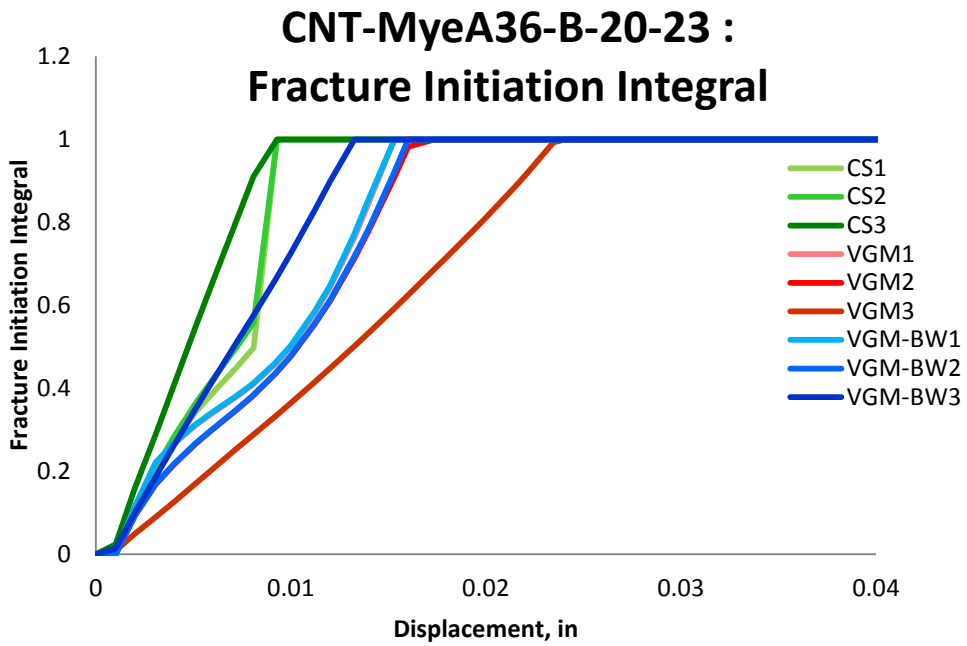

Figure 6.21: Variation of fracture initiation integral value with displacement for different elements laid out through the thickness of simulation of CNT-MyeA36-B-20-23 specimen for the three finite element deletion strategies

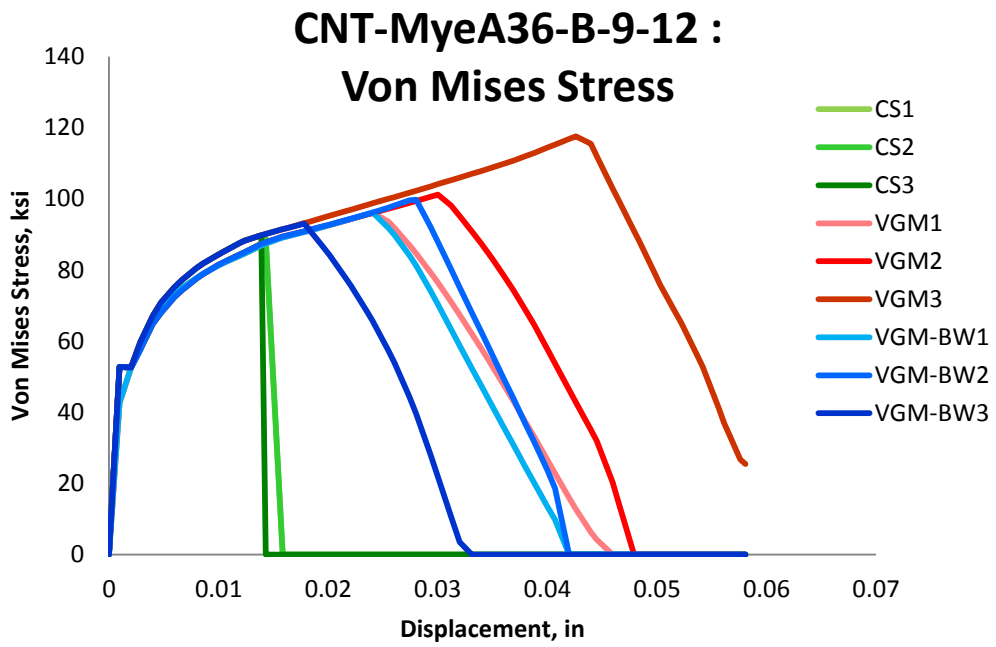

Figure 6.22: Variation of von Mises Stress with displacement for different elements laid out through the thickness of simulation of CNT-MyeA36-B-9-12 specimens for the three finite element deletion strategies

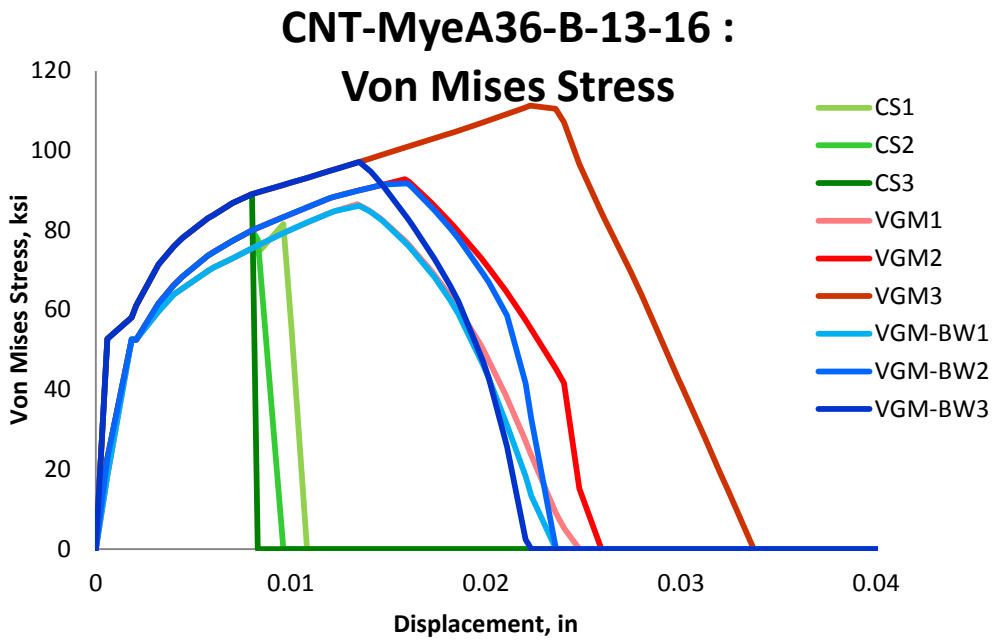

Figure 6.23: Variation of von Mises Stress with displacement for different elements laid out through the thickness of simulation of CNT-MyeA36-B-13-16 specimen for the three finite element deletion strategies

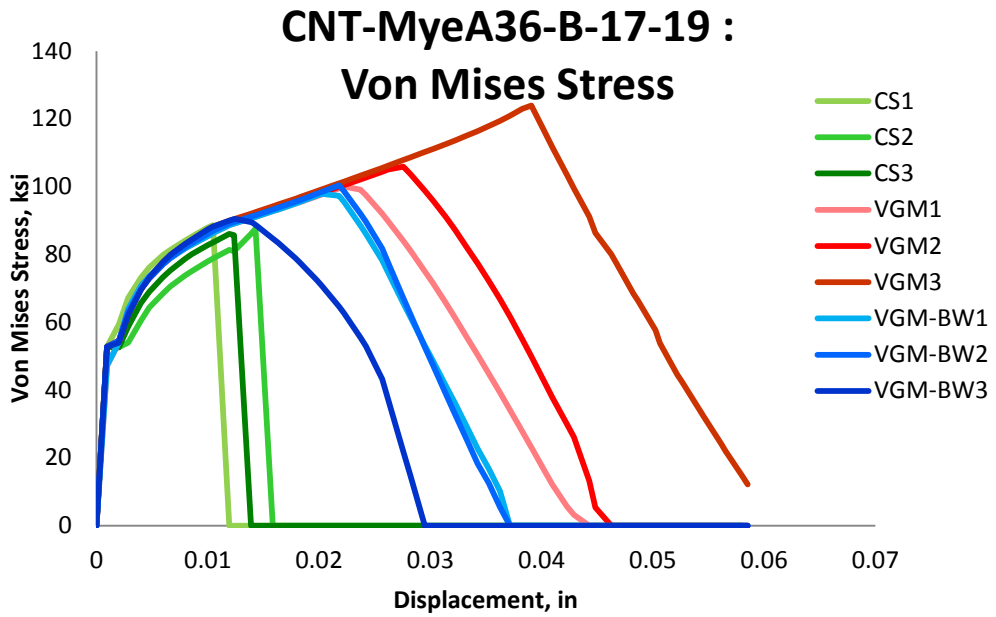

Figure 6.24: Variation of von Mises Stress with displacement for different elements laid out through the thickness of simulation of CNT-MyeA36-B-17-19 specimen for the three finite element deletion strategies

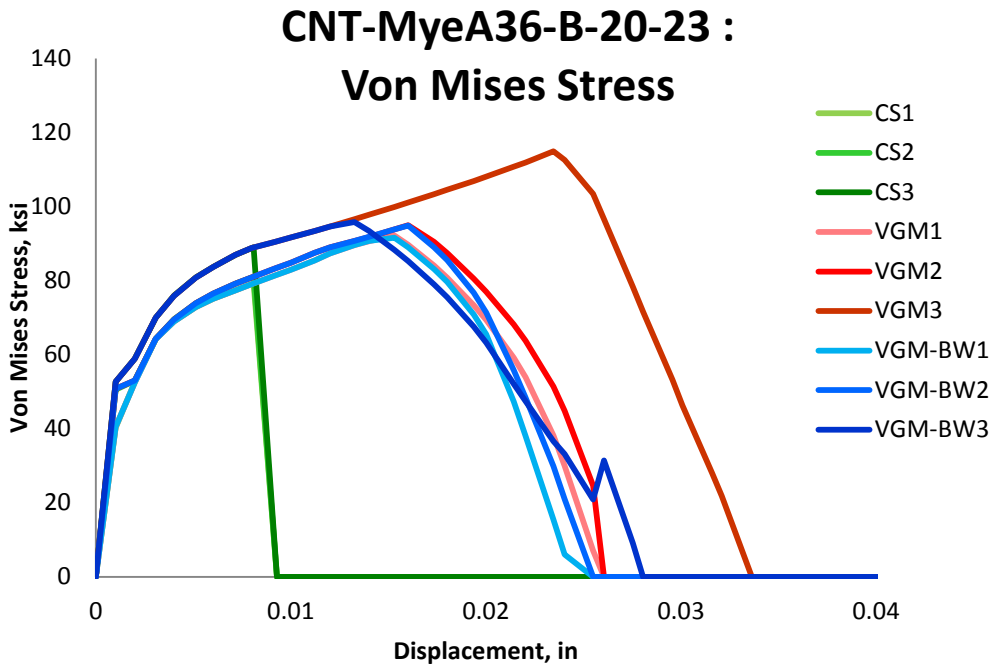

Figure 6.25: Variation of von Mises Stress with displacement for different elements laid out through the thickness of simulation of CNT-MyeA36-B-20-23 specimen for the three finite element deletion strategies

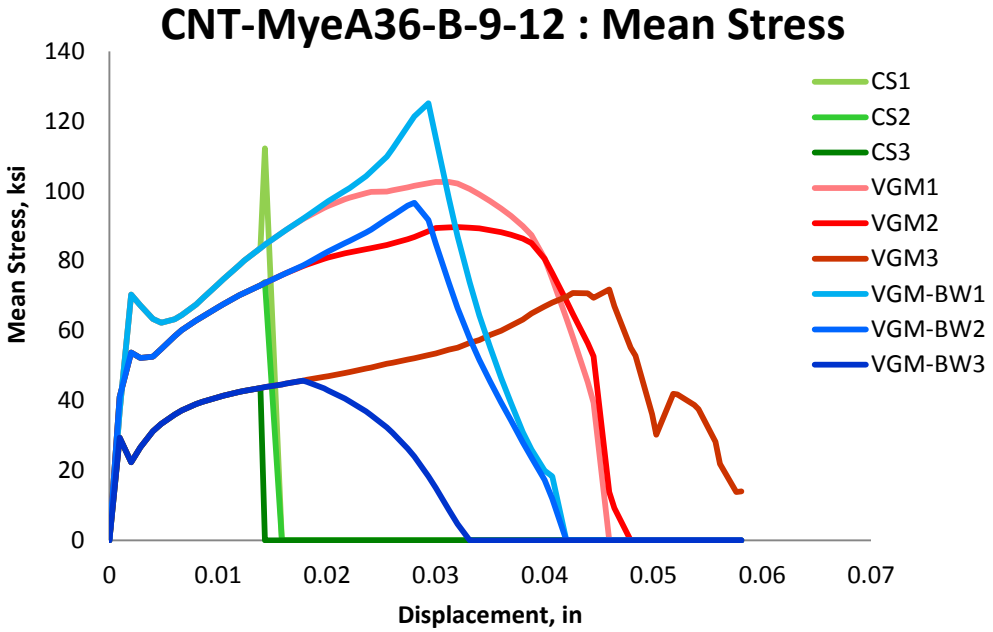

Figure 6.26: Variation of mean stress with displacement for different elements laid out through the thickness of simulation of CNT-MyeA36-B-9-12 specimens for the three finite element deletion strategies

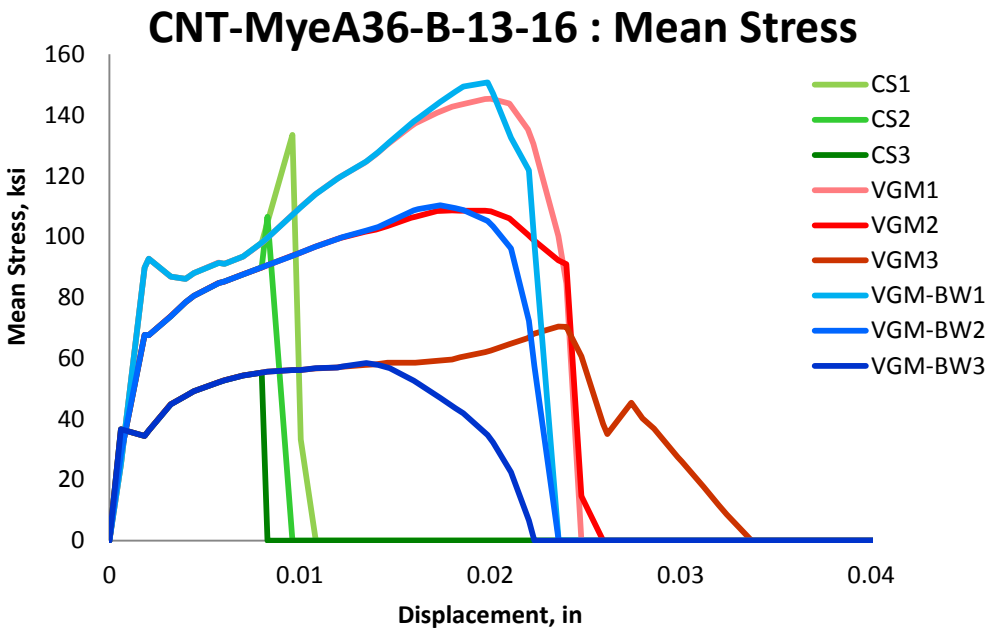

Figure 6.27: Variation of mean stress with displacement for different elements laid out through the thickness of simulation of CNT-MyeA36-B-13-16 specimen for the three finite element deletion strategies

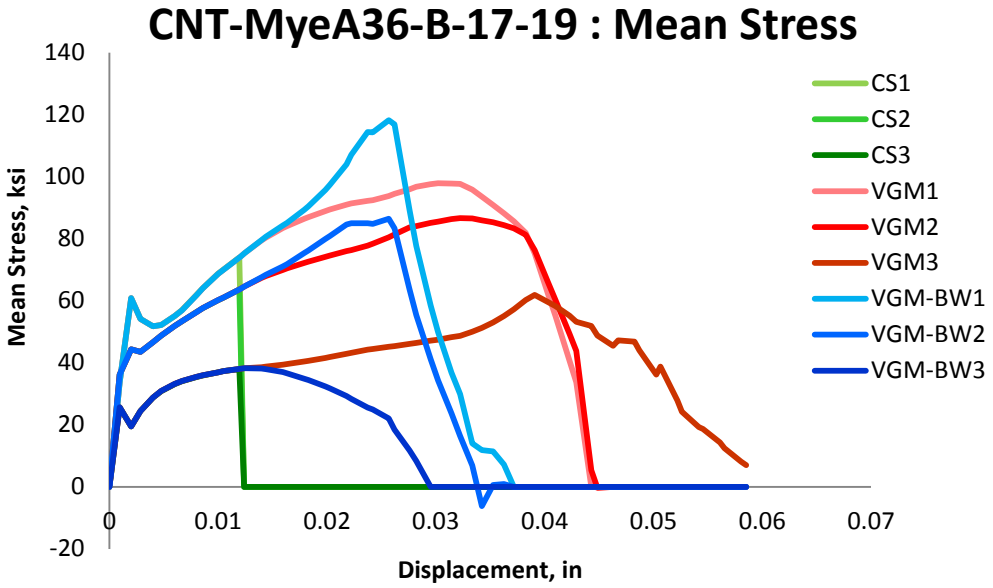

Figure 6.28: Variation of mean stress with displacement for different elements laid out through the thickness of simulation of CNT-MyeA36-B-17-19 specimen for the three finite element deletion strategies

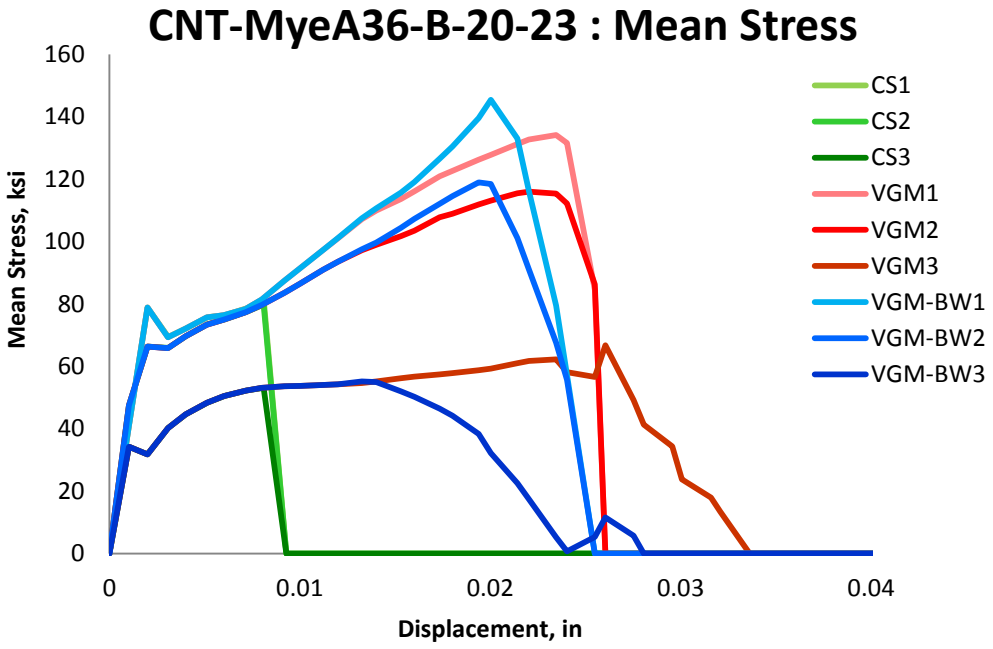

Figure 6.29: Variation of mean stress with displacement for different elements laid out through the thickness of simulation of CNT-MyeA36-B-20-23 specimen for the three finite element deletion strategies

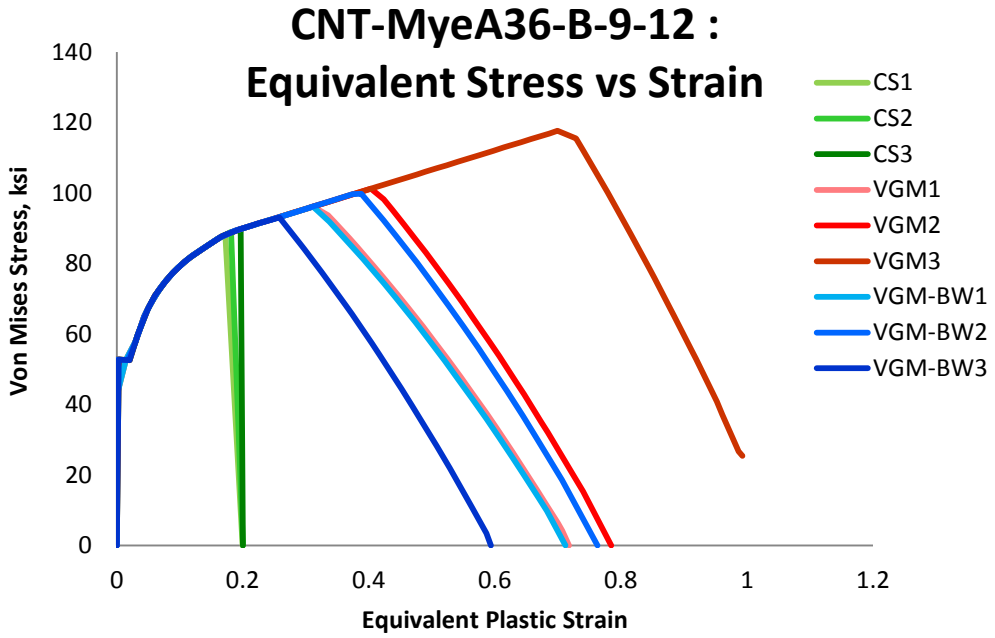

Figure 6.30: Variation of von Mises Stress with equivalent plastic strain for different elements laid out through the thickness of simulation of CNT-MyeA36-B-9-12 specimens for the three finite element deletion strategies

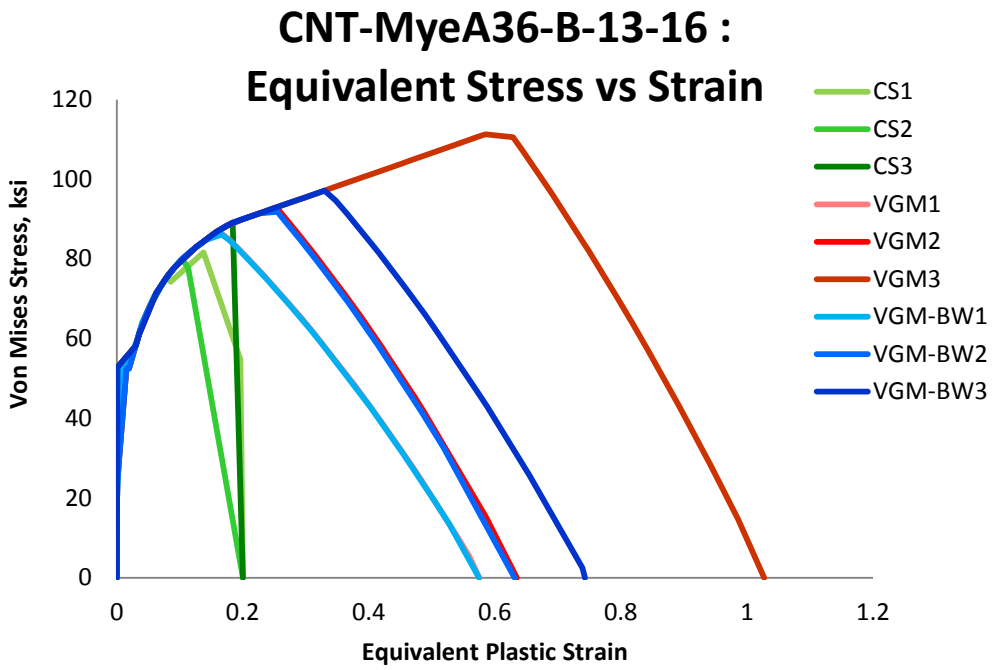

Figure 6.31: Variation of von Mises Stress with equivalent plastic strain for different elements laid out through the thickness of simulation of CNT-MyeA36-B-13-16 specimen for the three finite element deletion strategies

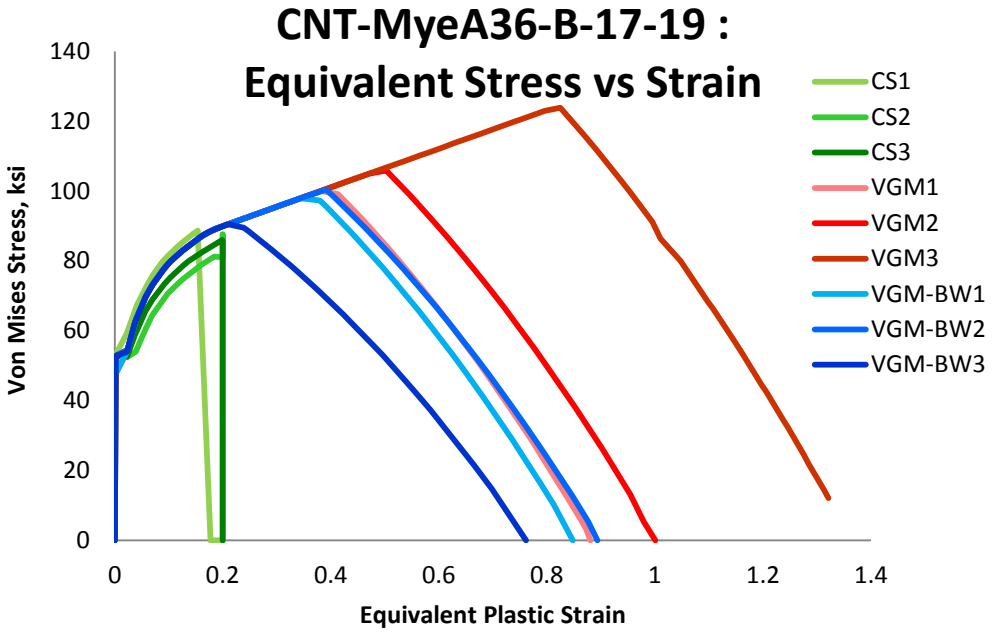

Figure 6.32: Variation of von Mises Stress with equivalent plastic strain for different elements laid out through the thickness of simulation of CNT-MyeA36-B-17-19 specimen for the three finite element deletion strategies

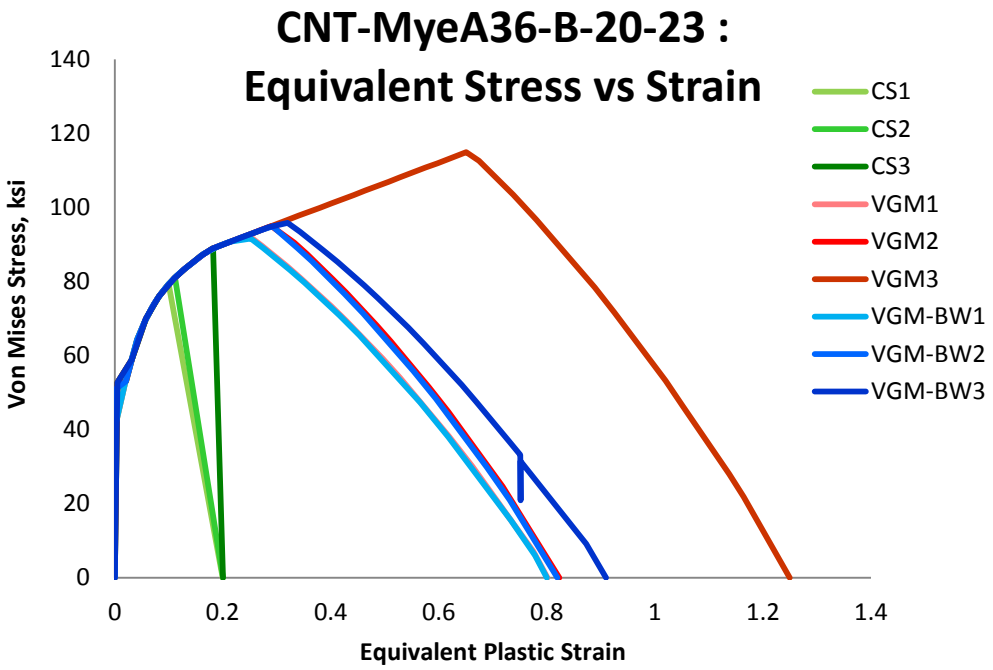

Figure 6.33: Variation of von Mises Stress with equivalent plastic strain for different elements laid out through the thickness of simulation of CNT-MyeA36-B-20-23 specimen for the three finite element deletion strategies

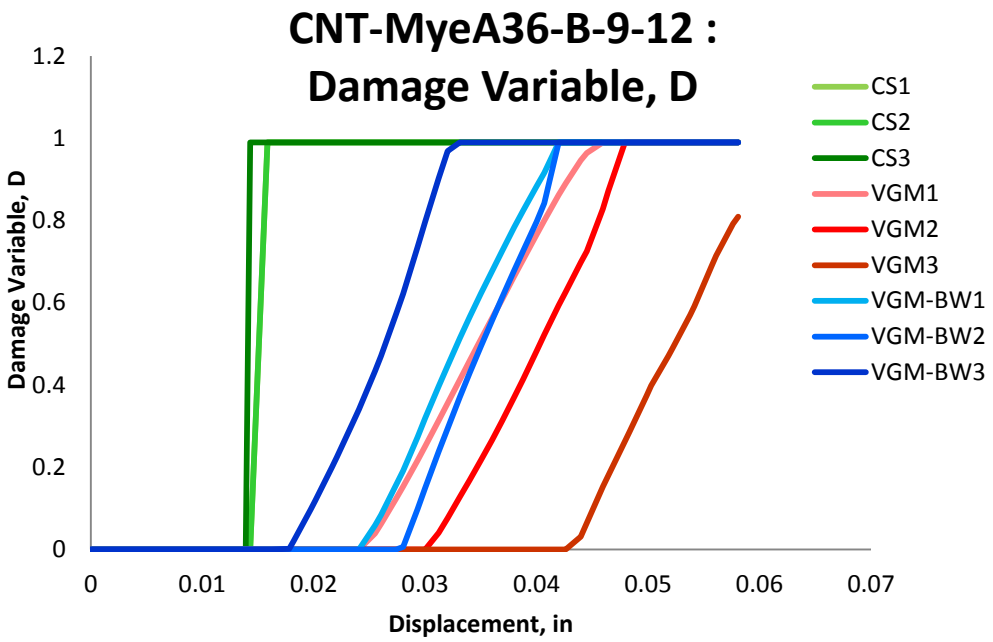

Figure 6.34: Variation of Damage Variable with displacement for different elements laid out through the thickness of simulation of CNT-MyeA36-B-9-12 specimens for the three finite element deletion strategies

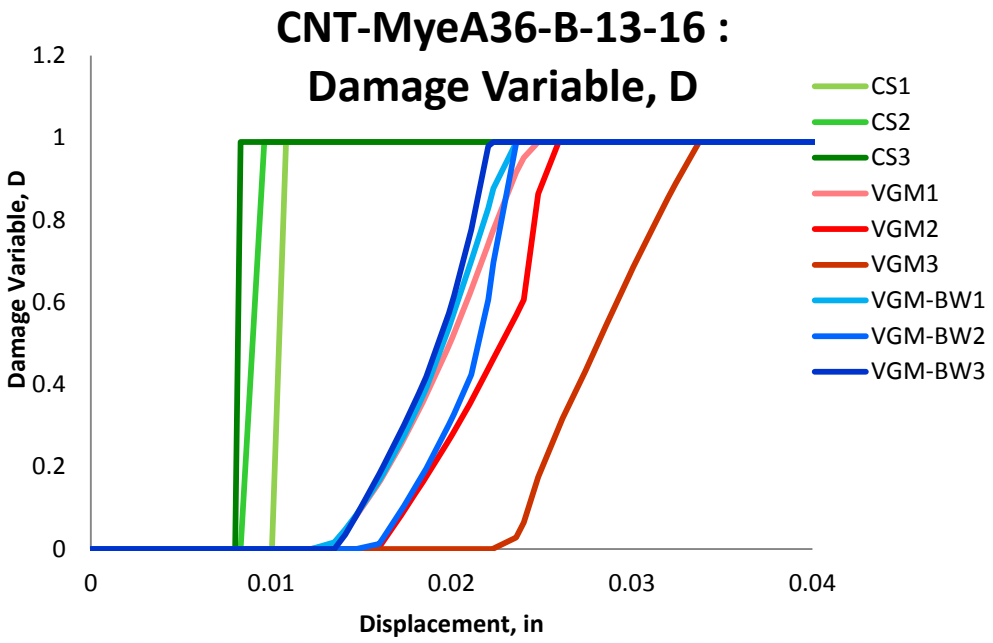

Figure 6.35: Variation of Damage Variable with displacement for different elements laid out through the thickness of simulation of CNT-MyeA36-B-13-16 specimen for the three finite element deletion strategies

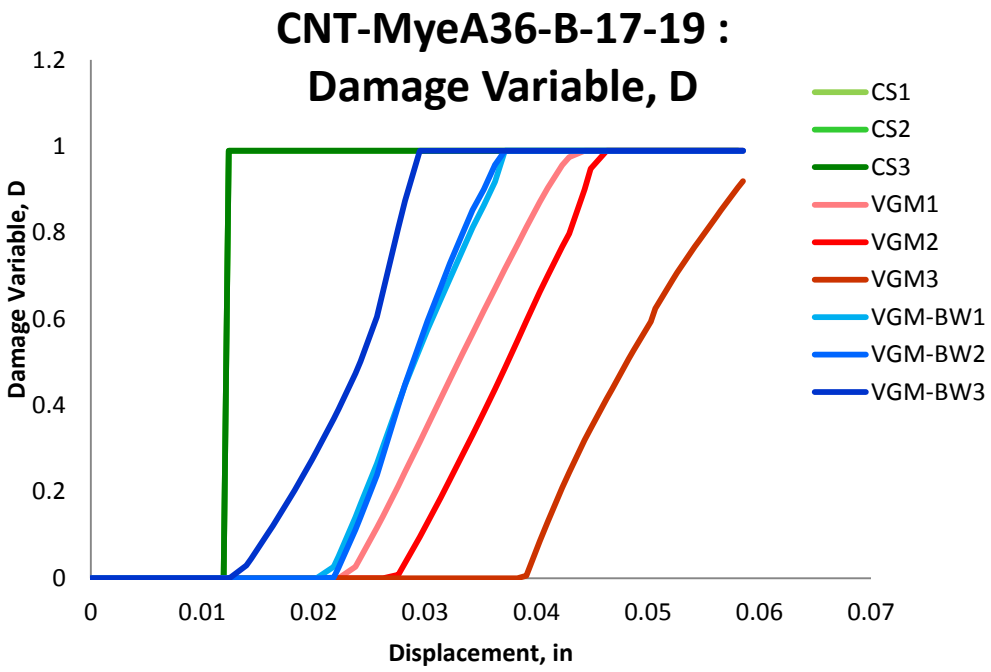

Figure 6.36: Variation of Damage Variable with displacement for different elements laid out through the thickness of simulation of CNT-MyeA36-B-17-19 specimen for the three finite element deletion strategies

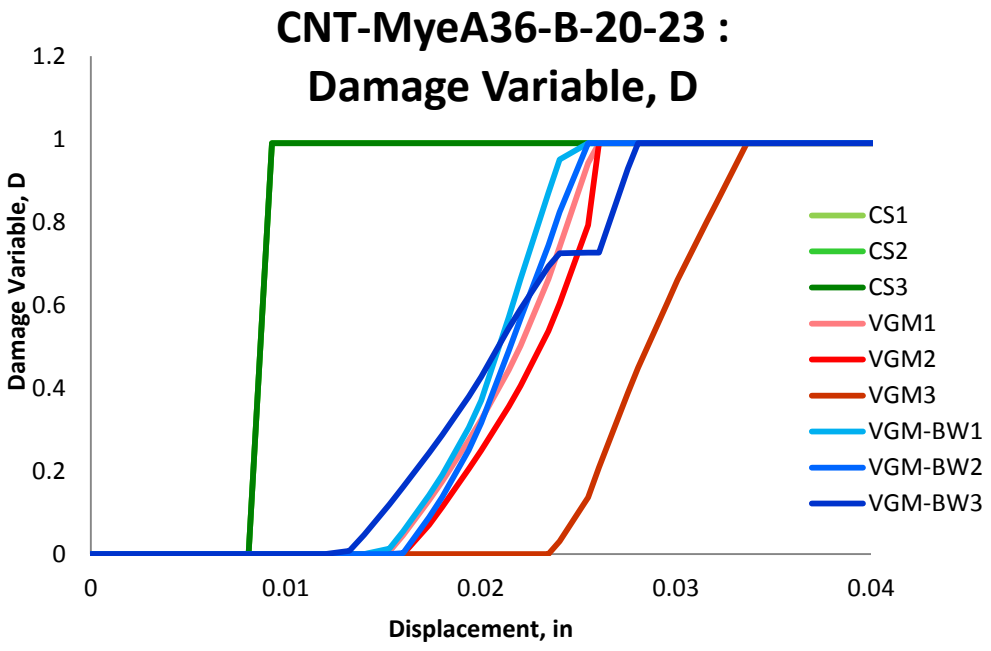

Figure 6.37: Variation of Damage Variable with displacement for different elements laid out through the thickness of simulation of CNT-MyeA36-B-20-23 specimen for the three finite element deletion strategies

6.1.1 Summary

Structural steel of type A36 was validated through comparison to CNTs with different notched radius and notch root diameters than the specimens used for calibration. This enforced a different triaxiality range throughout the loading for validation specimens than for calibration ones. The results show that the VGM calibrated fracture locus was able to capture the fracture behavior well in a different triaxiality range while the VGM-BW and Constant Strain approaches were not able to capture fracture behavior well. In addition, the following observations could be made:

- For CS simulations, dynamic instabilities were observed. These results highlight the issue of using CS strategy, which can induce significant dynamic instabilities during collapse modeling forcing significant error into models prediction.
- The VGM-BW and VGM strategies which model softening through the Hillerborg Model do not show any signs of dynamic instability for these specimens.
- After initiation of softening, triaxiality is dramatically increased for the inner elements but not for the outer one. The equivalent plastic strain for the outer element in the VGM and to a lesser extent the VGM-BW simulations continues to have a near vertical slope to triaxiality throughout the entire loading excursion and is not strongly affected by softening. The difference in force-displacement curves of VGM and VGM-BW finite element deletion strategies is most distinctive in the outer element.
- In the VGM simulations fracture initiates at the center of the specimen and propagates outward in agreement to the conclusions found in the literature. However the CS and VGM-BW simulations have the fracture start from the outside.

- In VGM simulations, the elements on the surface of the specimens exhibit much larger strain energy using the same material model than those at the center. However, for VGM-BW, no apparent trend is observable, and CS simulations have immediate failure for all of the three elements.

6.2 Plate Specimens

Another experimental test that was used for validation purposes was a pull-plate specimen. The pull-plate specimens used for validation were originally designed to study fracture under conditions representative of a bolted end of a tension member (Kanvinde et al. 2004). The specimens are designated as bolt-hole pull-plates BH-KanHPS70W-P-1-2 and BH-KanHPS70W-P-1-2 in Figure 6.38 and were used to validate type A572 Grade 50 and HPS70W steels, respectively. The specimens were cut from a plate with 2” x 1” x 6” dimensions and with the central 3 inches of the plate milled down to a thickness of 0.375 inches. In addition, the load is applied to the specimens at its ends by pins connected to the actuator. The average displacement reading was used for comparison to finite element simulation results. A one-eighth symmetrical model with appropriate symmetrical boundary conditions was used to simulate the pull-plate specimens. The plasticity and fracture model data inputs are described in Table 6.3. For the experimental results, fracture initiated on the specimen’s hole’s outside surface from the center of the specimen (Kanvinde et al. 2004). Figure 6.39 shows the selected finite elements for study of fracture initiation and propagation. The figure also shows the general boundary conditions used for the finite element simulations.

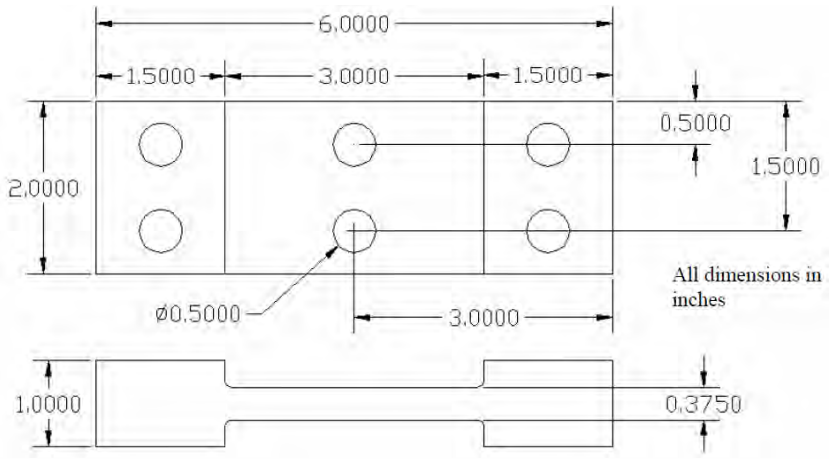

Figure 6.38: Experimental setup (Kanvinde et al. 2004) of a pull-plate BH-KanA572-P-1 and BH-KanHPS70W-P-1-2 specimens

Table 6.3: Plasticity and fracture model inputs for BH-KanA572-P-1, BH-KanHPS70W-P-1-2, DB-KanA572-P-1, and DB-KanHPS70W-P-1-2 specimens

		Fracture Model Input		
Test	**Plasticity Model Input**	**VGM**	**VGM-BW**	**CS**
BH-KanA572-P-1	CNT-KanA572-P-A	CNT-KanA572-P-A	TC-KanA572-P-A	0.2
BH-KanHPS70W-P-1-2	CNT-KanHPS70W-P-A	CNT-KanHPS70W-P-A	TC-KanHPS70W-P-A	0.2
DB-KanA572-P-1	CNT-KanA572-P-A	CNT-KanA572-P-A	TC-KanA572-P-A	0.2
DB-KanHPS70W-P-1-2	CNT-KanHPS70W-P-A	CNT-KanHPS70W-P-A	TC-KanHPS70W-P-A	0.2

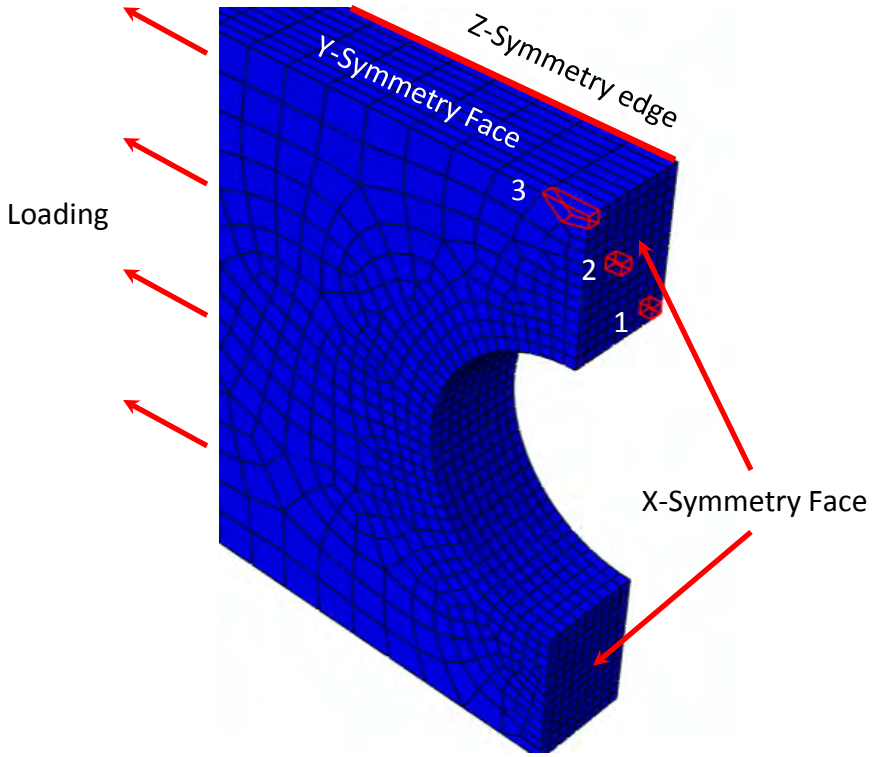

Figure 6.39: Elements selected for studying fracture initiation and propagation parameters in VGM-BW, VGM, and CS approaches for BH-KanA572-P-1 and BH-KanHPS70W-P-1-2 and the overall boundary conditions used for finite element simulations

In above discussion of the CNT specimens, it was mentioned that the three strategies predicted different locations of fracture initiation and direction of fracture propagation.

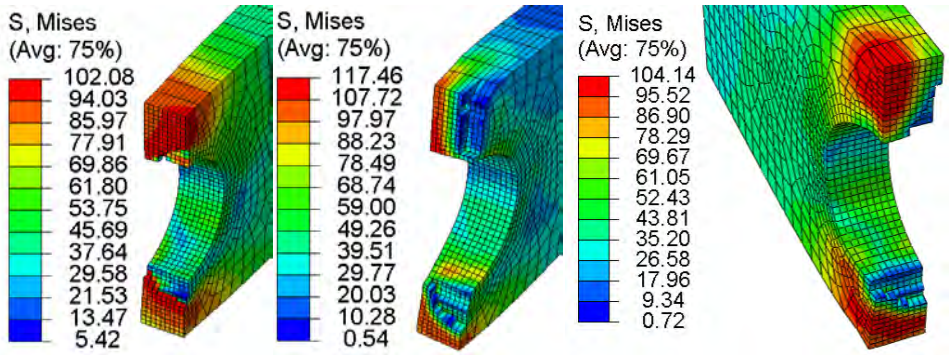

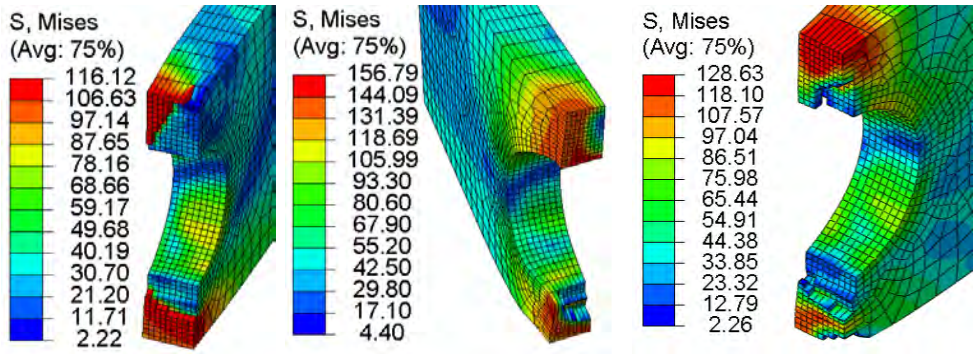

Figure 6.40 shows typical locations and propagation of fracture in these bolt-hole pull-plate specimens for different finite element deletion strategies. The red boxes highlight the location of fracture represented by finite element deletion in all of the following contour plots. The VGM criteria closely followed the experimental observations with fracture originating on the outside surface of the specimen hole from the center of the specimen and propagating to the outer surface of the specimen. However, fracture also quickly initiated on the inside surface of the specimen hole in the center of the specimen. For the CS and VGM-BW simulations, the fracture occurred simultaneously on the outer and inner surfaces of the specimen hole in the center of the specimen and propagated outward. As the loading progressed the VGM-BW simulation had fracture occur on the surface of the specimen independent from the crack propagating from the inside out. This type of fracture is not reported in the experimental test results or literature and no physical explanation could be found. However, the overall fracture propagation of fracture initiating at the center of the specimen and propagating outwards was capture by VGM-BW and CS strategies. Figure 6.41 and Figure 6.42 show the force-displacement results from the CS, VGM, and VGM-BW simulations. The CS underpredicts the force-displacement capacity of the plate by more than 50% for both materials. The VGM-BW strategy also significantly underpredicts the plates' capacity while the VGM predicts the

strength of the BH-KanA572-P-1 specimen well and has a near perfect fit for the BH-KanHPS70W-P-1-2 specimen. It should be noted that the experimental softening curve of these specimens consists of only two data points and a line that connects these points. In addition, for these bolt-hole pull-plate specimens, the dynamic instability in CS simulations is not that significant but is still present, while the VGM and VGM-BW, again, have no dynamic instability issues. To better understand these issues, the variation of fracture parameters are plotted and discussed below in similar manner to the previous section.

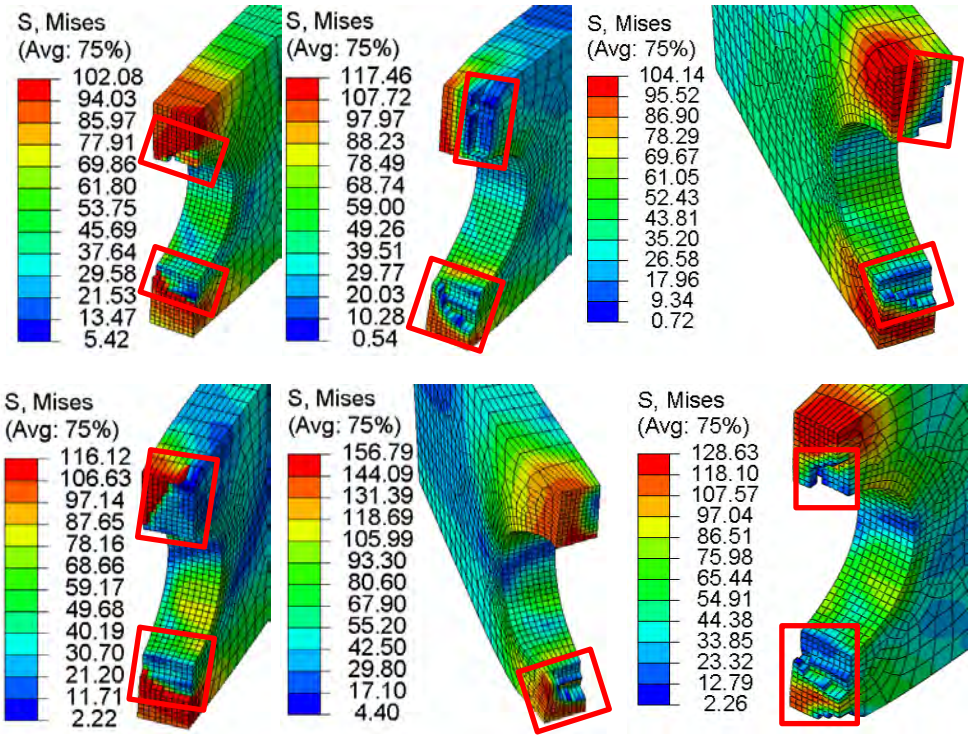

Figure 6.40: Simulation results (Kanvinde et al. 2004) of a BH-KanA572-P-1 specimen on top and BH-KanHPS70W-P-1-2 specimen on bottom with contours representing von Mises stress (ksi): CS (left), VGM (middle), VGM-BW (right)

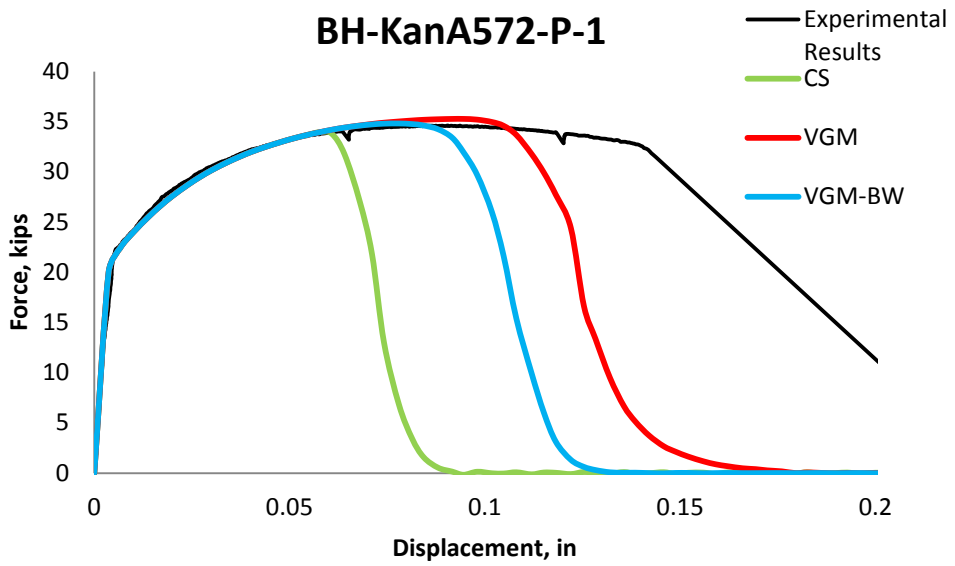

Figure 6.41: Validation results for pull-plate specimen BH-KanA572-P-1

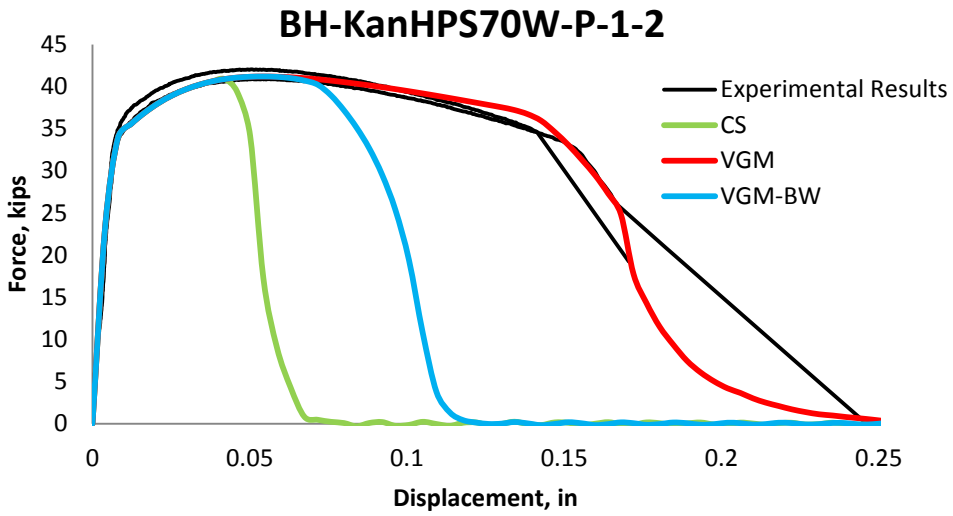

Figure 6.42: Validation results for pull-plate specimen BH-KanHPS70W-P-1-2

The variation of triaxiality with displacement is plotted for the three elements across the thickness of the specimen for the three finite element deletion strategies in Figure 6.43 and Figure 6.44. As in CNT specimens, the triaxiality is the same in each element throughout the loading excursion until the point of softening. After this point, the value of triaxiality is different for the three strategies. Most elements experience a significant increase in triaxiality before

failure except for the inside element 1 during the CS simulation. The curves in these two figures look very similar, suggesting that triaxiality variation during loading of a specimen is mainly governed by the geometry of the specimen and to a lesser extent the material of the specimen, since geometry is the same for the two specimens while the material is different. The equivalent plastic strain is plotted in Figure 6.45 and Figure 6.46. The figures show that for VGM simulations the inside element 1 reached the highest strain value of 100% and the element on the outside reached the lowest value for HPS70W material specimen. The slope of the equivalent plastic strain versus displacement curve increases at softening initiation.

The fracture locus is plotted in Figure 6.47 and Figure 6.48. In these figures, it is seen that the triaxiality range for the two materials is approximately the same, becoming wider with increasing equivalent plastic strain. The fracture locus for the CS is defined by a line at 0.2 equivalent plastic strain. The fracture locus for the three strategies is very similar to each other in this triaxiality range of 0.4 to 0.6 for BH-KanA572-P-1 specimen. However, the force-displacement results are different. The main difference is that CS does not include softening while VGM and VGM-BW do. This highlights the effect that softening can have on the global behavior of a structure. In this case, the difference in force-displacement capacity between CS and VGM strategies is approximately 40% and 15% between VGM and VGM-BW strategies. This smaller difference between the VGM and VGM-BW strategies is due to the fact that two elements initiate softening through the VGM criteria while the third one is affected by Bao-Wierzbicki criteria. For the BH-KanHPS70W-P-1-2 specimen the difference between the VGM and VGM-BW model is much larger because all three elements in the VGM-BW simulation initiated fracture based on Bao-Wierzbicki criteria.

The variation of the value of fracture initiation integral is shown in Figure 6.49 and Figure 6.50. In the VGM-BW and CS simulations the three elements follow distinctly different paths from each other, while the two inner elements in the VGM simulations have very similar paths. Element 3 on the outside surface has the smallest slope and reaches the highest displacement value, before initiating fracture, for all of the three strategies. As one moves inward the slope of the value of this integral increases due to higher triaxiality. This signifies that fracture will initiate at the center of the specimen before it does on the surface of the specimen.

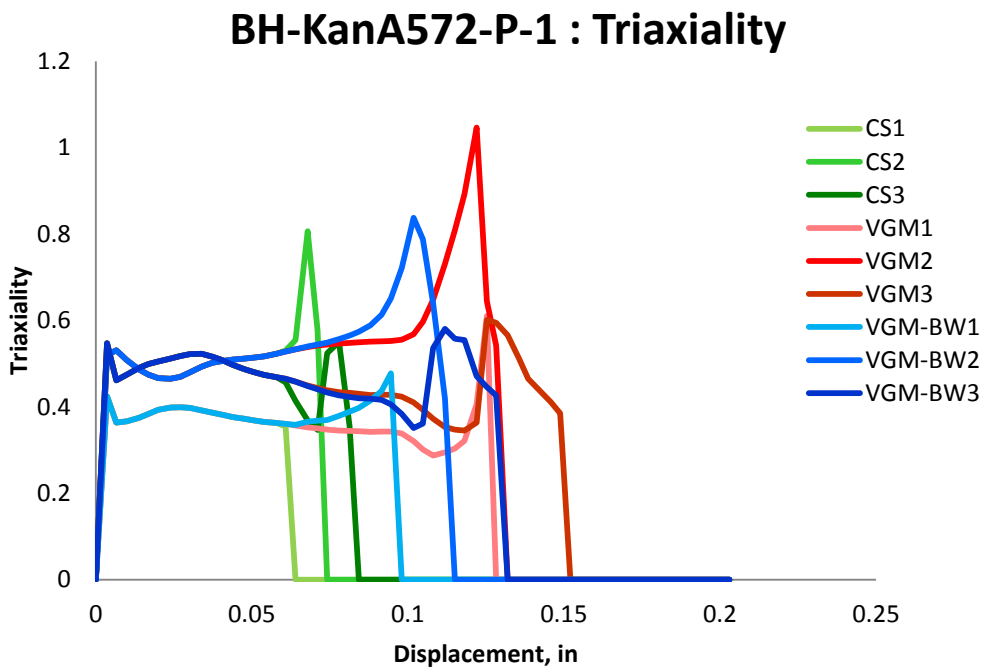

Figure 6.43: Variation of triaxiality with displacement for different elements laid out through the thickness of simulation of BH-KanA572-P-1 specimen for the three finite element deletion strategies

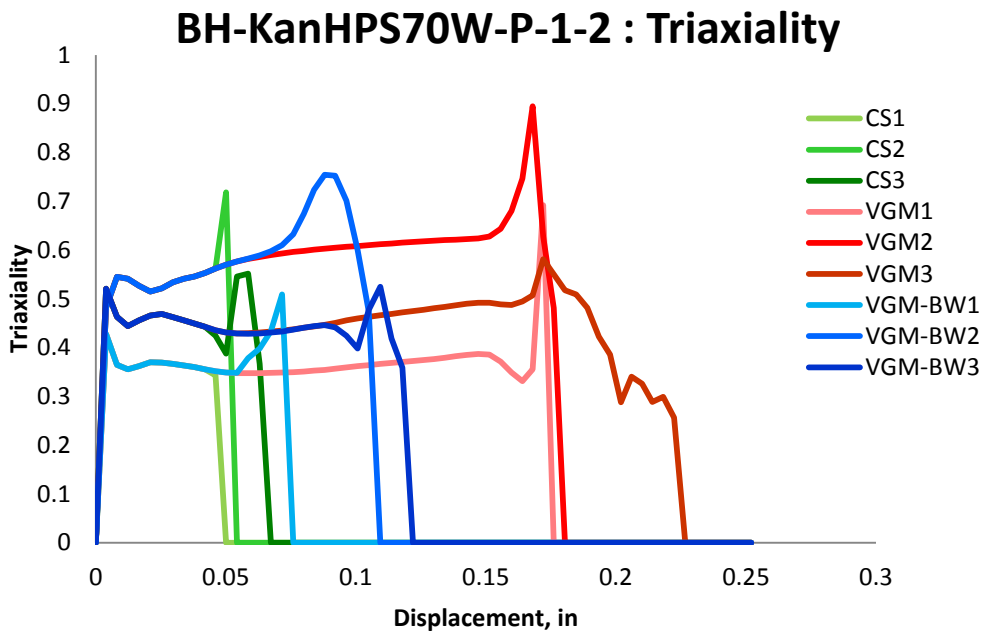

Figure 6.44: Variation of triaxiality with displacement for different elements laid out through the thickness of simulation of BH-KanHPS70W-P-1-2 specimens for the three finite element deletion strategies

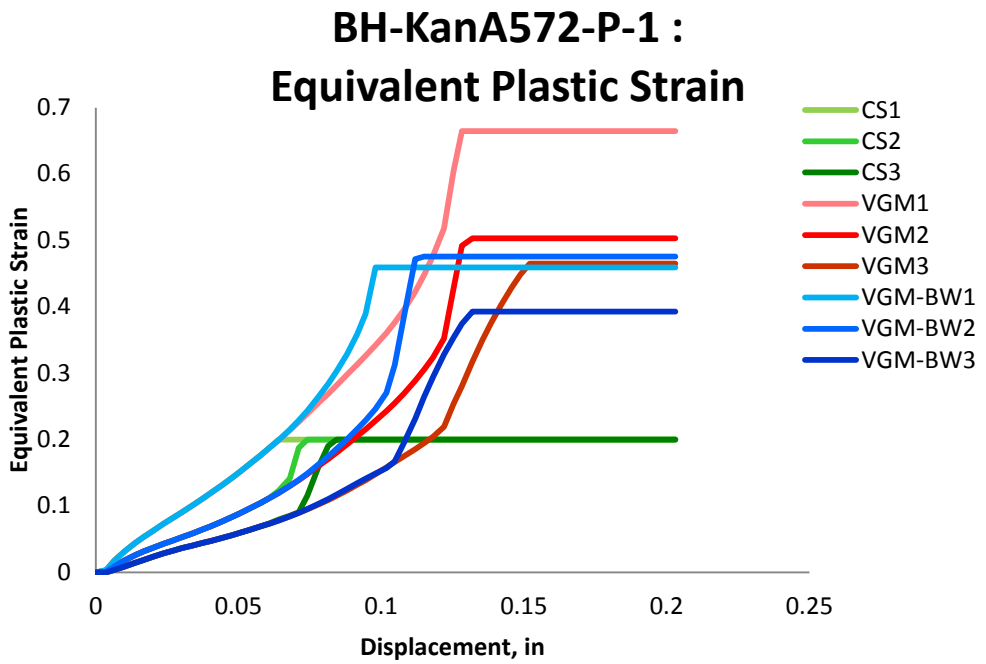

Figure 6.45: Variation of equivalent plastic strain with displacement for different elements laid out through the thickness of simulation of BH-KanA572-P-1 specimen for the three finite element deletion strategies

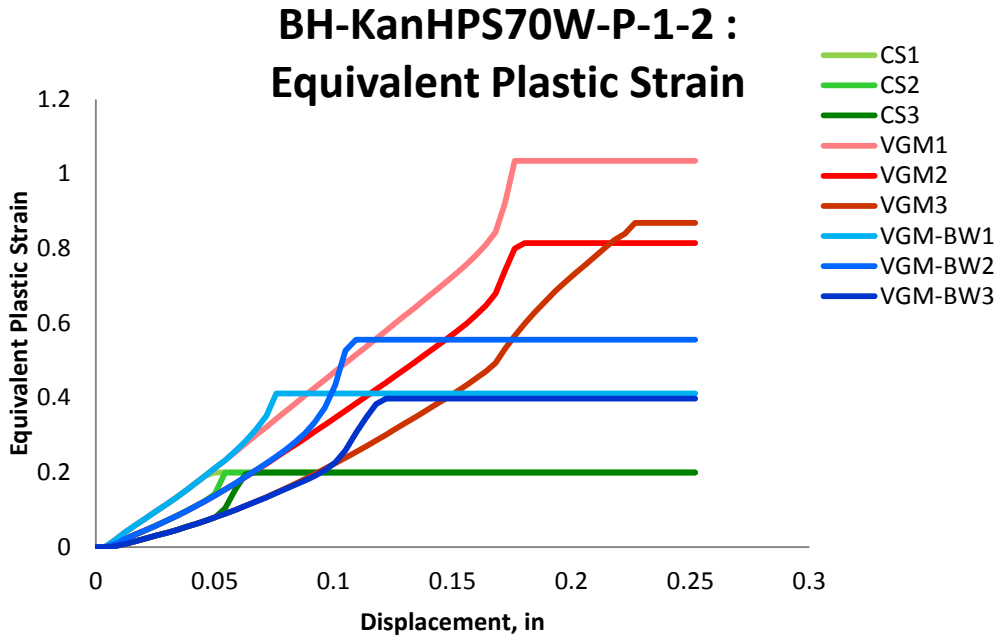

Figure 6.46: Variation of equivalent plastic strain with displacement for different elements laid out through the thickness of simulation of BH-KanHPS70W-P-1-2 specimens for the three finite element deletion strategies

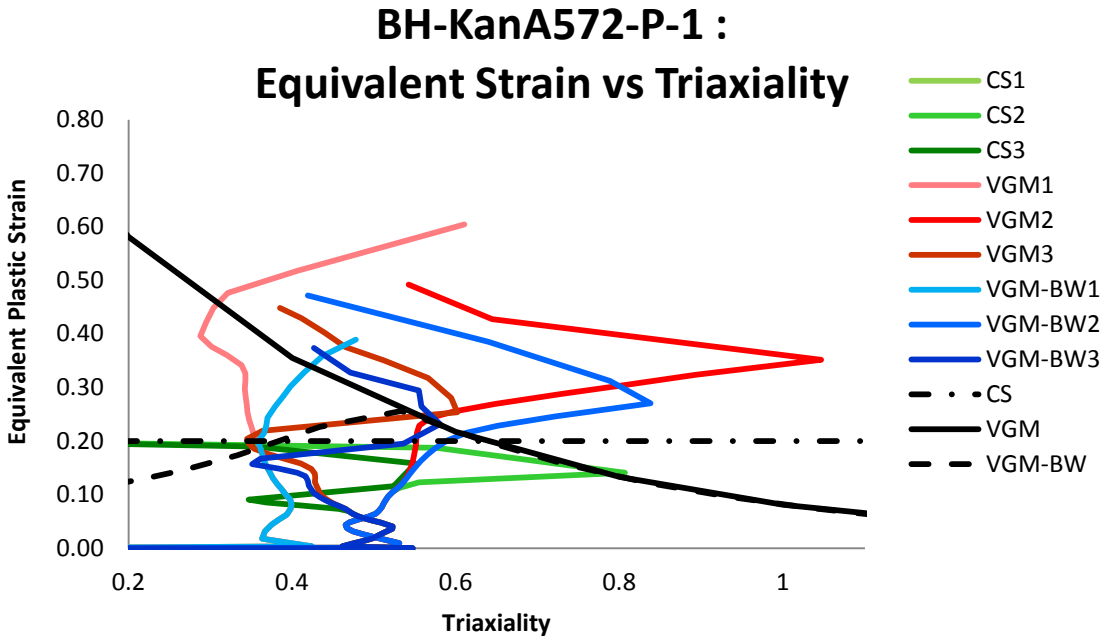

Figure 6.47: Variation of equivalent plastic strain with triaxiality for different elements laid out through the thickness of simulation of BH-KanA572-P-1 specimen for the three finite element deletion strategies

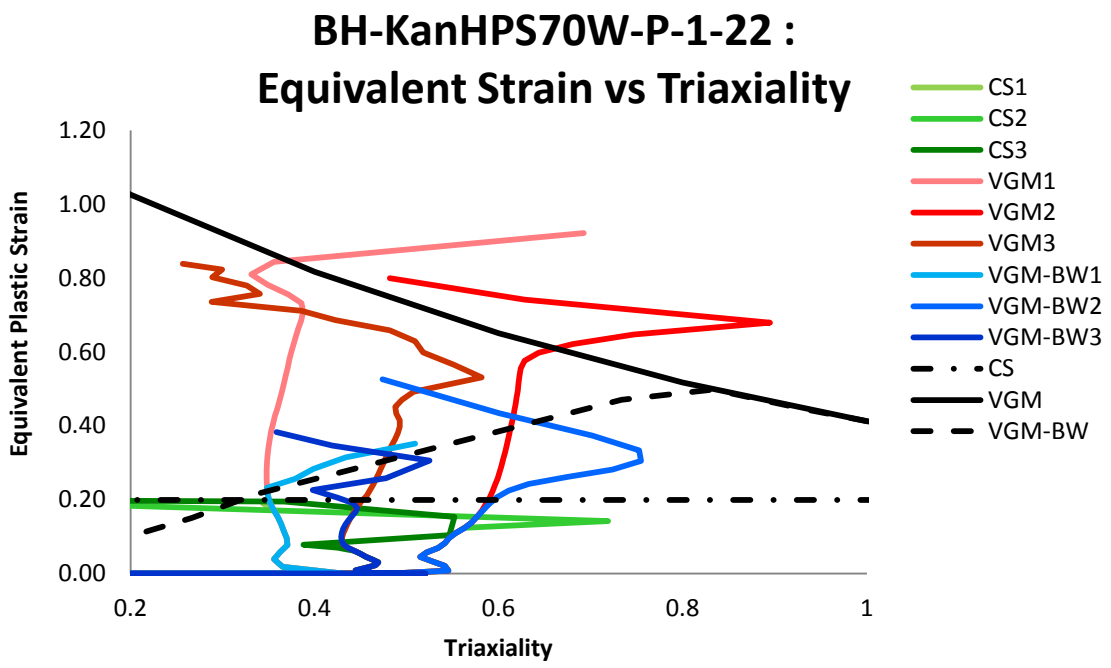

Figure 6.48: Variation of equivalent plastic strain with triaxiality for different elements laid out through the thickness of simulation of BH-KanHPS70W-P-1-2 specimens for the three finite element deletion strategies

There is a similar trend in the varition of von Mises stress with displacement shown in Figure 6.51 and Figure 6.52. The two inner elements, 1 and 2, for the VGM simulation initiate softening at approximately the same displacement, with very similar softening curves. However, the stress level between these two elements is significantly different signifying that fracture criteria was satisfied in these two elements at approximately similar displacement. The softening curve is distinct for all of the three elements in the VGM-BW and CS simulation. In addition, these two strategies have a clear trend of having a greater displacement value at fracture initiation point and softening for elements located farther from the hole's outside surface of the specimen. However, the stress values have the opposite trend. This means that the elements on the outside experience less stress per displacement than those at the center. Therefore, in these specimens the stress redistribution is such that the material on the inside

contributes more to resisting the load than the material on the outside until significant deformation has occurred, which would force stress redistribution to the outside material.

The mean stress variation throughout the loading excursion is plotted in Figure 6.53 and Figure 6.54. The mean stress in two of the elements for the three finite element deletion strategies dramatically increases right before softening. As elements are deleted on the through thickness surface, more stress is redistributed to the elements that still have load carrying capacity. With this stress redistribution, the mean stress increases for element 1 and 2, with the tendency for those elements to elongate in the primary loading direction, while other elements in non primary sides of the element offering resistance to the lateral deformation of the element. This is not the case for the third element on the surface of the specimen. The reason for this is that this element has one free surface that is free to deform due to Poisson's effect, therby decreasing the stress in the non primary loading directions.

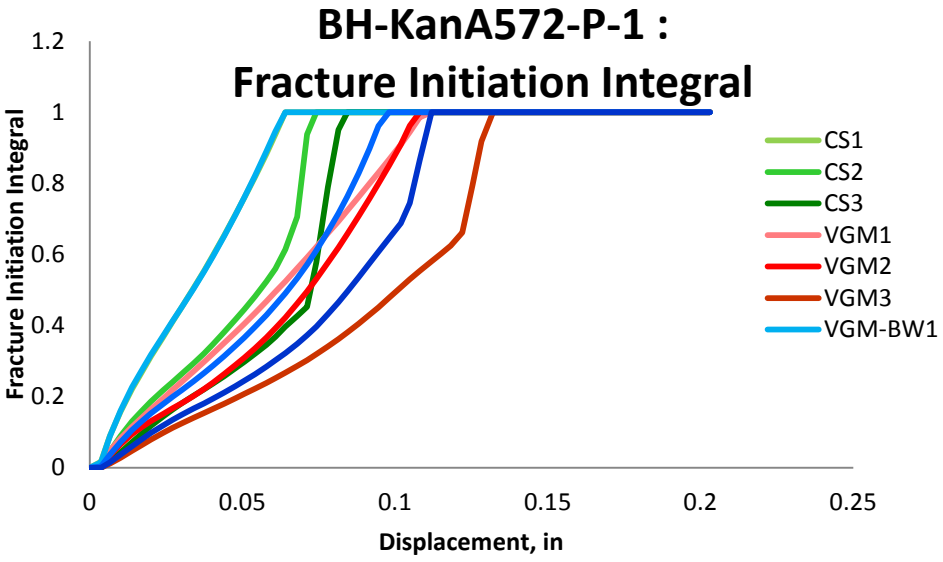

Figure 6.49: Variation of fracture initiation integral value with displacement for different elements laid out through the thickness of simulation of BH-KanA572-P-1 specimen for the three finite element deletion strategies

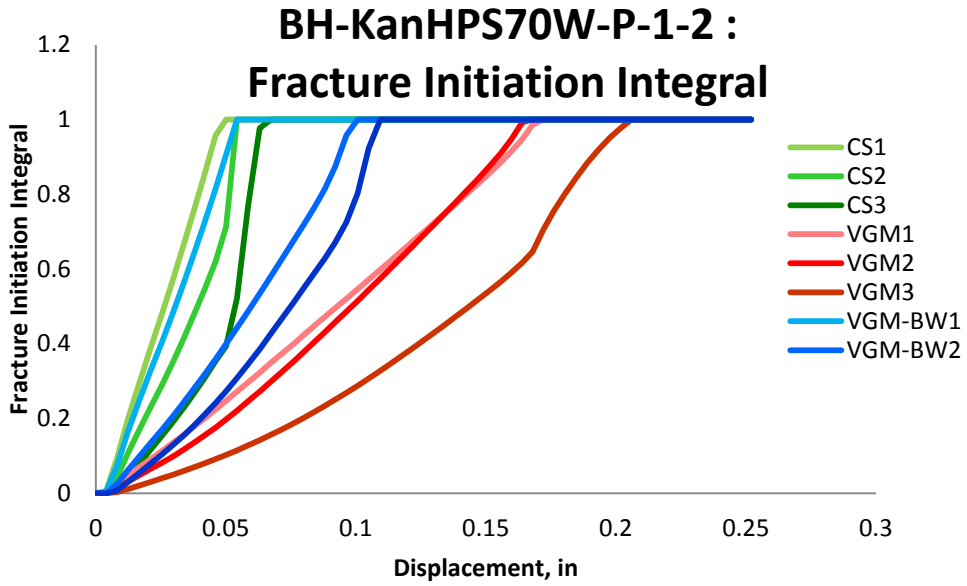

Figure 6.50: Variation of fracture initiation integral value with displacement for different elements laid out through the thickness of simulation of BH-KanHPS70W-P-1-2 specimens for the three finite element deletion strategies

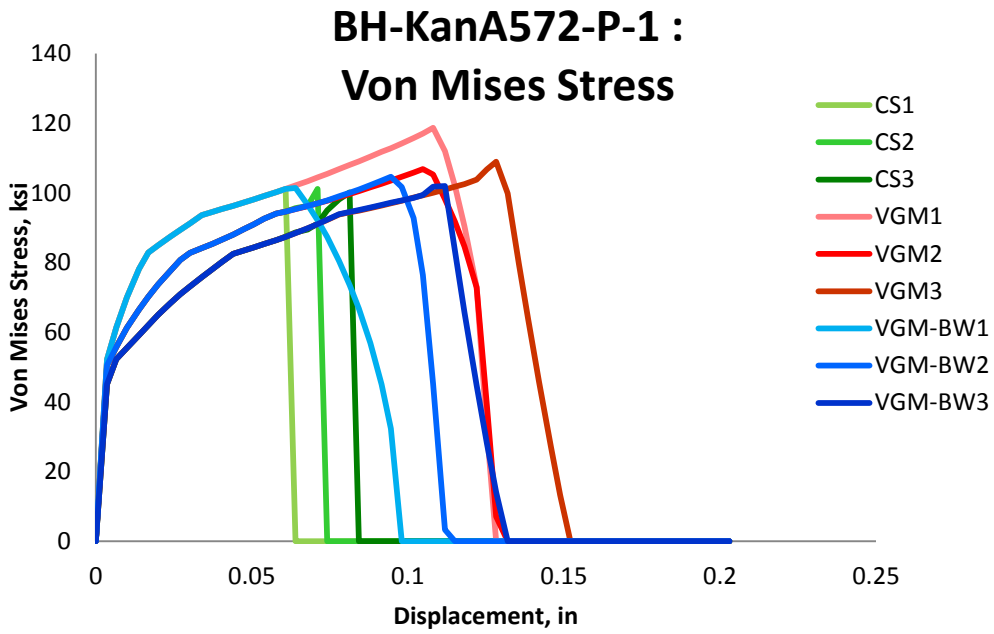

Figure 6.51: Variation of von Mises Stress with displacement for different elements laid out through the thickness of simulation of BH-KanA572-P-1 specimen for the three finite element deletion strategies

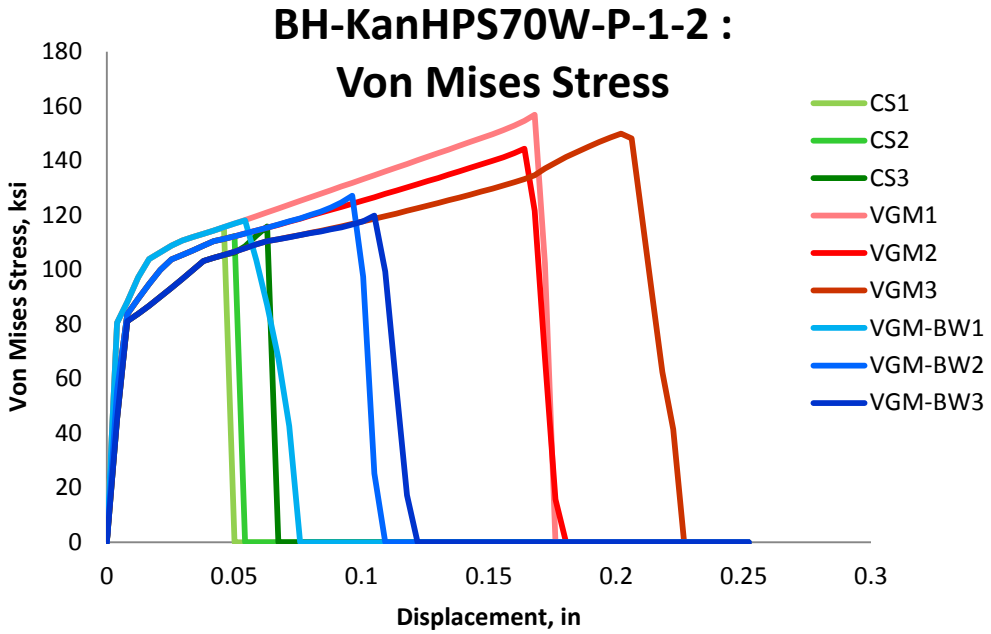

Figure 6.52: Variation of von Mises Stress with displacement for different elements laid out through the thickness of simulation of BH-KanHPS70W-P-1-2 specimens for the three finite element deletion strategies

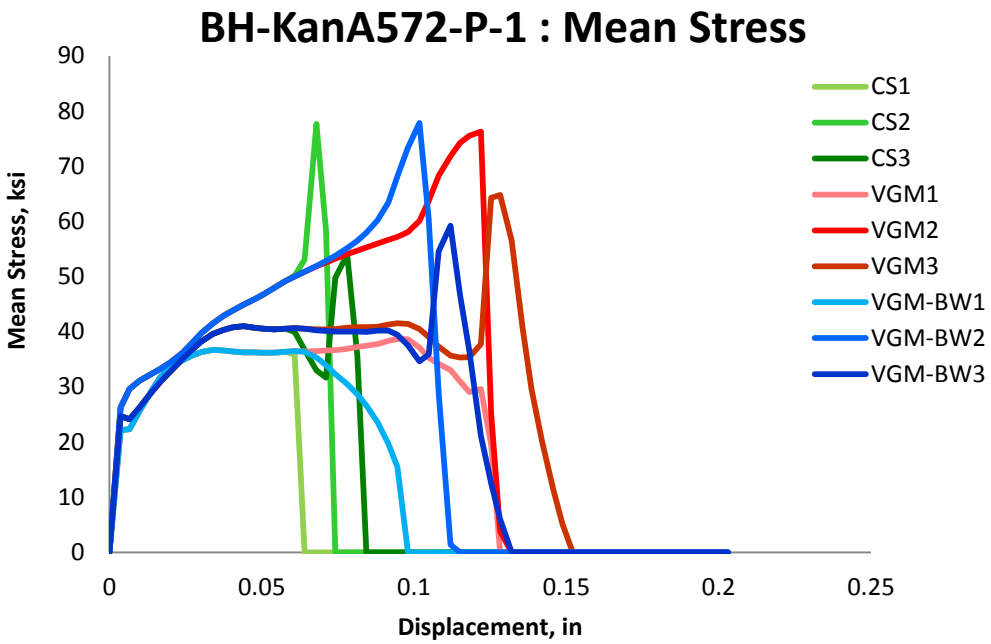

Figure 6.53: Variation of mean stress with displacement for different elements laid out through the thickness of simulation of BH-KanA572-P-1 specimen for the three finite element deletion strategies

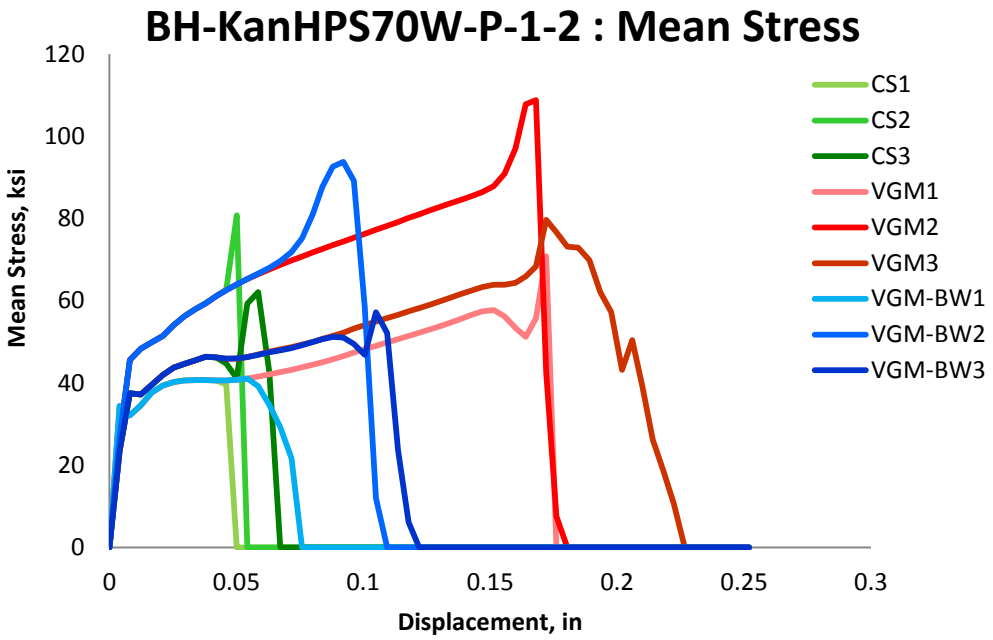

Figure 6.54: Variation of mean stress with displacement for different elements laid out through the thickness of simulation of BH-KanHPS70W-P-1-2 specimens for the three finite element deletion strategies

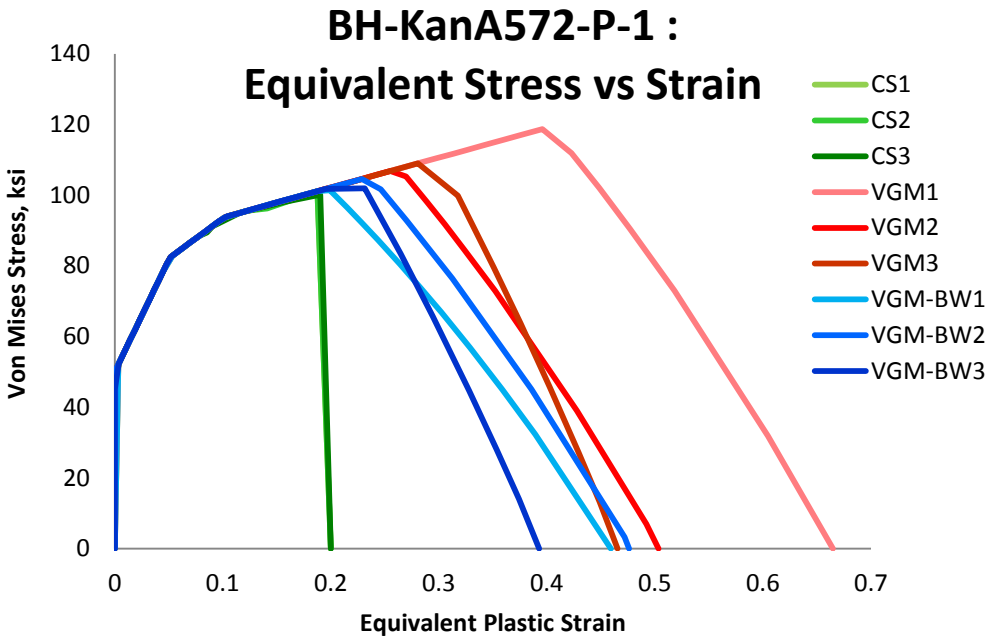

Figure 6.55: Variation of von Mises Stress with equivalent plastic strain for different elements laid out through the thickness of simulation of BH-KanA572-P-1 specimen for the three finite element deletion strategies

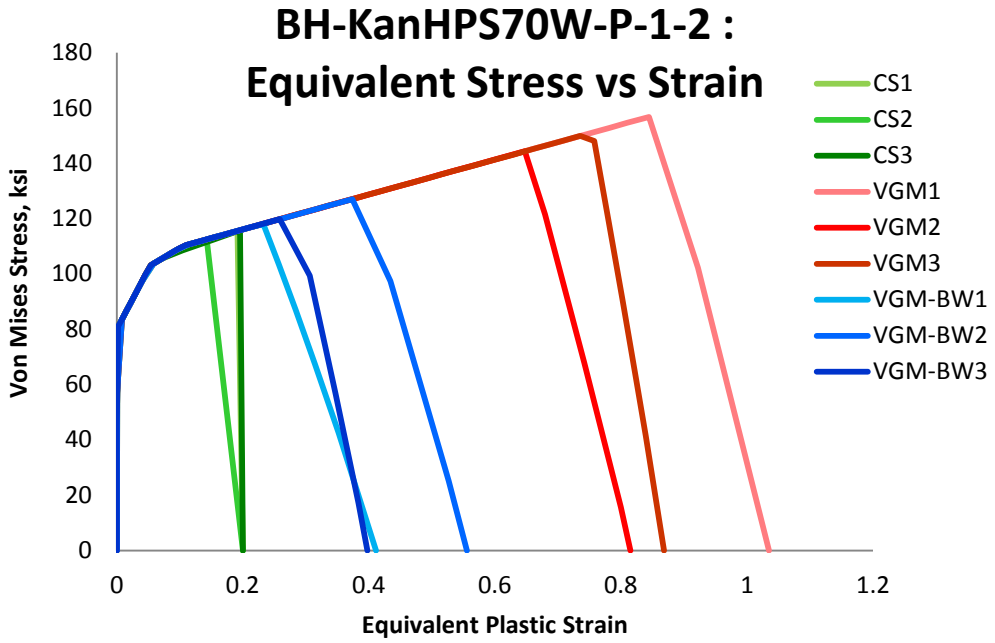

Figure 6.56: Variation of von Mises Stress with equivalent plastic strain for different elements laid out through the thickness of simulation of BH-KanHPS70W-P-1-2 specimens for the three finite element deletion strategies

Figure 6.55 and Figure 6.56 show the variation of von Mises equivalent stress with equivalent plastic strain. These figures show the extent to which the finite element deletion strategy affects the material capacity. The VGM strategy allows twice as much of strain energy in an element than VGM-BW and three times that of CS strategy in the BH-KanHPS70W-P-1-2 specimen and to a lesser extent in BH-KanA572-P-1 specimen. This allows the element to reach higher stress levels at larger equivalent plastic strain levels. Therefore, it is vital to accurately model material behavior to avoid under- and overpredictions of structural performance during collapse. In addition, the inner element reaches the highest values of stress and strain and element number 2 reaches the lowest values for the VGM and VGM-BW simulations due to higher triaxiality. The variation of the value of the damage variable is plotted in Figure 6.57 and Figure 6.58. For the BH-KanA572-P-1 specimen, the curves of damage variable at the

integration point of the elements for the three finite element deletion strategies are all fairly close to each other. The elements on the inside have their damage variable curves at a lower displacement value than those elements that are on the outside surface of the specimen signifying that fracture propagates from inside out. This is true for the BH-KanHPS70W-P-1-2 specimen, with an exception that there is a greater distance between each of the curves and finite element deletion strategies. The reason for the larger difference between each curve in the BH-KanHPS70W-P-1-2 specimen than in the BH-KanA572-P-1 specimen lies in the ductility of the material. The HPS70W is a high performance bridge steel with a larger yield stress and fracture initiation equivalent plastic strain values for the fracture locus than A572 Grade 50 steel material.

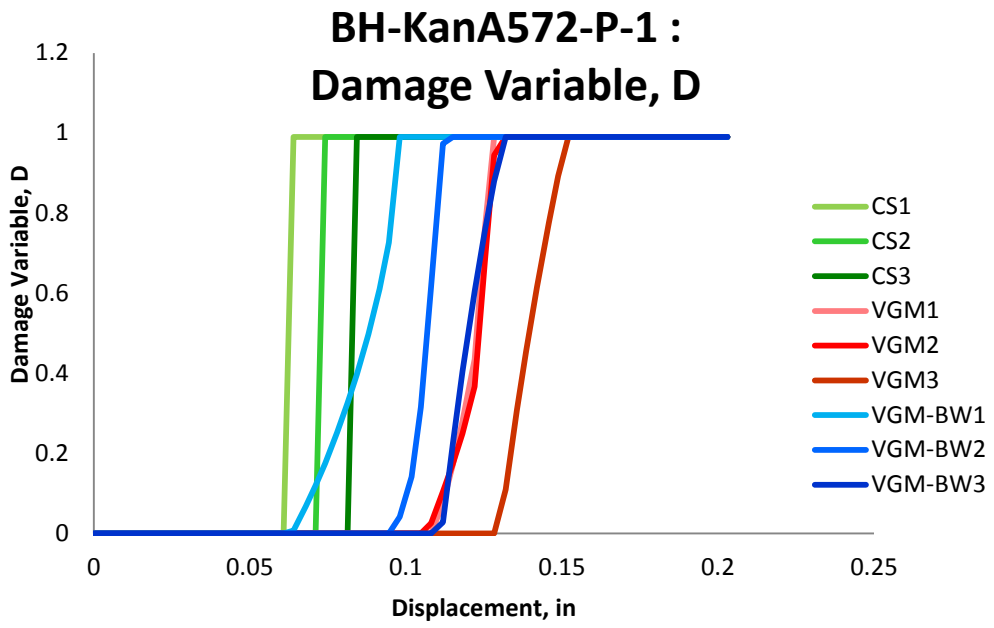

Figure 6.57: Variation of Damage Variable with displacement for different elements laid out through the thickness of simulation of BH-KanA572-P-1 specimen for the three finite element deletion strategies

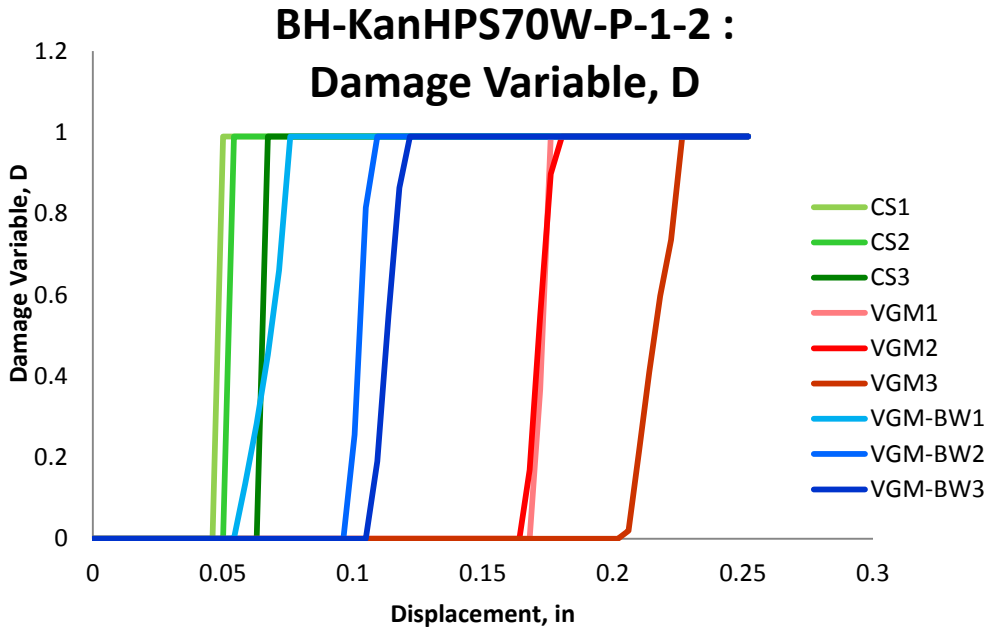

Figure 6.58: Variation of Damage Variable with displacement for different elements laid out through the thickness of simulation of BH-KanHPS70W-P-1-2 specimen for the three finite element deletion strategies

In addition to these specimens, type A572 Grade 50 and HPS70W steels were also validated through comparison to another set of pull-plate specimens, dog-bone pull-plates, designated as DB-KanA572-P-1 and DB-KanHPS70W-P-1-2 in

Table 6.1. These specimens were designed to model the reduced beam section connection (RBS). Though the RBS connection has the potential to prevent sudden and brittle failures, such as those in welded connections, there is always the possibility of ductile fracture under large plastic strains at the reduced section (Kanvinde et al. 2004). These pull-plate specimens were loaded through pins at their ends connected to an actuator. The central part of the plates is narrowed down to a width of 1 inch for type A572 Grade 50 and 0.9 inches for type HPS70W steel. The average displacement reading at the specimen ends was used for comparison to finite element simulation results. A one-eighth-symmetrical model with appropriate

symmetrical boundary conditions was used to simulate the dog-bone pull-plate specimens. The plasticity and fracture model data inputs are described in Table 6.3. In the experiments, fracture propagated quickly, which suggests that ductile initiation takes place over a large area and then all of a sudden the material fails by a mixture of tearing and ductile mechanisms (Kanvinde et al. 2004). This was evident in experiments from the fracture surfaces that have the appearance of ductile tearing dimples, smooth shear lips, as well as shiny cleavage facets (Kanvinde et al. 2004). Thus, it is not clear which mechanism governed the failure. Experimental test setups can be seen in Figure 6.59. Figure 6.60 shows the selected finite elements for study of fracture initiation and propagation parameters. This figure also shows the general boundary conditions used in finite element simulations.

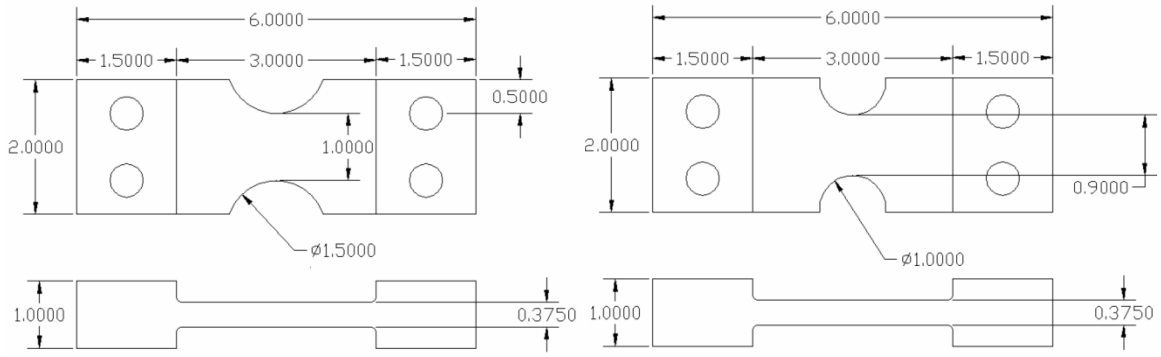

Figure 6.59: Experimental setup (Kanvinde et al. 2004) of a pull-plate DB-KanA572-P-1 specimen (left) and DB-KanHPS70W-P-1-2 specimen (right)

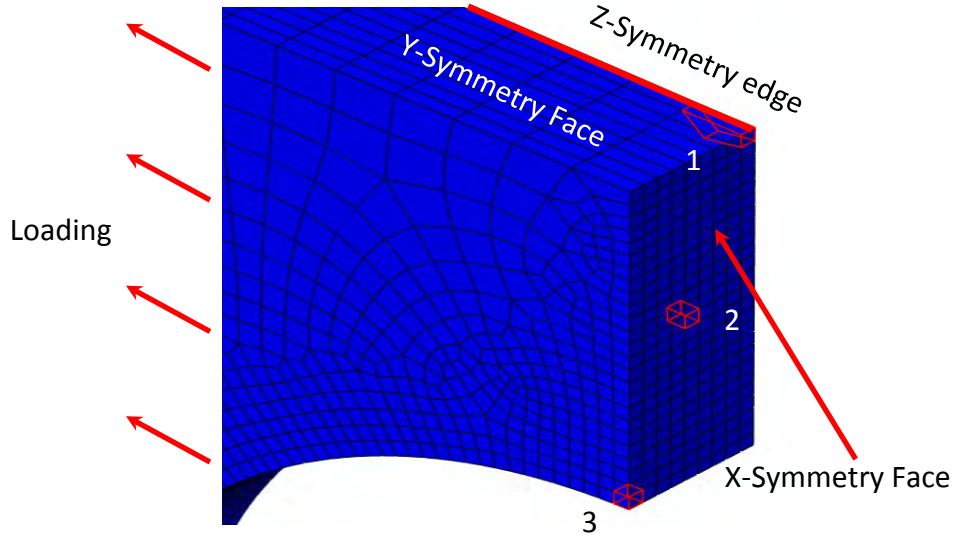

Figure 6.60: Elements selected for studying fracture initiation and propagation parameters in VGM-BW, VGM, and CS approaches for DB-KanA572-P-1 and DB-KanHPS70W-P-1-2 and the overall boundary conditions used for finite element simulations

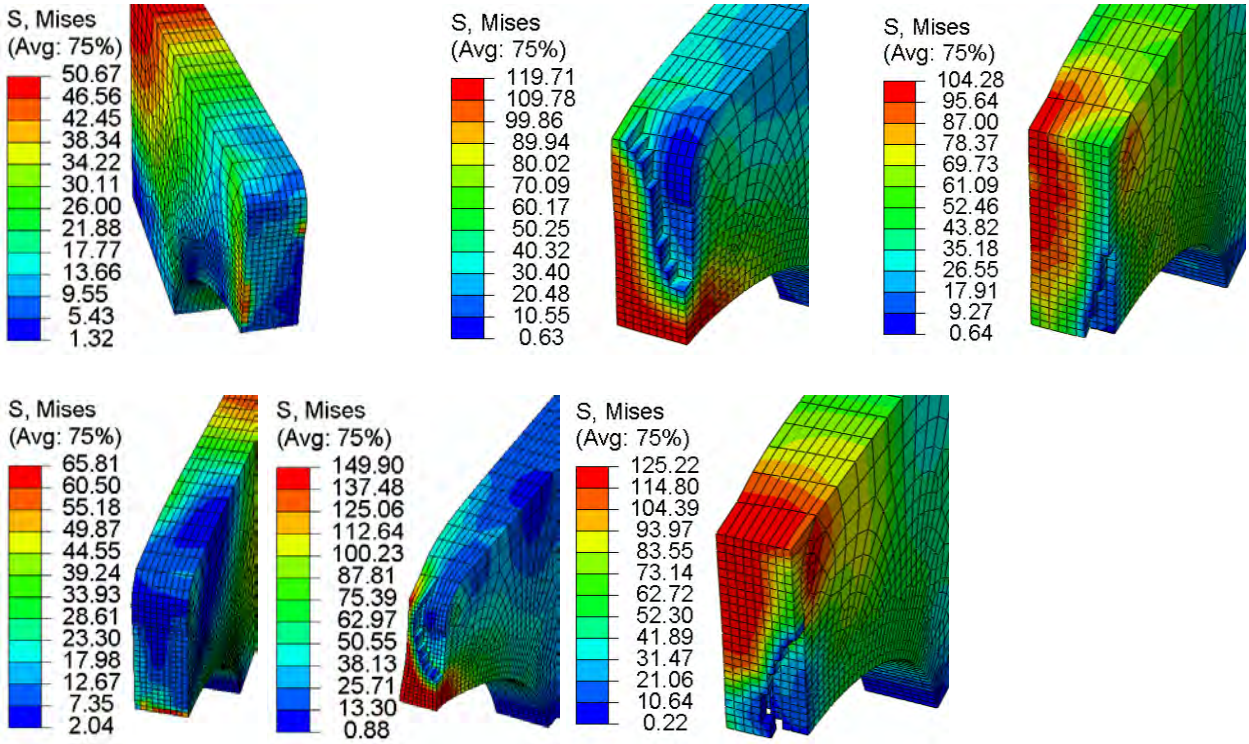

Figure 6.61 shows typical fracture locations and propagation direction in these dog-bone-pull-plate specimens for different finite element deletion strategies. The each strategy predicted a different fracture initiation location and propagation direction in both specimens. The CS

simulations showed a sudden fracture through the material thickness and height. The elements were deleted so quickly that it caused significant dynamic instabilities in the specimen. However, it seems to correspond to the observed sudden fracture of the specimens in the experimental tests. The VGM simulations showed fracture initiating at the center of the specimen, away from the edge of the notch, with fast fracture propagation to the surface of the specimen. Since, the VGM criterion overestimates the mix-mode fracture and completely ignores the negative triaxiality of shear fracture, it is questionable, without more detailed experimental observations, if VGM properly captured the fracture behavior. However, in the literature on CNT specimens, fracture initiates at the center of the specimen, and this plate could be looked at as a notched specimen (Kuwamura et al. 1997; Anderson 2005). On the other hand, VGM-BW simulation showed an opposite trend to that of VGM. Fracture initiated at the center of the specimen on the surface of the notch and propagated outwards, towards the elevation-view center of the specimen. Even though VGM-BW fracture locus captures the complete triaxiality range, it is doubtful that fracture behaved in the experimental test as exhibited in the VGM-BW simulation.

Figure 6.62 and Figure 6.63 show the force-displacement results from the CS, VGM, and VGM-BW simulations for DB-KanA572-P-1 and DB-KanHPS70W-P-1-2 specimens. As in the bolt-hole specimens, the CS underpredicts the force-displacement capacity of the plate by more than 50% on average. The VGM-BW strategy also significantly underpredicts the plates' capacity while the VGM underpredicts the capacity of the DB-KanA572-P-1 specimen but overpredicts the capacity of the DB-KanHPS70W-P-1-2. In addition, for these dog-bone specimens, the dynamic instability in the CS simulations is very significant, but is not present in the VGM and

VGM-BW. To better understand these issues, the variation of fracture parameters are plotted and discussed below in a similar fashion to the previous section.

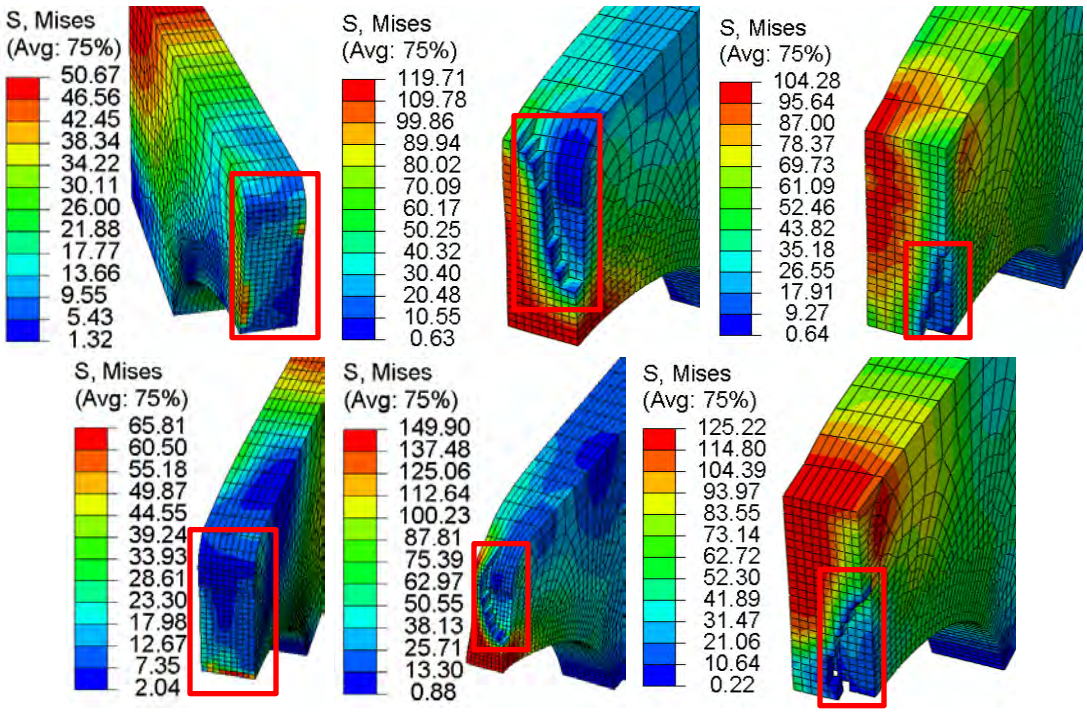

Figure 6.61: Simulation results (Kanvinde et al. 2004) of a dog-bone pull-plate DB-KanA572-P-1 specimen on top and DB-KanHPS70W-P-1-2 on the bottom with contours representing von Mises stress (ksi): CS (left), VGM (middle), VGM-BW (right)

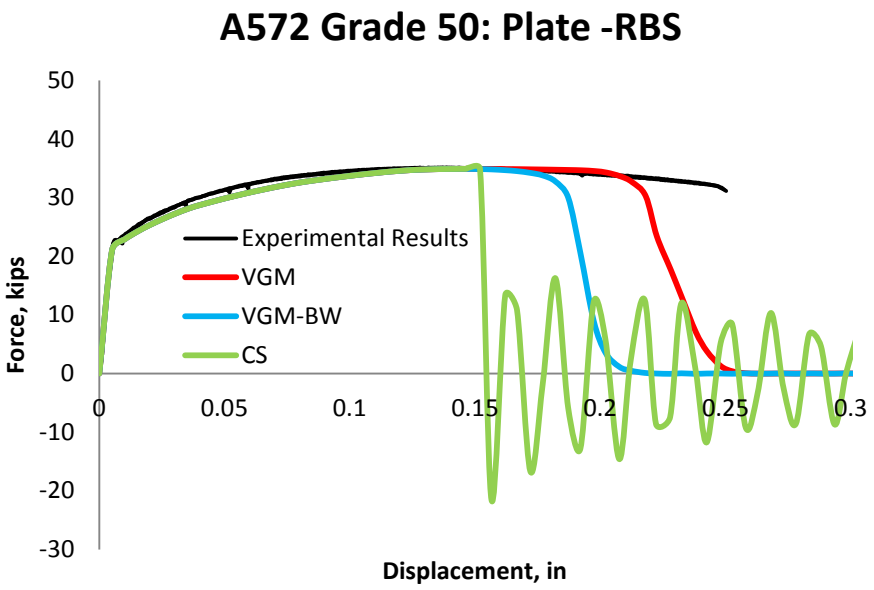

Figure 6.62: Validation results for pull-plate specimen DB-KanA572-P-1

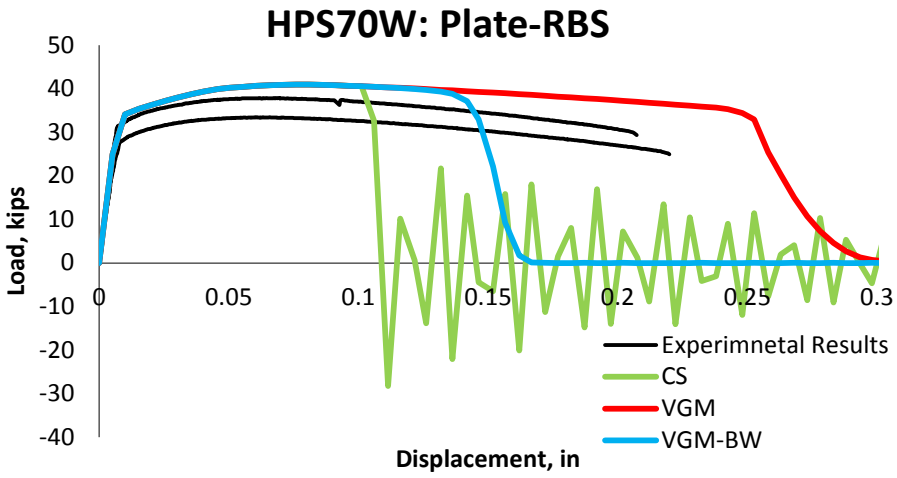

Figure 6.63: Validation results for pull-plate specimen DB-KanHPS70W-P-1-2

Triaxiality versus displacement is plotted for the three elements across the thickness of the specimen, for the three finite element deletion strategies, in Figure 6.64 and Figure 6.65. As in bolt-hole specimens, the triaxiality is the same in each element throughout the loading excursion until the point of softening, for the three finite element deletion strategies. After this

point, the value of triaxiality is different for the three strategies. Most elements experience an increase in triaxiality before failure in the VGM and VGM-BW simulations, except for the inside element 1 and the elements in the CS simulation. The triaxiality increase for DB-KanA572-P-1 specimen is not as significant as for DB-KanHPS70W-P-1-2 specimen, due to the fact that HPS70W is a more ductile metal. The triaxiality for the third element in the VGM-BW simulation goes negative after reaching its peak value. The reason for this is that this element was part of a piece that was cut off from the rest of the specimen in the simulation, due to fracture propagating in a slant manner towards the far end of the specimen. The equivalent plastic strain is plotted in Figure 6.66 and Figure 6.67. The figures show that, as for the bolt-hole specimens, the elements in VGM simulations reached the highest strain values and elements in CS simulations the lowest. For the DB-KanA572-P-1 specimen, the three elements for the three strategies follow a very similar path to each other, but in DB-KanHPS70W-P-1-2 the third element starts to follow a distinctive path, even before reaching softening. This is most like due to the slant fracture propagation.

The fracture locus is plotted in Figure 6.68 and Figure 6.69. It is seen in these figures that the triaxiality range for the two materials is approximately the same, becoming wider with increasing equivalent plastic strain. The fracture locus for the three strategies is very similar to each other in this triaxiality range of 0.35 to 0.5 for DB-KanA572-P-1 specimen. However, the force-displacement results are different. This again confirms the effect that softening can have on the global behavior of a structure. In this case, the difference in force-displacement capacity between VGM and the other two strategies is approximately 15%. Two of the elements have a different triaxiality versus equivalent plastic strain paths in the VGM and VGM-BW simulations

for the DB-KanA572-P-1, and all of the three elements have different paths for the DB-KanHPS70W-P-1-2 specimen. The third element located on the outside surface has a near vertical path showing that is not effected by softening.

The variation of the value of fracture initiation integral is shown in Figure 6.70 and Figure 6.71. In all of the three simulations, elements 1 and 2 follow similar paths while the outside elements follow a distinguishable path from the other two elements. Element 3 has the smallest slope and reaches the highest displacement value before initiating fracture for VGM simulations, with an opposite trend for CS and VGM-BW simulations. For the VGM simulation, as one moves inward, the slope of the value of this integral increases due to a higher triaxiality prevalent in inner elements. The difference between the different strategies in fracture initiation integral curves is much more distinguishable in the DB-KanHPS70W-P-1-2 specimen then in DB-KanA572-P-1 specimen due to a higher ductility of the material in the former.

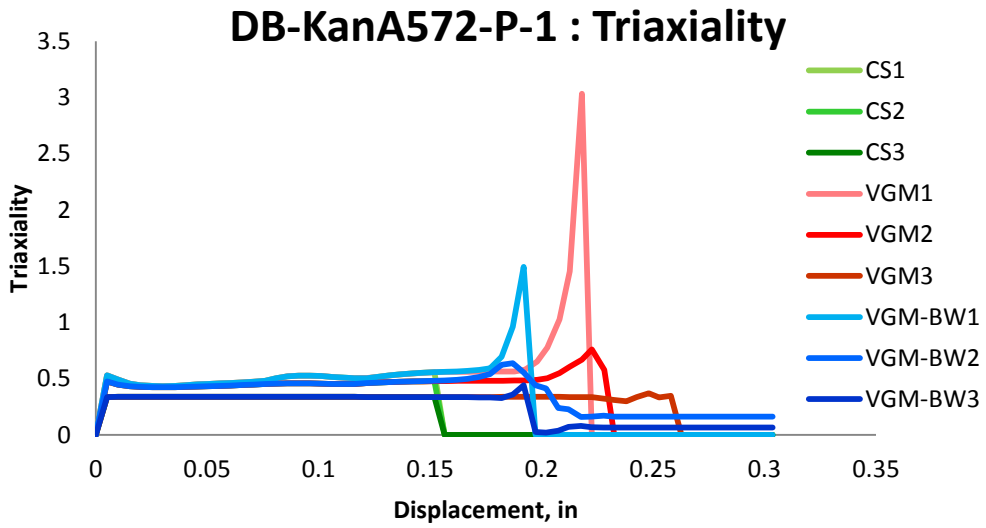

Figure 6.64: Variation of triaxiality with displacement for different elements laid out through the thickness of simulation of DB-KanA572-P-1 specimen for the three finite element deletion strategies

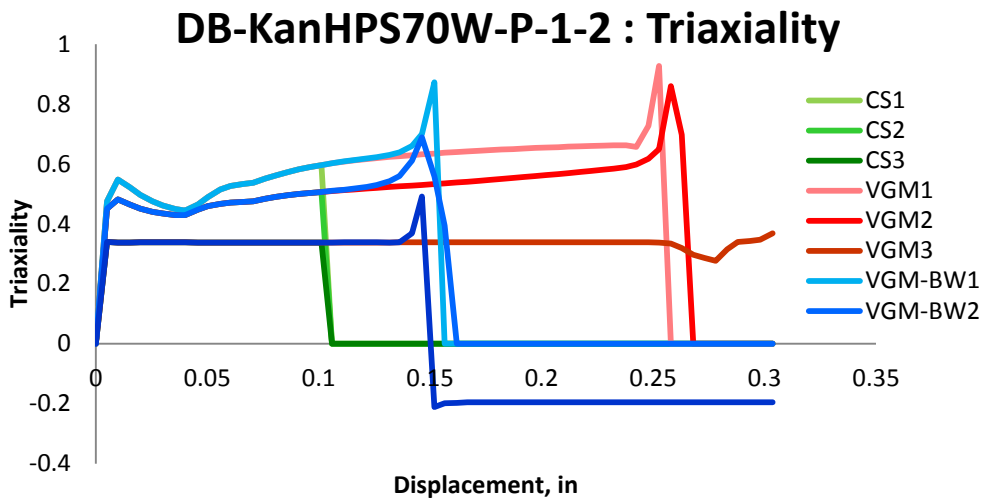

Figure 6.65: Variation of triaxiality with displacement for different elements laid out through the thickness of simulation of DB-KanHPS70W-P-1-2 specimens for the three finite element deletion strategies

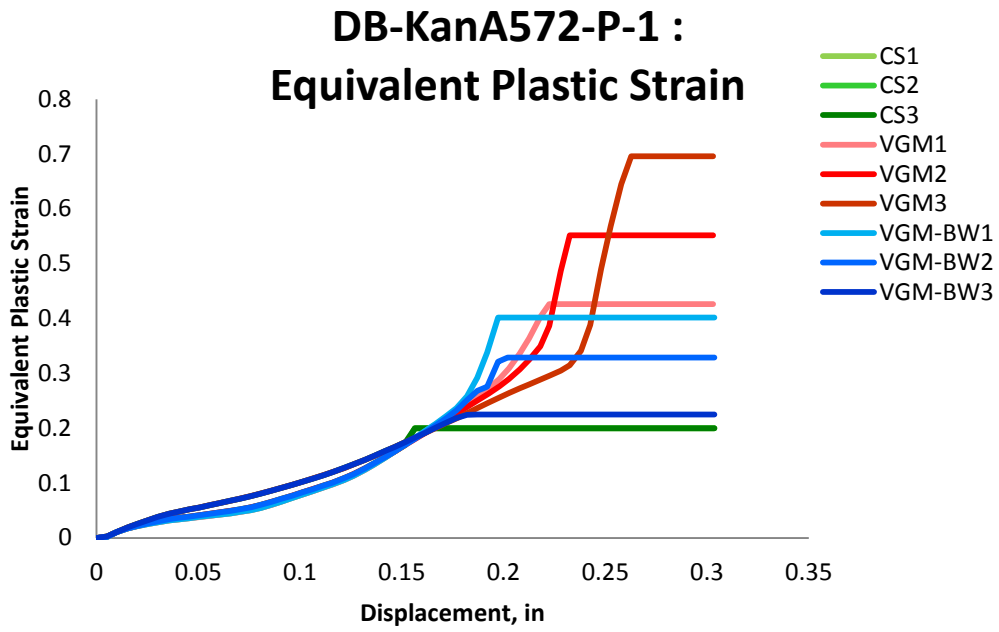

Figure 6.66: Variation of equivalent plastic strain with displacement for different elements laid out through the thickness of simulation of DB-KanA572-P-1 specimen for the three finite element deletion strategies

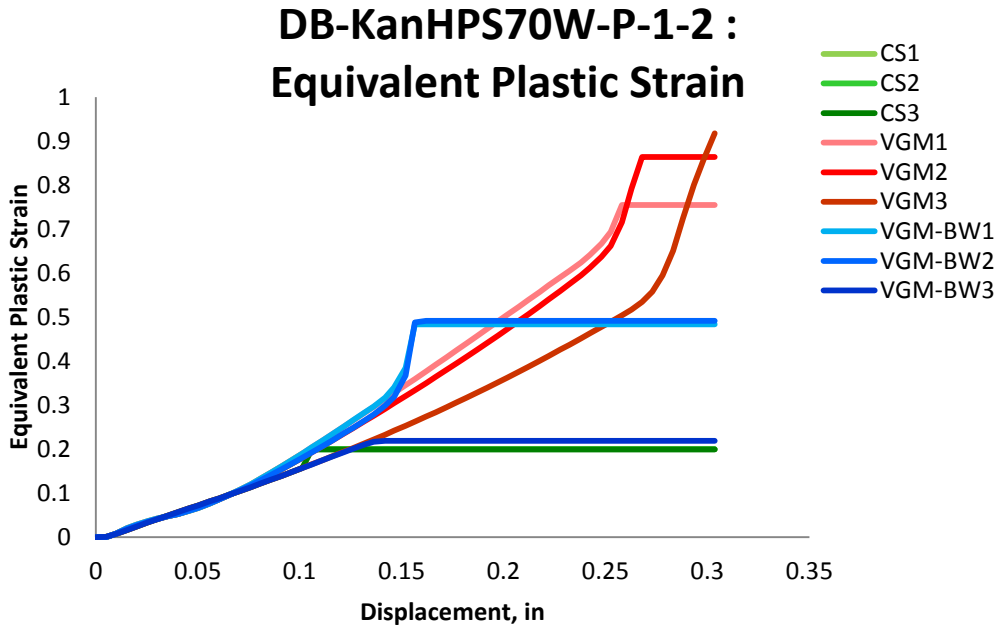

Figure 6.67: Variation of equivalent plastic strain with displacement for different elements laid out through the thickness of simulation of DB-KanHPS70W-P-1-2 specimens for the three finite element deletion strategies

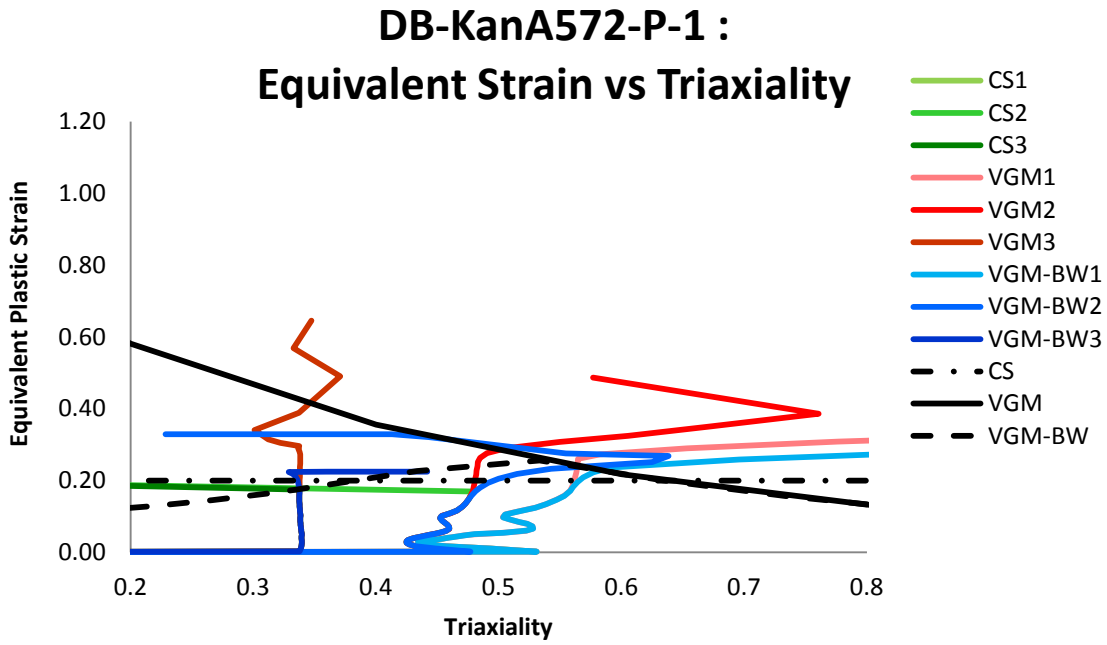

Figure 6.68: Variation of equivalent plastic strain with triaxiality for different elements laid out through the thickness of simulation of DB-KanA572-P-1 specimen for the three finite element deletion strategies

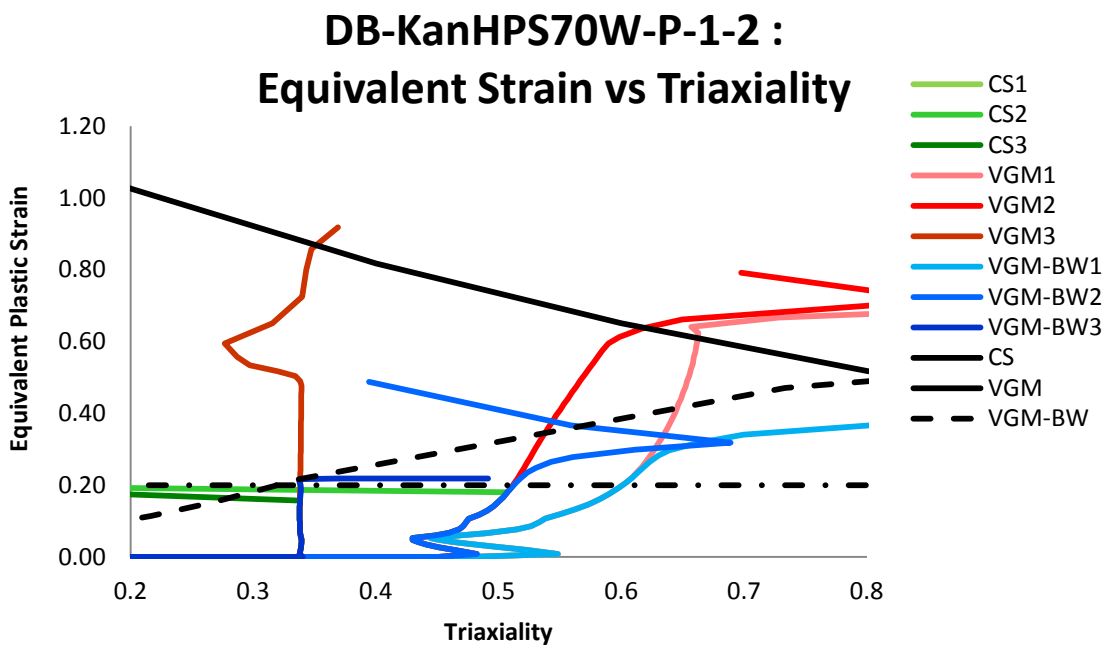

Figure 6.69: Variation of equivalent plastic strain with triaxiality for different elements laid out through the thickness of simulation of DB-KanHPS70W-P-1-2 specimens for the three finite element deletion strategies

There is a similar trend in the varition of von Mises stress with displacement, shown in Figure 6.72 and Figure 6.73. The VGM and VGM-BW curves for the three elements are distiguishable from each other, with the VGM strategy having a greater difference between the elements than the VGM-BW. In addition, specimen DB-KanHPS70W-P-1-2 has more differences between elements per each simulation and between the finite element deletion strategies than is seen in DB-KanA572-P-1 specimen. In the CS simulations, all of the three elements failed suddenly, which is shown by all of the elements initiating softening at the same displacement value and following the same softening curve. The flat horizontal lines, in Figure 6.72, show that elements 2 and 3 were not deleted for the VGM-BW model but were part of a piece that was cut off from the rest of the specimen by the slanted fracture propagation. The reason for the horizontal

lines is that the plot uses a node on the outside edge at the beginning of the notch to measure displacement, while von Mises stress is measured within the element

The mean stress variation throughout the loading excursion is plotted in Figure 6.74 and Figure 6.75. The mean stress in two of the elements for the VGM-BW strategy dramatically increases during softening, while only one element sees this type of increase in the VGM simulations. This is due to stress redistribution and is similar to was observed in the bolt-hole specimens. As elements are deleted on the through thickness surface, more stress is redistributed to the elements that still have load carrying capacity. The curves representing elements in CS simulations do not show such a trend. Since the CS simulations had sudden failure of all the elements across the thickness, such mean stress increase is not observed. In addition, as opposed to von Mises stress, the mean stress value is the same for the three finite element deletion strategies per element until initiation of softening.

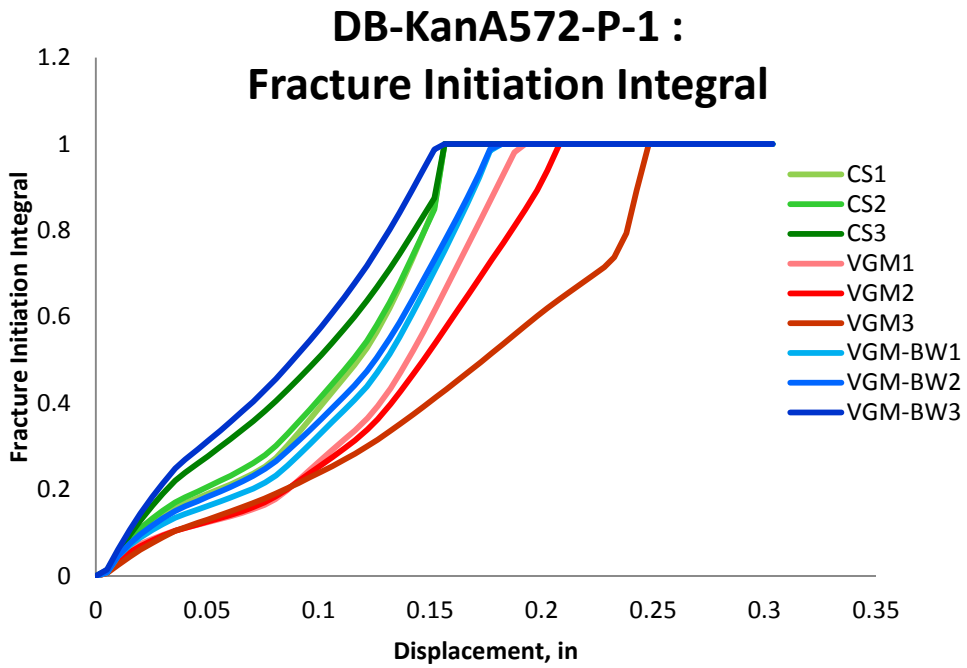

Figure 6.70: Variation of fracture initiation integral value with displacement for different elements laid out through the thickness of simulation of DB-KanA572-P-1 specimen for the three finite element deletion strategies

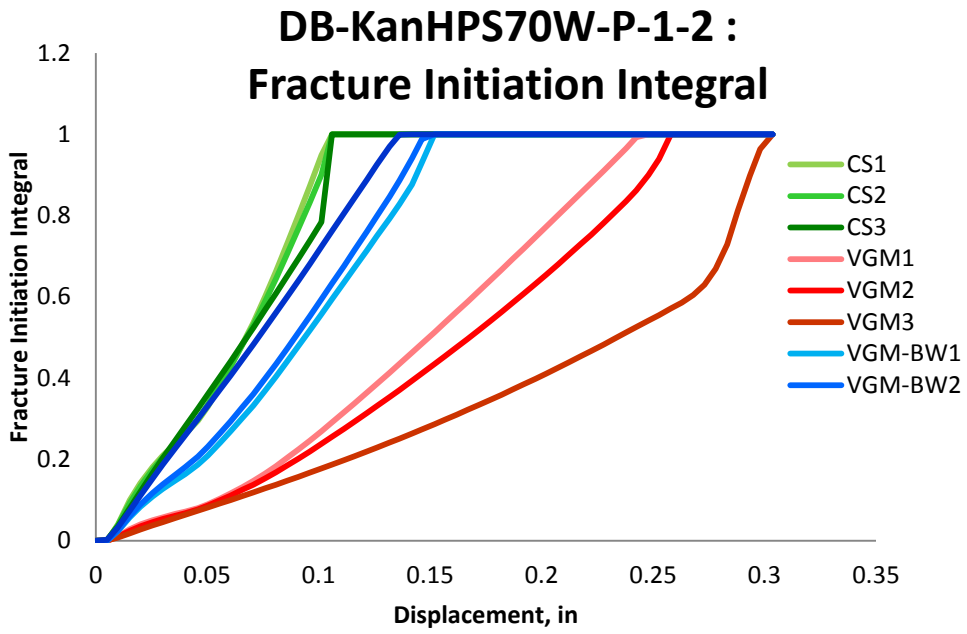

Figure 6.71: Variation of fracture initiation integral value with displacement for different elements laid out through the thickness of simulation of DB-KanHPS70W-P-1-2 specimens for the three finite element deletion strategies

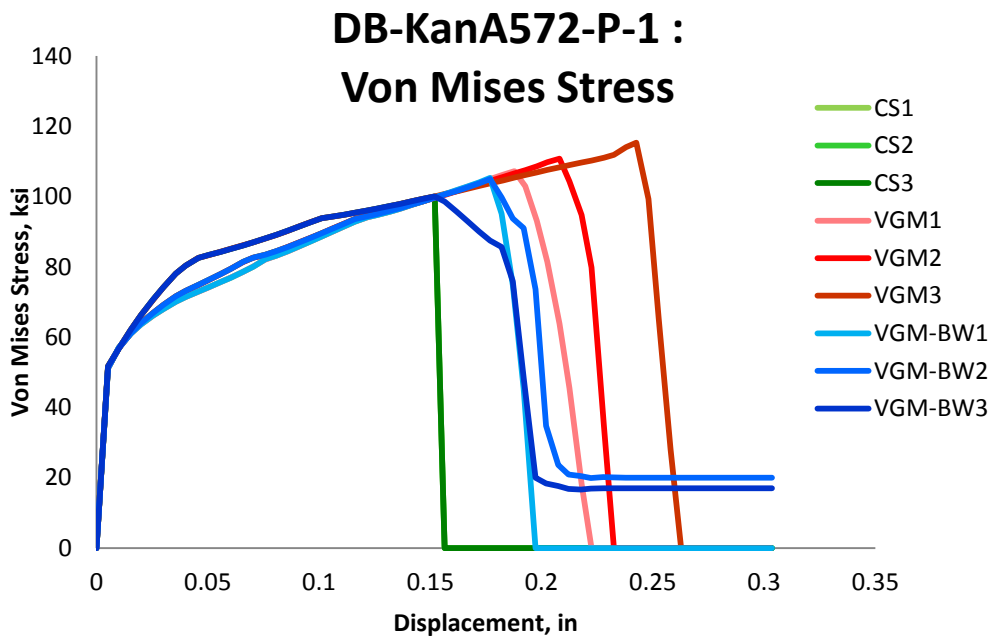

Figure 6.72: Variation of von Mises Stress with displacement for different elements laid out through the thickness of simulation of DB-KanA572-P-1 specimen for the three finite element deletion strategies

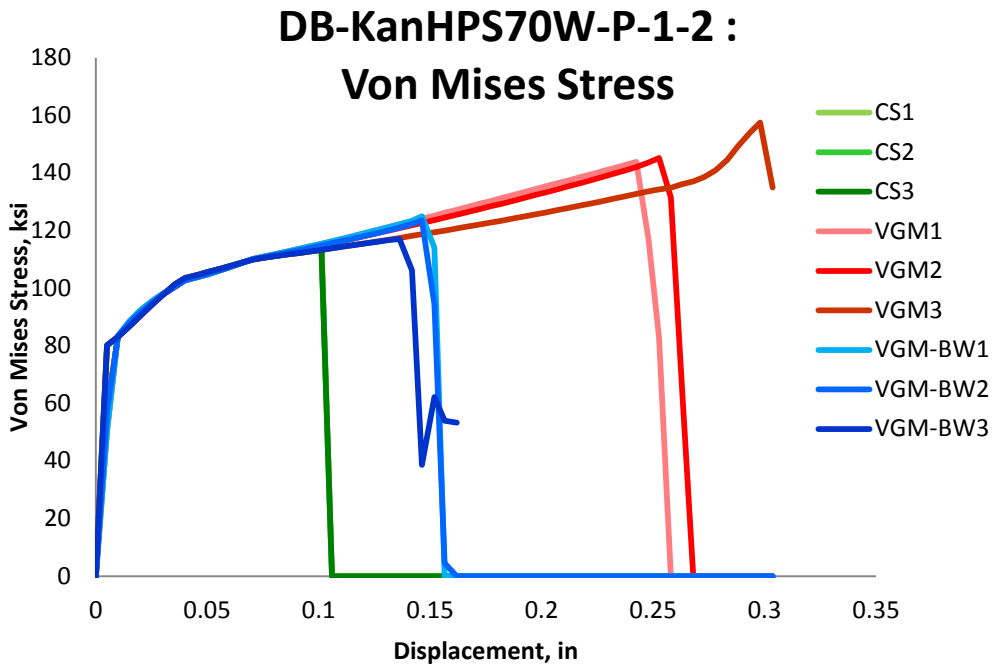

Figure 6.73: Variation of von Mises Stress with displacement for different elements laid out through the thickness of simulation of DB-KanHPS70W-P-1-2 specimens for the three finite element deletion strategies

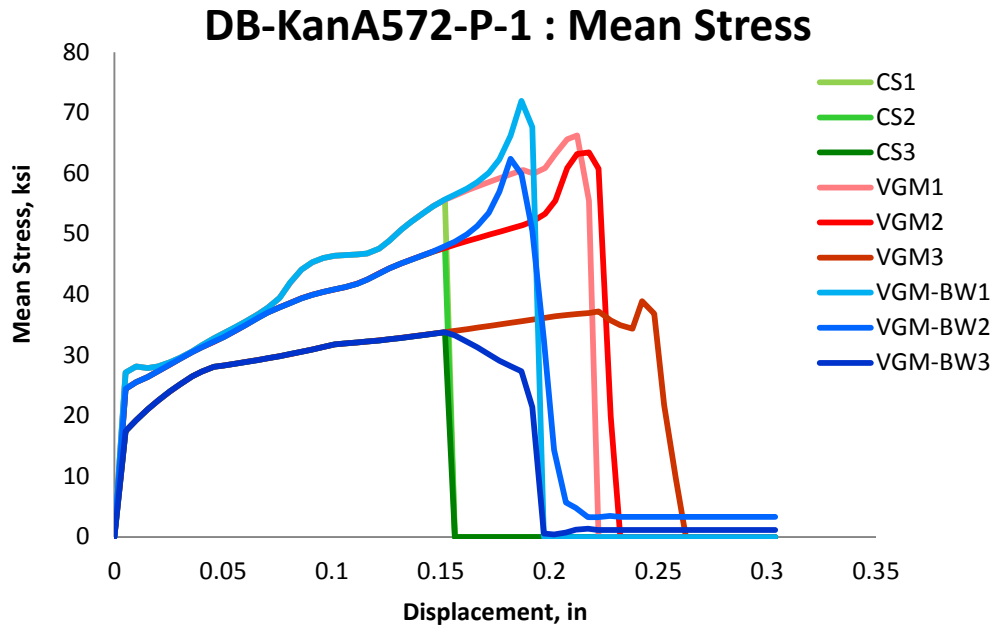

Figure 6.74: Variation of mean stress with displacement for different elements laid out through the thickness of simulation of DB-KanA572-P-1 specimen for the three finite element deletion strategies

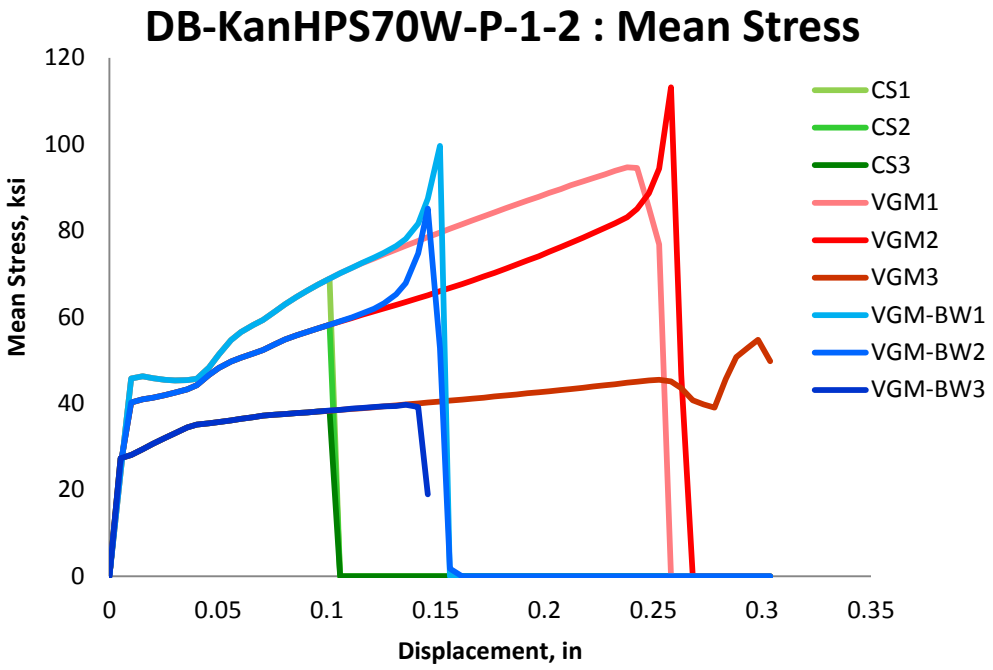

Figure 6.75: Variation of mean stress with displacement for different elements laid out through the thickness of simulation of DB-KanHPS70W-P-1-2 specimens for the three finite element deletion strategies

Figure 6.76 and Figure 6.77 show the variation of von Mises equivalent stress with equivalent plastic strain. The VGM finite element deletion strategy, for the dog-bone specimens, allowed twice as much strain energy in an element than VGM-BW, and three times that of CS strategy, in the DB-KanHPS70W-P-1-2 and to a lesser extent in DB-KanA572-P-1 specimen. The outside element attains the greatest amount of strain energy in the VGM simulation, while the inner element 1 attains the least amount. The VGM-BW simulation shows an opposite trend. This is directly related to the chosen fracture locus for these models. The variation of the value of the damage variable is plotted in Figure 6.78 and Figure 6.79. The damage variable curves, for the three finite element deletion strategies, are distinguishable from each other but not from each

element due to the sudden fracture propagation. The elements on the inside have their damage variable curves at a lower displacement value than those elements that are on the outside surface of the specimen, signifying that they initiated fracture and failed at a lower global displacement value. There is a greater distance between each of the curves for DB-KanHPS70W-P-1-2 than for DB-KanA572-P-1 specimen. The reason for this lies in the ductility and the fracture locus of the material. The type HPS70W is a high perfornce bridge steel with a larger yield stress and fracture initiation equivalent plastic strain values for the fracture locus than type A572 Grade 50 steel material.

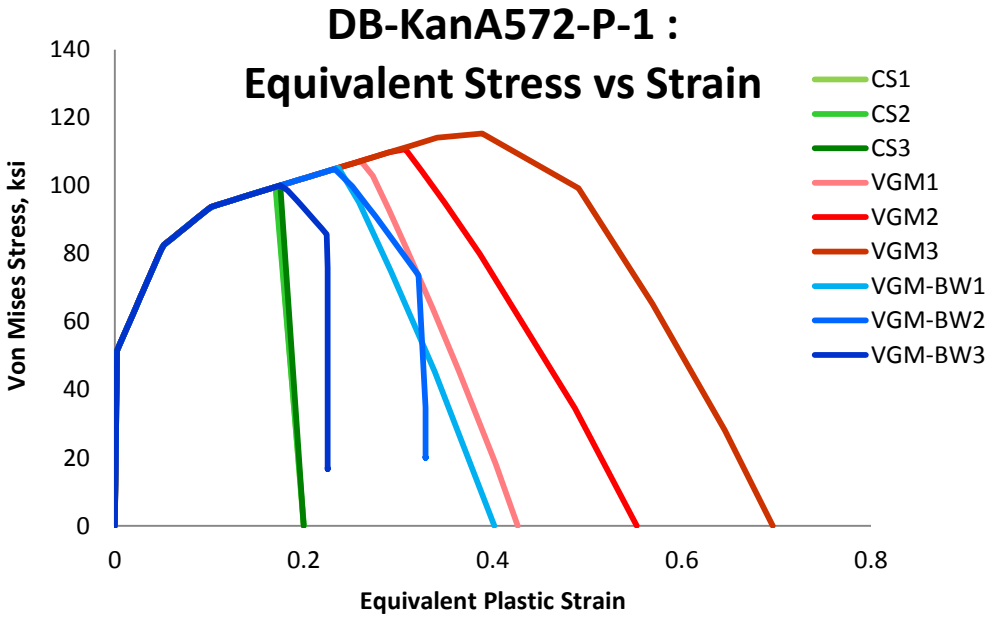

Figure 6.76: Variation of von Mises Stress with equivalent plastic strain for different elements laid out through the thickness of simulation of DB-KanA572-P-1 specimen for the three finite element deletion strategies

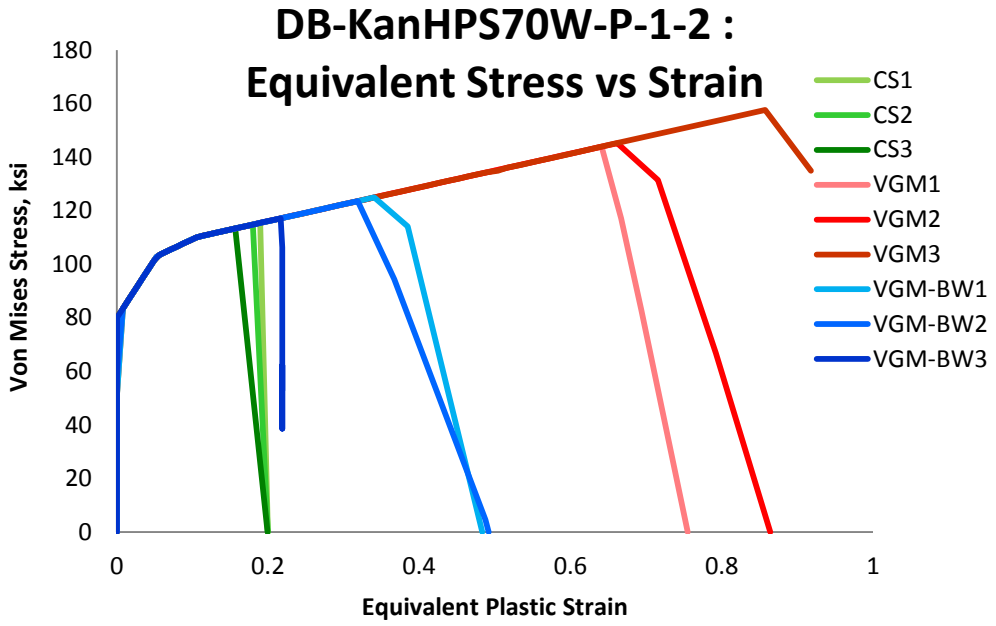

Figure 6.77: Variation of von Mises Stress with equivalent plastic strain for different elements laid out through the thickness of simulation of DB-KanHPS70W-P-1-2 specimens for the three finite element deletion strategies

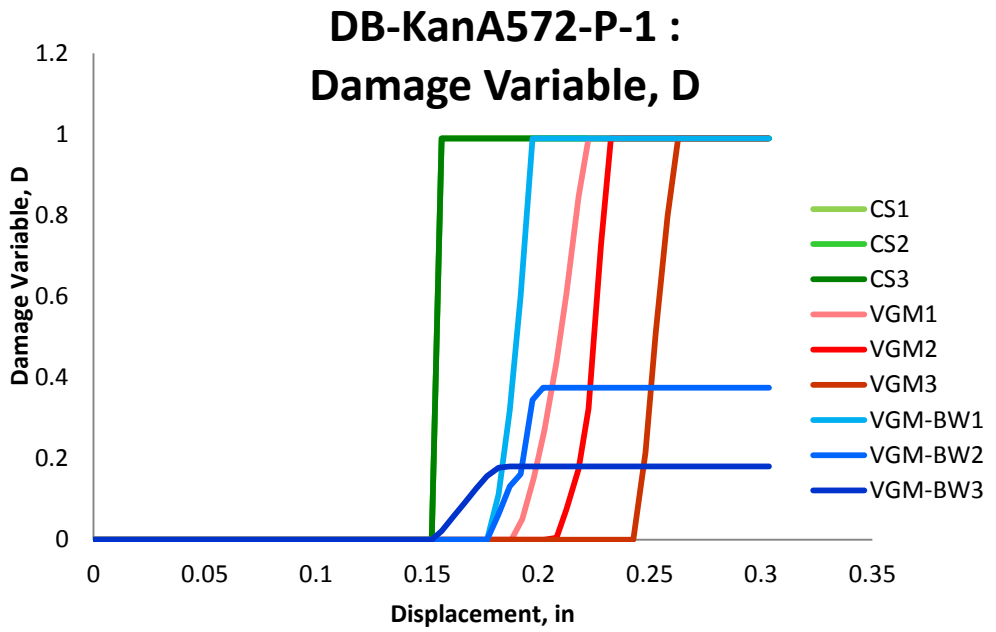

Figure 6.78: Variation of Damage Variable with displacement for different elements laid out through the thickness of simulation of DB-KanA572-P-1 specimen for the three finite element deletion strategies

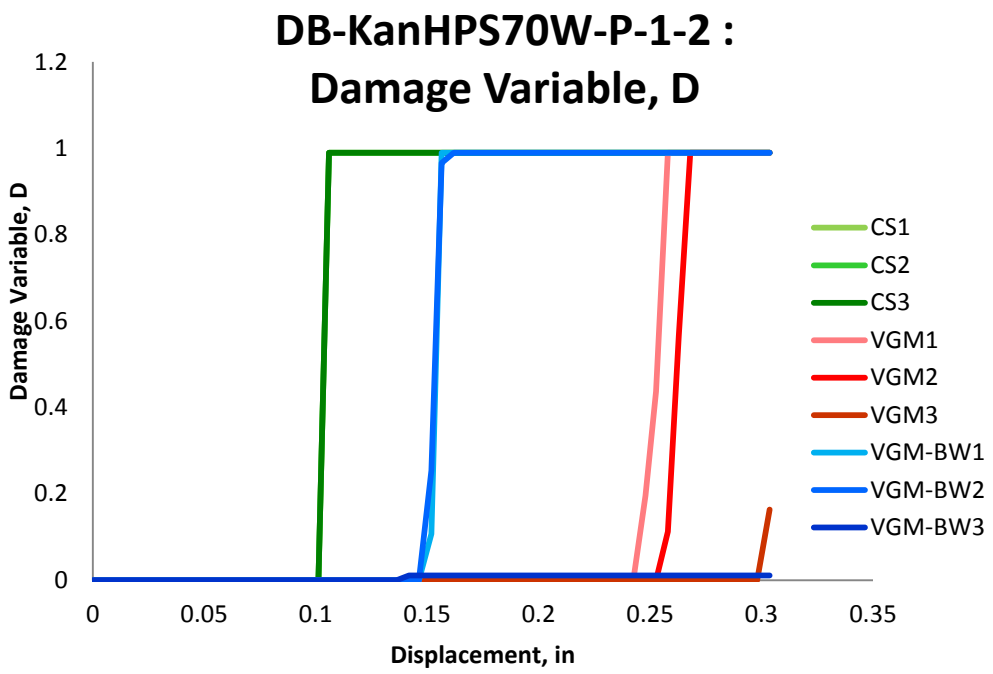

Figure 6.79: Variation of Damage Variable with displacement for different elements laid out through the thickness of simulation of DB-KanHPS70W-P-1-2 specimen for the three finite element deletion strategies

6.2.1 Summary

Structural steel type A572 Grade 50 and HPS70W, taken from a plate, were validated through comparison to a set of bolt-hole and dog-bone pull-plate specimens, which were loaded in tension and designed to study fracture under conditions representative of the bolted end of a tension member and reduce beam section. The VGM criteria closely followed the experimental observations of bolt-hole specimens, with fracture originating on the hole's outside surface from the center of the specimen and propagating to the outer surface of the specimen. For the CS and VGM-BW simulations, fracture occurred simultaneously on the outer and inner edges of the specimen's hole, in the center of the specimen, and propagated outwards. In addition, all of the three strategies had different fracture initiation and propagation prediction for both dog-bone specimens. The CS simulations showed a sudden fracture through the material thickness

and height, which seems to correspond to observed sudden fracture of the specimens in the experimental tests. The VGM simulations showed fracture initiating at the center of the specimen, away from the edge of the notch, with fast fracture propagation to the surface of the specimen. VGM-BW simulation showed an opposite trend to that of VGM. The fracture initiated at the center of the specimen, on the edge of the notch, and propagated inward towards the center of the specimen. Overall, VGM seems to perform better in locating facture initiation and properly modeling fracture propagation.

In addition, further results show that the calibrated fracture locus was able to capture fracture behavior well for VGM strategy but not for the VGM-BW and Constant Strain. From these results other observations could be made:

- The Constant Strain (CS) approach significantly underestimated the fracture equivalent plastic strain at fracture initiation resulting in inaccurate results.
- Similarly to the CNT specimens, after initiation of softening, triaxiality increases for the inner elements but not for the outer ones. The equivalent plastic strain for the outer element continues to have a near vertical slope to triaxiality throughout the entire loading excursion, and is not affected by softening. In addition, there is a significant difference in the triaxiality range of the outer and the inner elements.
- Triaxiality is governed mainly by the geometry of the specimen and to a lesser extent the material of the specimen.
- Incorporating softening into the material fracture model has significant effect on the global response of the pull-plate specimen

- The mean stress in an inside element increases before failure

6.3 Compact Tension Specimen

In addition to the pull-plate specimens, compact tension (CT) specimens were used in the validation process. The experimental CT specimens were similar to the Edge Notched Tension (SENT) specimen, defined by ASTM E399, but instead of having an atomically sharp crack, through fatigue-precracking, the specimens had a machined notch with notch radius equaling 0.03125 inches (Kanvinde et al. 2004). The purpose for this deviation from ASTM E399 standard was to test more realistic defect/flaw situations in structural connections, which have strong stress concentrations, but not necessarily sharp cracks (Kanvinde et al. 2004). The experiments were performed for type A572 Grade 50 taken from a plate, type A572 Grade 50 taken from a wide flange section, and type HPS70W steels. For type A572 Grade 50 taken from a plate (CT-KanA572-P-1-3), type A572 Grade 50 taken from a wide flange (CT-KanA572-W-4-6), and type HPS70W (CT-KanHPS70W-P-1-3) steels, a specimen with a thickness of 1 inch was used, but for the other set of type A572 grade 50 taken from a wide flange (CT-KanA572-W-1-3) experiments a specimen with a thickness of 0.5 inches was used to study the effect of triaxiality and constraint on fracture prediction. The specimen with 0.5 inch thickness has lower constraint and therefore higher ductility than the 1.0 inch thick specimen. The experimental test setups of the compact tension specimens are shown in Figure 6.80. The repeated unloading in HPS70W experimental tests was originally used for determining the critical *J* value by measuring the slope of the loading curve, which correlates to the current crack length (Anderson 2005). The

CT specimen was loaded through pins at its upper and lower ends connected to an actuator. A quarter-symmetrical model, with appropriate symmetrical boundary conditions, was used to simulate the CT specimens shown in Figure 6.81 with the chosen set of elements for study of the variation of fracture initiation and propagation parameters. In the experimental tests, the blunt crack led to large deformations of the specimens before fracture with extensive necking and bulging, which is shown in Figure 6.82 (Kanvinde et al. 2004). In general, the fracture surface morphology of the compact tension specimen that exhibit ductile crack growth show the crack tunneling through the center of the specimen (Anderson 2005). The reason for this is that the crack grows preferentially in the region of high confinement or triaxiality, which is at the center of the specimen. While the crack lags behind and occurs at 45° angle to the applied load on the surfaces, resulting with a flat region in the central part of the specimen and a 45° shear lips on the edges (Anderson 2005). As the thickness of the specimen decreases the flat region decreases. The data points used in plasticity and fracture models are described in Table 6.4. In the simulations, the three finite element deletion strategies all had unique fracture propagation behavior, but all had fracture initiate at the center of the specimen. Figure 6.83 shows the fracture of a CT-KanA572-P-1-3 specimen for CS, VGM and VGM-BW simulations. The three simulations showed some extent of necking at the notch with almost no bulging. It is not clear if all of the experimental test specimens had bulging. In the three simulations the fracture initiated in the center of the specimen and propagated outward through a tunneling effect. A tunneling effect is more prominent in the VGM and VGM-BW simulation than in CS simulation. The VGM and VGM-BW simulations do not show signs of shear lips, while the CS simulation shows more of an upward crack on the outside edges than a shear lip. This could be due to the

fact that facture has not occurred on the surface at the current displacement and further loading would have showed shear lip fracture. Figure 6.87 shows the force versus load line displacement plot for experimental test and simulation results. The CS had the closest fit to the experimental results. The VGM and VGM-BW had almost identical results due to high constraint of the specimen which forced critical elements to be governed by the VGM and not the B-W criteria.

Table 6.4: Plasticity and fracture model inputs for CT-KanA572-P-1-3, CT-KanHPS70W-P-1-3, CT-KanA572-W-1-3, and CT-KanA572-W-4-6 specimens

		Fracture Model Input		
Test	**Plasticity Model Input**	**VGM**	**VGM-BW**	**CS**
CT-KanA572-P-1-3	CNT-KanA572-P-A	CNT-KanA572-P-A	TC-KanA572-P-A	0.2
CT-KanHPS70W-P-1-3	CNT-KanHPS70W-P-A	CNT-KanHPS70W-P-A	TC-KanHPS70W-P-A	0.2
CT-KanA572-W-1-3	CNT-KanA572-W-L-A	CNT-KanA572-W-L-A	TC-KanA572-W-L-A	0.2
CT-KanA572-W-4-6	CNT-KanA572-W-L-A	CNT-KanA572-W-L-A	TC-KanA572-W-L-A	0.2

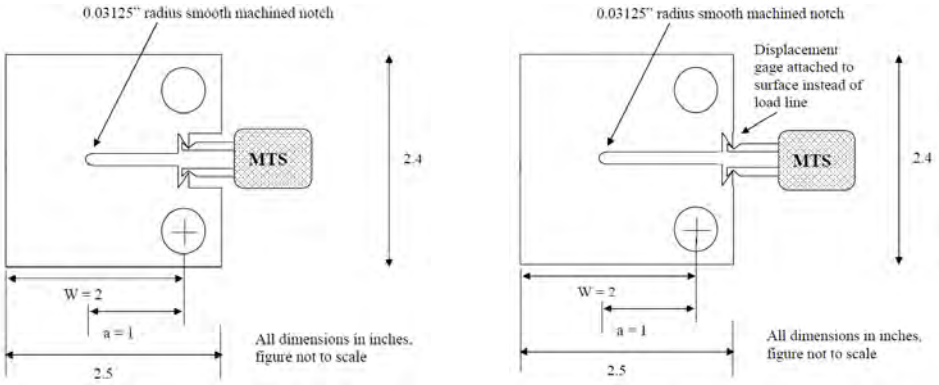

Figure 6.80: Experimental setup (Kanvinde et al. 2004) for specimens CT-KanA572-P-1-3, CT-KanA572-W-1-3, and CT-KanA572-W-4-6 (left); and for specimen CT-KanHPS70W-P-1-3 (right)

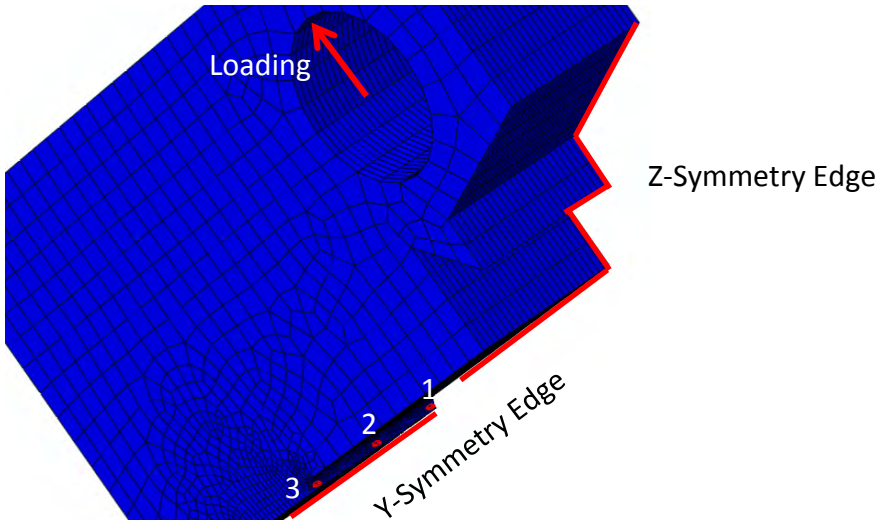

Figure 6.81: Elements selected for studying fracture initiation and propagation parameters in VGM-BW, VGM, and CS strategies with simulation boundary conditions for specimens CT-KanA572-P-1-3, CT-KanA572-W-1-3, CT-KanA572-W-4-6 (left), and CT-KanHPS70W-P-1-3

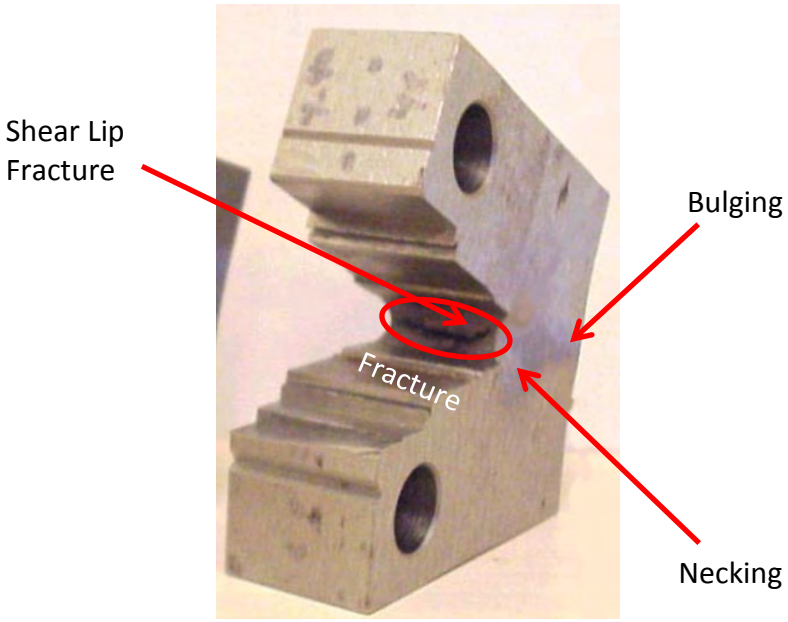

Figure 6.82: Fractured compact tension specimen with visible fracture, necking, and bulging (Kanvinde et al. 2004)

Figure 6.84 and Figure 6.85 show the fracture of a CT-KanA572-W-1-3 and CT-KanA572-W-4-6 specimens for CS, VGM and VGM-BW simulations, respectively. VGM and VGM-BW simulations

of the CT-KanA572-W-1-3 and CT-KanA572-W-4-6 specimens showed severe necking at the notch and bulging at the back end. For the CT-KanA572-W-1-3 specimen the necking and bulging was more severe than for CT-KanA572-W-4-6 specimen, probably due to the higher thickness of the latter specimen. The CS simulation showed minor necking and bulging for both specimen types. This is probably because in the CS simulation the back end fractured. This type of fracture is not reported in the literature. In all of the finite element deletion strategies of the two specimens, fracture initiated at the center of the specimen and propagated outward through a tunneling effect. The VGM simulation does not show signs of shear lips, while the CS simulation shows severe shear lips at the notch edge shown in Figure 6.84 and Figure 6.85. The VGM-BW shows shear lips for both of the specimens. Figure 6.88 and Figure 6.89 show force versus load line displacement plot for experimental test and simulation results of CT-KanA572-W-1-3 and CT-KanA572-W-4-6 specimen, respectively. The VGM had the closest fit to the experimental results. The VGM and VGM-BW simulation results were fairly close to one another with VGM-BW underpredicting the response. The CS simulation results show that the CS strategy severely underpredicted the force-displacement response primarily due to the fracture at the back end of the specimen which does not represent experimental test results found in the literature. The VGM had the best force-displacement prediction while the VGM-BW simulation captured a more complete behavior of fracture propagation in the compact tension specimens.

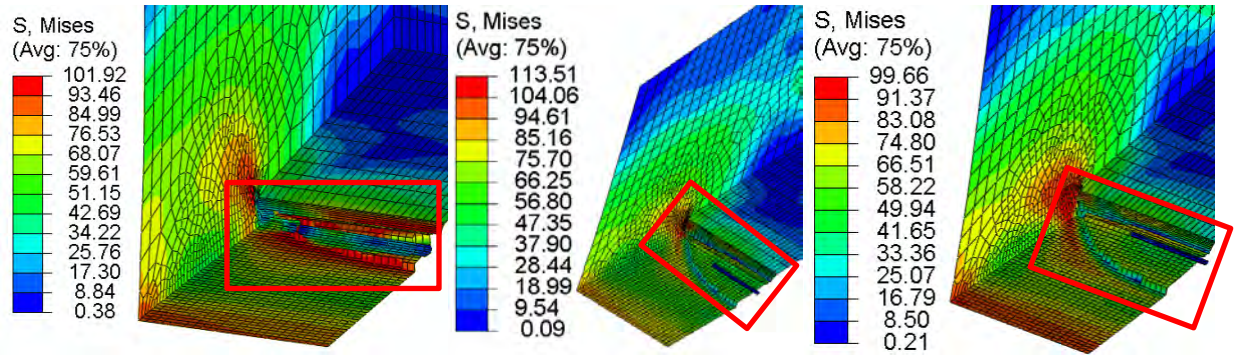

Figure 6.83: Simulation results (Kanvinde et al. 2004) of a compact tention CT-KanA572-P-1-3 specimen with contours representing von Mises stress (ksi): CS (left), VGM (middle), VGM-BW (right)

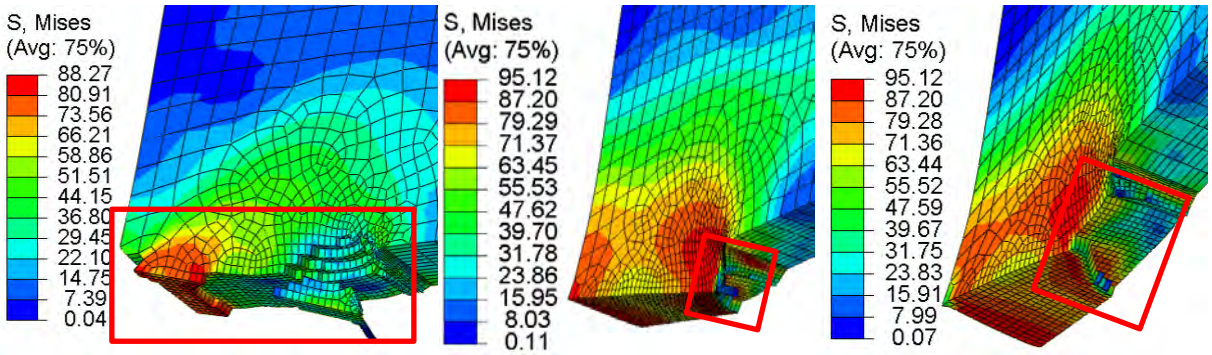

Figure 6.84: Simulation results (Kanvinde et al. 2004) of a compact tention CT-KanA572-W-1-3 specimen with contours representing von Mises stress (ksi): CS (left), VGM (middle), VGM-BW (right)

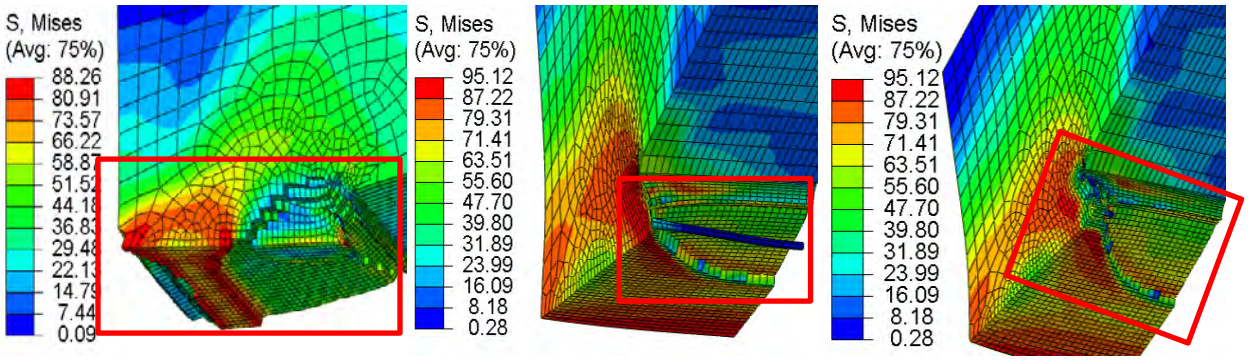

Figure 6.85: Simulation results (Kanvinde et al. 2004) of a compact tention CT-KanA572-W-4-6 specimen with contours representing von Mises stress (ksi): CS (left), VGM (middle), VGM-BW (right)

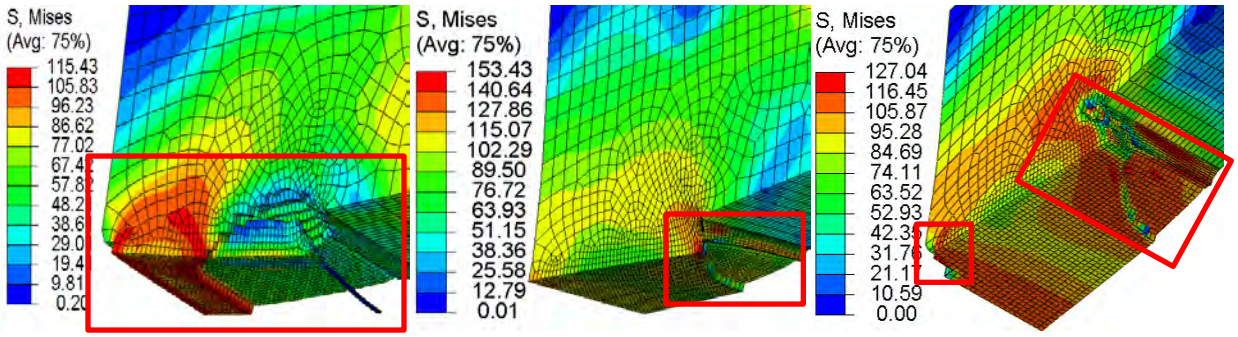

Figure 6.86: Simulation results (Kanvinde et al. 2004) of a compact tention CT-KanHPS70W-P-1-3 specimen with contours representing von Mises stress (ksi): CS (left), VGM (middle), VGM-BW (right)

Figure 6.86 shows the fracture of a CT-KanHPS70W-P-1-3 specimen for CS, VGM and VGM-BW simulations, respectively. VGM and VGM-BW simulations showed severe necking at the notch and some bulging at the back end. Bulging was most severe in VGM simulation due to fracture occurring in the back end of the specimen in VGM-BW and CS simulations. In general, the CS simulation showed minor necking and bulging. All of the finite element deletion strategies had fracture initiated at the center of the specimen and propagated outward and inward through a tunneling effect. The tunneling effect is more properly captured in the VGM and VGM-BW simulations than in CS. The VGM simulation does not show signs of shear lips while the CS simulation shows severe shear lips at the notch edge. The VGM-BW shows some shear lip fracture. Figure 6.90 shows force versus mouth opening displacement plot for experimental test and simulation results. The VGM had the closest fit to the experimental results. The VGM and VGM-BW simulation results were fairly close to one another with VGM-BW underpredicting the response. The CS simulation results show that the CS strategy severely underpredicted the force-displacement response primarily due to the fracture at the back end of the specimen which is not represent experimental test results found in the literature and not being able to

properly capture the tunneling effect. The VGM had the best force-displacement prediction while the VGM-BW simulation captured a more compete behavior of fracture propagation in the compact tension specimens except for the minor back end fracture which is not reported in experimental test results. Overall, for the four types of specimens, the VGM criteria gives the best force-displacement prediction while the CS and VGM-BW usually underpredict except for the CT-KanA572-P-1-3 specimen. In addition, the prediction is better for a thinner specimen than for a thicker one suggesting that the calibrated fracture locus at higher triaxiality is too low. On the other hand, the VGM-BW which accounts for shear and mix-mode fracture most accurately represents fracture propagation by properly capturing the tunneling effect and shear lip fracture on the edge surface of the specimens.

Below a detailed description is provided on the variation of fracture initiation and propagation parameters in elements that are located through the thickness of the specimens for the three finite element deletion strategies.

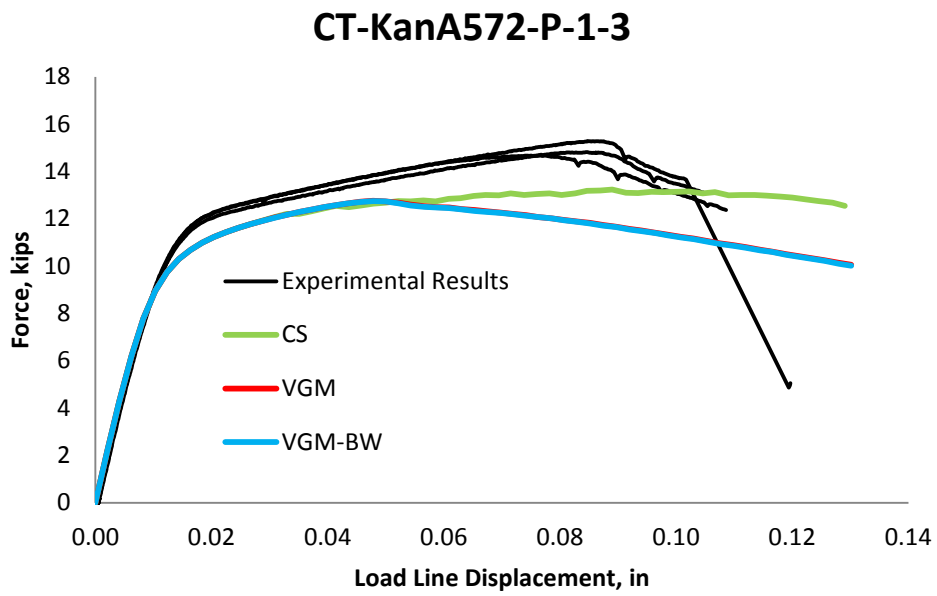

Figure 6.87: Force versus load line displacement validation results for compact tension specimen CT-KanA572-P-1-3

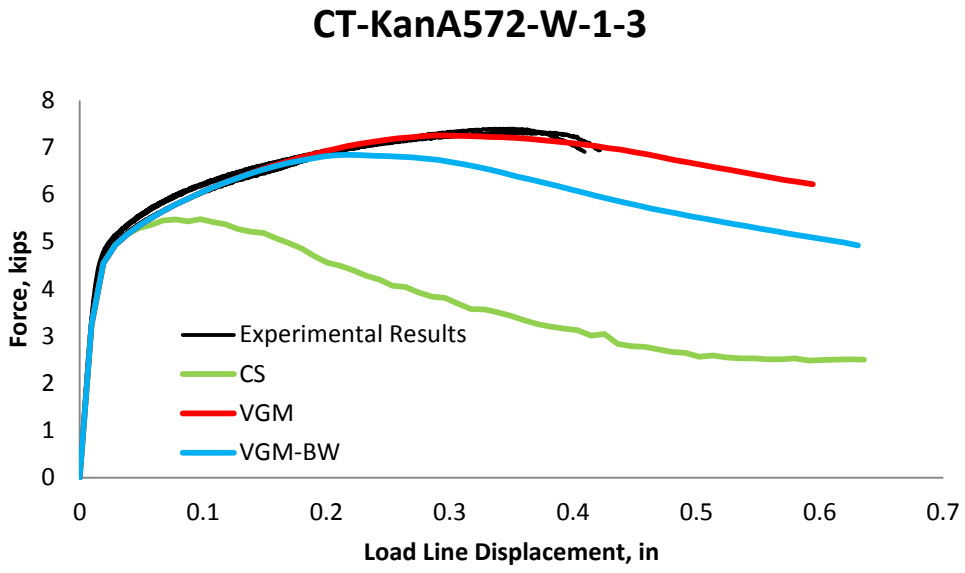

Figure 6.88: Force versus load line displacement validation results for a compact tension specimen CT-KanA572-W-1-3

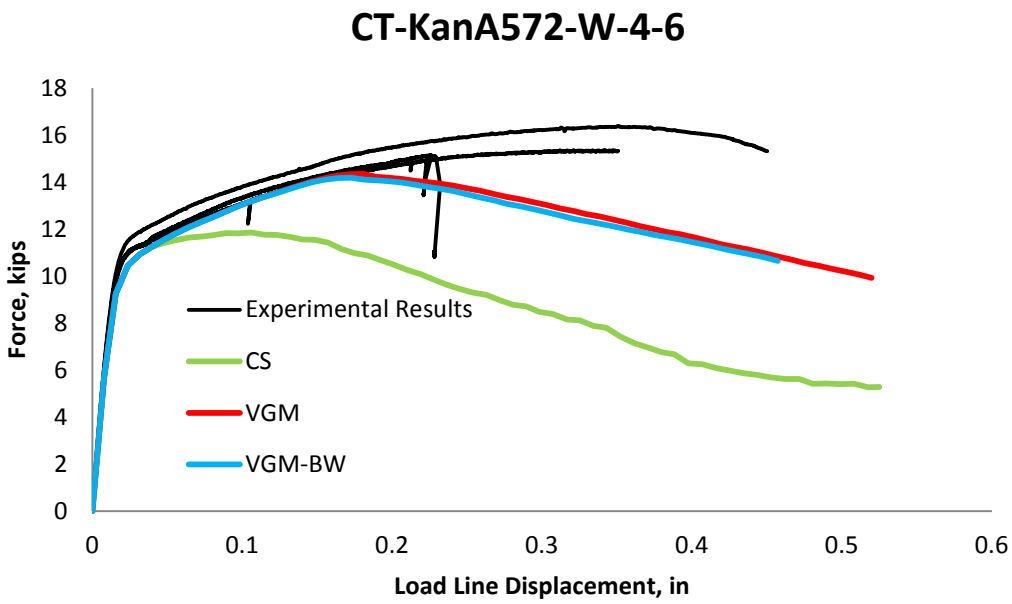

Figure 6.89: Force versus load line displacement validation results for a compact tension specimen CT-KanA572-W-4-6

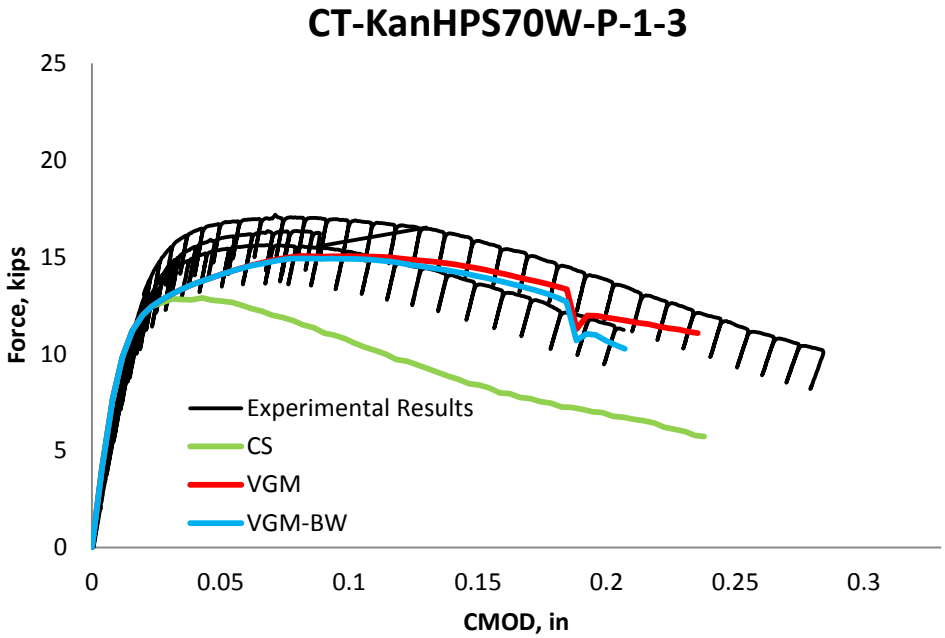

Figure 6.90: Force versus crack mouth opening displacement validation results for compact tention specimen CT-KanHPS70W-P-1-3

Triaxiality versus displacement is plotted for the three elements across the thickness of the four specimens for the three finite element deletion strategies in Figure 6.91, Figure 6.92, Figure 6.93, and Figure 6.94. As in previous specimens, the triaxiality is the same throughout the loading excursion until the point of softening for the three finite element deletion strategies for the CT-KanA572-P-1-3 and CT-KanHPS70W-P-1-3 specimens but not for CT-KanA572-W-1-3 and CT-KanA572-W-4-6 specimens, which had minor differences in triaxiality values between the finite element deletion strategies. After this point, the value of triaxiality is different for the three strategies. Most elements experience an increase in triaxiality before failure in the VGM and VGM-BW simulations. Figure 6.91 and Figure 6.93 show results for specimens with different materials but the same geometrical parameters, which should suggests that the triaxiality levels until softening of the elements should be very similar between materials. The triaxiality range is in fact approximately the same around 0.6 to 0.9 triaxiality but CT-KanA572-P-1-3 specimen has a constant triaxiality value until softening and the CT-KanA572-W-4-6 specimen has a declining triaxiality value. The reason for this is in the definition of the plasticity range of inputs with CT-KanA572-P-1-3 having isotropic plastic hardening defined up to an equivalent plastic strain value of 0.8 while CT-KanA572-W-4-6 up to 0.3. After reaching the strain level of 0.3 the material does not exhibit further hardening but keeps the yield stress constant as in perfectly plastic condition.

The equivalent plastic strain is plotted in Figure 6.95, Figure 6.96, Figure 6.97, and Figure 6.98. The figures show that the equivalent plastic strain in VGM simulations reached the highest values and in CS simulations the lowest. For VGM simulations the outside element reached the

highest strain value and the inner element the lowest. The VGM-BW simulation had an opposite trend.

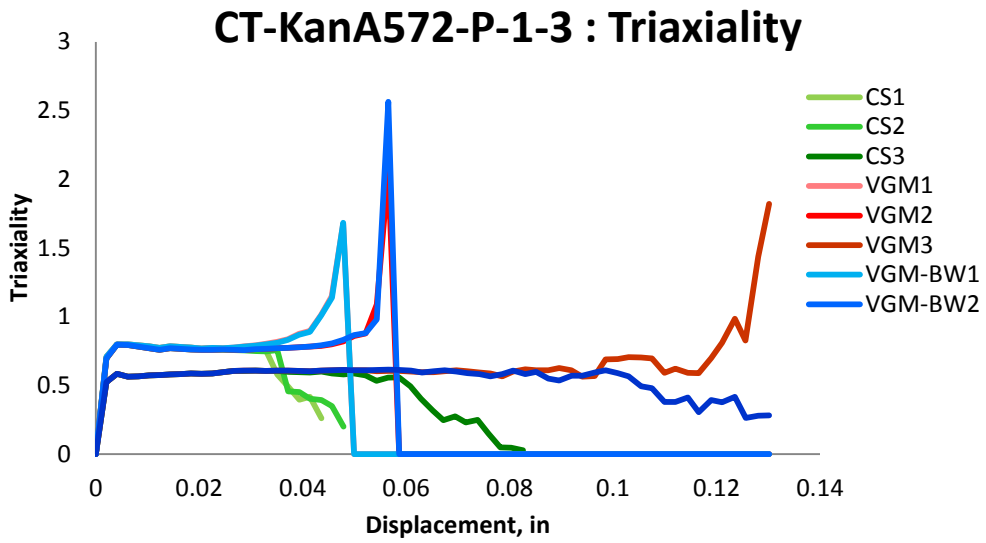

Figure 6.91: Variation of triaxiality with displacement for different elements laid out through the thickness of simulation of CT-KanA572-P-1-3 specimens for the three finite element deletion strategies

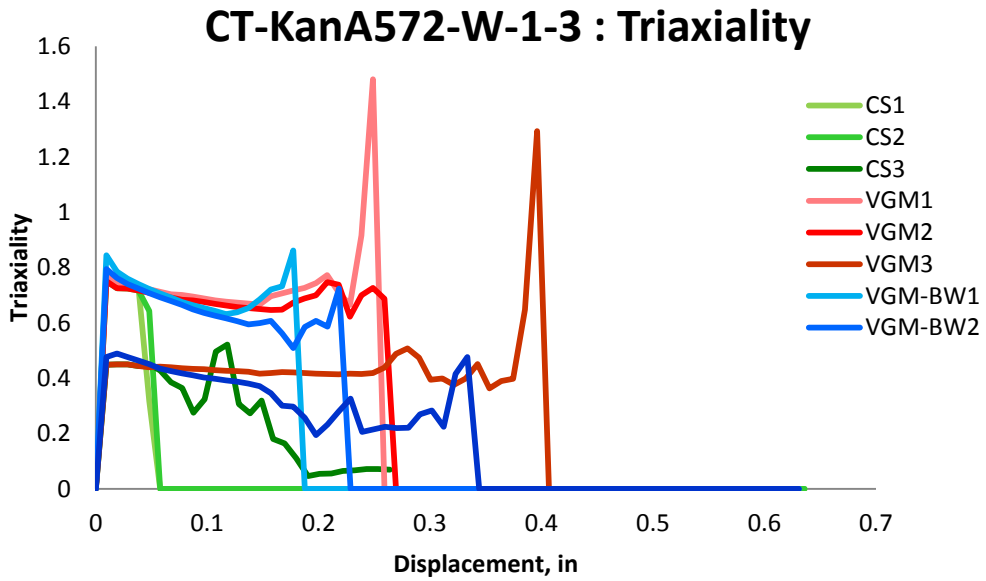

Figure 6.92: Variation of triaxiality with displacement for different elements laid out through the thickness of simulation of CT-KanA572-W-1-3 specimens for the three finite element deletion strategies

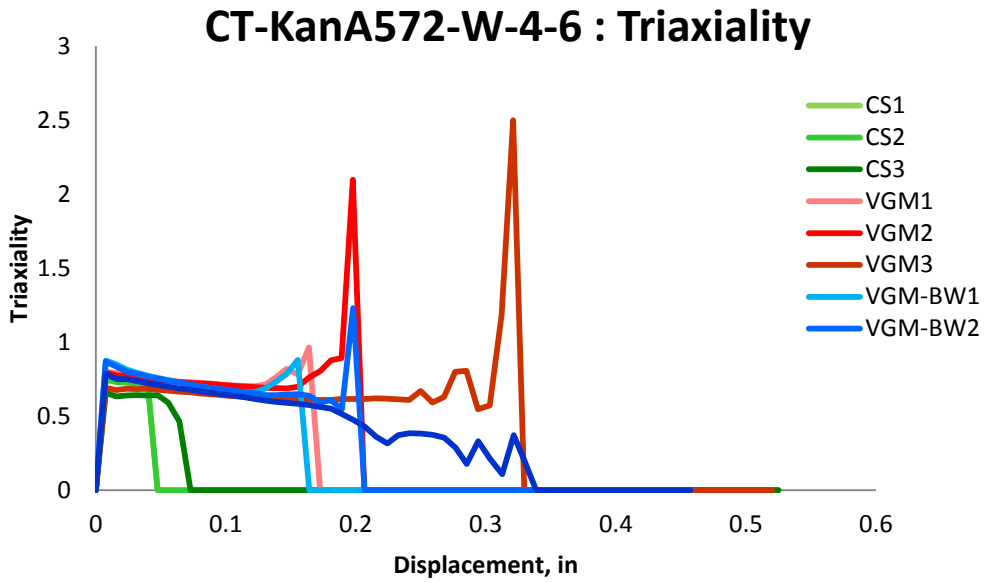

Figure 6.93: Variation of triaxiality with displacement for different elements laid out through the thickness of simulation of CT-KanA572-W-4-6 specimens for the three finite element deletion strategies

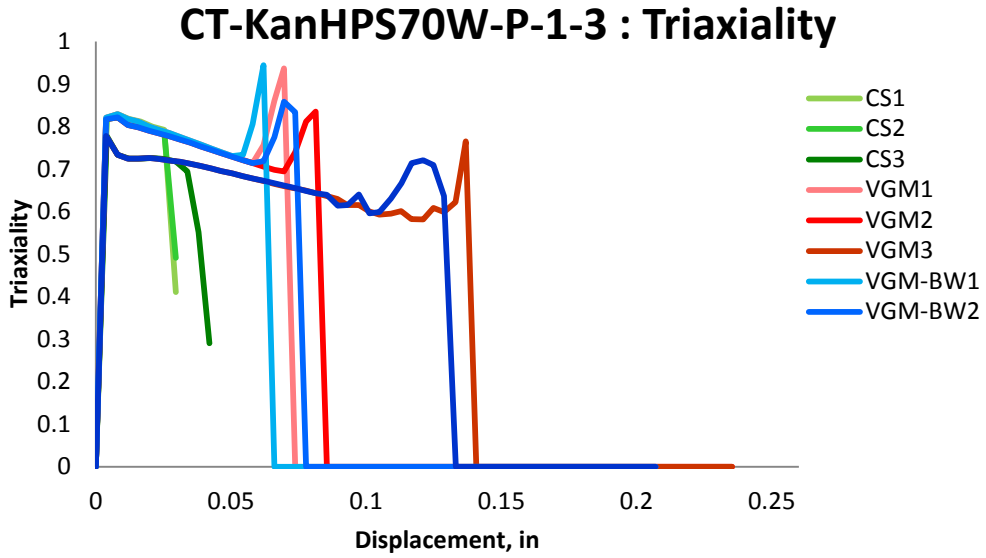

Figure 6.94: Variation of triaxiality with displacement for different elements laid out through the thickness of simulation of CT-KanHPS70W-P-1-3 specimens for the three finite element deletion strategies

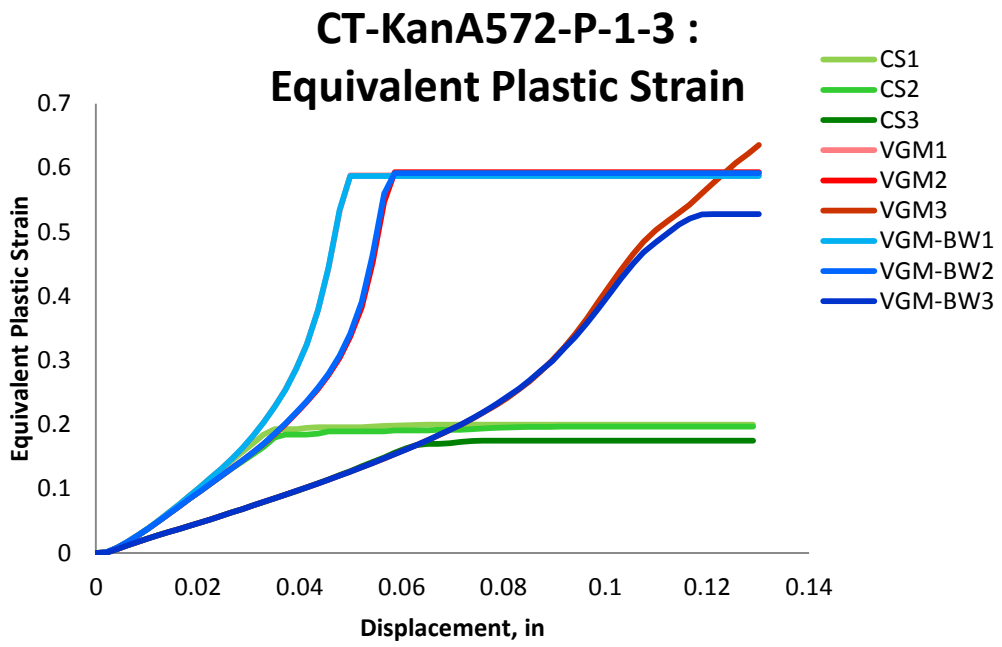

Figure 6.95: Variation of equivalent plastic strain with displacement for different elements laid out through the thickness of simulation of CT-KanA572-P-1-3 specimens for the three finite element deletion strategies

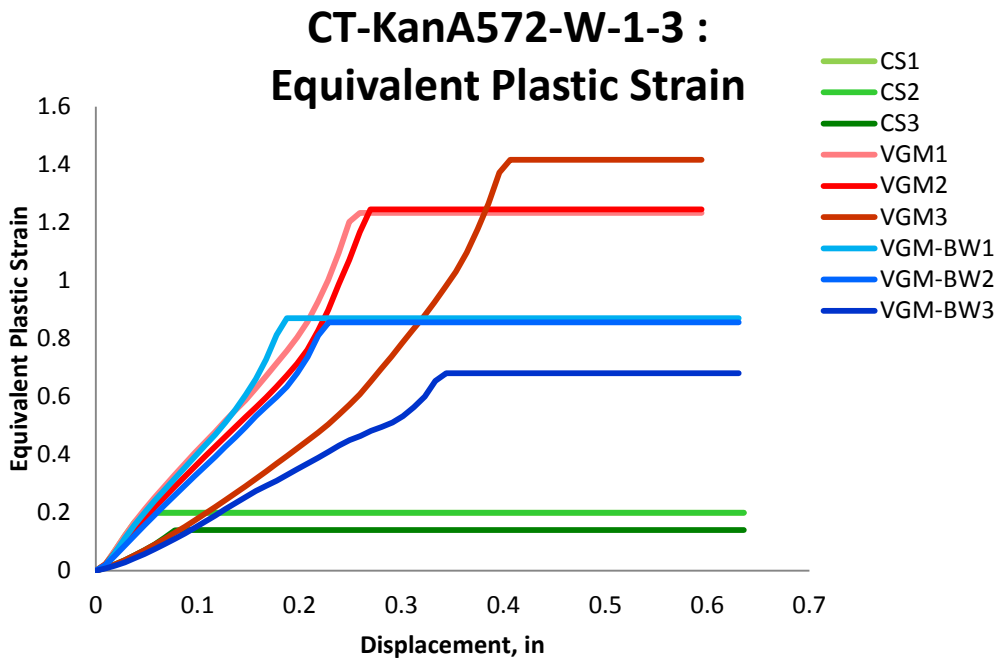

Figure 6.96: Variation of equivalent plastic strain with displacement for different elements laid out through the thickness of simulation of CT-KanA572-W-1-3 specimens for the three finite element deletion strategies

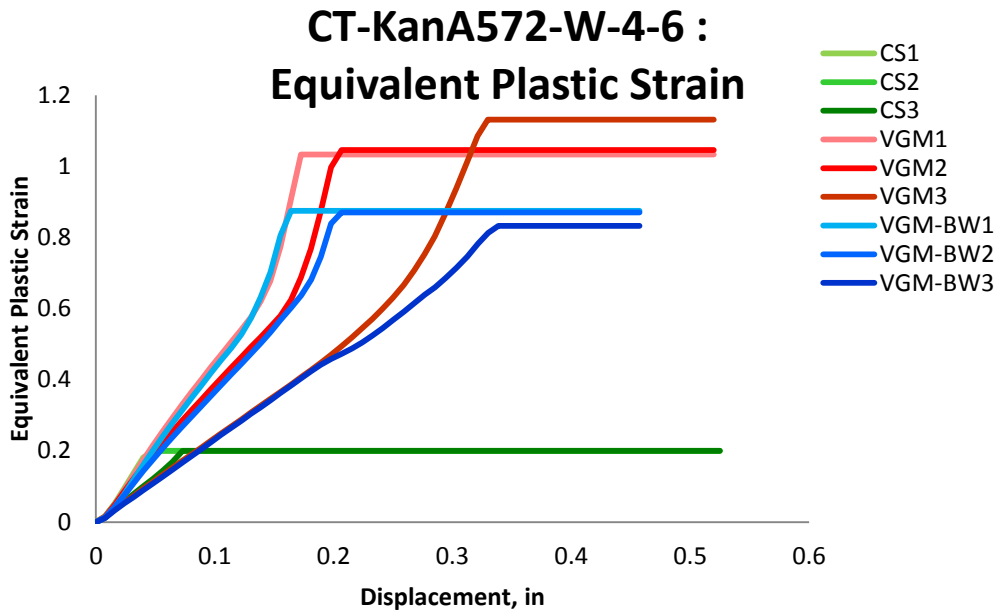

Figure 6.97: Variation of equivalent plastic strain with displacement for different elements laid out through the thickness of simulation of CT-KanA572-W-4-6 specimens for the three finite element deletion strategies

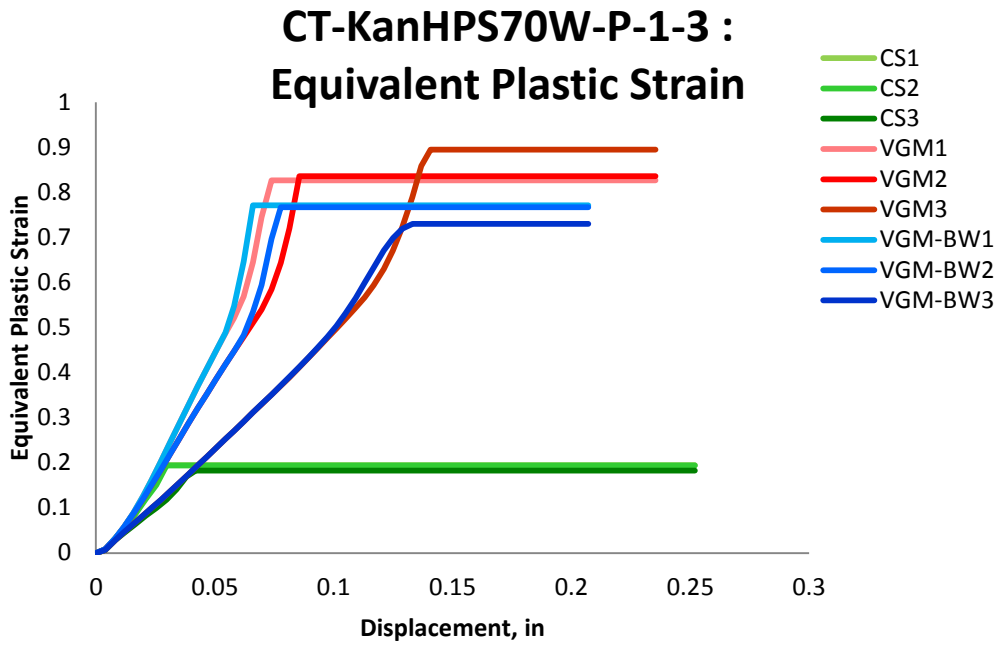

Figure 6.98: Variation of equivalent plastic strain with displacement for different elements laid out through the thickness of simulation of CT-KanHPS70W-P-1-3 specimens for the three finite element deletion strategies

The fracture locus is plotted in Figure 6.99, Figure 6.100, Figure 6.101, and Figure 6.102. The triaxiality range varied from approximately 0.4 to 0.8 for the CT-KanA572-W-1-3 specimen and 0.6 to 0.9 for the other three specimens. It can be seen that triaxiality on the surface of the specimens is lower for the thinner specimen. The thinner specimen has more ductility than the thicker, allowing for less confinement. In addition, as the equivalent plastic strain grows there is a tendency for triaxiality to decline forcing less confinement on the plastic flow in an element. The plasticity is defined up to 1.386 equivalent plastic strain for CT-KanHPS70W-P-1-3 specimen; therefore, the elements experienced hardening throughout the loading process as apposed to the CT-KanA572-W-1-3 and CT-KanA572-W-4-6 specimens. The reason for the declining triaxiality is most probably due to a physical phenomena that as the elements are elongated they reduce the confinement imposed on each other. The fracture locus for the three strategies is very similar to each other in this triaxiality range of 0.6 to 0.8 for CT-KanA572-P-1-3 specimen. However the force-displacement results are different. This again confirms the effect that softening can have on the global behavior of a structure. The curves for the three finite element strategies of the three elements should follow the exact same path until they reach softening, after which the curves diverge. This is not the case for CT-KanA572-W-1-3 and CT-KanA572-W-4-6 specimens. This is due to fracture occuring in different ways and at other locations affecting the response at the chosen elements.

The variation of the value of fracture initiation integral which is shown in Figure 6.103, Figure 6.104, Figure 6.105, and Figure 6.106 follows simmilar trend where the difference between finite element deletion strategies for an element are attributed to failure occuring at other parts of the specimen and affecting results of the element. As one moves inward the slope of

the value of this integral increases due to higher triaxiality. When an element did not reach a value of 1 for the fracture initiation integral it means that it was not deleted but was separated from the rest of the strucutre by a fracture propagating in nearby elements.

The varition of von Mises stress with displacement is shown in Figure 6.107, Figure 6.108, Figure 6.109, and Figure 6.110. The curves for VGM and VGM-BW simulations for the three elements follow a similar trend as other parameters previously mentioned. For the three out of four specimens the von Mises stress versus displacmenet curves for VGM and VGM-BW follow distinct paths, which signifies that for the three specimens the elements behaved in the lower triaxiality region, where VGM and VGM-BW predict different equivalent plastic strain at fracture initiation. For the CT-KanA572-P-1-3 specimen, the three elements reached their critical equivalent plastic strain value at almost the same values for the three finite element deletion strategies, which signifies that the elements for the three strategies exhibited higher triaxiality. The CS failure is more gradual than in the previous sections. This allows for stress redistribution to occur and limits any dynamic instabilities that might occur. The flat horizontal top of the curves is due to elements reaching equivalent plastic strain values above those for which plasticity was defined creating perfectly plastic stress condition.

The mean stress variation through out the loading excursion is plotted Figure 6.111, Figure 6.112, Figure 6.113, and Figure 6.114. The mean stress does not increase during softening for the three finite element deletion strategies as in previous sections. Only the outside element of the thin CT-KanA572-W-1-3 specimen has any such increase before failure. These specimens are thick enough to allow fracture to propagate and for stress in the specimen to redistribute.

In addition, the softening for the outside element has vibrations due to the edge fracture occuring with some degree of slant at the edges of the specimen above the chosen elements.

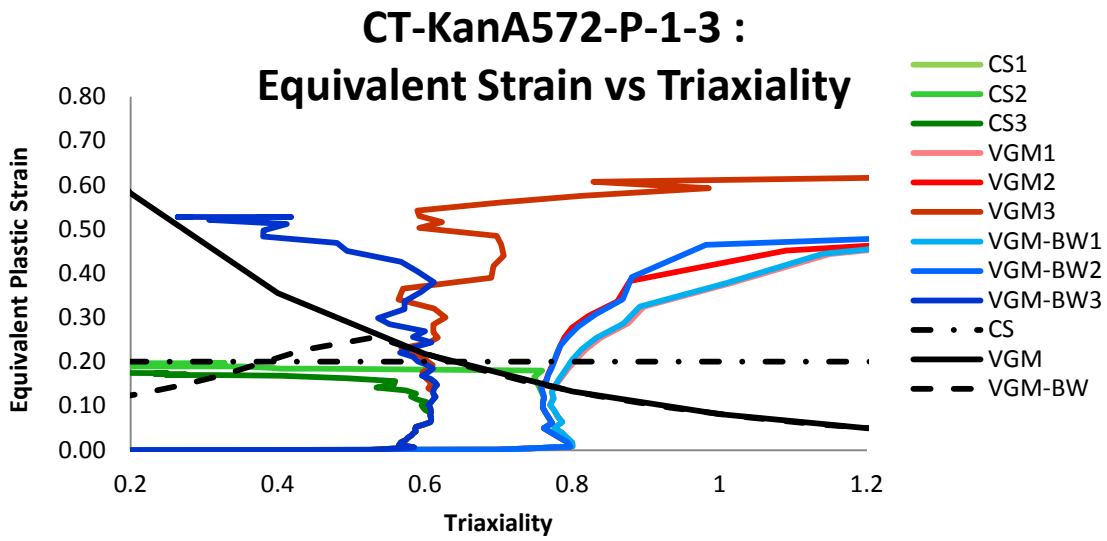

Figure 6.99: Variation of equivalent plastic strain with triaxiality for different elements laid out through the thickness of simulation of CT-KanA572-P-1-3 specimens for the three finite element deletion strategies

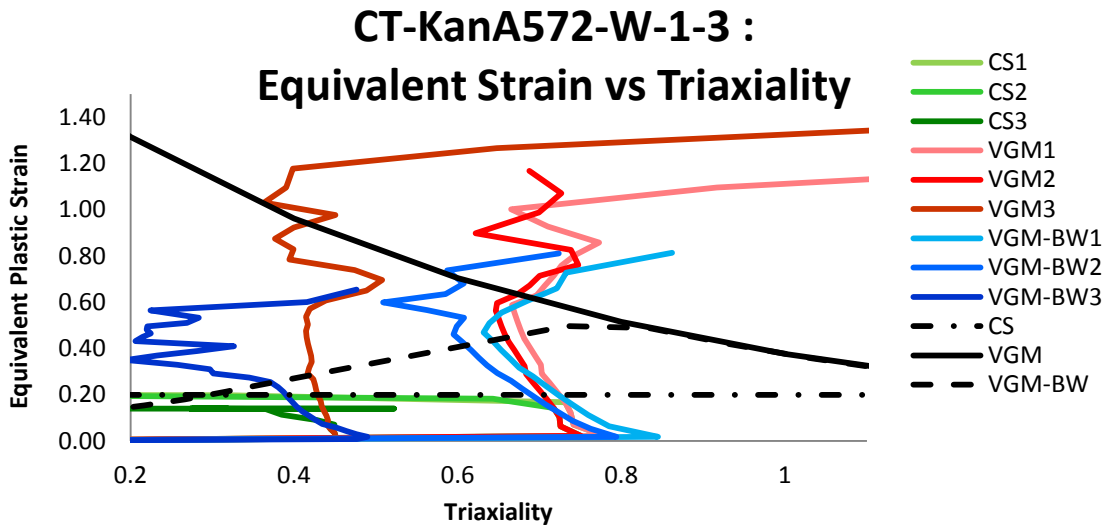

Figure 6.100: Variation of equivalent plastic strain with triaxiality for different elements laid out through the thickness of simulation of CT-KanA572-W-1-3 specimens for the three finite element deletion strategies

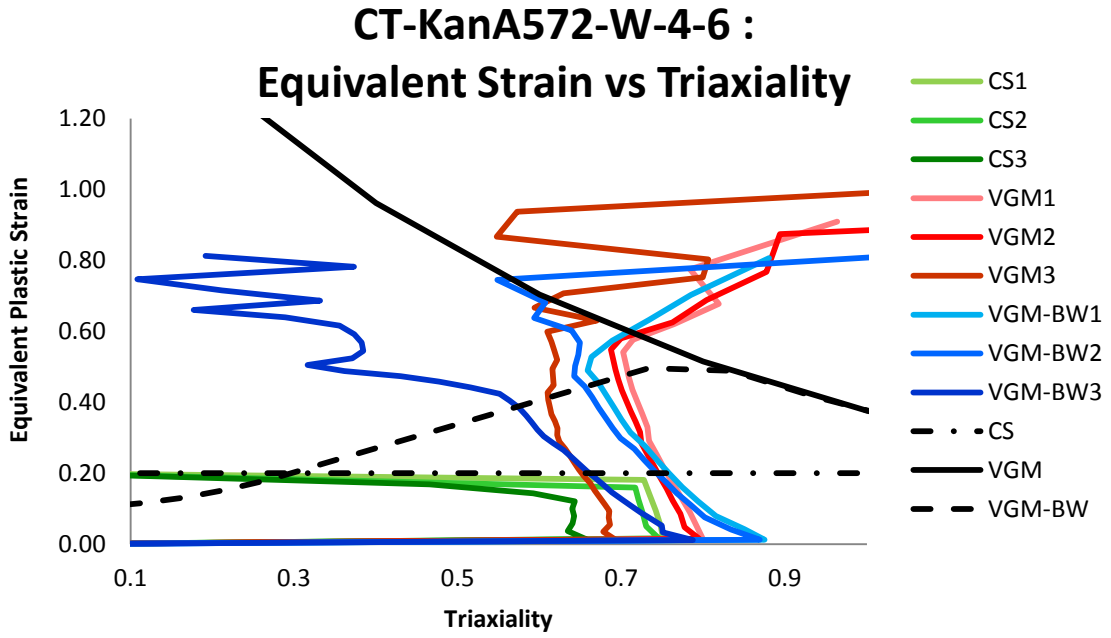

Figure 6.101: Variation of equivalent plastic strain with triaxiality for different elements laid out through the thickness of simulation of CT-KanA572-W-4-6 specimens for the three finite element deletion strategies

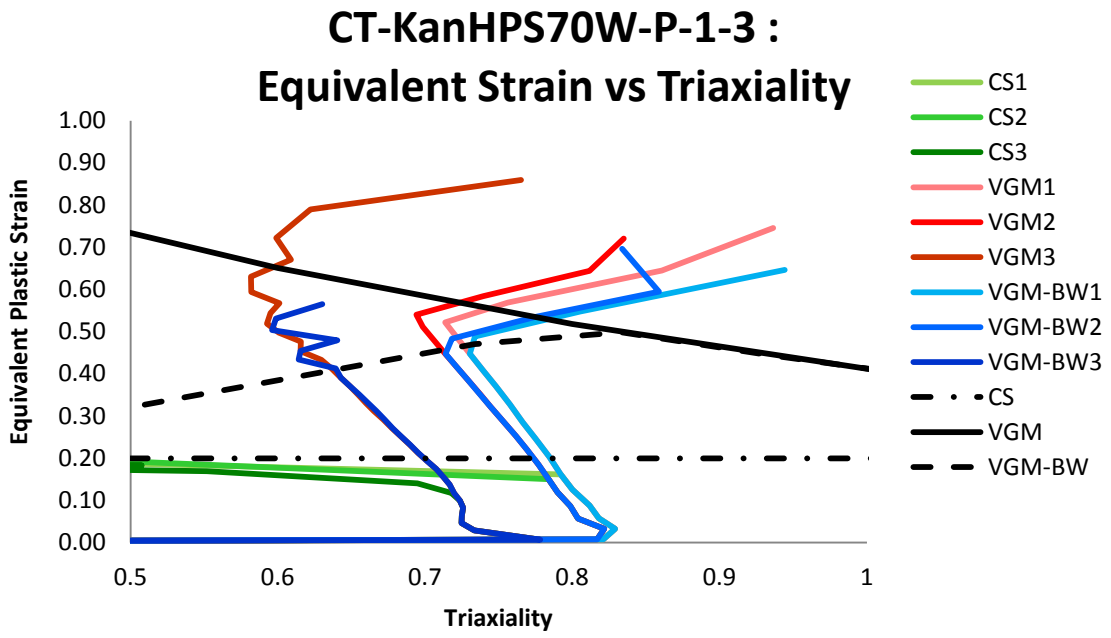

Figure 6.102: Variation of equivalent plastic strain with triaxiality for different elements laid out through the thickness of simulation of CT-KanHPS70W-P-1-3 specimens for the three finite element deletion strategies

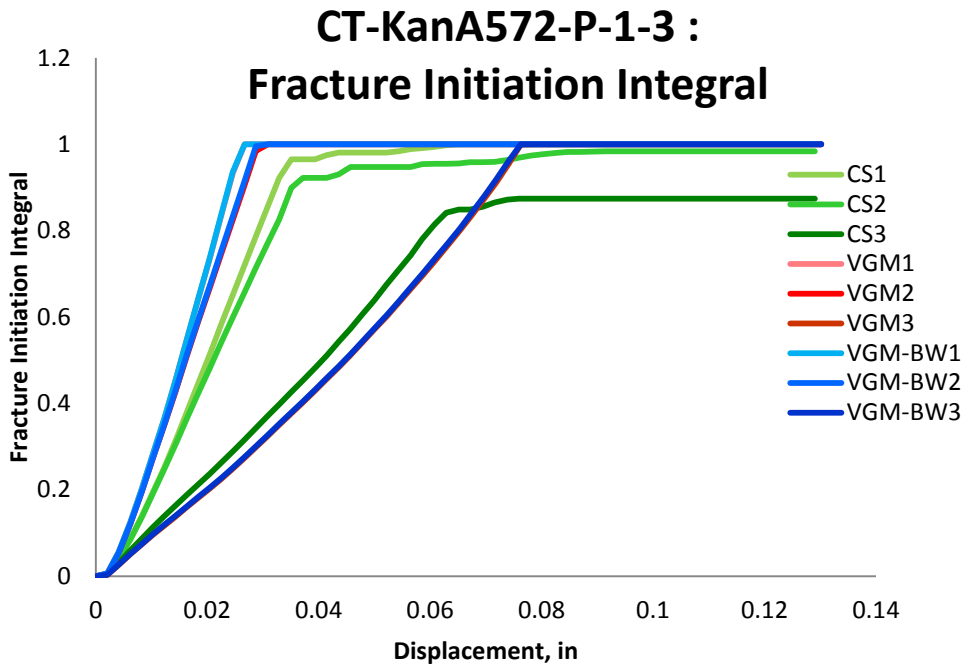

Figure 6.103: Variation of fracture initiation integral value with displacement for different elements laid out through the thickness of simulation CT-KanA572-P-1-3 specimens for the three finite element deletion strategies

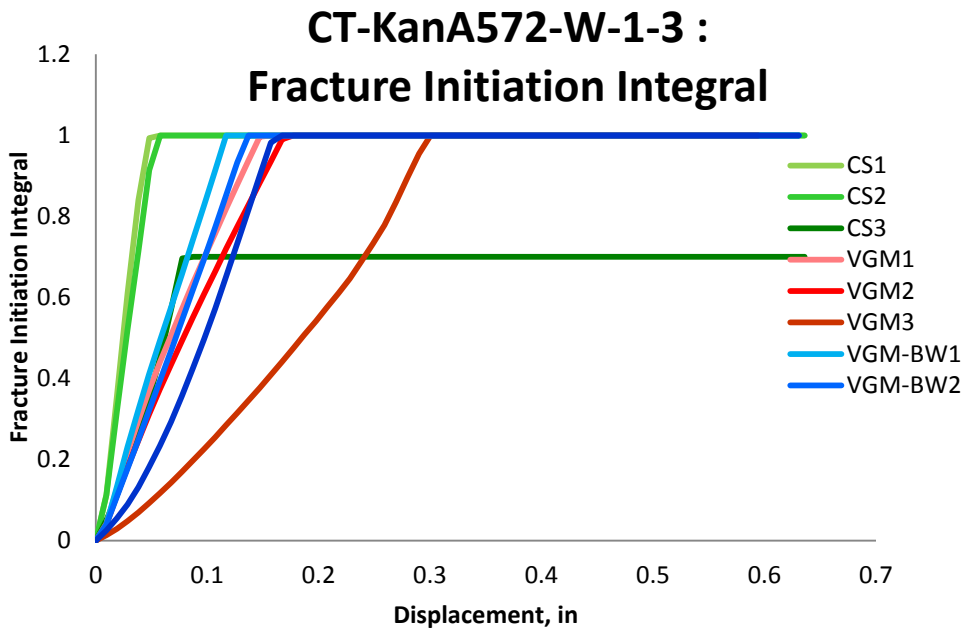

Figure 6.104: Variation of fracture initiation integral value with displacement for different elements laid out through the thickness of simulation of CT-KanA572-W-1-3 specimens for the three finite element deletion strategies

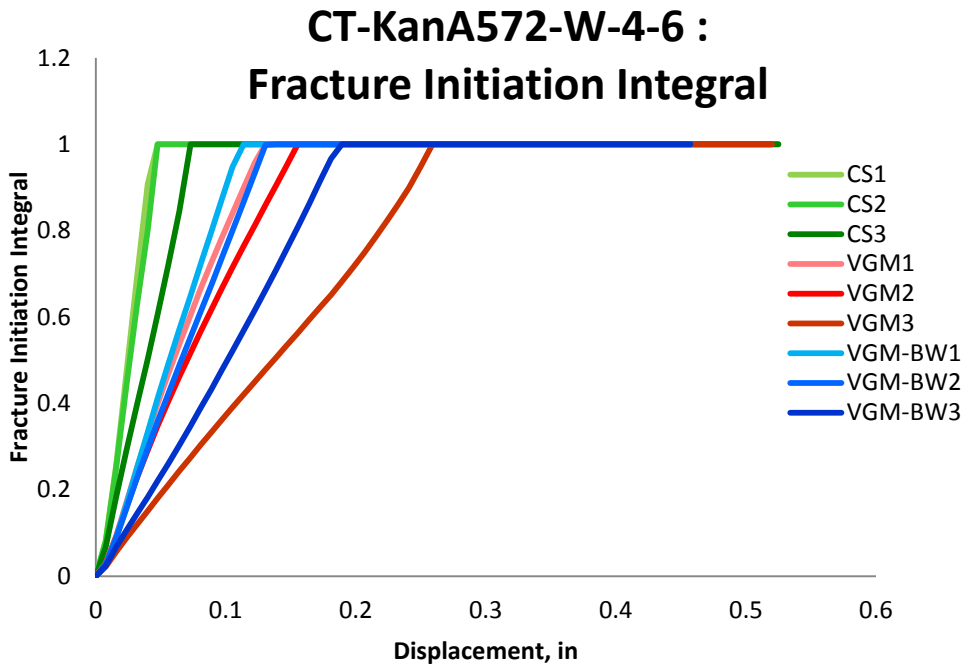

Figure 6.105: Variation of fracture initiation integral value with displacement for different elements laid out through the thickness of simulation of CT-KanA572-W-4-6 specimens for the three finite element deletion strategies

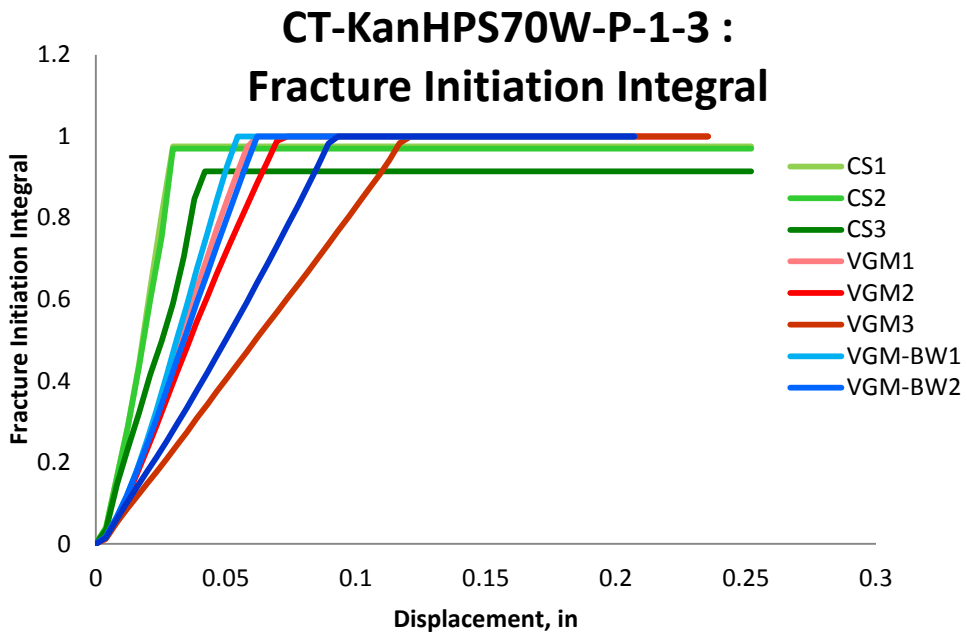

Figure 6.106: Variation of fracture initiation integral value with displacement for different elements laid out through the thickness of simulation of CT-KanHPS70W-P-1-3 specimens for the three finite element deletion strategies

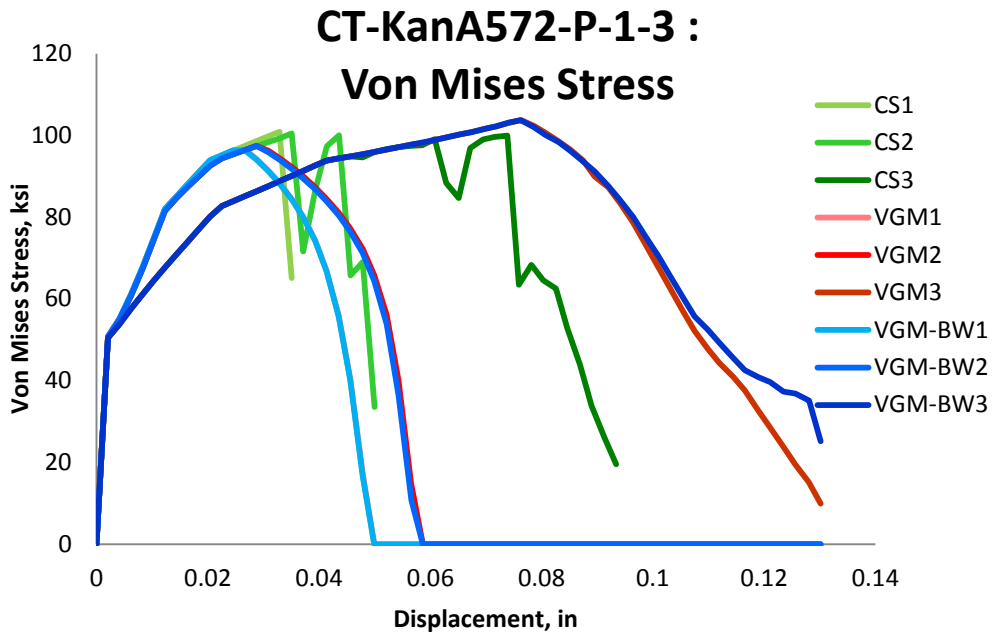

Figure 6.107: Variation of von Mises Stress with displacement for different elements laid out through the thickness of simulation of CT-KanA572-P-1-3 specimens for the three finite element deletion strategies

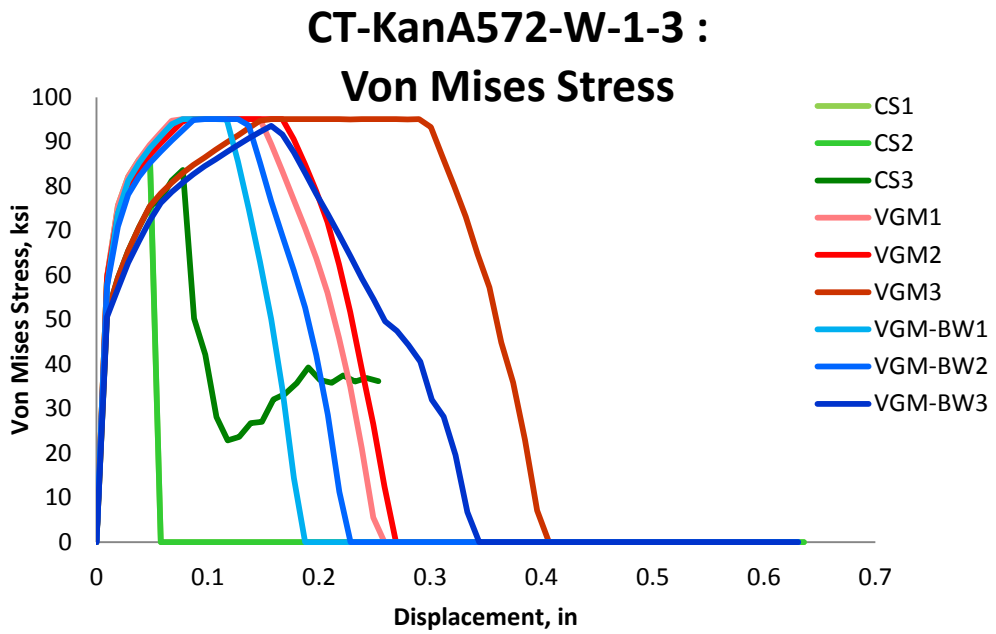

Figure 6.108: Variation of von Mises Stress with displacement for different elements laid out through the thickness of simulation of CT-KanA572-W-1-3 specimens for the three finite element deletion strategies

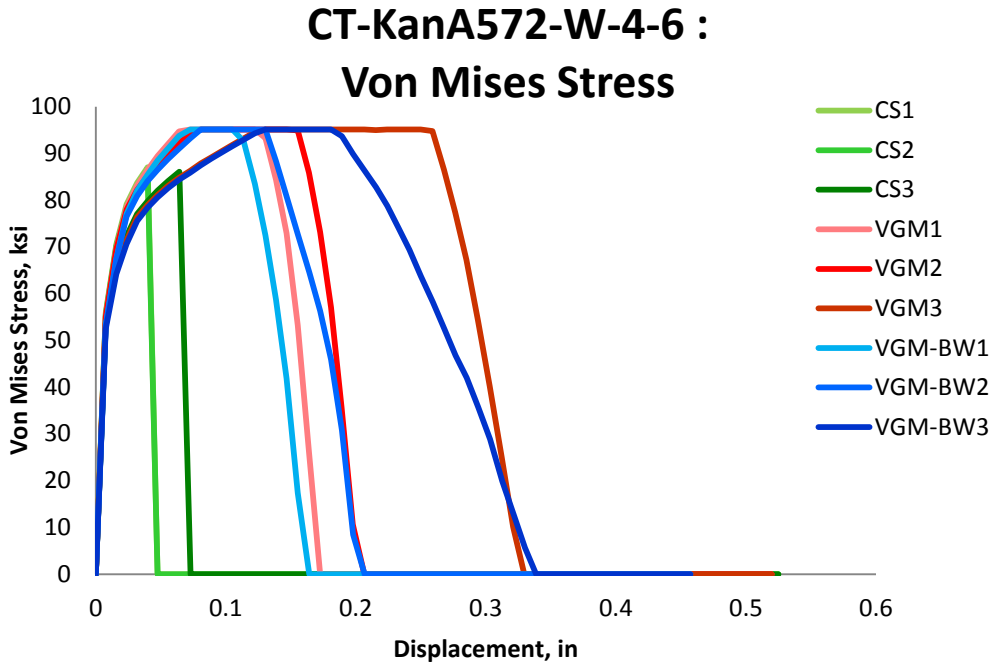

Figure 6.109: Variation of von Mises Stress with displacement for different elements laid out through the thickness of simulation of CT-KanA572-W-4-6 specimens for the three finite element deletion strategies

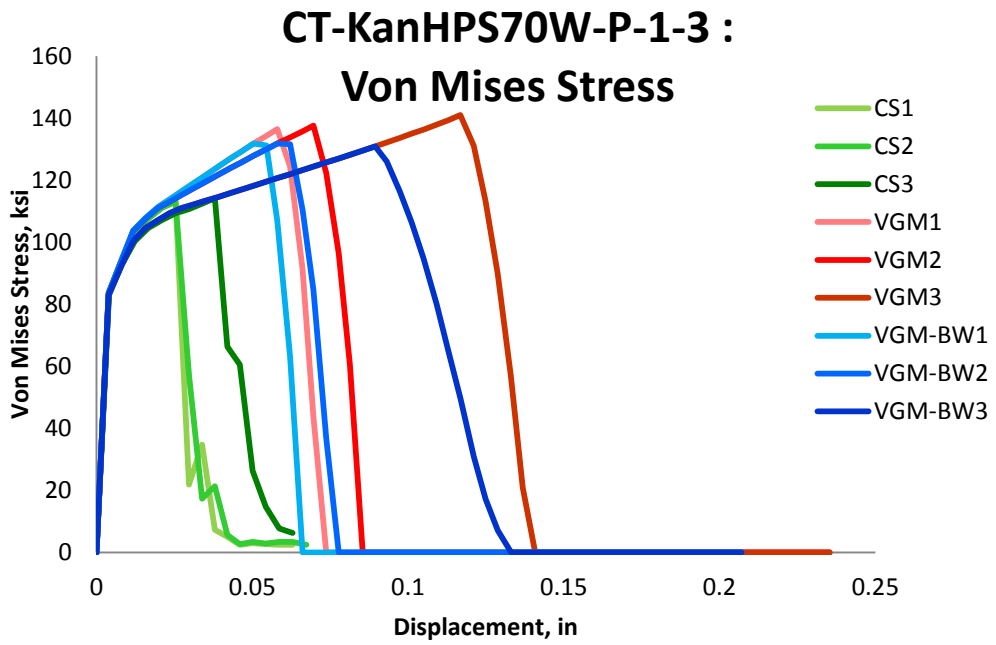

Figure 6.110: Variation of von Mises Stress with displacement for different elements laid out through the thickness of simulation of CT-KanHPS70W-P-1-3 specimens for the three finite element deletion strategies

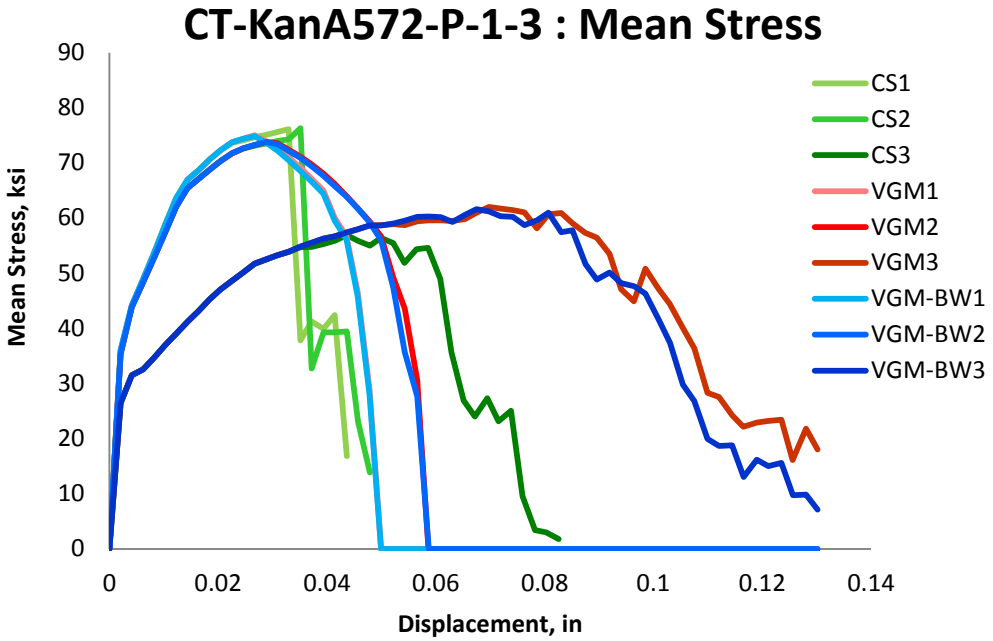

Figure 6.111: Variation of mean stress with displacement for different elements laid out through the thickness of simulation of CT-KanA572-P-1-3 specimens for the three finite element deletion strategies

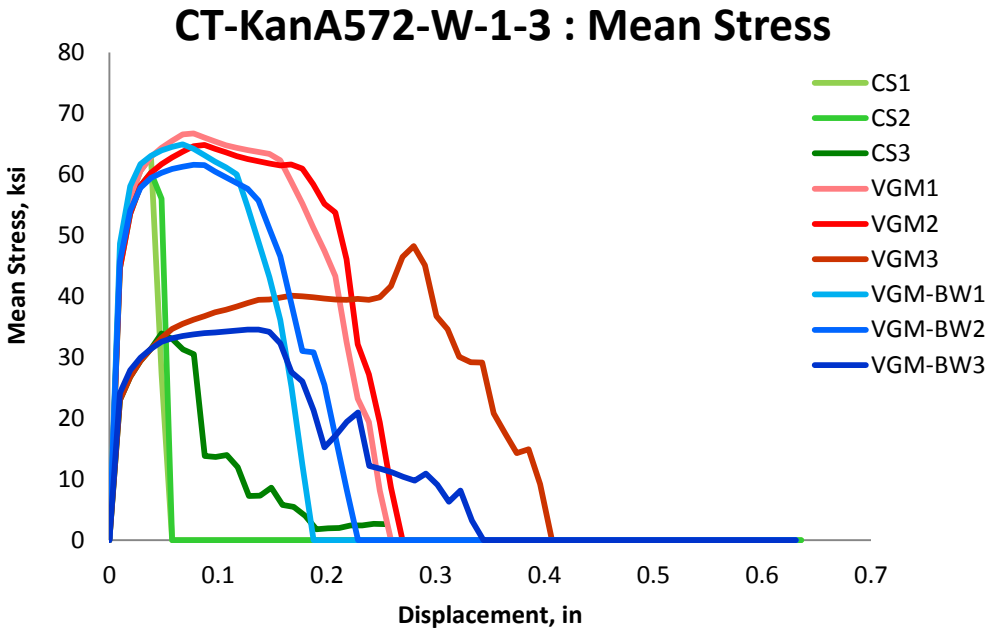

Figure 6.112: Variation of mean stress with displacement for different elements laid out through the thickness of simulation of CT-KanA572-W-1-3 specimens for the three finite element deletion strategies

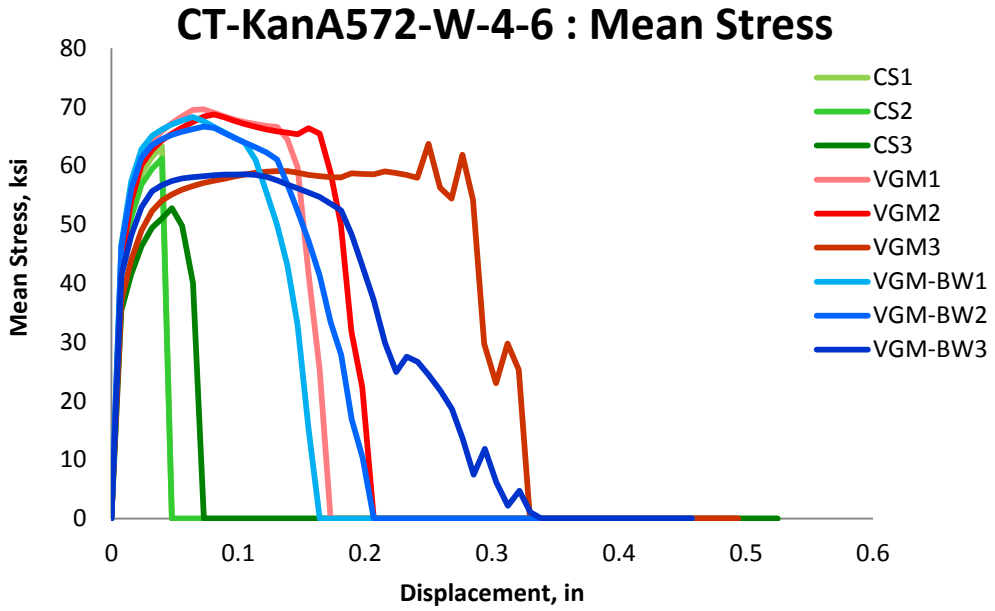

Figure 6.113: Variation of mean stress with displacement for different elements laid out through the thickness of simulation of CT-KanA572-W-4-6 specimens for the three finite element deletion strategies

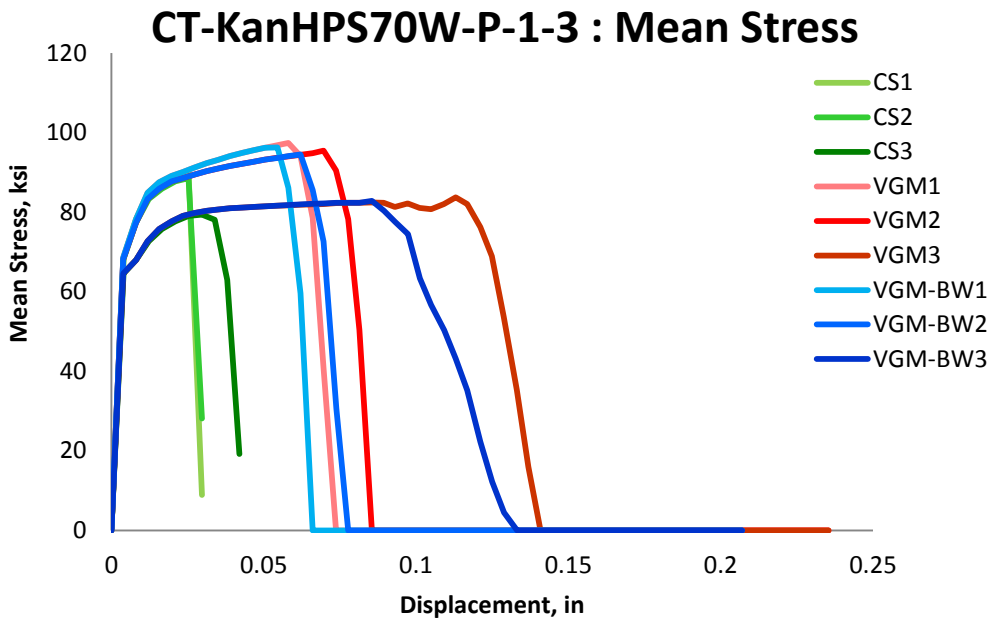

Figure 6.114: Variation of mean stress with displacement for different elements laid out through the thickness of simulation of CT-KanHPS70W-P-1-3 specimens for the three finite element deletion strategies

Figure 6.115, Figure 6.116, Figure 6.117, and Figure 6.118 show the variation of von Mises equivalent stress vs. equivalent plastic strain. As in the previous specimens, the VGM finite element deletion strategy allowed twice as much of strain energy in an element than VGM-BW and three times that of CS strategy for most specimens. This allows the element to reach higher stress at larger equivalent plastic strain levels. Due to the lower triaxiality levels the outside element attains the greatest amount of strain energy for the VGM simulation while the inner element 1 attains the least amount. The VGM-BW simulation shows an opposite trend. The reason for this is the increasing critical equivalent plastic strain value as triaxiality decreases for the VGM fracture locus and a decreasing critical equivalent plastic strain value for Bao-Wierzbicki fracture locus used in VGM-BW strategy. The variation of the value of the damage variable is plotted in Figure 6.119, Figure 6.120, Figure 6.121, and Figure 6.122. The damage variable curves for the three finite element deletion strategies are distinguishable from each strategy and from each element due to fracture tunneling effect. The fracture tunneling effect causes the crack to propagate more inward than outward and since the three finite element deletion strategies have distinctive fracture locus this propagation is different for each strategy. This causes different stress redistribution to occur and different stress-strain based parameters at the elements' integration points for different finite element deletion strategies. In addition, the elements on the inside have their damage variable curves at a lower displacement value than those elements that are on the outside surface of the speciemen signifying that they initiated fracture and failed at a lower global specimen displacement value.

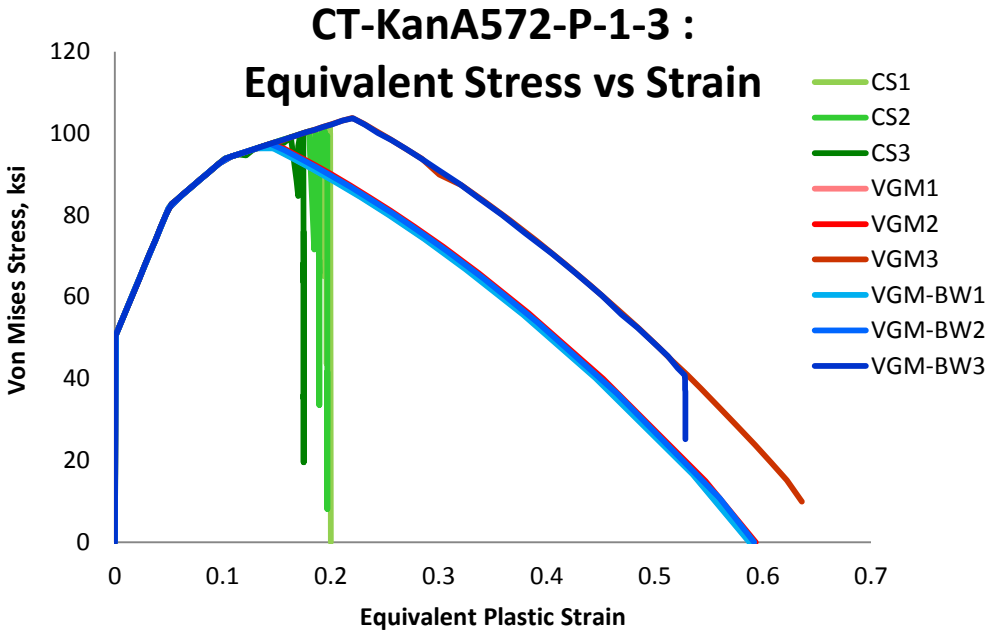

Figure 6.115: Variation of von Mises Stress with equivalent plastic strain for different elements laid out through the thickness of simulation of CT-KanA572-P-1-3 specimens for the three finite element deletion strategies

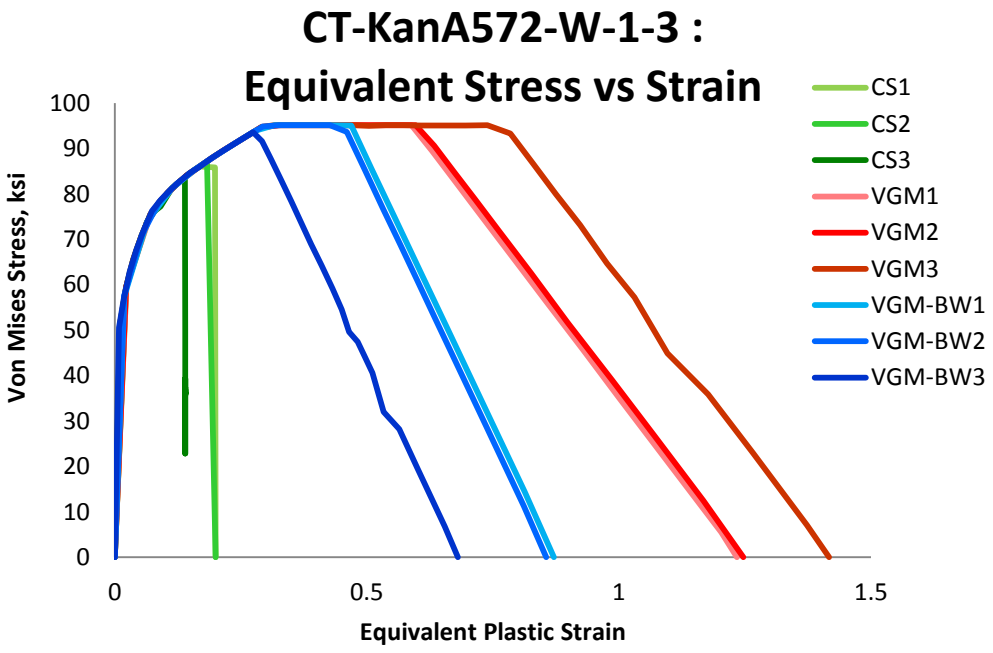

Figure 6.116: Variation of von Mises Stress with equivalent plastic strain for different elements laid out through the thickness of simulation of CT-KanA572-W-1-3 specimens for the three finite element deletion strategies

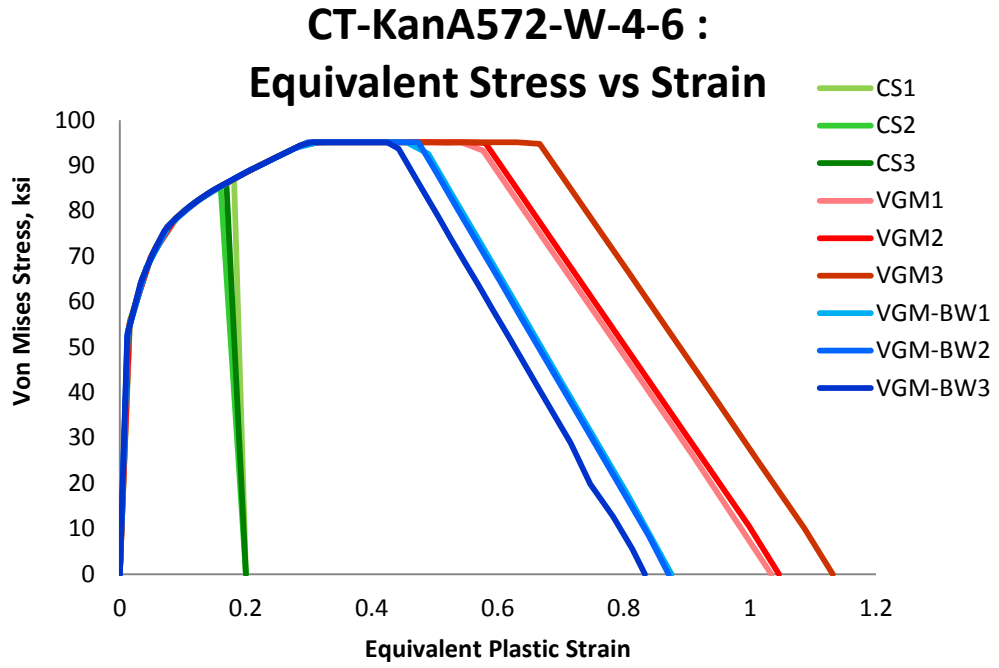

Figure 6.117: Variation of von Mises Stress with equivalent plastic strain for different elements laid out through the thickness of simulation of CT-KanA572-W-4-6 specimens for the three finite element deletion strategies

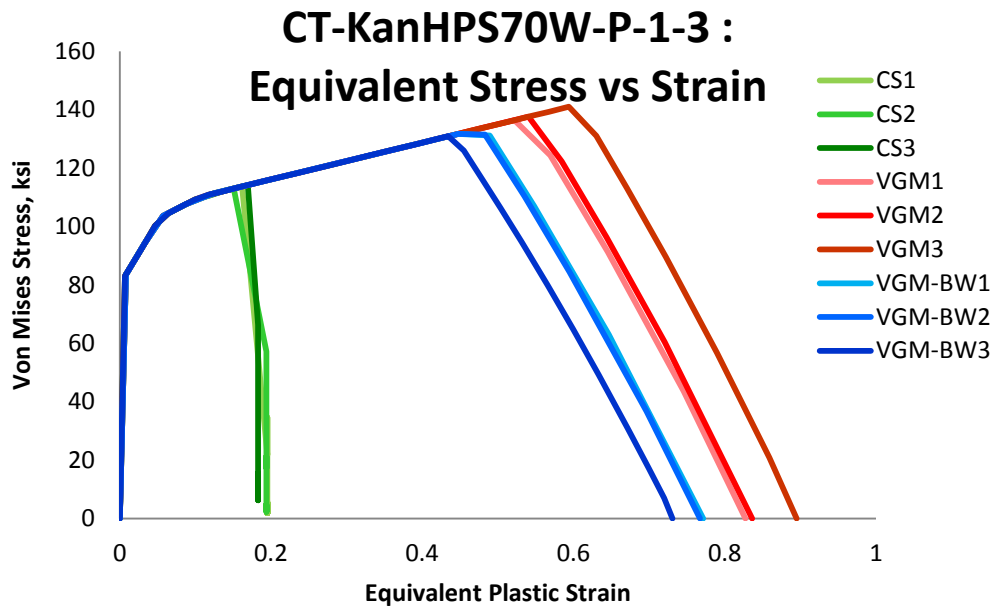

Figure 6.118: Variation of von Mises Stress with equivalent plastic strain for different elements laid out through the thickness of simulation of CT-KanHPS70W-P-1-3 specimens for the three finite element deletion strategies

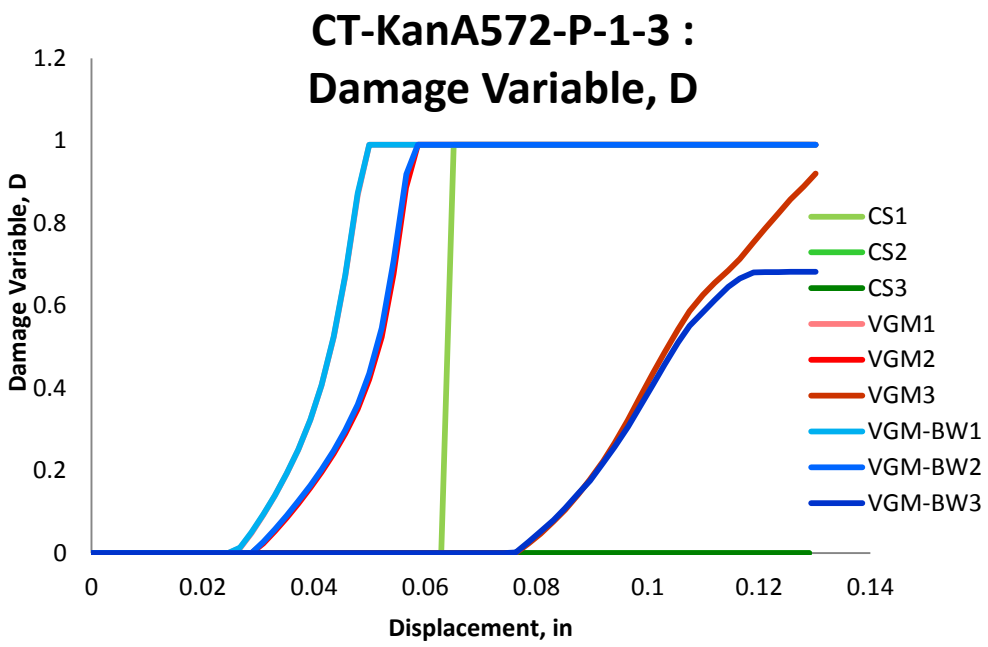

Figure 6.119: Variation of Damage Variable with displacement for different elements laid out through the thickness of simulation of CT-KanA572-P-1-3 specimens for the three finite element deletion strategies

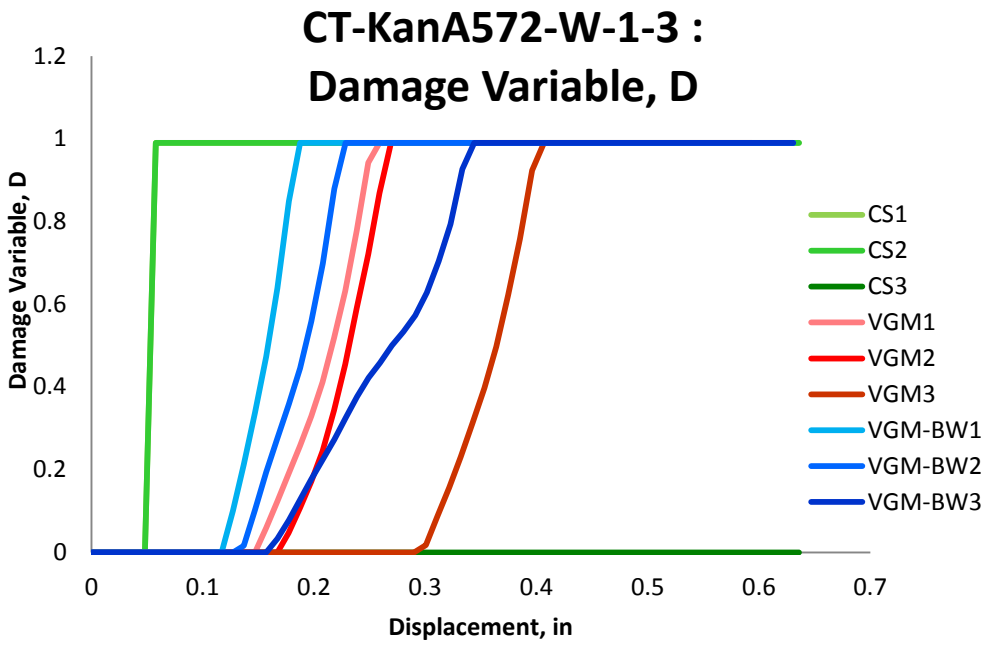

Figure 6.120: Variation of Damage Variable with displacement for different elements laid out through the thickness of simulation of CT-KanA572-W-1-3 specimens for the three finite element deletion strategies

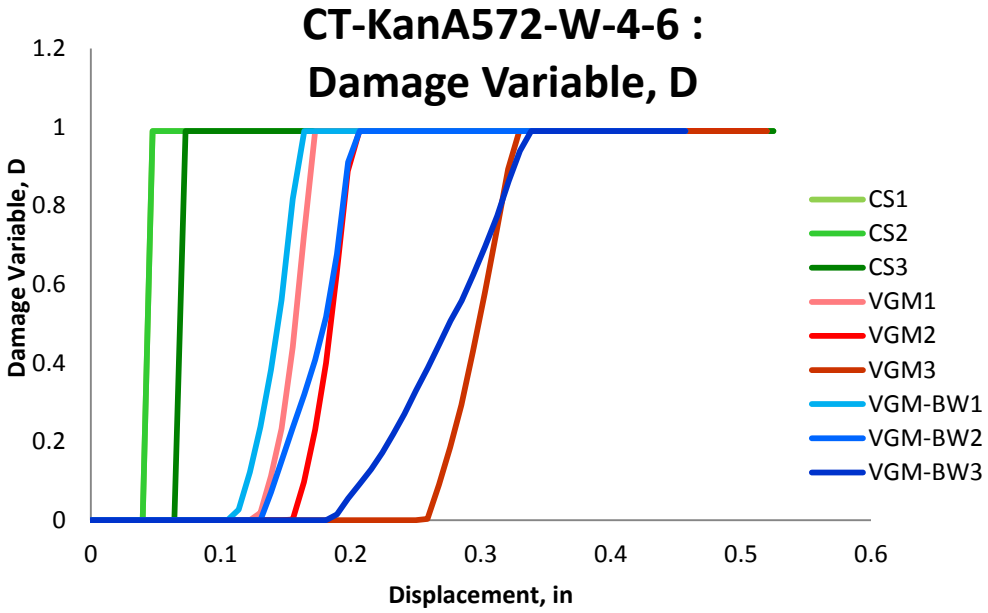

Figure 6.121: Variation of Damage Variable with displacement for different elements laid out through the thickness of simulation of CT-KanA572-W-4-6 specimens for the three finite element deletion strategies

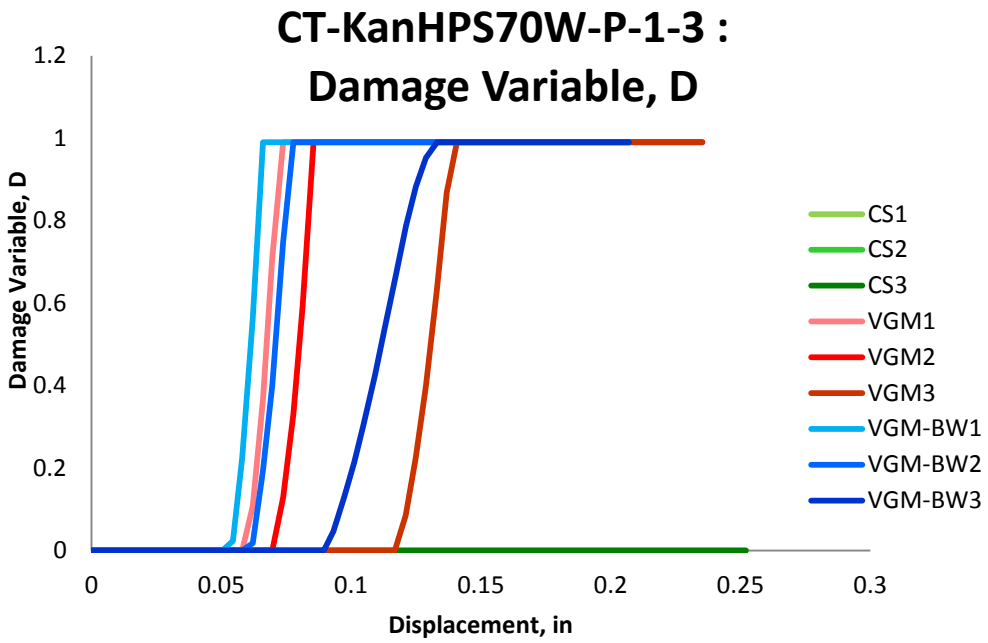

Figure 6.122: Variation of Damage Variable with displacement for different elements laid out through the thickness of simulation of CT-KanHPS70W-P-1-3 specimens for the three finite element deletion strategies

6.3.1 Summary

Structural steel A572 Grade 50 taken from a plate and a W-Section, and HPS70W taken from a plate, were validated through comparison to compact tension specimens loaded in vertical tension through pins at its upper and lower ends connected to an actuator. In the simulations the three finite element deletion strategies all had unique fracture propagation behavior while all had fracture initiate at the center of the specimen. Overall, for the three types of specimens, the VGM criterion gives the best force-displacement predictions while the CS and VGM-BW usually underpredicting except for the CT-KanA572-P-1-3 specimen. In addition, the prediction is better for a thinner specimen than for a thicker one, suggesting that the calibrated fracture locus at higher triaxiality is too low. On the other hand, the VGM-BW approach, which accounts for shear and mix-mode fracture, most accurately represents fracture propagation by properly capturing the tunneling effect and shear lip fracture on the edge surface of the specimens. However, VGM-BW simulations have minor fracture occurring at the end of the specimen, which is not recorded in experimental tests. This is due to having a fracture locus in the negative triaxiality region.

From these results other observations could be made

- The VGM did not model the shear lip fracture behavior but captured the crack tunneling and the surface of the specimen necking and bulging.
- The variation of triaxiality is more affected by the geometry of the specimen than the material it is made from.

- The hardening of the material keeps the triaxiality approximately constant throughout the loading process until softening.
- The fracture locus and softening models have a significant effect on the global response of the structure

6.4 Three-Point Bending Specimen

The last small test that was used for validation purposes was a three-point bending test. The Single Edge Notched Bending (SENB) specimen is a three-point bending test based on ASTM E399 standard. The specimen had a thickness of 1 inch, height of 2 inches, and an 8 inch span as shown in Figure 6.123. The specimen is side-grooved to a thickness of 0.8 inches at the crack location to promote a uniform constraint across the crack width and encourage straight-through crack growth to avoid faster crack growth in the center than the edges of the specimen, which is the tunneling effect observed in compact tension specimens discussed in the previous section (Kanvinde et al. 2004). The crack was first machined and then fatigue precracked to extend and sharpen the crack tip for a distance of 0.16 inches beyond the machined crack. The repeated unloading was used for determining the critical *J* value by measuring the slope of the loading curve, which correlates to the current crack length (Anderson 2005). The data points in the plasticity and fracture models are described by Table 6.5. No description of the fracture propagation is provided in the original paper but due to many similarities between the three-point bending specimen and the compact tension specimen the failure propagation should be similar. However, it is not expected to have any of

the tunneling effect encountered in the compact tension specimens due to the side grooves. A quarter-symmetrical model with appropriate symmetrical boundary conditions was used to simulate this specimen which is shown in Figure 6.124 with the location of finite elements chosen through the thickness of the specimen at the location of fracture for study of the variation of fracture parameters through the loading of the specimen.

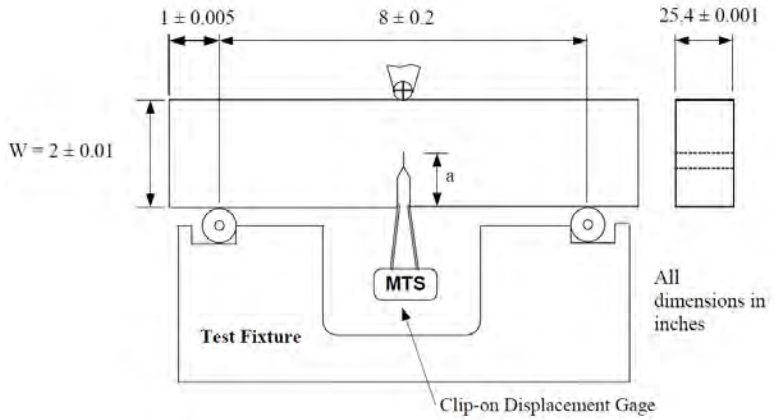

Figure 6.123: Experimental test setup with corresponding dimmensions (Kanvinde et al. 2004)

Table 6.5: Plasticity and fracture model inputs for 3PB-KanA572-W-1-2 specimen

		Fracture Model Input		
Test	**Plasticity Model Input**	**VGM**	**VGM-BW**	**CS**
3PB-KanA572-W-1-2	CNT-KanA572-W-L-A	CNT-KanA572-W-L-A	TC-KanA572-W-L-A	0.2

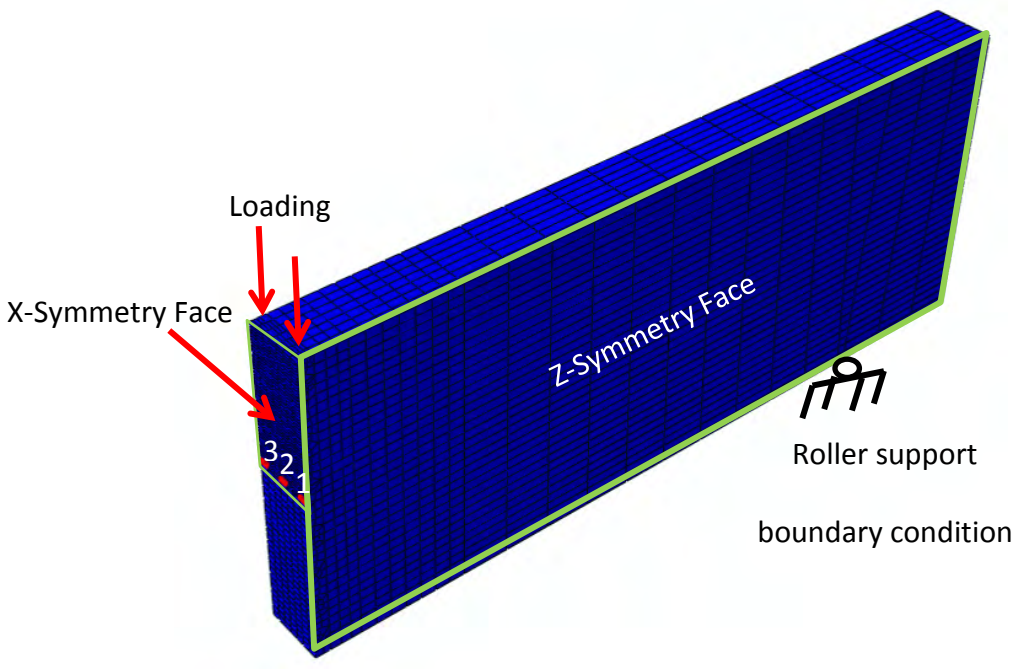

Figure 6.124: Elements selected for studying fracture initiation and propagation parameters in VGM-BW, VGM, and CS strategies with simulation boundary conditions for 3PB-KanA572-W-1-2 specimen

Fracture occurred at the center of the specimen and propagated outward for all of the simulations. In addition, all three finite deletion strategies showed some crack tunneling effect. The VGM and VGM-BW had a more pronounced tunneling effect than did CS strategy. The crack in the CS and VGM-BW simulations had a tendency to propagate at an angle from the vertical towards the back end roller support of the specimen while the VGM simulation showed a more vertical propagation. The force versus the crack mouth opening displacement plot is shown in Figure 6.126 for the three finite element deletion strategies. All three strategies performed well in capturing the force displacement curve of the experimental test results. The VGM and VGM-BW did not show any difference between each other, signifying that the specimen experienced high triaxiality at the crack tip. Below a detailed description is provided on the variation of

fracture initiation and propagation parameters in elements that are located through the thickness of the specimens for the three finite element deletion strategies.

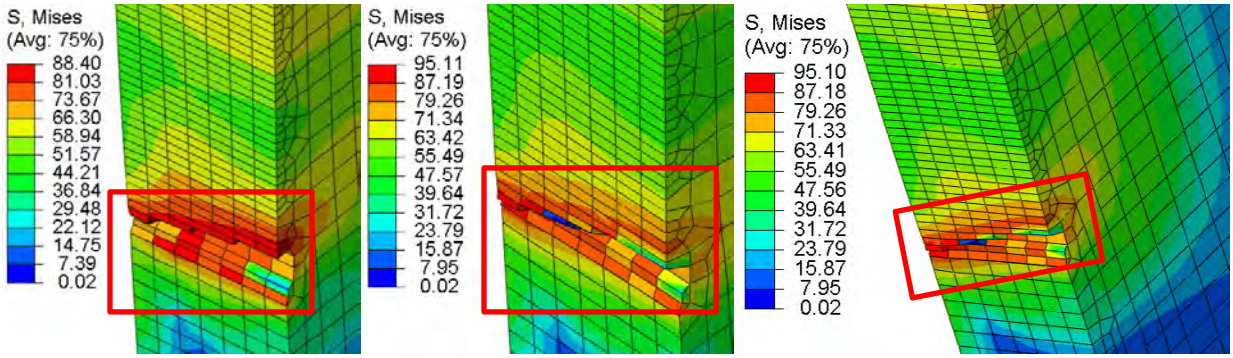

Figure 6.125: Simulation results of a compact tention 3PB-KanA572-W-1-2 specimen with contours representing von Mises stress (ksi): CS (left), VGM (middle), VGM-BW (right)

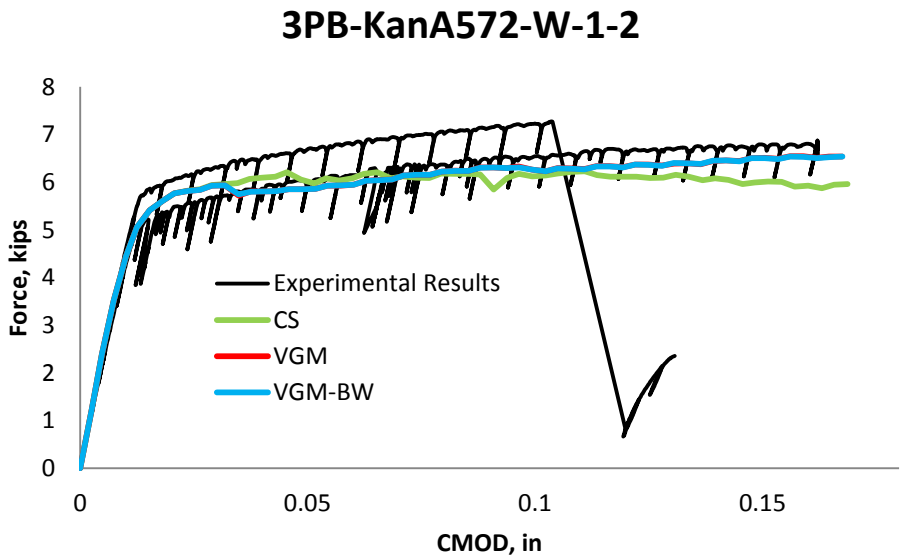

Figure 6.126: Validation results for SENB 3PB-KanA572-W-1-2 specimen

Triaxiality versus displacement is plotted for the three elements across the thickness of the specimen for the three finite element deletion strategies in Figure 6.127. As in previous specimens, the triaxiality is the same throughout the loading excursion until the point of softening for the three finite element deletion strategies. In addition, the two inner elements had approximately the same triaxiality paths for the VGM and VGM-BW simulations while the

third outside element had minor differences between the simulations. In addition, the two inside elements experience an increase in triaxiality before failure in the three simulations while the outer element does not. The increase in triaxiality before final element deletion is due to an increase in confinement in the inner parts of the specimen during large plastic deformation of the material while elements on the outside surface of the specimen do not experience such confinement due to a free surface which allows for necessary plastic flow to occur to reduce confinement on the element.

The equivalent plastic strain is plotted in Figure 6.128. The figures show that the equivalent plastic strain in VGM and VGM-BW simulations followed the same equivalent plastic strain path during loading. The maximum value of equivalent plastic strain reached in the SENB specimen was much lower than in the CT specimens due to a side-groove that enforced constant constrain through thickness of the SENB specimen.

The equivalent plastic strain versus triaxiality path of the element with associated fracture locus of the material is plotted in Figure 6.129. The triaxiality range in the SENB specimen was much higher than for the CT specimens varying from approximately 0.9 to 3.5. In addition, as the equivalent plastic strain grows there is a tendency for triaxiality to decline forcing less confinement on the plastic flow in an element. The reason for the declining triaxiality is most probably due to a physical phenomena of plastic hardening of the material while the triaxiality starts to increase after the material starts to soften. The fracture locus for the three strategies is very similar for this specimen and the force-displacement results are similar as well. This suggests that inclusion of softening did not have a major impact on the global behavior of the

structure most likely due to the small size of the fracture propagation compared to the size of the specimen.

The variation of the value of fracture initiation integral which is shown in Figure 6.130 follows simmilar trend where no appperent difference between finite element deletion strategies of VGM and VGM-BW for an element are seen. As one moves inward the slope of the value of this integral increases due to higher triaxiality. The results of CS simulations show that the path of fracture initiation integral for the three elements falls between the inner two elements and the outer element of the VGM and VGM-BW simulations. This can be seen in the above Figure 6.129 as well, where for the two inside elements the fracture locus for the VGM and VGM-BW is lower than for the CS and for the outside third element it is higher.

The varition of von Mises stress with displacement is shown Figure 6.131. This figure shows the same trend where the two inner elements in the CS strategy reached higher maximum stress value and failed at a higher displacement value and for the outside third element the CS had lower maximum stress level and failed at a lower displacement value than in VGM and VGM-BW simulations. In addition, even though immediate failure is seen of the elements in CS simulation, no dynamic instability is created. This is most likely do the fact that the crack propagation and size are small compared to the overall size of the specimen and all dynamic vibrations get absorbed by the specimen. In other words, the specimen size allows for stress redistribution to occur and limits any dynamic instabilities that might occur. In addition, the state of stress in the specimen is such that the softening curve for the three simulations is very similar causing similar global performance.

The mean stress variation throughout the loading excursion is plotted in Figure 6.132. The mean stress does not increase during softening for the three finite element deletion strategies as in previous specimens. Only the outside element for the VGM and VGM-BW simulation has any such increase before failure. This is due to the specimen being thick enough to allow fracture to properly propagate and for stress in the specimen to redistribute.

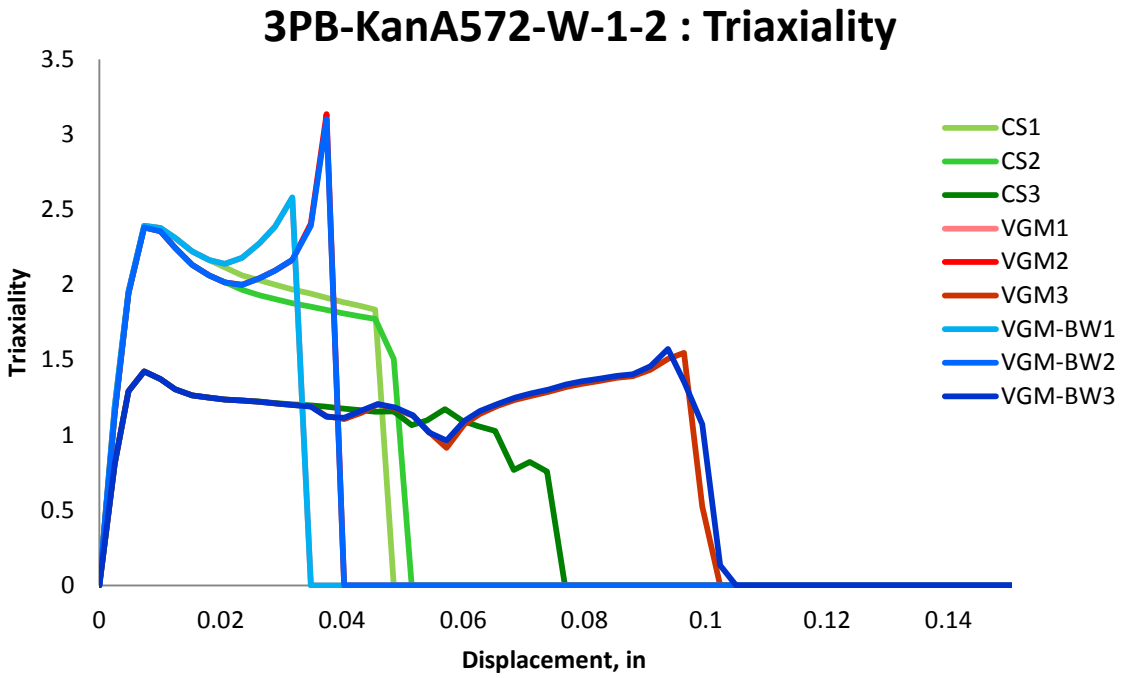

Figure 6.127: Variation of triaxiality with displacement for different elements laid out through the thickness of simulation of 3PB-KanA572-W-1-2 specimens for the three finite element deletion strategies

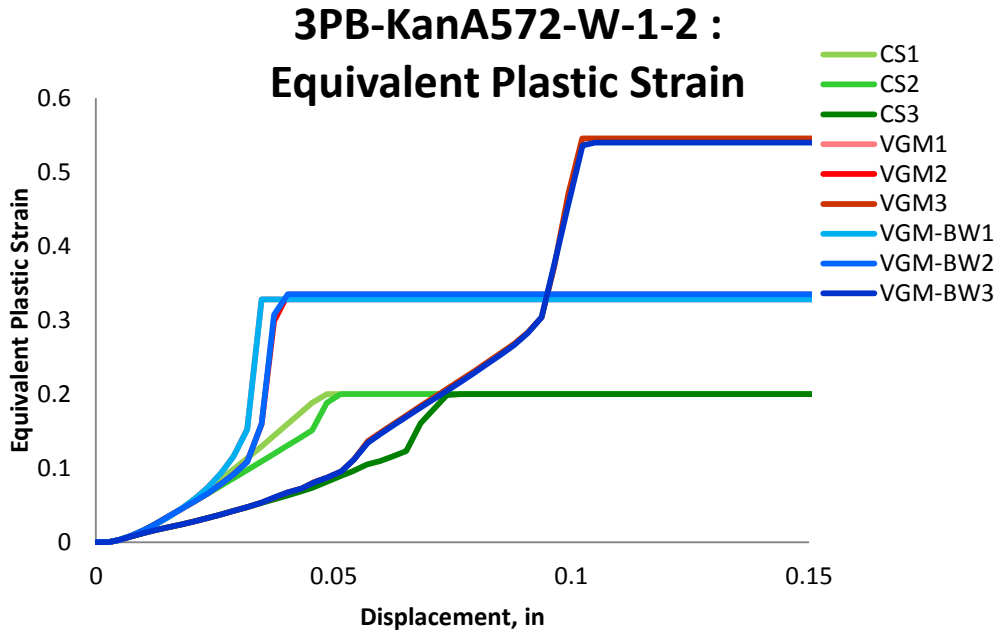

Figure 6.128: Variation of equivalent plastic strain with displacement for different elements laid out through the thickness of simulation of 3PB-KanA572-W-1-2 specimens for the three finite element deletion strategies

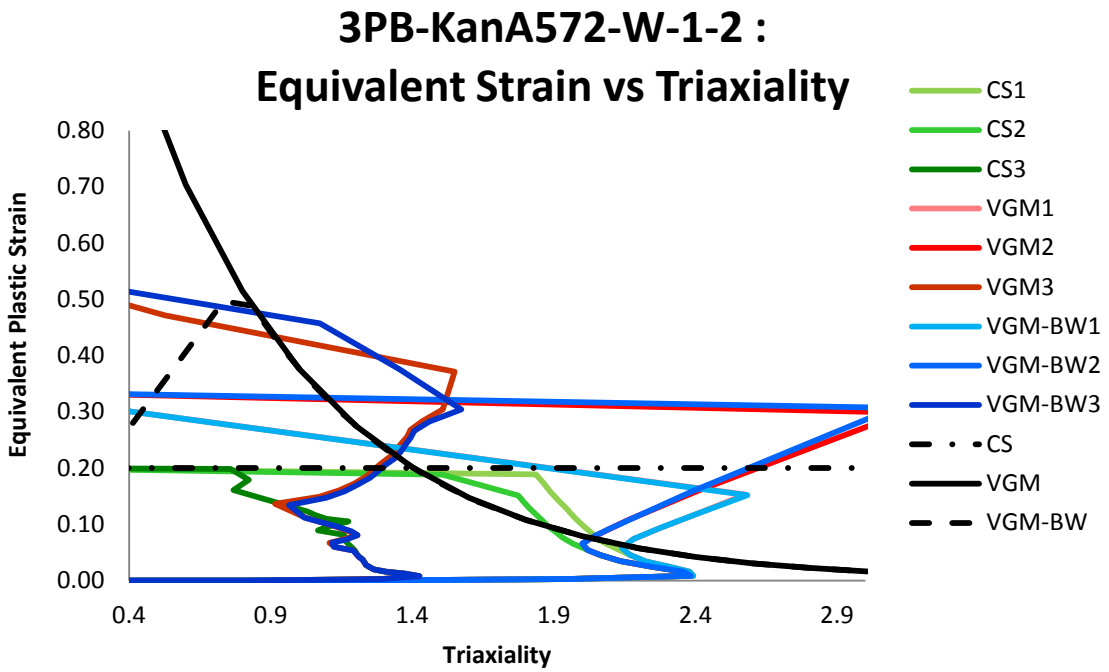

Figure 6.129: Variation of equivalent plastic strain with triaxiality for different elements laid out through the thickness of simulation of 3PB-KanA572-W-1-2 specimens for the three finite element deletion strategies

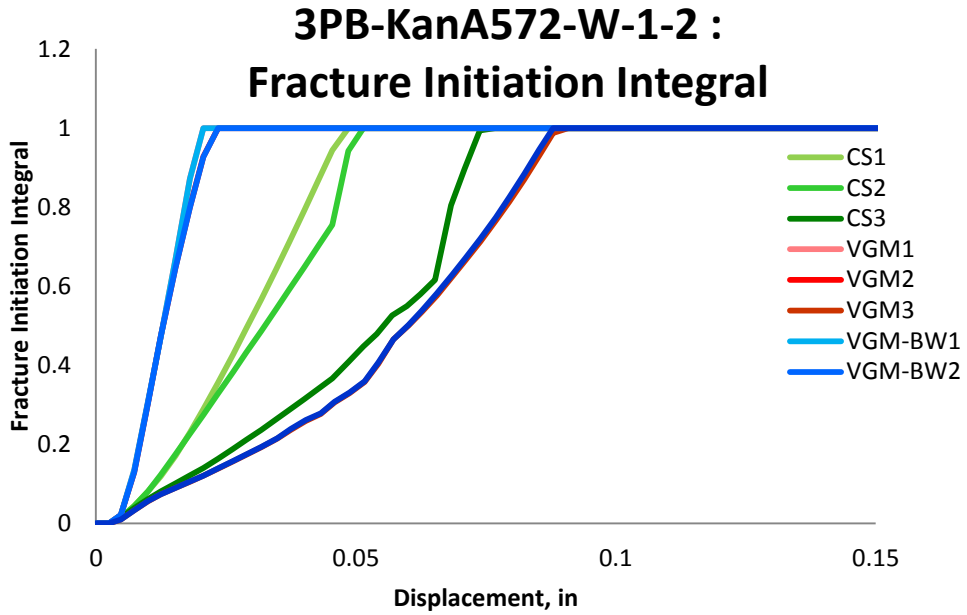

Figure 6.130: Variation of fracture initiation integral value with displacement for different elements laid out through the thickness of simulation 3PB-KanA572-W-1-2 specimens for the three finite element deletion strategies

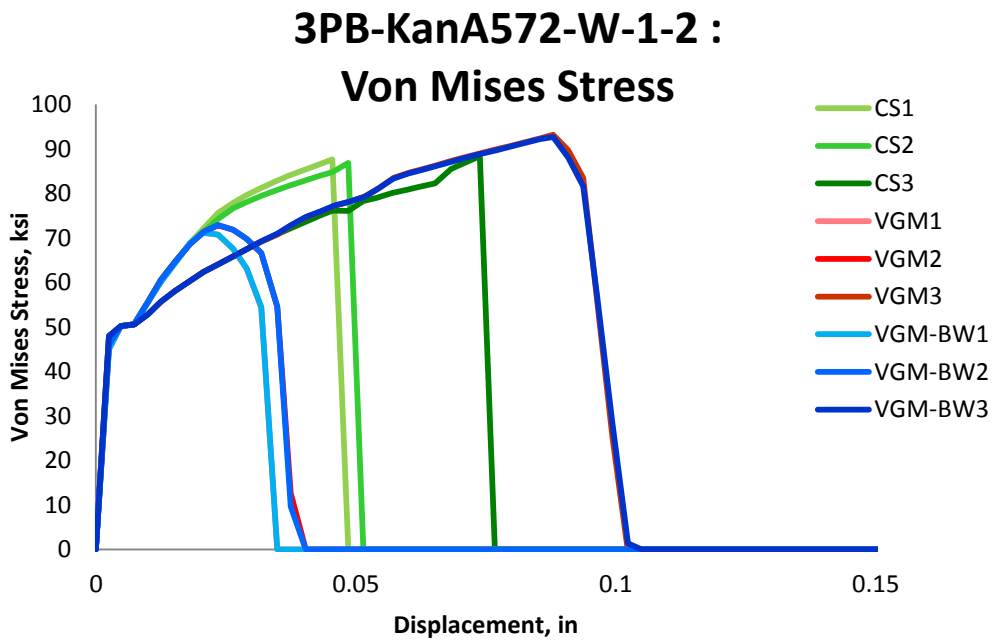

Figure 6.131: Variation of von Mises Stress with displacement for different elements laid out through the thickness of simulation of 3PB-KanA572-W-1-2 specimens for the three finite element deletion strategies

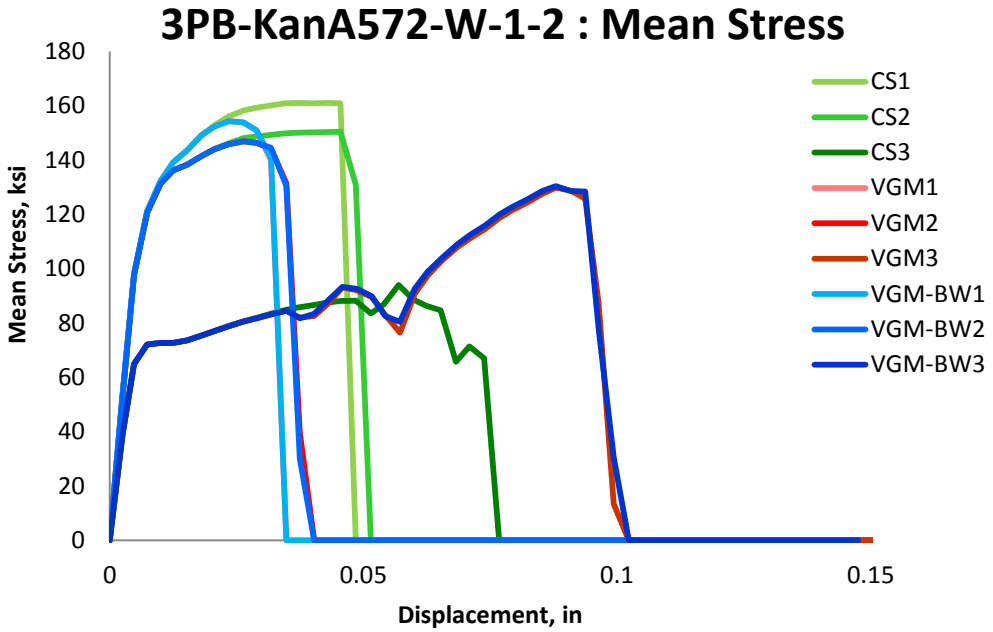

Figure 6.132: Variation of mean stress with displacement for different elements laid out through the thickness of simulation of 3PB-KanA572-W-1-2 specimens for the three finite element deletion strategies

Figure 6.133 shows the variation of von Mises equivalent stress with equivalent plastic strain. The figure shows that in the VGM and VGM-BW simulations the outside element achieves twice as much strain energy than the elements on the inside. It is interesting to note that there is a small difference between the two inside elements due to a similar state of triaxiality during loading. This again confirms the common notion that triaxiality is constant through the thickness of the specimen but closer to the surface of the specimen it declines rapidly due to a change from plain strain to plain stress conditions (Anderson 2005). On the other hand, the CS strategy does not capture such conditions but provides an average strain energy capacity.

The variation of the value of the damage variable is plotted in Figure 6.134. In general, the elements on the inside have their damage variable curves at a lower displacement value than

those elements that are on the outside surface of the speciemen signifying that they initiated fracture and failed at a lower global specimen displacement value.

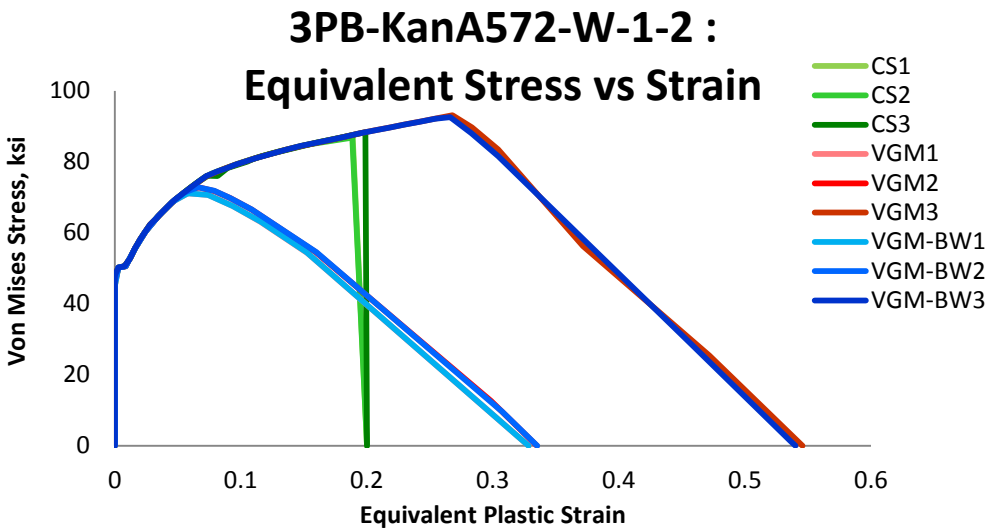

Figure 6.133: Variation of von Mises Stress with equivalent plastic strain for different elements laid out through the thickness of simulation of 3PB-KanA572-W-1-2 specimens for the three finite element deletion strategies

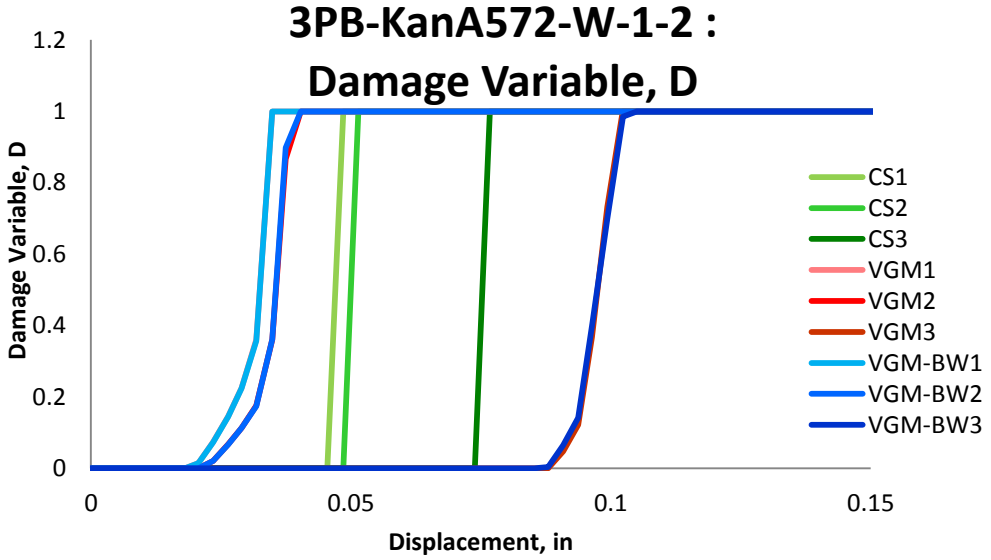

Figure 6.134: Variation of Damage Variable with displacement for different elements laid out through the thickness of simulation of 3PB-KanA572-W-1-2 specimens for the three finite element deletion strategies

6.4.1 Summary

In this section structural steel A572 Grade 50 taken from a W-Section was validated through comparison to experimental test results of a SENB specimen based on ASTM E399 standard. No description of the fracture propagation is provided in the original paper. In the three simulations with different element deletion strategies fracture occurred at the center of the specimen and propagated outward. In addition, all three finite deletion strategies showed some crack tunneling effect. The VGM and VGM-BW had a more pronounced tunneling effect than did CS strategy. All three strategies performed well in capturing the force displacement curve of the experimental test results.

Other observations made

- In the SENB specimen there is a significant difference in material behavior between the outer edge and the inner part of the specimen. This is shown in triaxiality, equivalent plastic strain, and other stress-strain fracture parameters variations throughout the loading. The figures confirm that the inner part of the specimen is under a plane strain conditions while the surface is under plane stress. The CS completely ignores these effects while trying to provide an average of the material fracture capacity but the VGM and VGM-BW account for these changes by modeling fracture initiation based on triaxiality.
- The side-groove of the specimen was successful at avoiding crack tunneling and shear lip fracture.

- During hardening of the material the equivalent plastic strain will increase with decreasing triaxiality but it will increase with an increase in triaxiality during softening for the material.

6.5 Double Angle Connection

The first connection test used for validation was a bolted double-angle beam connection. The beam was a W18x45 section and the connection was designed so that bearing strength controlled the allowable end reaction and that the beam experienced only a portion of the total allowable beam shear capacity (Birkemoe et al. 1978). The beam was connected with double angles to a column stub and loaded near the reaction to preclude flexural failure of the beam (Birkemoe et al. 1978). The applied load and the smaller of the two beam reactions were measured to determine the load on the test connection. The exact location of the vertical loading and boundary conditions was not specified in the original paper (Birkemoe et al. 1978). The materials used were G40.21 Grade 44W steel and ASTM A325 bolts. The data points into the plasticity and fracture models are described by Table 6.6. For simulation, A572 Grade 50 steel calibrated constitutive properties and fracture parameters from CNT-KanA572-W specimens were used to model G40.21 Grade 44W steel (McAllister et al. 2008). The experimental test setup of the connection is shown in Figure 6.135. Finite element simulation results were compared to the nominal shear load on connection versus the net deflection of the end of the beam with respect to the column . The finite element model with associated boundary conditions and loading is shown in Figure 6.136. In the simulation model, the meshing

for the beam and column had a maximum finite element size of 0.5 inches but around the connection the beam, column, double angle, and bolts used a maximum finite element size of 0.04 inches.

Table 6.6: Plasticity and fracture model inputs for DAC-BirG40.21-W-1 specimen

		Fracture Model Input		
Part	**Plasticity Model Input**	**VGM**	**VGM-BW**	**CS**
Angle	DAC-BirG40.21-W-1	CNT-KanA572-W-L-A	TC-KanA572-W-L-A	0.2
Bolts	Bolt-SadA490-B-A	-	Bolt-SadA490-B-A	0.2
Beam	DAC-BirG40.21-W-1	CNT-KanA572-W-L-A	TC-KanA572-W-L-A	0.2
Column	DAC-BirG40.21-W-1	CNT-KanA572-W-L-A	TC-KanA572-W-L-A	0.2

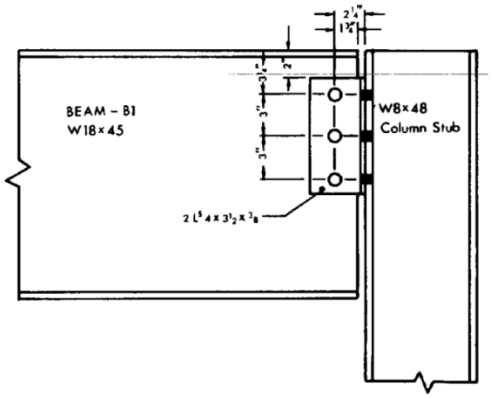

Figure 6.135: Experimental test setup with corresponding dimmensions (Birkemoe et al. 1978)

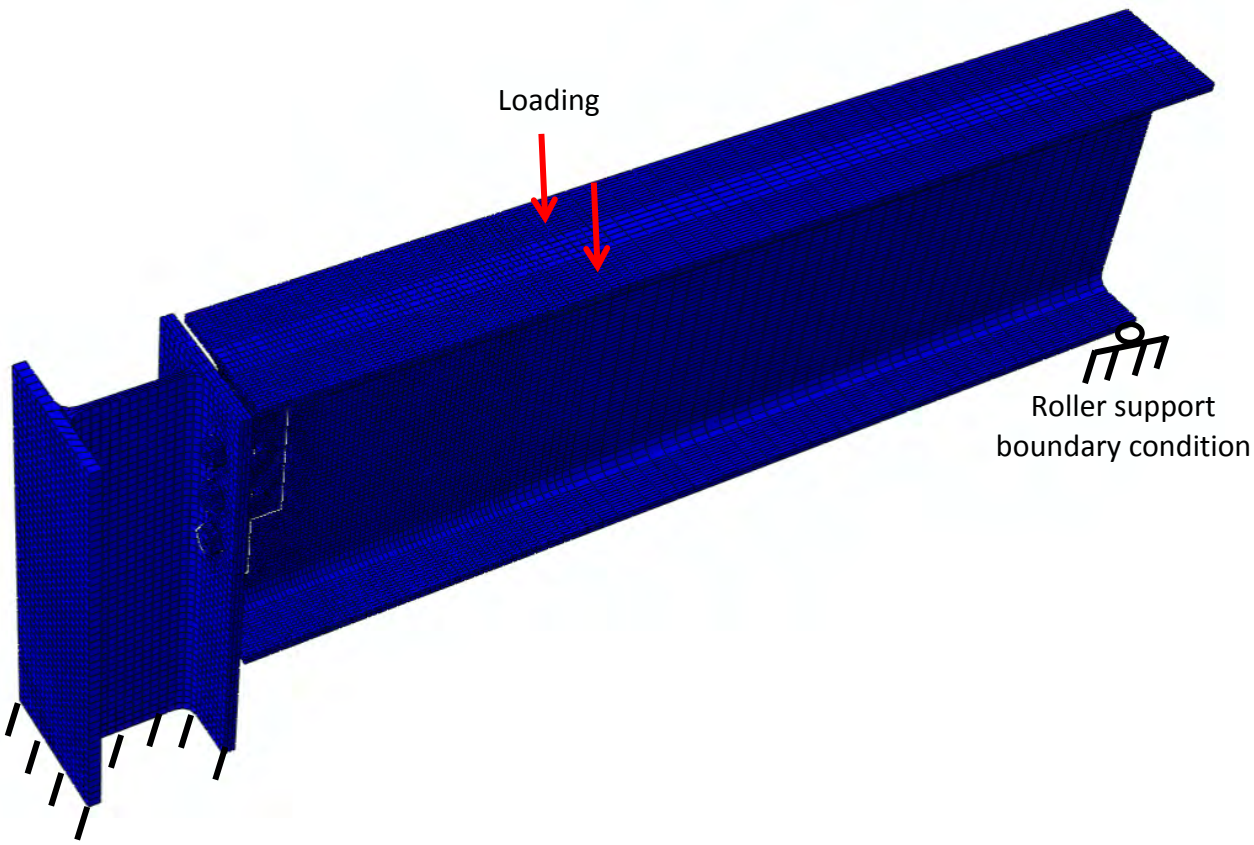

Figure 6.136: Finite Element Model for the CS, VGM, and VGM-BW simulations with boundary conditions and loading

Fracture occurred at the lower bolt hole of the beam web in the experimental test results shown in Figure 6.137. In the three simulations the fracture propagated very quickly with bolts ripping out through the beam web. The location of fracture initiation and propagation in the three simulations are shown in Figure 6.138. For the CS and VGM-BW approaches, the fracture started with the top bolt ripping the beam web, followed by fracture at the middle and bottom bolts. This is opposite to what was reported in the paper of bottom bolt ripping the beam web first. The reason could be due to the fact that since the exact location of the loading was unknown, the simulation could have experienced more moment than seen in the experimental test. In addition, the CS and VGM-BW simulation had fracture at the roller support and the loading location. This is not reported in the literature. For the VGM simulations the lower bolt

was the first one to rip through the beam web and then the two other bolts followed. This follows the experimental test results closer than the CS and VGM-BW simulations but it is still suspected that the connection experienced more moment in the simulation than it did in the actual experiment. This is due to some beam web buckling being observed in the three simulations. However, the fracture for the three bolt holes in the VGM simulation was located right above the holes with a small angle to the y-axis which shows that the connection failed due to shear loading.

Figure 6.137 : Fractured beam web of a double angle bolted connection (Birkemoe et al. 1978)

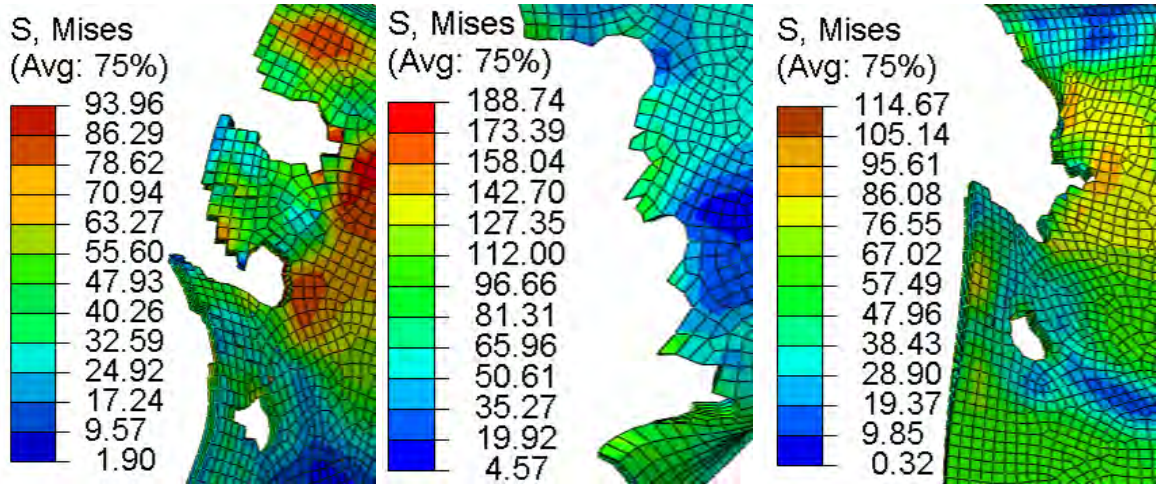

Figure 6.138: Simulation results of a DAC-BirG40.21-W-1 specimen with contours representing von Mises stress (ksi): CS (left), VGM (middle), VGM-BW (right)

The force-displacement plot for the three finite element deletion strategies is shown in Figure 6.139. For the three simulations the shear failure was sudden and no differences are seen between the three simulations prior to fracture. This is because the three simulations behaved the same up to the point of fracture. After this point the beam web fractured suddenly for the three simulations. Almost no fracture propagation occurred which could differentiate the three force-displacement plots.

The simulation model with associated boundary conditions and elements selected for studying the variation of stress-strain fracture parameters throughout the loading process is shown in Figure 6.140.

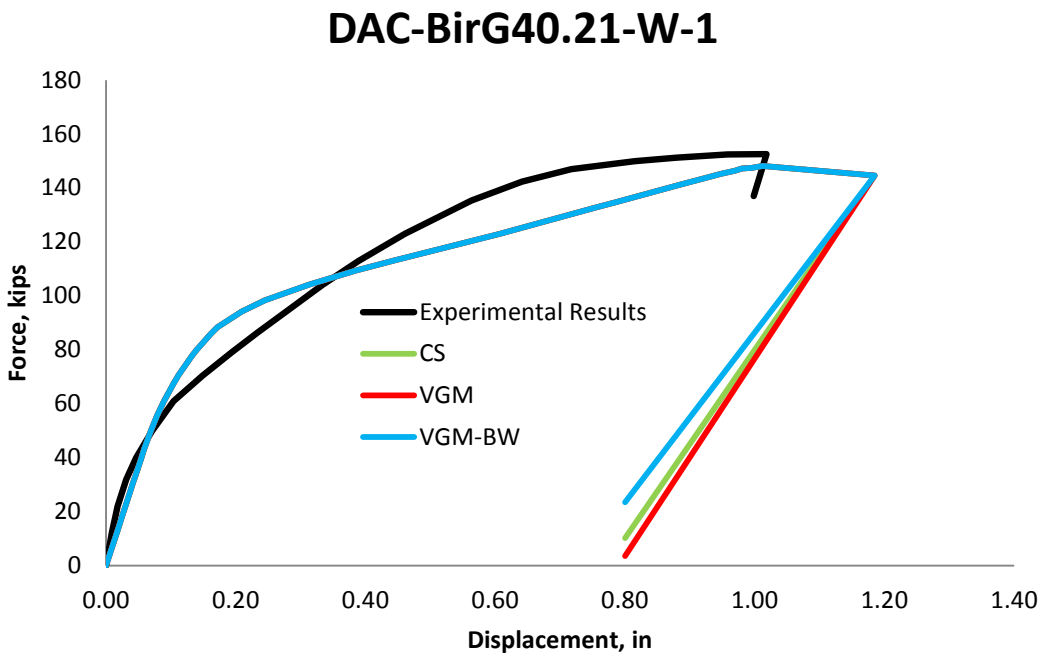

Figure 6.139: Validation results for DAC-BirG40.21-W-1 specimen

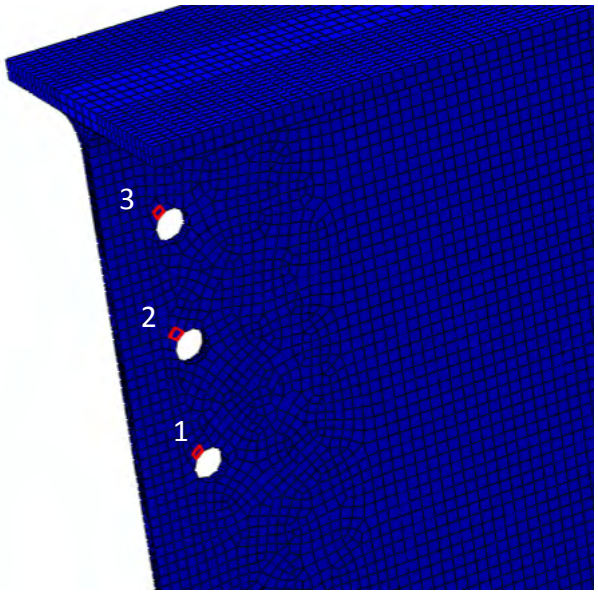

Figure 6.140: Elements selected for studying fracture initiation and propagation parameters in VGM-BW, VGM, and CS strategies for DAC-BirG40.21-W-1 specimen

Triaxiality versus displacement is plotted for the three finite elements across the web of the specimen for the three finite element deletion strategies in Figure 6.141. The triaxiality is the same throughout the loading excursion until the point of softening for the three finite element deletion strategies. The three strategies do not differ from each other since fracture initiation and element deletion occurred at the same displacement value in the three simulations. Each element has a distinctive path; the third element which is located at the top bolt hole has the lowest negative triaxiality and the bolt on the bottom has the greatest negative triaxiality. This relationship changes throughout the loading process, with the third element eventually having a greater negative triaxiality than the first element. Since the triaxiality is so negative it shows that the connection was loaded with a shear type loading and the elements experienced significant compression.

The equivalent plastic strain is plotted in Figure 6.142. The figure reveals that the first element located at bottom bolt hole has the highest equivalent plastic strain and the third element

located at the top bolt hole has the lowest. This confirms that the overall loading on the connection was a shear load. Overall, the maximum values of equivalent plastic strain attained were significantly lower than the ones in previous specimens, where positive triaxiality prevailed throughout the critical areas of the specimen.

The equivalent plastic strain versus triaxiality path of the element with associated fracture locus of the material is plotted in Figure 6.143. The triaxiality range in this double angle connection specimen was much lower than any of the previous specimens varying from approximately -0.6 to -0.4. Even though the triaxiality range is very different than in the previous simulations the same trend of increasing equivalent plastic strain with decreasing triaxiality throughout the loading is retained. This confirms that the reason for the declining triaxiality is most probably due to a physical phenomena of plastic hardening of the material. Once softening is initiated the triaxiality starts to dramatically increase with increase of the equivalent plastic strain. Even though the three simulations follow different paths after initiating softening all of the elements where deleted at the next time step.

The variation of the value of fracture initiation integral is shown in Figure 6.144. The figure shows that for most of the loading process the elements remained elastic or had very little amount of plastification for the VGM and VGM-BW simulations. In addition, it is seen that the three strategies converged at a fracture initiation integral value of 1 at the same displacement value signifying sudden shear type failure for the three simulations. The varition of von Mises stress with displacement is shown Figure 6.145. This figure shows the same trend where the three strategies follow the same path. Element 1, located at the bottom bolt hole, has the

highest value of von Mises stress throughout the loading while the third element has the lowest value. In addition, the first element has higher slope for the von Mises stress than the other two elements signifying that at the initaition of the loading the material around the bottom bolt hole provided more resistance to the shear loading than the material located around the other two bolt holes. The mean stress variation through out the loading excursion is plotted in Figure 6.146. The negative mean stress signifies a compressive hydrostatic stress condition on the element. As with the von Mises stress the first element has the highest value of mean stress throughout the loading and the third element the lowest. In addition, the mean stress slope is greatest for the first element. This again confirms that at the beginning stages of loading the specimen the material around the bottom bolt hole provided more resistance than the material around the other two bolt holes.

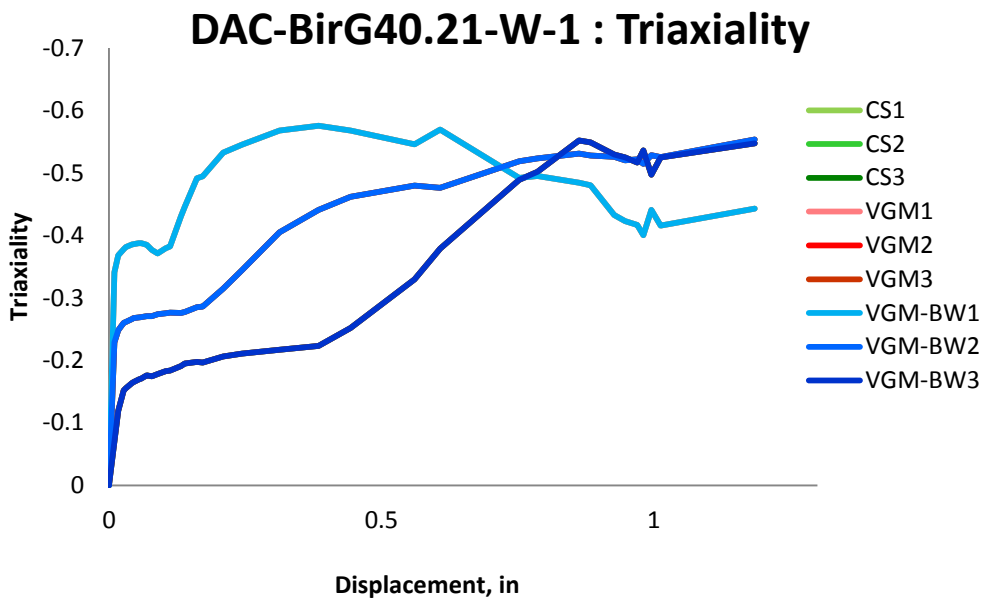

Figure 6.141: Variation of triaxiality with displacement for different elements laid out through the thickness of simulation of DAC-BirG40.21-W-1 specimens for the three finite element deletion strategies

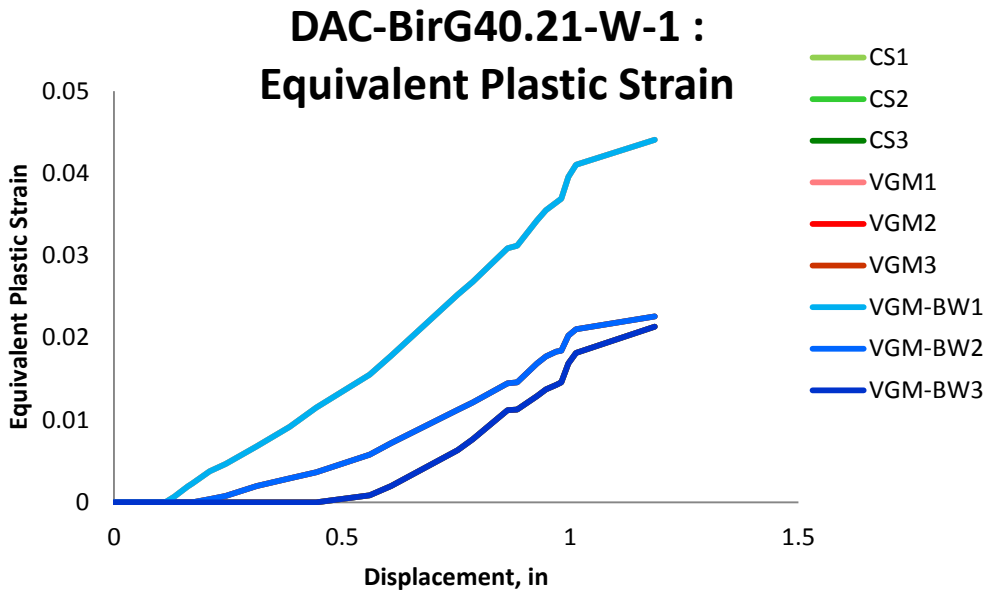

Figure 6.142: Variation of equivalent plastic strain with displacement for different elements laid out through the thickness of simulation of DAC-BirG40.21-W-1 specimens for the three finite element deletion strategies

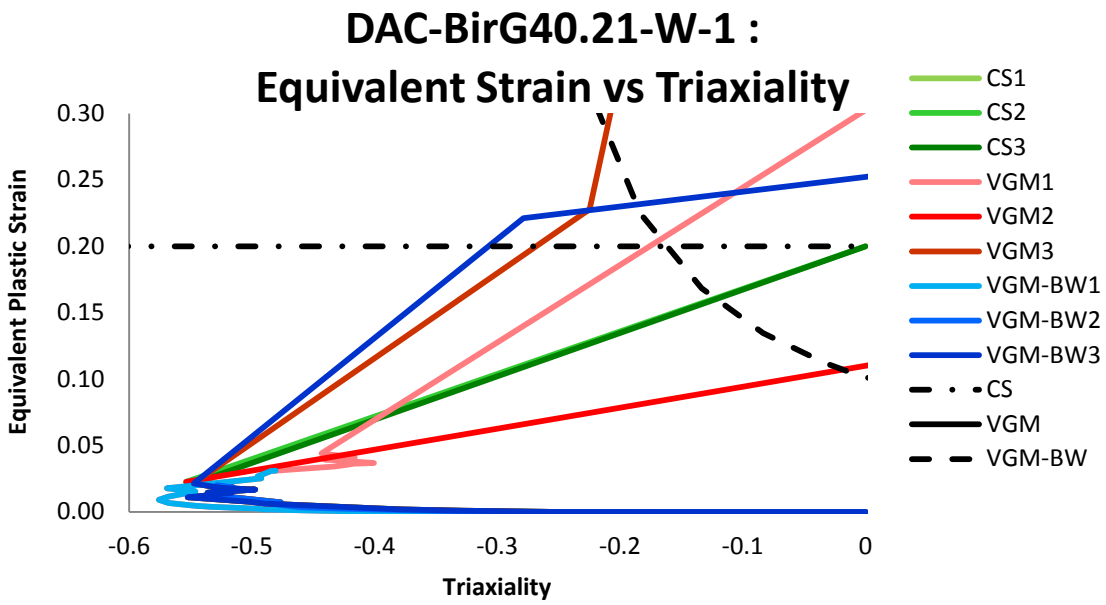

Figure 6.143: Variation of equivalent plastic strain with triaxiality for different elements laid out through the thickness of simulation of DAC-BirG40.21-W-1 specimens for the three finite element deletion strategies

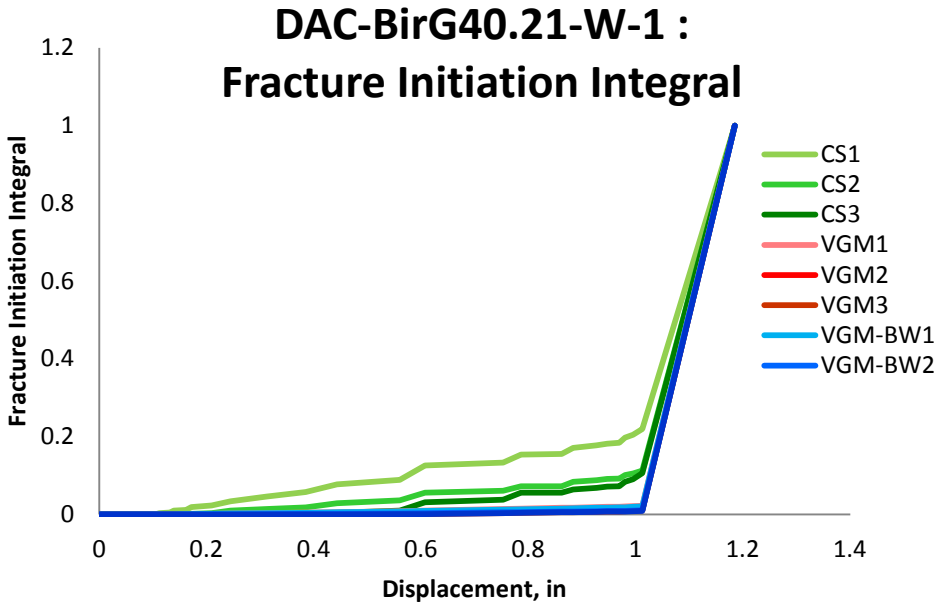

Figure 6.144: Variation of fracture initiation integral value with displacement for different elements laid out through the thickness of simulation DAC-BirG40.21-W-1 specimens for the three finite element deletion strategies

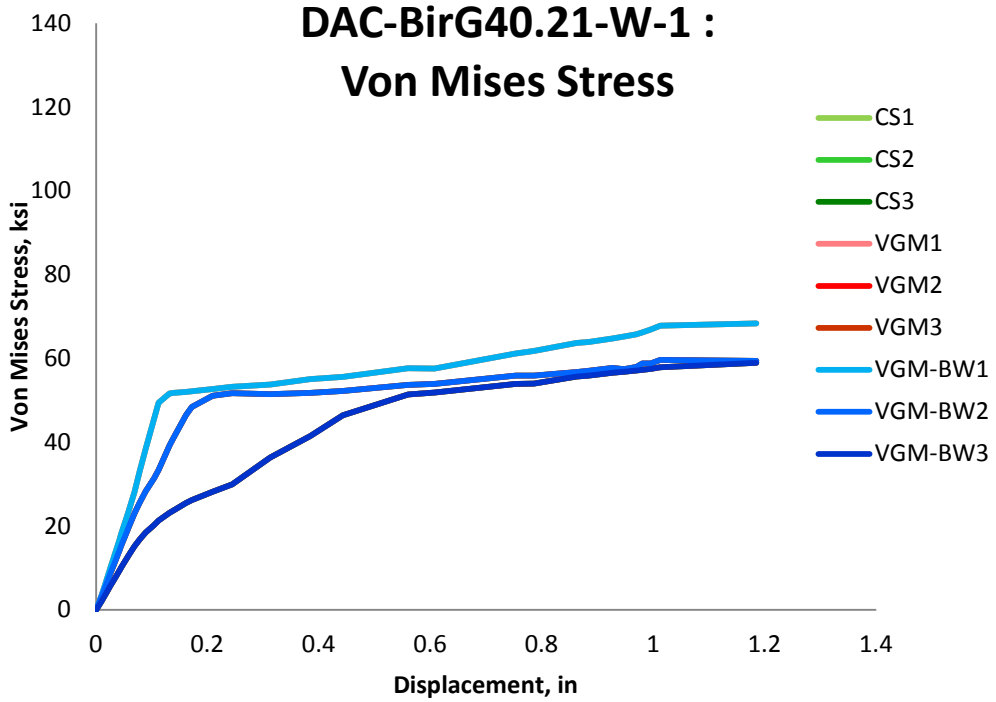

Figure 6.145: Variation of von Mises Stress with displacement for different elements laid out through the thickness of simulation of DAC-BirG40.21-W-1 specimens for the three finite element deletion strategies

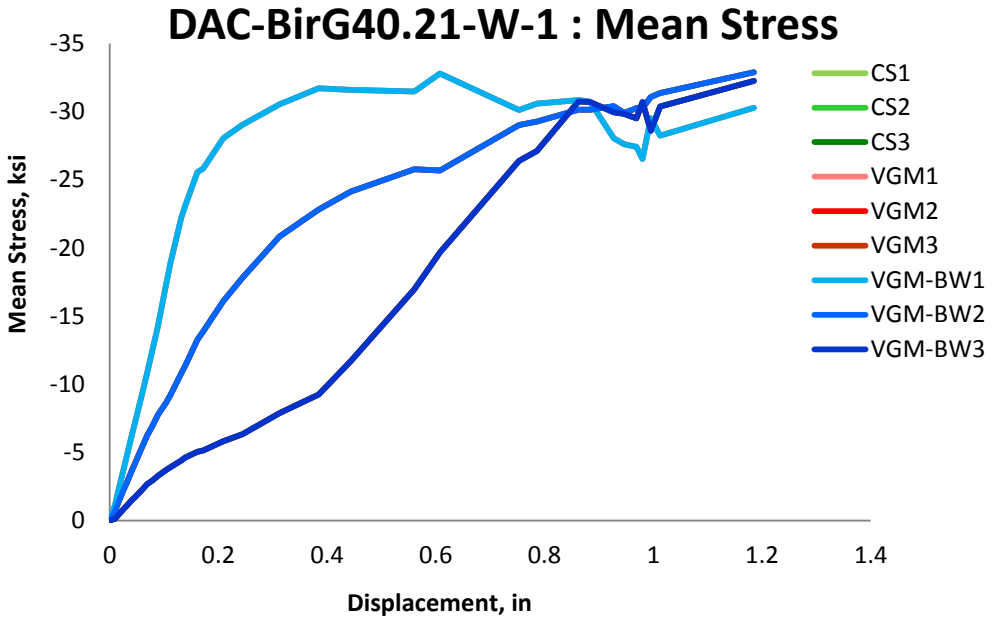

Figure 6.146: Variation of mean stress with displacement for different elements laid out through the thickness of simulation of DAC-BirG40.21-W-1 specimens for the three finite element deletion strategies

Figure 6.147 shows the variation of von Mises equivalent stress with equivalent plastic strain. The figure shows that in the VGM simulation the first element achieved twice as much strain energy as the elements located at the top two bolt holes. As in previous simulations the CS provides the least strain energy while the VGM the greatest amount. However, the curves of the three simulations after a point approximately where the CS elements start to soften are composed of two data points due to a sudden failure of the connection under shear loading. The variation of the value of the damage variable is plotted in Figure 6.148. All of the three elements in the three simulations had elements fail at the same time at about displacement of 1 inch.

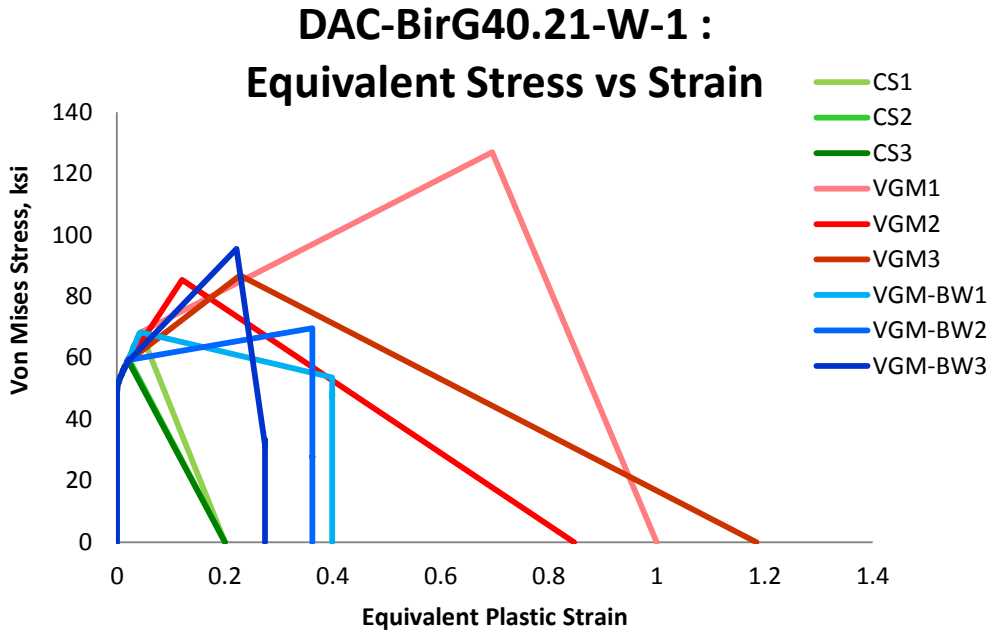

Figure 6.147: Variation of von Mises Stress with equivalent plastic strain for different elements laid out through the thickness of simulation of DAC-BirG40.21-W-1 specimens for the three finite element deletion strategies

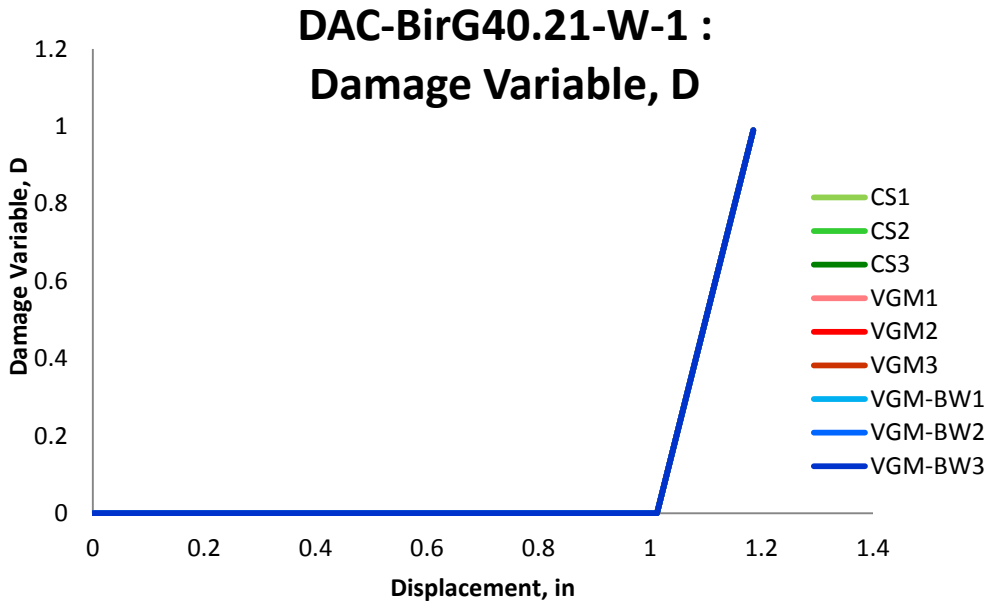

Figure 6.148: Variation of Damage Variable with displacement for different elements laid out through the thickness of simulation of DAC-BirG40.21-W-1 specimens for the three finite element deletion strategies

6.5.1 Summary

In this section structural steel G40.21 Grade 44W steel taken from a W-Section modeled by the fracture and constitutive behavior of CNT-KanA572-W specimen was validated through comparison to experimental test results of a bolted double-angle beam connection. Fracture occurred at the lower bolt hole of the beam web in the experimental test results. In the three simulations the fracture propagated very quickly, with bolts ripping through the beam web. For the CS and VGM-BW the fracture started with the top bolt ripping the beam web. For the VGM simulations the lower bolt was the first one to rip through the beam web and then the two other bolts followed. For the three simulations, the shear failure was sudden and no differences are seen between the three simulations in the force-displacement results.

Other observations could be made

- The material around the lowest bolt hole provides most of the initial resistance to the shear load with material around the upper bolt holes providing more resistance as the load progresses
- Equivalent plastic strain has a positive relationship with triaxiality while material is experiencing plastic hardening and negative relationship when it softens.
- Triaxiality greatly increases right before failure and finite elements fail in the positive triaxiality region for the three finite element deletion strategies.

6.6 Moment Restraining Connection

The three strategies to finite element fracture initiation and material softening with subsequent element deletion were also validated through comparison to different beam-to-column

moment resisting connections. The experimental tests that were used for validation were performed at Lehigh University for the purpose of examining beam-to-column web moment connections from the viewpoint of strength, stiffness, and ductility and to consider connection stiffening when required to attain the desire connection, load or stiffness (Rentschler et al. 1978). The experimental work consisted of four full-scale beam-to-column web connection assemblages representing an exterior column. Each assemblage consisted of an 18 foot column and a beam approximately five feet long connected at the midheight of the column. The column had fixed ends so that the distance between the inflection points was deemed to be approximately 12 feet (Rentschler et al. 1978). An axial load was applied at the top end of the column while the bottom end was bolted to the floor. Once the axial load of 1520 kips in increments of 250 kips was applied to the column, an upward load to the beam end was applied by hydraulic jack in increments of 25 kips until significant deflections were observed (Rentschler et al. 1978). Each assemblage contained different geometries of welding and bolting the beam to the column. The specimens were designed in accordance to the AISC Specification (AISC 1970) of the time and welds were designed to AWS Specifications of the time (AWS 1969) to resist the moment and shear generated by the full factored load (Rentschler et al. 1978). A W14x246 column section was used and a W27x94 beam section was used for all of the tests. A572 Grade 50 steel was used for all specimens, along with ASTM 490 bolts. The weld material was E70XX using flux cored arc welding (FCAW) (Rentschler et al. 1978). The constitutive and fracture parameters calibrated in Chapter 5 were used in finite element simulations to test the predictive nature and accuracy of the approach. The overall

layout of the experimental test specimens is shown in

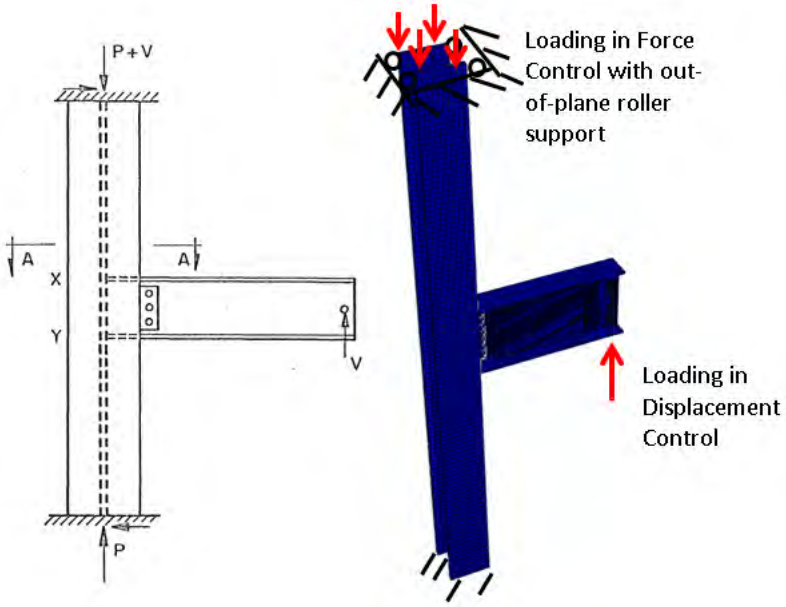

Figure 6.149. The details of each connection can be seen in figures from Figure 6.150 to Figure 6.153. For more information on the experimental setups see (Rentschler et al. 1978). The general finite element model for the four specimens with corresponding boundary conditions is

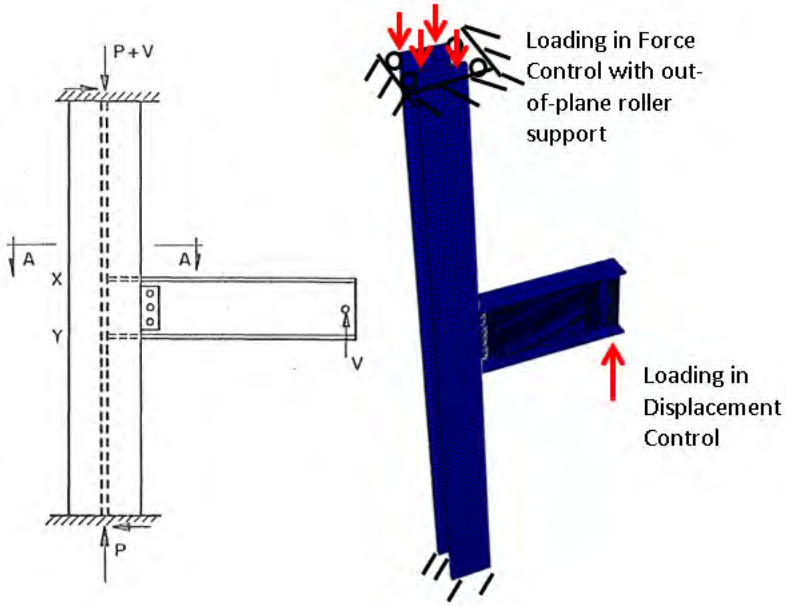

seen in

Figure 6.149. For the finite element model, a minimum of 2 elements through thickness was maintained, with maximum allowable element size ranging from 0.125 inches near the critical areas to 2 inches in regions far away from the connection. This resulted in approximately 44,000, 56,000, 98,000, and 44,000 elements for specimens MRC-RenA572-W-14-1, MRC-RenA572-W-14-2, MRC-RenA572-W-14-3, and MRC-RenA572-W-14-4, respectively. The data points for plasticity and fracture model inputs are described in Table 6.7, Table 6.8, Table 6.9, and Table 6.10 for MRC-RenA572-W-14-1, MRC-RenA572-W-14-2, MRC-RenA572-W-14-3, and MRC-RenA572-W-14-4, respectively.

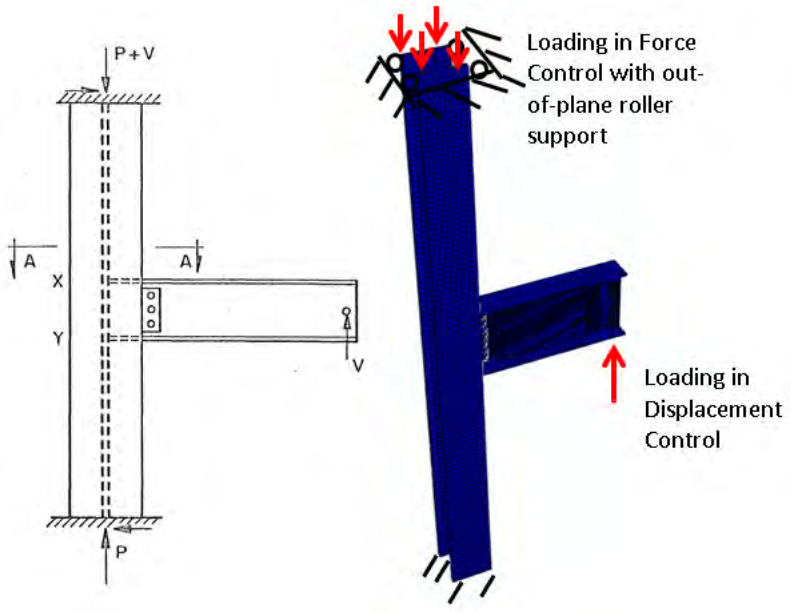

Figure 6.149: Layout of the experimental test setup for the four specimens (left) (Rentschler et al. 1978) and finite element model with associated boundary conditions (right) for MRC-RenA572-W-14-1, MRC-RenA572-W-14-2, MRC-RenA572-W-14-3, and MRC-RenA572-W-14-4 specimens

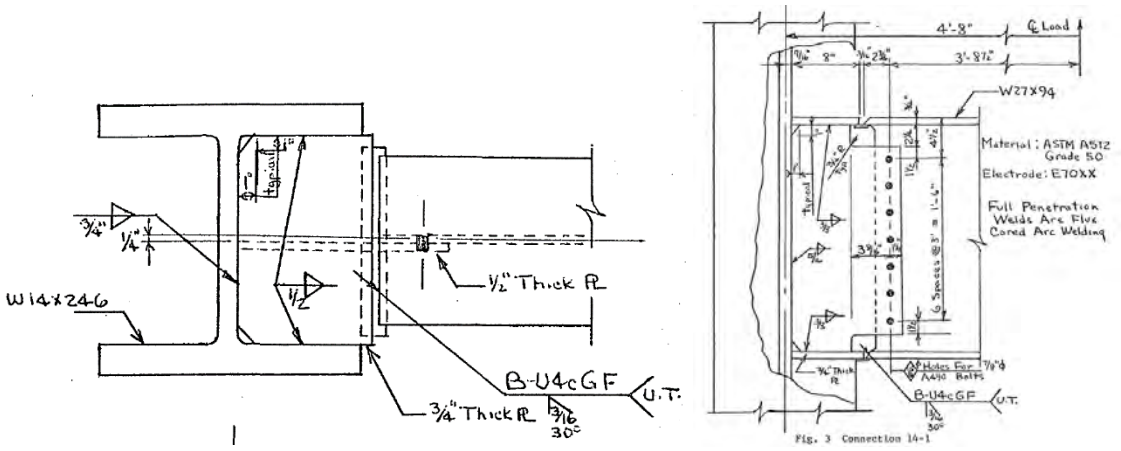

Figure 6.150: Flange-welded web-bolted connection of specimen MRC-RenA572-W-14-1 (Rentschler et al. 1978)

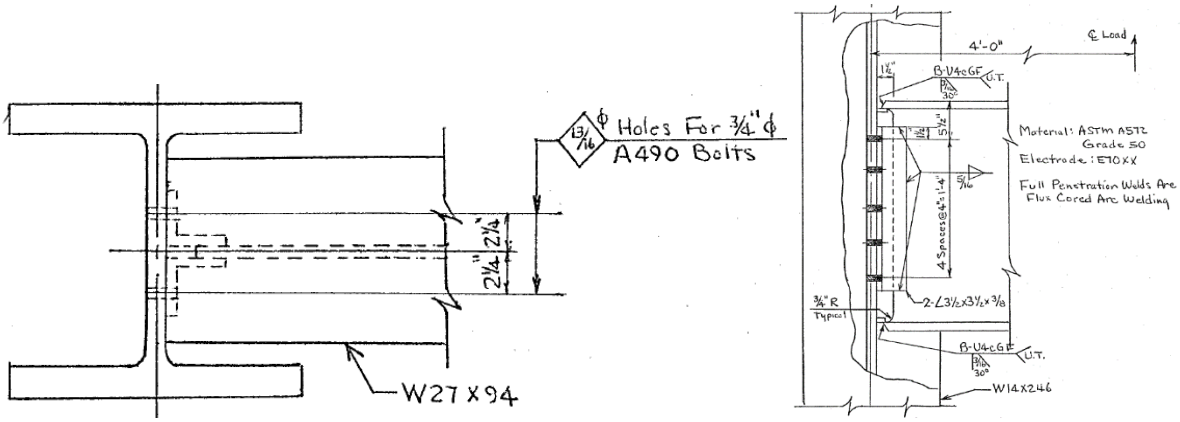

Figure 6.151: Flange-welded web-welded connection of specimen MRC-RenA572-W-14-2 (Rentschler et al. 1978)

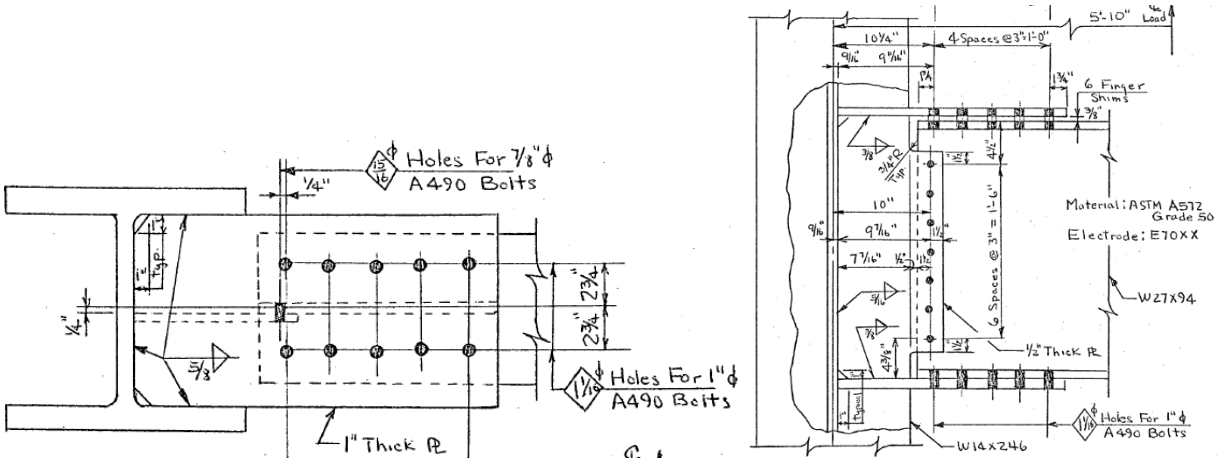

Figure 6.152: Fully-bolted connection of specimen MRC-RenA572-W-14-3 (Rentschler et al. 1978)

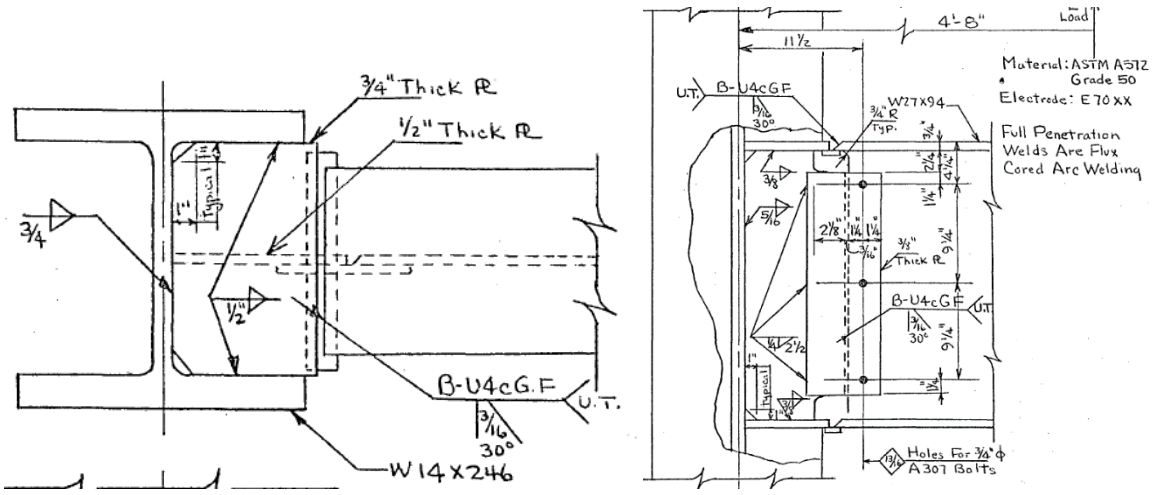

Figure 6.153: Fully-welded connection of specimen MRC-RenA572-W-14-4 (Rentschler et al. 1978)

Table 6.7: Plasticity and fracture model inputs for MRC-RenA572-W-14-1 specimen

		Fracture Model Input		
Part	**Plasticity Model Input**	**VGM**	**VGM-BW**	**CS**
Insert	CNT-KanA572-W-L-A	CNT-KanA572-W-L-A	TC-KanA572-W-L-A	0.2
Bolt	Bolt-SadA490-B-A	-	Bolt-SadA490-B-A	0.2
Beam	CNT-KanA572-W-LA	CNT-KanA572-W-L-A	TC-KanA572-W-L-A	0.2
Column	CNT-KanA572-W-L-A	CNT-KanA572-W-L-A	TC-KanA572-W-L-A	0.2
Weld	TC-NgE70T-8K6-P-A	LPT-NgE70T-8K6-P-A	TC-NgE70T-8K6-P-A	0.2

Table 6.8: Plasticity and fracture model inputs for MRC-RenA572-W-14-2 specimen

		Fracture Model Input		
Part	**Plasticity Model Input**	**VGM**	**VGM-BW**	**CS**
Angle	CNT-KanA572-W-L-A	CNT-KanA572-W-L-A	TC-KanA572-W-L-A	0.2
Bolt	Bolt-SadA490-B-A	-	Bolt-SadA490-B-A	0.2
Beam	CNT-KanA572-W-LA	CNT-KanA572-W-L-A	TC-KanA572-W-L-A	0.2
Column	CNT-KanA572-W-L-A	CNT-KanA572-W-L-A	TC-KanA572-W-L-A	0.2
Weld	TC-NgE70T-8K6-P-A	LPT-NgE70T-8K6-P-A	TC-NgE70T-8K6-P-A	0.2

Table 6.9: Plasticity and fracture model inputs for MRC-RenA572-W-14-3 specimen

		Fracture Model Input		
Part	**Plasticity Model Input**	**VGM**	**VGM-BW**	**CS**
Insert	CNT-KanA572-P-A	CNT-KanA572-P-A	TC-KanA572-P-A	0.2
Bolt	Bolt-SadA490-B-A	-	Bolt-SadA490-B-A	0.2
Beam	CNT-KanA572-P-A	CNT-KanA572-P-A	TC-KanA572-P-A	0.2
Column	CNT-KanA572-P-A	CNT-KanA572-P-A	TC-KanA572-P-A	0.2
Finger Shim	CNT-KanA572-P-A	CNT-KanA572-P-A	TC-KanA572-P-A	0.2

Table 6.10: Plasticity and fracture model inputs for MRC-RenA572-W-14-4 specimen

		Fracture Model Input		
Part	**Plasticity Model Input**	**VGM**	**VGM-BW**	**CS**
Insert	CNT-KanA572-W-LA	CNT-KanA572-W-LA	TC-KanA572-W-L-A	0.2
Bolt	Bolt-SadA490-B-A	-	Bolt-SadA490-B-A	0.2
Beam	CNT-KanA572-W-LA	CNT-KanA572-W-L-A	TC-KanA572-W-L-A	0.2
Column	CNT-KanA572-W-L-A	CNT-KanA572-W-L-A	TC-KanA572-W-L-A	0.2
Weld	TC-NgE70T-8K6-P-A	LPT-NgE70T-8K6-P-A	TC-NgE70T-8K6-P-A	0.2

For specimen MRC-RenA572-W-14-1, in the experimental test the failure consisted of tearing that propagated quickly across the entire width of the tension flange connection plate in the region of the transverse groove weld. In the VGM and VGM-BW simulations the failure propagated quickly in the weld of the tension flange. This coincides with the experimental test results. Judging from the value of the fracture initiation integral, the crack started from the lower edges of the tension flange and quickly propagated through the thickness of the flange.

The fracture location and the finite element model of this specimen are shown in

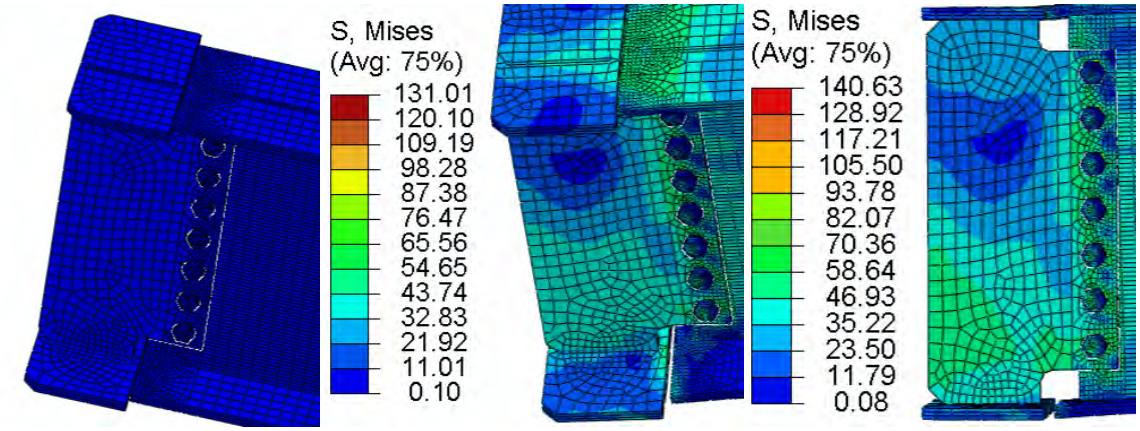

Figure 6.154. The CS simulation showed very different failure propagation. The first failure was the fracture occurring in the edges of the compression flange. After this a crack started to propagate in the tension flange from the outside edges inward. After the tension flange was fractured approximately 50 percent of the bolts severed. This fracture propagation process in the CS simulation is shown in

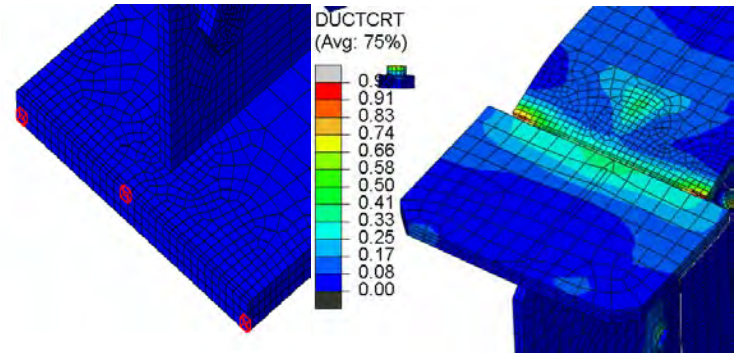

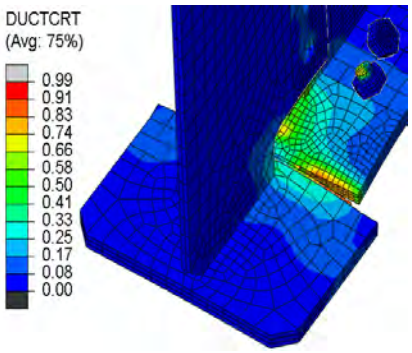

Figure 6.155. This type of fracture is not reported in the experimental test results. This behavior is clearly seen in the force-displacement plot shown in Figure 6.156. The CS simulation overpredicts the load capacity of the moment resisting connection. The VGM and the VGM-BW simulations have very similar results. The results underpredict the overall capacity of the sub-assemblage by approximately five percent.

For specimen MRC-RenA572-W-14-2, in the experimental test the fracture occurred at the weld connecting the beam flange to the column web. In the VGM and VGM-BW simulations the failure occurred instantaneously in the tension flange of the beam connecting to the column web. This again coincides with the experimental test results. As with the previous sub-assemblage specimen the values of fracture initiation integral along the flange thickness indicate that the crack started from the lower edges of the tension flange and quickly propagated through the thickness of the flange. The fracture location and the finite element

model of this specimen MRC-RenA572-W-14-2 is shown in

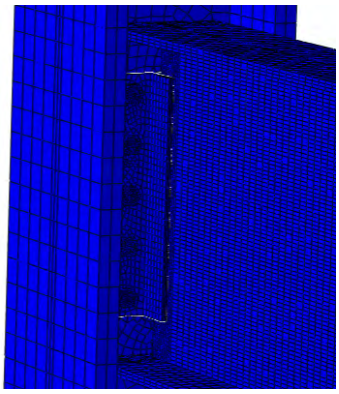

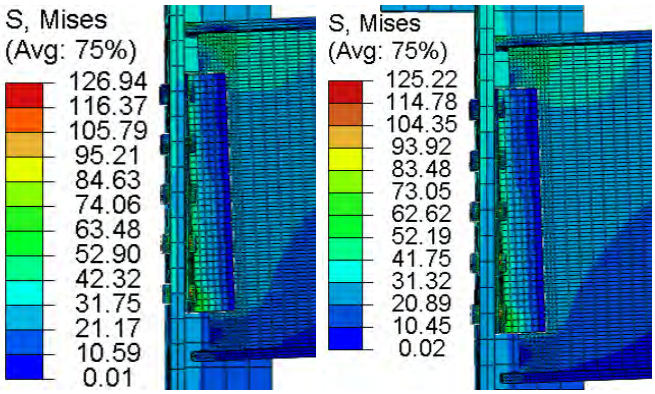

Figure 6.157. The CS simulation again showed very different failure propagation. The first damage to occur was fracture in the tension flange of the beam. After this some minor fracture occurred at the edge of the compression beam flange. The fractures at the beam flanges were not sudden like they were in the VGM and VGM-BW simulations and did not completely propagate through the flange thickness. This fracture propagation process in the CS simulation is shown in Figure 6.158. As in the CS simulation of the previous sub-assemblage specimen this type of fracture is not reported in the experimental test results. The force-displacement plot is shown in Figure 6.159. The CS simulation significantly overpredicted the capacity of this moment resisting connection. The VGM and the VGM-BW simulations underpredict the overall capacity of the sub-assemblage. The VGM simulation has a closer prediction to the real capacity of the sub-assemblage.

In the experimental test of specimen MRC-RenA572-W-14-3, the fracture occurred in the tension flange connection plate. The finite element model and the selected elements for studying the fracture initiation and propagation related parameters are shown in Figure 6.160. The VGM and VGM-BW simulations had different fracture locus for the base material but the same for the bolts. In the VGM and VGM-BW simulations the failure occurred in the bolts in the tension flange and the web of the beam. At first the bolts in the tension flange that are closest to the column fractured. After this the bolts connecting the web of the beam quickly fractured from the lowest bolt to the top bolt in the web. Right before the top bolt in the beam web fractured the bolts in the tension flange started to fracture from the bolts farthest away from the column propagating inwards. No fracture occurred in the tension flange of the beam and the connecting plate. This does not coincide with experimental test results. The reason for this is that the fracture locus used for the bolts is an underestimate of the fracture capacity of the bolts used in the experimental testing of this specimen. This shows the need for calibrating the B-W model to experimental test directly through the use of PSO or a similar approach described in Section 5.3 of this work. This would have likely improved the results. Since fracture occurred in the bolts that had the same fracture locus for the VGM and VGM-BW simulations the results are the same and only one would be discussed. The CS showed different failure propagation. The first bolt to sever was the one connecting the beam web to the connector plate located at the top right below the compression flange. After this the bolts in the beam web quickly fractured downward in addition to the bolts in the compression flange fracturing suddenly. As in the CS simulation of the previous sub-assemblage specimens, this type of fracture is not reported in the experimental test results. The fractures of the connection specimen for the CS

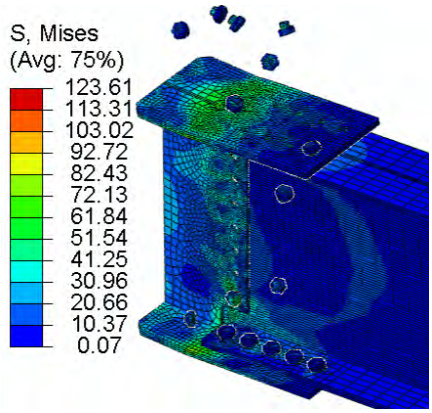

and VGM/VGM-BW are shown in

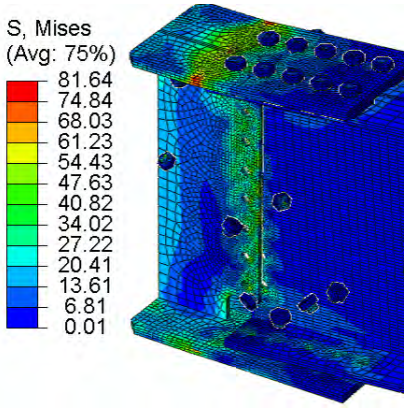

Figure 6.161 (fractured bolts are shown in mid-flight in the figure). The force-displacement plot is shown in Figure 6.162. The VGM/VGM-BW simulation slightly underpredicts the overall fracture capacity of the sub-assemblage. The VGM simulation has a closer prediction to the real capacity of the sub-assemblage.

The failure of MRC-RenA572-W-14-4 was determined by large beam deflections and no fracture was reported. In the VGM and VGM-BW simulations the failure propagated quickly in the tension flange of the beam connecting to the insert tension flange and propagated very quickly through the weld connecting the beam web and the web of the insert. In the VGM-BW simulation the fracture propagated faster than in VGM simulation. As with the previous sub-assemblage specimen, the values of fracture initiation integral along the flange thickness

indicate that the crack started from the lower edges of the tension flange and quickly propagated through the thickness of the flange and then the beam web. The fracture location and the finite element model of this specimen MRC-RenA572-W-14-4 is shown in

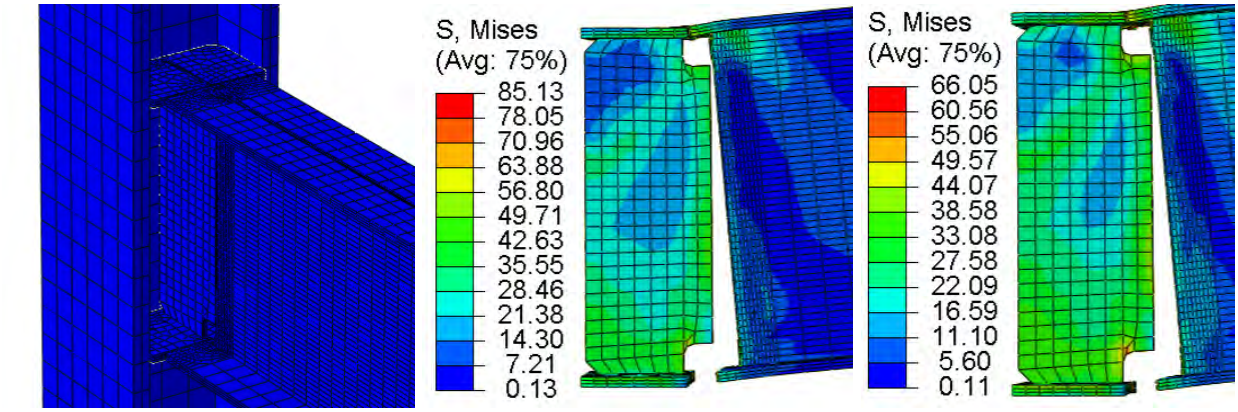

Figure 6.163. In the CS simulation, the fracture propagation was different than in the VGM and VGM-BW simulations. The fracture started at a corner of a tension and compression flange at the same time. The fracture at the edge of the compression flange was on the opposite side of the beam than the fracture at the edge of the tension flange. The fracture propagated inward from the two edges while the other two diagonal edges did not have any fracture. When fracture in the tension flange reached the center of the beam flange the weld connecting beam web and insert fractured. The fracture of the beam web was sudden, propagating to the very top near the compression flange. This fracture propagation process in the CS simulation is

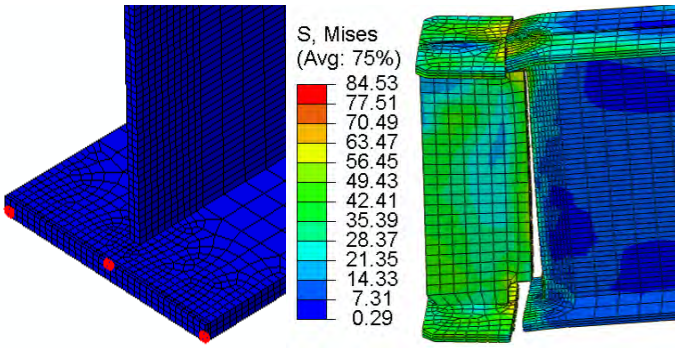

shown in

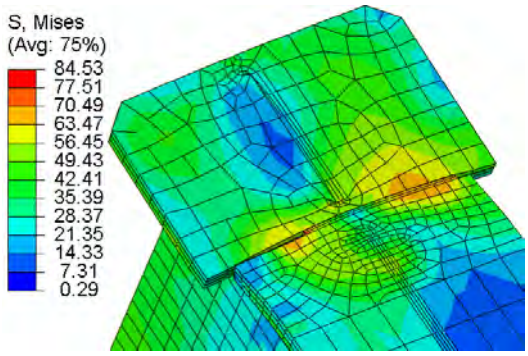

Figure 6.164. The force-displacement plot is shown in Figure 6.165. The VGM and the VGM-BW simulations significantly underpredict the overall capacity of the sub-assemblage. In addition, the simulations experience vibration due to the assembly being only connected at the compression flange after fracture and not offering much resistance to the further loading of the assembly. The CS simulation significantly overpredicts the capacity of the connection.

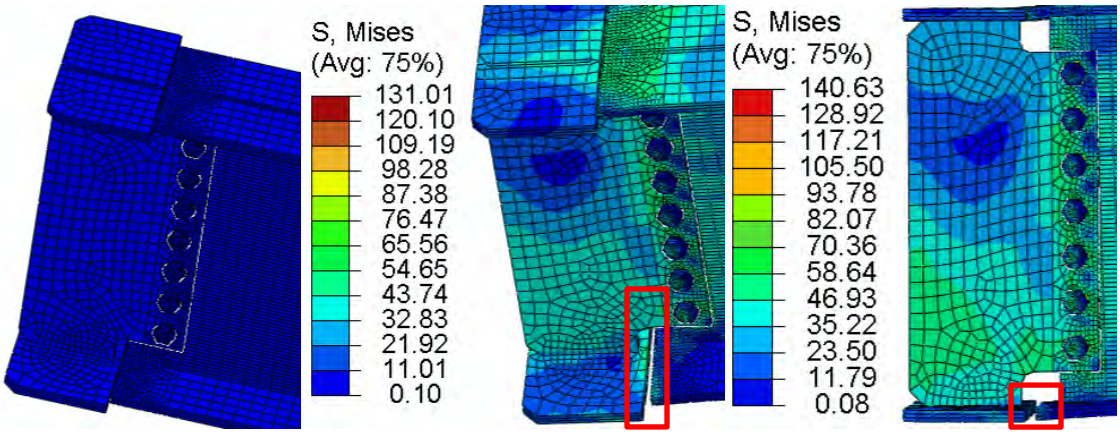

Figure 6.154: Finite element model (left) and simulation results (Rentschler et al. 1978) of a moment resisting connection MRC-RenA572-W-14-1 specimen with contours representing von Mises stress (ksi): VGM (middle), VGM-BW (right)

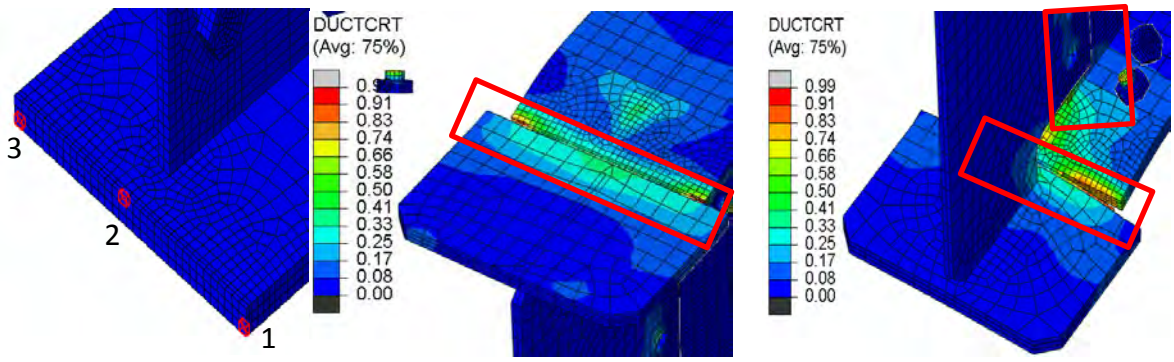

Figure 6.155: Simulation results (Rentschler et al. 1978) of a moment resisting connection MRC-RenA572-W-14-1 specimen with contours representing the value of fracture initiation integral: chosen elements' location (left), CS fracture of compression flange (middle), CS fracture of tension flange and severed bolts (right)

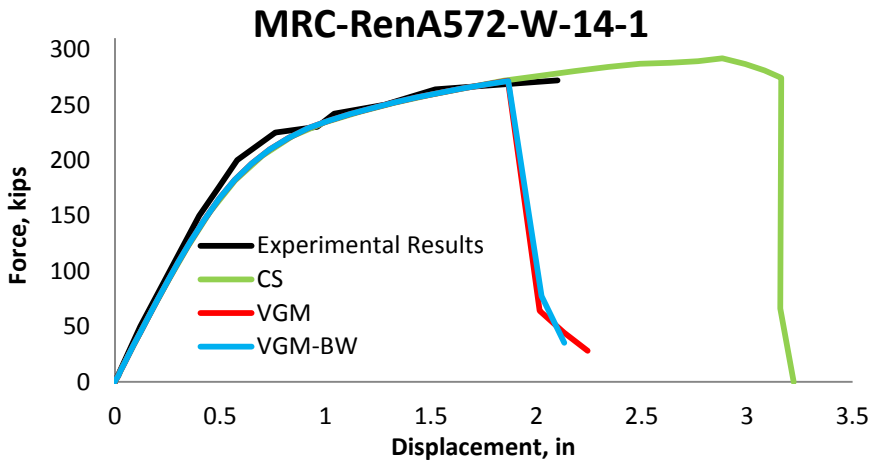

Figure 6.156: Validation results for beam to column web connections MRC-RenA572-W-14-1 specimen

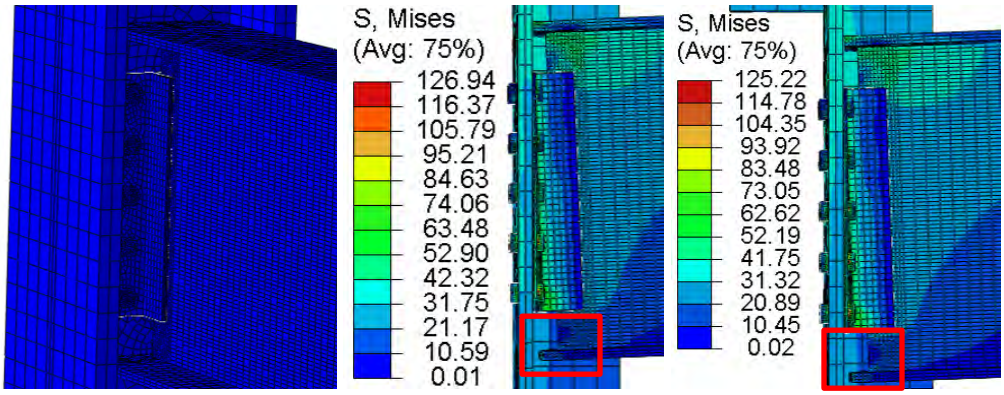

Figure 6.157: Finite element model (left) and simulation results (Rentschler et al. 1978) of a moment resisting connection MRC-RenA572-W-14-2 specimen with contours representing von Mises stress (ksi): VGM (middle), VGM-BW (right)

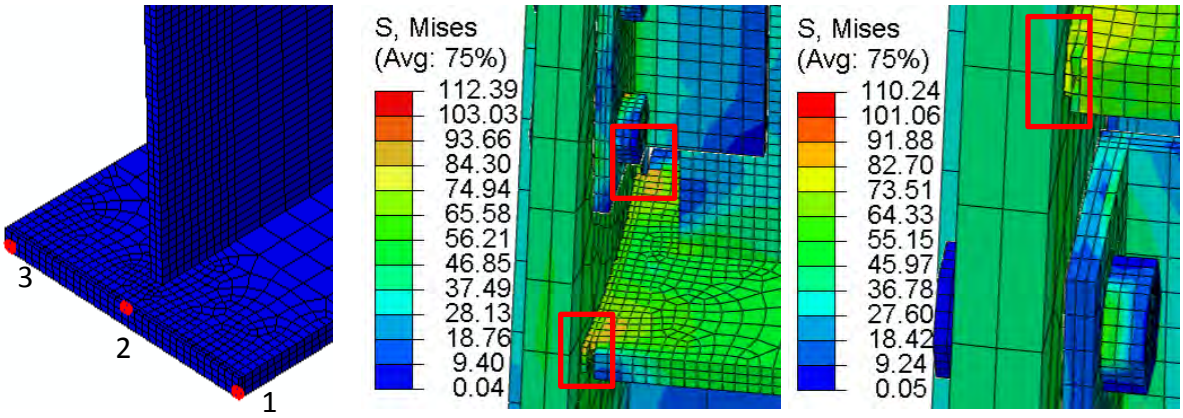

Figure 6.158: Simulation results (Rentschler et al. 1978) of a moment resisting connection MRC-RenA572-W-14-2 specimen with contours representing von Mises stress (ksi): chosen elements' location (left), CS lower flange fracture (middle), CS upper flange fracture (right)

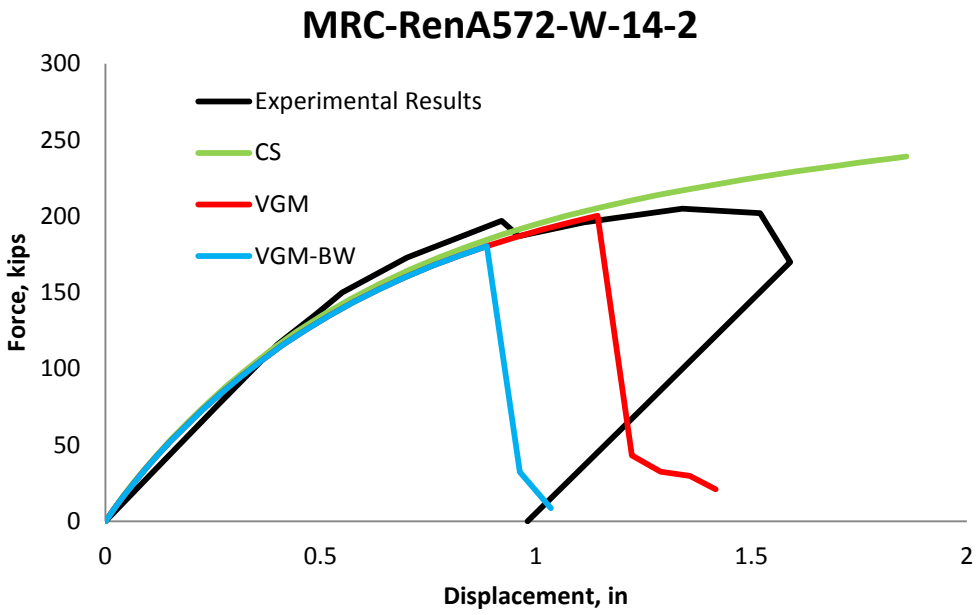

Figure 6.159: Validation results for beam to column web connections MRC-RenA572-W-14-2 specimen

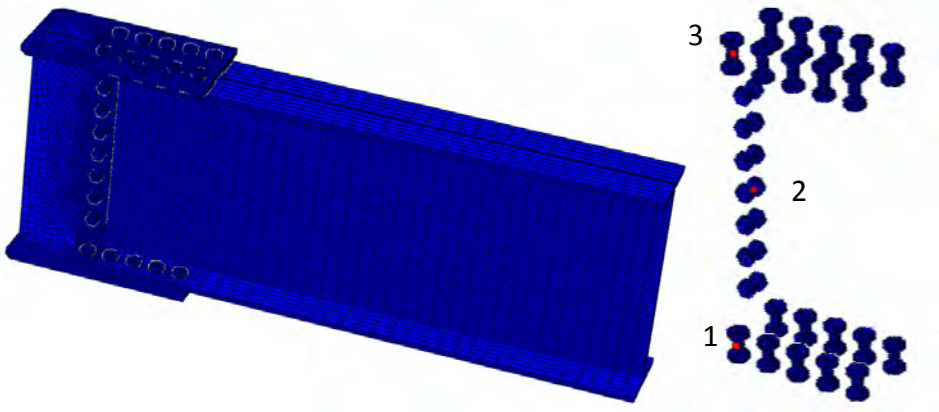

Figure 6.160: Finite element model (left) and selected elements for study of the variation of fracture parameters throughout the loading of a moment resisting connection MRC-RenA572-W-14-3 specimen

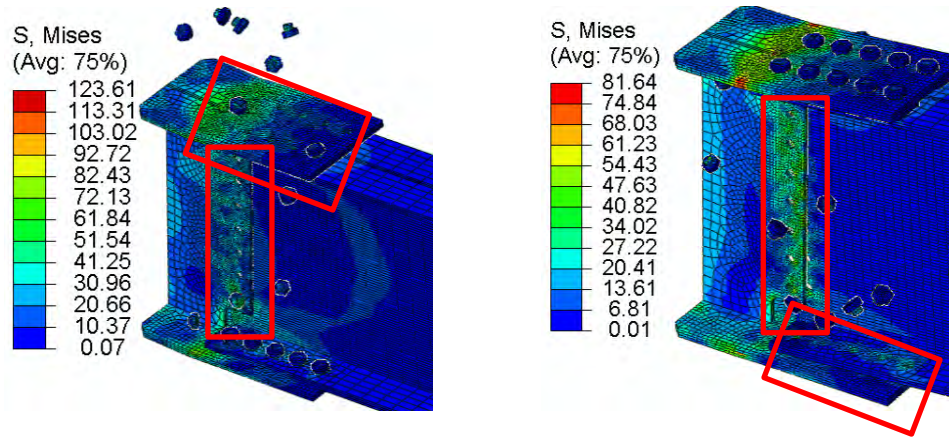

Figure 6.161: Simulation results (Rentschler et al. 1978) of a moment resisting connection MRC-RenA572-W-14-3 specimen with contours representing von Mises stress (ksi): CS (left), VGM and VGM-BW (right)

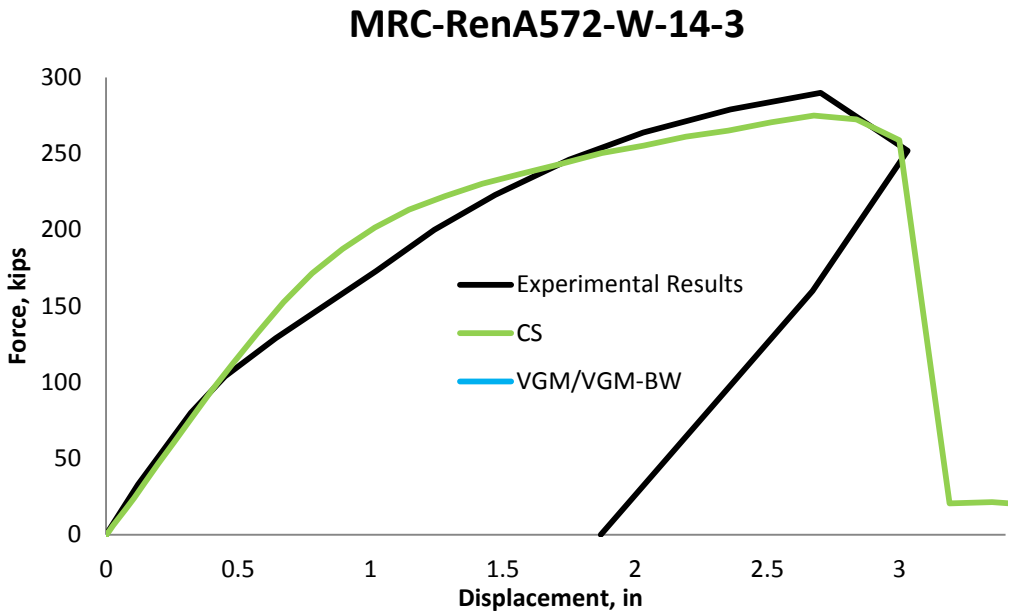

Figure 6.162: Validation results for beam to column web connections MRC-RenA572-W-14-3 specimen

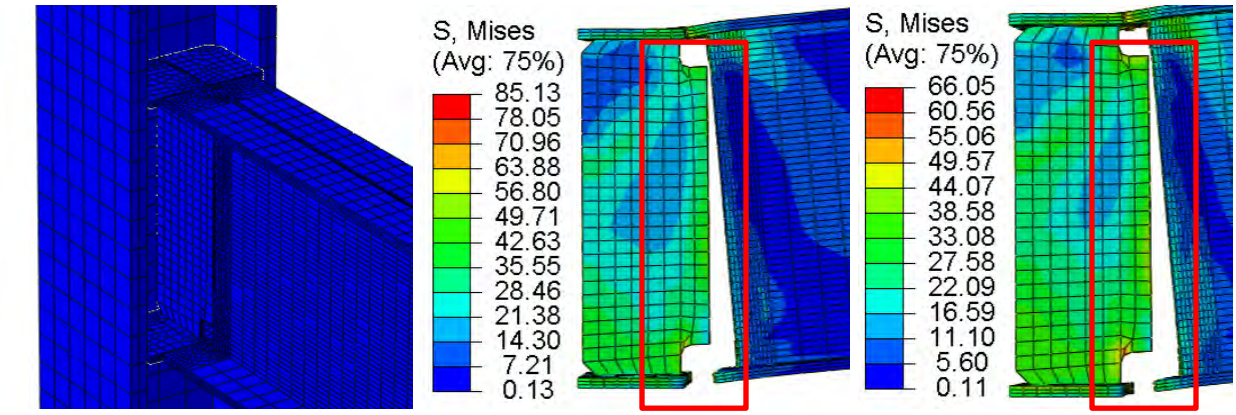

Figure 6.163: Finite element model (left) and simulation results (Rentschler et al. 1978) of a moment resisting connection MRC-RenA572-W-14-4 specimen with contours representing von Mises stress (ksi): VGM (middle), VGM-BW (right)

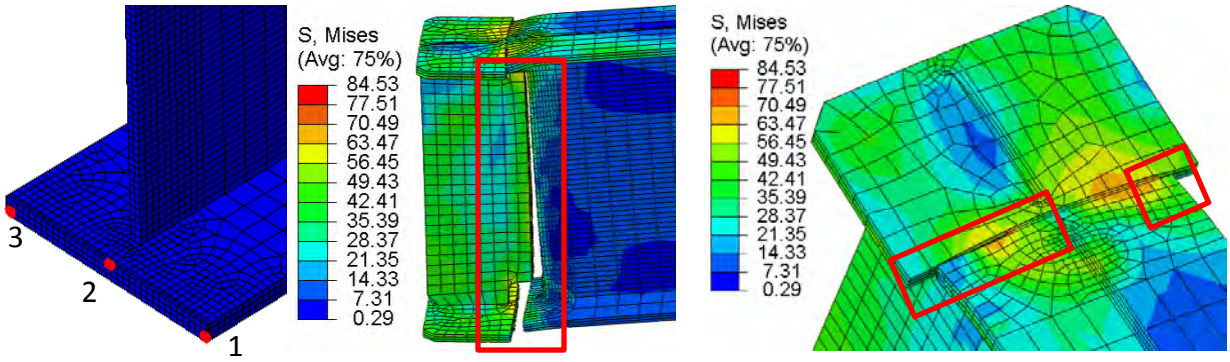

Figure 6.164: Simulation results (Rentschler et al. 1978) of a moment resisting connection MRC-RenA572-W-14-2 specimen with contours representing von Mises stress (ksi): chosen elements' location (left), CS lower flange fracture (middle), CS upper flange fracture (right)

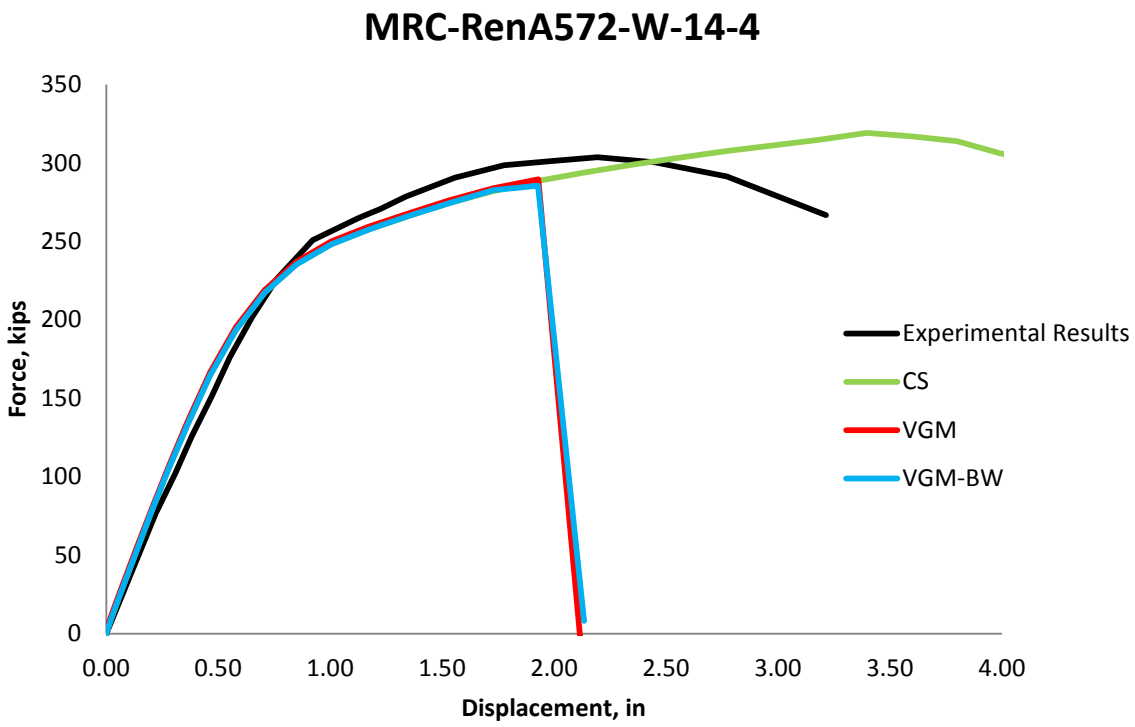

Figure 6.165: Validation results for beam to column web connections MRC-RenA572-W-14-4 specimen

Below a detailed description is provided on the variation of fracture initiation and propagation parameters in elements that are located through the thickness of the specimens for the three finite element deletion strategies shown in Figure 6.155, Figure 6.158, Figure 6.160, and Figure 6.164.

Triaxiality versus displacement is plotted for the three elements across the thickness of the tension flange in MRC-RenA572-W-14-1, MRC-RenA572-W-14-2, and MRC-RenA572-W-14-4 specimens and in the bolts shown by Figure 6.160 for the MRC-RenA572-W-14-3 specimen for the three finite element deletion strategies in Figure 6.166, Figure 6.167, Figure 6.168, and Figure 6.169, respectively. For specimen MRC-RenA572-W-14-1 the VGM, VGM-BW, and CS have almost identical triaxiality variation throughout the loading process. The outside edge

elements, 1 and 3, have a higher triaxiality value than the middle element. The middle element experiences a small amount of compression at the beginning of the loading process because the element is located on top of the tension flange and only the column is loaded at this time. The triaxiality values remain almost constant throughout the loading process for the three elements after the initiation increase. The biggest difference between the CS simulation and the other two simulations is that in CS simulation the elements reached a much larger displacement value. In addition, in the CS simulation element 3 experienced a spike before failure while others did not. For specimen MRC-RenA572-W-14-2 the three simulations had almost identical triaxiality variation through the loading process with elements in CS reaching higher displacement than in the VGM and VGM-BW simulation. The middle element in the tension flange had negative triaxiality throughout the loading process due to the beam web being welded to the angles thereby imposing high restraint against vertical movement right at the lower corner of the angle creating compression in the top elements of the tension flange. Again, the middle element in CS simulation is not deleted because fracture does not propagate through the tension flange completely. For specimen MRC-RenA572-W-14-3, the elements were chosen inside the bolts because that is where the failure occurred. The bolts were subjected to shear loading in the three simulations. The element in the bottom bolt for the CS and VGM and VGM-BW stayed in the positive triaxiality region with some attenuation. Eventually the bottom bolt in the CS simulation experiences high positive triaxiality, which signifies tension. The element in the middle bolt located in the beam web experiences some negative triaxiality at the beginning but then goes into lower positive triaxiality region. In the CS simulation, the element in the middle bolt also experiences higher positive triaxiality signifying

tension loading on the bolt. This bolt does not fail in the CS simulation. The element in the top bolt located in the compression flange experiences shear loading throughout the first half of the loading process but then transitions into compressive negative triaxiality for the VGM and VGM-BW simulations. In the CS simulation the element in the top bolt stays in the lower positive triaxiality region signifying shear loading throughout the loading process. The triaxiality variation in the MRC-RenA572-W-14-4 specimen remains in the positive high triaxiality region for the three elements across the tension flange in the three simulations. Overall, the elements in the CS simulation experience a smaller triaxiality but achieve far greater displacement than the elements in VGM and VGM-BW simulations.

The equivalent plastic strain is plotted in Figure 6.170, Figure 6.171, Figure 6.172, and Figure 6.173. For the MRC-RenA572-W-14-1 specimen in the three simulations the edge elements had similar variation of equivalent plastic strain throughout loading while the middle element had different behavior for each simulation. It is interesting to note that edge elements in the three simulations all reached an equivalent plastic strain value of approximately 0.2. The middle elements reach a much smaller strain value in the VGM and VGM-BW simulations while in the CS simulation the middle element reaches about the same strain value as the edge elements. A similar behavior can be seen in MRC-RenA572-W-14-2 specimen. The edge elements in the three simulations followed a gradual equivalent plastic strain growth. The middle elements for the three simulations reach a much smaller maximum strain value. Overall, the elements in the CS simulation reached higher equivalent plastic strain values than in the other two simulations. The variation of equivalent plastic strain is different for the MRC-RenA572-W-14-3 specimen than in the other specimens. In the VGM and VGM-BW simulations the element in the middle

bolt reaches the highest strain value while the element in the top bolt reaches the minimum. In the CS simulation both the element in the middle and top bolt reach maximum strain value while the element in the bottom bolt reaches a much smaller equivalent plastic strain value. However, in all of the simulations there is a very dramatic and almost sudden increase in the strain value. In the MRC-RenA572-W-14-4 specimen the variation of equivalent plastic strain value follows a similar trend as in the first two specimens. The elements on the edges of the tension flange reach high equivalent plastic strain values while the middle elements reaches a low strain value with an exception to the middle CS element, which also reaches the maximum strain value.

The fracture locus is plotted in Figure 6.174, Figure 6.175, Figure 6.176, and Figure 6.177. For MRC-RenA572-W-14-1 specimen the edge elements are mainly influenced by the VGM fracture locus for the VGM and VGM-BW simulations. The middle element behavior in the fracture locus plane is different for the VGM and VGM-BW because is it mainly subjected to lower triaxiality. The equivalent plastic strain in the VGM and VGM-BW simulations grows with minimal change in triaxiality signifying sudden failure. The CS simulation follows a similar trend with almost vertical growth of equivalent plastic strain with triaxiality for the edge elements. This trend is repeated in MRC-RenA572-W-14-2 and MRC-RenA572-W-14-4 specimens. For the MRC-RenA572-W-14-3 specimen the triaxiality range in the three simulations is similar, ranging from 0.2 to 0.5 triaxiality. This signifies that the bolts in the three simulations experience shear and tension loading. The three bolts start out with shear loading being imposed on them but as the loading progresses the state of stress changes to one of tension shown in the fracture locus plots.

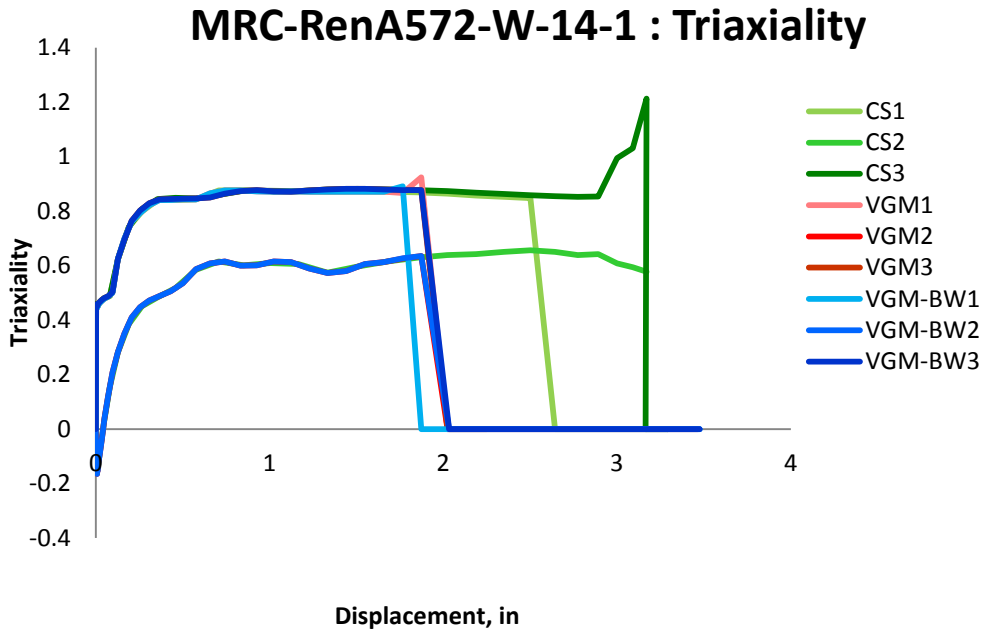

Figure 6.166: Variation of triaxiality with displacement for different elements laid out through the thickness of the tension flange of MRC-RenA572-W-14-1 specimen for the three finite element deletion strategies

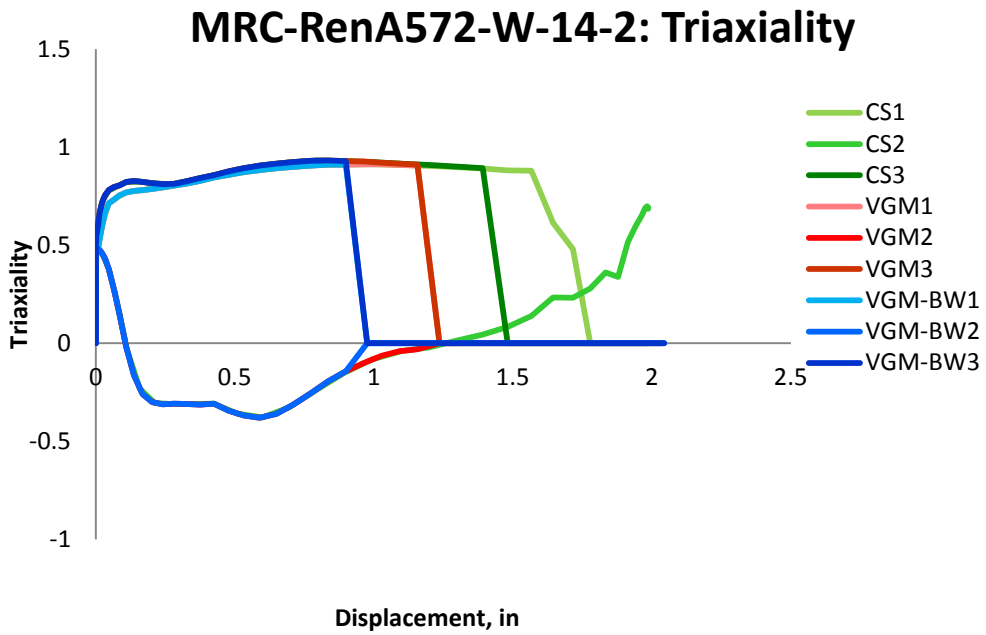

Figure 6.167: Variation of triaxiality with displacement for different elements laid out through the thickness of the tension flange of MRC-RenA572-W-14-2 specimen for the three finite element deletion strategies

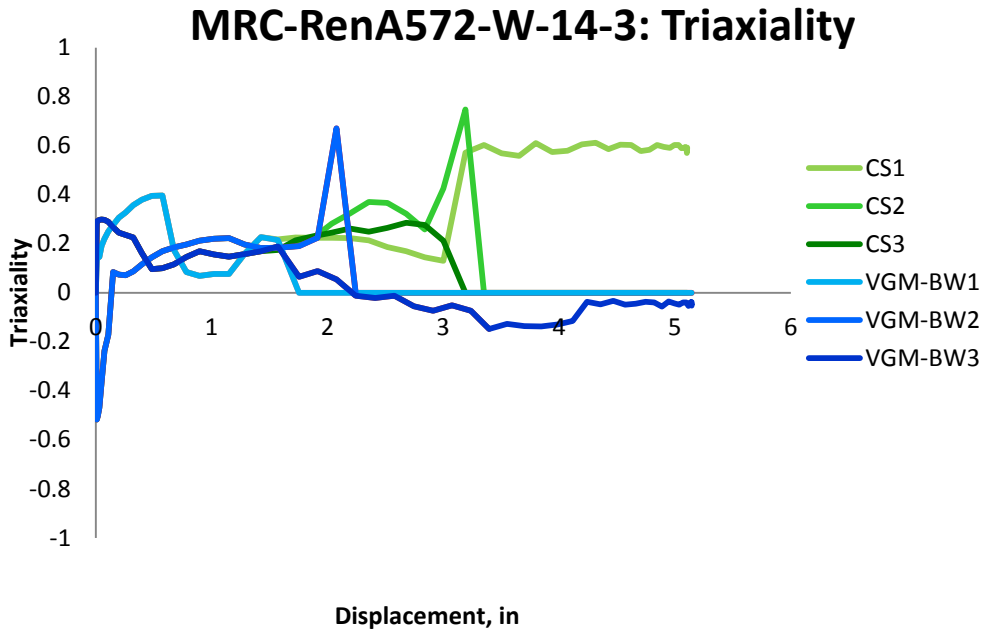

Figure 6.168: Variation of triaxiality with displacement for different elements laid out in the bolts of MRC-RenA572-W-14-3 specimen for the three finite element deletion strategies

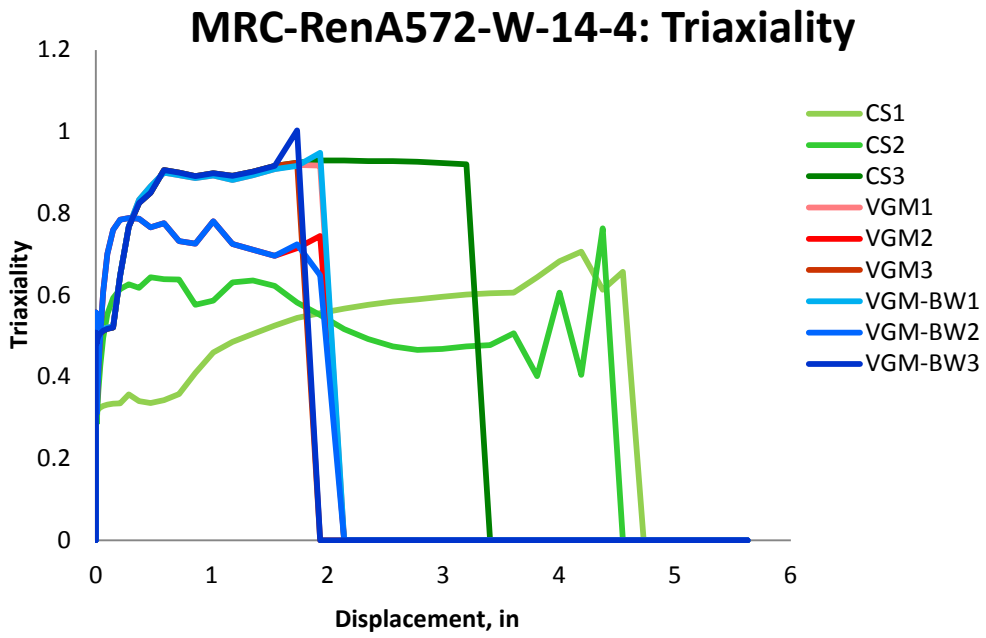

Figure 6.169: Variation of triaxiality with displacement for different elements laid out through the thickness of the tension flange of MRC-RenA572-W-14-4 specimen for the three finite element deletion strategies

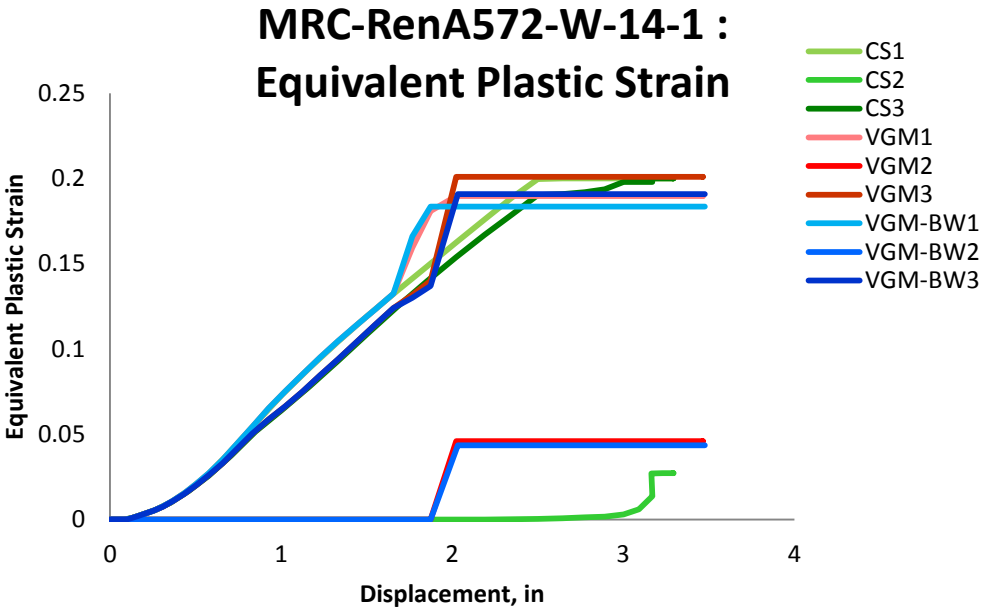

Figure 6.170: Variation of equivalent plastic strain with displacement for different elements laid out through the thickness of the tension flange of MRC-RenA572-W-14-1 specimen for the three finite element deletion strategies

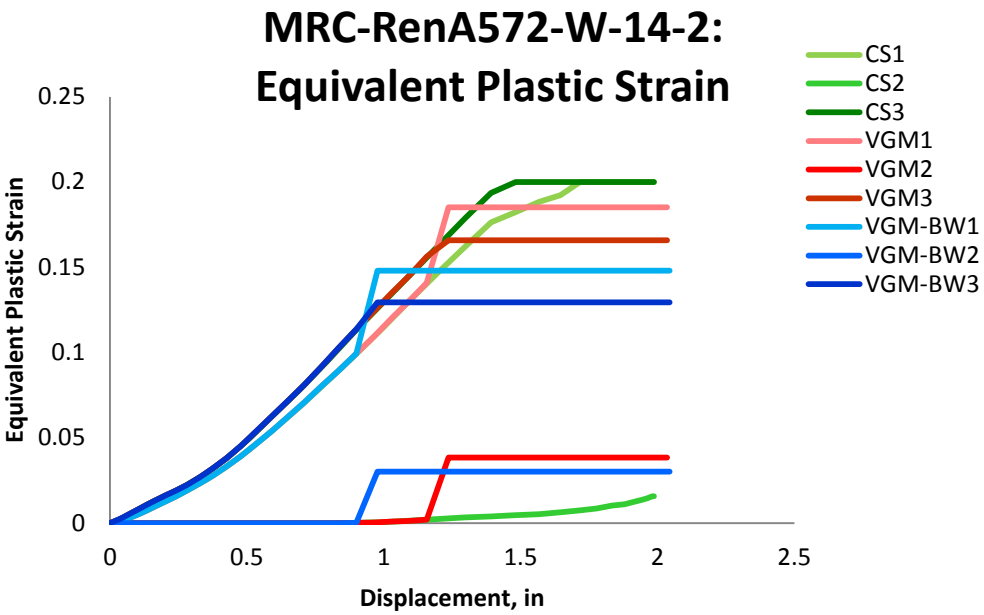

Figure 6.171: Variation of equivalent plastic strain with displacement for different elements laid out through the thickness of the tension flange of MRC-RenA572-W-14-2 specimen for the three finite element deletion strategies

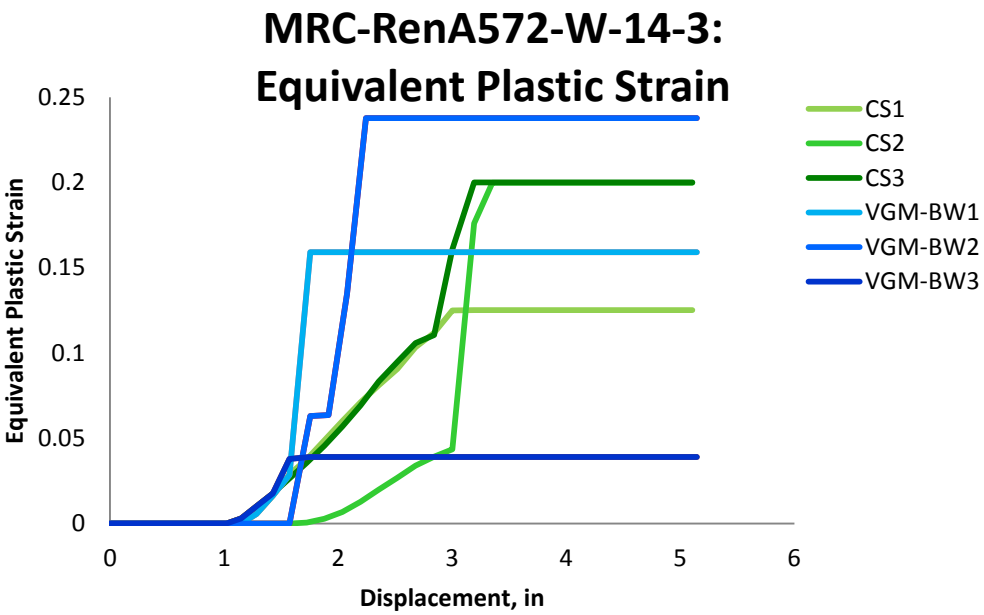

Figure 6.172: Variation of equivalent plastic strain with displacement for different elements laid out in the bolts of MRC-RenA572-W-14-3 specimen for the three finite element deletion strategies

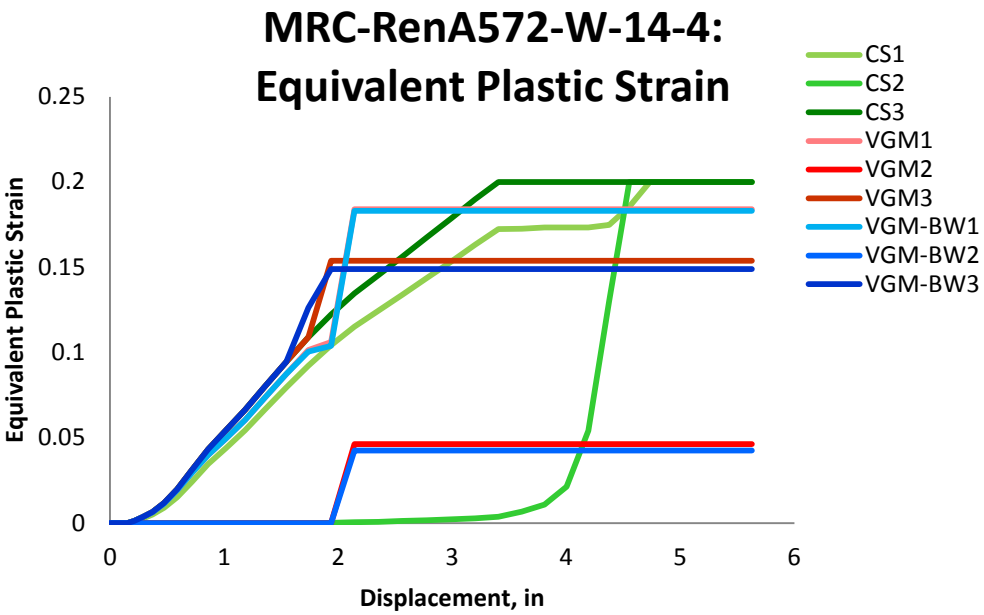

Figure 6.173: Variation of equivalent plastic strain with displacement for different elements laid out through the thickness of the tension flange of MRC-RenA572-W-14-4 specimen for the three finite element deletion strategies

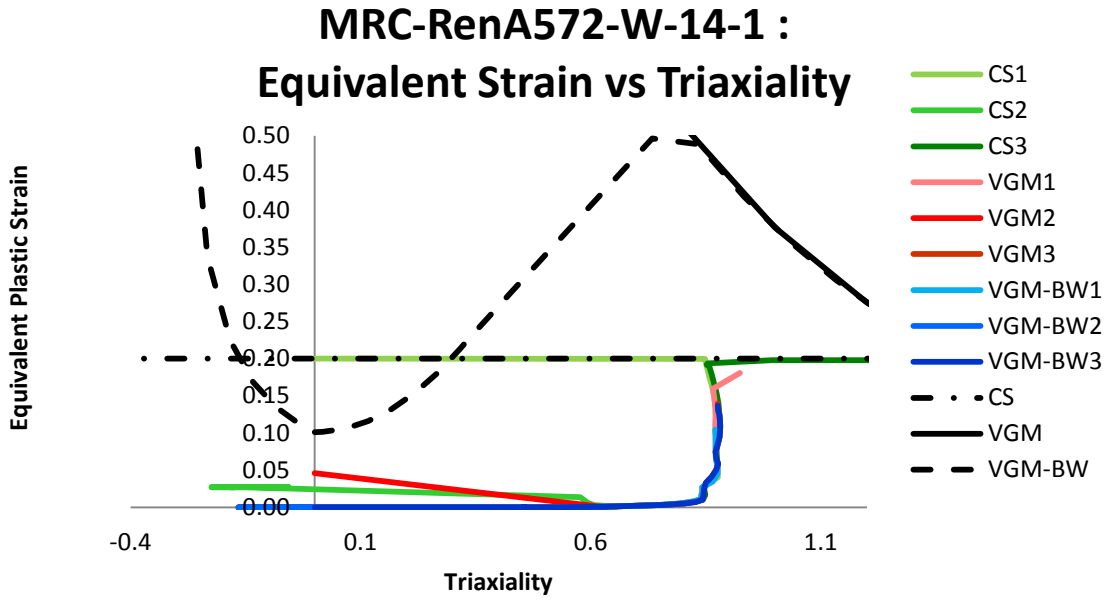

Figure 6.174: Variation of equivalent plastic strain with triaxiality for different elements laid out through the thickness of the tension flange of MRC-RenA572-W-14-1 specimen for the three finite element deletion strategies

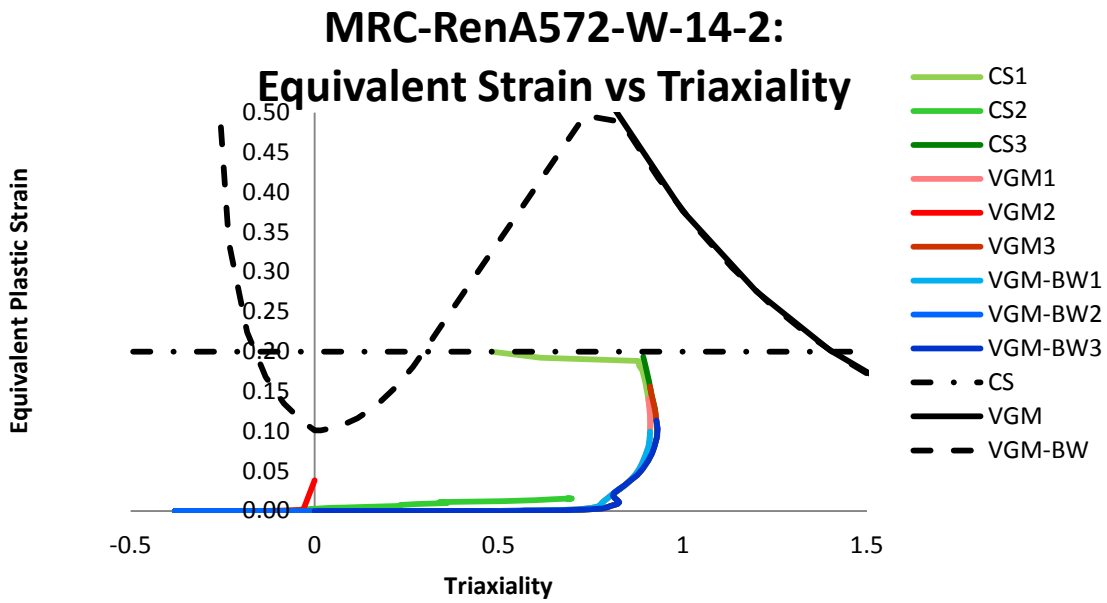

Figure 6.175: Variation of equivalent plastic strain with triaxiality for different elements laid out through the thickness of the tension flange of MRC-RenA572-W-14-2 specimen for the three finite element deletion strategies

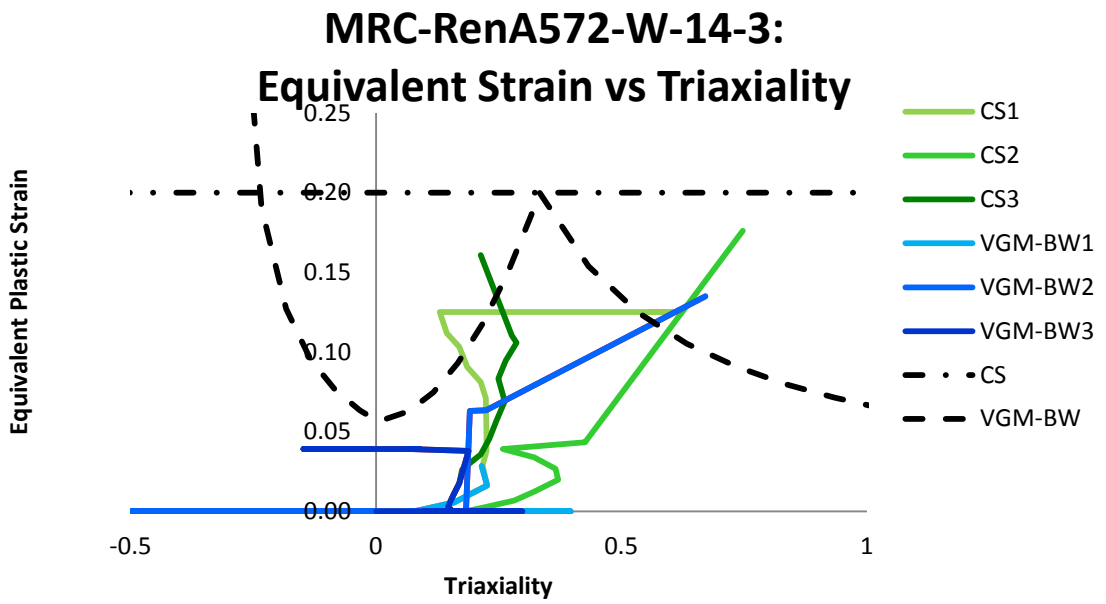

Figure 6.176: Variation of equivalent plastic strain with triaxiality for different elements laid out in the bolts of MRC-RenA572-W-14-3 specimen for the three finite element deletion strategies

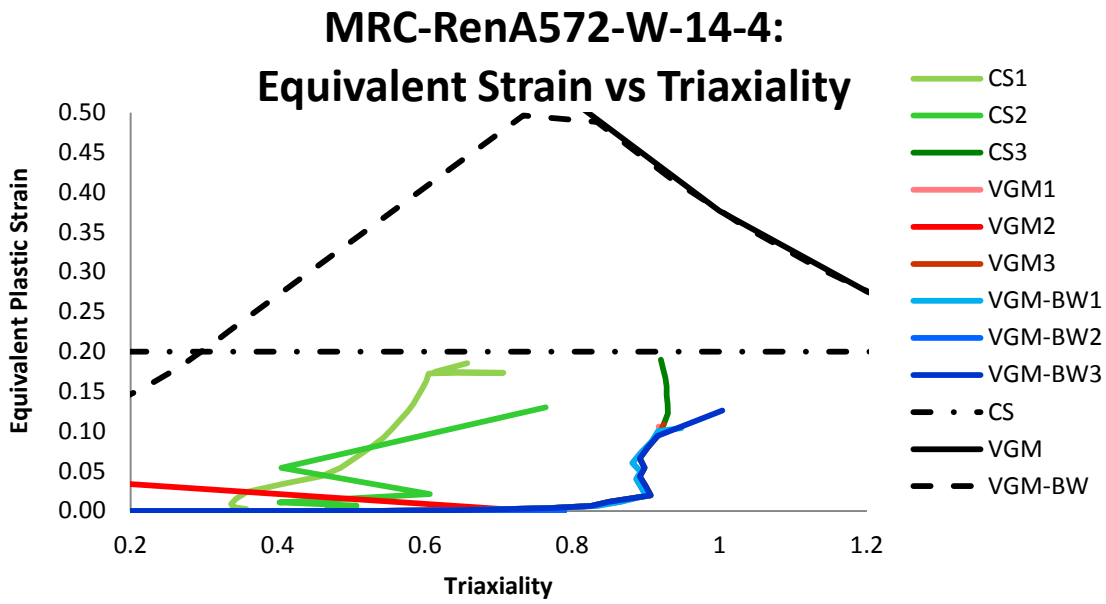

Figure 6.177: Variation of equivalent plastic strain with triaxiality for different elements laid out through the thickness of the tension flange of MRC-RenA572-W-14-4 specimen for the three finite element deletion strategies

The variation of the value of fracture initiation integral is shown in Figure 6.178, Figure 6.179, Figure 6.180, and Figure 6.181. In the MRC-RenA572-W-14-1 specimen the CS simulation shows that the critical value of the fracture initiation integral for the edge elements was reached at a higher displacement value than in the other two simulations. The middle element did not see any growth in the integral value until much later in the loading process. The middle element never reached the critical value signifying that the tension flange did not facture completely through the middle. In the VGM and VGM-BW simulations all three element across the tension flange reached the critical value. The edge elements saw growth in the integral value early on in the loading while the middle element did not see any growth until right before fracture. This shows that the middle part of the tension flange did not experience plastic behavior until right before fracture. This limits the deformation capacity of the specimen. The MRC-RenA572-W-14-2 specimen experienced similar behavior in the VGM and VGM-BW simulations. While the edges of the tension flange saw plastification from the beginning of the loading the middle part of the tension flange did not see almost any plastic behavior but went from elastic behavior to fracture almost instantaneously. In the CS simulation, the edges of the tension flange saw a more gradual growth of the fracture initiation integral compared to the other two simulations. The middle element remained mainly elastic until much later in the simulation. It saw very little plastic behavior and was not deleted. In the MRC-RenA572-W-14-3 specimen the bolts also remained elastic until right before fracture occurred in the VGM-BW/VGM simulation. The element in the bottom and top bolt began to plastify at approximately the same displacement but the bottom bolt started to soften while the top bolt remain plastic throughout the loading. The middle bolt also saw a quick transition from elastic to softening behavior with little plastic

behavior. In the CS simulation the bottom bolt did not sever but experienced significant plastic behavior without reaching softening. The middle and top bolt experienced a more gradual growth of the fracture initiation integral than in the VGM-BW/VGM simulation. The elements on the edge of the tension flange in MRC-RenA572-W-14-4 specimen experienced gradual growth in the fracture initiation integral for the three simulations. The growth of the integral was more gradual in the CS than in the VGM and VGM-BW simulations. The element in the middle of the tension flange remained elastic throughout the loading process until right before fracture for the three simulations.

The varition of von Mises stress with displacement is shown in Figure 6.182, Figure 6.183, Figure 6.184, and Figure 6.185. In the MRC-RenA572-W-14-1 specimen the three simulations show that the elements on the edges of the tension flange experienced higher von Mises stress throughout the loading process than the element in the middle of the flange. All elements in the VGM and VGM-BW simulations failed at the same displacement signifying that the tension flange experienced a sudden fractured through its entire thickness. In the CS simulation each element failed at different displacement values which are higher than in the other simulations for the corresponding element. A similar trend is observed in the MRC-RenA572-W-14-2 specimen with an exception that the elements in the VGM simulation reach higher displacement values than in the VGM-BW simulation. The bolts in MRC-RenA572-W-14-3 specimen reach higher maximum value of von Mises stress in the VGM-BW/VGM and CS simulations than in the previous specimens. The growth of the von Mises stress is much more gradual than in the tension flange. The top bolt in the VGM-BW simulation experienced softening at the same displacement as the bottom bolt but did not fail. The same occurred for

the bottom bolt in the CS simulation when the top bolt started to soften. The reason for constant stress after the failure of the other bolt is because of failure of bolts through the height of the web which allowed for more beam displacement without imposing more stress on the bolts. The bolts in the CS simulation reach higher displacement and von Mises stress values than in VGM-BW simulation. The variation of von Mises Stress in MRC-RenA572-W-14-4 specimen followed a similar trend as in MRC-RenA572-W-14-1 and MRC-RenA572-W-14-2 specimens. The stress at the edges of the tension flange was much greater throughout the loading process than at the middle of the flange for the three simulations. The element in the middle of the flange experienced a much more gradual growth in the von Mises stress value than at the flange edges. The elements in the CS simulation reached a much higher displacement value than in VGM and VGM-BW simulations.

The mean stress variation throughout the loading excursion is plotted Figure 6.186, Figure 6.187, Figure 6.188, and Figure 6.189. For MRC-RenA572-W-14-1 specimen the variation of mean stress for the three simulations follows the same trend as with von Mises stress. The edges on the tension flange experience higher mean stress than the middle of the flange for the VGM, VGM-BW, and CS simulations. For the MRC-RenA572-W-14-2 specimen the edges of the flange for the three simulations experience a constant increase in the mean stress. The elements in the CS simulation reached a higher displacement than the in the other two simulations. The middle of the flange experienced a negative mean stress throughout the loading process signifying compression. For the VGM and VGM-BW simulations the three elements all failed at the same displacement signifying a sudden fracture across the flange thickness. For the MRC-RenA572-W-14-3 specimen the bolts experienced a positive mean

stress in the CS and VGM-BW simulation throughout the loading except for the top bolt in the VGM-BW simulation where it experienced small amount of negative mean stress after the lower and most of the web bolts fractured. The elements in the MRC-RenA572-W-14-4 specimen followed the similar trend as in the MRC-RenA572-W-14-1 and MRC-RenA572-W-14-2 specimens. The edges experienced higher mean stress throughout the loading than the middle portion of the tension flange. The CS simulation had more fracture occur on one side of the flange than on the other.

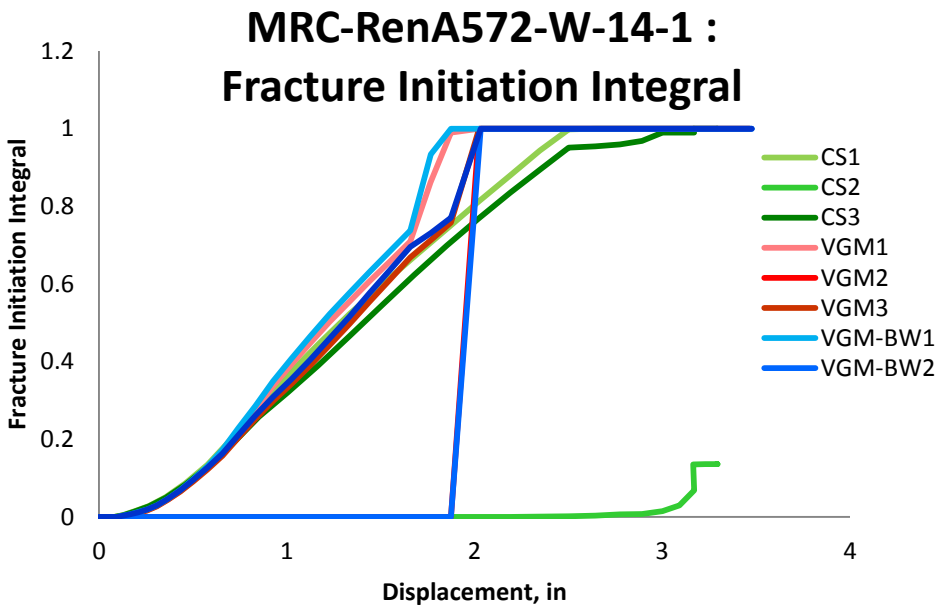

Figure 6.178: Variation of fracture initiation integral value with displacement for different elements laid out through the thickness of the tension flange of MRC-RenA572-W-14-1 specimen for the three finite element deletion strategies

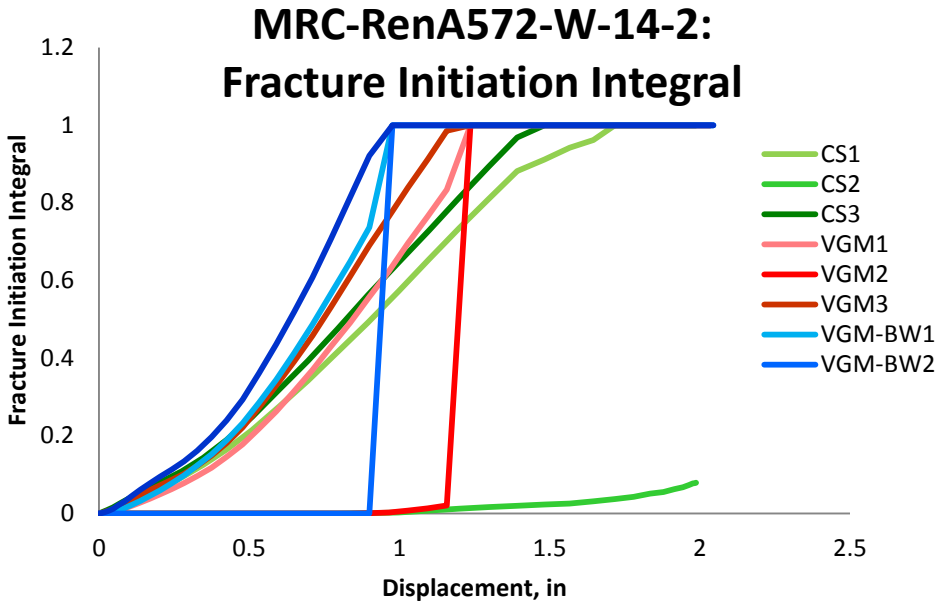

Figure 6.179: Variation of fracture initiation integral value with displacement for different elements laid out through the thickness of the tension flange of MRC-RenA572-W-14-2 specimen for the three finite element deletion strategies

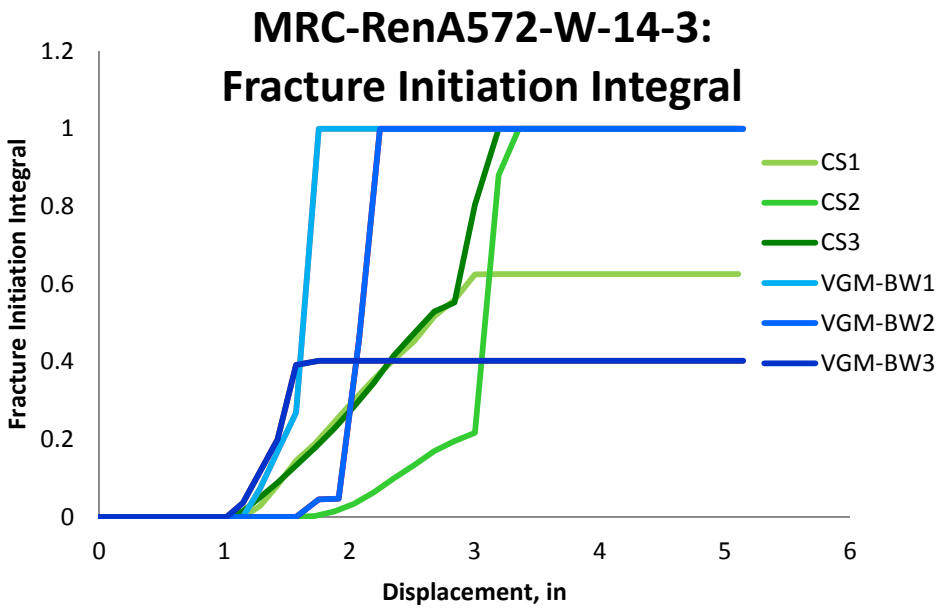

Figure 6.180: Variation of fracture initiation integral value with displacement for different elements laid out in the bolts of MRC-RenA572-W-14-3 specimen for the three finite element deletion strategies

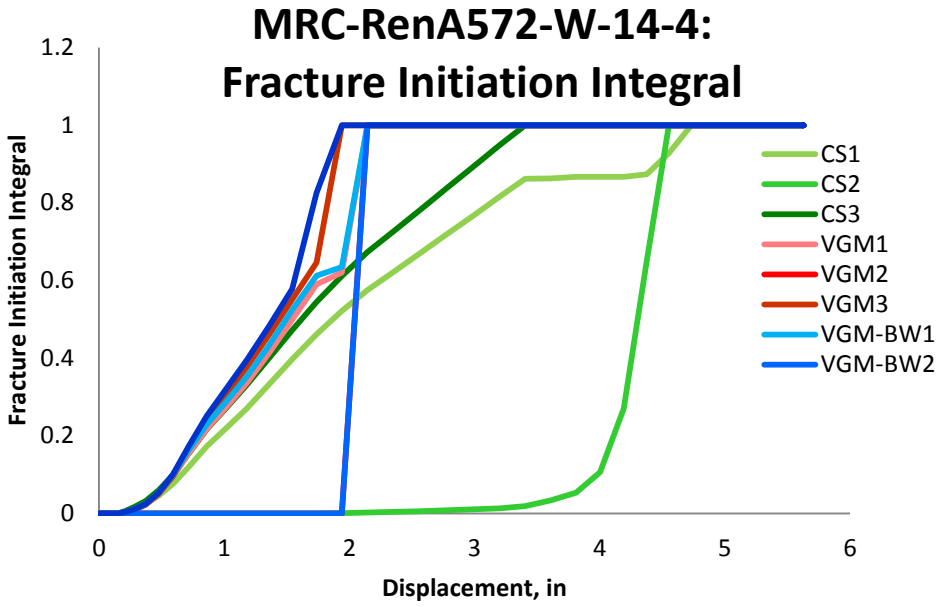

Figure 6.181: Variation of fracture initiation integral value with displacement for different elements laid out through the thickness of the tension flange of MRC-RenA572-W-14-4 specimen for the three finite element deletion strategies

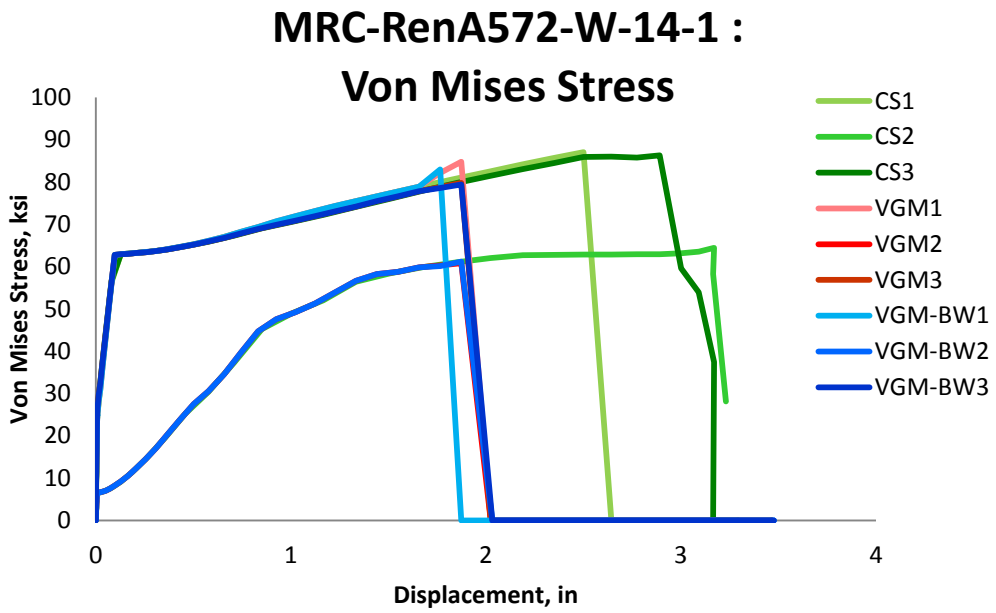

Figure 6.182: Variation of von Mises Stress with displacement for different elements laid out through the thickness of the tension flange of MRC-RenA572-W-14-1 specimen for the three finite element deletion strategies

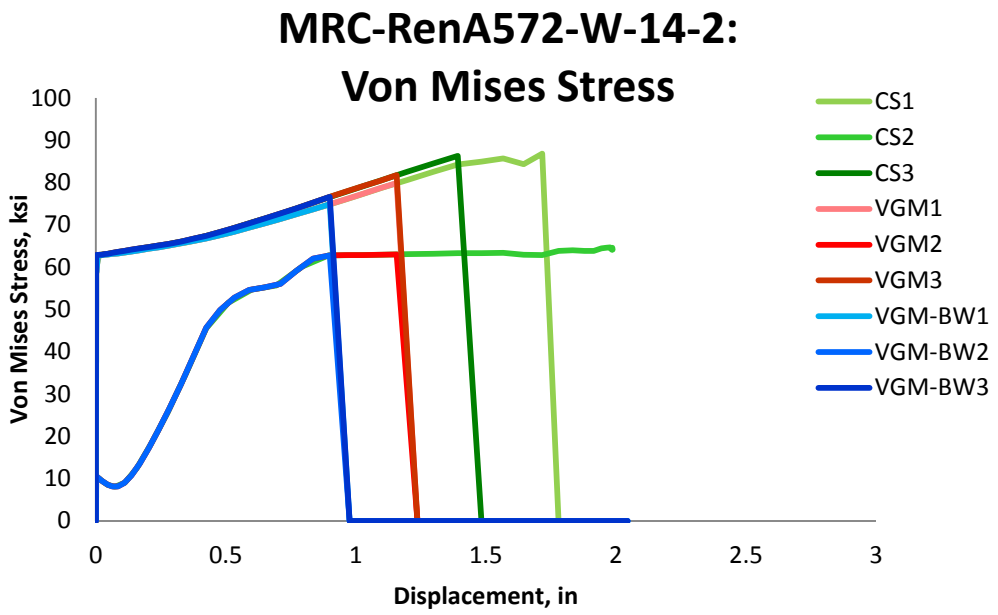

Figure 6.183: Variation of von Mises Stress with displacement for different elements laid out through the thickness of the tension flange of MRC-RenA572-W-14-2 specimen for the three finite element deletion strategies

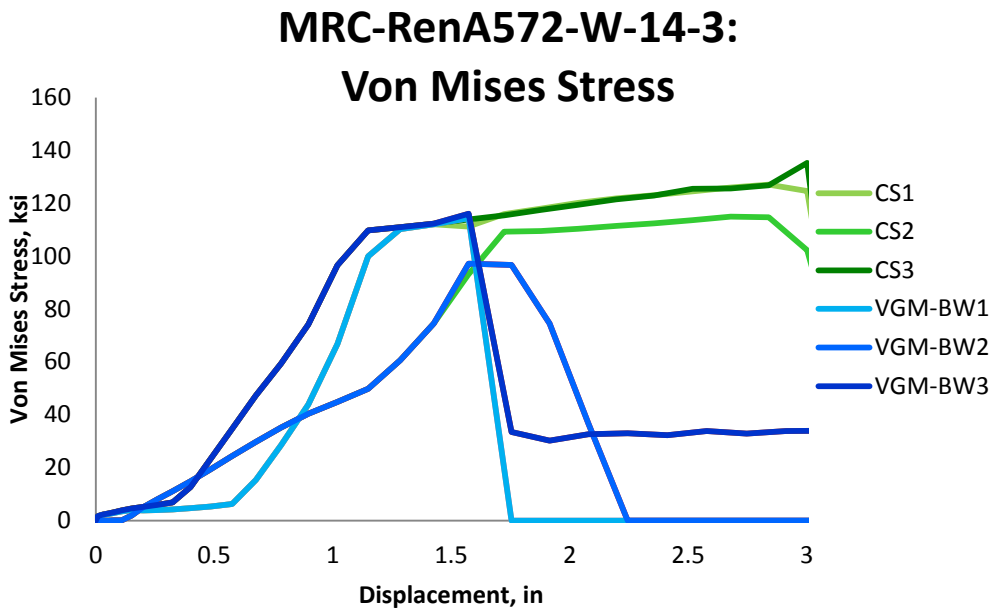

Figure 6.184: Variation of von Mises Stress with displacement for different elements laid out in the bolts of MRC-RenA572-W-14-3 specimen for the three finite element deletion strategies

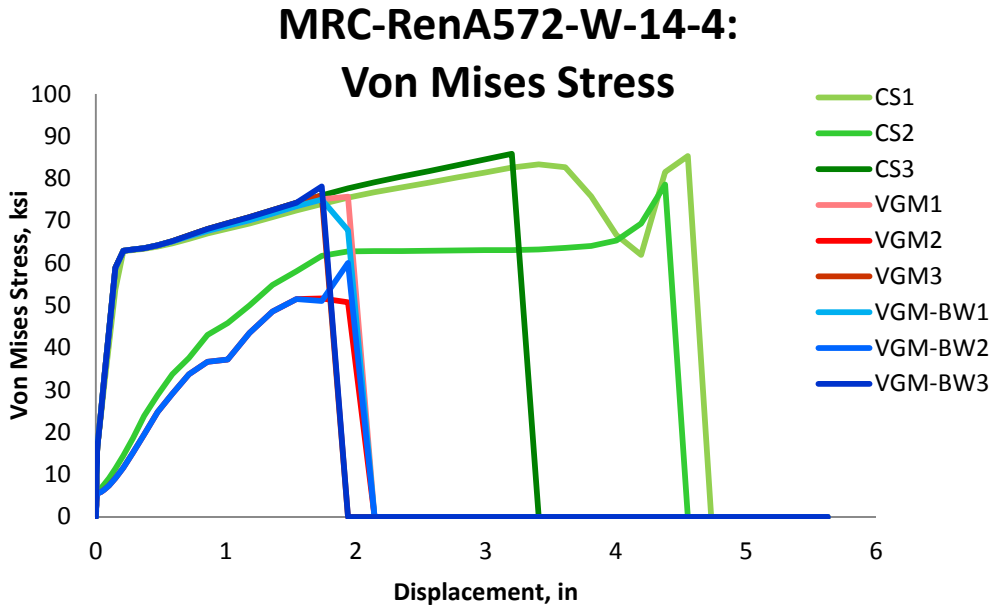

Figure 6.185: Variation of von Mises Stress with displacement for different elements laid out through the thickness of the tension flange of MRC-RenA572-W-14-4 specimen for the three finite element deletion strategies

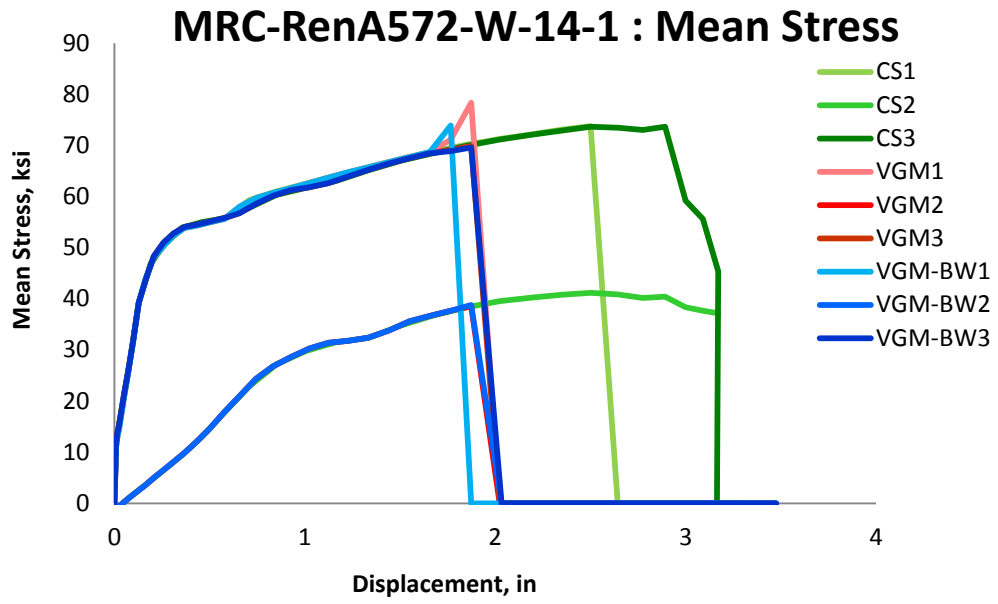

Figure 6.186: Variation of mean stress with displacement for different elements laid out through the thickness of the tension flange of MRC-RenA572-W-14-1 specimen for the three finite element deletion strategies

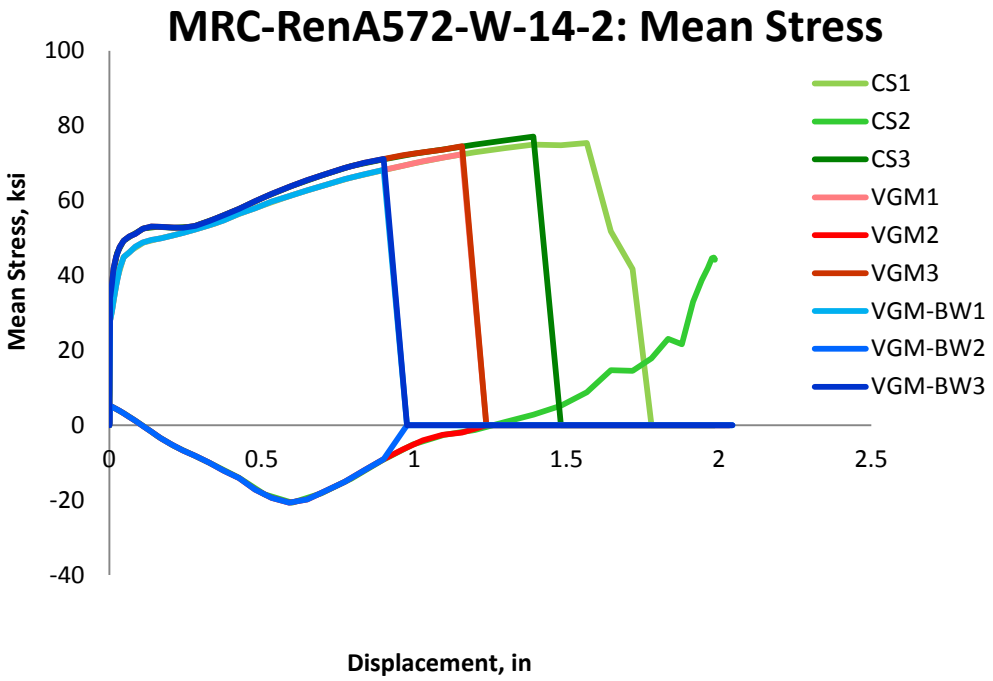

Figure 6.187: Variation of mean stress with displacement for different elements laid out through the thickness of the tension flange of MRC-RenA572-W-14-2 specimen for the three finite element deletion strategies

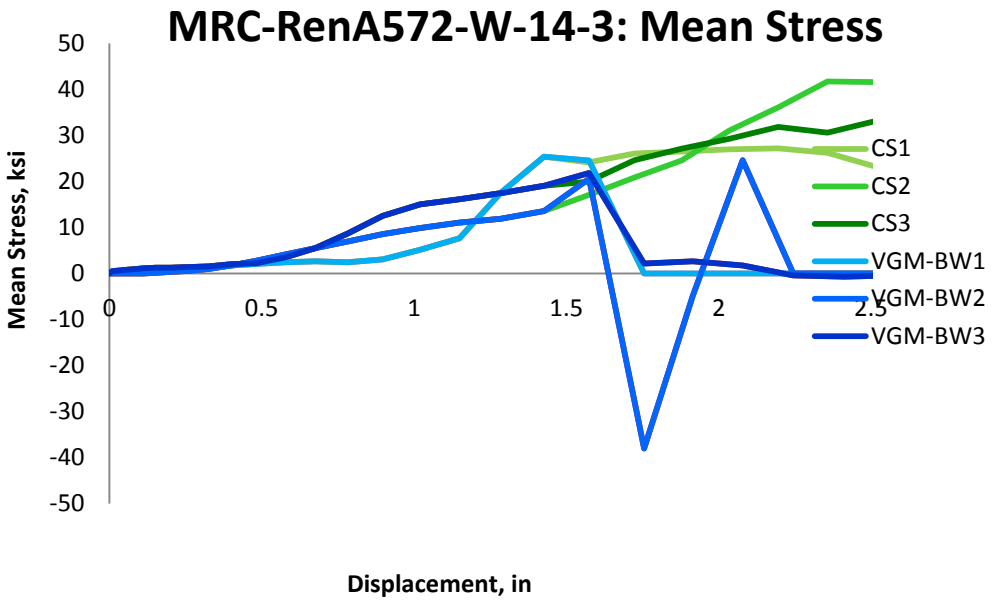

Figure 6.188: Variation of mean stress with displacement for different elements laid out in the bolts of MRC-RenA572-W-14-3 specimen for the three finite element deletion strategies

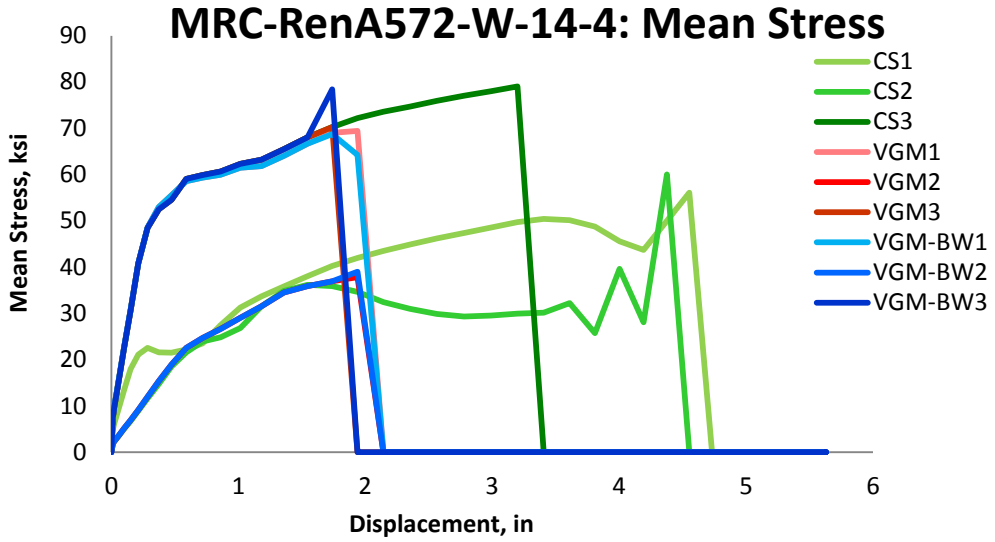

Figure 6.189: Variation of mean stress with displacement for different elements laid out through the thickness of the tension flange of MRC-RenA572-W-14-4 specimen for the three finite element deletion strategies

Figure 6.190, Figure 6.191, Figure 6.192, and Figure 6.193 show the variation of von Mises equivalent stress with equivalent plastic strain. For the MRC-RenA572-W-14-1 specimen, Figure 6.190 shows that the elements on the edges of the tension flange saw plastic behavior while the elements in the middle of the flange went from elastic behavior to fracture in the VGM and VGM-BW simulation. In the CS simulation the middle element saw very small amount of plasticity before failure. The elements on the flange edges in CS simulation achieved much larger equivalent plastic strain and strain energy than in the other two simulations. For the MRC-RenA572-W-14-2 specimen the edge elements experienced plastic behavior before fracture while the elements at the center of the flange went from elastic behavior to failure. In the VGM simulation the elements achieved higher equivalent plastic strain values than in the VGM-BW simulations. For the MRC-RenA572-W-14-3 specimen the elements in CS and VGM-BW simulations experienced a very gentle softening slope for the two bolts that fractured in each respective simulation. On the other hand, the top bolt in the VGM-BW simulation and the

bottom bolt in the CS simulation experienced a very steep softening slope. Most bolts in the two simulations experienced some plastic behavior with an exception of the middle bolt in the VM-BW simulation. In the MRC-RenA572-W-14-4 specimen the elements follow a similar von Mises stress versus equivalent plastic strain trend as MRC-RenA572-W-14-1 and MRC-RenA572-W-14-2 specimen for the three simulations. The elements located on the edges of the tension flange experienced significant plastic behavior while the elements located at the middle of the tension flange went from elastic behavior to failure.

The variation of the value of the damage variable is plotted in Figure 6.194, Figure 6.195, Figure 6.196, and Figure 6.197. The figures show that for the four specimens the slope of the damage variable is very steep. This signifies that the elements failed almost immediately after reaching the fracture initiation integral value of 1. This shows that these connections offer a lot of stiffness and constraint to plastic deformation of the material at critical locations.

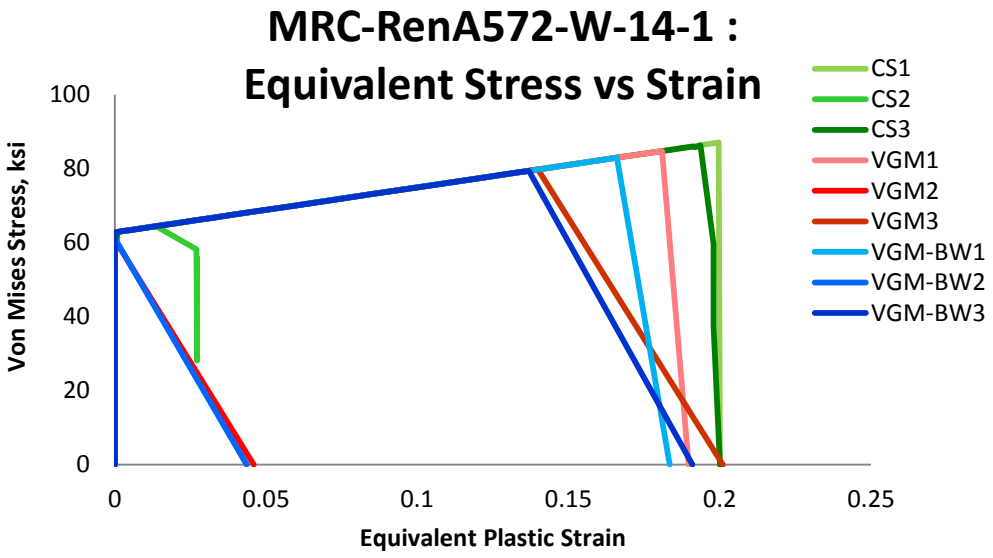

Figure 6.190: Variation of von Mises Stress with equivalent plastic strain for different elements laid out through the thickness of the tension flange of MRC-RenA572-W-14-1 specimen for the three finite element deletion strategies

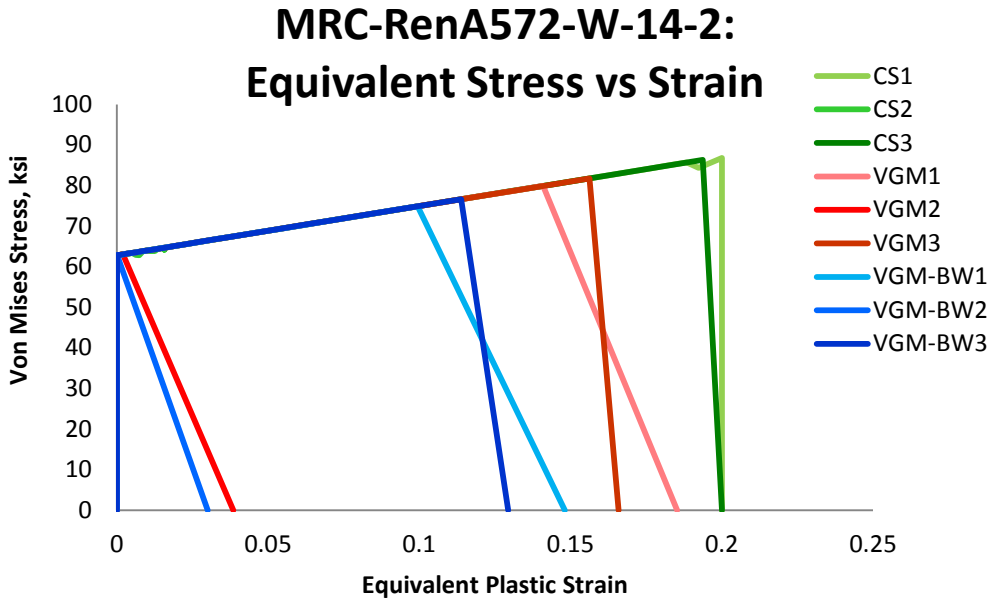

Figure 6.191: Variation of von Mises Stress with equivalent plastic strain for different elements laid out through the thickness of the tension flange of MRC-RenA572-W-14-2 specimen for the three finite element deletion strategies

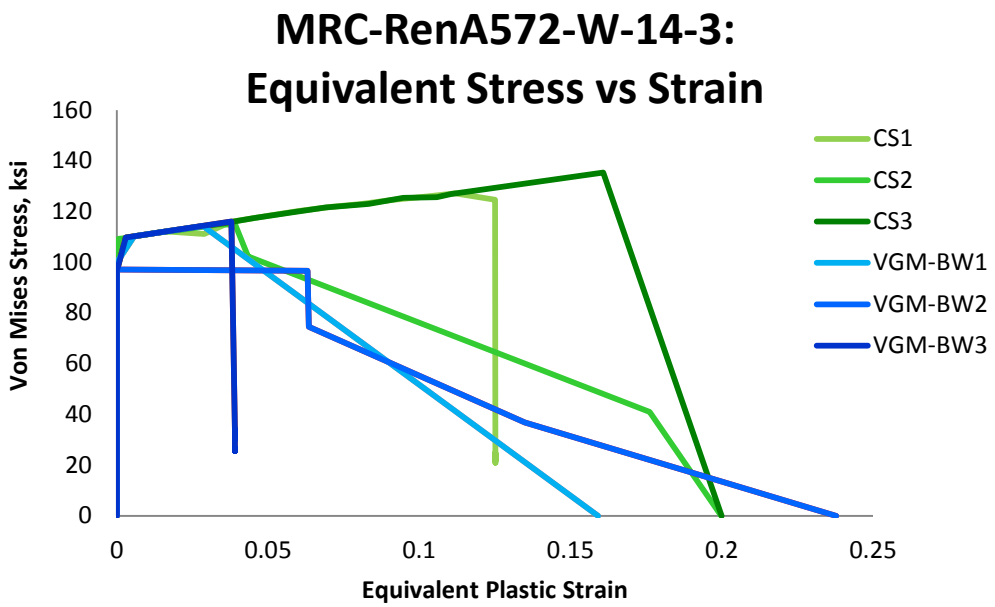

Figure 6.192: Variation of von Mises Stress with equivalent plastic strain for different elements laid out in the bolts of MRC-RenA572-W-14-3 specimen for the three finite element deletion strategies

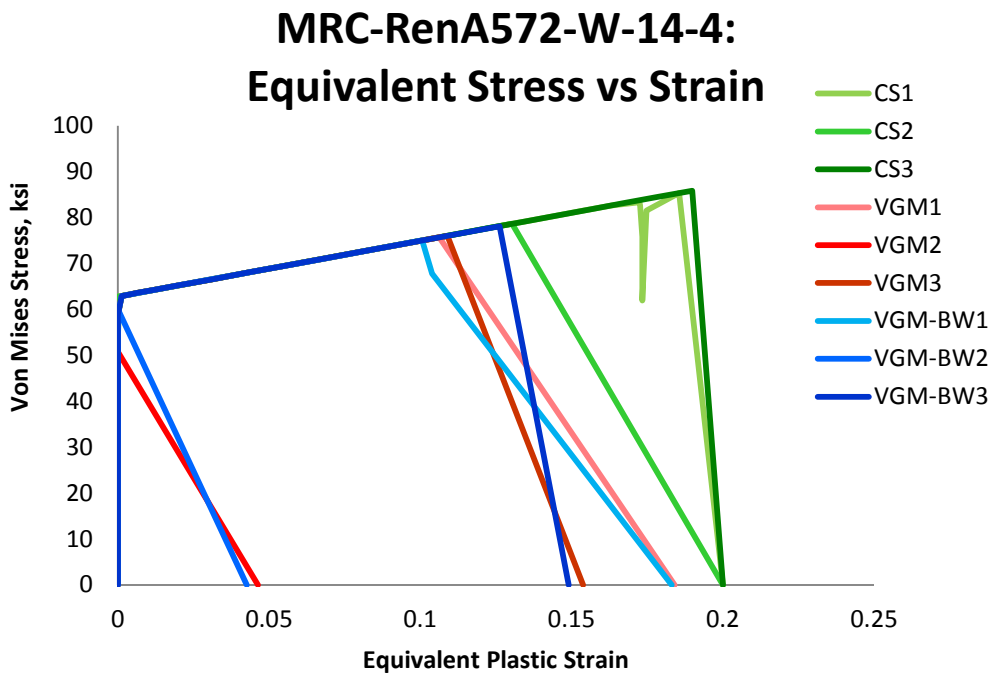

Figure 6.193: Variation of von Mises Stress with equivalent plastic strain for different elements laid out through the thickness of the tension flange of MRC-RenA572-W-14-4 specimen for the three finite element deletion strategies

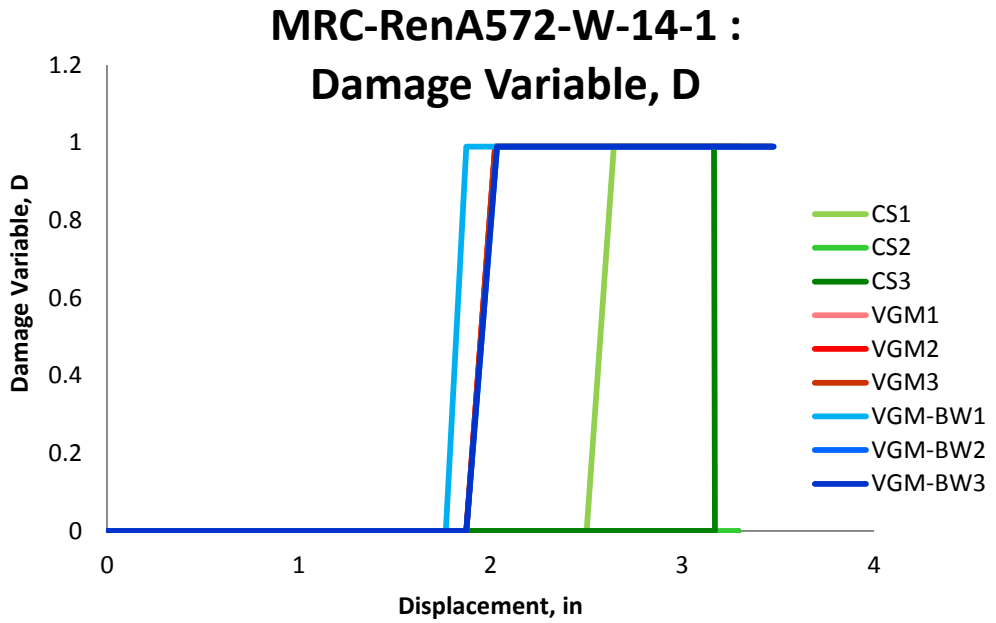

Figure 6.194: Variation of Damage Variable with displacement for different elements laid out through the thickness of the tension flange of MRC-RenA572-W-14-1 specimen for the three finite element deletion strategies

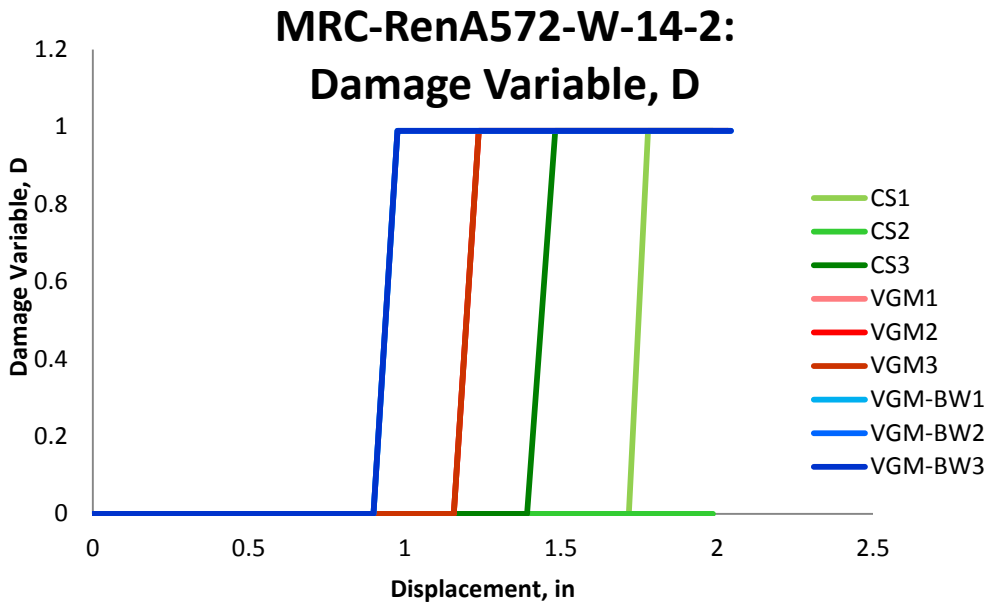

Figure 6.195: Variation of Damage Variable with displacement for different elements laid out through the thickness of the tension flange of MRC-RenA572-W-14-2 specimen for the three finite element deletion strategies

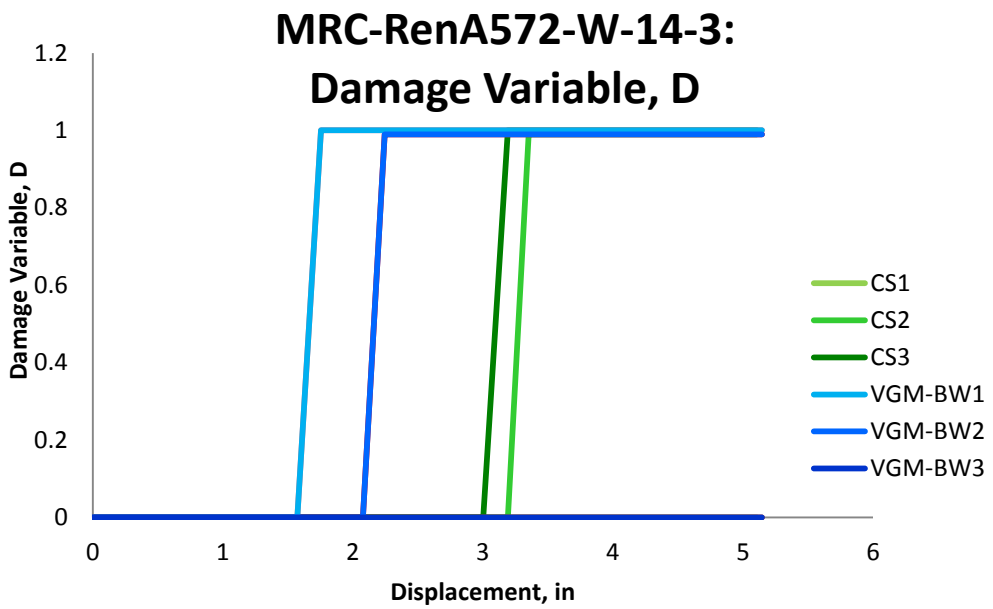

Figure 6.196: Variation of Damage Variable with displacement for different elements laid out in the bolts of MRC-RenA572-W-14-3 specimen for the three finite element deletion strategies

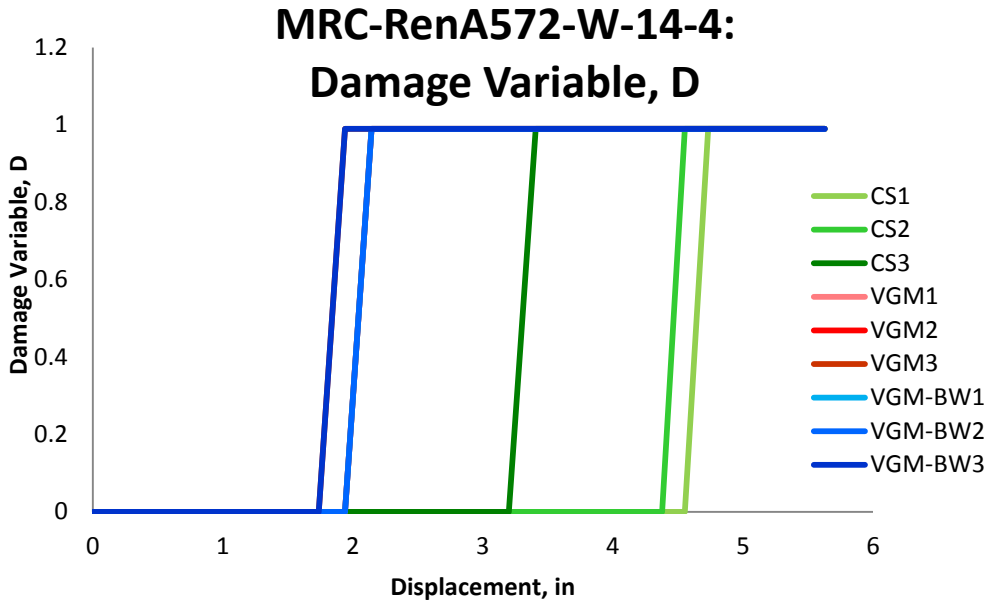

Figure 6.197: Variation of Damage Variable with displacement for different elements laid out through the thickness of the tension flange of MRC-RenA572-W-14-4 specimen for the three finite element deletion strategies

6.6.1 Summary

Structural steel A572 Grade 50 taken from a W-Section and ASTM A490 bolt material were validated through comparison to experimental test results of moment resisting connection specimens. The experimental work consisted of four full-scale beam-to-column web connection assemblages representing an exterior column. Each assemblage contained different geometries of welding and bolting the beam to the column. For specimen MRC-RenA572-W-14-1, in the experimental test the failure consisted of a tearing that propagated quickly across the entire width of the tension flange connection plate in the region of the transverse groove weld. In the VGM and VGM-BW simulations the failure occurred instantaneously in the tension flange in the weld. The CS simulation showed a type of fracture that is not reported in the experimental test

results. For specimen MRC-RenA572-W-14-2, in the experimental test fracture occurred at the weld connecting the beam flange to the column web. In the VGM and VGM-BW simulations the failure occurred quickly in the tension flange of the beam connecting to the column web. The fractures in the CS simulation at the beam flanges were not sudden like they were in the VGM and VGM-BW simulations and did not completely propagate through the flange thickness. In the experimental test of specimen MRC-RenA572-W-14-3, the fracture occurred in the tension flange connection plate. In the VGM and VGM-BW simulations the failure occurred in the bolts in the tension flange and the web of the beam. In the CS simulation the first bolt of sever was the one connecting the beam web to the connector plate located at the top right below the compression flange. This does not coincide with experimental test results. The failure of MRC-RenA572-W-14-4 was determined by large beam deflections and no fracture was reported. In the VGM and VGM-BW simulations the failure occurred instantaneously in the tension flange of the beam connecting to the insert tension flange and propagated very quickly through the weld connecting the beam web and the web of the insert. In the CS simulation the fracture started at a corner of a tension and compression flange at the same time.

Overall, it could be said that VGM most closely captures the location of fracture initiation and its subsequent propagation even throughout a complicated connection specimen. In addition, VGM captures the force-displacement behavior fairly well. The reason for underpredicting is most like due the absence of a CNT specimen with a higher notch radius like 0.25 inches to calibrate to the lower triaxiality region. This material only had two different notch sized specimens for the PSO to calibrate the VGM parameters. The VGM-BW simulation underpredicts the force-displacement capacity and sometimes allows for non-physical fracture

to occur. However the triaxiality range in these specimens is such that VGM captures it well and VGM-BW is not needed. The CS cannot locate or capture the fracture propagation accurately but for these specimens it predicts the force-displacement behavior satisfactorily with some overprediction. In addition, the following observations were made:

- The tension flange experiences a variation of triaxiality through its thickness. While the edges of the flange see significant plastic behavior, the middle of the flange goes from elastic behavior to failure due to the high constraint.
- Fracture occurs suddenly across the tension flange of a moment resisting connection

6.7 NIST Welded Unreinforced Flange-Bolted Web Connection and Reduced Beam Section Subassemblage

The three finite element deletion strategies were also validated through comparison to welded unreinforced flange-bolted web (WUF-B) and reduce beam section (RBS) beam-column sub-assemblages. (Sadek et al. 2010) conducted an experimental and computational study to investigate the behavior of steel moment connections under scenarios in which a column is removed due to an extreme event. A series of subassemblages were tested by applying vertical axial compression load to a column that lacked support at its bottom end and that was connected on either side to girders using either WUF-B or RBS moment connections (Sadek et al. 2010). The girders were also connected to supporting columns at their far ends by using the

WUF-B and RBS connection, respectively (Sadek et al. 2010). The testing continued until fracture occurred at the connection ends and significant load-carrying capacity of the connections was lost. The connections were designed to meet seismic design criteria (Sadek et al. 2010). Two types of steels were used, A992 for beams, columns, and doubler plates, and A36 for shear tabs and continuity plates (Sadek et al. 2010). The WUF-B connection used ASTM A490 bolts. The edge columns were braced to prevent them deflecting into the center. Lateral support was provided to beams at midspan and center column at its bottom (Sadek et al. 2010). Due to an actuator stroke length of 20 inches the WUF-B and RBS connections required an unloading and readjustment of the actuator for reloading (Sadek et al. 2010). The experimental test setup is shown in Figure 6.198. For finite element simulations, a minimum of 2 elements through thickness was maintained with maximum allowable element size ranging from 0.2 inches near the critical areas to 2 inches in regions far away from the connection region. The data point inputs into the plasticity and fracture models are shown in Table 6.11 and Table 6.12. In the experimental test of the WUF-B connection, the beam top flange near the center column buckled first, then a shear failure of the lowest and middle bolts occurred, and finally fracture of the bottom beam flange near the center column occurred (Sadek et al. 2010). This damage is shown in Figure 6.199. In the CS simulation, the WUF-B sub-assemblage fracture originated from the center of the bottom weld access hole and quickly propagating outward through the tension flange section. The compression flange did not buckle and only the lowest bolt fractured with some damage visible in the other two bolts. In the VGM simulation the failure sequence followed that of the experiment. The compression flange first buckled. Then the lower bolt severed followed by the middle bolt and then the top bolt. After this fracture

initiated at the center of the bottom weld access hole and propagated outward through the thickness of the flange. The fracture initiation and propagation for CS and VGM simulations are shown in

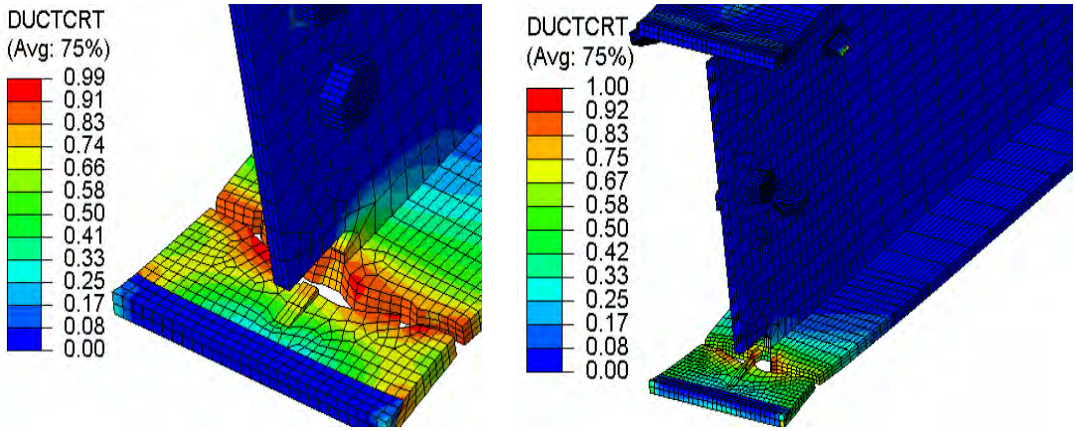

Figure 6.200. In the VGM-BW simulation, the buckling of the compression flange occurred first. Then fracture initiated at the lowest bolt. After this, the second and the top bolt severed. This was accompanied with fracture initiating at the center of the bottom weld access hole. At the same time the edges of the tension flange fractured. Afterwards the fracture at the center of weld access hole propagated outwards through the tension flange. The fracture initiation and propagation for VGM-BW simulation is shown in Figure 6.201. In Figure 6.201, it looks as if the bolts did not sever, but they are completely severed on the other side of the beam web. In the experimental testing of RBS sub-assemblage fracture first occurred at the bottom beam flange in the middle of the reduced section and then propagated until the specimen could no longer carry the applied load (Sadek et al. 2010). This damage pattern was repeated in all three simulations. The fracture initiated at the edges for the VGM-BW and at the center for CS and VGM simulations of the tension flange right below the web and propagated outward through the flange and upward through the web. The crack through the tension flange was straight for CS and VGM simulations and at an angle to the longitudinal direction of the beam in the VGM-

BW simulation. In addition, in the CS simulation, the crack propagated through more than half the web height while in VGM and VGM-BW simulations the upward propagation was smaller. The fracture initiation and propagation for the RBS specimen is shown in g of the tension flange (right)

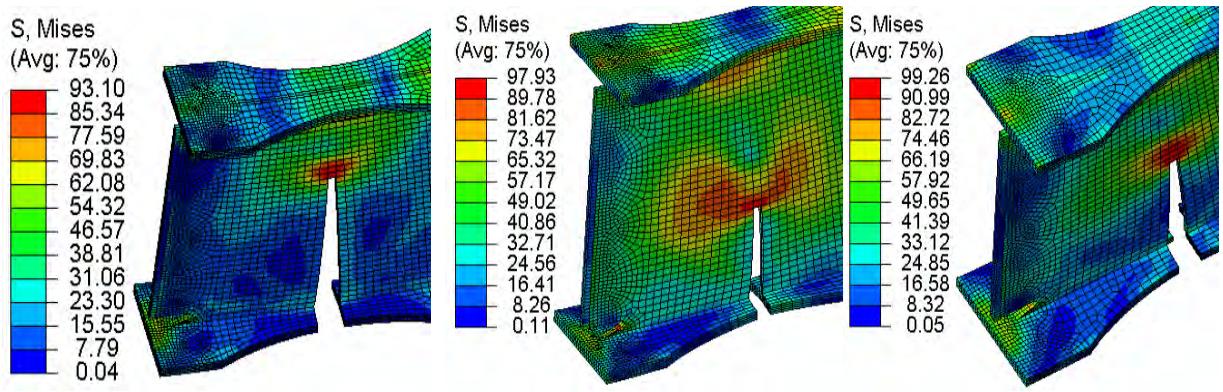

Figure 6.202.

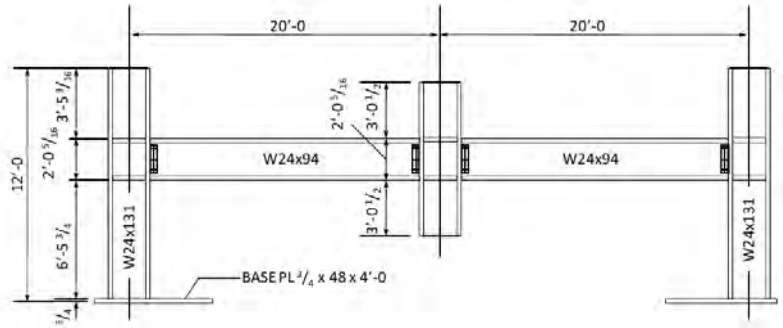

Figure 6.198: Experimental setup for specimens WUFB-SadA992-W-1 and RBS-SadA992-W-1

Figure 6.199: Fractured WUFB-SadA992-W-1 (left) and RBS-SadA992-W-1 (right) specimens (Sadek et al. 2010)

Table 6.11: Plasticity and fracture model inputs for WUFB-SadA992-W-1 specimen

		Fracture Model Input		
Part	**Plasticity Model Input**	**VGM**	**VGM-BW**	**CS**
Continuity Plate	CNT-MyeA36-B-A	CNT-MyeA36-B-A	TC-MyeA36-B-A	0.2
Bolt	Bolt-SadA490-B-A	Bolt-SadA490-B-A	Bolt-SadA490-B-A	0.2
Beam	TC-SadA992-W-W-A	CNT-KanA572-W-L-A	TC-KanA572-W-L-A	0.2
Column	TC-SadA992-Col-F-A	CNT-KanA572-W-L-A	TC-KanA572-W-L-A	0.2
Weld	TC-MyeE70-T6-W-T-A	LPT-NgE70T-8K6-P-A	TC-NgE70T-8K6-P-A	0.2

Table 6.12: Plasticity and fracture model inputs for RBS-SadA992-W-1 specimen

		Fracture Model Input		
Part	**Plasticity Model Input**	**VGM**	**VGM-BW**	**CS**
Continuity Plate	CNT-MyeA36-B-A	CNT-MyeA36-B-A	TC-MyeA36-B-A	0.2
Doubler Plate	CNT-MyeA36-B-A	CNT-MyeA36-B-A	TC-MyeA36-B-A	0.2
Beam	TC-SadA992-W-W-A	CNT-KanA572-P-A	TC-KanA572-P-A	0.2
Column	TC-SadA992-Col-F-A	CNT-KanA572-P-A	TC-KanA572-P-A	0.2
Weld	TC-NgE70T-7K2-P-A	LPT-NgE70T-8K6-P-A	TC-NgE70T-8K6-P-A	0.2

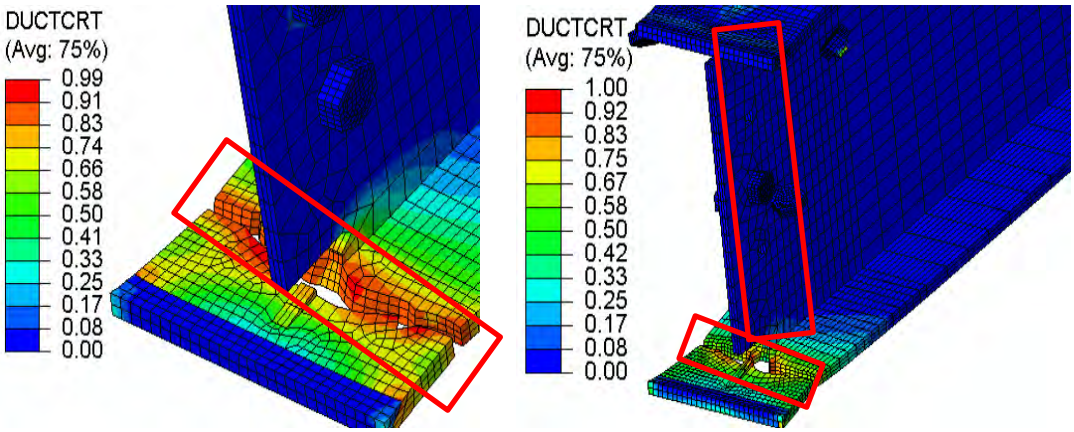

Figure 6.200: Simulation results (Sadek et al. 2010) WUFB-SadA992-W-1 specimen with contours representing fracture initiation integral: CS (left), VGM (right)

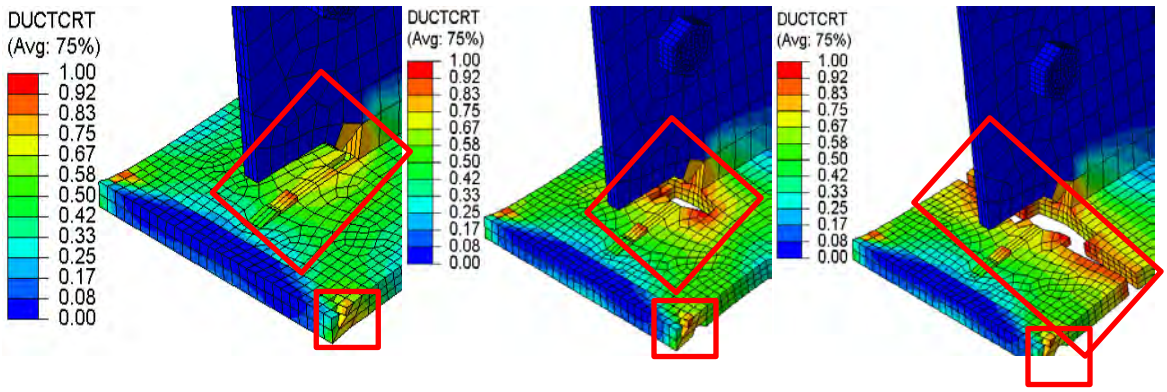

Figure 6.201: Simulation results (Sadek et al. 2010) WUFB-SadA992-W-1 specimen with contours representing von Mises stress (ksi): VGM-BW fracture initiation (left), VGM-BW intermediate fracture (middle), VGM-BW severing of the tension flange (right)

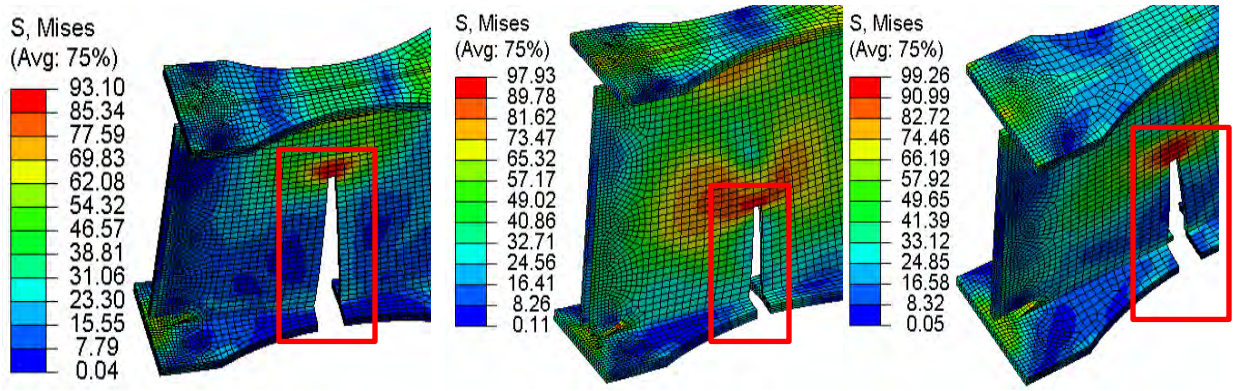

Figure 6.202: Simulation results (Sadek et al. 2010) RBS-SadA992-W-1 specimen with contours representing von Mises stress (ksi): CS (left), VGM (middle), VGM-BW (right)

Figure 6.203 and Figure 6.204 show the force-displacement plot for the WUF-B and RBS sub-assemblage specimens. In the specimens, the VGM simulation attained results that match closely with the experimental test results capturing the force value throughout the loading at the correct displacement for the WUF-B and RBS sub-assemblage specimens. For the WUF-B sub-assemblage specimen the VGM-BW and CS initiated fracture too soon which prevented them to capture properly the unloading of the sub-assemblage. In the RBS specimen the VGM-

BW simulation underestimated the capacity of the sub-assemblage but the results are still judged to be acceptable. However, the CS simulation severely underestimated the force-displacement capacity of the RBS sub-assemblage specimen. Figure 6.205 and Figure 6.206 show the selected elements in the WUF-B and RBS sub-assemblages for which a detailed description is provided on the variation of fracture initiation and propagation parameters in elements that are located through the thickness of the specimens for the three finite element deletion strategies.

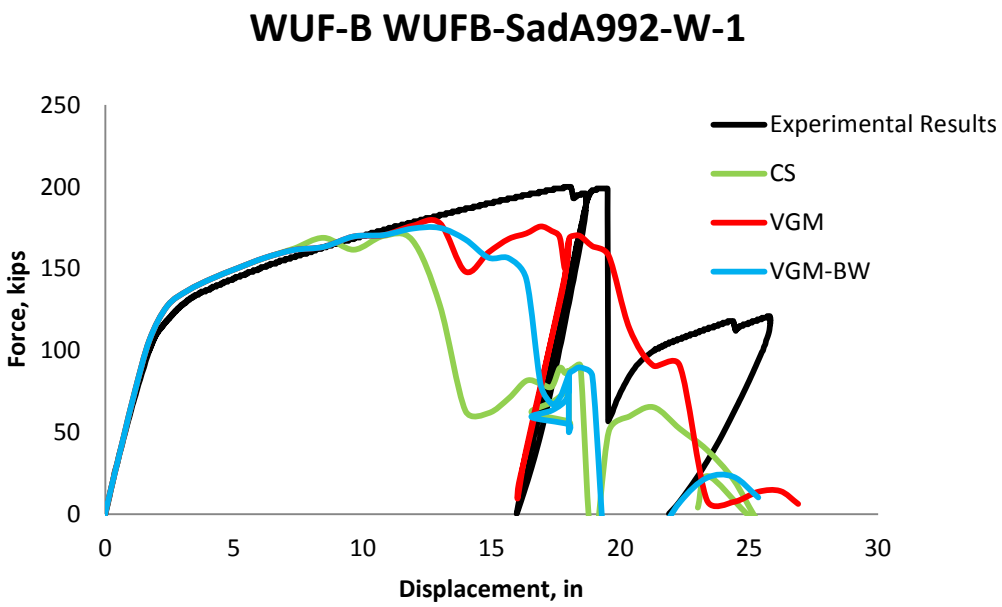

Figure 6.203: Force versus displacement validation results for WUF-B WUFB-SadA992-W-1 specimen

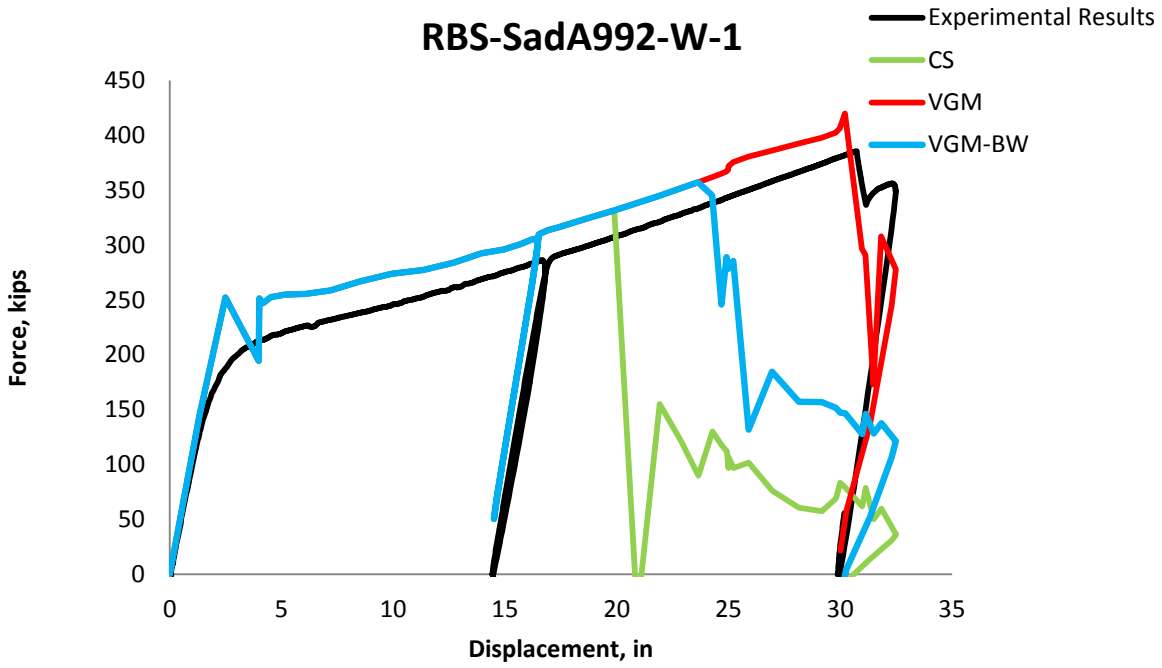

Figure 6.204: Force versus displacement validation results for a RBS RBS-SadA992-W-1 specimen

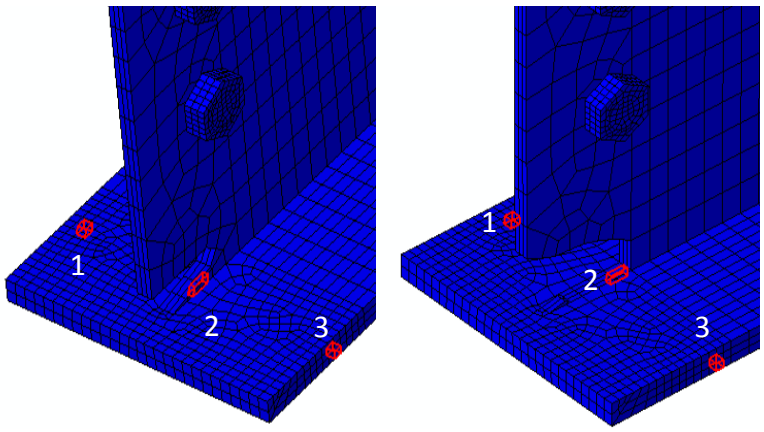

Figure 6.205: Elements selected for studying fracture initiation and propagation parameters in CS and VGM (left), and VGM-BW (right) simulations of WUFB-SadA992-W-1 specimen with some elements removed from visualization to improve clarity

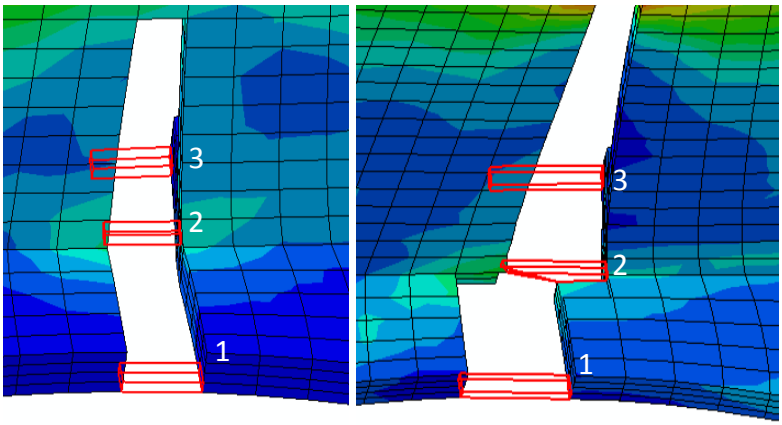

Figure 6.206: Elements selected for studying fracture initiation and propagation parameters in CS and VGM (left), and VGM-BW (right) strategies in RBS-SadA992-W-1 specimen located at the center of the reduce beam section

Triaxiality is plotted versus displacement for the three elements across the thickness of the tension flange of the WUF-B and RBS sub-assemblage specimens for the three finite element deletion strategies in Figure 6.207 and Figure 6.208. In the WUF-B specimen, after the initial spike, the triaxiality levels off and remains constant for the three elements in the three simulations with an exception of element 2 in VGM-BW simulation which has a constant decrease in the triaxiality value. Most elements experienced a spike in triaxiality before failure. In the RBS specimen, the triaxiality is exactly the same throughout the loading excursion until the point of softening for the three finite element deletion strategies. After this point the value of triaxiality is different for the three strategies. Only the middle element experiences an increase in triaxiality before failure in the VGM-BW simulation while no other element experiences similar increase before softening in the other two simulations. During the unloading, the triaxiality for the three elements in the three simulations goes negative due to a change from tensile to compressive loading.

The equivalent plastic strain is plotted in Figure 6.209 and Figure 6.210 for WUF-B and RBS sub-assemblage specimens, respectively. For the WUF-B specimen the elements in the CS and VGM-BW simulations reached approximately the same equivalent plastic strain values. The elements in VGM simulation reached much greater strain value than in the other two simulations. It is interesting to note that for the WUF-B the middle element had a higher slope of equivalent plastic strain to displacement value than the elements located at the edges of the tension flange. This is most likely due to the weld access hole, which keeps the triaxiality lower than it would have been without it throughout the loading process as seen in the moment connection simulations of the previous section. Figure 6.210 show that the VGM simulations of RBS sub-assemblage reached the highest strain values and CS the lowest in the chosen elements. For the RBS specimen the two elements on the edges of the flanges follow the same path until softening initiation in the three simulations while the middle elements all follow a different path. The flat plateau in the middle of the plot is due to the elastic unloading.

The fracture locus is plotted in Figure 6.211 and Figure 6.212 for WUF-B and RBS sub-assemblage specimens, respectively. In the WUF-B sub-assemblage specimen the triaxiality range is fairly small during the time with the elements are experiencing plastic hardening. During softening the elements experience more of a divergence from each other. Elements in the VGM simulation experience an increase in the value of triaxiality with increase of equivalent plastic strain signifying that the specimen was not able to deform quickly enough to keep the triaxiality constant. The triaxiality ranges from approximately 0.4 to 0.6. In the RBS specimen the triaxiality range for the three elements in the three simulations is very small, ranging from 0.34 to 0.4. In addition, the triaxiality remains virtually constant with a near vertical equivalent

plastic strain growth. The plot does not show any softening in the three elements for the three simulations signifying that the fracture was sudden and that it propagated quickly signifying that fracture criteria was satisfied for the entire flange at the same time. The first two horizontal plateaus represent the elastic unloading of the RBS specimen. It is interesting to note that the elements in the WUF-B specimen have a much wider spread in the fracture locus plane than elements in the RBS specimen, which signifies that the RBS specimen was able to adjust to the loading by deforming better than WUF-B.

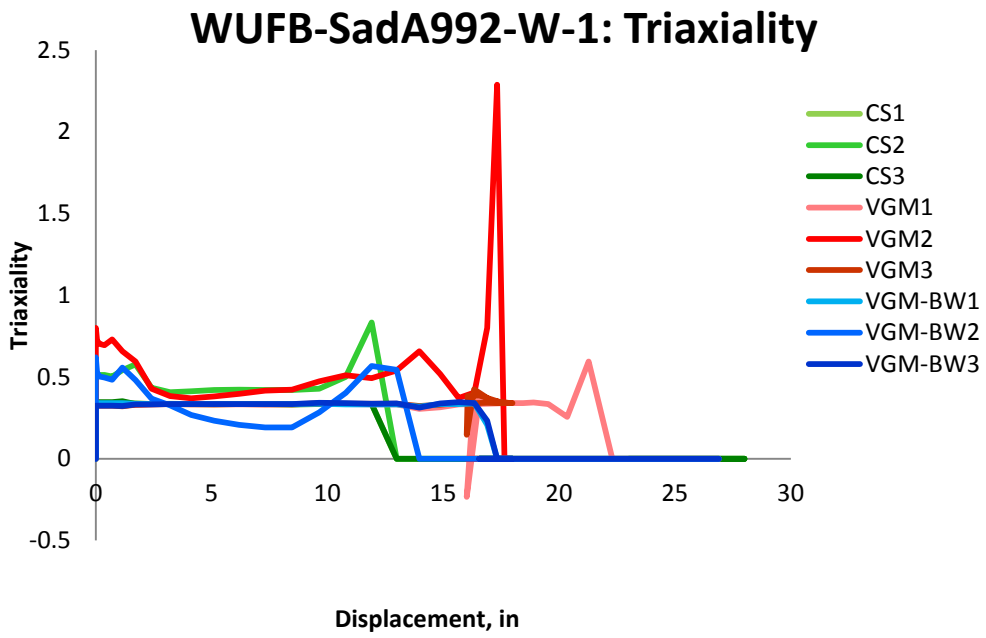

Figure 6.207: Variation of triaxiality with displacement for different elements laid out through the thickness of the tension flange of WUFB-SadA992-W-1 specimen for the three finite element deletion strategies

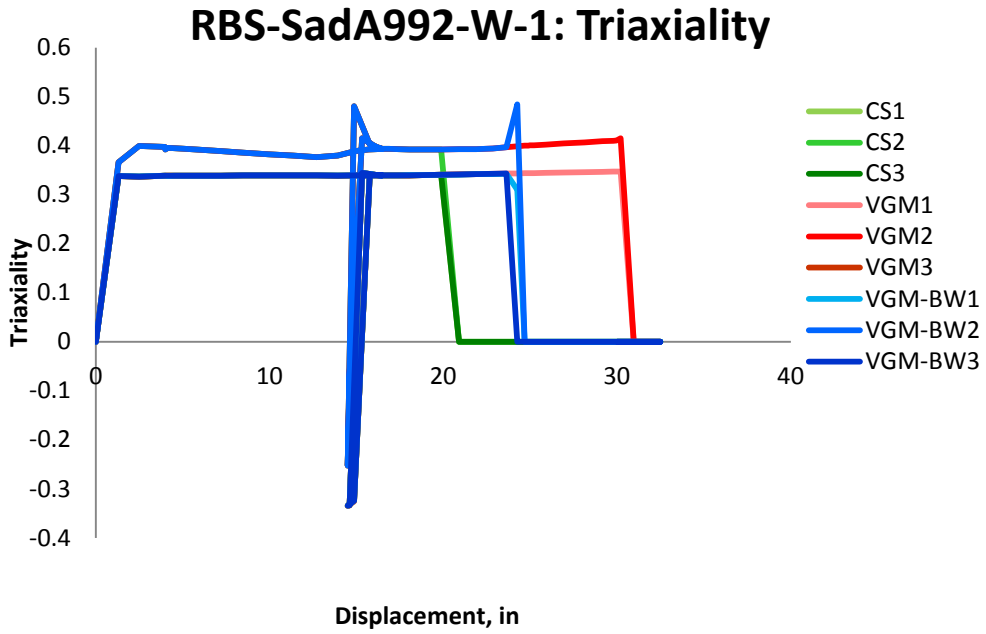

Figure 6.208: Variation of triaxiality with displacement for different elements laid out through the thickness of the tension flange of RBS-SadA992-W-1 specimens for the three finite element deletion strategies

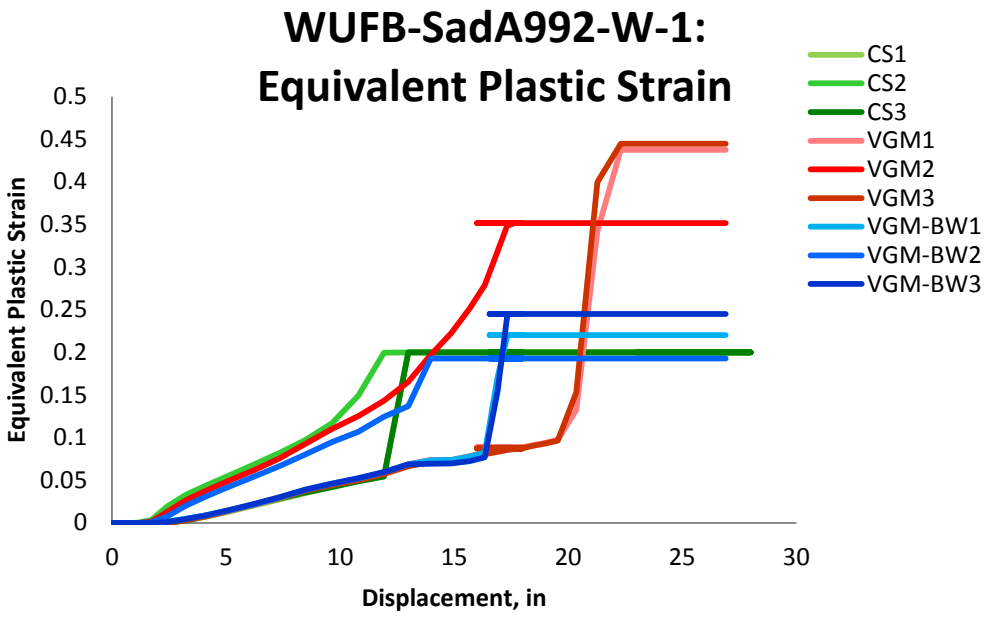

Figure 6.209: Variation of equivalent plastic strain with displacement for different elements laid out through the thickness of the tension flange of WUFB-SadA992-W-1 specimen for the three finite element deletion strategies

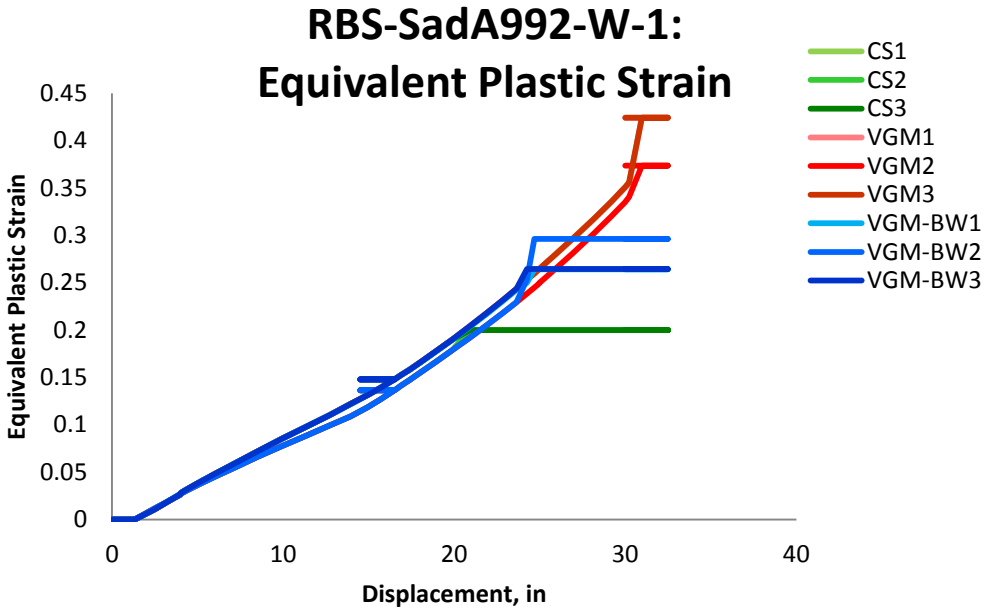

Figure 6.210: Variation of equivalent plastic strain with displacement for different elements laid out through the thickness of the tension flange of RBS-SadA992-W-1 specimens for the three finite element deletion strategies

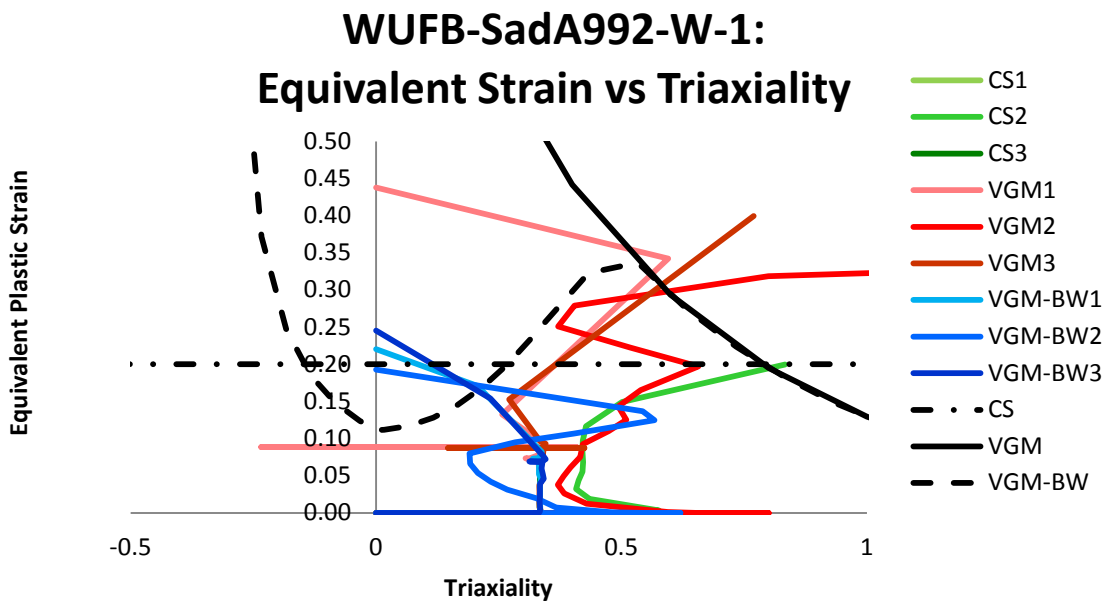

Figure 6.211: Variation of equivalent plastic strain with triaxiality for different elements laid out through the thickness of the tension flange of WUFB-SadA992-W-1 specimen for the three finite element deletion strategies

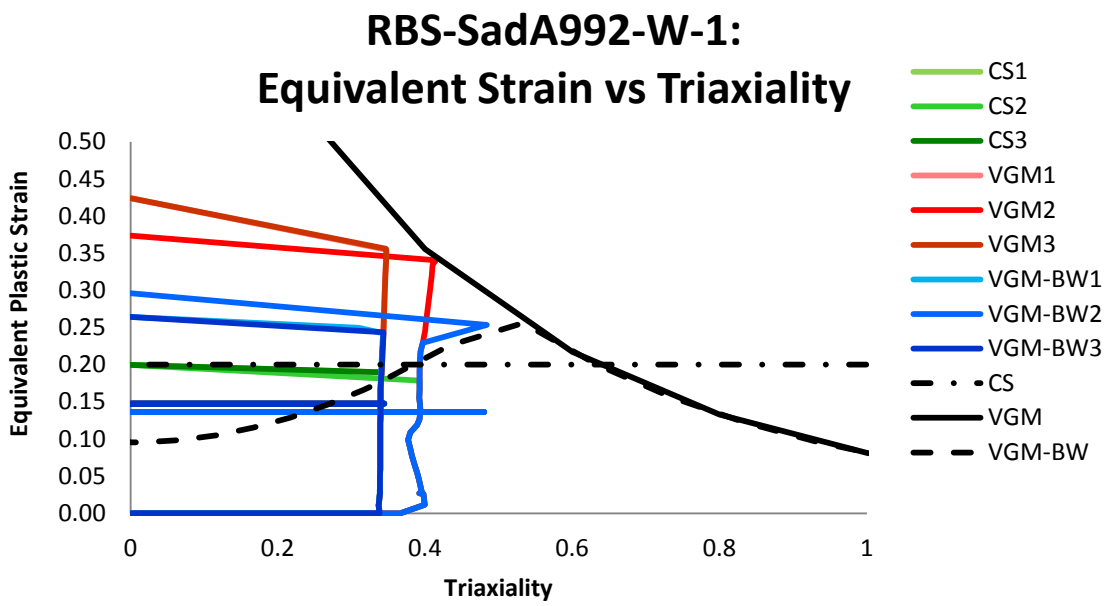

Figure 6.212: Variation of equivalent plastic strain with triaxiality for different elements laid out through the thickness of the tension flange of RBS-SadA992-W-1 specimens for the three finite element deletion strategies

The variation of the value of fracture initiation integral is shown in Figure 6.213 and Figure 6.214 for the WUF-B and RBS sub-assemblage specimens, respectively. In the WUF-B and RBS specimens the three simulations have different curves for the elements. The VGM simulation has the least slope in its curves while the CS simulation has the highest slope. This reflects the fracture initiation locus with VGM having the highest and the CS having the lowest equivalent plastic strain at fracture initiation in this perticular triaxiality range. In the simulations of WUF-B the elements located on the edges of the tension flange experience a smaller slope throughout the loading process with almost immediate initiation of softening afterwards. This is due to bolt fracture after which the demand on the edge elements in the flange increases. The middle element located in the tension flange right below the weld access hole has a higher slope and smoother curve throughout the loading process. This is different in the RBS specimen where the middle element has smaller slope that the other elements for the CS and VGM-BW

simulation but not for VGM simulation. The small plateaus in the middle signify the elastic unloading of the RBS specimen.

The varition of von Mises stress with displacement is shown in Figure 6.215 and Figure 6.216 for the WUF-B and RBS sub-assemblage specimens, respectively. In the WUF-B specimen, the three elements in the VGM-BW and CS simualtions and the middle element in the VGM simulation fail before the unloading of the specimen. The sharp fall of von Mises stress for VGM-BW and VGM simulation is related to the fracture of the bolts. In the RBS specimen, the three elements in the three finite element deletion strategies follow the approximately the same von Mises stress path with displacement with an exception for the inner and edge elements in VGM-BW simulation during softening. The edge element failed before the other edge element and the middle element. This signifies that in the VGM-BW simulation fracture initiated at an edge and propageted through the whole flange thickness fairly quickly. For the VGM and CS simulation all elements failed at the same displacement signifying sudden crack through flange thickness.

The mean stress variation through the loading excursion is plotted in Figure 6.217 and Figure 6.218 for the WUF-B and RBS sub-assemblage specimens, respectively. In the WUF-B and RBS specimens the edge elements and the middle element follow distinctive paths for the three simulations. For the WUF-B specimen the mean stress value for the edge elements is higher than for the middle element throughout the loading process for the VGM and CS simulations but not for VGM-BW simulation. In addition, the middle elements experience an increase in mean stress value right before failure while the edge elements due not in the three simulations. The mean stress in the middle element is higher than in the edge elements in the three

simulations for the RBS speciment. Only the middle element in the VGM-BW simulation experiences an increase before softening. In addition, the edge elements do experience a compressive mean stress during elastic unloading. Overall, the curves for the RBS specimen simualtions resemble the triaxiality variation with displacement but not so much for the WUF-B specimen. This shows that the mean stress had a pronounced effect on the triaxiality of the chosen elements in the three simulaitons for the RBS speicmen.

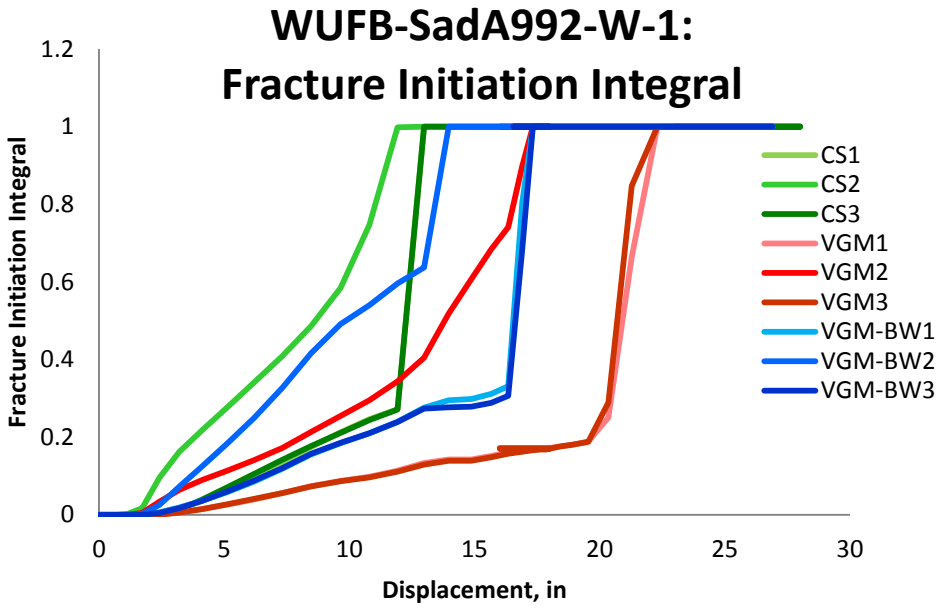

Figure 6.213: Variation of fracture initiation integral value with displacement for different elements laid out through thickness of the tension flange of WUFB-SadA992-W-1 specimen for the three finite element deletion strategies

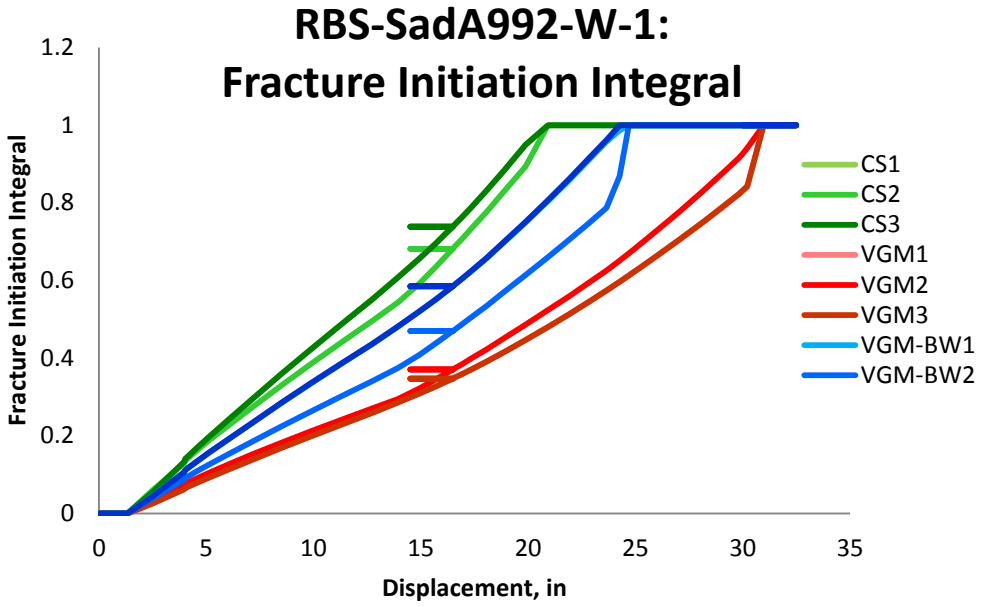

Figure 6.214: Variation of fracture initiation integral value with displacement for different elements laid out through the thickness of the tension flange of RBS-SadA992-W-1 specimens for the three finite element deletion strategies

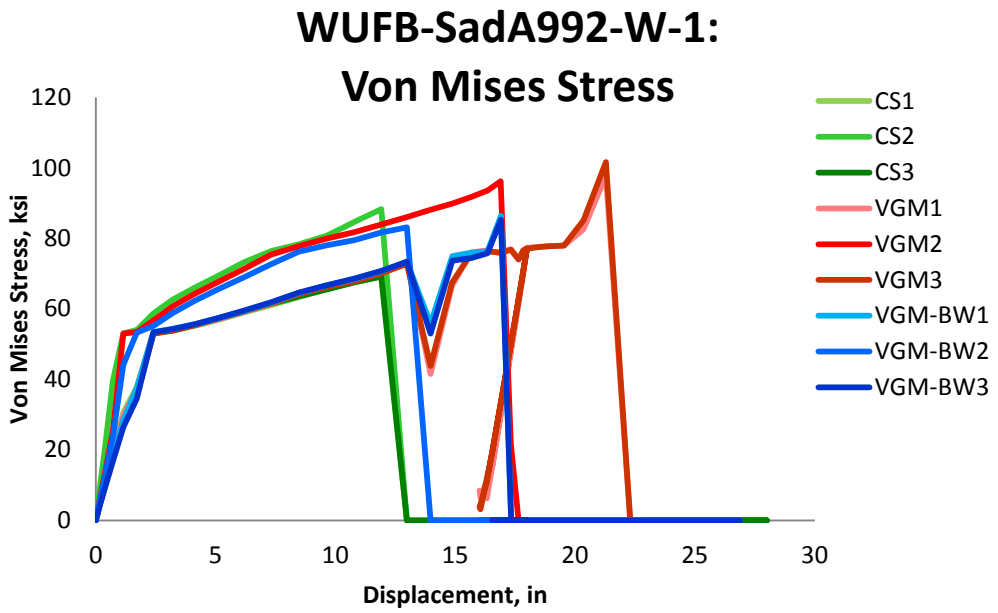

Figure 6.215: Variation of von Mises Stress with displacement for different elements laid out through the thickness of the tension flange of WUFB-SadA992-W-1 specimen for the three finite element deletion strategies

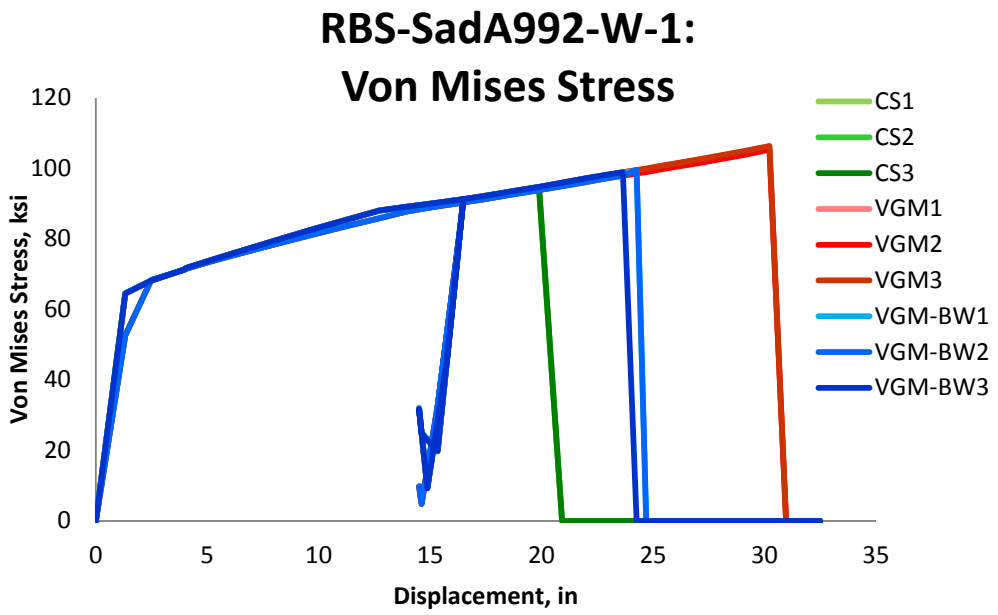

Figure 6.216: Variation of von Mises Stress with displacement for different elements laid out through the thickness of the tension flange of RBS-SadA992-W-1 specimens for the three finite element deletion strategies

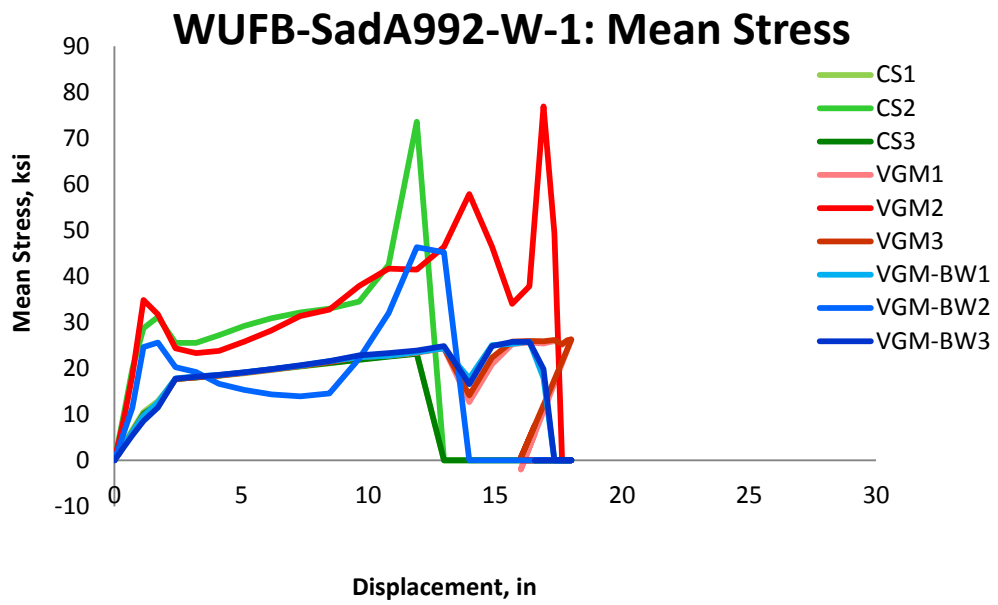

Figure 6.217: Variation of mean stress with displacement for different elements laid out through the thickness of the tension flange of WUFB-SadA992-W-1 specimen for the three finite element deletion strategies

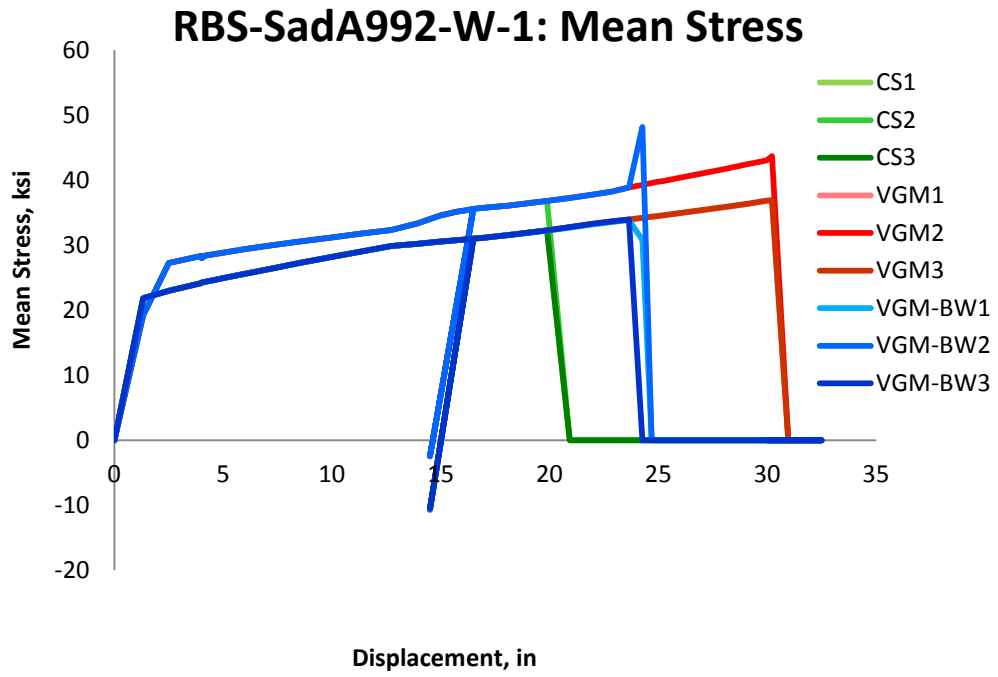

Figure 6.218: Variation of mean stress with displacement for different elements laid out through the thickness of the tension flange of RBS-SadA992-W-1 specimens for the three finite element deletion strategies

Figure 6.219 and Figure 6.220 show the variation of von Mises equivalent stress with equivalent plastic strain for the WUF-B and RBS sub-assemblage specimens, respectively. These figures show the extent to which the finite element deletion strategy affects the material capacity. In the WUF-B specimen the initial decline of von Mises stress for the VGM and VGM-BW simulations is due to the fracture of the bolts in the connection and the buckling of the compression flange. After this, the elements in the VGM simulation provide a significant amount of plastic deformation capacity and strain energy while in VGM-BW simulation this not the case. In addition, for VGM and VGM-BW simulations the edge elements provide more strain energy capacity than the inner middle element located at the weld access hole. In the CS simulation this is the opposite with the middle element provide more strain energy than the edge element. In the RBS specimen the VGM finite element deletion strategy allows the

elements to develop the highest strain energy while the CS strategy the lowest. From Figure 6.220 it can be seen that the unloading is elastic. In addition, for the CS and VGM simulations the edge elements follow exactly the same hardening and softening path while in the VGM-BW simulation this is not the case due to selected elements being picked on the crack path which was at an angle to the longitudinal axis of the beam.

The variation of the value of the damage variable is plotted in Figure 6.221 and Figure 6.222 for the WUF-B and RBS sub-assemblage specimens, respectively. In the WUF-B specimen the three simulations are distinguishable from each other. In addition, the inner and edge elements follow different paths in VGM and VGM-BW simulations. In the CS simulation all the three elements follow the same path indicating a sudden fracture. In the RBS sub-assemblage specimen the damage variable curves for the three finite element deletion strategies are distinguishable from each strategy but not from each element due to the sudden fracture propagation except for the VGM-BW simulation where the third element on the flange edge failed before the other two. The CS and VGM simulations show a similar slope of the damage variable while the VGM-BW has a steeper slope than the other two.

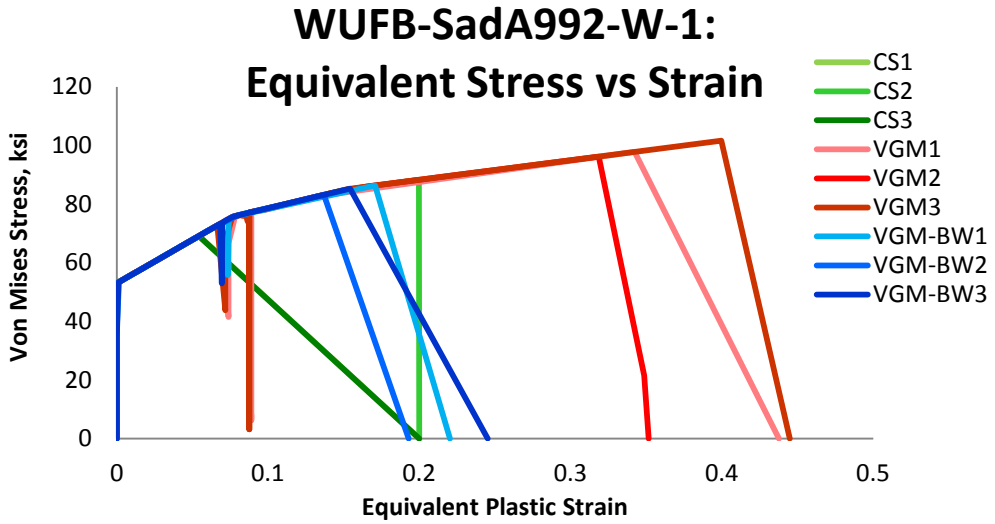

Figure 6.219: Variation of von Mises Stress with equivalent plastic strain for different elements laid out through the thickness of the tension flange of WUFB-SadA992-W-1 specimen for the three finite element deletion strategies

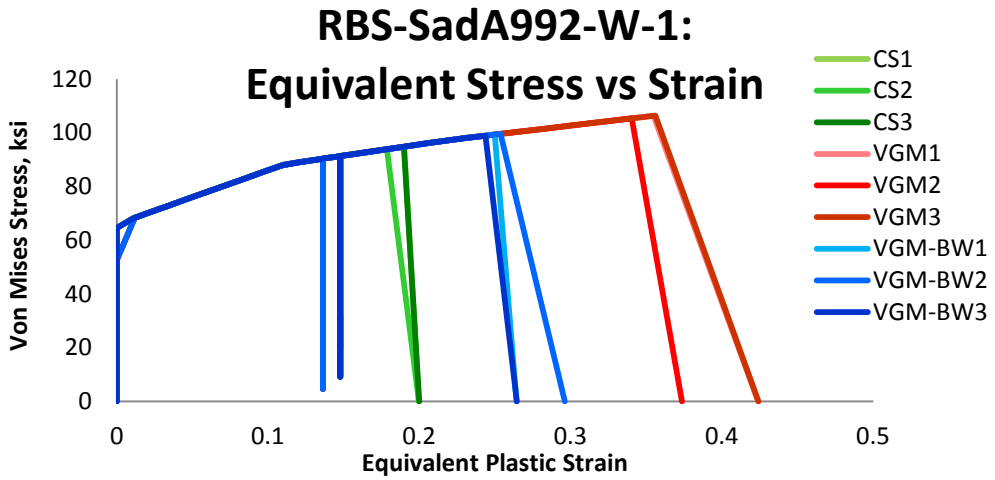

Figure 6.220: Variation of von Mises Stress with equivalent plastic strain for different elements laid out through the thickness of the tension flange of RBS-SadA992-W-1 specimens for the three finite element deletion strategies

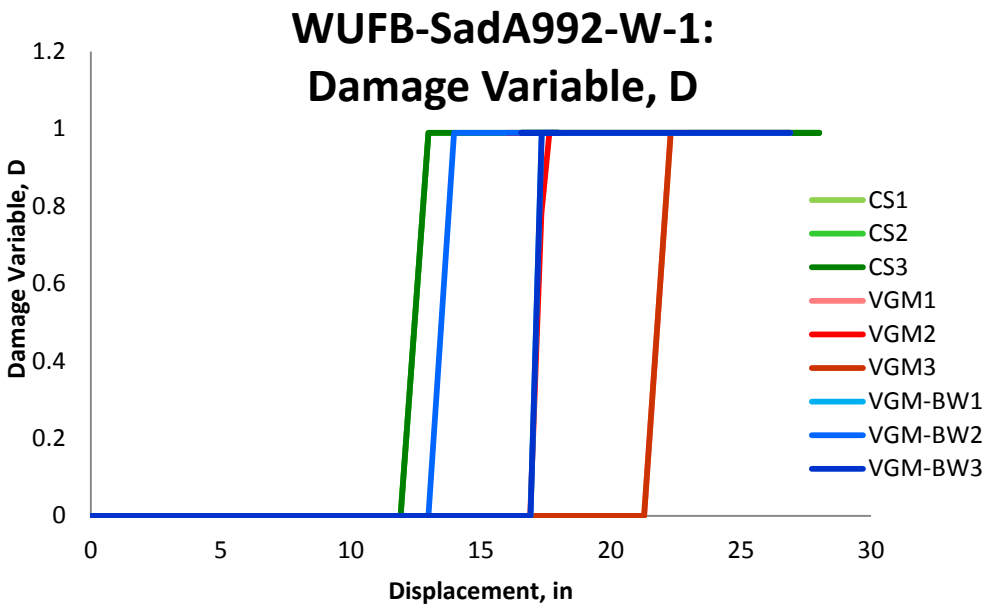

Figure 6.221: Variation of Damage Variable with displacement for different elements laid out through the thickness of the tension flange of WUFB-SadA992-W-1 specimen for the three finite element deletion strategies

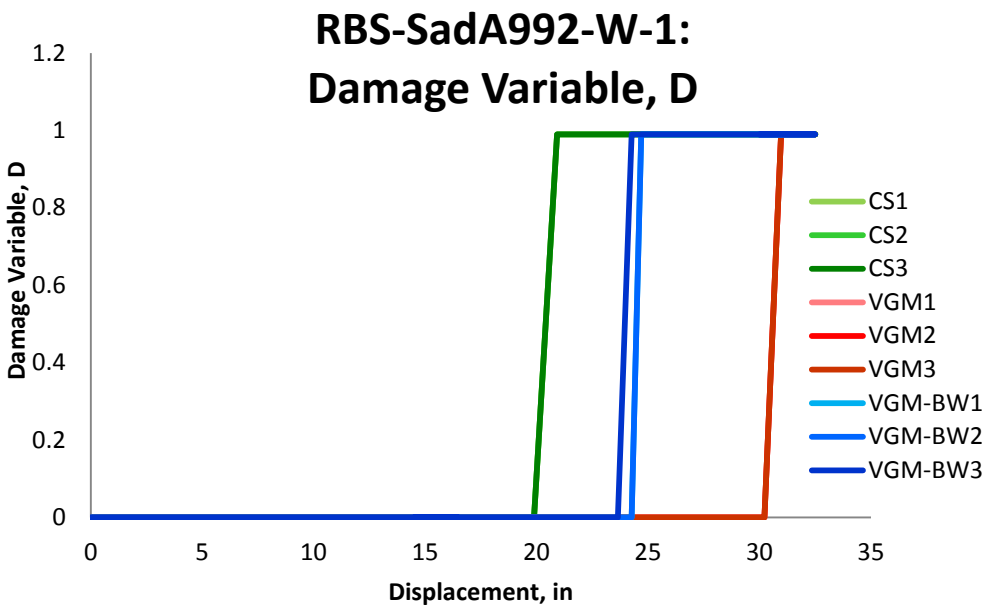

Figure 6.222: Variation of Damage Variable with displacement for different elements laid out through the thickness of the tension flange of RBS-SadA992-W-1 specimen for the three finite element deletion strategies

6.7.1 Summary

The three finite element deletion strategies were also validated through comparison to WUF-B and RBS beam-column subassemblages. The testing of the sub-assemblages continued until fracture occurred at the connection ends and significant load-carrying capacity of the connections was lost. In the experimental test of WUF-B connection, the beam top flange near the center column buckled first, then a shear failure of the lowest and middle bolts occurred, and finally fracture of the bottom beam flange near the center column occurred. In the VGM simulation the failure sequence followed that of the experiment. The VGM-BW closely followed the damage propagation, while CS did not follow the damage propagation seen in the experiment. In the experimental testing of RBS sub-assemblage fracture first occurred at the bottom beam flange in the middle of the reduced section and then propagated until the specimen could no longer carry the applied load. This damage pattern was repeated in all three simulations. Overall, the VGM performed best in capturing the fracture initiation and propagation in the WUF-B and RBS subassemblage specimens while the VGM-BW captured most of failure pattern, but predicted fracture where no fracture was observed in the experiment such as at the edges of the tension flange of the WUF-B specimen. The CS approach captured the fracture initiation and propagation in the RBS specimen but not in WUF-B specimen. In addition, the VGM-BW and CS underpredicted the capacity of the sub-assemblages while VGM had a very close prediction to the experimental capacity. Other observations that could be made are:

- Triaxiality reflects the importance of steel connection detailing. The WUF-B the middle element had a higher slope of equivalent plastic strain to displacement value than the

elements located at the edges of the tension flange. This is most likely due to the weld access hole, which is keeping the triaxiality lower than it would have been without it throughout the loading process as seen in the moment connection simulations of the previous section allowing the plastic flow to occur.

- The triaxiality range in the tension flange of the WUF-B and RBS connections is fairly small, ranging from 0.34 to 0.6 signifying a uniaxial to biaxial tensile loading.
- A repeated pattern is observed in moment–resisting connections that when triaxiality is fairly constant throughout the loading process through width of the tension flange with an increasing equivalent plastic strain a sudden fracture occurs throughout the thickness of the tension flange of the specimen. The opposite is true when there exists a significant triaxiality variation with increase in equivalent plastic strain in the tension flange.

Overall, the three finite element deletion strategies were able to capture the sudden fracture propagation through the thickness of the tension flange in the two specimens, while only the VGM was able to properly capture the failure of the bolts.

6.8 Steel Portal Moment Frame

In addition to establishing the validation against shear tab and moment connections, the validation platform also includes a steel portal moment frame. Schutz et al. (1953) loaded a portal frame with gravity and lateral loads to determine its collapse strength. The large-scale specimen was fabricated from 12WF36 for both the beam and columns, with a beam span of 30

feet and a column height of 10 feet. Measured cross-sectional properties of the 12WF26 member were measured by the original author and used in finite element simulations in this work. Gravity and lateral loads were applied at the one-third points of the beam and windward column, respectively. The experimental layout of the portal frame is shown in Figure 6.223. Hydraulic jacks were used to apply the loading; one actuator was used for each of the two vertical loads, and one horizontal actuator was used for the two horizontal loads using a special pinned load distribution test setup (Schutz et al. 1953). The column bases were mounted on knife edges so that a pin ended condition was maintained throughout the test (Schutz et al. 1953). The distance between the column bases was kept constant by means of tie rods. A horizontal reaction was used at the base of the windward column (Schutz et al. 1953). The test was planned so that the movement caused by the horizontal load would take place at the column bases, leaving the ends of the beam restrained horizontally from lateral drift (Schutz et al. 1953). Surveying instruments were used to determine the deflected shape of the frame. The monotonic loading regime was carried out continuously until inelastic lateral-torsional buckling occurred in the leeward column. The mechanical properties of the steel used were determined by standard tension and compression coupon tests taken from several locations in the cross-section of the beam (the columns were made from the same section) by the original author (Schutz et al. 1953). The steel used was ASTM A7-50T (ASTM A7, 1967) and all three steel members needed to form the frame (one beam, two columns) were cut from a single length beam. Based on the reported chemical composition and mechanical properties, the ASTM A7-50T is very similar to the current ASTM A36 steel (ASTM A36, 2008). The A7 and A373 steels were consolidated in 1967 into the A36 steel specification. From the coupon test results, the

yield strength and ultimate strength with strain hardening were provided by the original author but not used in finite element simulations in this work. In the finite element simulations the ASTM A7-50T will be modeled as ASTM A36 steel. The reason for this was to test the predictive nature of the proposed approach since many older steel structures are still in use today with no available material information. The data point inputs for plasticity and fracture models are shown in Table 6.13. The portal frame was modeled as a single unit made out of base metal type A36, with plastic and fracture parameters calibrated in Chapter 5 of this work. The weld material was ignored because no detailed information on the weld material was provided to account for it in finite element simulation, and no failure occurred in the original experiment. Collapse in this specimen was determined by the formation of severe plastic hinges until such a point as the load-carrying capacity of the frame decreased significantly. Specific cases of fracture were not mentioned in the reporting of the experiment (Schutz et al. 1953). However, Figure 6.225 shows severe plastic deformation occurring. The finite element simulations were carried out to larger displacement values than in the actual experiment to see if fracture initiation would be predicted after the maximum experimental displacement. The finite element model used for the three simulations with associated boundary conditions is shown in Figure 6.224. In the CS and VGM-BW finite element simulations fracture occurred at a displacement much larger than the experimental maximum displacement. In the CS simulation, the first failure occurred as a buckling of the inside flange of the leeward column and the compression flange of the beam. This intensified as the loading progressed. After this the leeward column web and the beam web buckled. Fracture first initiated in the inside flange of the leeward column and propagated so as to severe the column flange in two halves separating

it from the web. This damage progression is shown in Figure 6.226. In the VGM simulation the damage progressed similar to that in the CS simulation with the buckling of the leeward column flange and web and of compressive beam flange. However, in the VGM simulation no fracture occurred. In fact, the fracture initiation integral only reached a maximum value of approximately 0.33 signifying no fracture initiation occurred. In the VGM-BW simulation the damage progressed similar to the other two simulations. At first, the buckling of the inside flange of the leeward column and the compressive flange of the beam occurred followed by the buckling of the leeward column web and beam web. Fracture initiated at the junction of the leeward column web and the inside flange. The extensive buckling of the inside leeward column flange caused it to separate from the column web. The fracture initiation and propagation in the VGM-BW simulation is shown in Figure 6.227.

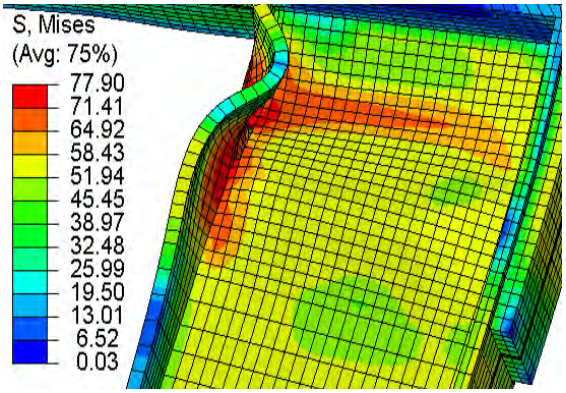

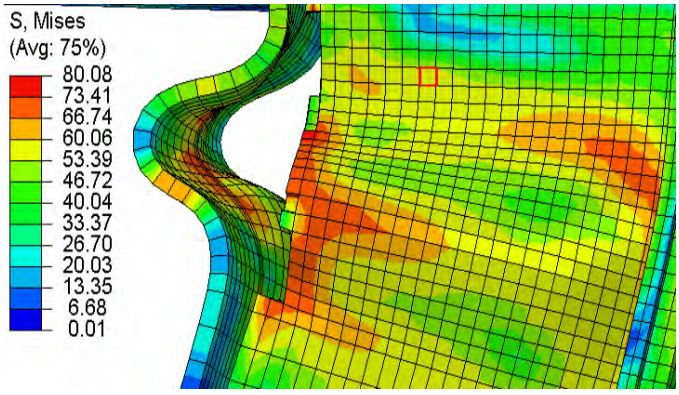

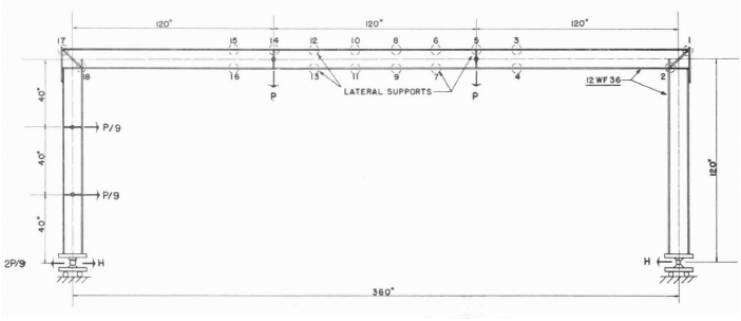

Figure 6.223: Portal frame Portal-SchA7-W-1 dimensions and lateral and base support details (Schutz et al. 1953)

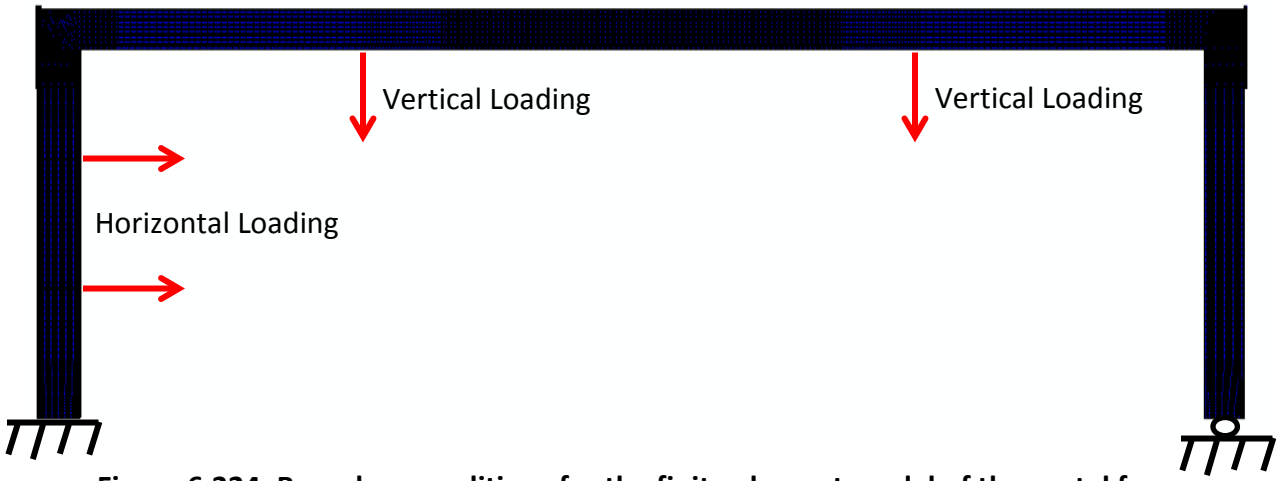

Figure 6.224: Boundary conditions for the finite element model of the portal frame

Table 6.13: Plasticity and fracture model inputs for Portal-SchA7-W-1 specimen

		Fracture Model Input		
Part	**Plasticity Model Input**	**VGM**	**VGM-BW**	**CS**
Beam	CNT-MyeA36-B-A	CNT-MyeA36-B-A	TC-MyeA36-B-A	0.2
Column	CNT-MyeA36-B-A	CNT-MyeA36-B-A	TC-MyeA36-B-A	0.2

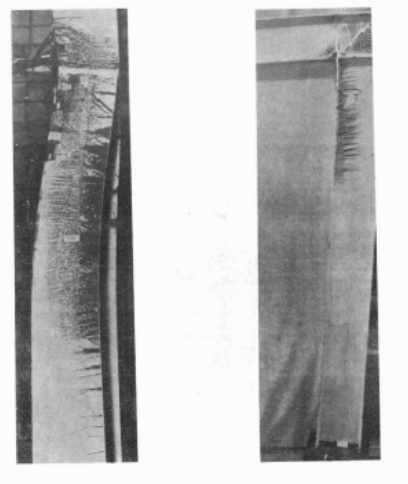

Figure 6.225: Leeward column: inside of the flange (left) and side view (right) (Schutz et al. 1953)

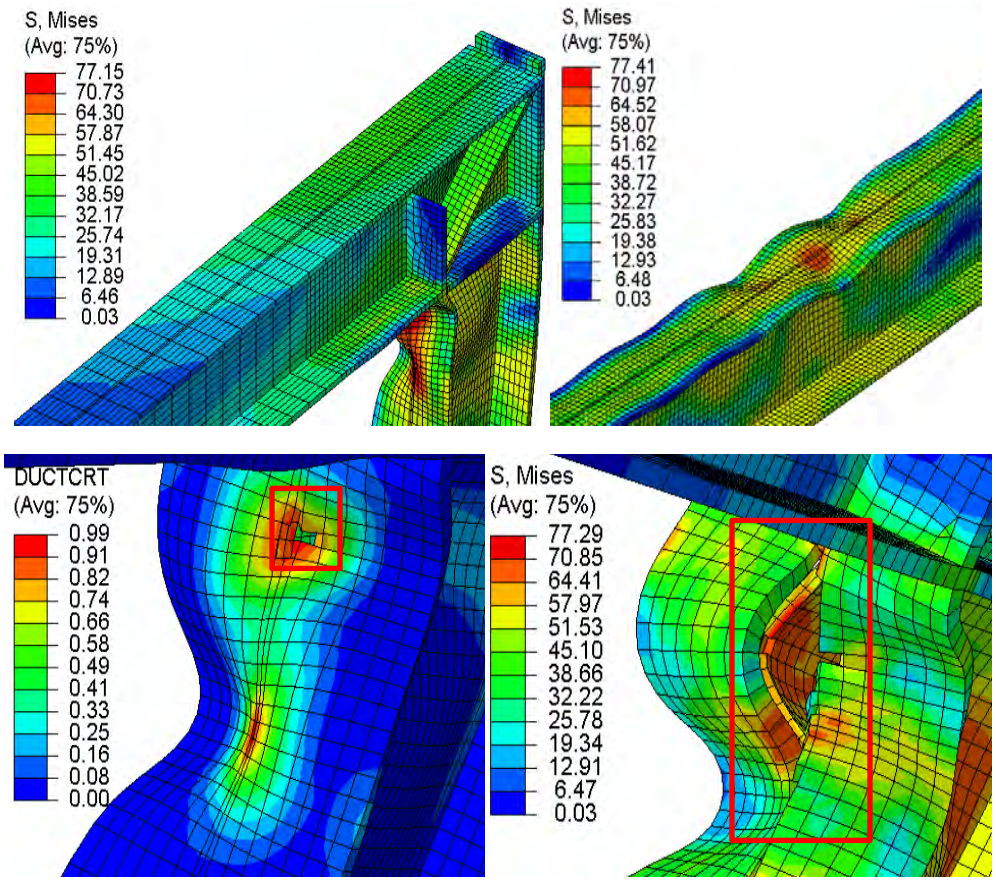

Figure 6.226: Simulation results of a portal Portal-SchA7-W-1 specimen with contours representing von Mises stress (ksi) and fracture initiation integral: CS leeward column flange and web buckle (top left), CS compression beam flange buckle (top right), CS fracture initiation (bottom left), and CS fracture propagation (bottom right)

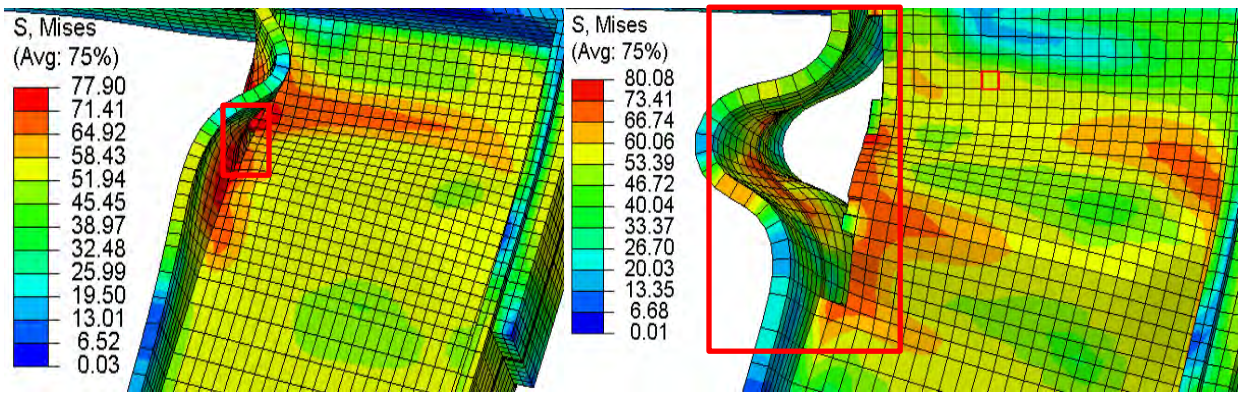

Figure 6.227: Simulation results of a portal Portal-SchA7-W-1 specimen with contours representing von Mises stress (ksi): VGM-BW fracture initiation (left), and VGM-BW fracture propagation (right)

Figure 6.228 and Figure 6.229 show the vertical load versus vertical center displacement plot and vertical load versus horizontal displacement at the top of the windward beam-column knee connection for the experimental and simulation results, respectively. Up to the displacement value of the experimental test results the three simulations show approximately the same results. This confirms that in the experimental test there was no fracture because none of the three simulations show any sign of fracture until much larger displacement. Since the VGM simulation did not see any fracture it follows a continual decline in force capacity of the portal frame with significant plastic hinges forming in the leeward knee connection and in the center of the beam. The VGM-BW and CS simulation follow very similar paths. The initial divergence from the VGM curve signifies fracture. The VGM-BW simulation has a smooth divergence from the VGM curve, while the CS simulation has a more abrupt divergence. In addition, the CS simulation shows more vibration in the force-displacement curve due to a more abrupt nature of the fracture that was seen in the simulation. However, the VGM-BW and the CS simulations predict a similar force-displacement behavior, which signifies that this portal frame is constructed to be ductile and develop plastic hinges and is not susceptible to fractures.

Elements selected for study of the fracture initiation and propagation parameters were located near the intersection of the leeward column inside flange and web. First element was located on the surface of the inside flange where fracture initiated for the CS simulation. The other two elements were the elements that were located in the column web at the flange-web intersection. The third element was located higher than the second element. The chosen element locations are shown in Figure 6.230.

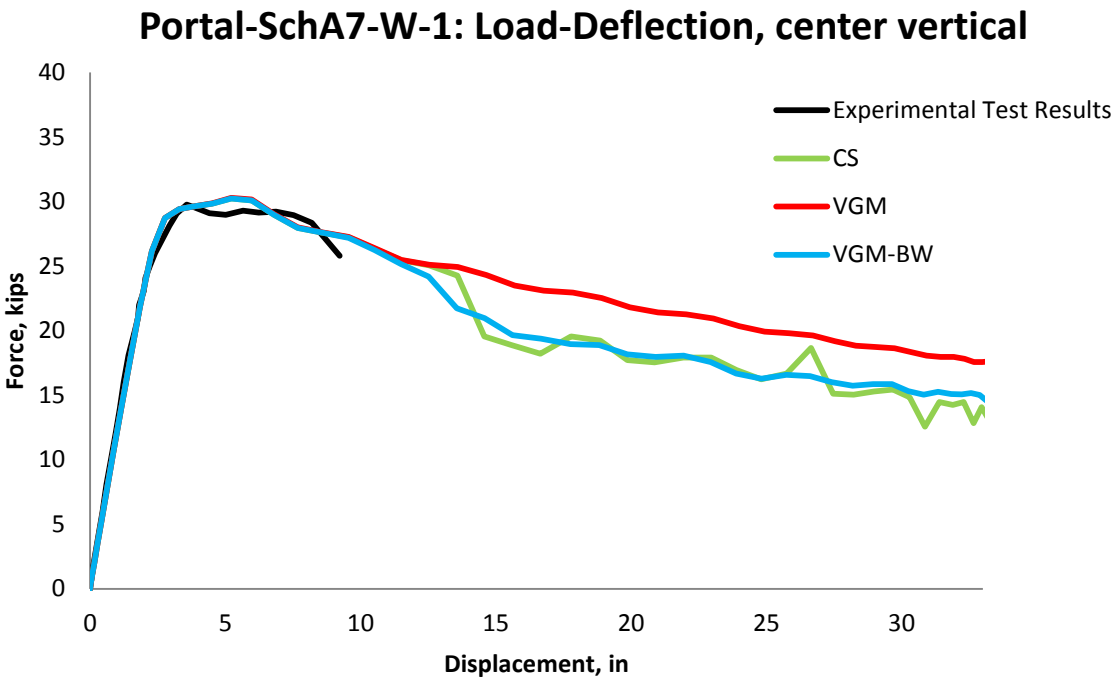

Figure 6.228: Validation results for Portal-SchA7-W-1 in vertical load-vertical deflection curves (Schutz et al. 1953)

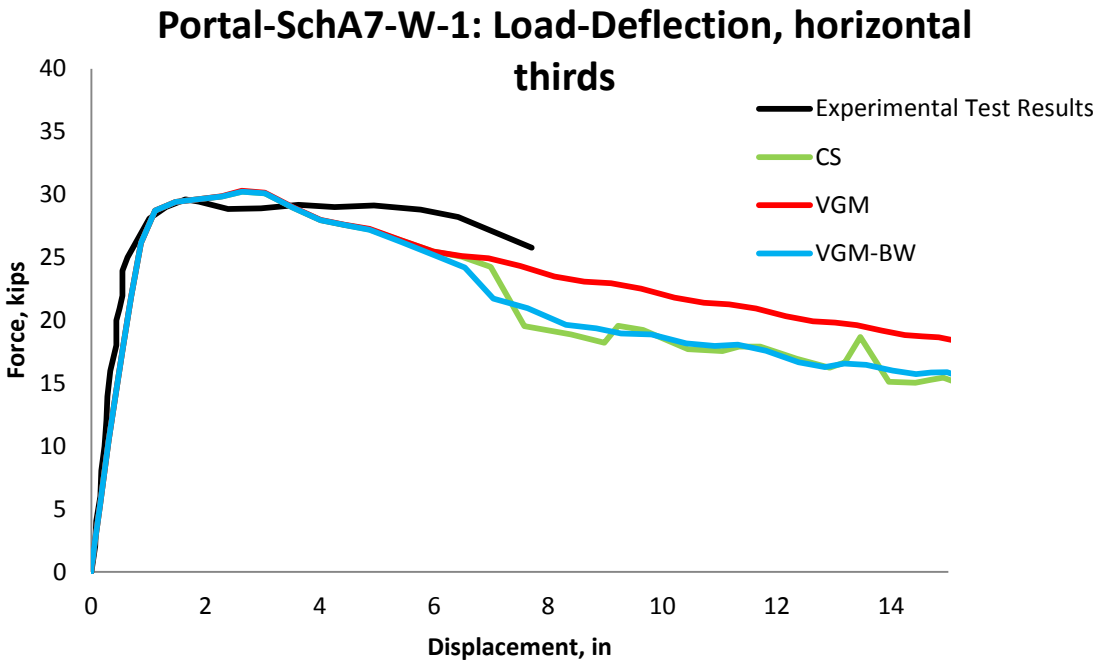

Figure 6.229: Validation results for Portal-SchA7-W-1 in vertical load-horizontal deflection curves (Schutz et al. 1953)

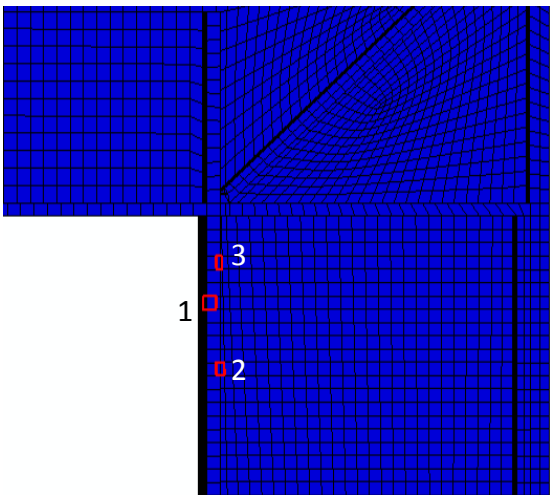

Figure 6.230: Elements chosen for fracture initiation and propagation study for Portal-SchA7-W-1 specimen

The triaxiality versus vertical displacement is plotted for the three chosen elements in the leeward column of the specimen for the three finite element deletion strategies in Figure 6.231. The triaxiality path in the three simulations for each element is different from each other from the beginning of the loading process. This is probably due to different damages occurring early

on in the loading such as buckling of the beam and column flanges and web. Each element experiences an initial spike and fall due to buckling of the inside flange in the leeward column. Elements 1 and 3 mainly experience negative triaxiality throughout the loading which signifies that they are under a compressive stress. In the VGM-BW simulation elements 1 and 3 experienced spikes in in negative triaxiality due to buckling of the column web. In the VGM simulation no fracture occurred and the triaxiality of the chosen elements has a constant slope throughout the loading process after the initial spike.

The equivalent plastic strain is plotted in Figure 6.232. The figures show that the equivalent plastic strain in the three simulations did not follow the same equivalent plastic strain path during loading. In the VGM simulation, the elements follow a path similar to a power law. This signifies that the rate of plastic deformation at the top of the leeward column declined as the loading progressed. The CS and VGM-BW simulations did not show this type of behavior for second and third elements. In these elements the equivalent plastic strain had a change in its slope after fracture, which resulted in a significant increase of the equivalent plastic strain. The first element reached approximately the same equivalent plastic strain value in CS and VGM-BW simulations.

The equivalent plastic strain versus triaxiality path of the element with associated fracture locus of the material is plotted in Figure 6.233. The triaxiality range for the top part of the inside flange of leeward column is between -0.7 to 0.5. Only element 2 experiences positive triaxiality while elements 1 and 3 experience more negative triaxiality throughout the loading. In addition, elements 1 and 3 have a more vertical equivalent plastic strain growth with triaxiality

than element 2 does. Since the top element is in compression and bottom element is in tension for most of the loading with the middle element being around zero triaxiality, this shows that a significant moment was acting in the column-beam connection.

The variation of the value of fracture initiation integral is shown in Figure 6.234. The elements in VGM simulation had a steady increase in the value of the fracture initiation integral. The curves for element 1 and 2 are very similar to each other. In the CS simulation the first element had the steepest slope while in the VGM-BW simulation element 2 failed first. In the VGM-BW simulation the fracture initiation integral does not grow much for most of the loading while in CS simulation the third element has a fairly steep curve throughout the loading process. The curve for element 1 was similar for CS and VGM-BW simulation.

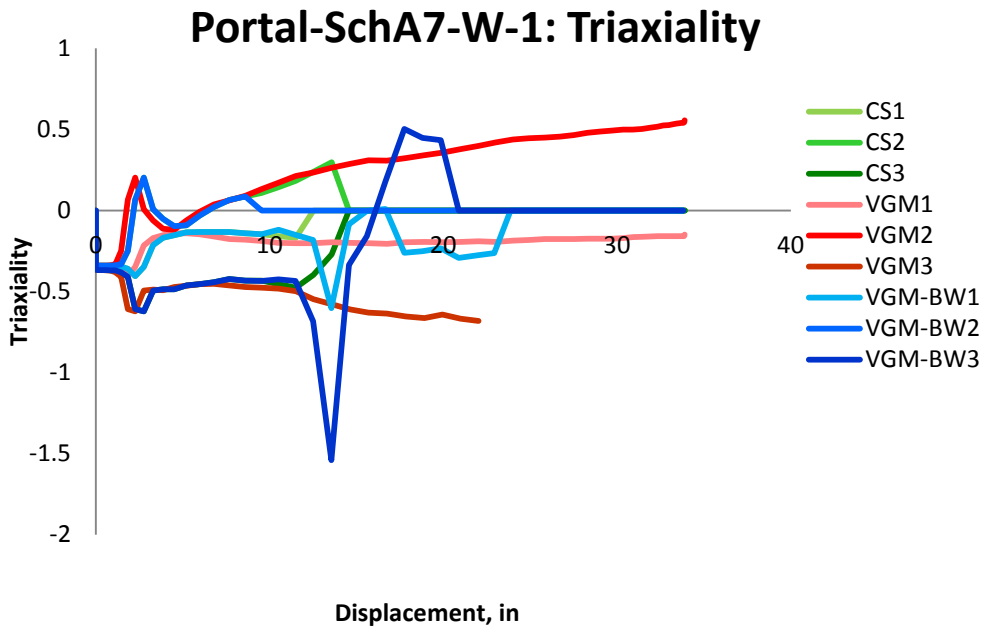

Figure 6.231: Variation of triaxiality with vertical displacement for different elements laid out through the leeward column of Portal-SchA7-W-1 specimens for the three finite element deletion strategies

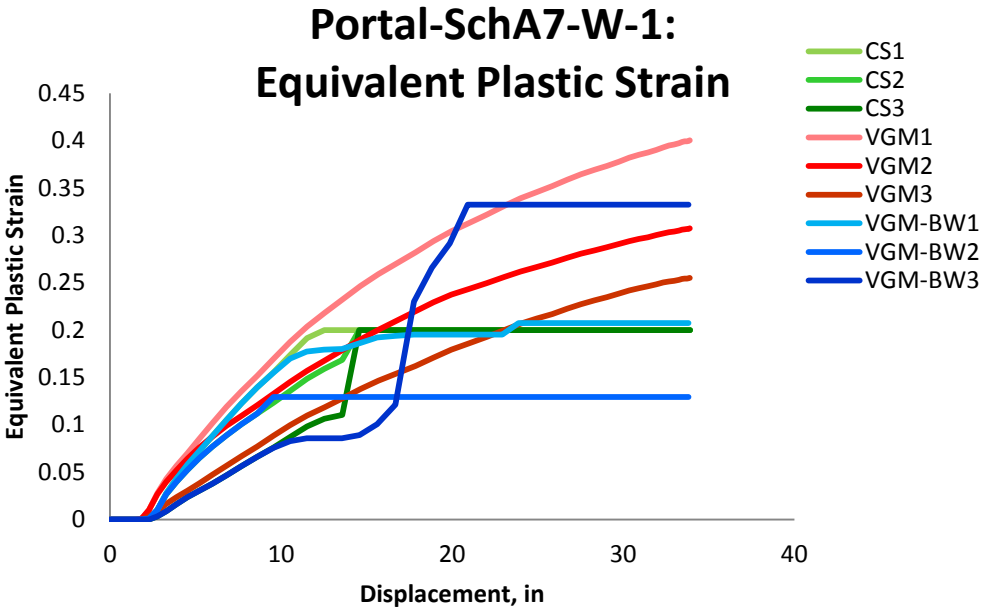

Figure 6.232: Variation of equivalent plastic strain with vertical displacement for different elements laid out through the leeward column of Portal-SchA7-W-1 specimens for the three finite element deletion strategies

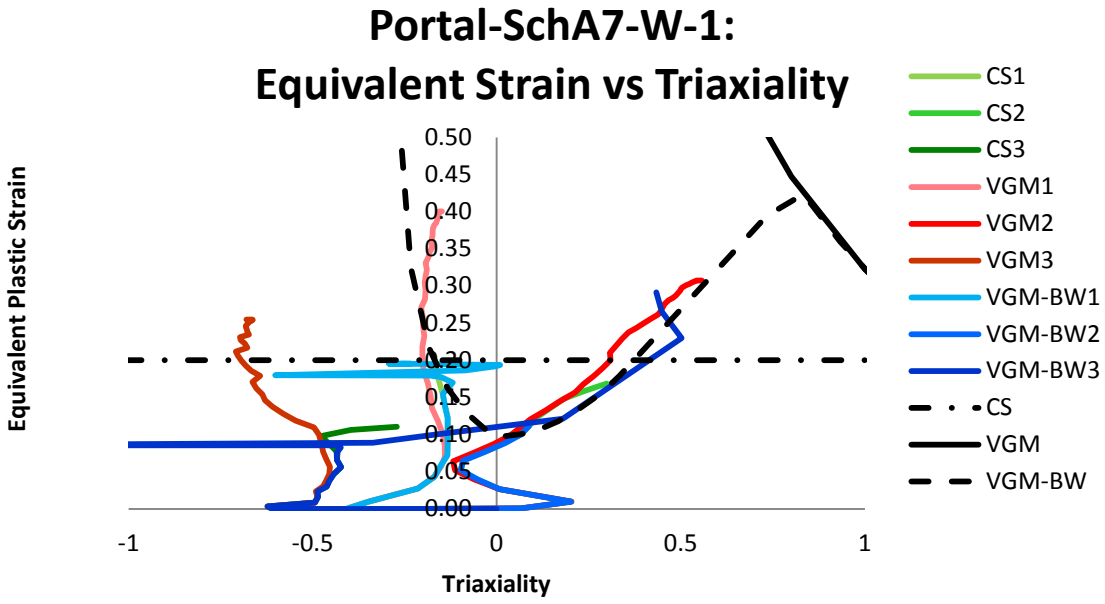

Figure 6.233: Variation of equivalent plastic strain with triaxiality for different elements laid out through the leeward column of Portal-SchA7-W-1 specimens for the three finite element deletion strategies

The varition of von Mises stress with displacement is shown Figure 6.235. The elements in the VGM simulation show a constant hardening of von Mises stress. The sudden doward slope of the elements in the VGM simualtion does not signify softening initiation but rather damage such as buckling that is occuring near the elements that is not changing the displacement but still lowers the stress level. The earliest element to fail in the three simulations is element 2 in the VGM-BW simulation. The plot shows that fracture occurred more sudden in the CS simulation because all of the elements failed at about the same displacement while in VGM-BW simulation the damage propagation was more gradual. The steep fall in the VGM-BW simulation is due to a fracture propagating between the column web and inside flange which is causing sever buckling of the column web and flange. The elements regain their strength and arest the crack propagation until they themselves fail.

The mean stress variation throughout the loading excursion is plotted in Figure 6.236. The variation of mean stress has similarities to the variation of triaxiality with displacement. This shows that mean stress reflects the triaxiality of an element more than von Mises stress. The path of mean stress in the three simulations for each element is different from each other from the beginning of the loading. Each element experiences an initial spike and fall due to buckling of the inside flange in the leeward column. Elements 1 and 3 mainly experience negative mean stress throughout the loading. In the VGM-BW simulation elements 1 and 3 experienced spikes in negative mean stress due to buckling of the column web and flange because of crack propagation separating it from the web. In the VGM simulation no fracture occurred and the mean stress of the chosen elements has a constant slope throughout the loading process after the initial spike.

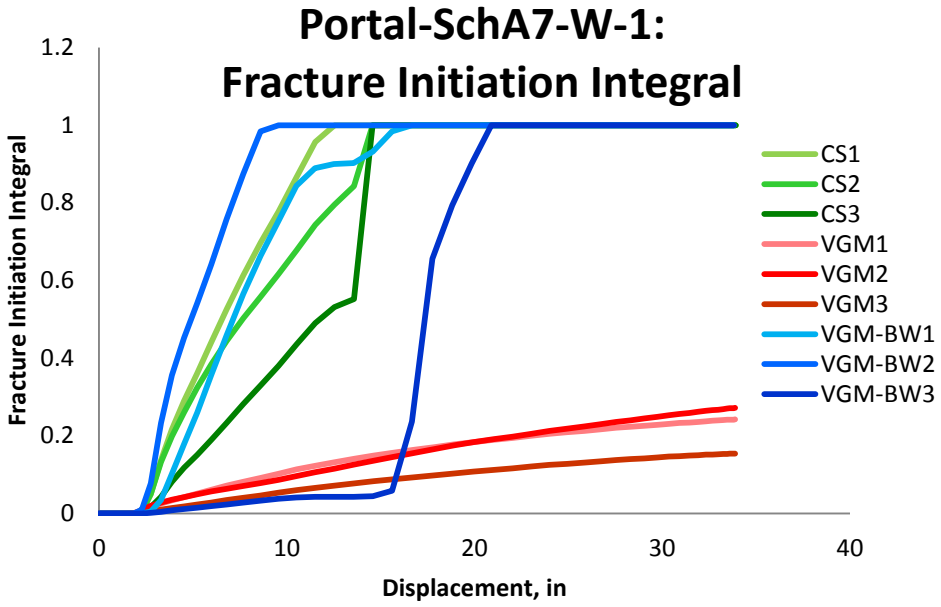

Figure 6.234: Variation of fracture initiation integral value with vertical displacement for different elements laid out through the leeward column of Portal-SchA7-W-1 specimen for the three finite element deletion strategies

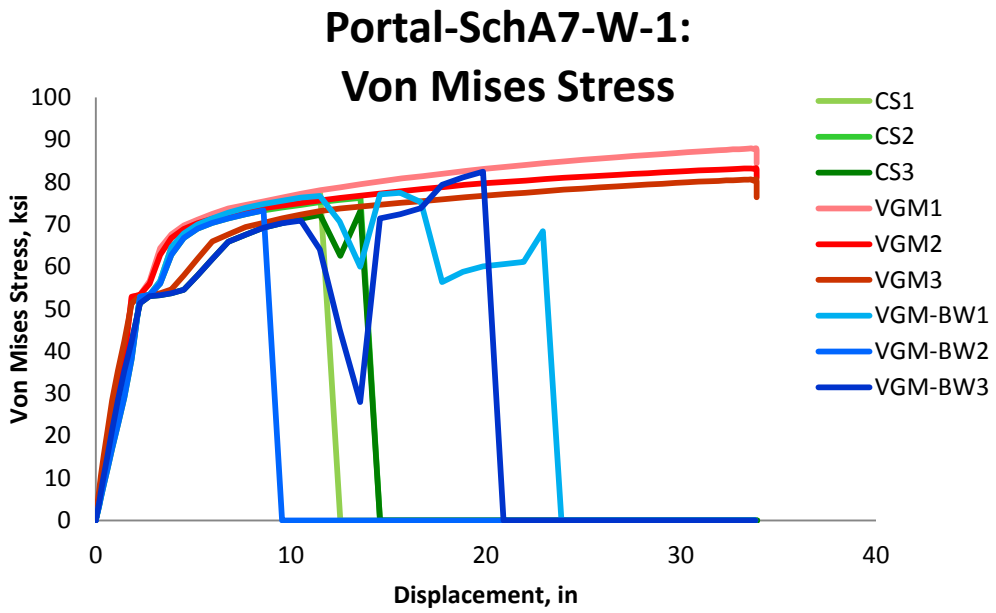

Figure 6.235: Variation of von Mises Stress with vertical displacement for different elements laid out through the leeward column of Portal-SchA7-W-1 specimens for the three finite element deletion strategies

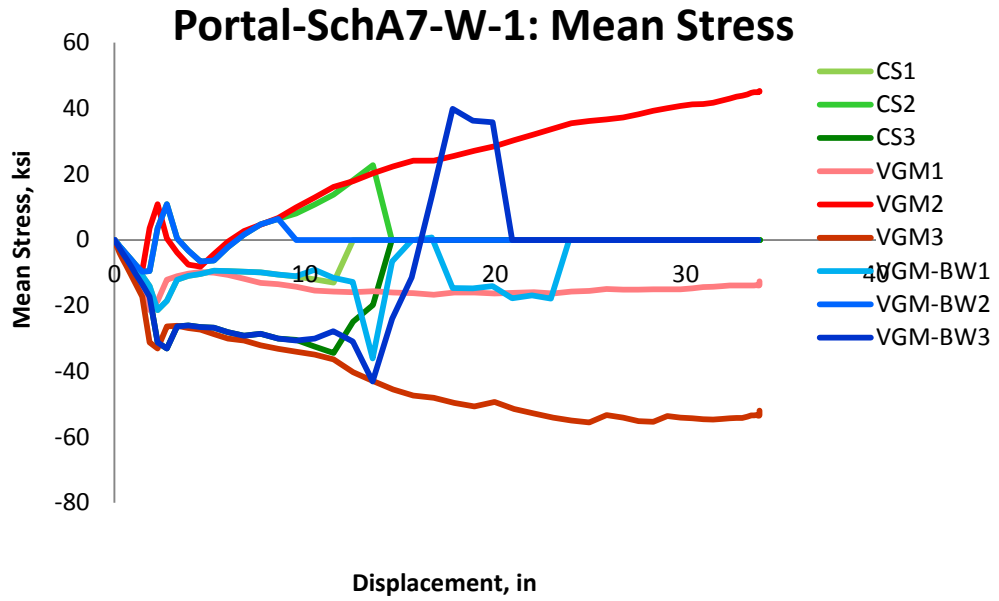

Figure 6.236: Variation of mean stress with vertical displacement for different elements laid out through the leeward column of Portal-SchA7-W-1 specimens for the three finite element deletion strategies

Figure 6.237 shows the variation of von Mises equivalent stress with equivalent plastic strain for the three elements located in the top of the leeward column at the inside flange and web intersection. The figure shows that the earliest element to fail is the second element in the VGM-BW simulation. For the VGM-BW simulation the third element located at the top of the leeward column achieved the highest equivalent plastic strain and strain energy out of the three elements. For the CS and VGM simulations the third element achieved the least amount of equivalent plastic strain energy. In these simulations the first element achieved the greatest amount of plastic deformation. This signifies that the fracture propagation in the VGM-BW simulation is probably not correct.

The variation of the value of the damage variable is plotted in Figure 6.238 for the three elements in the three simulations. No fracture was observed in the VGM simulation. The CS and

VGM-BW damage variable curves show a similar trend to the previous plots. The second element in the VGM-BW simulation failed first. The first element failed first in the CS simulation. In CS simulation elements 2 and 3 failed at the same displacement. This signifies that the crack in the intersection of the leeward column inside flange and web was sudden in CS simulation. In the VGM-BW simulation the first element was the last to fail. In addition, there is a big difference between when each element begins to soften and is deleted. This shows that the fracture of the leeward column web and inside flange was more gradual and was accompanied by larger plastic deformation. All the elements in the CS and VGM-BW simulation had the damage variable curves with similar steep slopes.

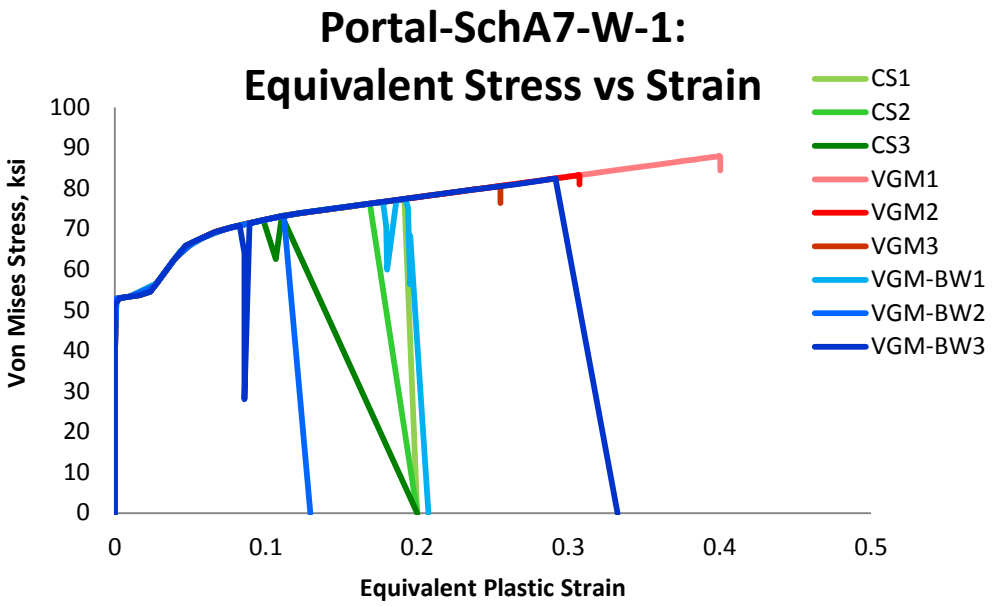

Figure 6.237: Variation of von Mises Stress with equivalent plastic strain for different elements laid out through the leeward column of Portal-SchA7-W-1 specimens for the three finite element deletion strategies

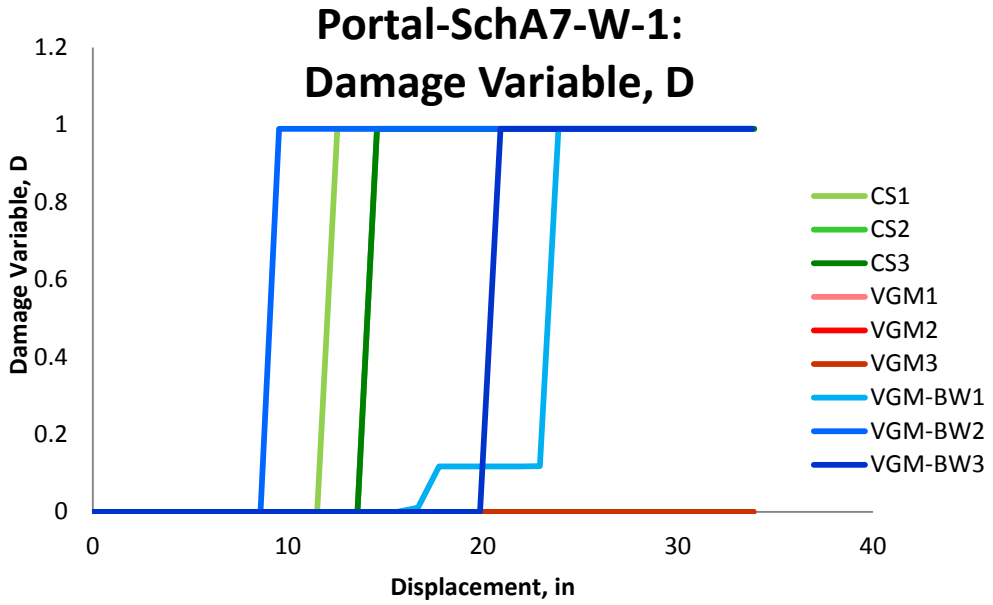

Figure 6.238: Variation of Damage Variable with vertical displacement for different elements laid out through the leeward column of Portal-SchA7-W-1 specimens for the three finite element deletion strategies

6.8.1 Summary

In this section the three finite element deletion strategies were validated against a steel portal moment frame. Monotonic loading regime was carried out continuously on the portal frame until inelastic lateral-torsional buckling occurred in the leeward column. Collapse in this specimen was determined by the formation of severe plastic hinges until such a point as the load-carrying capacity of the frame decreased significantly. Specific cases of fracture were not mentioned in the reporting of the experiment(Schutz et al. 1953)(Schutz et al. 1953)(Schutz et al. 1953)(Schutz et al. 1953)(Schutz et al. 1953)(Schutz et al. 1953). The finite element simulations were carried out to larger displacement than in the actual experiment to see if fracture initiation would be predicted after the maximum experimental displacement. In the CS and VGM-BW finite element simulations fracture occurred at a displacement much larger than the experimental maximum displacement. In the VGM simulation no fracture occurred. Overall,

since CS and VGM-BW simulations predict different fracture initiation and propagation and VGM has no fracture at all it is difficult to decide if fracture would behave in the same manner as in the VGM-BW or CS simulations. Judging from the fact that only element 2 acts in the positive triaxiality region it could be assumed that fracture would occur at the flange-web intersection a little ways down from the knee beam-column connection. However, the portal frame clearly had significant deformation without exhibiting fracture.

6.9 Multi-Story Steel Braced Frame

In addition to validating to a portal frame experiment, the validation set includes the comparison of the proposed element deletion approaches to experimental results of a series of steel braced multi-story frames. The large-scale braced frames were three-story two-bay structures that are 30 feet high with a 15 feet bay spacing (Yura 1965). Continuous welded construction was used on all the test specimens, which were fabricated from ASTM A36 steel, to have beam-to-column fully-restrained connections (Yura 1965). Four types of tests and measurements were performed to determine the material and sectional properties: tension tests, cross-section measurements, beam tests, and residual stress measurements. The static yield stress, ultimate stress, percent elongation in 8 inches, strain-hardening modulus, and ratio of strain at strain-hardening to yield strain were provided from tension coupon results by the original author, which were taken from the web and flange of beam and column sections. In simulating the braced frame specimens and to test the predictive capability of the proposed approach, the calibrated constitutive and fracture parameters were used instead of the

measured ones. The cross-sectional properties were measured by micrometers and vernier calipers. All of the three frames have the same geometry and cross-section sizes (Yura 1965). The exterior columns are 6WF20, the interior are 6WF25, and all of the beams are 12B16.5. In addition, the two beams at each story were cut from a single length steel section so that beam properties are the same for a given story. Each diagonal brace consists of two 1 inch diameter rods and are prestressed to offset any slackening due to column shortening under axial load. Exterior beam-to-column connections, column fixity to the base, general member layout, and loading locations are shown in Figure 6.239 and Figure 6.240 (Yura 1965). The columns were welded to a 2½ inch thick base plate and the plate was prestressed to the foundation by means of two 3 inch diameter anchor bolts.

Strain gages were used on the braces, beams, and columns to indicate the strains in the members (Yura 1965). The moment and axial loads were calculated from the strain readings and the measured material properties. Deflections of the structure were measured by transits and levels sighting on scales. Column deflections were measured at 30 inch intervals along their lengths, and the deflections of each beam were recorded at the ends, load points, and centerline (Yura 1965). In addition, the rotations of the joints and bases in each frame were measured by electrical and mechanical gages.

The braced frames (Yura 1965) and their corresponding loadings are shown in Figure 6.241. These frames were tested to study their behavior for determining the strength of braced multi-story steel frames subjected to symmetrical and unsymmetrical vertical gravity loading and horizontal wind loading (Yura 1965). The loading conditions vary for each test. The gravity

loading on the top story is 0.75 of the gravity loading on the lower floors to prevent the formation of a mechanism in the top story. Checkerboard gravity loading was used to create bending moments in the interior column. The columns are loaded about their strong axis and are continuous from the base to the top story. Vertical loads were applied to the test frame 40.5 inches from the centerline of the beams (Yura 1965). Lateral loads were applied at each floor level by hydraulic jacks acting in tension. Movement of the test frame out-of-plane was prevented by lateral bracing, which was supported by the loading frame, as shown in Figure 6.242. In addition, it was shown that the forces in the diagonal bracing due to unsymmetrical vertical loads become significant once first plastic hinges are formed in the braced frames (Yura 1965). Diagonal bracing was designed to carry the entire applied lateral load so as to minimize second-order effects (Yura 1965). The finite element model for the three braces and the location of the element chosen to perform a fracture initiation and propagation study are shown in

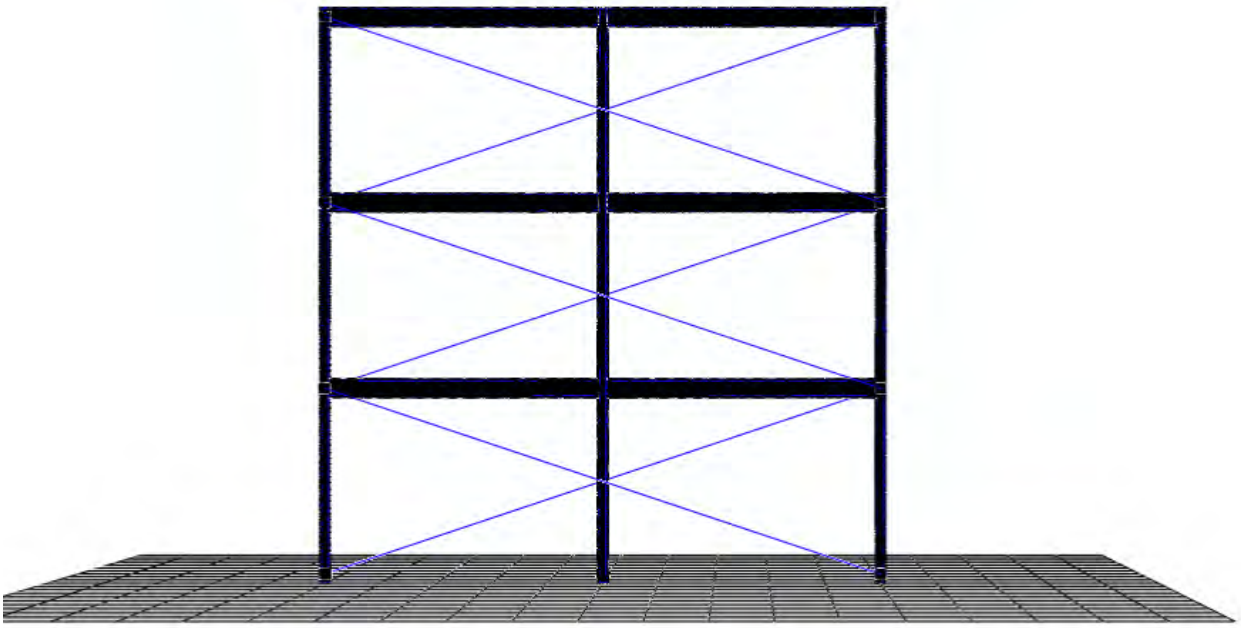

Figure 6.243. The data point inputs for the plasticity and fracture models are shown in Table 6.14.

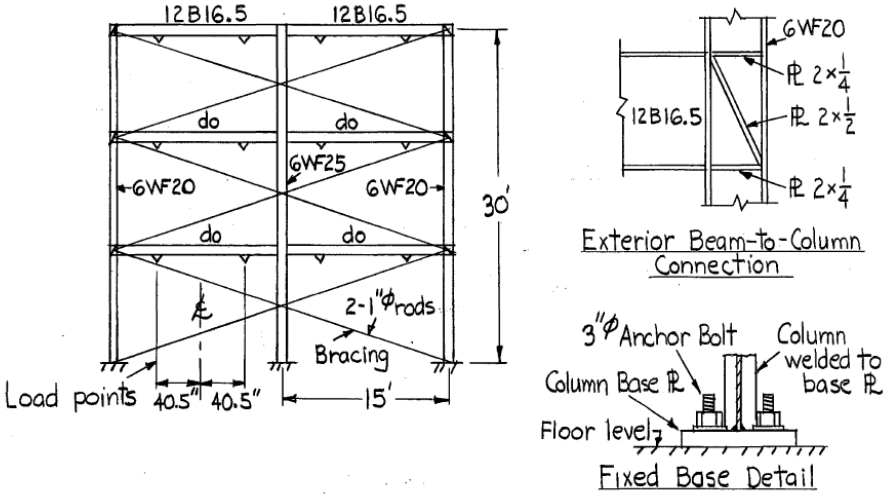

Figure 6.239: Braced frame test specimen (Yura 1965)

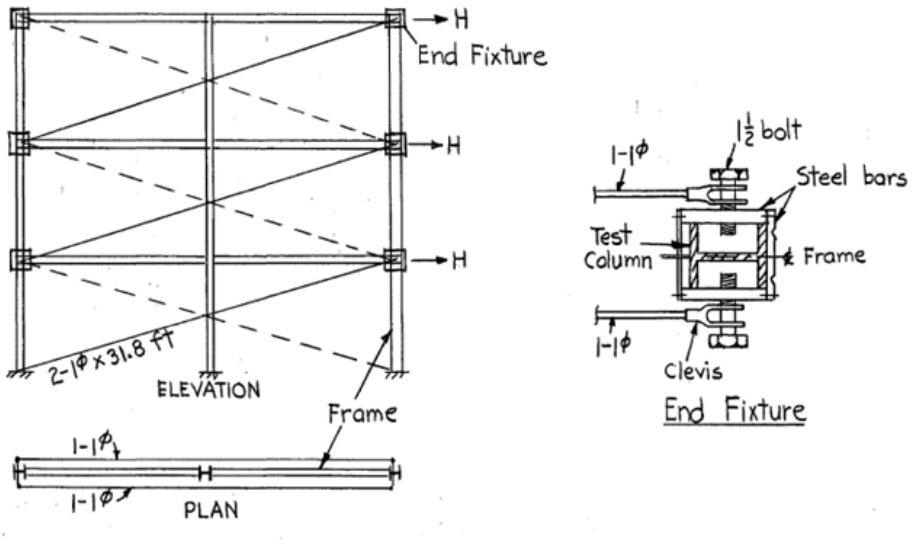

Figure 6.240: Experimental test bracing system (Yura 1965)

TEST NO.	TYPE OF TEST	LOADING CONDITION
Brace-YurA36-W-1	Braced Frame	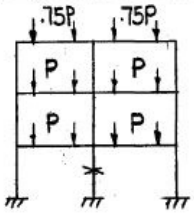 Full Dead and Live Loads
Brace-YurA36-W-2	Braced Frame	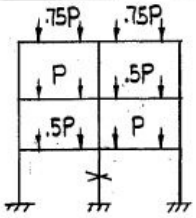 Checkerboard
Brace-YurA36-W-3	Braced Frame	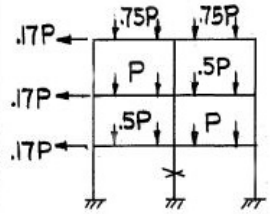 Checkerboard plus Wind

Figure 6.241: Shows the proposed braced frame experiments against which to validate [after(Yura 1965)]

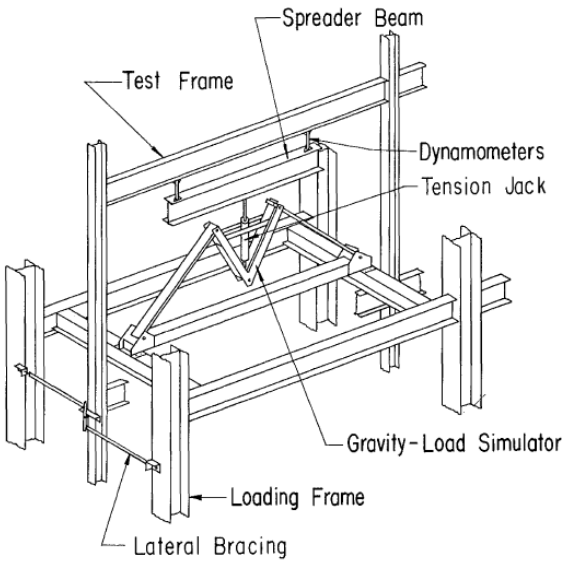

Figure 6.242: Typical bay loading and out-of-plane bracing arrangement (Yura 1965)

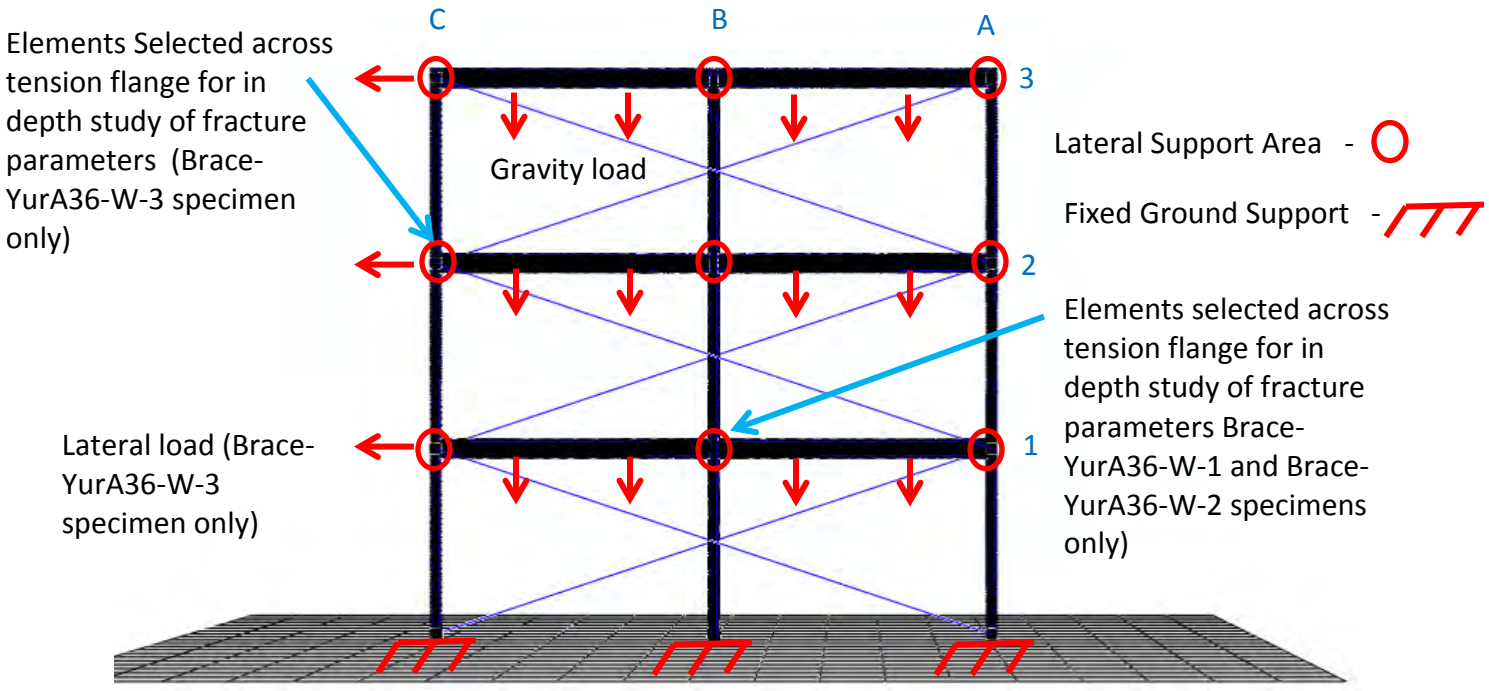

Figure 6.243: Finite element model with its boundary conditions, loading, and location of elements selected for study of fracture parameters for Brace-YurA36-W-1, Brace-YurA36-W-2, and Brace-YurA36-W-3 specimens

Table 6.14: Plasticity and fracture model inputs for Brace-YurA36-W-1, Brace-YurA36-W-2, and Brace-YurA36-W-3 specimens

		Fracture Model Input		
Part	**Plasticity Model Input**	**VGM**	**VGM-BW**	**CS**
Anchor Plate	CNT-MyeA36-B-A	CNT-MyeA36-B-A	TC-MyeA36-B-A	0.2
Beam	CNT-MyeA36-B-A	CNT-MyeA36-B-A	TC-MyeA36-B-A	0.2
Brace	Elasticity Only	-	-	-
Column	CNT-MyeA36-B-A	CNT-MyeA36-B-A	TC-MyeA36-B-A	0.2
Stiffener	CNT-MyeA36-B-A	CNT-MyeA36-B-A	TC-MyeA36-B-A	0.2
Weld	TC-NgE70T-7K2-P-A	LPT-NgE70T-7K2-P-A	TC-NgE70T-8K6-P-A	0.2

In the experimental testing of the braced frames several plastic hinges are developed during loading, although fracture is not mentioned explicitly. In addition, Figure 6.244 shows a possible location of a fracture, where it seems that the beam on the left has its flanges separated from the column. In the VGM simulation of the Brace-YurA36-W-1 specimen, the first fracture occurred at a displacement of 11.5 inches in the tension flange of the BC1 beam at the exterior end. Before this fracture occurred, severe plastic deformation and buckling occurred in all of the beams in the frame. The fracture started at the edge of the tension flange due to eccentric loading imposed by the plastic buckling of the beam. Soon after this, fracture occurred in the middle of the tension flange at the interior column connection. The crack propagated through the tension flange and downward through the web of the beam for all of the frame beams. The damage propagation was very similar for the CS and VGM-BW simulations. The first fracture in the VGM-BW simulation occurred at a displacement of 17.5 inches and at the edge of the beam AB1 inside tension flange. This is higher than in the VGM simulation because in the VGM simulation, the weld material was modeled as weld metal with no hardness specified, while for

the VGM-BW simulation weld was modeled as weld with hardness specified, as shown in Table 6.14. This only delayed the fracture and did not change damage propagation. First fracture in the CS simulation occurred at a displacement value of 21.5 inches at the edge of the beam AB1 inside tension flange. Fracture propagated from the edge of the tension flange and down the beam web. Overall, for Brace-YurA36-W-1 specimen the predominant failure was out-of-plane buckling of the beams and not by fracture. The deformation propagation for the VGM simulation is shown in

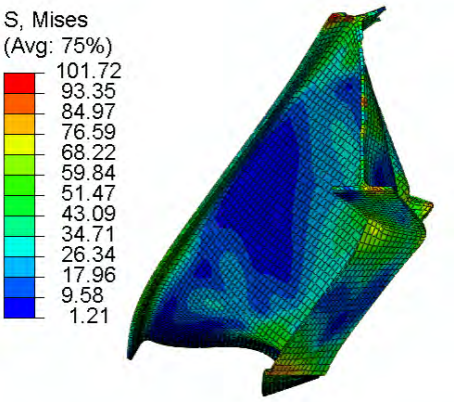

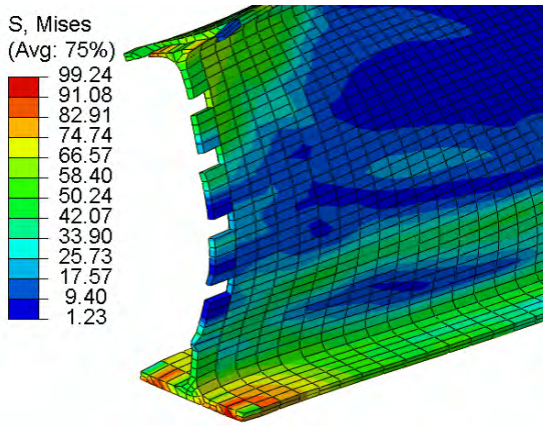

Figure 6.245 with similar deformation occurring for VGM-BW and CS simulation.

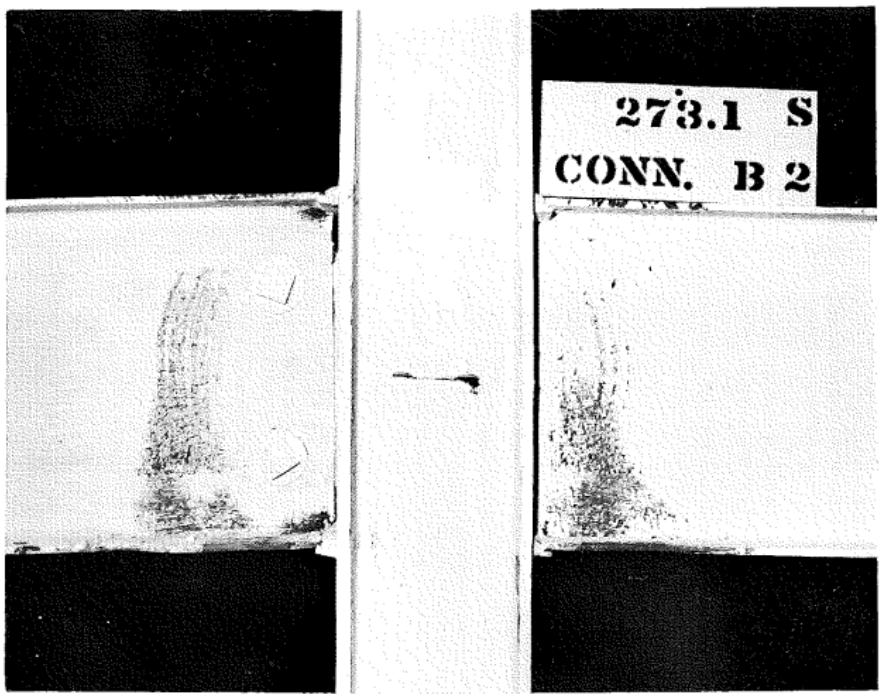

Figure 6.244: Possible fracture location in Brace-YurA36-W-1 specimen (Yura 1965)

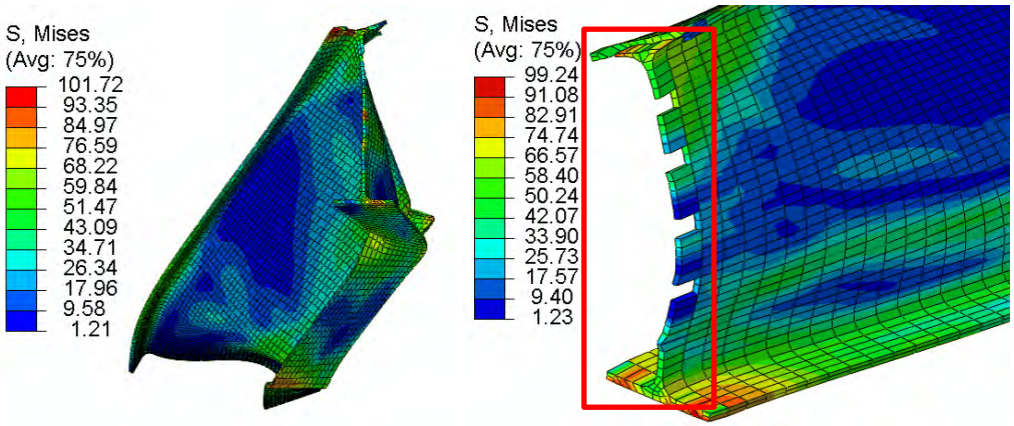

Figure 6.245: Simulation results of a braced frame Brace-YurA36-W-1 specimen with contours representing von Mises stress (ksi): VGM beam buckling looking through along beam axis (left), VGM fracture (right)

In all simulations of the Brace-YurA36-W-2 specimen, before fracture occurred, severe plastic deformation and buckling occurred in all of the frame beams. In the VGM simulation of the Brace-YurA36-W-2 specimen first fracture occurred at displacement of 8.9 inches in the tension flange of the BC2 beam at the exterior end and then at a displacement of 10.5 inches in the

exterior tension flange of beam AB1. The fracture started at the edge of the tension flange of beam BC2 due to eccentric loading imposed by the plastic buckling of the beam and in the middle of the of the tension flange in beam AB1. Soon after this, fracture occurred in the tension flange at the interior column connection. The crack propagated through the tension flange and downward through the web of the beam for all of the frame beams. The damage propagation was very similar in the CS and VGM-BW simulations. First fracture in the VGM-BW simulation occurred at a displacement of 14 inches and at the edges of exterior tension flanges of beams AB1 and BC2. As in the simulation of Brace-YurA36-W-1 specimen the displacement in VGM-BW is higher than in the VGM simulation because in the VGM simulation weld material was modeled with no hardness while for the VGM-BW simulation weld with hardness was used to model the weld material. This only delayed the fracture and did not change damage propagation. First fracture in the CS simulation occurred at a displacement value of 16.6 inches at the edge of the inside tension flange of beam AB1. After this, the edge of the exterior tension flange of beam AB1 fractured. Fracture propagated from the edge of the tension flange and down the beam web. Overall, for the Brace-YurA36-W-2 specimen, the predominant failure was out-of-plane buckling of the beams and not by fracture. The deformation propagation for the VGM simulation is shown in Figure 6.246, with similar deformation occurring for VGM-BW and CS simulation.

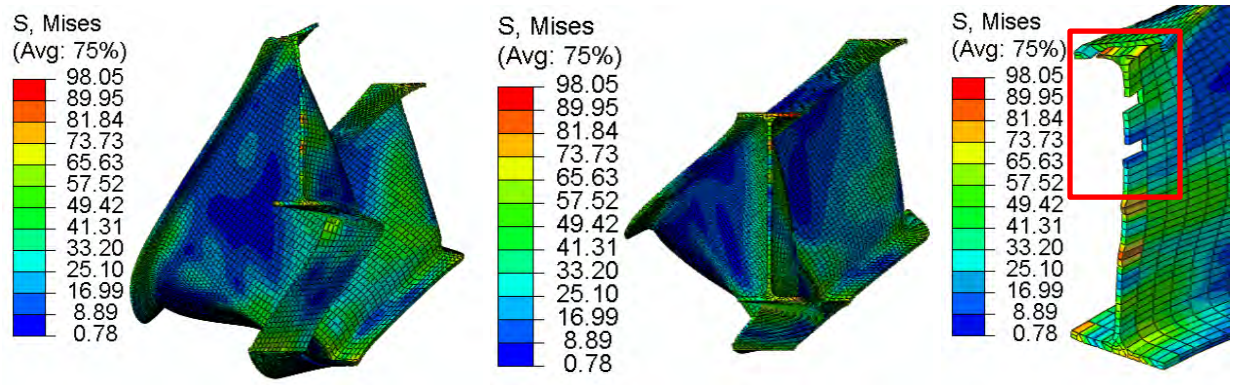

Figure 6.246: Simulation results of a braced frame Brace-YurA36-W-2 specimen with contours representing von Mises stress (ksi): VGM BC2 beam buckling looking along beam axis (left), VGM BC1 beam buckling looking along beam axis (left), VGM fracture (right)

As in the previous two specimens, all simulations of the Brace-YurA36-W-3 specimen experienced severe plastic deformation and buckling in all of the frame beams before fracture occurred. In the VGM simulation of the Brace-YurA36-W-3 specimen, the first fracture occurred at a displacement of 8 inches in the tension flange of the BC2 beam at the exterior end. Beam BC2 was then almost completely separated from the exterior column before fracture occurred at an interior tension flanges of beams AB1 and BC2 and exterior tension flange of AB1 at a displacement of 13.2 inches. The fracture started at the middle of the tension flange. The crack propagated through the tension flange and downward through the web of the beam. The damage propagation was very similar for the CS and VGM-BW simulations. First fracture in the VGM-BW simulation occurred at a displacement of 11.4 inches and at the edges of exterior tension flanges of beam BC2. Sever buckling of all of the beams occurred before fracturing the edge of an interior tension flange of beam AB1 at a displacement of 15 inches. As in the previous simulations, the displacement in VGM-BW is higher than in the VGM simulation because in the VGM simulation weld material was modeled with no hardness while for the VGM-BW simulation weld with hardness was used to model the weld material. First fracture in

the CS simulation occurred at a displacement value of 15.8 inches at the edge of the exterior tension flange of beam BC2. In the CS simulation the beams sustained extensive deformation after the first fracture before experiencing any other fractures. The next fracture occurred at a compression flange of beam AB1 approximately a quarter of the beam length away from the inside column. This occurred at a displacement of approximately 20.8 inches. Overall, for the Brace-YurA36-W-3 specimen, the predominant failure was out-of-plane buckling of the beams and not by fracture. The deformation propagation for the VGM simulation is shown in Figure 6.247 with similar deformation occurring for VGM-BW and CS simulation.

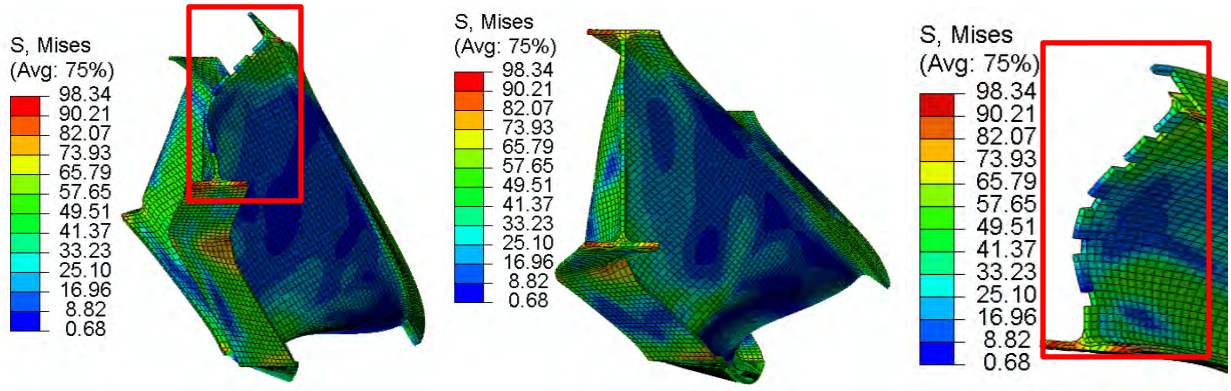

Figure 6.247: Simulation results of a braced frame Brace-YurA36-W-3 specimen with contours representing von Mises stress (ksi): VGM BC2 beam buckling looking along beam axis (left), VGM BC1 beam buckling looking along beam axis (left), VGM fracture (right)

Finite element deletion strategies are validated against experimental test results expressed as the applied load versus the deflection at beam centerline for a respective beam in the braced frame. Two validation results are shown in Figure 6.248 to Figure 6.253 for the simulation results of the three braced frames. The first plot shows the simulation results up to 4 inches which is around the maximum experimental displacement achieved at the center of a respective beam. The second plot shows the simulation results up to a center beam displacement of 20 inches. As can be seen from Figure 6.248, Figure 6.250, and Figure 6.252

which show results up to 4 inches, there are no differences between the three finite element deletion strategies up to the maximum experimental displacement. Therefore, no fracture occurred in the three simulations. This confirms that there was no fracture in the experimental test of braced frames. In fact, as was already mentioned above fracture occurred at a minimum displacement of 8 inches which is more than twice the maximum experimental displacement. Figure 6.249, Figure 6.251, and Figure 6.253 show the validation results up to a center beam displacement of 20 inches. In these plots the difference between the three finite element deletion strategies is clear after approximate displacement of 10 inches. The VGM simulation had fracture occur at the smallest displacement out of the three approaches. Therefore, the force-displacement curve in the VGM simulations had the steepest and the earliest decline. The CS and VGM-BW simulations showed very similar force-displacement capacity of the braced frame under the three different types of loading schemes with the CS simulation providing a small fraction more capacity than VGM-BW. Overall, the frames under the three different types of loading schemes and the three simulations failed by plastic deformation and buckling of the beams' web and not by fracture. Fracture occurred only after the out-of-plane buckling deformation made the beam unsafe.

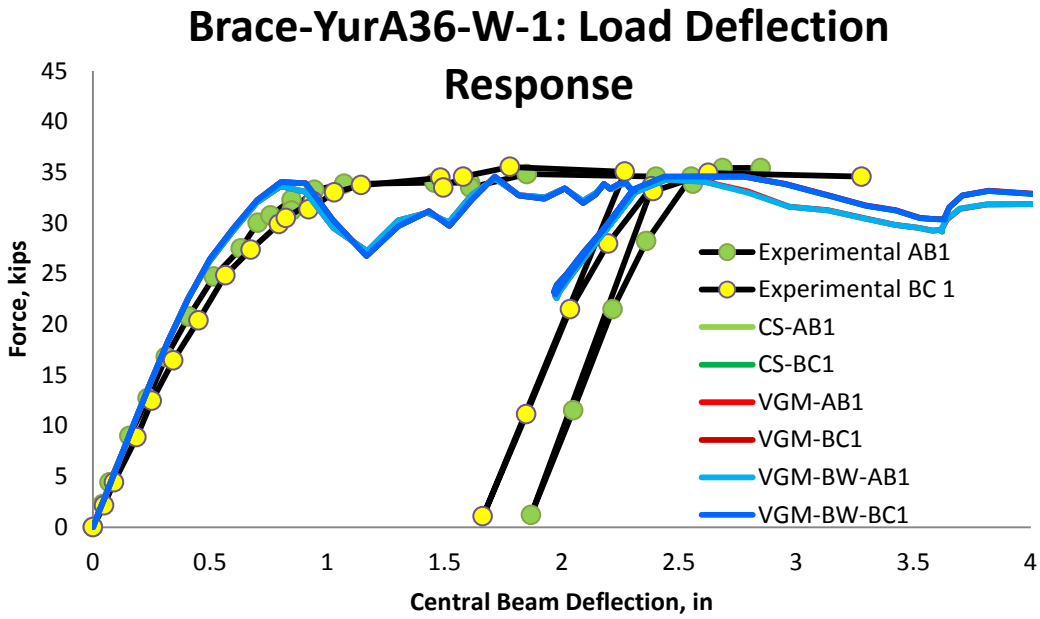

Figure 6.248: Validation results for Brace-YurA36-W-1 specimen up to experimental displacement

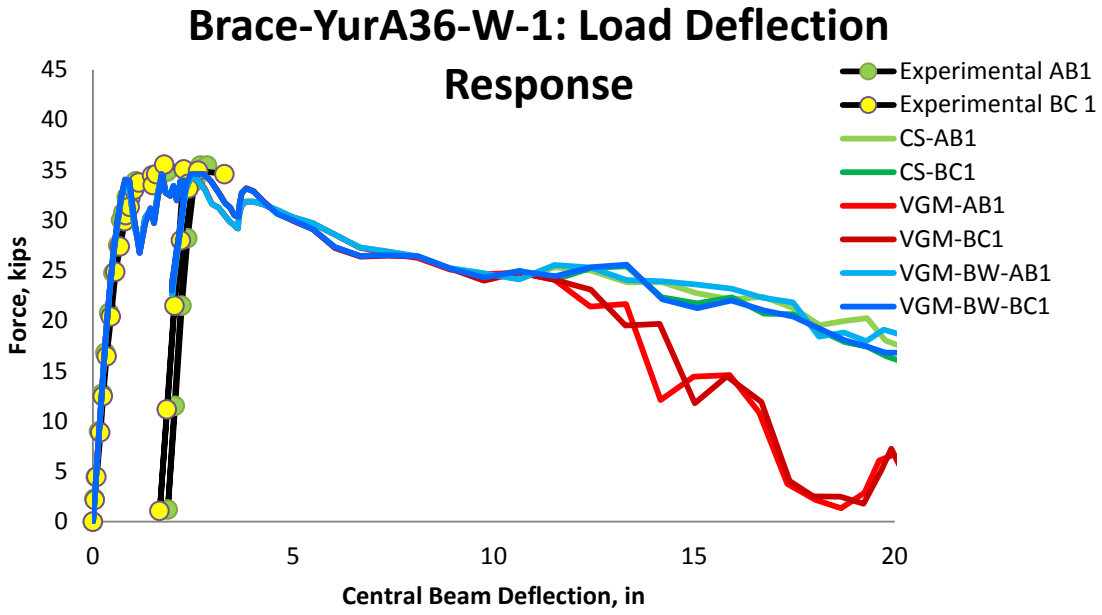

Figure 6.249: Validation results for Brace-YurA36-W-1 specimen up displacement of 20 inches

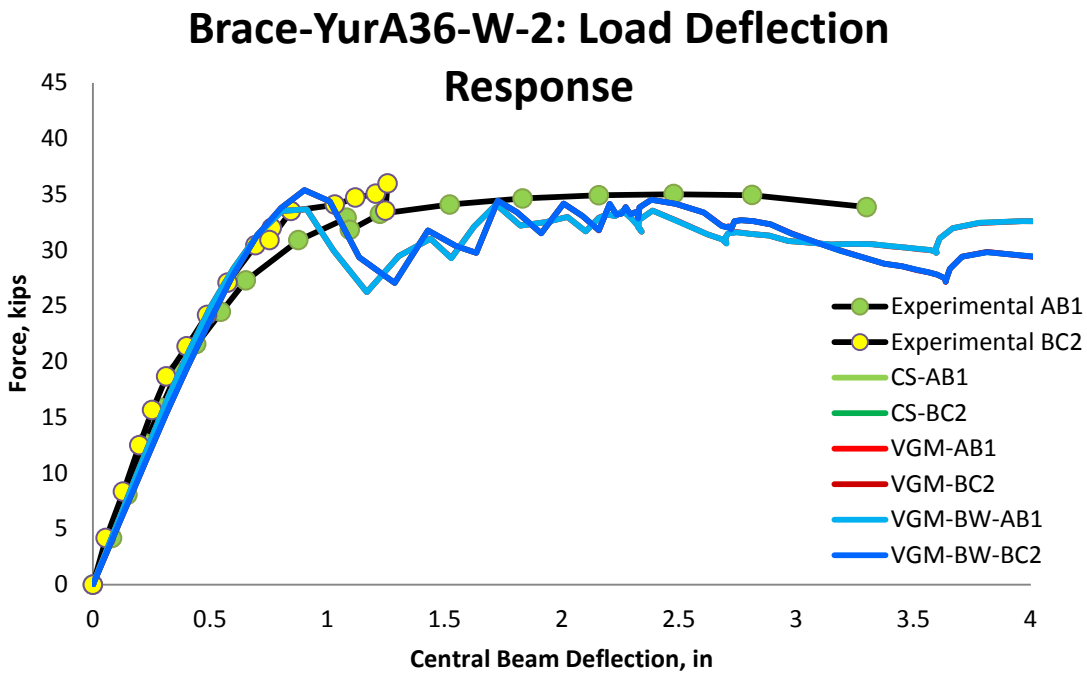

Figure 6.250: Validation results for Brace-YurA36-W-2 specimen up to experimental displacement

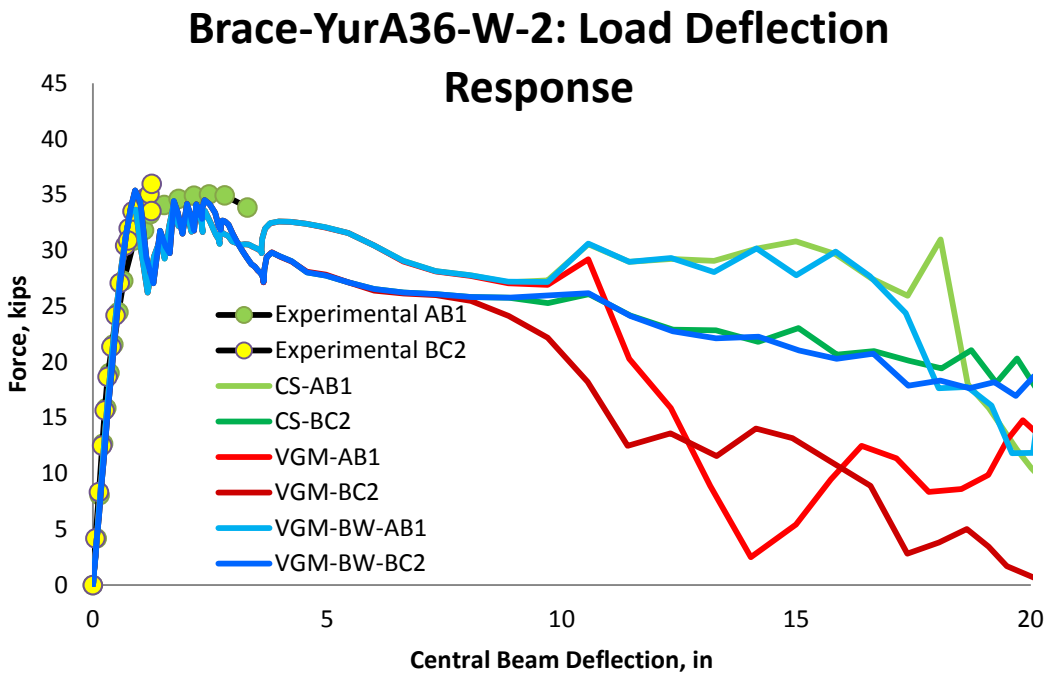

Figure 6.251: Validation results for Brace-YurA36-W-2 specimen up displacement of 20 inches

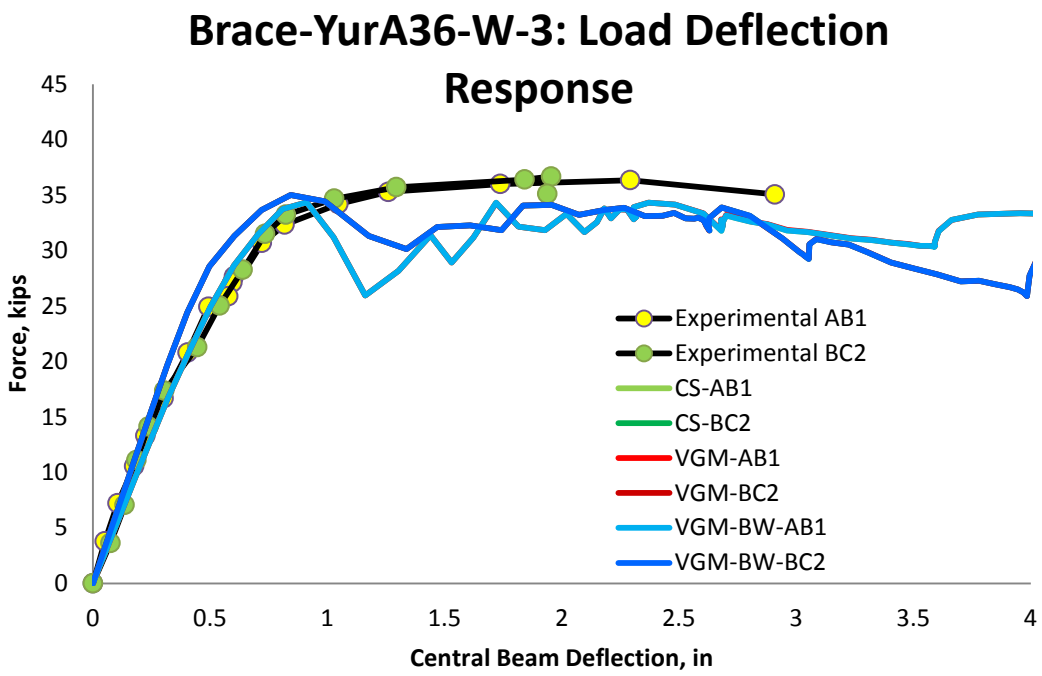

Figure 6.252: Validation results for Brace-YurA36-W-3 specimen up to experimental displacement

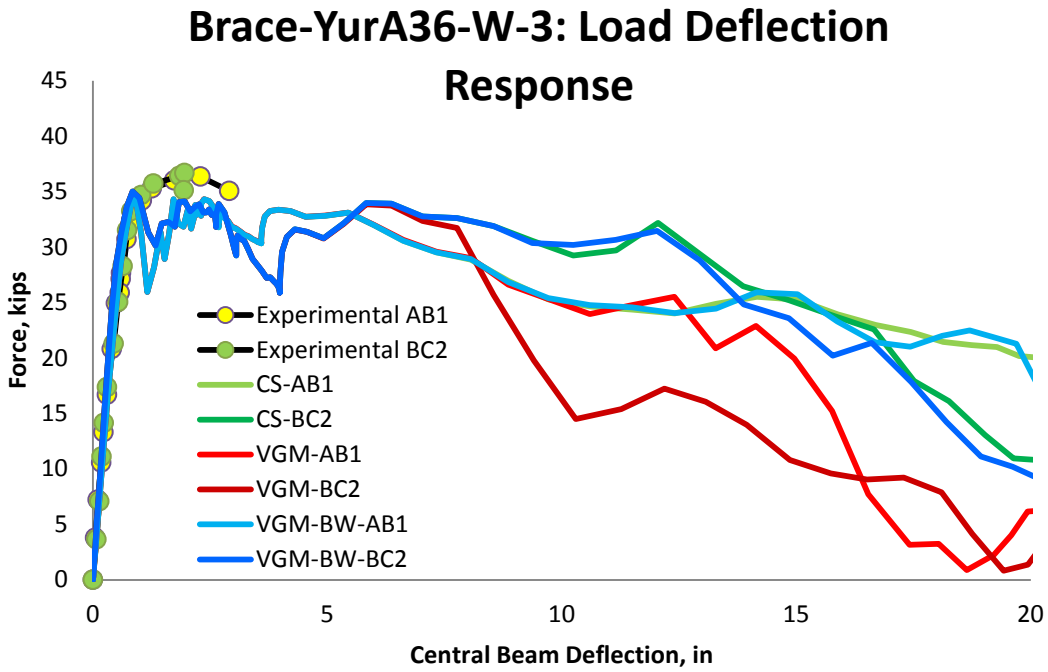

Figure 6.253: Validation results for Brace-YurA36-W-3 specimen up displacement of 20 inches

Below a detailed description is provided on the variation of fracture initiation and propagation parameters in elements that are located through the thickness of the tension beam flanges in the three specimens for the three finite element deletion strategies.

Triaxiality versus displacement is plotted for the three elements across the thickness of the tension beam flanges in the Brace-YurA36-W-1, Brace-YurA36-W-2, and Brace-YurA36-W-3 specimens for the three finite element deletion strategies in Figure 6.254, Figure 6.255, and Figure 6.256, respectively. For the Brace-YurA36-W-1 specimen, the difference between the three simulations is only seen later on in the loading process. In the three simulations the fact that the first element is in negative traxiality signifying compression and the third element is in positive triaxiality signifying tension which are located at the opposite edges from each other on the same tension flange shows the sever buckling that occurred during higher displacement values. The buckling forced one edge to be in tension while the other in compression. The triaxiality for element 1 and 3 in the VGM simulation deviated from the other two simulations at approximately 13 inches of displacement. In the VGM simulation once the middle element failed it forced the element in compression to go into tension. Hence, in the VGM simulation fracture started in the middle of the tension flange but did not propagate all the way through the flange thickness until much later at which point the beam has already failed by buckling. In the VGM-BW simulation fracture occurred at an edge of the tension flange and then propagated through the flange thickness. Similar behavior was observed in the CS simulation except that fracture occurred at the middle and edge element at the same dispacement value. The initial vibration is due to material in the beam becoming plastic and initial out-of-plane buckling that occurred in the beginning of the simulation. For the Brace-YurA36-W-2 specimen

the triaxiality variation in the elements for the three simulations was similar to that of the Brace-YurA36-W-1 specimen. As in Brace-YurA36-W-1 specimen the difference between the three simulations is only seen later on in the loading process. Overall, the elements failed sooner for the three simulations than in Brace-YurA36-W-1 specimen due to checkered loading applied to Brace-YurA36-W-2 specimen. In the three simulations sever buckling of the beam web caused the first element to be in negative traxiality signifying compression and the third element to be in positive triaxiality signifying tension which are located at the opposite edges from each other on the same tension flange. The triaxiality for element 1 and 3 in the VGM simulation deviated from the other two simulations at approximately 10 inches of displacement. In the VGM simulation once the middle element failed it forced the element in compression to go into tension. Hence, in the VGM simulation fracture started in the middle of the tension flange but did not propagate all the way through the flange thickness until much later at which point the beam has already failed by buckling. In the VGM-BW simulation the edge element 3 failed first and then the middle element followed. The other edge element stayed in the negative triaxiality region. Similar behavior was observed in the CS simulation except that fracture occurred at approximately the same dispacement value for the three elements. The initial vibration is due to material in the beam becoming plastic and initial out-of-plane buckling that occurred in the beginning of the simulation. The edge elements in the VGM simulation failed at a higher displacement value than other elements in other simulations. For the Brace-YurA36-W-3 specimen the triaxiality variation in the elements for the three simulations was different to the other specimens. However the difference between the three simulations is only seen later on in the loading process similar to other specimens. In the three

simulations sever buckling of the beam web caused the third element to be in negative traxiality signifying compression and the first element to be in positive triaxiality signifying tension which are located at the opposite edges from each other on the same tension flange. The triaxiality for element 1 and 3 in the VGM simulation deviated from the other two simulations at approximately 5 inches of displacement. In the VGM simulation once the middle element failed it forced the element in compression to go into tension. Hence, as for other specimens in the VGM simulation fracture started in the middle of the tension flange but did not propagate all the way through the flange thickness until much later at which point the beam has already failed by buckling. In the VGM-BW simulation the edge element 1 failed first and then the middle element followed but the other edge element stayed in the negative triaxiality region. Similar behavior was observed in the CS simulation. The initial vibration is again due to material in the beam becoming plastic and initial out-of-plane buckling that occurred in the beginning of the simulation. The edge elements in the VGM simulation failed at a higher displacement value than other elements in other simulations.

The equivalent plastic strain is plotted in Figure 6.257, Figure 6.258, and Figure 6.259. For the Brace-YurA36-W-1 specimen in the three simulations the edge and middle elements had similar variation of equivalent plastic strain throughout loading until a displacement of approximately 11 inches when the strain in the elements for VGM simulation starts to digress from the other two simulations. In the VGM simulation the third element on the edge of the flange has higher strain value than the middle and element 1. This shows that initially the first element did not experience significant plastic deformation. This changed when element three and element 2 reached a plateau which caused element one to deform at a high plastic strain rate. In the VGM

simulation element 1 was able to reach greater equivalent plastic strain than the other two elements while in VGM-BW simulation the middle element reached the highest strain value. Overall, the VGM allowed the elements to reach higher equivalent plastic strain values than VGM-BW and CS simulations. The behavior of equivalent plastic strain in Brace-YurA36-W-2 specimen is similar to that of Brace-YurA36-W-1 specimen. For the Brace-YurA36-W-2 specimen in the three simulations the elements had similar variation of equivalent plastic strain throughout loading until a displacement of approximately 8 inches when the strain in the elements for VGM simulation starts to digress from the other two simulations. In the VGM simulation the third element on the edge of the flange has higher strain value than the middle and element 1. This shows that initially the first element did not experience significant plastic deformation. This changed when element three and element 2 reached a plateau which caused element one to deform at a high plastic strain rate. The plateau is due to extremely severe lateral buckling of the beam web occurring at the middle of the beam. In the VGM simulation element 1 was able to reach greater equivalent plastic strain than the other two elements while in VGM-BW simulation the middle element reached the highest strain value. Overall, the VGM simulation allowed the elements to reach higher equivalent plastic strain values than VGM-BW and CS simulations. The behavior of equivalent plastic strain in Brace-YurA36-W-3 specimen is somewhat different than in Brace-YurA36-W-1 and Brace-YurA36-W-2 specimens. For the Brace-YurA36-W-3 specimen in the three simulations the elements had similar variation of equivalent plastic strain throughout loading until a displacement of approximately 6 inches when the strain in the elements for VGM simulation starts to digress from the other two simulations. In the VGM simulation the first element on the edge of the flange has higher strain

value than the middle and element 3. This shows that initially the third element did not experience significant plastic deformation. This changed when element 1 and element 2 reached a plateau which caused element 3 to deform at a high plastic strain rate but equivalent plastic strain in element 3 did not reach the value of the other two elements. The plateau is due to extremely severe lateral buckling of the beam web occurring at the middle of the beam. In the VGM simulation element 1 and 2 reached similar equivalent plastic strain value while in VGM-BW simulation the middle element reached the highest strain value. Overall, the elements in the three simulations reached similar equivalent plastic strain values. The fracture locus is plotted in Figure 6.260,

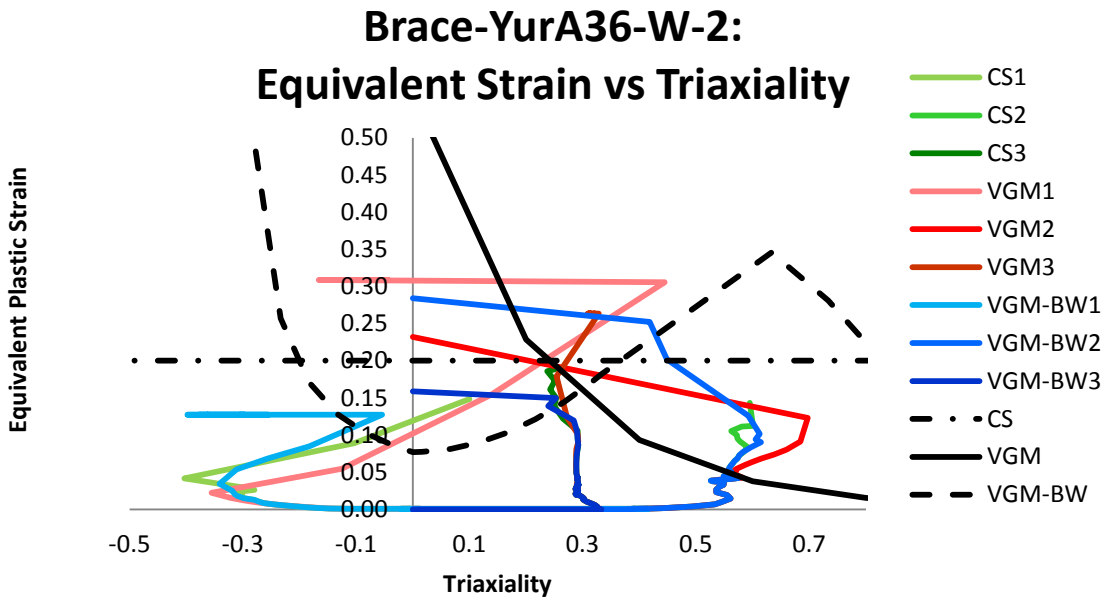

Figure 6.261, and Figure 6.262. In the Brace-YurA36-W-1 specimen the triaxiality range for the chosen elements in the fracture locus is quite large, ranging from negative 0.5 to positive 0.7. In the three simulations, element 1 experiences a decline in triaxiality with increase of equivalent plastic strain during initial loading while element 2 experiences an increase in triaxiality.

Element 3 has a near vertical growth of equivalent plastic strain with minimal changes in triaxiality. The plateau seen in element 2 and 3 is due to initial lateral buckling of the beam web. The behavior of elements in the equivalent plastic strain and triaxiality plane for Brace-YurA36-W-2 specimen is similar to that of Brace-YurA36-W-1 specimen. In the Brace-YurA36-W-2 specimen the triaxiality range for the chosen elements in the fracture locus ranges from negative 0.4 to positive 0.7. In the three simulations, element 1 experiences a decline in triaxiality with increase of equivalent plastic strain during initial loading while element 2 experiences an increase in triaxiality. Element 3 has a near vertical growth of equivalent plastic strain with minimal changes in triaxiality. The behavior of elements in the equivalent plastic strain and triaxiality plane for Brace-YurA36-W-3 specimen is different than in Brace-YurA36-W-1 and Brace-YurA36-W-2 specimens. In the Brace-YurA36-W-3 specimen the triaxiality range for the chosen elements in the fracture locus ranges from negative 0.7 to positive 0.8. In the VGM-BW and CS simulations, element 3 experiences a decline in triaxiality with increase of equivalent plastic strain during initial loading while element 2 experiences an increase in triaxiality. For the three simulation element 1 has a near vertical growth of equivalent plastic strain with minimal changes in triaxiality. In the VGM simulation element 3 goes into positive triaxiality making the three elements across the tension flange in positive triaxiality region signifying tension loading on the flange. Hence, in the VGM simulation the beam experienced smaller lateral buckling of its web than in other two simulations.

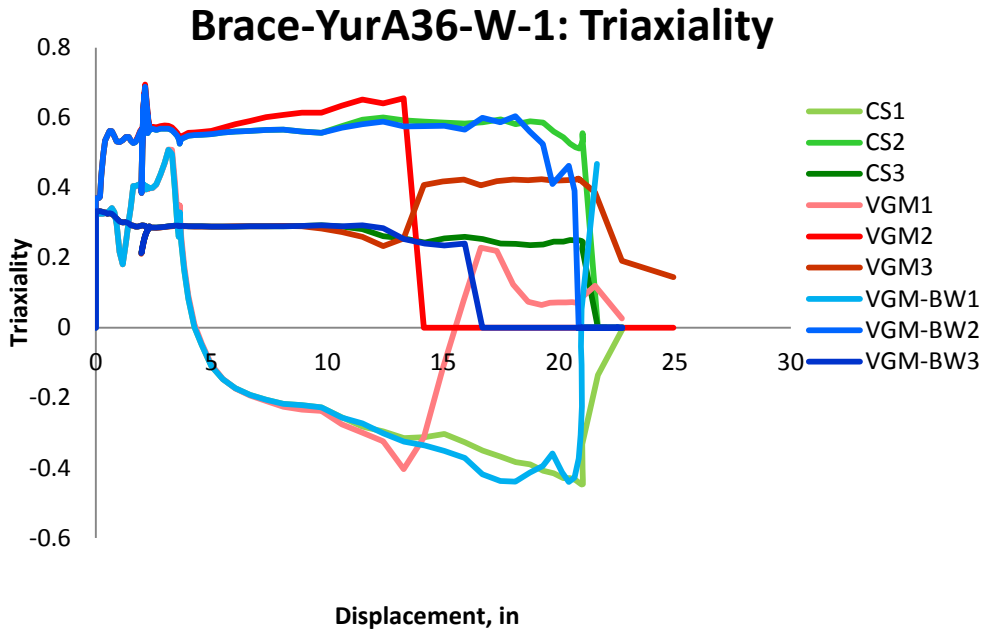

Figure 6.254: Variation of triaxiality with displacement for different elements laid out through the thickness of the tension flange of Brace-YurA36-W-1 specimen for the three finite element deletion strategies

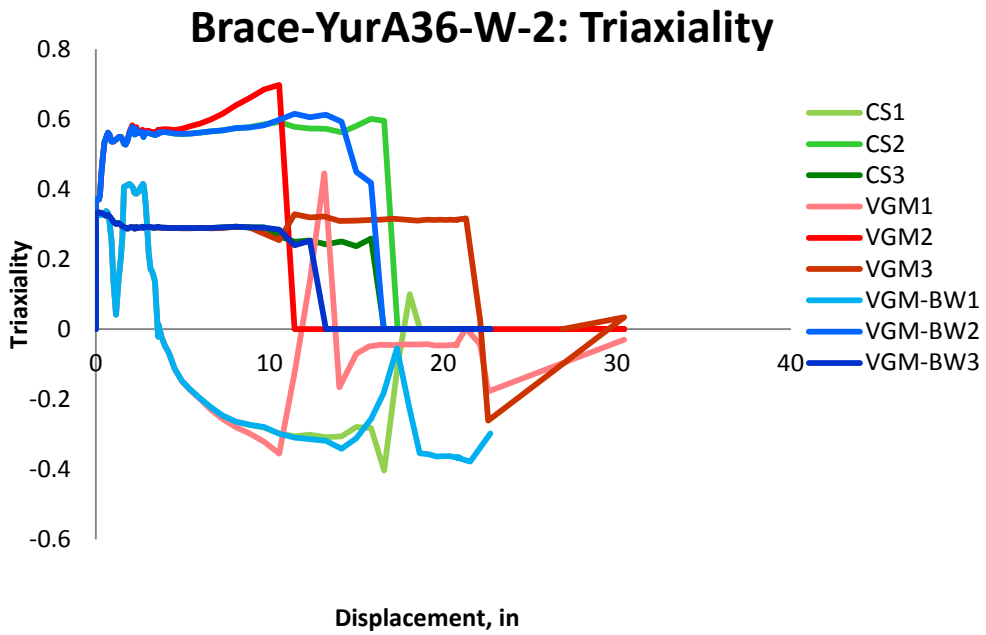

Figure 6.255: Variation of triaxiality with displacement for different elements laid out through the thickness of the tension flange of Brace-YurA36-W-2 specimen for the three finite element deletion strategies

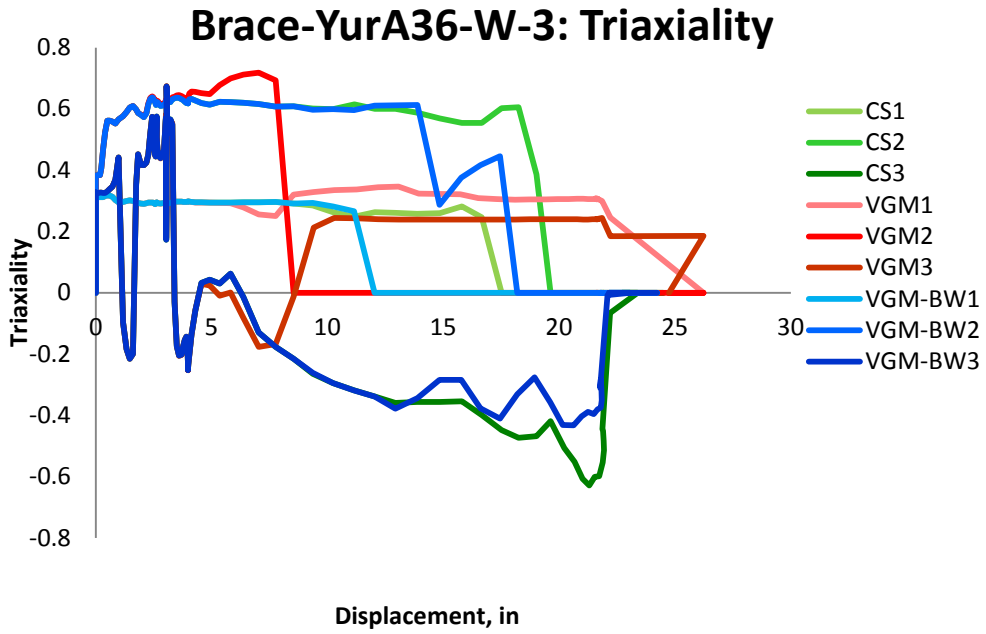

Figure 6.256: Variation of triaxiality with displacement for different elements laid out through the thickness of the tension flange of Brace-YurA36-W-3 specimen for the three finite element deletion strategies

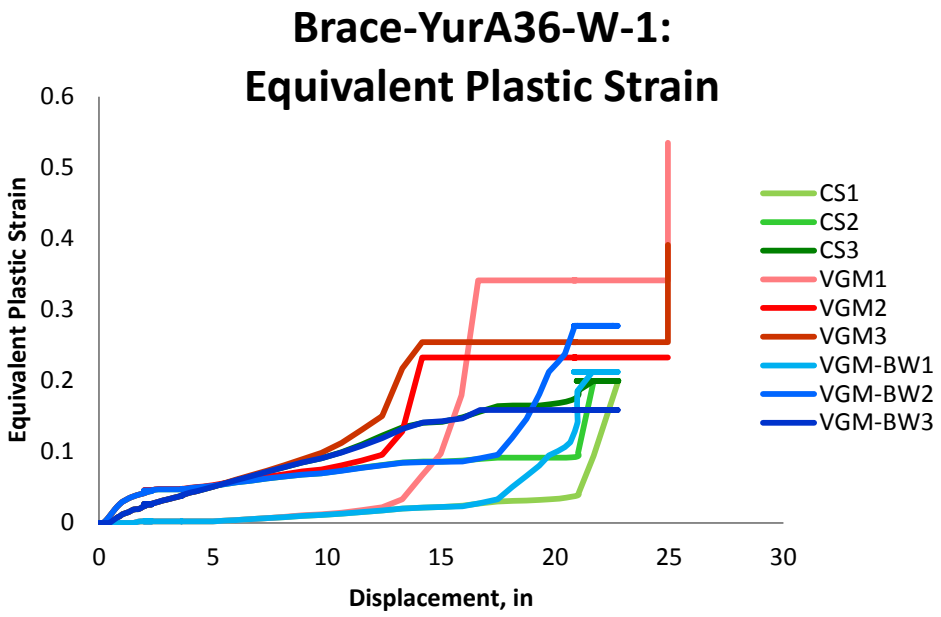

Figure 6.257: Variation of equivalent plastic strain with displacement for different elements laid out through the thickness of the tension flange of Brace-YurA36-W-1 specimen for the three finite element deletion strategies

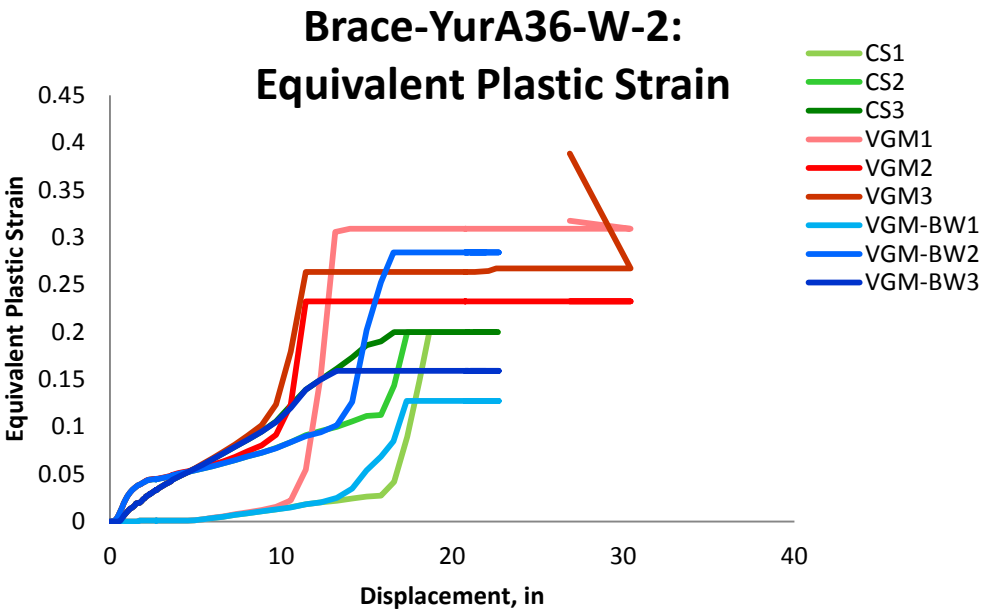

Figure 6.258: Variation of equivalent plastic strain with displacement for different elements laid out through the thickness of the tension flange of Brace-YurA36-W-2 specimen for the three finite element deletion strategies

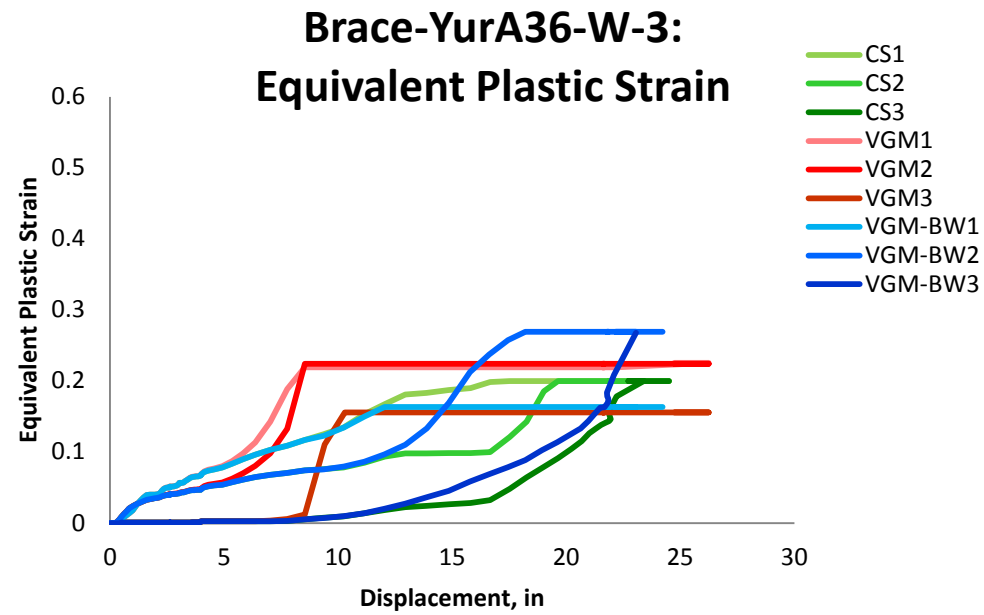

Figure 6.259: Variation of equivalent plastic strain with displacement for different elements laid out through the thickness of the tension flange of Brace-YurA36-W-3 specimen for the three finite element deletion strategies

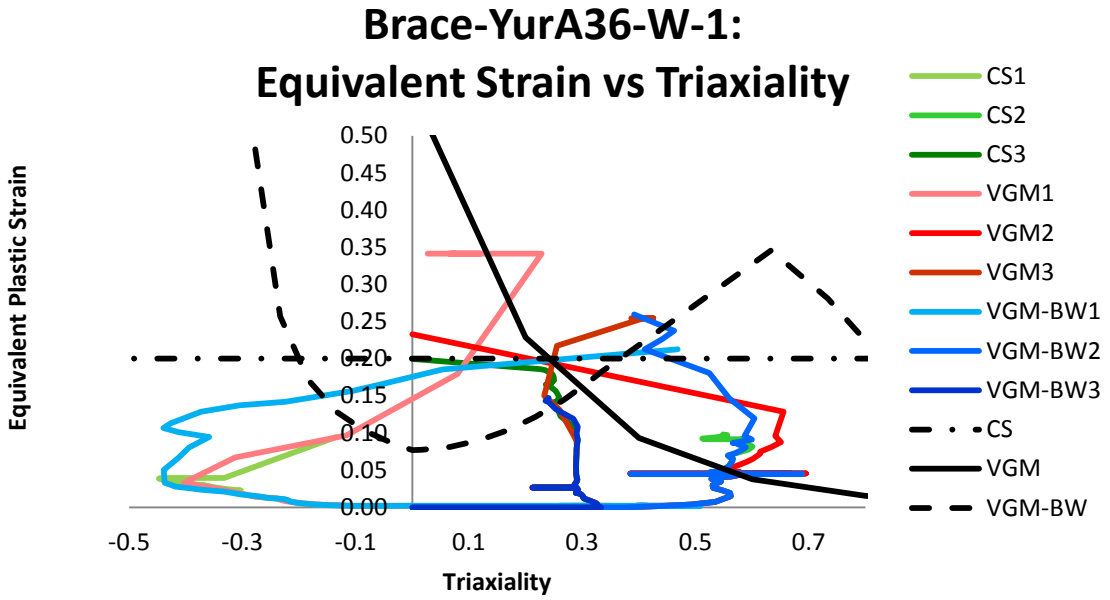

Figure 6.260: Variation of equivalent plastic strain with triaxiality for different elements laid out through the thickness of the tension flange of Brace-YurA36-W-1 specimen for the three finite element deletion strategies

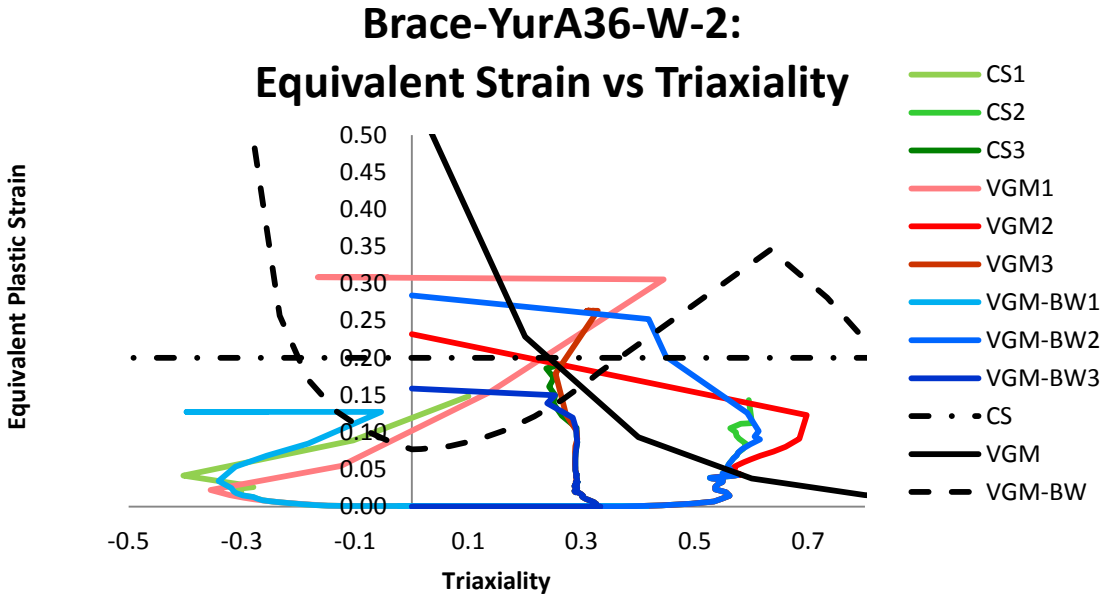

Figure 6.261: Variation of equivalent plastic strain with triaxiality for different elements laid out through the thickness of the tension flange of Brace-YurA36-W-2 specimen for the three finite element deletion strategies

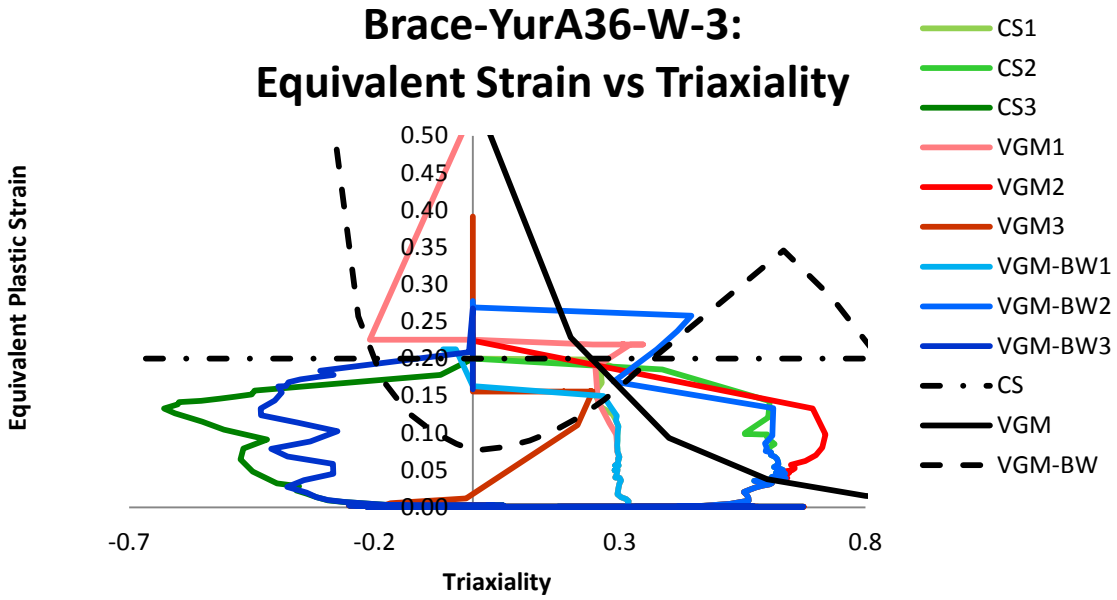

Figure 6.262: Variation of equivalent plastic strain with triaxiality for different elements laid out through the thickness of the tension flange of Brace-YurA36-W-3 specimen for the three finite element deletion strategies

The variation of the value of fracture initiation integral is shown in Figure 6.263, Figure 6.264, and Figure 6.265. For the Brace-YurA36-W-1 specimen in VGM simulation the middle element has the highest fracture initiation integral growth. The middle element initiated softening in the initial part of the loading process at approximately 4 inches of displacement. This is close to maximum experimental displacement value. Other edge elements initiated softening much later in the simulation. The third element had an almost constant slope throughout the loading process while element 1 experienced a sudden increase in the value of fracture initiation integral. In the VGM-BW simulation, element 3 experienced similar variation throughout the loading process as in VGM simulation while in CS simulation the element had a lower slope than in the other two simulations. Element one experienced a sudden increase at the later part of the loading process. This behavior is also seen in the middle elements in VGM-BW and CS simulations. Figure 6.263 also confirms that fracture initiated at the edge of the tension flange

for VGM-BW and CS simulation while for VGM simulation fracture initiated at the center of the flange. Similar behavior was observed for Brace-YurA36-W-2 specimen. For the Brace-YurA36-W-2 specimen in VGM simulation the middle element has the highest fracture initiation integral growth. The middle element initiated softening in the initial part of the loading process at approximately 4 inches of displacement. This is close to maximum experimental displacement value. Other edge elements initiated softening much later in the simulation. The third element had an almost constant slope throughout the loading process while element 1 experienced a sudden increase in the value of fracture initiation integral. For the other two simulations element one also experienced a sudden increase at the later part of the loading process. In the VGM-BW simulation, element 3 experienced similar variation throughout the loading process as in VGM simulation while in CS simulation the element had a lower slope than in the other two simulations. Figure 6.264 also confirms that fracture initiated at the edge of the tension flange for VGM-BW and CS simulation while for VGM simulation fracture initiated at the center of the flange. Similar behavior was observed for Brace-YurA36-W-3 specimen. For the Brace-YurA36-W-3 specimen in VGM simulation the middle element has the highest fracture initiation integral growth. The middle element initiated softening in the initial part of the loading process at approximately 3 inches of displacement. This is below the maximum experimental displacement value. Other edge elements initiated softening much later in the simulation. The third element had an almost constant slope throughout the loading process while element 1 experienced a sudden increase in the value of fracture initiation integral. For the other two simulations element one also experienced a sudden increase at the later part of the loading process. In the VGM-BW simulation, element 3 experienced similar variation throughout the

loading process as in VGM simulation while in CS simulation the element had a lower slope than in the other two simulations. Figure 6.265 also confirms that fracture initiated at the edge of the tension flange for VGM-BW and CS simulation while for VGM simulation fracture initiated at the center of the flange.

The varition of von Mises stress with displacement is shown in Figure 6.266, Figure 6.267, and Figure 6.268. In the Brace-YurA36-W-1 specimen the variation of von Mises Stress is simlar for the three simulations up to a displacement value of 8 inches. The middle element in VGM simulation deviates from other two simulations due to softening being initiated early on in the loading process as described above. Element 2 and three experience sudden drop in stress capacity at aprroximately the same displacement but element three does not fail but caries small amount of laod through the remaining displacement. Element 1 experiences a sudden increase of stress followed by a suddent decrease. This behavior is seen to a lesser extent for element 1 in the other two simulations. The edge elements in VGM simulation experience a plateau in von Mises stress while this is not observed in the other two simulations. In VGM-BW and CS simulations, the elements experience hardening until right before failure. The elements fail with a sudden decrease of von Mises stress value. The initial vibration due to lateral buckling of the beam web in the initial displacement is observed in the elements 1 and 2 but not in element 3. Similar behavior of the von Mises stress variation in Brace-YurA36-W-2 specimen is observed as in Brace-YurA36-W-1 specimen. In the Brace-YurA36-W-2 specimen the variation of the von Mises Stress is simlar for the three simulations up to a displacement value of 8 inches. The middle element in VGM simulation deviates from other two simulations due to softening being initiated early on in the loading process as described above. Element 2

and three experience sudden drop in stress capacity at aprroximately the same displacement but element three does not fail but caries small amount of laod through the remaining displacement. This shows that the middle element failed first. Element 1 experiences a sudden increase of stress followed by a suddent decrease. The edge elements in VGM simulation experience a plateau in von Mises stress while this is not observed in the other two simulations. In VGM-BW and CS simulations, the elements experience hardening until right before failure. The elements fail with a sudden decrease of von Mises stress value. The initial vibration due to lateral buckling of the beam web in the initial displacement is observed in the elements 1 and 2 but not in element 3. Somewhat different behavior of von Mises stress variation is observed in Brace-YurA36-W-3 specimen as in Brace-YurA36-W-1 and Brace-YurA36-W-2 specimens. In the Brace-YurA36-W-3 specimen the Variation of von Mises Stress is simlar for the three simulations up to a displacement value of 5 inches. The middle element in VGM simulation deviates from other two simulations due to softening being initiated early on in the loading process as described above. Element 2 and 1 experience sudden drop in stress capacity at aprroximately the same displacement but element 1 does not fail but caries small amount of laod through the remaining displacement. This shows that the middle element failed first. Element 3 experiences a couple of sudden increases of stress followed by a suddent decrease. The edge elements in VGM simulation experience a plateau in von Mises stress while this is not observed in the other two simulations. In VGM-BW and CS simulations, the elements experience hardening until right before failure. The elements fail with a sudden decrease of von Mises stress value. The initial vibration due to lateral buckling of the beam web in the initial displacement is observed mainly in the element 3 for the three simulations.

The mean stress variation throughout the loading excursion is plotted Figure 6.269, Figure 6.270, and Figure 6.271. For the Brace-YurA36-W-1 specimen the variation of mean stress is similar between the three simulation up to a displacement value of approximately 11 inches. The middle and the edge element 3 have positive values of mean stress while element 1 has negative which signifies an overall tensile and compressive loading on the element, respectively. The variation of mean stress follows very closely to that of triaxiality. When the middle element fails element 1 goes from negative to positive mean stress value. In addition, in the VGM simulation the edge elements experience a plateau of mean stress after a sudden decrease while this is not observed in the other two simulations. For the VGM-BW and CS simulations the mean stress variation is very similar between them with an exception that mean stress for the elements in VGM-BW simulation fails at a smaller displacement value than in CS simulation. The variation of mean stress for Brace-YurA36-W-2 is similar to that of Brace-YurA36-W-1 specimen. For the Brace-YurA36-W-2 specimen the Variation of mean stress is similar between the three simulation up to a displacement value of approximately 11 inches. The variation of mean stress follows very closely to that of triaxiality. The middle and the edge element 3 have positive values of mean stress while element 1 has negative. When the middle element fails element 1 goes from negative to positive mean stress value. In addition, in the VGM simulation the edge elements experience a plateau of mean stress after a sudden decrease while this is not observed in the other two simulations. For the VGM-BW and CS simulations the mean stress variation is again very similar between them with an exception that mean stress for the elements in VGM-BW simulation fails at a smaller displacement value than in CS simulation. The variation of mean stress for Brace-YurA36-W-3 is similar to that of Brace-

YurA36-W-1 and Brace-YurA36-W-2 specimens. For the Brace-YurA36-W-3 specimen the variation of mean stress is similar between the three simulation up to a displacement value of approximately 8 inches. The variation of mean stress again follows very closely to that of triaxiality. The middle and the edge element 1 have positive values of mean stress while element 3 has negative. When the middle element fails element 3 goes from negative to positive mean stress value for VGM simulation but not in the VGM-BW and CS simulation where it remains in the negative mean stress region. In addition, in the VGM simulation the edge elements experience a plateau of mean stress after a sudden decrease and increase while this is not observed in the other two simulations. For the VGM-BW and CS simulations the mean stress variation is again very similar between them with an exception that mean stress for the elements in VGM-BW simulation fails at a smaller displacement value than in CS simulation.

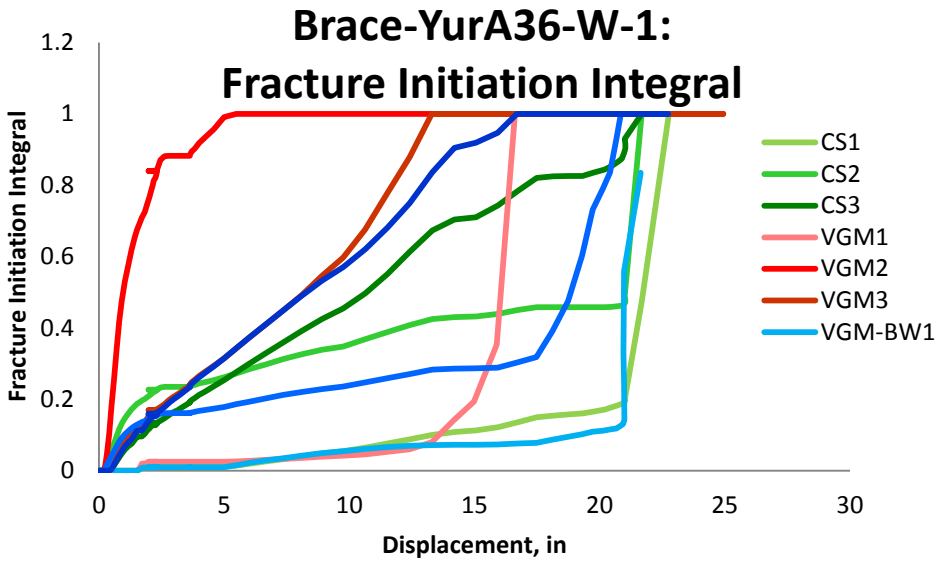

Figure 6.263: Variation of fracture initiation integral value with displacement for different elements laid out through the thickness of the tension flange of Brace-YurA36-W-1 specimen for the three finite element deletion strategies

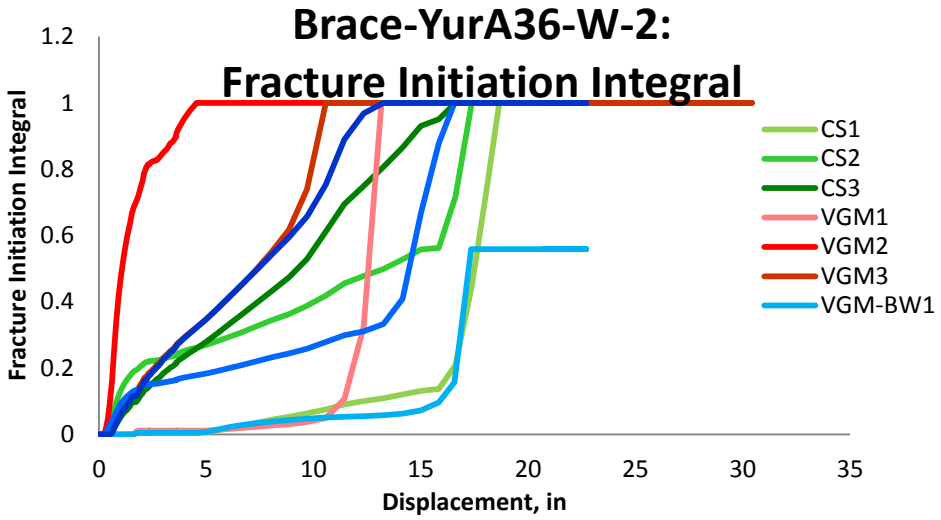

Figure 6.264: Variation of fracture initiation integral value with displacement for different elements laid out through the thickness of the tension flange of Brace-YurA36-W-2 specimen for the three finite element deletion strategies

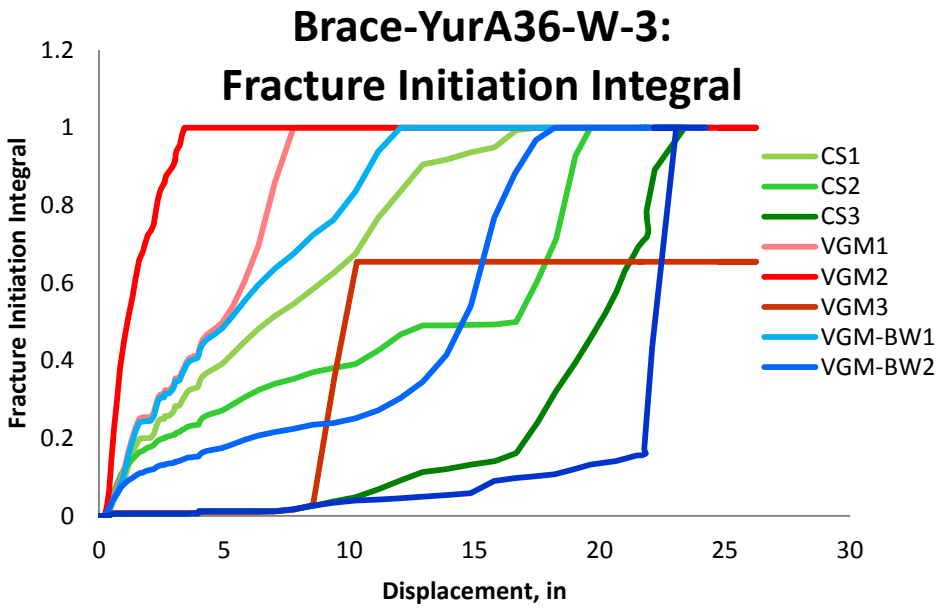

Figure 6.265: Variation of fracture initiation integral value with displacement for different elements laid out through the thickness of the tension flange of Brace-YurA36-W-3 specimen

for the three finite element deletion strategies

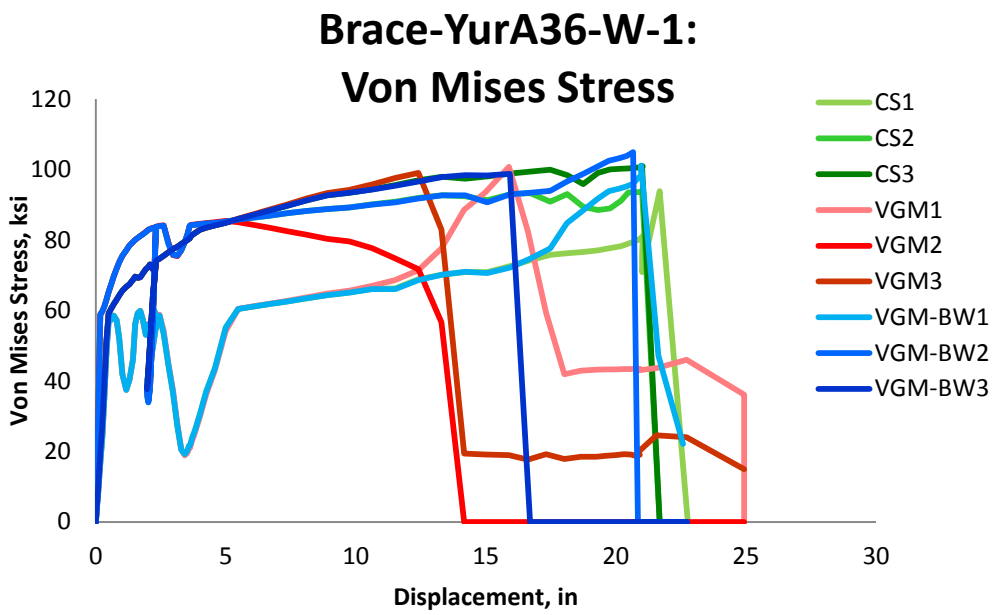

Figure 6.266: Variation of von Mises Stress with displacement for different elements laid out through the thickness of the tension flange of Brace-YurA36-W-1 specimen for the three finite element deletion strategies

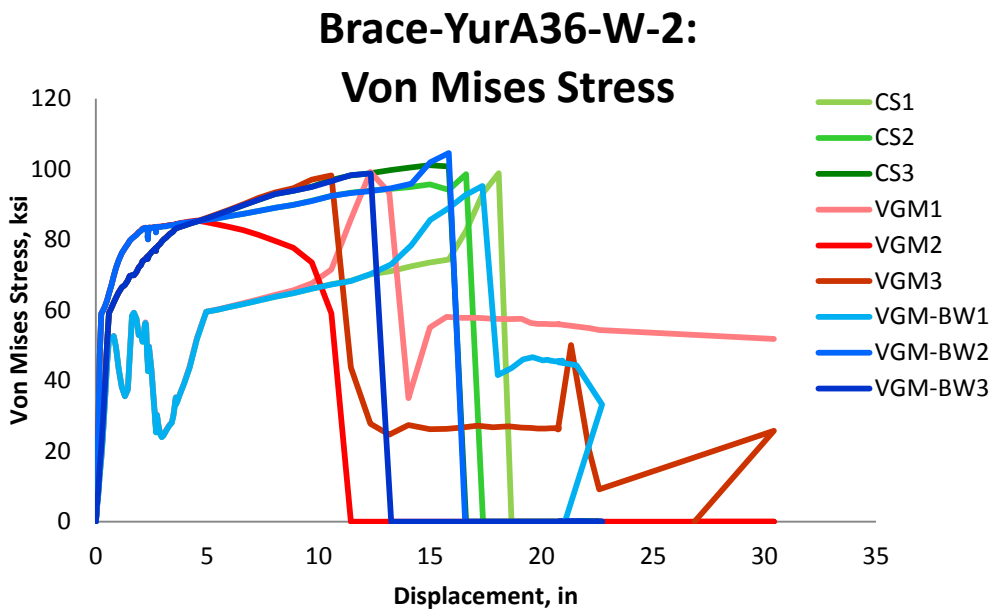

Figure 6.267: Variation of von Mises Stress with displacement for different elements laid out through the thickness of the tension flange of Brace-YurA36-W-2 specimen for the three finite element deletion strategies

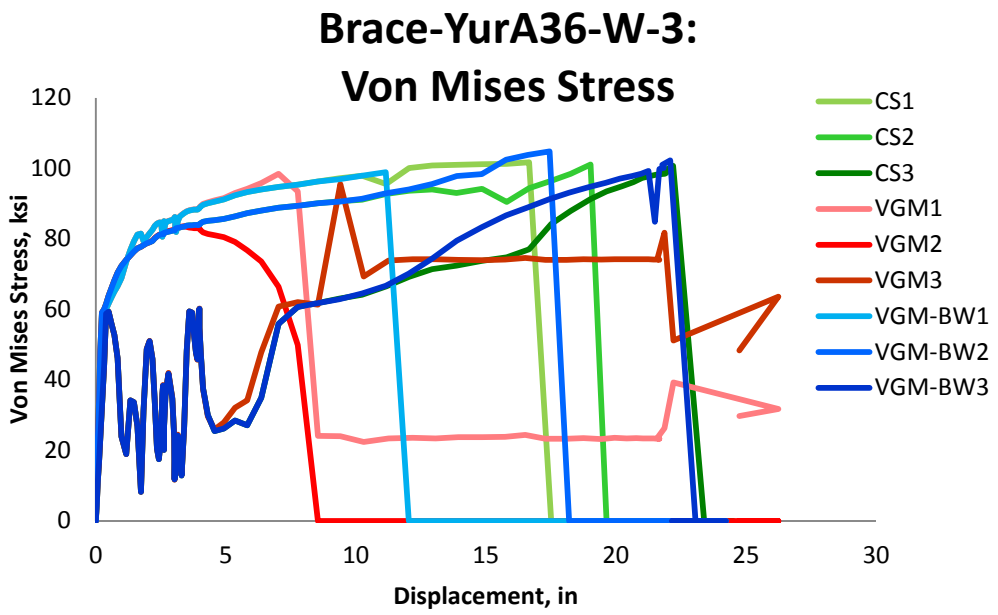

Figure 6.268: Variation of von Mises Stress with displacement for different elements laid out through the thickness of the tension flange of Brace-YurA36-W-3 specimen for the three finite element deletion strategies

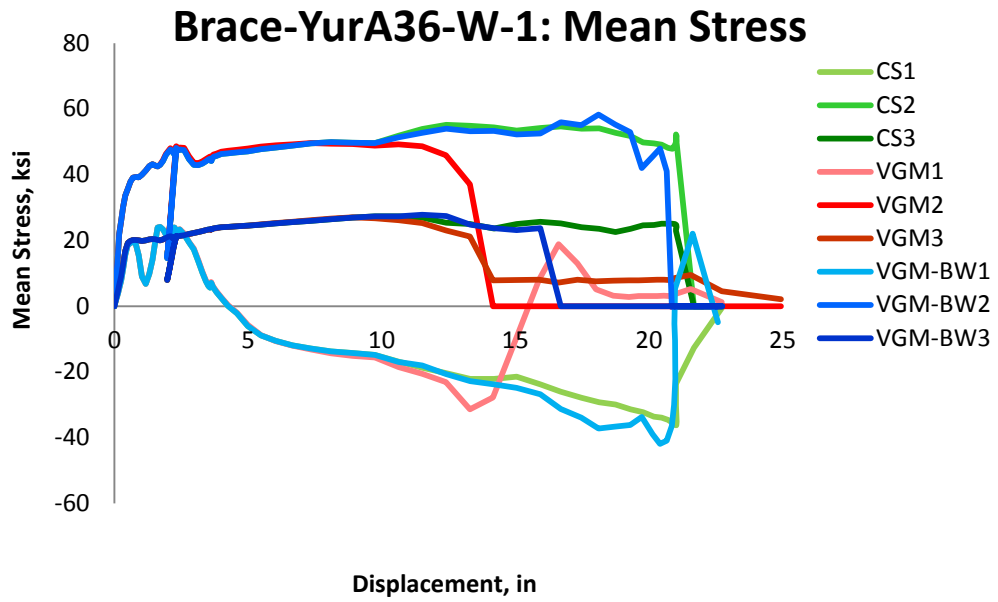

Figure 6.269: Variation of mean stress with displacement for different elements laid out through the thickness of the tension flange of Brace-YurA36-W-1 specimen for the three finite element deletion strategies

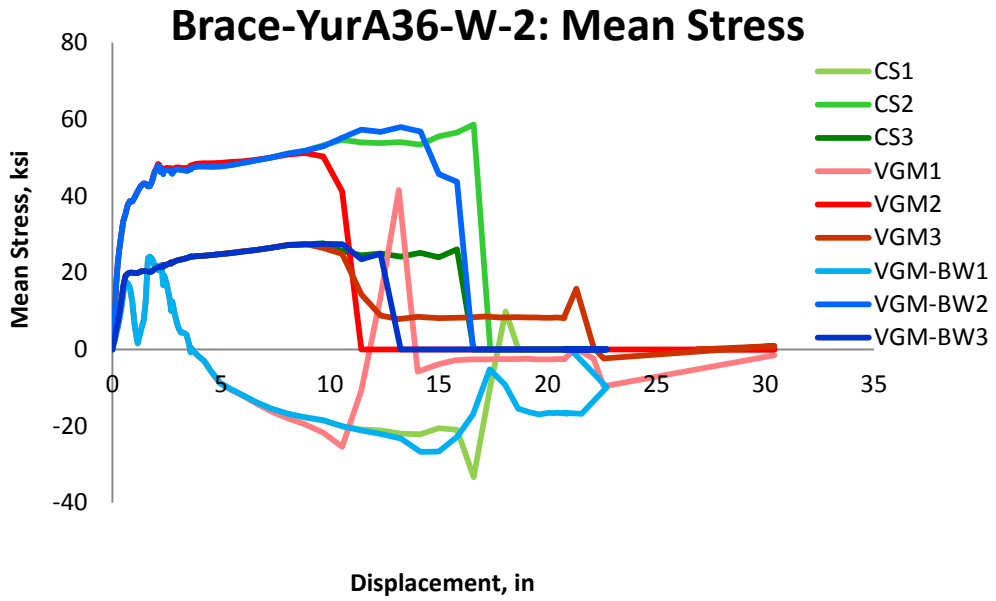

Figure 6.270: Variation of mean stress with displacement for different elements laid out through the thickness of the tension flange of Brace-YurA36-W-2 specimen for the three finite element deletion strategies

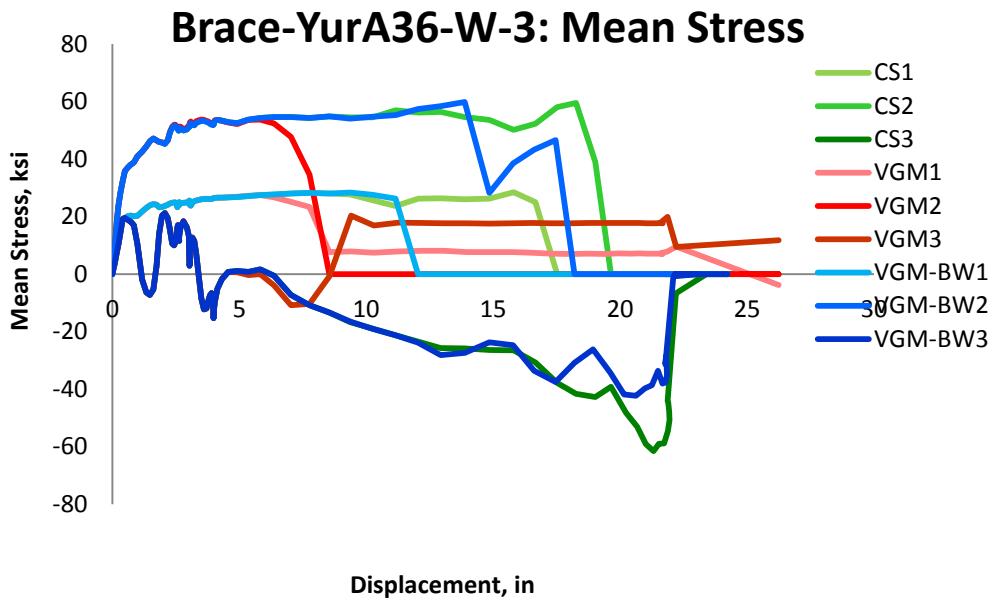

Figure 6.271: Variation of mean stress with displacement for different elements laid out through the thickness of the tension flange of Brace-YurA36-W-3 specimen for the three finite element deletion strategies

Figure 6.272, Figure 6.273, and Figure 6.274 show the variation of von Mises equivalent stress with equivalent plastic strain. For Brace-YurA36-W-1 specimen in the VGM simulation the edge

elements attain higher stress and strain values than does the middle element while in VGM-BW simulation the middle element attains higher values. In CS simulation the middle and first element fail at approximately similar strain values. In VGM-BW simultion the softening is sudden while in CS and more so in VGM simulation the softening is more gradual. In the VGM simulation there is large difference between the curves of each elements while in VGM-BW and CS simulations the difference is much smaller between each curve. Similar behavior is observed in the Brace-YurA36-W-2 specimen. For Brace-YurA36-W-2 specimen the VGM simulation has the edge elements again attain higher stress and strain values than the middle element while in VGM-BW simulation the middle element attains higher values. In CS simulation the middle and first element fail at approximately similar strain values. In VGM-BW simultion the softening is sudden while in CS and more so in VGM simulation the softening is more gradual. In the VGM simulation there is large difference between the curves of each elements while in VGM-BW and CS simulations the difference is much smaller between each curve. Different behavior is observed in the Brace-YurA36-W-3 specimen. In the VGM-BW simulation the elements achieved higher strain values than in the other two simualtions. The middle element failed after the two edge elements in the VGM-BW simulation. Sudden softening was again observed in the VGM-BW simulation. The elements in CS simulation all failed at similar strain values signifying a very sudden fracture across the tension flange of the beam. In the VGM simulation the middle element failed first followed by the edge elements. After the failure of the middle element the third element experienced a sudden load increase failing soon after. The slope of the softening curve in VGM simulation is more gradual than in the other two simulations.

The variation of the value of the damage variable is plotted in Figure 6.275, Figure 6.276, and Figure 6.277. For the Brace-YurA36-W-1 specimen in the VGM simulation the middle element failed first followed by the edge elements which had a plateau for the later part of the loading most likely due to severe lateral beam web buckling. These edge elements had a sudden failure. For VGM-BW simulation the edge element failed first followed by the middle element. The other edge element did not fail. In the CS simulation the three elements failed at approximately the same displacement value. For the Brace-YurA36-W-2 specimen in the VGM simulation the middle element failed first followed by the edge element which had a plateau for the later part of the loading most likely due to severe lateral beam web buckling. The edge element 1 did not fail signifying that fracture did not propagate through the flange thickness. For VGM-BW simulation the edge element failed first followed by the middle element. The other edge element did not fail. In the CS simulation the three elements failed at approximately the same displacement value. For the Brace-YurA36-W-3 specimen in the VGM simulation the middle element failed first followed by the edge element which had a plateau for the later part of the loading most likely due to severe lateral beam web buckling. The edge element 3 did not fail signifying that fracture did not propagate through the flange thickness. For VGM-BW simulation the edge element failed first followed by the middle element and then followed by the other edge element. In the CS simulation the order of failure followed that of VGM-BW simulation.

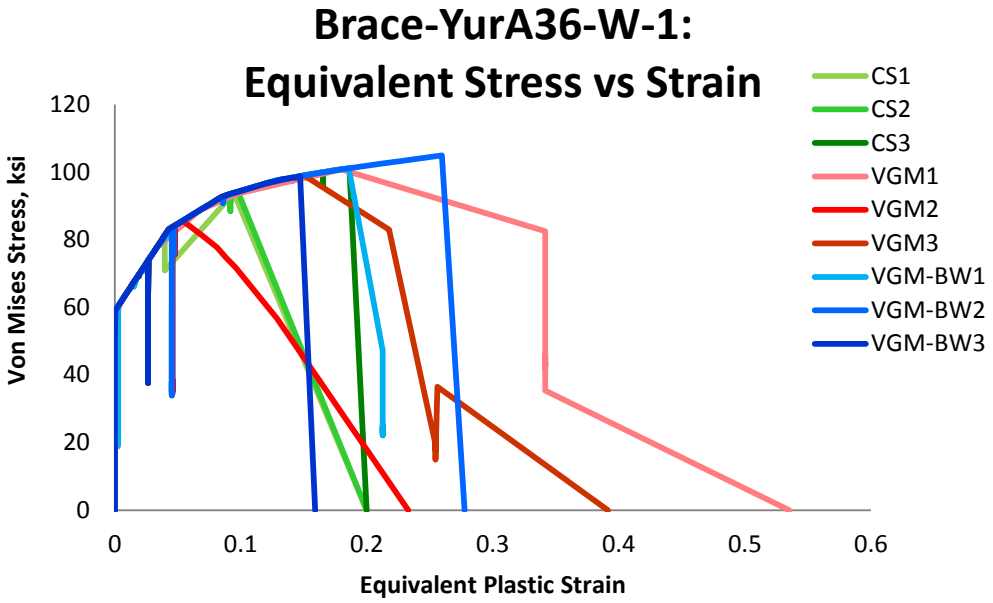

Figure 6.272: Variation of von Mises Stress with equivalent plastic strain for different elements laid out through the thickness of the tension flange of Brace-YurA36-W-1 specimen for the three finite element deletion strategies

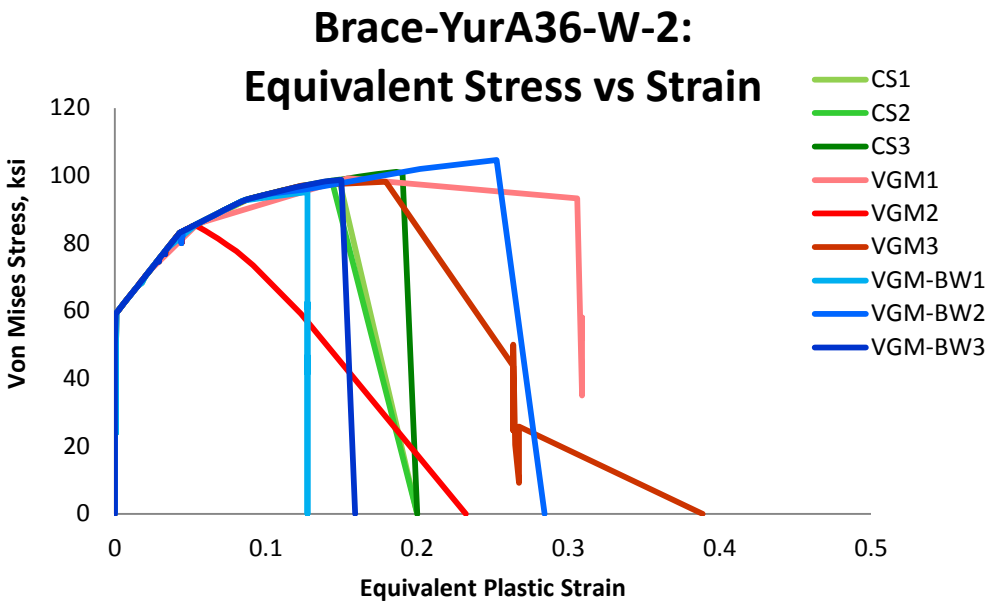

Figure 6.273: Variation of von Mises Stress with equivalent plastic strain for different elements laid out through the thickness of the tension flange of Brace-YurA36-W-2 specimen for the three finite element deletion strategies

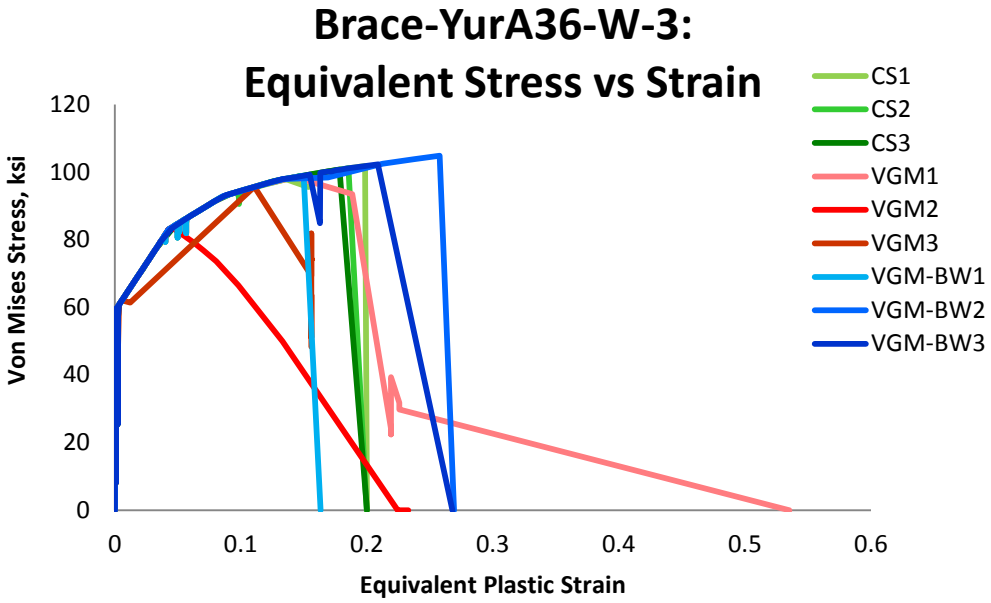

Figure 6.274: Variation of von Mises Stress with equivalent plastic strain for different elements laid out through the thickness of the tension flange of Brace-YurA36-W-3 specimen for the three finite element deletion strategies

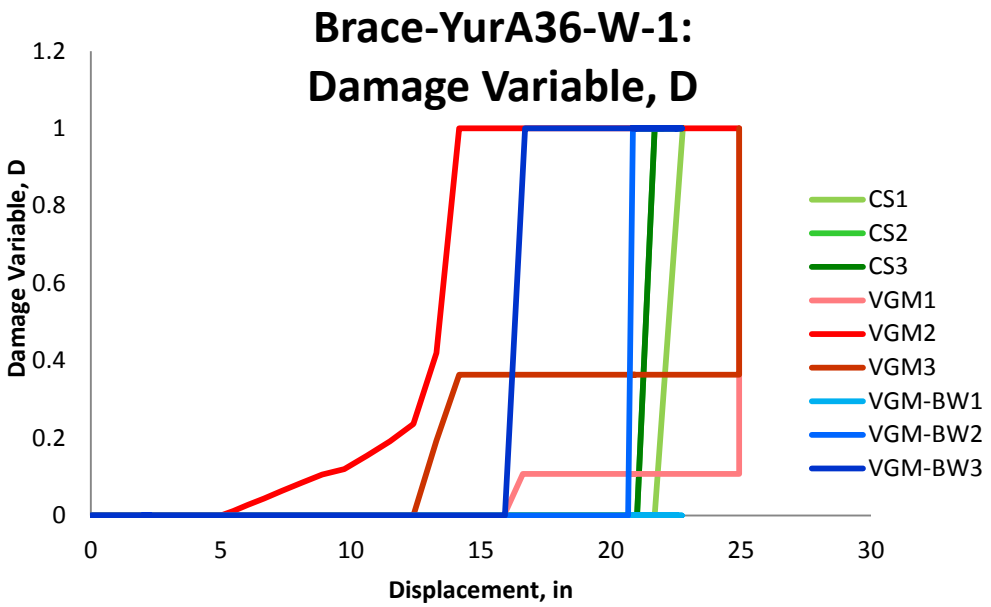

Figure 6.275: Variation of Damage Variable with displacement for different elements laid out through the thickness of the tension flange of Brace-YurA36-W-1 specimen for the three finite element deletion strategies

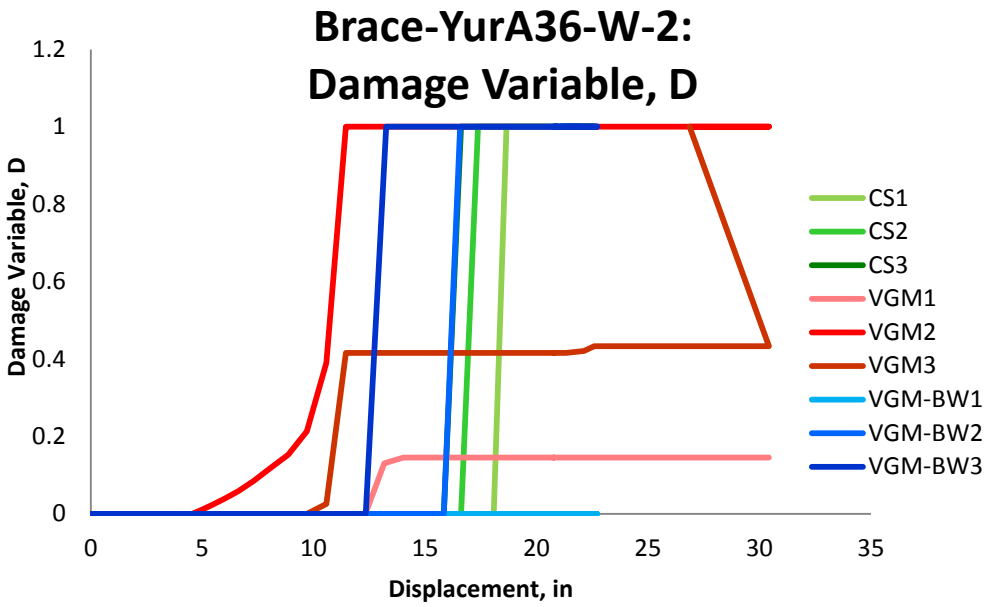

Figure 6.276: Variation of Damage Variable with displacement for different elements laid out through the thickness of the tension flange of Brace-YurA36-W-2 specimen for the three finite element deletion strategies

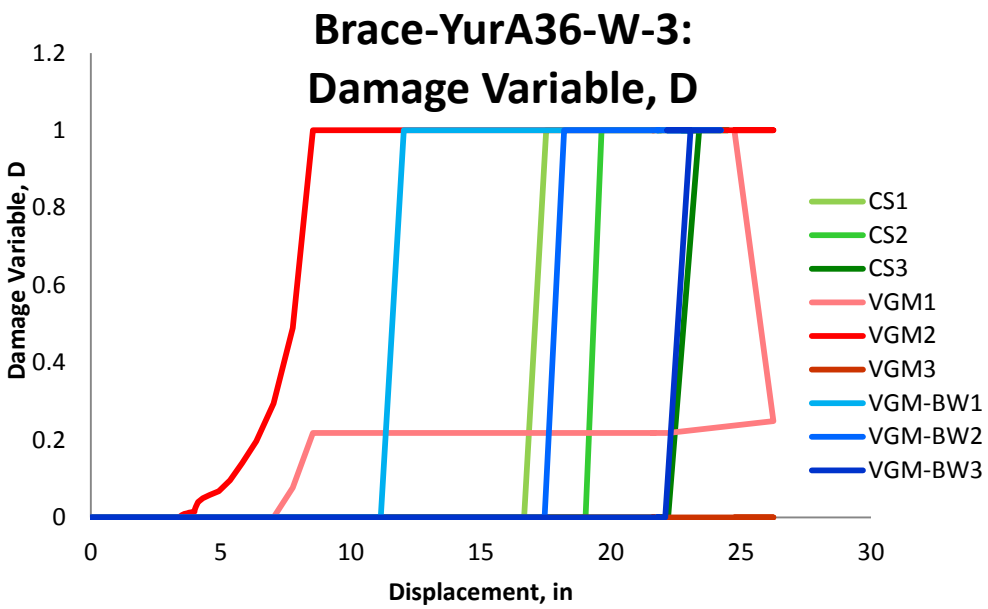

Figure 6.277: Variation of Damage Variable with displacement for different elements laid out through the thickness of the tension flange of Brace-YurA36-W-3 specimen for the three finite element deletion strategies

6.9.1 Summary

In this validation study, construction steel material A36 and weld E70 with and without hardness were validated against experimental test results of the three three-story-braced frames which differed from each other by the applied loading configuration. In the experimental testing of the braced frames several plastic hinges are developed during the loading process, although fracture is not mentioned explicitly. Overall, for the three braced frame specimens the predominant failure was out-of-plane buckling of the beams and not fracture. Judging from the results of the simulations it could be concluded that fracture did not occur in the experimental tests of the three braced frames and that the primary failure mode was the buckling of the beam webs. This was due to the frame allowing for structural parts to deform in such a way as to allow plastic flow in the material which relates to lower triaxiality. In addition, in the VGM simulation, the fracture of the tension flange had a high tendency to start in the middle of the flange while in the other two simulations the edge of the flange was the most likely location of fracture initiation. Since fracture did not occur in the experimental tests it cannot be concluded which of the simulations were more accurate in predicting failure. It is interesting to note that beam buckling caused some elements of the tension flange to be in compression and increased the triaxiality range experienced by the elements. In addition, even though the connections performed in a ductile fashion and avoided fracture until the beam failed by severe buckling.

7 Conclusions

7.1 Summary of the Element Deletion Strategy

This work has focused on implementing finite element deletion strategies to simulate fracture initiation, propagation and softening, and eventual finite element deletion, which represents material dissociation, within the context of continuum finite element modeling to be used in collapse modeling of steel structures. Motivation for this study came from the fact that most studies on collapse of steel structures do not account for material dissociation or fracture in their modeling and those that do have not used a broad range of experimental test results of

steel connections and of multi-story steel structures undergoing collapse to comprehensively validate the models used.

The state-of-the-art structural collapse models of steel structures have used the constant critical strain approach to model fracture in steel members (Khandelwal et al. 2009; Sadek et al. 2010; Szyniszewski et al. 2012). In this approach, a critical equivalent plastic strain at fracture is specified at an integration point of a finite element. Upon reaching this equivalent plastic strain at an integration point of the finite element, the element is suddenly removed (Khandelwal et al. 2008). The constant critical strain approach is used most often in modeling collapse of steel structures because of its practicality, ease of use, and a lack of complexity in the model itself. However, this may create an oversimplified model for a complex fracture process that occurs during collapse of steel structures. This means that the calibrated critical strain may be valid only for a situation that has similar boundary conditions, geometrical configuration, and loading history as the experimental setup that was used for calibration. For all other cases, it will typically either overpredict or underpredict the results. The constant critical strain approach simplifies the fracture initiation process to a single value of critical strain while ignoring ductile fracture's dependence on stress triaxiality. In Chapter 3 of this report it was shown through literature review that triaxiality and equivalent plastic strain are the two most important quantities in determining fracture in ductile metals. Other important parameters in determining fracture initiation in ductile metals were also reviewed. In addition, the Constant Strain approach suffers from not implementing softening defined by the degradation of finite element's stress and stiffness. Preliminary studies in the literature have shown that an alternative approach that includes material softening leading to finite element deletion has the

potential to yield better results (Bao et al. 2004; Wierzbicki et al. 2005; Khandelwal et al. 2009; Sadek et al. 2010). The approach should be firmly grounded in micromechanical fracture models that can account for different state of stress and strain, coupled with stress softening to delete a finite element.

In this work, two other models are proposed to be used for finite element deletion in steel structures: the Void Growth Model (VGM) and the hybrid of VGM and Bao-Wierzbicki Model (VGM-BW), which are compared to the current state-of-the-art in collapse modeling of steel strutures, the constant critical strain approach. The VGM model was developed by (Rice et al. 1969) for high triaxiality regions. It is based on the conclusion reached by Rice et al. (1969) that equivalent plastic strain to fracture was an exponential function of triaxiality. To account for lower triaxiality regions, parts of the Bao-Wierzbicki criterion (Bao et al. 2004) were utilized. Bao et al. (2004) propose a piecewise fracture initiation model that accounts for a complete range of triaxiality. The Bao-Wierzbicki criterion is a compromise between accuracy and practicality. To improve this criterion, it was combined with the VGM criterion which determined the critical equivalent plastic strain at higher triaxiality regions. In addition, softening and finite element deletion in the VGM and VGM-BW approaches is modeled through the Hillerborg Model (Hillerborg et al. 1976). This is done by allowing for monotonically decreasing stress and stiffness during softening. This approach, in addition to mitigating spatial mesh dependency, allows for minimizing spurious transient effects of dynamic instabilities upon element deletion that may cause inaccuracy of the results. Overall, the chosen approaches implement fracture micromechanical models that are based on stress triaxiality,

which allows for better prediction of fracture location and propagation direction than the current critical strain approach.

These fracture initiation micromechanical models are then calibrated and validated through comparison with a comprehensive set of experimental test results, ranging from coupon tests through to complete structures subjected to collapse. The VGM model parameters were calibrated through comparison to circumferentially notched tensile coupon specimens by the Particle Swarm Optimization (PSO) algorithm. The PSO algorithm requires the definition of an objective or error function that determines the quality of the fit between the experimental and computational results. This approach tries to minimize the objective function, which is defined in the force-displacement space by running a nonlinear finite element simulation which generates load-displacement curve for a given design point, which is a candidate parameter set for the VGM fracture model. Overall, satisfactory results were attained. Unfortunately no experimental coupon specimens were available for lower and negative triaxiality regions. Therefore, Bao-Wierzbicki model was calibrated analytically through the use of the plastic hardening relationship obtained through the standard tensile coupon specimens. This was shown to be possible through obtaining an empirical relationship of the hardening exponents of the material and the equivalent plastic strain at fracture initiation. In addition, the variation of fracture initiation and propagation parameters was studied in detail through VGM simulations of the circumferentially notched tensile specimens. In addition, no strong relationship was found between the Charpy V-Notch experimental test results and the VGM and Bao-Wierzbicki parameters.

Finally, this work presented the validation of the VGM, VGM-BW, and the CS approaches to finite element deletion. The accuracy of the validation results was decided through comparison of the experimental and simulation force-displacement result and if the model was able to properly capture the fracture initiation and propagation seen in the experimental testing. This showed how much triaxility is dictating fracture in steel structures since both the VGM and B-W models are dependent on triaxiality, but the constant critical strain approach is not. In addition, the plotted fracture initiation and propagation parameters show the triaxiality range that is dominate during fracture at critical locations, and the general behavior associated with those parameters. The validation set included circumferentially notched tension specimens, plate specimens with holes and cutouts, compact tension specimens, single edge notch bending specimens, shear tab connections, moment-resisting connections, a portal frame, and three multi-story braced frames, which were used to validate each finite element deletion strategy through the above mentioned criteria.

7.2 Conclusions

The chosen fracture initiation approaches, VGM, VGM-BW, and CS, all use local stress and strain derived quantities, such as equivalent plastic strain and triaxiality, to model the initiation of softening and associated degradation of stress and stiffness of the finite element. After the parameters of the VGM, B-W, and Hillerborg models were calibrated for particular structural steels analytically and based on the use of CNT and tensile lapped specimens, they were validated through comparison with a broad array of experimental test results of steel structures and compared to the CS approach. Through these calibration and validation simulations and

fracture initiation and propagation plots,it was concluded that triaxiality is critical in properly determining the location of fracture initiation and propagation direction and to properly account for - stress and stiffness degradation in collapse modeling fo steel structures. It was also concluded that VGM-BW approached lacked the advantage of being calibrated to the experimental test results directly. In addition, when the fracture locus is defined in negative triaxiality it allows for nonphysical fracture, which was not observed in experimental tests to occur in the CS and VGM-BW simulations. This highlights the need for further research into the topic of fracture cut-off and how to properly account for negative triaxiality regions. (Bao et al. 2004) . The CS approach often performed poorly in determining the fracture initiation and propagation direction and capturing the force-displacement capacity of many of the specimens. Overall, the VGM approach had the best performance in determining fracture behavior and capturing the force-displacement capacity. However, CS is computationally less burdensome in calibration and the VGM-BW approach is very promising if calibrated directly to experimental test results.

7.2.1 Influence of Triaxiality on Fracture and Limitations of the Element Deletion Strategies

The influence of triaxiality was first studied in the calibration and then validation of CNT specimens. The first observation is that the material on the outer surface has less constraint to plastic flow and thus less triaxiality than elements at the center (Anderson 2005). However, for each element it could be seen that triaxiality does not vary much throughout loading until it reaches softening after which an increase in triaxiality is usually observed. Another important observation that could be made is that softening of stress and stiffness dramatically increases triaxiality in an element for all elements through the thickness of the specimen except for the

outer ones. The elements on the outer surface attain greater strain values than those that are at the center. It could also be observed that as the notch radius decreases of the CNT specimen the overall triaxiality range increases. Also, it is shown that the material in the center of the specimen will initiate softening sooner than the material on the outer surface. In addition, the larger notch radius of the CNT specimen allows for more use of the material on the surface of the notch than smaller notch sizes by increasing the relative amount of deformation the material on the surface can achieve to those in the center. Overall, this allows for the elements on the surface of the specimens to exhibit much larger strain energy using the same material model than those at the center. This behavior is significant, with elements on the surface achieving strain energy almost as twice as large as those at the center. This all signifies that triaxiality plays a critical role in the mechanical use of the material. As triaxiality increases the use of the material defined by equivalent plastic stress, strain, and strain energy decreases which signifies that structural detailing is very important in avoiding fracture and in effective use of the material. In addition the CNT validation results show that the calibrated fracture locus was able to capture the fracture behavior well in a different triaxiality range for the VGM strategy, but not for the VGM-BW and CS. A general trend is seen in the three simulations of the CNT specimens in that after initiation of softening triaxiality is dramatically increased for the inner elements but not for the outer ones. In general, the CS approach significantly underestimated the fracture equivalent plastic strain in CNT specimens resulting in inaccurate results. In the VGM simulations, fracture initiates at the center of the specimen and propagates outward, in agreement to the conclusions found in the literature. The CS and VGM-BW

simulations have the fracture start from the outside but the VGM-BW is able to capture shear lip fracture.

In the simulations of plate specimens with holes and cutouts (bolt-hole and dog-bone specimens), the VGM criteria closely followed the experimental observations with fracture originating on the outside edge of the specimen hole from the inside of the specimen and propagating to the outer surface of the specimen. However, fracture also quickly initiated on the inside edge of the specimen hole in the center of the specimen. For the CS and VGM-BW simulations, the fracture occurred simultaneously on the outer and inner edge of the specimen hole in the center of the specimen and propagated outward. As the loading progressed, the VGM-BW simulation had fracture occur on the surface of the specimen. In the experimental testing of dog-bone specimens, fracture propagated quickly, which suggests that the ductile initiation takes place over a large area and then all of a sudden the material fails by a mixture of tearing and ductile mechanisms. All of the three strategies had different fracture initiation and propagation for both specimens. The CS simulations showed a sudden fracture through the material thickness and height, which seems to correspond to observed sudden fracture of the specimens in the experimental tests. The VGM simulations showed fracture initiating at the center of the specimen away from the edge of the notch with fast fracture propagation to the surface of the specimen. VGM-BW simulation showed an opposite trend to that of VGM. The fracture initiated at the center of the specimen on the surface of the notch and propagated inward towards the center of the specimen. Overall, in these simulations the VGM approach performed better in locating facture initiation and properly modeling fracture propagation. Similarly to the CNT specimens, after initiation of softening, triaxiality is generally significantly

increased for the inner elements but not for the outer ones. The equivalent plastic strain for the outer element continues to have a near vertical slope relative to triaxiality throughout the entire loading excursion and is not affected by softening. In addition, there is a significant difference in the triaxiality range of the outer and the inner elements. However, for the VGM-BW approach, no apparent trend is observable and CS simulations have immediate failure for all of the three elements. From these validation simulations, it could be concluded that triaxiality is governed mainly by the geometry of the specimen and to a lesser extent the material of the specimen and that incorporating softening into the material fracture model has significant effect on the global response of the structure. In addition, the CS approach significantly underestimated the fracture equivalent plastic strain resulting in inaccurate results. The VGM had the most accurate prediction of the force-displacement capacity while the VGM-BW and the CS significantly underestimated the capacity.

In the compact tension specimens, the VGM criterion gave the best force-displacement predictions while the CS and VGM-BW usually underpredicting. In addition, the prediction is better for a thinner specimen than for a thicker one suggesting that the calibrated fracture locus at higher triaxiality is too low. On the other hand, the VGM-BW, which accounts for shear and mix-mode fracture, most accurately represented fracture propagation by properly capturing the tunneling effect and shear lip fracture on the edge surface of the specimens. However, VGM-BW simulations had minor fracture occurring at the back end of the specimen which is not recorded in experimental tests. In the VGM simulation, shear lip fracture behavior was not captured. However, it captured the crack tunneling effect and surface of the specimen necking and bulging. Again it is observed that the variation of triaxiality is more affected by the

geometry of the specimen than the material it is made out of. In addition, it was observed that the hardening of the material keeps the triaxiality approximately constant throughout the loading process until softening, which increases the triaxiality.

For the SENB specimens, no description of the fracture propagation was provided in the original paper. In the three simulations with different element deletion strategies, fracture occurred at the center of the specimen and propagated outward. In addition, all three finite deletion strategies showed some crack tunneling effect. The VGM and VGM-BW had a more pronounced tunneling effect than the CS strategy. All three strategies performed well in capturing the force-displacement curve of the experimental test results. In addition, it was observed that in the SENB specimen, there is a significant difference in behavior of fracture parameters between the outer edge and the inner part of the specimen. This is shown in triaxiality, equivalent plastic strain, and other stress-strain fracture parameters variations throughout the loading. The inner part of the specimen is under plane strain conditions, while the surface is under plane stress. The CS approach ignores these effects, while trying to provide an average of the material fracture capacity, but the VGM and VGM-BW account for these changes by modeling fracture initiation based on triaxiality. It was also observed that during hardening of the material the equivalent plastic strain will increase with decreasing triaxiality, but it will increase with an increase in triaxiality during softening for the material.

In the three simulations of a bolted double-angle beam connection, the fracture propagated very quickly, with bolts ripping through the beam web. For the CS and VGM-BW approaches, the fracture started with the top bolt ripping the beam web. For the VGM simulations, the

lower bolt was the first one to rip through the beam web and then the two other bolts followed. It was also observed that equivalent plastic strain had a positive relationship with triaxiality while the material is experiencing plastic hardening and a negative relationship when it softens. Triaxiality greatly increases right before failure and finite elements located in the beam web at the surface of bolt holes failed in the positive triaxiality region for the three finite element deletion strategies.

In addition, interesting observations in the simulation of moment-resisting connection specimens were made about the influence of triaxiality and performance of the finite element deletion approaches. For specimen MRC-RenA572-W-14-1, for the VGM and VGM-BW simulations, the failure occurred instantaneously in the tension flange in the weld. The value of the fracture initiation integral showed that the crack started from the lower edges of the tension flange and quickly propagated through the thickness of the flange. The CS simulation showed a type of fracture that is not reported in the experimental test results. For specimen MRC-RenA572-W-14-2, the VGM and VGM-BW simulations showed failure occurring instantaneously in the tension flange of the beam connecting to the column web. The values of fracture initiation integral along the flange thickness indicate that the crack started from the lower edges of the tension flange and quickly propagated through the thickness of the flange. The fractures in the CS simulation at the beam flanges were not sudden like they were in the VGM and VGM-BW simulations and did not completely propagate through the flange thickness. The VGM and the VGM-BW simulations underpredict the overall capacity of the sub-assemblage while the CS overpredicts it. In the experimental test of specimen MRC-RenA572-W-14-3, the VGM/VGM-BW simulation underpredicts the overall force-displacement capacity

of the sub-assemblage but the CS captures it accurately. However, none of the simulations properly captured the fracture behavior seen in the experiment. For specimen MRC-RenA572-W-14-4, the VGM and the VGM-BW simulations significantly underpredicted the overall force-displacement capacity of the sub-assemblage, while the CS simulation significantly overpredicted the capacity. Overall it could be said that VGM most closely captured the location of fracture initiation and its subsequent propagation for the moment resisting connections. In addition, the VGM approach captures the force-displacement behavior fairly accurately. The reason for underpredicting is most like due the absence of a CNT specimen with a higher notch radius like 0.25 inches to calibrate to the lower triaxiality region. This material only had two different notch sized specimens for the PSO to calibrate the VGM parameters. The VGM-BW simulation underpredicts the force-displacement capacity and sometimes allows for not physical fracture to occur. The CS cannot locate or capture the fracture propagation accurately for these specimens but it predicts the force-displacement behavior satisfactorily with some overprediction. In addition, it was observed that tension flange experiences a variation of triaxiality through its thickness. While the edges of the flange see significant plastic behavior, the middle of the flange goes from elastic behavior to failure due to the high constraint.

The three finite element deletion strategies were also validated through comparison to WUF-B and RBS beam-column subassemblages. In the VGM simulation of the WUF-B specimen, the failure sequence followed that of the experiment. The VGM-BW closely followed this damage propagation, while CS did not follow the damage propagation seen in the experiment. The damage pattern seen in the experimental test results of RBS was repeated in all three

simulations. Overall, the VGM approach performed best in capturing the fracture initiation and propagation in the WUF-B and RBS subassemblage specimens, while the VGM-BW captured some of the behavior well, but predicted fracture where no fracture was observed in the experiment, like the edges of the tension flange of the WUF-B specimen. The CS approach captureed the fracture initiation and propagation in the RBS specimen, but not in WUF-B specimens. In addition, the VGM-BW and CS approaches underpredicted the capacity of the sub-assemblages, while the VGM approach had a very close prediction to the experimental capacity. It was also shown that the triaxiality range in the critical locations for these specimens varied from 0.34 to 0.6. Therefore, there is no need for the fracture locus to be defined in negative triaxiality ranges for these specimens. In addition, it was observed that triaxiality is a good measure of ductility of steel connection detailing with weld access hole in WUF-B specimen helping to keep triaxiality low throughout the loading process allowing for plastic flow and avoiding highly confined fracture. Overall, the three finite element deletion strategies were able to capture the sudden fracture propagation through the thickness of the tension flange in the two specimens while only the VGM approach was able to properly capture the failure propagation of the bolts in WUF-B.

In the simulation of the portal frame, fracture was predicted by the VGM-BW and CS but not by VGM model, while no specific cases of fracture were mentioned in the experimental test results. In the CS and VGM-BW finite element simulations, fracture occurred at a displacement much larger than the experimental maximum displacement. Overall, since CS and VGM-BW simulations predict different fracture initiation and propagation and VGM has no fracture at all, it is difficult to decide if fracture would behave in the same manner as in the VGM-BW or CS

simulations. The simulations support the notion of portal frame being a ductile structural configuration and that it would fail through buckling far sooner than fracture.

In addition, three three-story-braced frames, which differed from each other by the applied loading configuration, were simulated by the three strategies. In the experimental testing of the braced frames several plastic hinges are developed during loading, although fracture is not mentioned explicitly. In the VGM simulation of the Brace-YurA36-W-1 specimen, fracture occurred at an edge of the exterior tension flange and at the center of the interior flange of beam AB1 specimen. Before fracture occurred severe plastic deformation and buckling occurred in all of the frame beams by lateral buckling of the beam web. The cracks propagated through the tension flange and downward through the web of the beam for all of the frame beams. The damage propagation was very similar for the CS and VGM-BW simulations, except fracture occurring at a larger displacement. Overall, in the simulation of Brace-YurA36-W-1 specimen, the predominant failure was out-of-plane buckling of the beams and not by fracture. In all simulations of the Brace-YurA36-W-2 specimen before fracture occurred severe plastic deformation and buckling occurred in all of the frame beams. In the VGM simulation, the first fracture occurred in the tension flange of the BC2 beam at the exterior end and then in the exterior tension flange of beam AB1. Soon after this, fracture occurred in the tension flange at the interior column connection. The damage propagation was very similar for the CS and VGM-BW simulations, except that fracture occurred at a much larger displacement. Overall, in the simulation of Brace-YurA36-W-2 specimen, the predominant failure was out-of-plane buckling of the beams and not by fracture. As in previous two specimens, all simulations of the Brace-YurA36-W-3 specimen experienced severe plastic deformation and buckling in all of the frame

beams before fracture occurred. In the VGM simulation of the Brace-YurA36-W-3 specimen, the first fracture occurred in the tension flange of the BC2 beam at the exterior end. After beam BC2 was almost completely separated from the exterior column before fracture occurred at an interior tension flanges of beams AB1 and BC2 and exterior tension flange of AB1. The damage propagation was very similar for the CS and VGM-BW simulations. Overall, in the simulation of Brace-YurA36-W-3 specimen the predominant failure was out-of-plane buckling of the beams and not by fracture. Judging from the results of the simulations, it is concluded that fracture did not occur in the experimental tests of the three braced frames and that the primary failure mode was the buckling of the beam webs. In the VGM simulation the fracture of the tension flange had a high tendency to start in the middle of the flange while in the other two simulation the edge of the flange was the most likely location of fracture initiation.

In conclusion, the two calibrated (VGM and VGM-BW) and current state-of-the-art (CS) finite element deletion strategies used in modeling collapse of steel structures are compared to each other and to the experimental test results. In particular, the force-displacement relationships are compared to determine if the approaches are able to properly capture the strength and deformation capacity of the specimen. In addition, the models are compared to see if they are able to predict the location and direction of fracture propagation accurately. It could be concluded that VGM model is able to accurately predict the force-displacement relationship, properly locate fracture initiation, and determine the direction of fracture propagation. The VGM-BW model underestimates the force-displacement capacity in most cases but can capture such fracture behavior as shear lip which the VGM model cannot. Two reasons exist for the underestimation of the VGM-BW. The first one deals with the fact that the lower and negative

triaxiality fracture locus was not calibrated through the use of PSO, which would have provided a better calibration, but through analytical methods which seem to underestimate the capacity. This is because there are inadequate experimental tests of structural steel in the literature to calibrate for low triaxiality. It is very likely that, with proper calibration, the VGM-BW model will be superior to the VGM model for cases that are dominated by low triaxility at their fracture locations. In addition, as was mentioned above, it is still not clear below what triaxiality value is fracture prevented from occurring. The VGM-BW assumed it to be -1/3 while others believe it to be 0. The results in this work highlights that a triaxiality value of zero could be a reasonable fracture cut-off value if calibration of the VGM-BW model to experiments in the negative triaxiality region proves to be insufficient for accuracy. This would prevent the fractures from occurring in the simulations that are not occurring in the experiments, as was sometimes encountered in the validation set of simulations. Since these nonphysical fractures affect the global response, the zero triaxiality to positive values would most likely improve the results of the VGM-BW model. Finally, the current state-of-the-art CS model did not perform well in capturing the force-displacement capacity of most specimens. In addition, it did not capture the fracture initiation location and propagation direction. It could be concluded that it would be very difficult for the CS model to capture the capacity and the physical behavior of fracture. Out of the three models, VGM is the best performing model so far and should be used in collapse modeling of steel structures to properly account for material separation through finite element deletion, but the VGM-BW has a potential to yield better and more consistent results if low triaxiality response can be calibrated to appropriate experiments. In addition, it

was found that positive triaxiality is most likely to be encountered in critical structural steel members under fracture.

7.3 Future Work

This work revealed that there is a need for more experimental test results for the calibration of the finite element deletion strategies. It is proposed that the VGM-BW type models with fracture locus defined up to -1/3 and with fracture locus defined up to 0 triaxiality be calibrated to a set of circumferentially notched tensile coupon specimens, compression cylinders or upsetting specimens, flat grooved specimens, round notches under compression specimens, flat dog-bone shear specimens, and other specimen types with different types of structural steels in order to calibrate the models through the use of the PSO algorithm or similar approach. These specimens would cover a large range of triaxiality, and calibrating the fracture locus to the force-displacement curve of the experimental test results would allow for the calibration of a VGM-BW type model. It is recommended that these specimens be in a set of three or more to avoid any outliers in material fracture and constitutive behavior in calibration of the fracture locus. In addition, these models should implement the Lode angle parameter to further improve the results, which would capture the effect of all of the most important parameters in fracture prediction. This would yield better and consistent results than shown in this work and shed light on the fracture cut-off for the calibrated fracture locus. This future work would allow structural engineers to perform collapse analysis of steel structures with more confidence and extract more informative results.

In addition, this approach should be implemented for cyclic material behavior. In the past, research such as (Kanvinde et al. 2004; Myers et al. 2009; Smith, Chris M. et al. 2013) have investigated the modification of the VGM to be used in cyclic fracture predictions of ductile structural steel metals, but so far these models have not been combined with damage mechanics to account for finite element deletion. If these models are calibrated to a comprehensive set of specimens that captures a large triaxiality range and validated against a comprehensive set of connection and frame specimens, then collapse of steel structures under the influence of earthquake loading could be investigated. This would shed light into the collapse limit state and influence of fracture on the capacity of steel structures under earthquake loading.

In addition, having a calibrated and validated fracture initiation and propagation model enables the execution of parametric investigations of numerous steel connection studies. For example, it was shown in this work that the older connections at Lehigh University had a very high triaxiality at the center of the tension flange, which encouraged early fracture, while a similar WUF-B connection kept the triaxiality at the center of the tension flange lower due to the weld access hole geometry. Similar improvement could be investigated through numerous simulations that employ the fracture initiation and propagation models calibrated and validated in this work.

References

ABAQUS 6.11-2 (2011). *Abaqus User Manual*, Dassault Systèmes Simulia Corp., Providence, Rhode Island.

AISC (1970). *Manual of Steel Construction.* 7th Edition, American Institute of Steel Construction,

Alashker, Y., El-Tawil, S., and Sadek, F. (2010). "Progressive Collapse Resistance of Steel-Concrete Composite Floors," *Journal of Structural Engineering,* 10(136), 1187-1196.

Alashker, Y., Li, H., and El-Tawil, S. (2011). "Approximations in Progressive Collapse Modeling," *Journal of Structural Engineering,* 9(137), 914-924.

Alves, M. l., and Jones, N. (1999). "Influence of Hydrostatic Stress on Failure of Axisymmetric Notched Specimens," *Journal of the Mechanics and Physics of Solids,* 3(47), 643-667.

Anderson, T. L. (2005). *Fracture Mechanics*, 3rd Edition, CRC Press, Taylor & Francis Group, Boca Raton, FL.

Argon, A., Im, J., and Safoglu, R. (1975). "Cavity Formation from Inclusions in Ductile Fracture," *Metallurgical Transactions A,* 4(6), 825-837.

Arndt, J., and Dahl, W. (1997). "Effect of Void Growth and Shape on the Initiation of Ductile Failure of Steels," *Computational Materials Science,* 1(9), 1-6.

ASTM A7. (1967). *Specification for Steel for Bridge and Building*. ASTM International, West Conshohocken, PA.

ASTM A36. (2008). *Standard Specification for Carbon Structural Steel*. ASTM International, West Conshohocken, PA.

ASTM E399. (2012). *Standard Test Method for Linear-Elastic Plane-Strain Fracture Toughness Kic of Metallic Materials*. ASTM International, West Conshohocken, PA.

Atkins, A. (1996). "Fracture in Forming," *Journal of Materials Processing Technology,* 1(56), 609-618.

Atkins, A. (1997). "Fracture Mechanics and Metal Forming: Damage Mechanics and the Local Approach of Yesterday and Today," *Fracture research in retrospect. Balkema, Rotterdam,* 327-350.

AWS (1969). *Code for Welding in Building Construction*. AWS D1.0-69, 9th Edition, American Welding Society,

Bai, Y., Teng, X., and Wierzbicki, T. (2009). "On the Application of Stress Triaxiality Formula for Plane Strain Fracture Testing," *Journal of Engineering Materials and Technology*, 2(131), 021002.

Bai, Y., and Wierzbicki, T. (2008). "A New Model of Metal Plasticity and Fracture with Pressure and Lode Dependence," *International Journal of Plasticity*, 6(24), 1071-1096.

Bao, Y. (2005). "Dependence of Ductile Crack Formation in Tensile Tests on Stress Triaxiality, Stress and Strain Ratios," *Engineering Fracture Mechanics*, 4(72), 505-522.

Bao, Y., and Wierzbicki, T. (2004). "On Fracture Locus in the Equivalent Strain and Stress Triaxiality Space," *International Journal of Mechanical Sciences*, 1(46), 81-98.

Bao, Y., and Wierzbicki, T. (2005). "On the Cut-Off Value of Negative Triaxiality for Fracture," *Engineering Fracture Mechanics*, 7(72), 1049-1069.

Barsoum, I., and Faleskog, J. (2007). "Rupture Mechanisms in Combined Tension and Shear—Experiments," *International Journal of Solids and Structures*, 6(44), 1768-1786.

Birkemoe, P. C., and Gilmore, M. I. (1978). "Behavior of Bearing Critical Double-Angle Beam Connections," *Engineering Journal*, 4(15), 109-115.

Blodgett, O. (1995). "Details to Increase Ductility in Smrf Connections," *The Welding Innovation Quarterly*, 12(2), 16-18.

Clausing, D. P. (1970). "Effect of Plastic Strain State on Ductility and Toughness," *International Journal of Fracture Mechanics*, 6(1), 71-85.

Cooper, J. D., Friedland, I. M., Buckle, I. G., Nimis, R. B., and Bobb, N. M. (1994). *The Northridge Earthquake: Progress Made, Lessons Learned in Seismic-Resistant Bridge Design*, Report #58, U.S. DOT Federal Highway Administration, Washington, D.C.

Coppola, T., Cortese, L., and Folgarait, P. (2009). "The Effect of Stress Invariants on Ductile Fracture Limit in Steels," *Engineering Fracture Mechanics*, 9(76), 1288-1302.

D'Escatha, Y., and Devaux, J. (1979). "Numerical Study of Initiation, Stable Crack Growth, and Maximum Load, with a Ductile Fracture Criterion Based on the Growth of Holes," *ASTM special technical publication*, 668, 229-248.

Del Valle, Y., Venayagamoorthy, G. K., Mohagheghi, S., Hernandez, J.-C., and Harley, R. G. (2008). "Particle Swarm Optimization: Basic Concepts, Variants and Applications in Power Systems," *Evolutionary Computation, IEEE Transactions on*, 2(12), 171-195.

Deng, K., Grondin, G. Y., and Driver, R. G. (2006). "Effect of Loading Angle on the Behavior of Fillet Welds," *Engineering Journal*, 1(43), 9-24.

e Meyers, M. A., and Chawla, K. K. (2009). "Mechanical Behavior of Materials,"

Ehlers, S. (2010). “Strain and Stress Relation until Fracture for Finite Element Simulations of a Thin Circular Plate,” *Thin-Walled Structures,* 1(48), 1-8.

Geltmacher, A. B., Koss, D., Matic, P., and Stout, M. (1996). “A Modeling Study of the Effect of Stress State on Void Linking During Ductile Fracture,” *Acta Materialia,* 6(44), 2201-2210.

Gurson, A. L. (1975). “Continuum Theory of Ductile Rupture by Void Nucleation and Growth. Part I. Yield Criteria and Flow Rules for Porous Ductile Media,” *Journal of Engineering Materials and Technology,* 99(1), 2-15.

Hancock, J., and Brown, D. (1983). “On the Role of Strain and Stress State in Ductile Failure,” *Journal of the Mechanics and Physics of Solids,* 1(31), 1-24.

Hillerborg, A., Modeer, M., and Petersson, P. E. (1976). “Analysis of Crack Formation and Crack Growth in Concrete by Means of Fracture Mechanics and Finite Elements,” *Cement and Concrete Research,* 6(6), 773-782.

Hooputra, H., Gese, H., Dell, H., and Werner, H. (2004). “A Comprehensive Failure Model for Crashworthiness Simulation of Aluminium Extrusions,” *International Journal of Crashworthiness,* 5(9), 449-464.

Huang, Y. (1991). “Accurate Dilatation Rates for Spherical Voids in Triaxial Stress Fields,” *Journal of Applied Mechanics,* 4(58), 1084-1086.

Inglis, C. (1997). “Stresses in a Plate Due to the Presence of Cracks and Sharp Corners,” *SPIE MILESTONE SERIES MS,* 137, 3-17.

Jamshidi, A., and Driver, R. (2013). *Structural Integrity of Composite Steel Gravity Frame Systems.* Paper presented at the Structures Congress 2013, ASCE, Pittsburgh, Pennsylvania.

Kanvinde, A. M., and Deierlein, G. G. (2004). *Micromechanical Simulation of Earthquake-Induced Fracture in Steel Structures,* Report #145, The John A. Blume Earthquake Engineering Center, Stanford, California.

Kaufmann, E. J., and Fisher, J. W. (1995). *Fracture Analysis of Failed Moment Frame Weld Joints Produced in Full-Scale Laboratory Tests and Buildings Damaged in the Northridge Earthquake,* SAC 95-08, SAC Joint Venture, Sacramento, California.

Kennedy, J. (1997). *The Particle Swarm: Social Adaptation of Knowledge.* Paper presented at the IEEE International Conference on Evolutionary Computation 1997, IEEE, Washington, D.C.

Khandelwal, K. (2008). “Multi-Scale Computational Simulation of Progressive Collapse of Steel Frames,” Ph.D. Dissertation, University of Michigan, Ann Arbor, Michigan.

Khandelwal, K., and El-Tawil, S. (2005). *Progressive Collapse of Moment Resisting Steel Frame Buildings.* Paper presented at the Structures Congress 2005, ASCE, New York, New York.

Khandelwal, K., and El-Tawil, S. (2007). "Collapse Behavior of Steel Special Moment Resisting Frame Connections," *Journal of Structural Engineering*, ASCE, 5(133), 646-655.

Khandelwal, K., El-Tawil, S., Kunnath, S. K., and Lew, H. (2008). "Macromodel-Based Simulation of Progressive Collapse: Steel Frame Structures," *Journal of Structural Engineering*, 7(134), 1070-1078.

Khandelwal, K., El-Tawil, S., and Sadek, F. (2009). "Progressive Collapse Analysis of Seismically Designed Steel Braced Frames," *Journal of Constructional Steel Research*, 3(65), 699-708.

Kofiani, K., Nonn, A., and Wierzbicki, T. (2013). "New Calibration Method for High and Low Triaxiality and Validation on Sent Specimens of Api X70," *International Journal of Pressure Vessels and Piping*, 111, 187-201.

Koplik, J., and Needleman, A. (1988). "Void Growth and Coalescence in Porous Plastic Solids," *International Journal of Solids and Structures*, 8(24), 835-853.

Kurishita, H., Kayano, H., Narui, M., Yamazaki, M., Kano, Y., and Shibahara, I. (1993). "Effects of V-Notch Dimensions on Charpy Impact Test Results for Differently Sized Miniature Specimens of Ferritic Steel," *Materials Transactions, JIM(Japan)*, 11(34), 1042-1052.

Kuwamura, H. (2003). "Classification of Material and Welding in Fracture Consideration of Seismic Steel Frames," *Engineering Structures*, 5(25), 547-563.

Kuwamura, H., Iyama, J., and Matsui, K. (2003). "Effects of Material Toughness and Plate Thickness on Brittle Fracture of Steel Members," *Journal of Structural Engineering*, 11(129), 1475-1483.

Kuwamura, H., and Yamamoto, K. (1997). "Ductile Crack as Trigger of Brittle Fracture in Steel," *Journal of Structural Engineering*, 6(123), 729-735.

Le Roy, G., Embury, J., Edwards, G., and Ashby, M. (1981). "A Model of Ductile Fracture Based on the Nucleation and Growth of Voids," *Acta Metallurgica*, 8(29), 1509-1522.

Lee, Y.-W., and Wierzbicki, T. (2004). *Quick Fracture Calibration for Industrial Use*, Report No. 115, Massachusetts Institute of Technology, Impact and Crashworthiness Laboratory.

Li, H., and El-Tawil, S. (2011). *Three-Dimensional Effects in Progressive Collapse Modeling.* Paper presented at the Structures Congress 2011, ASCE, Las Vegas, Nevada.

Li, H., and El-Tawil, S. (2012). *Role of Composite Action in Collapse Resistance of Steel Frame Buildings.* Paper presented at the Structures Congress 2012, ASCE, Chicago, Illinois.

Li, H., and El-Tawil, S. (2013). *Collapse Resistance Mechanisms in Steel Frame Buildings.* Paper presented at the Structures Congress 2013, ASCE, Pittsburgh, Pennsylvania.

Lu, L.-W., Ricles, J. M., Mao, C., and Fisher, J. W. (2000). "Critical Issues in Achieving Ductile Behaviour of Welded Moment Connections," *Journal of Constructional Steel Research,* 55, 325-341.

Main, J. A., and Sadek, F. (2009). *Development of 3d Models of Steel Moment-Frame Buildings for Assessment of Robustness and Progressive Collapse Vulnerability.* Paper presented at the Structures Congress 2009, ASCE, Austin, Texas.

McAllister, T. P., Gann, R. G., Averill, J. D., Gross, J. L., Grosshandler, W. L., Lawson, J. R., . . . Nelson, H. E. (2008). *Structural Fire Response and Probable Collapse Sequence of World Trade Center Building 7 (Volume 2),* Federal Building and Fire Safety Investigation of the World Trade Center Disaster, NIST NCSTAR 1-9, National Institute of Standards and Technology, U.S. Department of Commerce,

McClintock, F. (2003). "Slip Line Fracture Mechanics: A New Regime of Fracture Mechanics," *ASTM SPECIAL TECHNICAL PUBLICATION*, 1417, 3-56.

McClintock, F. A. (1968). "A Criterion for Ductile Fracture by the Growth of Holes," *Journal of Applied Mechanics,* 35, 363-371.

Mercury (2013). "5 Floors of Building Collapse," *San Jose Mercury News,* San Jose, California.

Miazga, G. S., and Kennedy, D. L. (1989). "Behaviour of Fillet Welds as a Function of the Angle of Loading," *Canadian Journal of Civil Engineering*, 4(16), 583-599.

Mirza, M., Barton, D., and Church, P. (1996). "The Effect of Stress Triaxiality and Strain-Rate on the Fracture Characteristics of Ductile Metals," *Journal of Materials Science,* 2(31), 453-461.

Miyazaki, Y., Abe, K., Ando, M., and et al. (2013). *Seismic Activity in Japan,* December 2, 2013, http://www.hp1039.jishin.go.jp/eqchreng/eqchrfrm.htm

Myers, A. T., Deierlein, G. G., and Kanvinde, A. (2009). *Testing and Probabilistic Simulation of Ductile Fracture Initiation in Structural Steel Components and Weldments,* Report #170, The John A. Blume Earthquake Engineering Center, Stanford, California.

Ng, K. F., Driver, R. G., and Grondin, G. Y. (2002). *Behaviour of Transverse Fillet Welds,* Structural Engineering Report #245, Department of Civil and Environmental Engineering, University of Alberta, Edmonton, Alberta, Canada.

Ojdrovic, R., Schafer, B., and Zarghamee, M. (2004). *Fracture and the Role of Triaxiality for Steel Structures.* Paper presented at the Structures Congress 2000, ASCE, Philadelphia, Pennsylvania.

Rentschler, G. P., Chen, W.-F., and Driscoll, G. C. (1978). *Tests of Beam-to-Column Web Moment Connections,* Report #405.9, Fritz Engineering Laboratory, Bethlehem, PA.

Rice, J. R., and Tracey, D. M. (1969). "On the Ductile Enlargement of Voids in Triaxial Stress Fields," *Journal of the Mechanics and Physics of Solids,* 3(17), 201-217.

SAC Joint Venture (1996). *Technical Report: Experimental Investigations of Beam-Column Subassemblages,* SAC 96-01, Sacramento, California.

Sadek, F., Main, J. A., Lew, H. S., Robert, S. D., Chiarito, V. P., and El-Tawil, S. (2010). *An Experimental and Computational Study of Steel Moment Connections under a Column Removal Scenario,* NIST Technical Note 1669, National Institute of Standards and Technology, U.S. Department of Commerce, Gaithersburg, Maryland.

Schafer, B., Ojdrovic, R., and Zarghamee, M. (2000). "Triaxiality and Fracture of Steel Moment Connections," *Journal of Structural Engineering,* 10(126), 1131-1139.

Schluter, N., Grimpe, F., Bleck, W., and Dahl, W. (1996). "Modelling of the Damage in Ductile Steels," *Computational Materials Science,* 7(1-2), 27-33.

Schutz, F. W., Schilling, C. G. J., and Beedle, L. S. (1953). *The Collapse Strength of a Welded Single Bay Frame,* Report #205D.5, Fritz Engineering Laboratory, Lehigh University, Bethlehem, Pennsylvania.

Smith, C. M. (2013). "A Stress-Weighted Damage Model for Ductile Fracture Initiation in Structural Steel under Cyclic Loading and Generalized Stress States," Ph.D. Dissertation, Stanford University, Stanford University.

Smith, C. M., Kanvinde, A. M., and Deierlein, G. G. (2013). "Optimal Calibration of Continuum Cyclic Constitutive Model for Structural Steel Using Particle Swarm Optimization," *Journal of Structural Engineering,* ASCE, submitted for publication.

Standard, A. (2009). "E23-09: Standard Test Method for Notched Bar Impact Testing of Metallic Materials," *Annual Book of ASTM Standards, ASTM, West Conshohocken, PA,*

Szyniszewski, S. (2009). *Dynamic Energy Based Method for Progressive Collapse Analysis.* Paper presented at the Structures Congress 2009, ASCE, Austin, Texas.

Szyniszewski, S. (2010). *Effects of Random Imperfections on Progressive Collapse Propagation.* Paper presented at the Structures Congress 2010, ASCE, Orlando, Florida.

Szyniszewski, S., and Krauthammer, T. (2012). "Energy Flow in Progressive Collapse of Steel Framed Buildings," *Engineering Structures,* 42, 142-153.

Thomason, P. (1985). "A Three-Dimensional Model for Ductile Fracture by the Growth and Coalescence of Microvoids," *Acta Metallurgica,* 6(33), 1087-1095.

Wierzbicki, T., Bao, Y., Lee, Y.-W., and Bai, Y. (2005). "Calibration and Evaluation of Seven Fracture Models," *International Journal of Mechanical Sciences*, 4(47), 719-743.

Xue, L., and Wierzbicki, T. (2008). "Ductile Fracture Initiation and Propagation Modeling Using Damage Plasticity Theory," *Engineering Fracture Mechanics*, 11(75), 3276-3293.

Yang, T.-S., and Popov, E. P. (1995). *Behavior of Pre-Northridge Moment Resisting Steel Connections*, Report #UCB/EERC-95/08, Earthquake Engineering Research Center, University of California at Berkeley, Berkeley, California.

Yu, H., and Jeong, D. (2010). "Application of a Stress Triaxiality Dependent Fracture Criterion in the Finite Element Analysis of Unnotched Charpy Specimens," *Theoretical and Applied Fracture Mechanics*, 1(54), 54-62.

Yura, J. A. (1965). *The Strength of Braced Multi-Story Steel Frames*, Report #273.28, Fritz Engineering Laboratory, Lehigh University, Bethlehem, Pennsylvania.

Appendix A: Particle Swarm Optimization Flowchart

This appendix provides a flowchart of how PSO was implemented in calibration of VGM criteria.

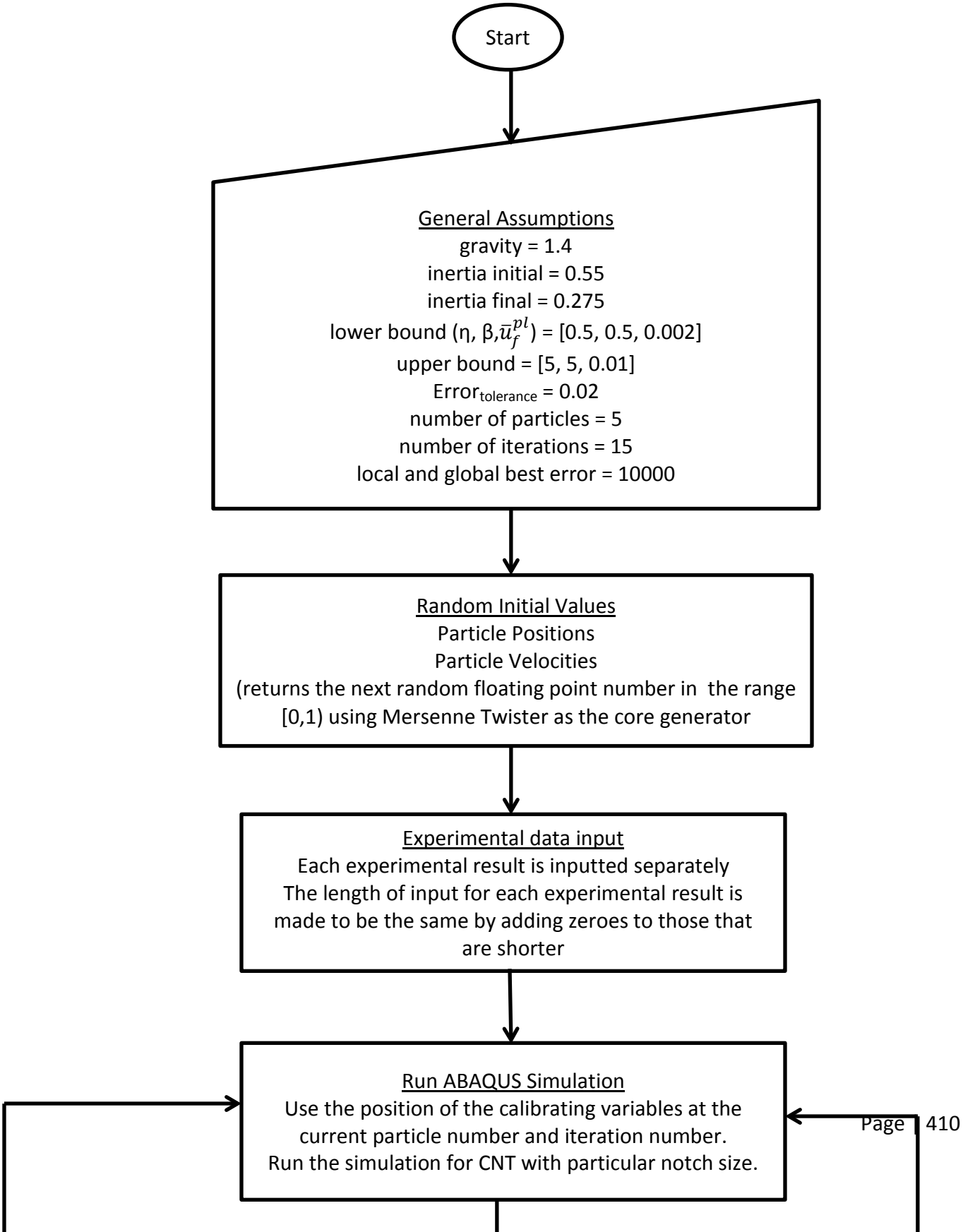

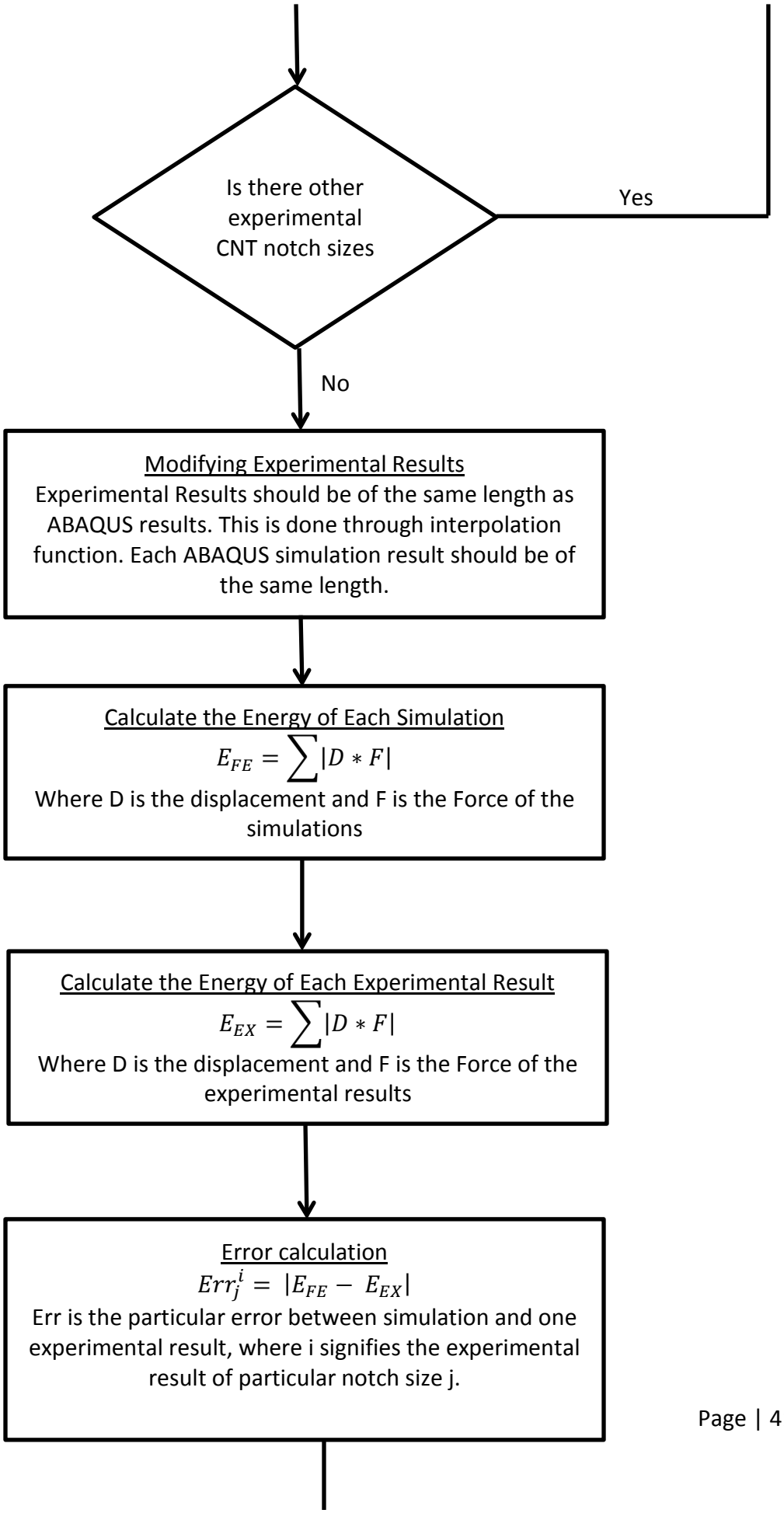
Is there other experimental CNT notch sizes
Yes
No
Modifying Experimental Results
Experimental Results should be of the same length as ABAQUS results. This is done through interpolation function. Each ABAQUS simulation result should be of the same length.
Calculate the Energy of Each Simulation
$E_{FE} = \sum |D * F|$
Where D is the displacement and F is the Force of the simulations
Calculate the Energy of Each Experimental Result
$E_{EX} = \sum |D * F|$
Where D is the displacement and F is the Force of the experimental results
Error calculation
$Err_j^i = |E_{FE} - E_{EX}|$
Err is the particular error between simulation and one experimental result, where i signifies the experimental result of particular notch size j.

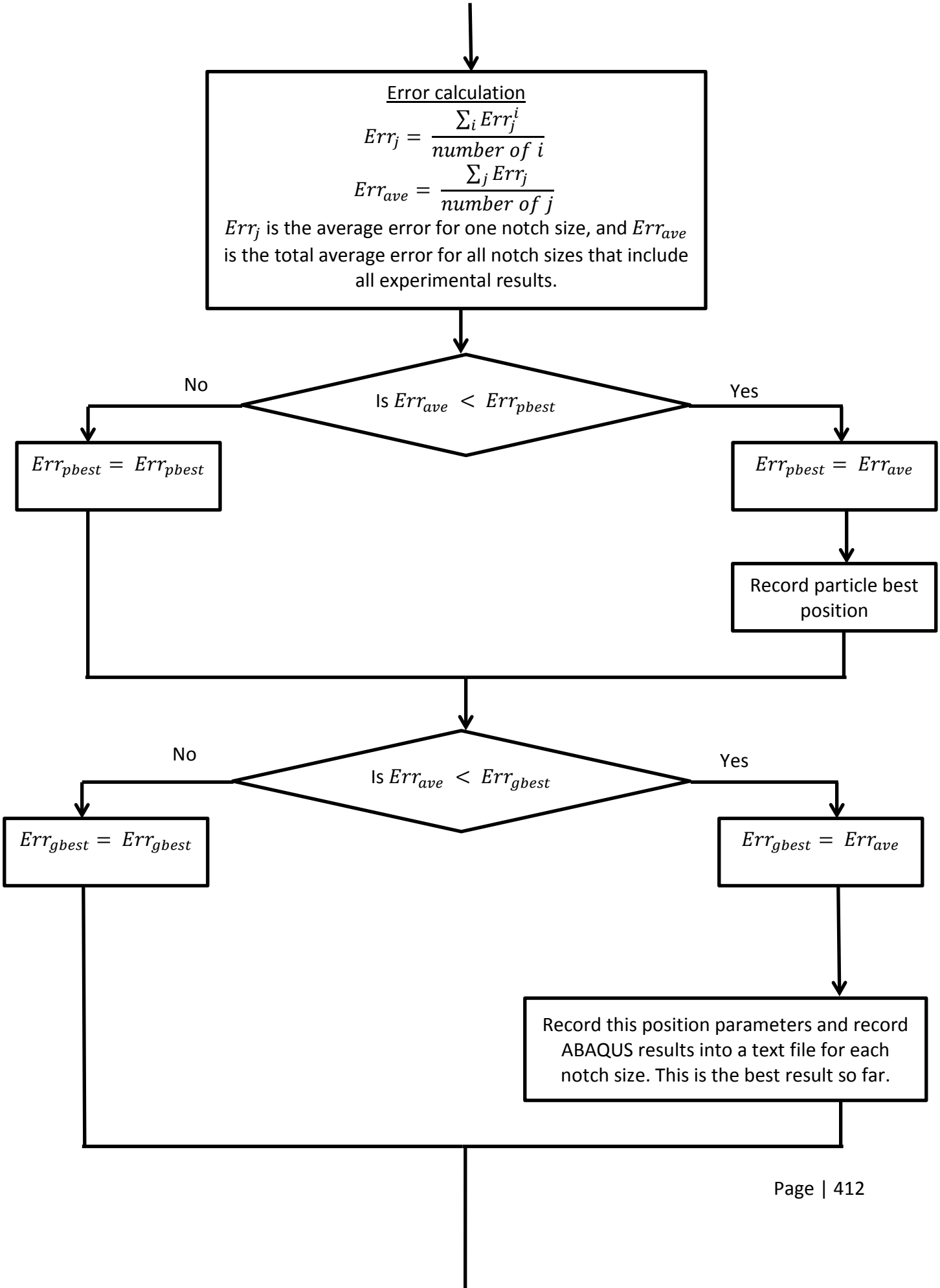
Error calculation
$Err_j = \frac{\sum_i Err_j^i}{number\ of\ i}$
$Err_{ave} = \frac{\sum_j Err_j}{number\ of\ j}$
Err_j is the average error for one notch size, and Err_{ave} is the total average error for all notch sizes that include all experimental results.
Is $Err_{ave} < Err_{pbest}$
No
Yes
$Err_{pbest} = Err_{pbest}$
$Err_{pbest} = Err_{ave}$
Record particle best position
Is $Err_{ave} < Err_{gbest}$
No
Yes
$Err_{gbest} = Err_{gbest}$
$Err_{gbest} = Err_{ave}$
Record this position parameters and record ABAQUS results into a text file for each notch size. This is the best result so far.

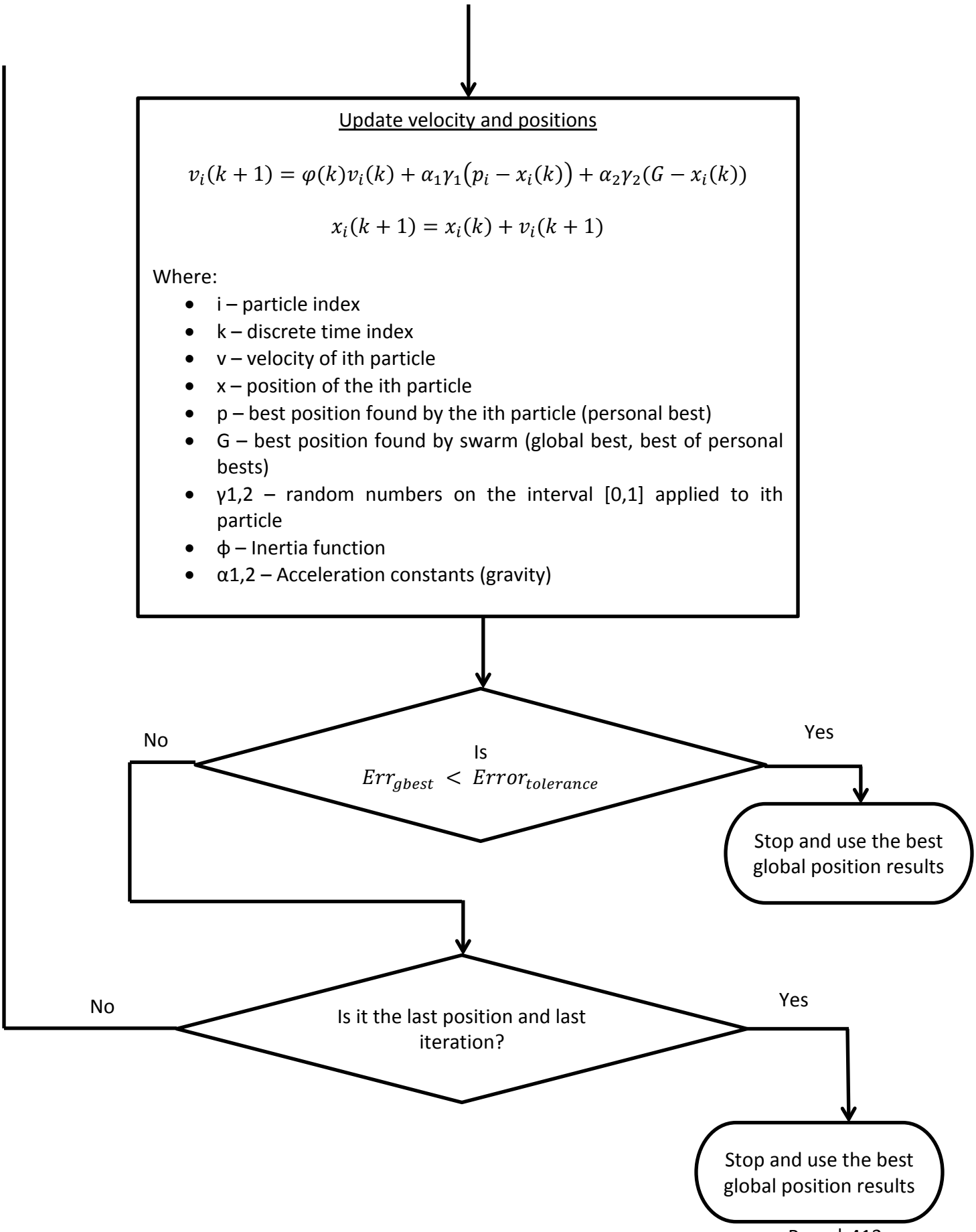
Update velocity and positions
$v_i(k+1) = \varphi(k)v_i(k) + \alpha_1\gamma_1(p_i - x_i(k)) + \alpha_2\gamma_2(G - x_i(k))$
$x_i(k+1) = x_i(k) + v_i(k+1)$
Where:
i – particle index
k – discrete time index
v – velocity of ith particle
x – position of the ith particle
p – best position found by the ith particle (personal best)
G – best position found by swarm (global best, best of personal bests)
γ1,2 – random numbers on the interval [0,1] applied to ith particle
ϕ – Inertia function
α1,2 – Acceleration constants (gravity)
Is $Err_{gbest} < Error_{tolerance}$
No
Yes
Stop and use the best global position results
Is it the last position and last iteration?
No
Yes
Stop and use the best global position results

Appendix B: Fracture Initiation and Propagation Parameter Variation in CNT Specimens used for Calibration

The following plots show the variation of triaxiality and related fracture parameters during loading and its effect on fracture in circumferentially notched tensile specimens used for calibration. The plots are from finite element simulations of different calibrated steels mentioned in Chapter 5 of this report. The modeling assumptions are the same as in Chapter 5. Figure 5.46, which shows the location of each of the elements through the thickness of the CNT specimens, is replotted here for clarity. For detailed documentation and explanation see Chapter 5.5.

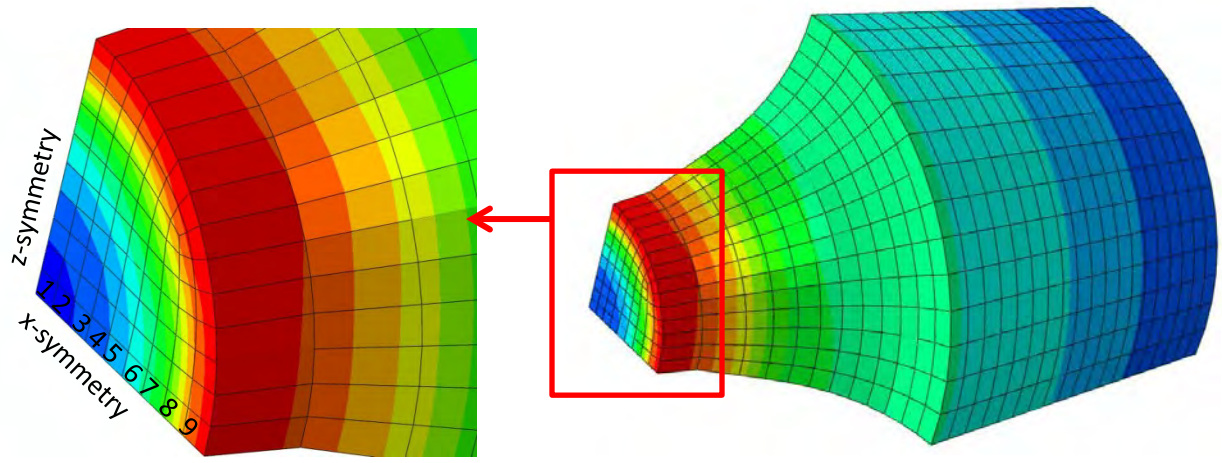

Figure B. 1: Location of each element through the thickness of the CNT specimen. The specimen is shown during loading with countors representing von Mises stress

B.1 CNT-MyeA36-B-A

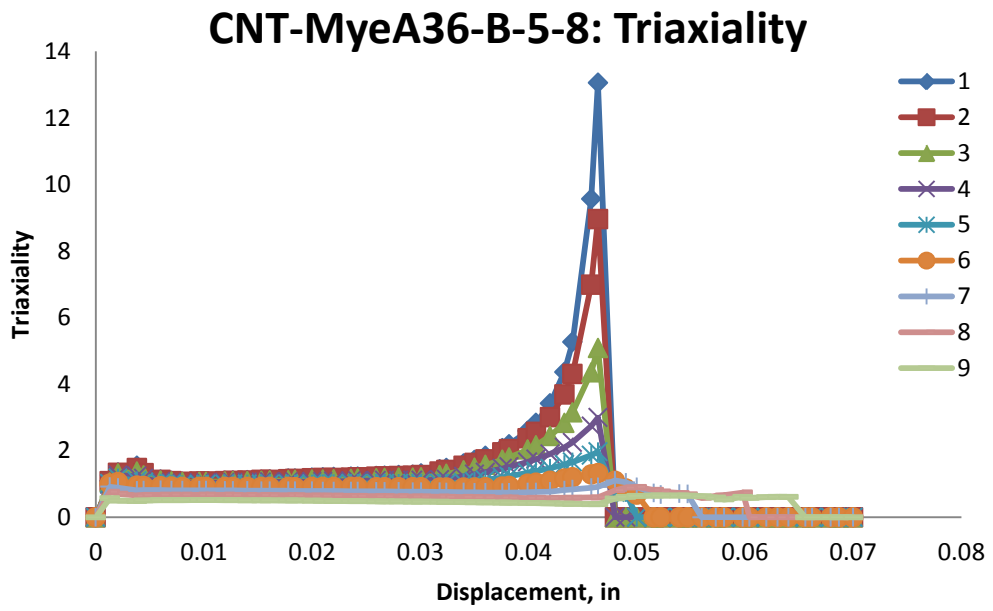

Figure B. 2: Variation of triaxiality with displacement for different elements laid out through the thickness of simulation of CNT-MyeA36-B-5-8 specimens

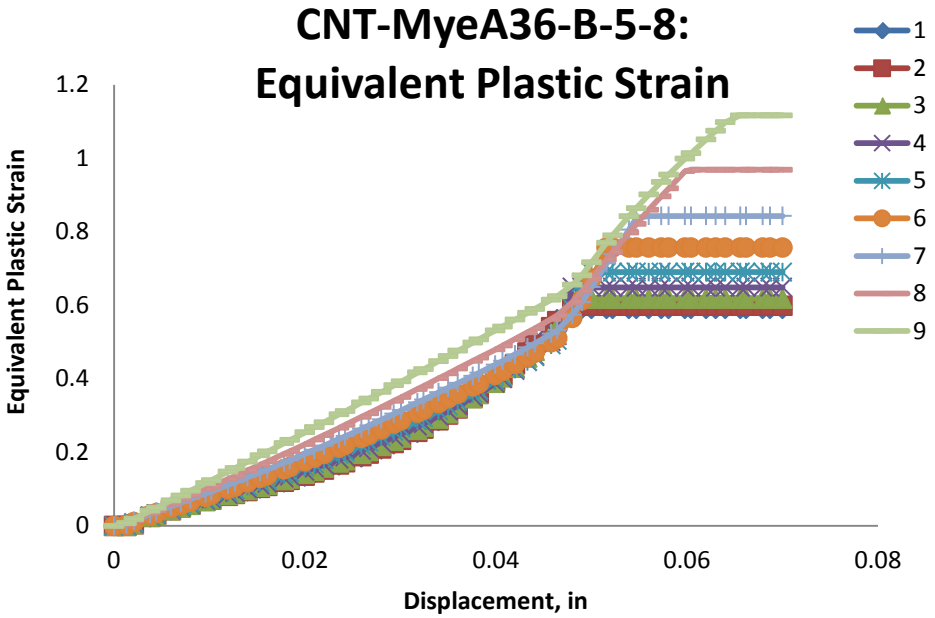

Figure B. 3: Variation of equivalent plastic strain with displacement for different elements laid out through the thickness of simulation of CNT-MyeA36-B-5-8 specimens

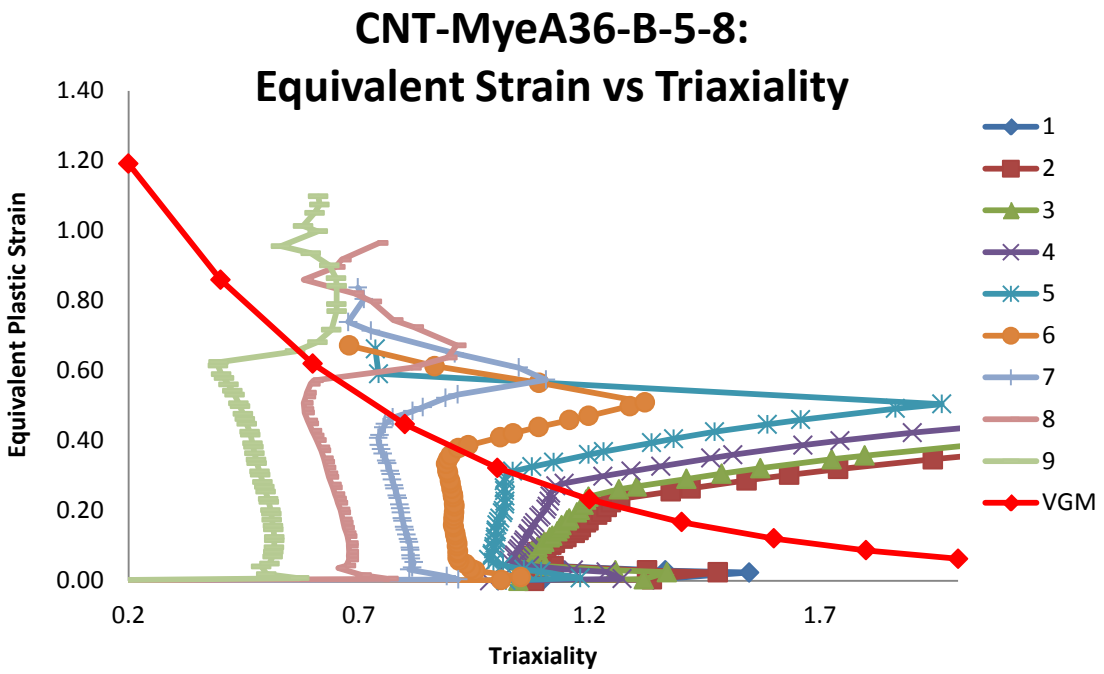

Figure B. 4: Variation of equivalent plastic strain versus triaxiality for different elements laid out through the thickness of simulation of CNT-MyeA36-B-5-8 specimens

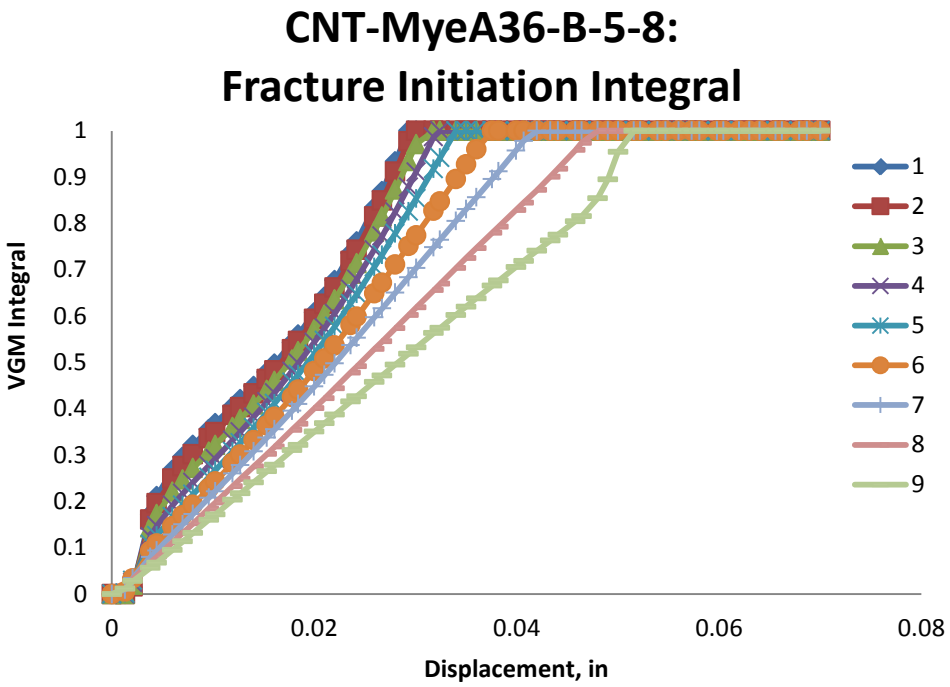

Figure B. 5: Value of fracture initiation integral for different elements laid out through the thickness of simulation of CNT-MyeA36-B-5-8 specimens

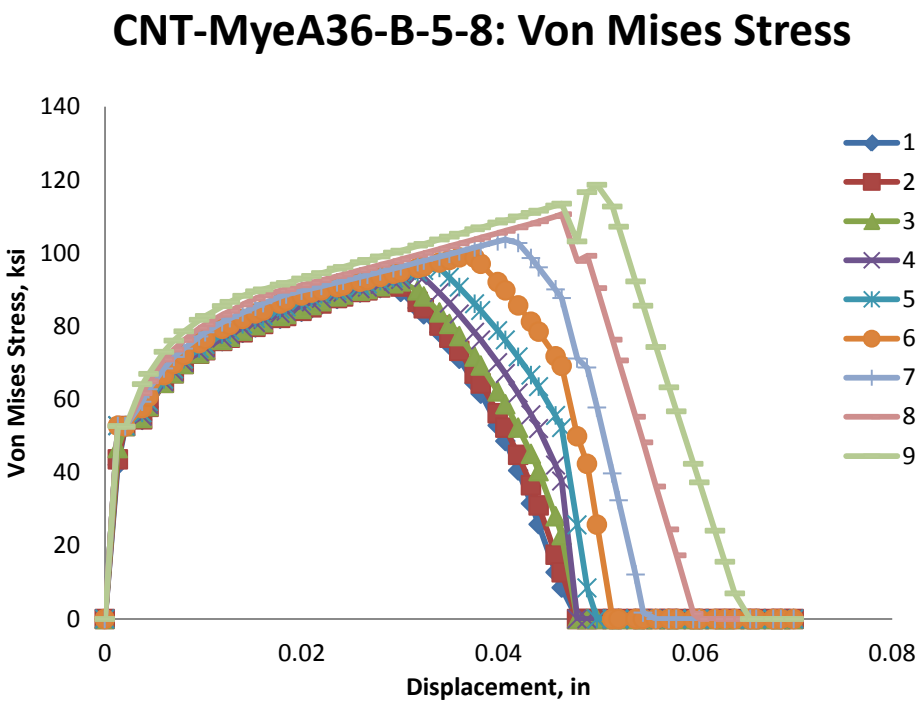

Figure B. 6: Variation of von Mises stress versus displacement for different elements laid out through the thickness of simulation of CNT-MyeA36-B-5-8 specimens

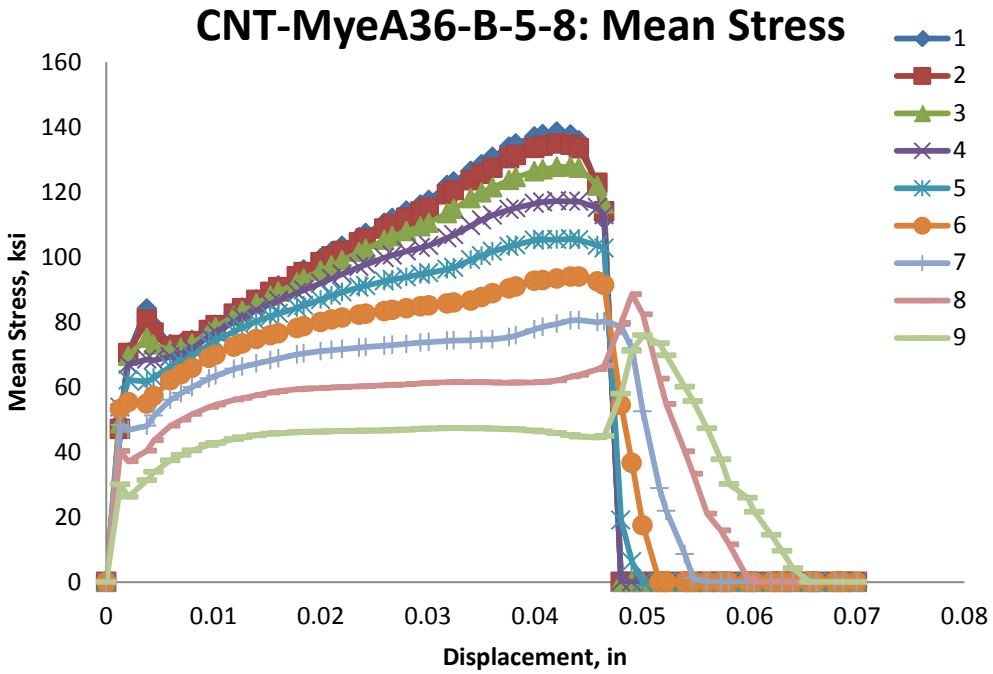

Figure B. 7: Variation of mean stress versus displacement for different elements laid out through the thickness of simulation of CNT-MyeA36-B-5-8 specimens

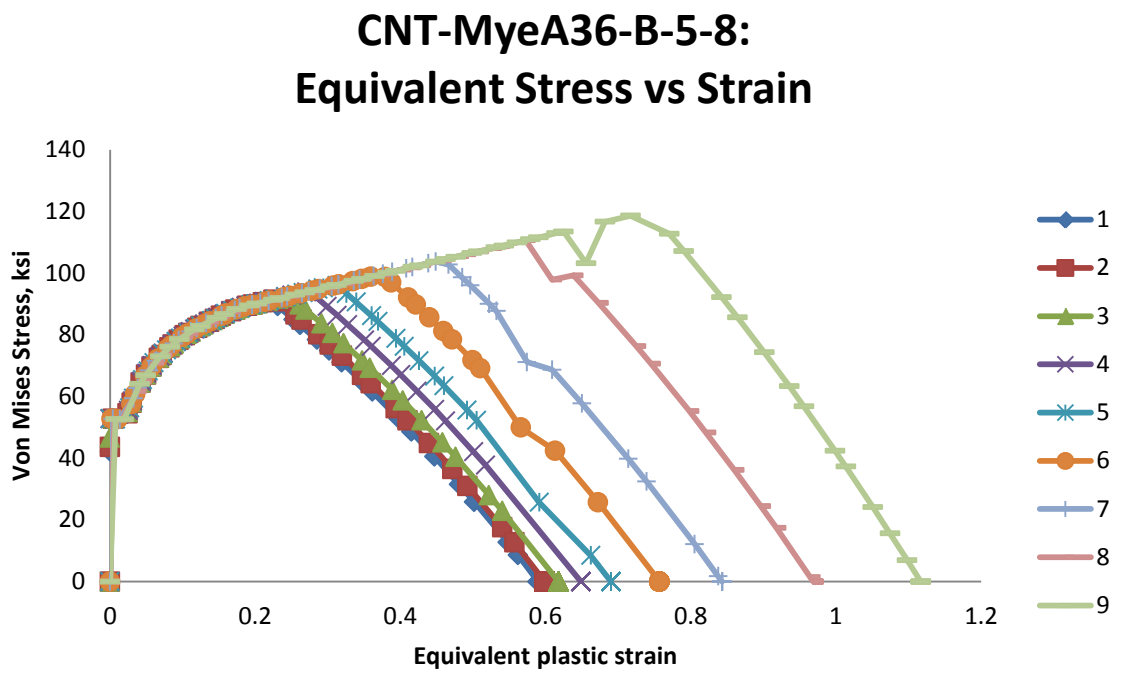

Figure B. 8: Variation of von Mises stress versus equivalent plastic strain for different elements laid out through the thickness of simulation of CNT-MyeA36-B-5-8 specimens

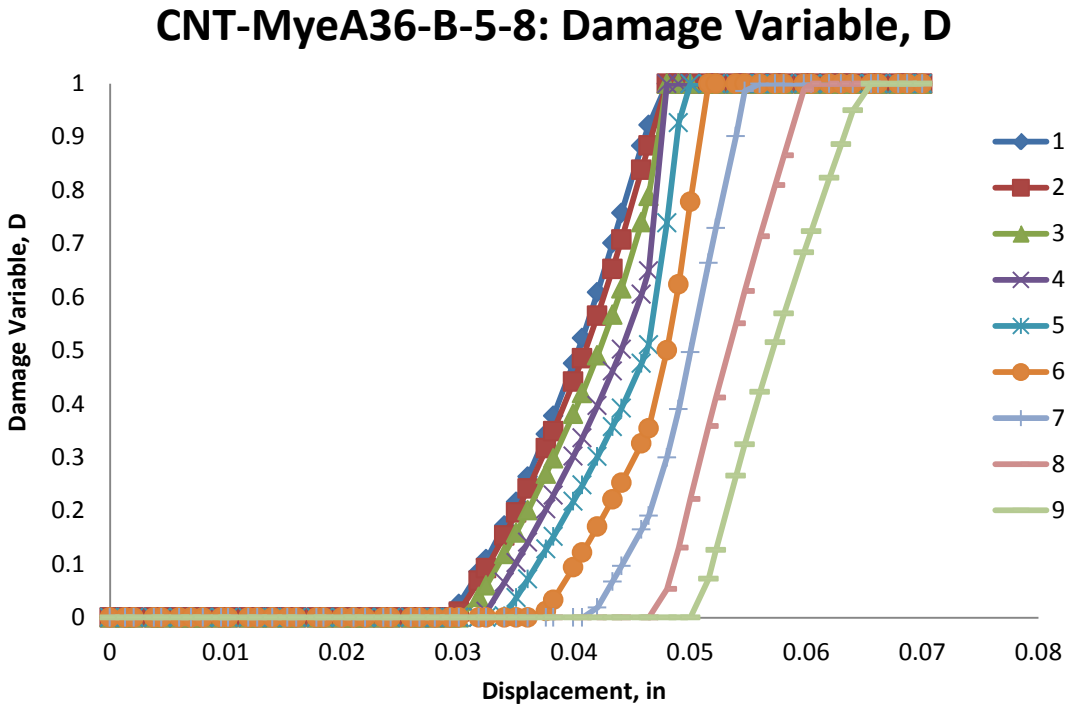

Figure B. 9: Variation of damage variable with displacement for different elements laid out through the thickness of simulation of CNT-MyeA36-B-5-8 specimens

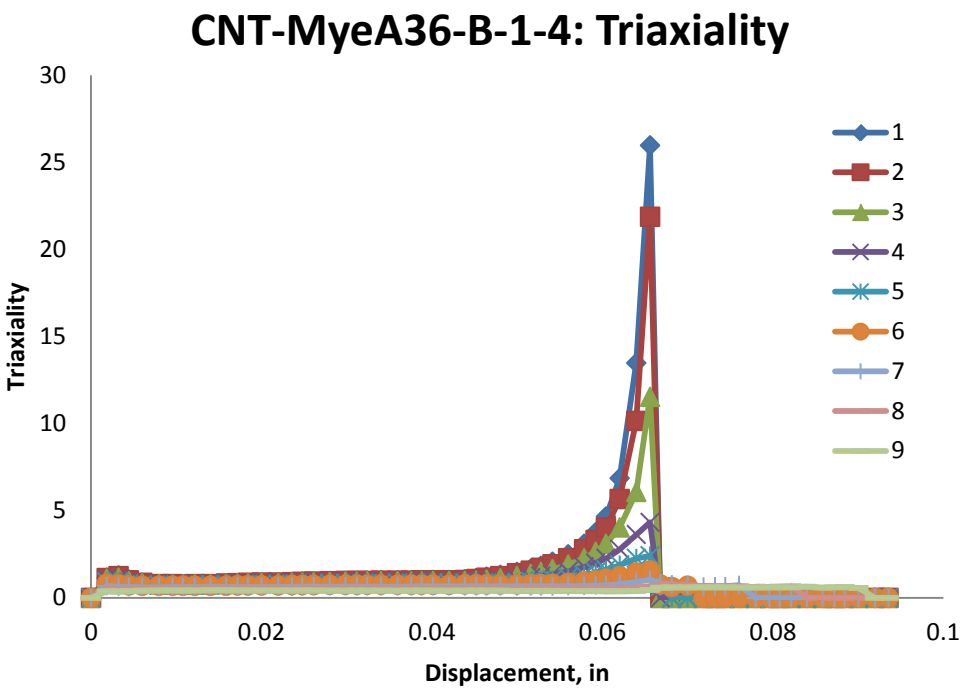

Figure B. 10: Variation of triaxiality with displacement for different elements laid out through the thickness of simulation of CNT-MyeA36-B-1-4 specimens

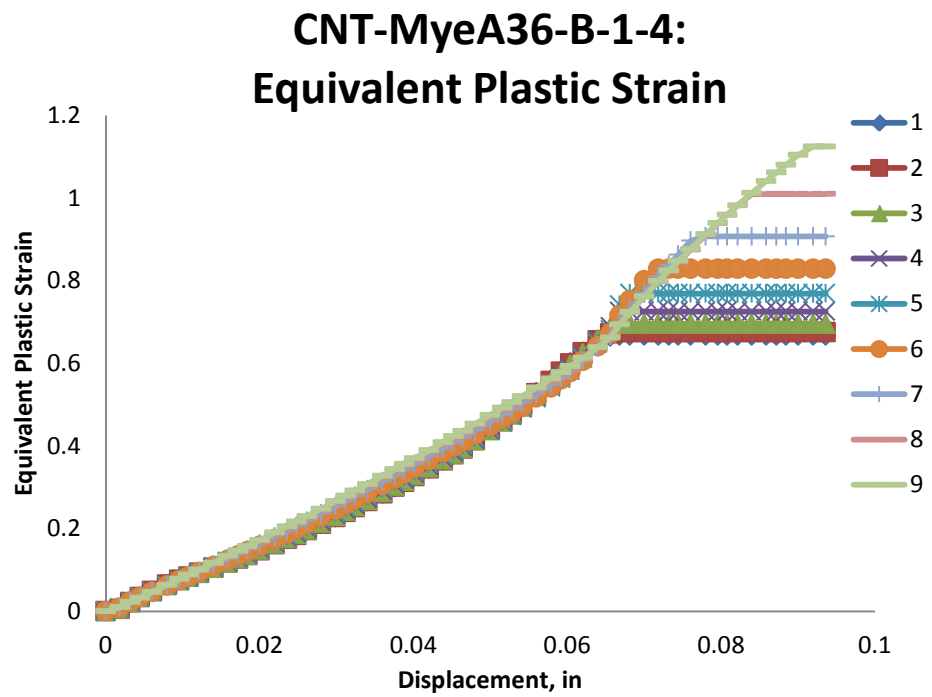

Figure B. 11: Variation of equivalent plastic strain with displacement for different elements laid out through the thickness of simulation of CNT-MyeA36-B-1-4 specimens

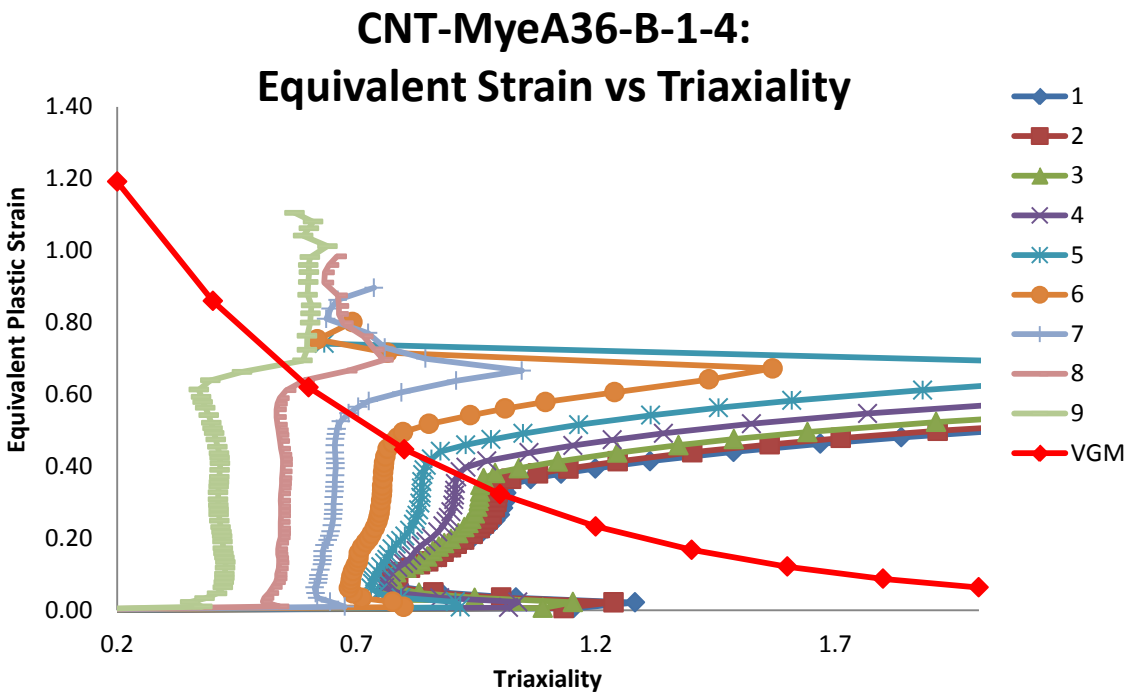

Figure B. 12: Variation of equivalent plastic strain versus triaxiality for different elements laid out through the thickness of simulation of CNT-MyeA36-B-1-4 specimens

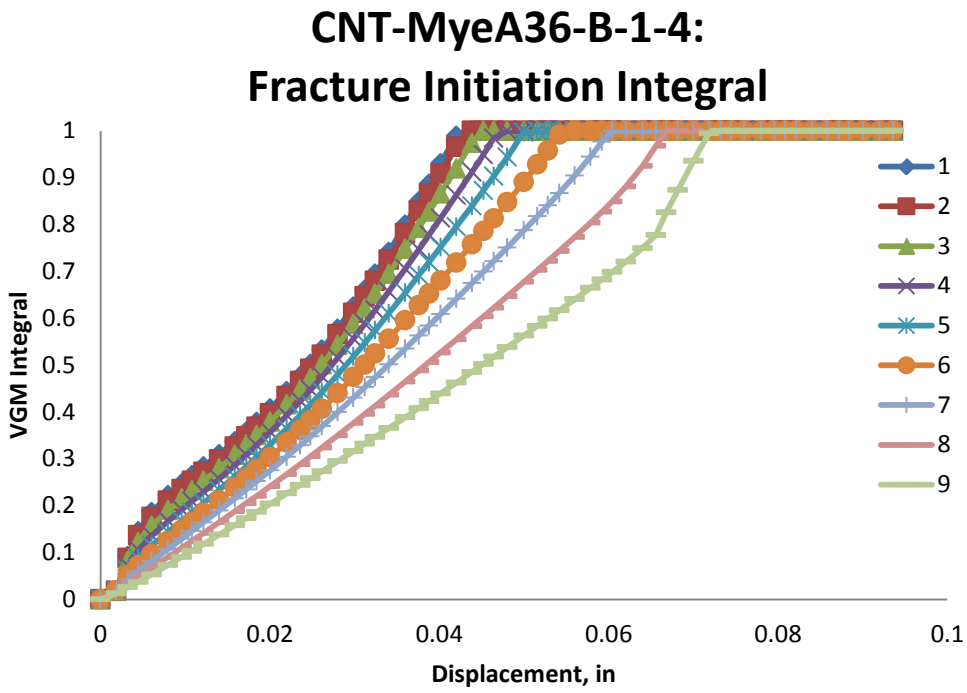

Figure B. 13: Value of fracture initiation integral for different elements laid out through the thickness of simulation of CNT-MyeA36-B-1-4 specimens

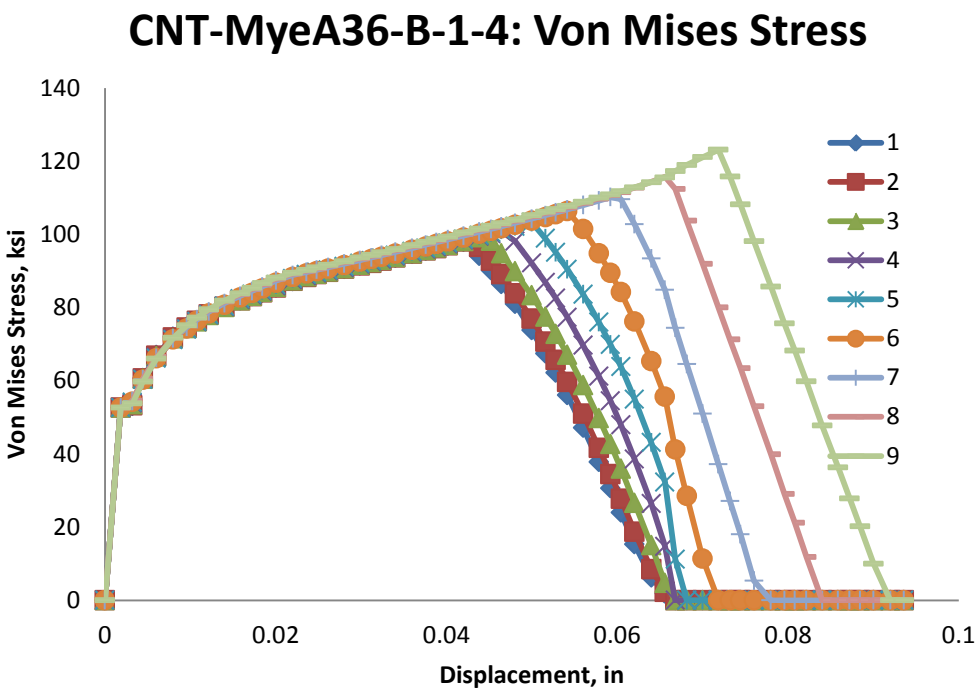

Figure B. 14: Variation of von Mises stress versus displacement for different elements laid out through the thickness of simulation of CNT-MyeA36-B-1-4 specimens

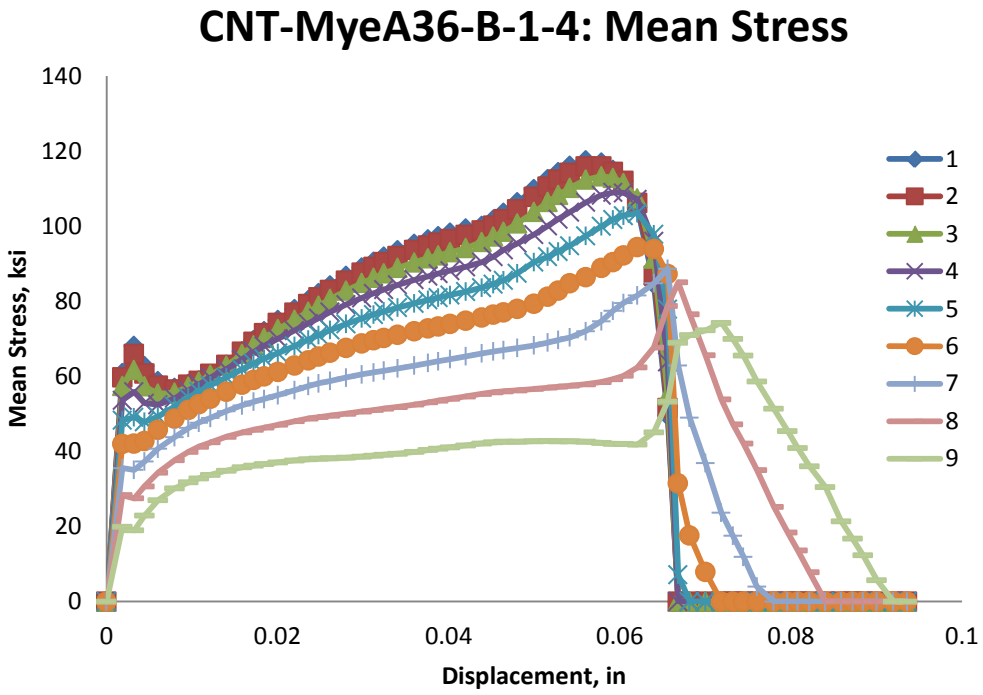

Figure B. 15: Variation of mean stress versus displacement for different elements laid out through the thickness of simulation of CNT-MyeA36-B-1-4 specimens

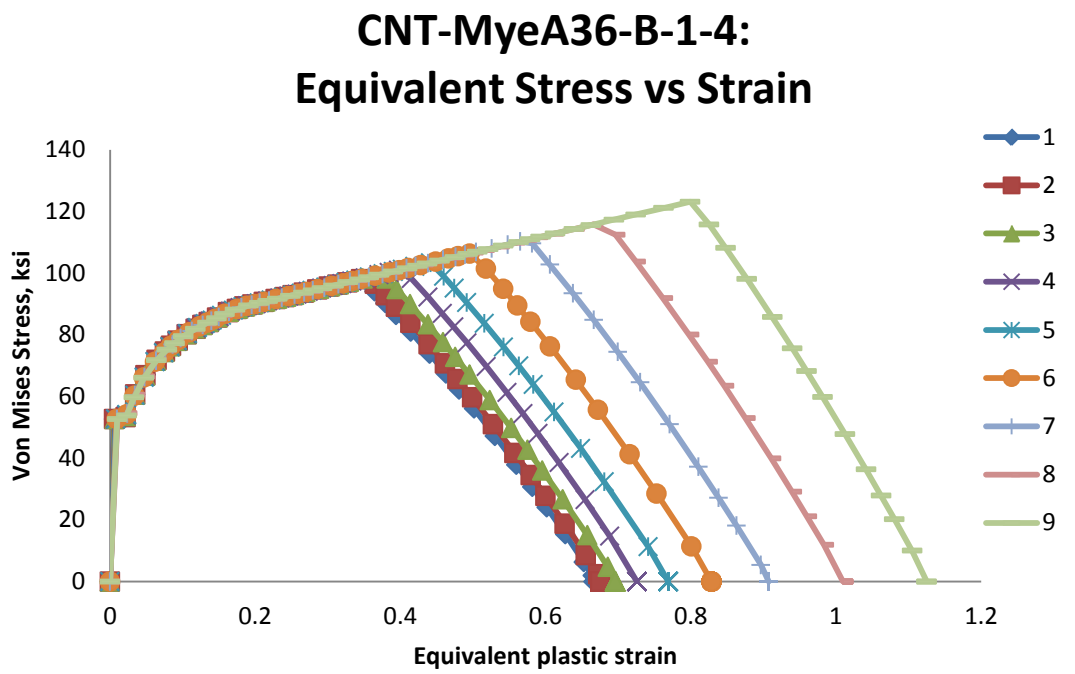

Figure B. 16: Variation of von Mises stress versus equivalent plastic strain for different elements laid out through the thickness of simulation of CNT-MyeA36-B-1-4 specimens

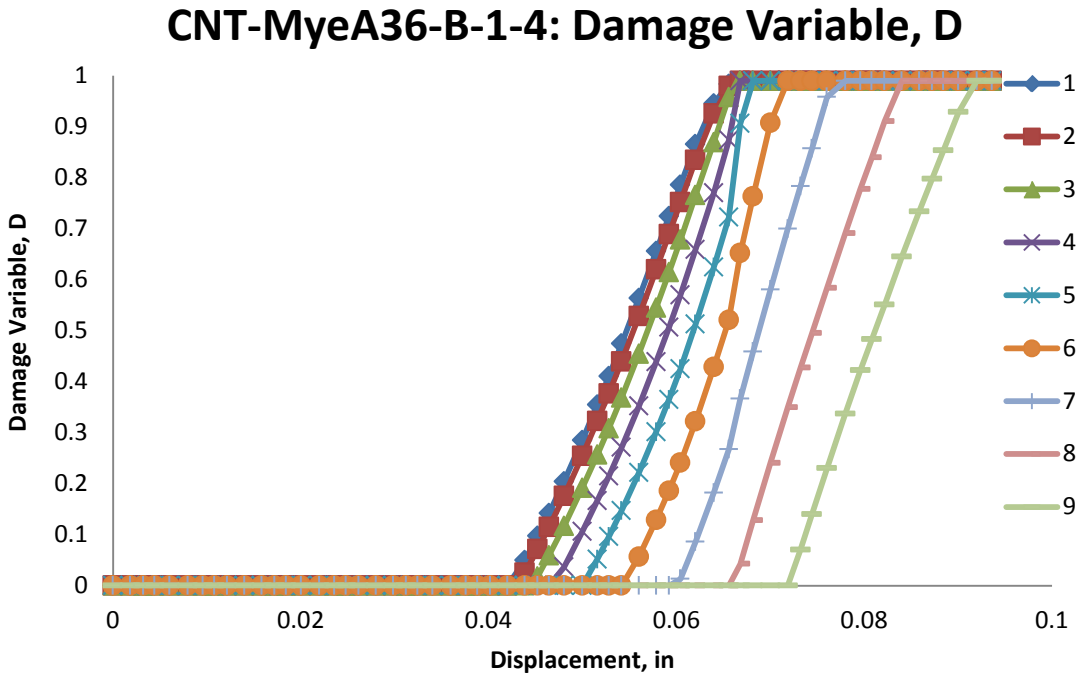

Figure B. 17: Variation of damage variable with displacement for different elements laid out through the thickness of simulation of CNT-MyeA36-B-1-4 specimens

B.2 CNT-MyeA992-W-L-A

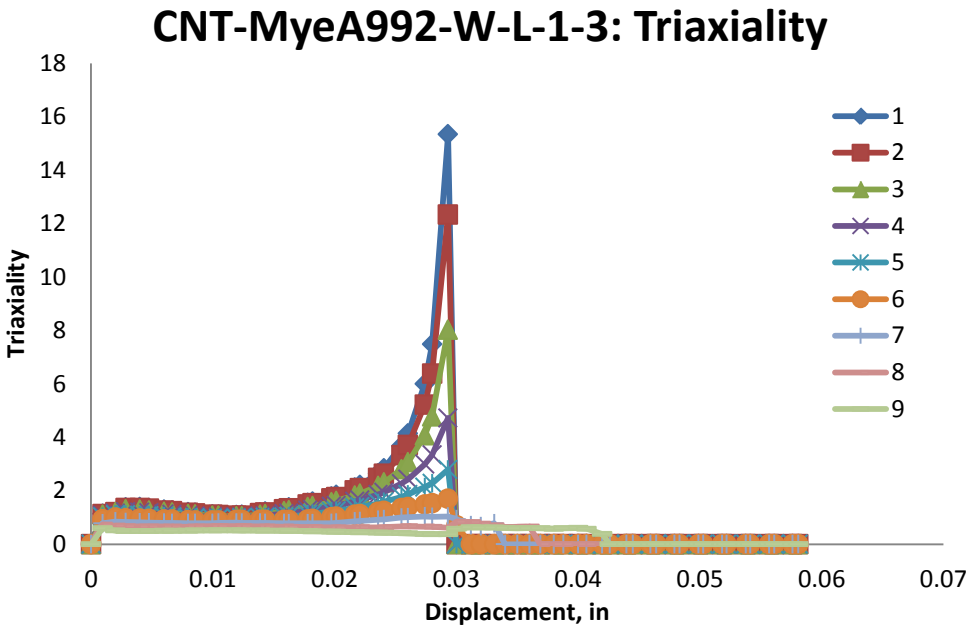

Figure B. 18: Variation of triaxiality with displacement for different elements laid out through the thickness of simulation of CNT-MyeA992-W-L-1-3 specimens

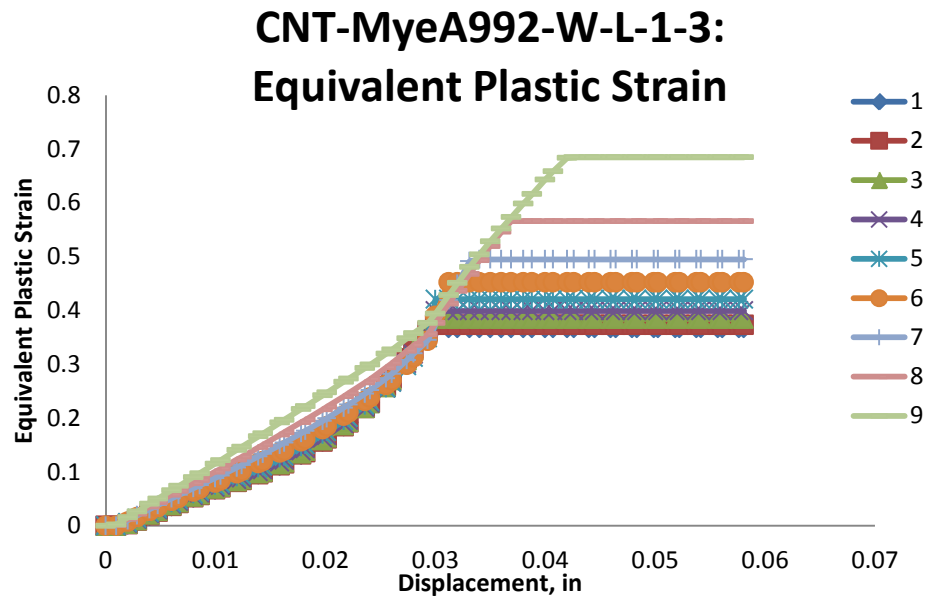

Figure B. 19: Variation of equivalent plastic strain with displacement for different elements laid out through the thickness of simulation of CNT-MyeA992-W-L-1-3 specimens

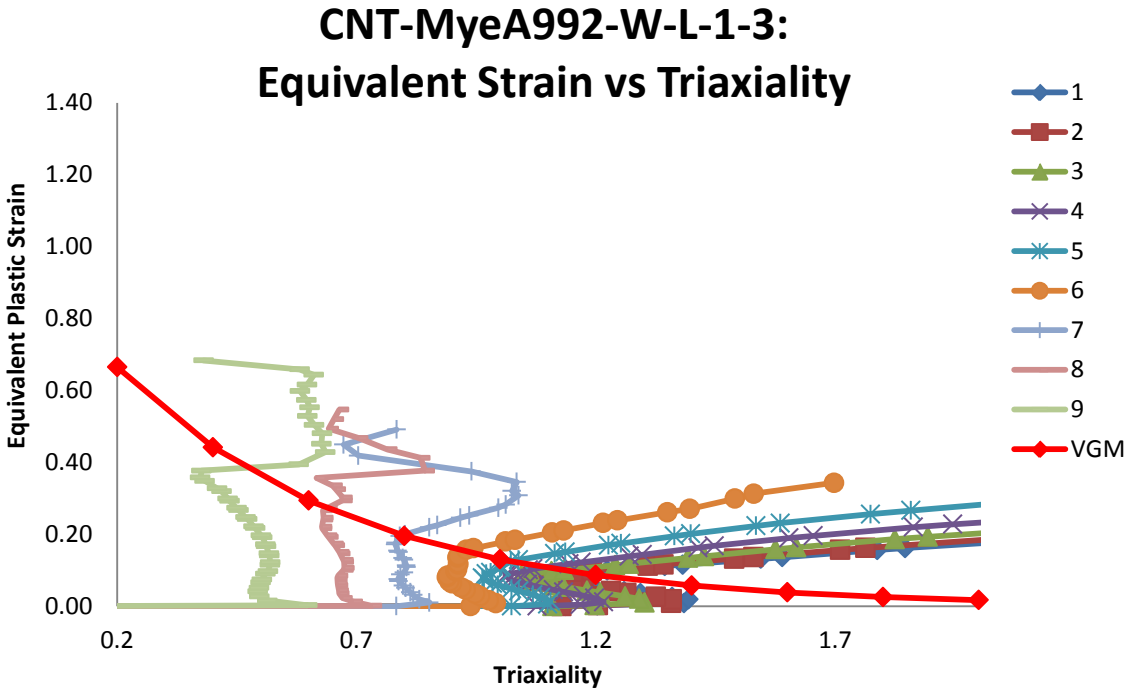

Figure B. 20: Variation of equivalent plastic strain versus triaxiality for different elements laid out through the thickness of simulation of CNT-MyeA992-W-L-1-3 specimens

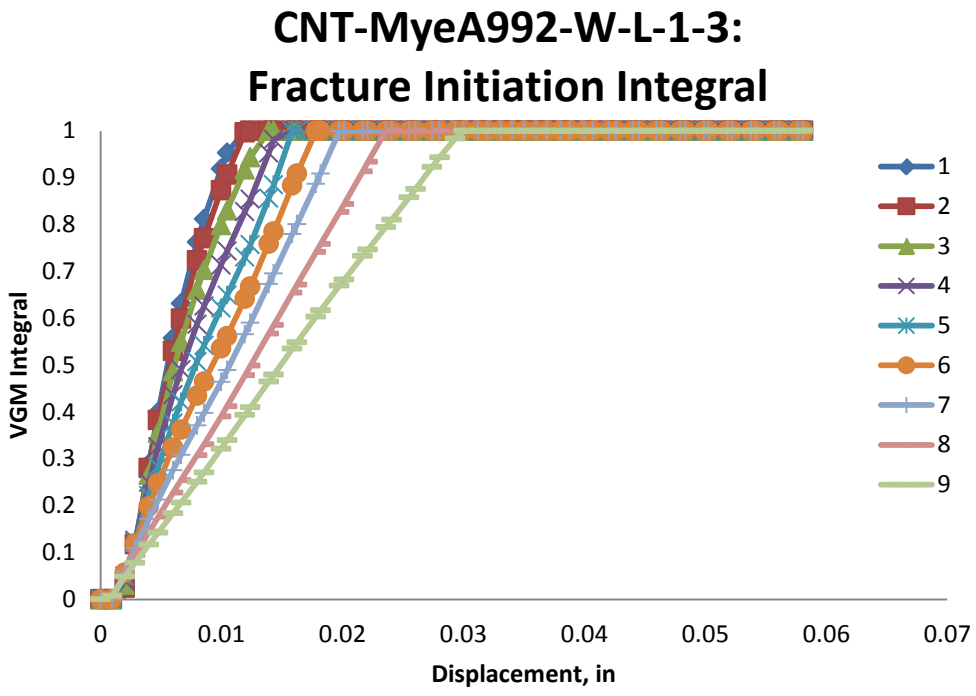

Figure B. 21: Value of fracture initiation integral for different elements laid out through the thickness of simulation of CNT-MyeA992-W-L-1-3 specimens

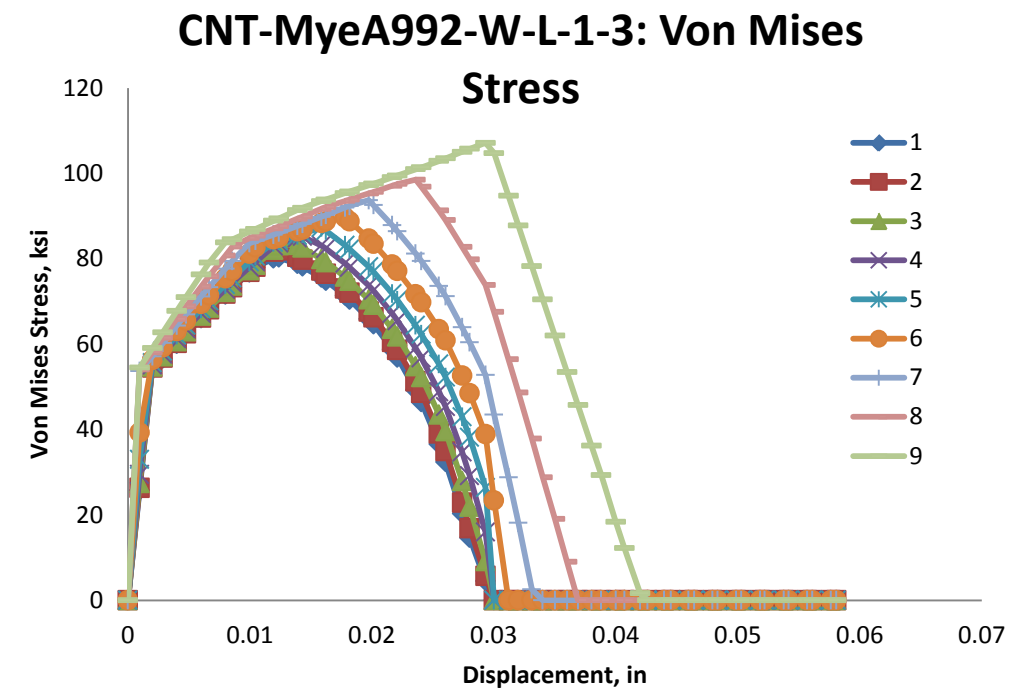

Figure B. 22: Variation of von Mises stress versus displacement for different elements laid out through the thickness of simulation of CNT-MyeA992-W-L-1-3 specimens

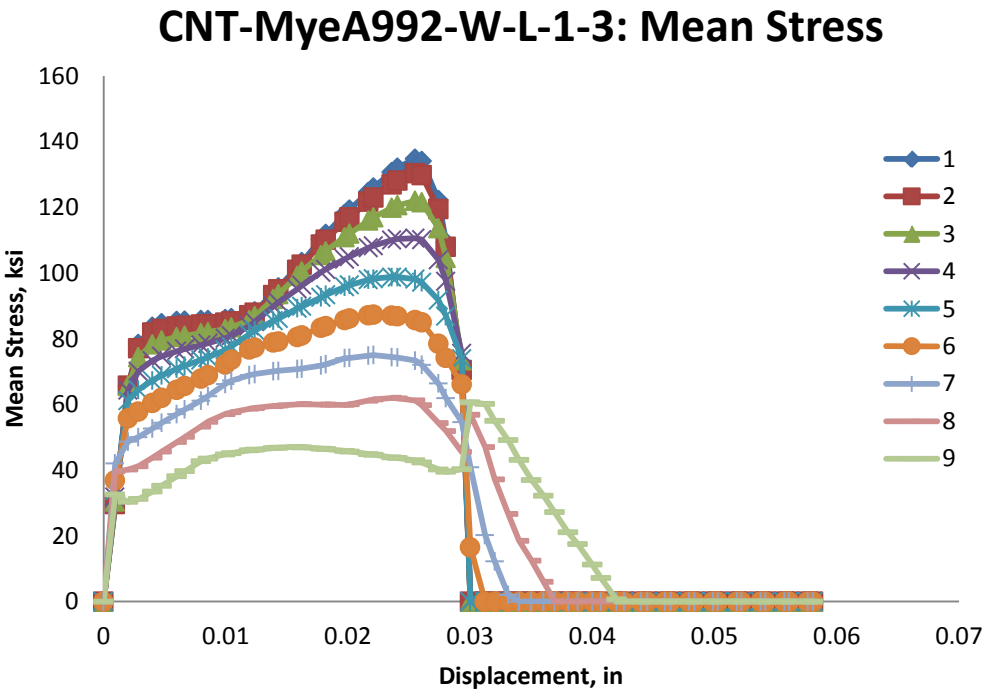

Figure B. 23: Variation of mean stress versus displacement for different elements laid out through the thickness of simulation of CNT-MyeA992-W-L-1-3 specimens

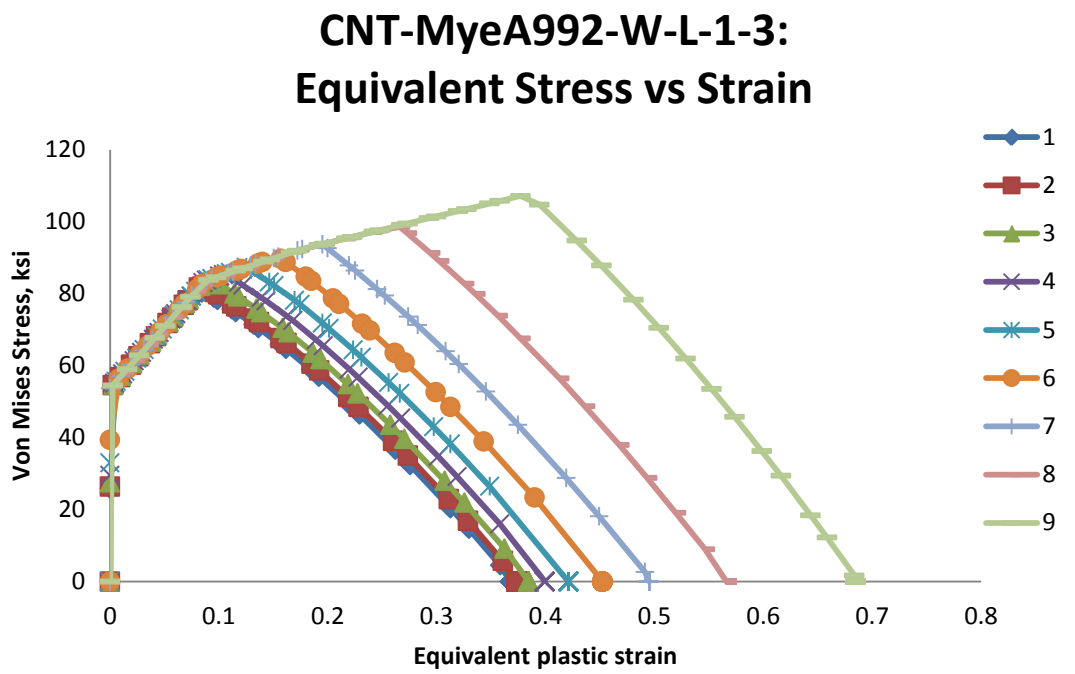

Figure B. 24: Variation of von Mises stress versus equivalent plastic strain for different elements laid out through the thickness of simulation of CNT-MyeA992-W-L-1-3 specimens

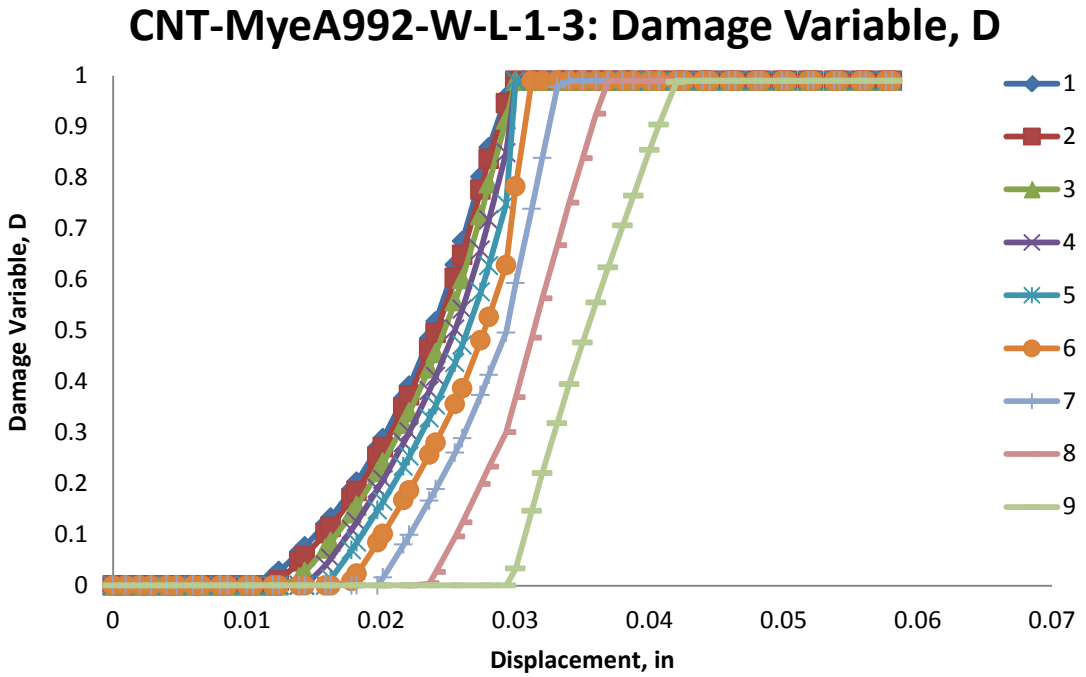

Figure B. 25: Variation of damage variable with displacement for different elements laid out through the thickness of simulation of CNT-MyeA992-W-L-1-3 specimens

B.3 CNT-MyeA992-W-T-A

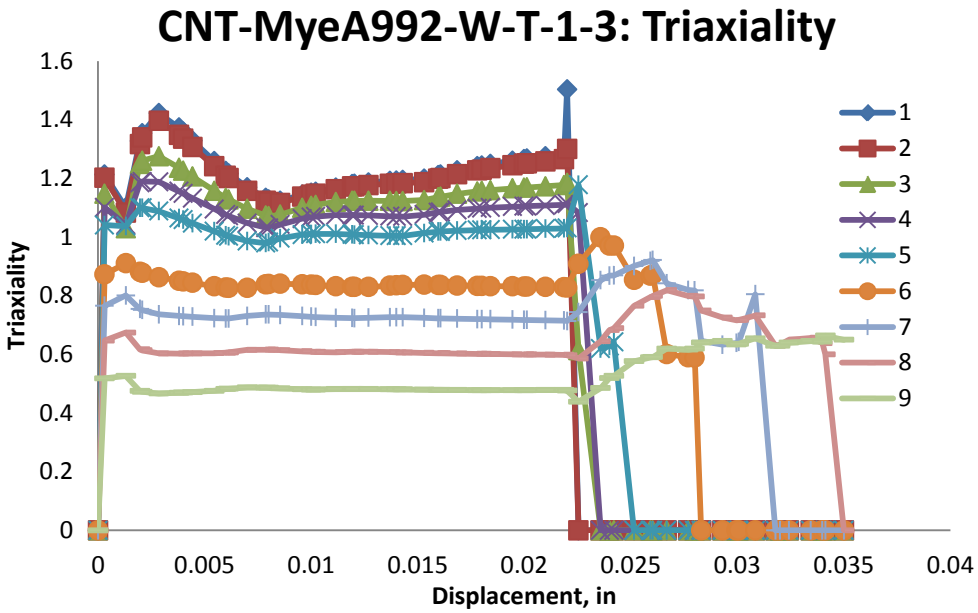

Figure B. 26: Variation of triaxiality with displacement for different elements laid out through the thickness of simulation of CNT-MyeA992-W-T-1-3 specimens

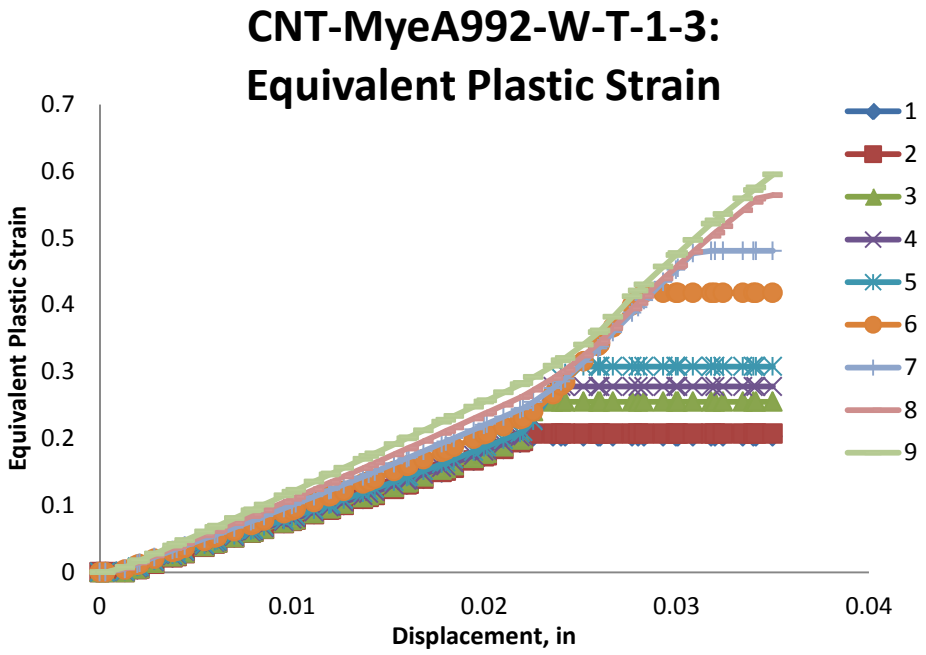

Figure B. 27: Variation of equivalent plastic strain with displacement for different elements laid out through the thickness of simulation of CNT-MyeA992-W-T-1-3 specimens

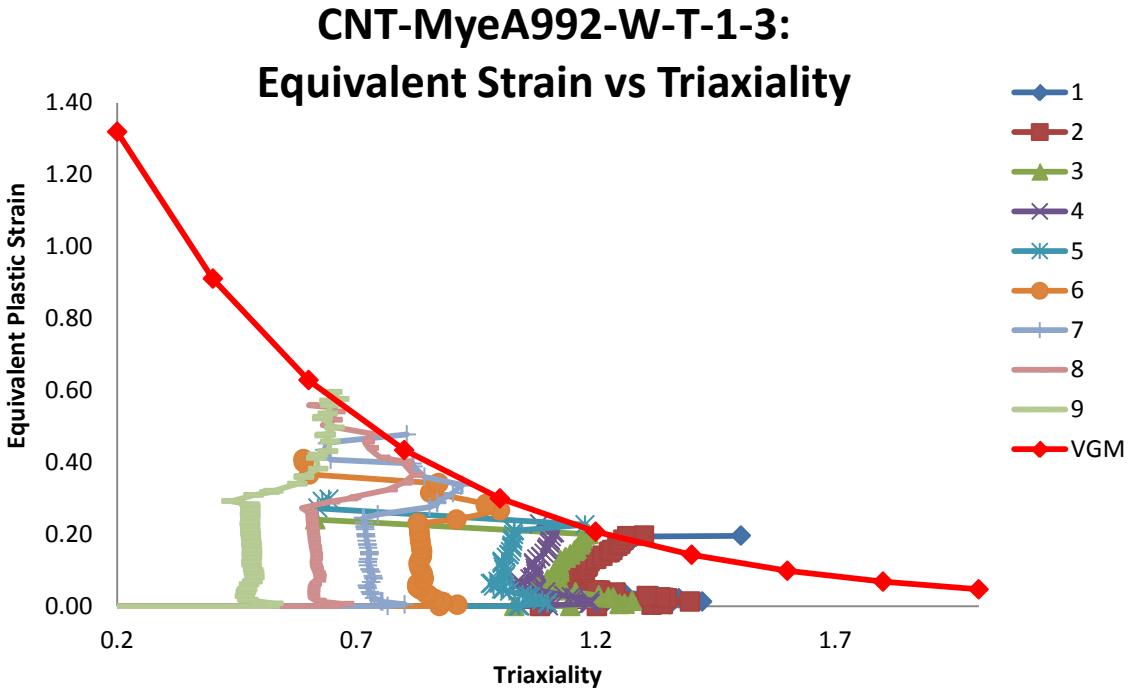

Figure B. 28: Variation of equivalent plastic strain versus triaxiality for different elements laid out through the thickness of simulation of CNT-MyeA992-W-T-1-3 specimens

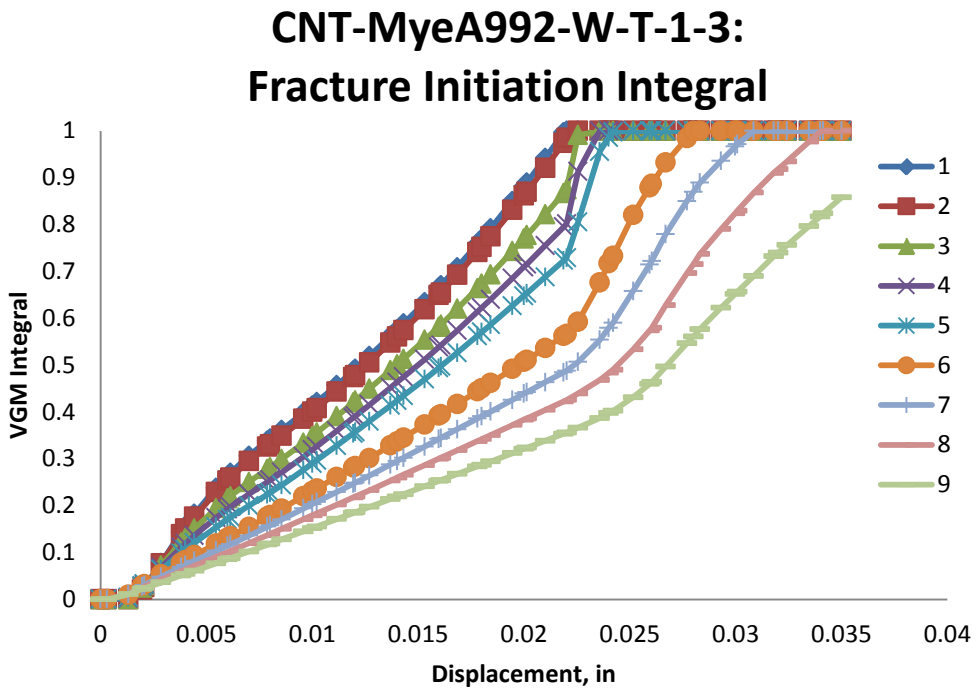

Figure B. 29: Value of fracture initiation integral for different elements laid out through the thickness of simulation of CNT-MyeA992-W-T-1-3 specimens

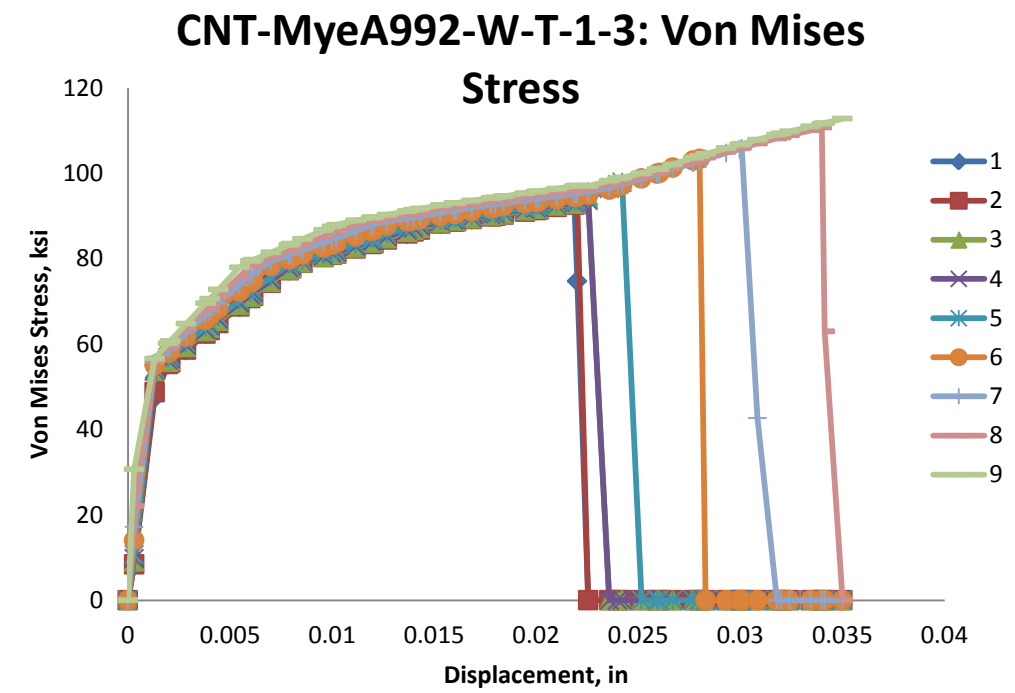

Figure B. 30: Variation of von Mises stress versus displacement for different elements laid out through the thickness of simulation of CNT-MyeA992-W-T-1-3 specimens

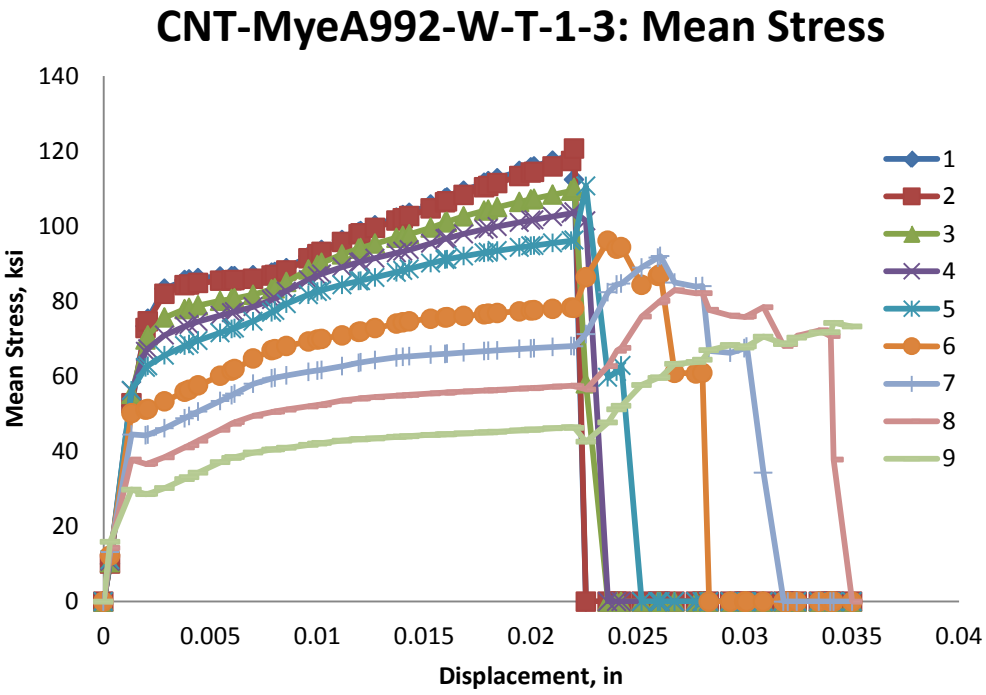

Figure B. 31: Variation of mean stress versus displacement for different elements laid out through the thickness of simulation of CNT-MyeA992-W-T-1-3 specimens

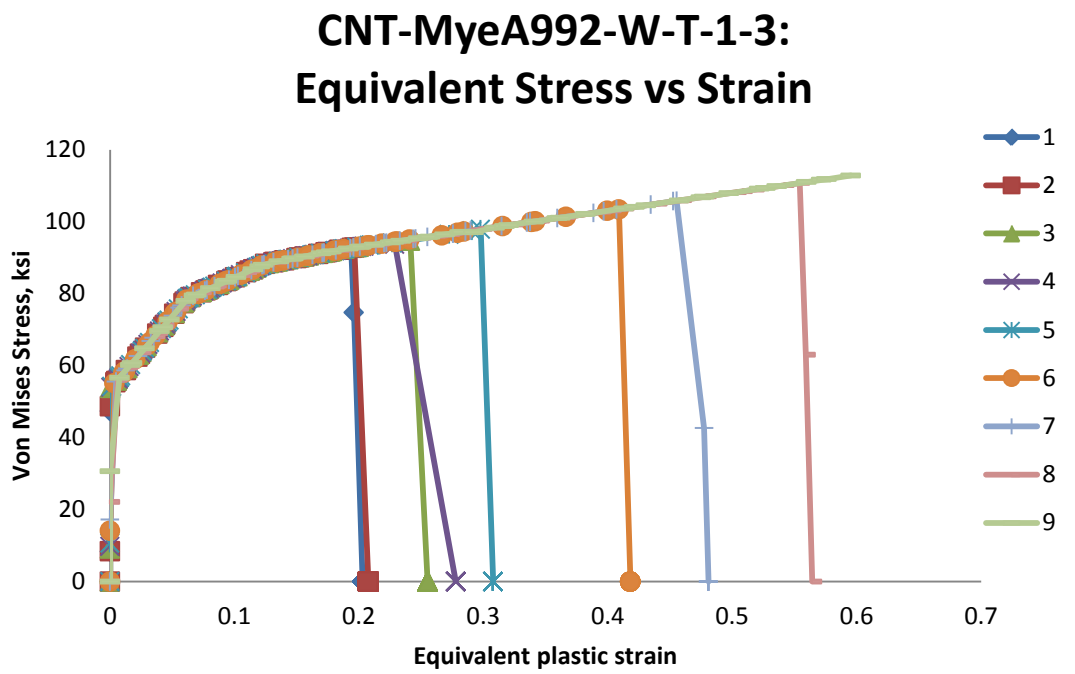

Figure B. 32: Variation of von Mises stress versus equivalent plastic strain for different elements laid out through the thickness of simulation of CNT-MyeA992-W-T-1-3 specimens

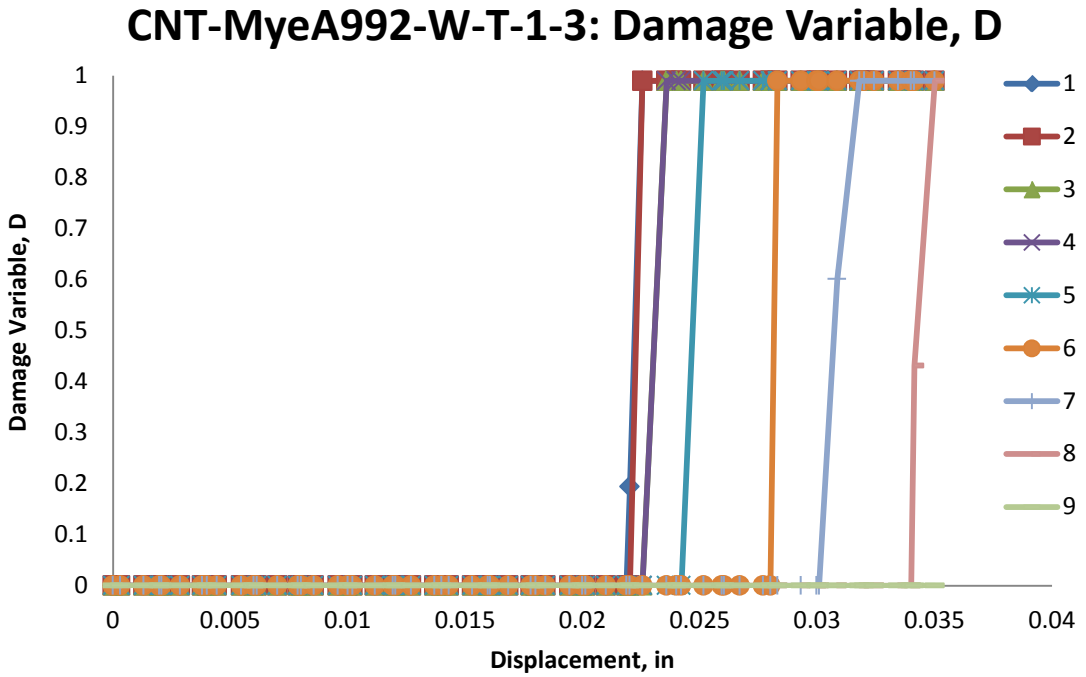

Figure B. 33: Variation of damage variable with displacement for different elements laid out through the thickness of simulation of CNT-MyeA992-W-T-1-3 specimens

B.4 CNT-KanA572-W-L-A

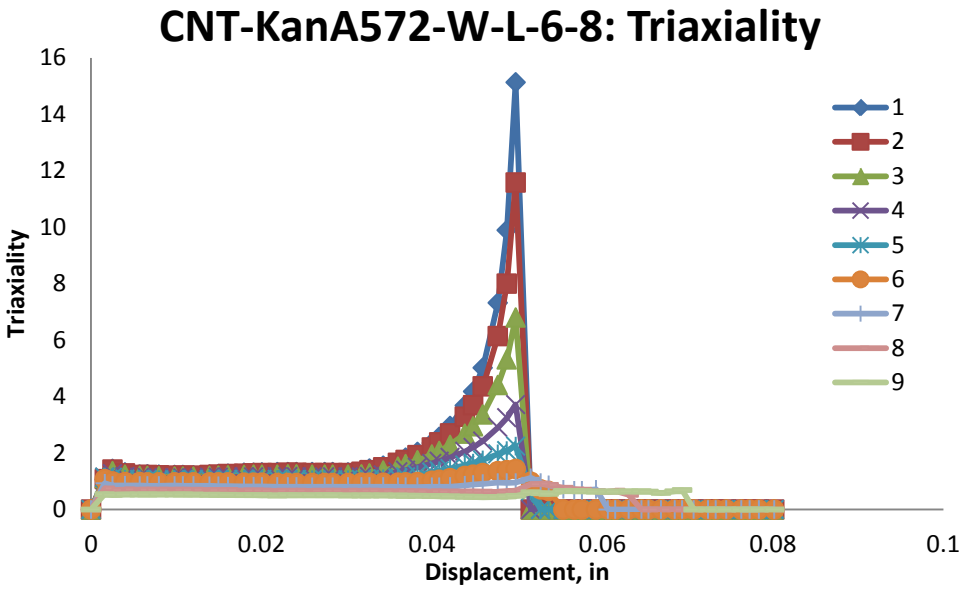

Figure B. 34: Variation of triaxiality with displacement for different elements laid out through the thickness of simulation of CNT-KanA572-W-L-6-8 specimens

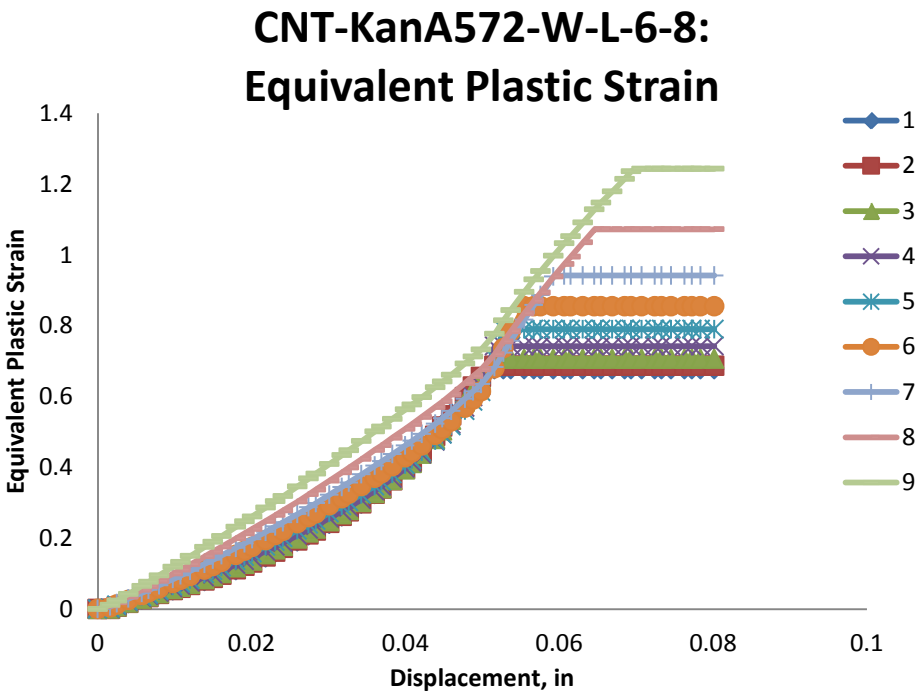

Figure B. 35: Variation of equivalent plastic strain with displacement for different elements laid out through the thickness of simulation of CNT-KanA572-W-L-6-8 specimens

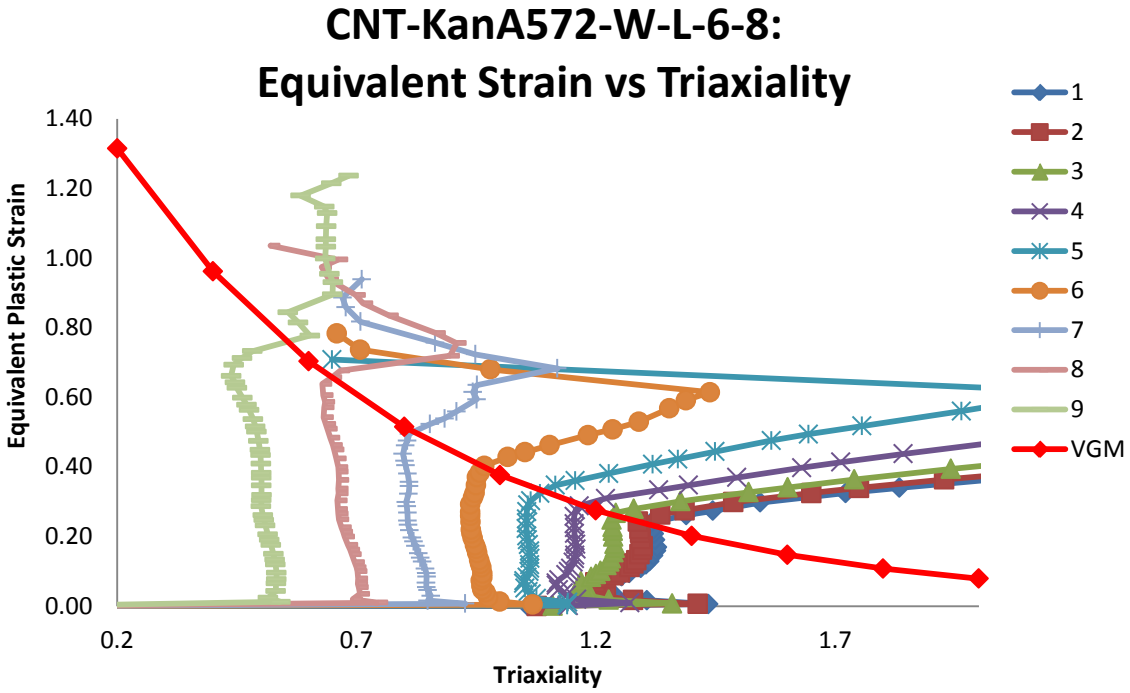

Figure B. 36: Variation of equivalent plastic strain versus triaxiality for different elements laid out through the thickness of simulation of CNT-KanA572-W-L-6-8 specimens

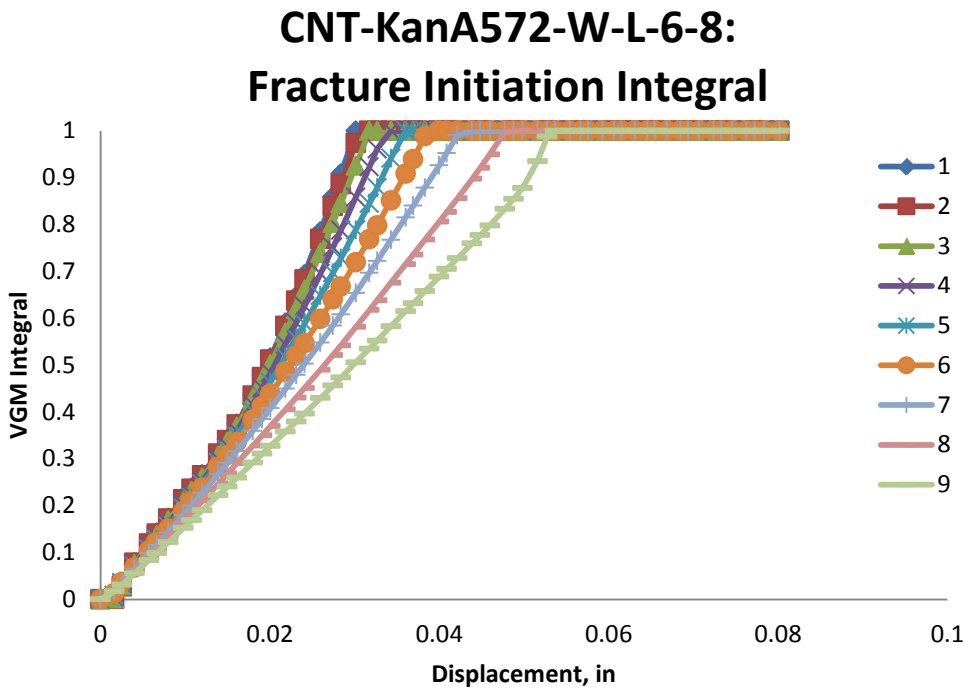

Figure B. 37: Value of fracture initiation integral for different elements laid out through the thickness of simulation of CNT-KanA572-W-L-6-8 specimens

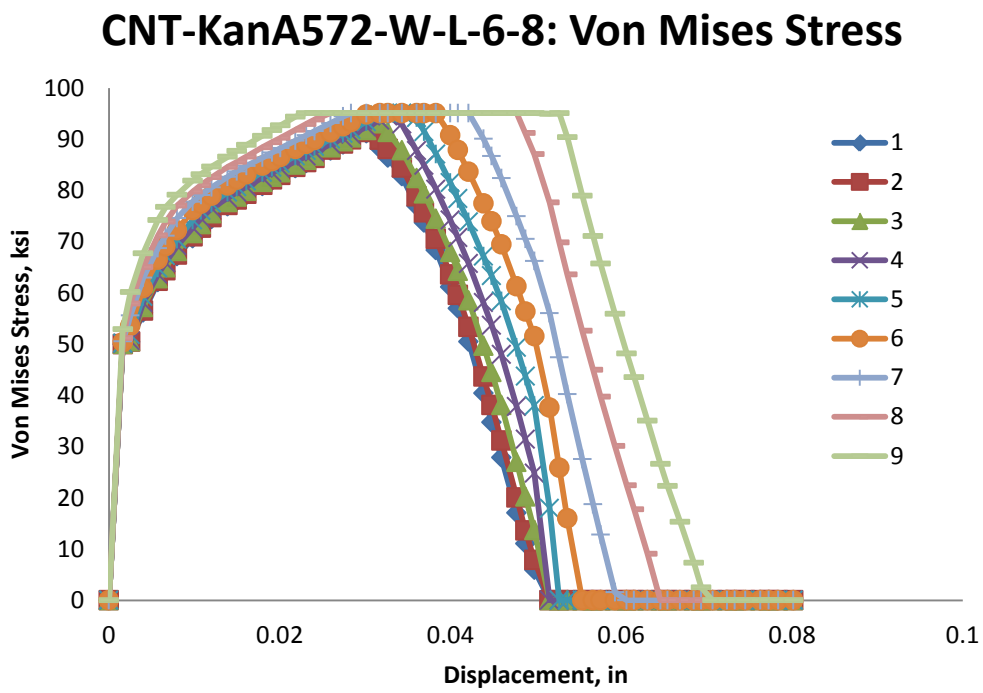

Figure B. 38: Variation of von Mises stress versus displacement for different elements laid out through the thickness of simulation of CNT-KanA572-W-L-6-8 specimens

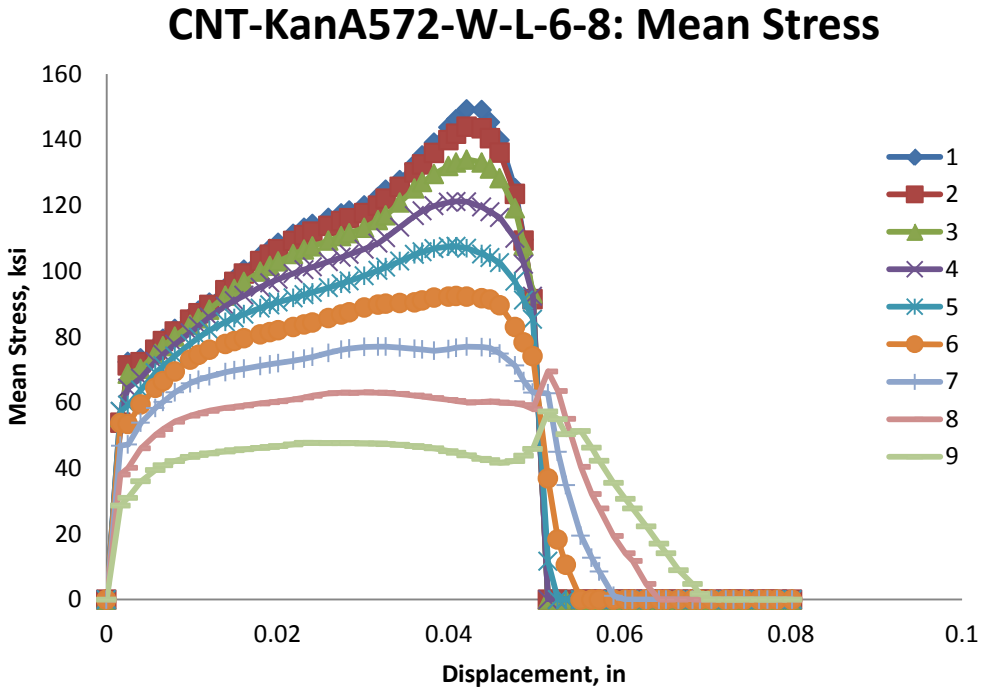

Figure B. 39: Variation of mean stress versus displacement for different elements laid out through the thickness of simulation of CNT-KanA572-W-L-6-8 specimens

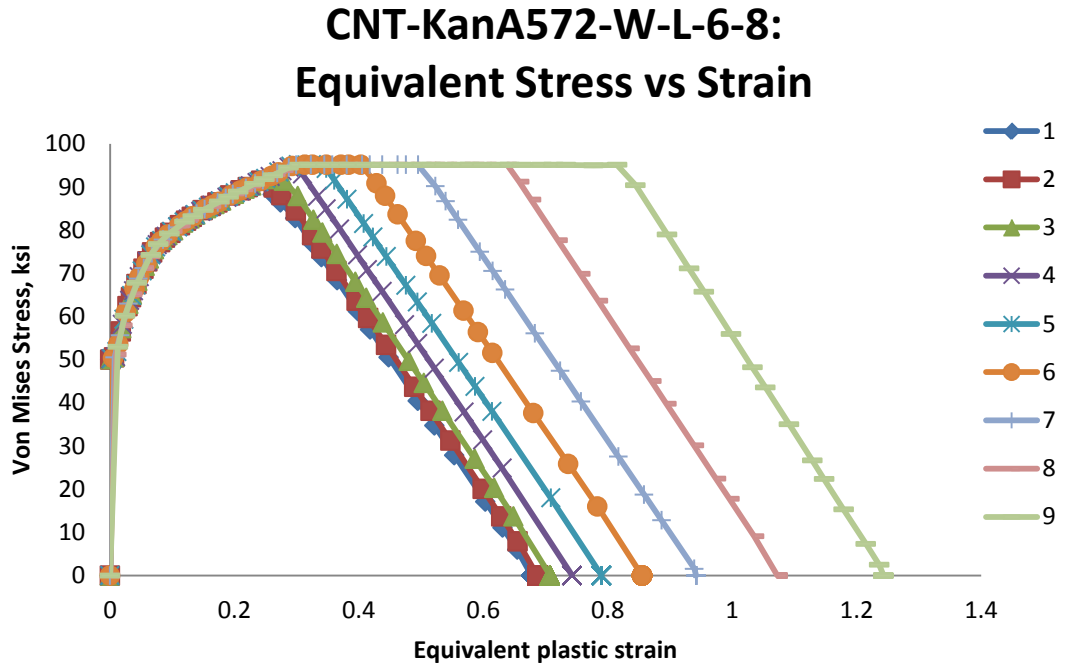

Figure B. 40: Variation of von Mises stress versus equivalent plastic strain for different elements laid out through the thickness of simulation of CNT-KanA572-W-L-6-8 specimens

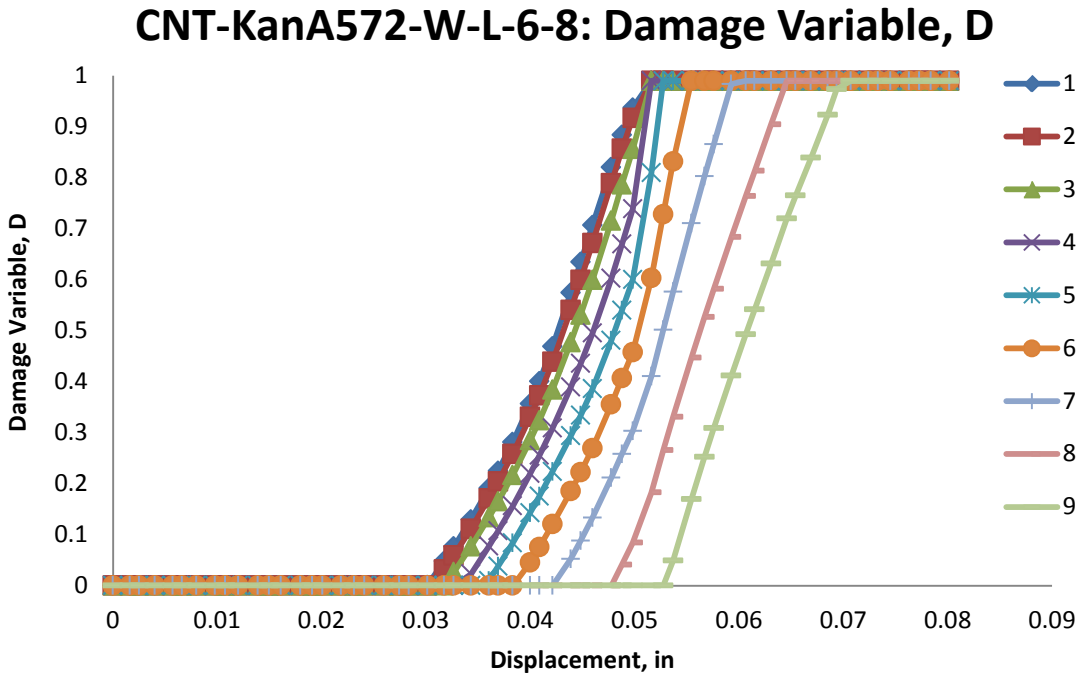

Figure B. 41: Variation of damage variable with displacement for different elements laid out through the thickness of simulation of CNT-KanA572-W-L-6-8 specimens

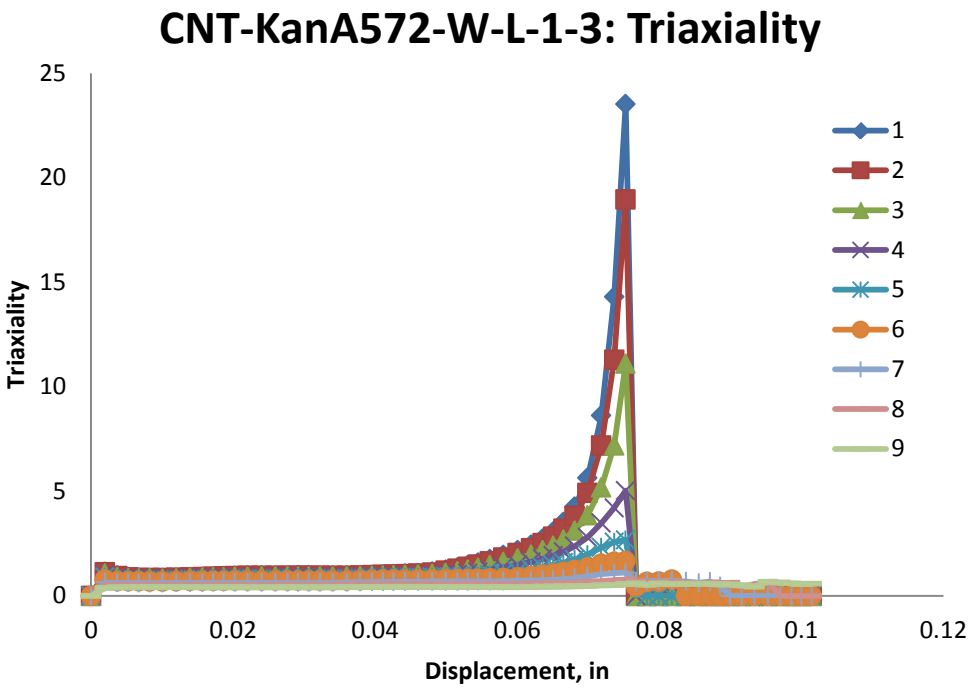

Figure B. 42: Variation of triaxiality with displacement for different elements laid out through the thickness of simulation of CNT-KanA572-W-L-1-3 specimens

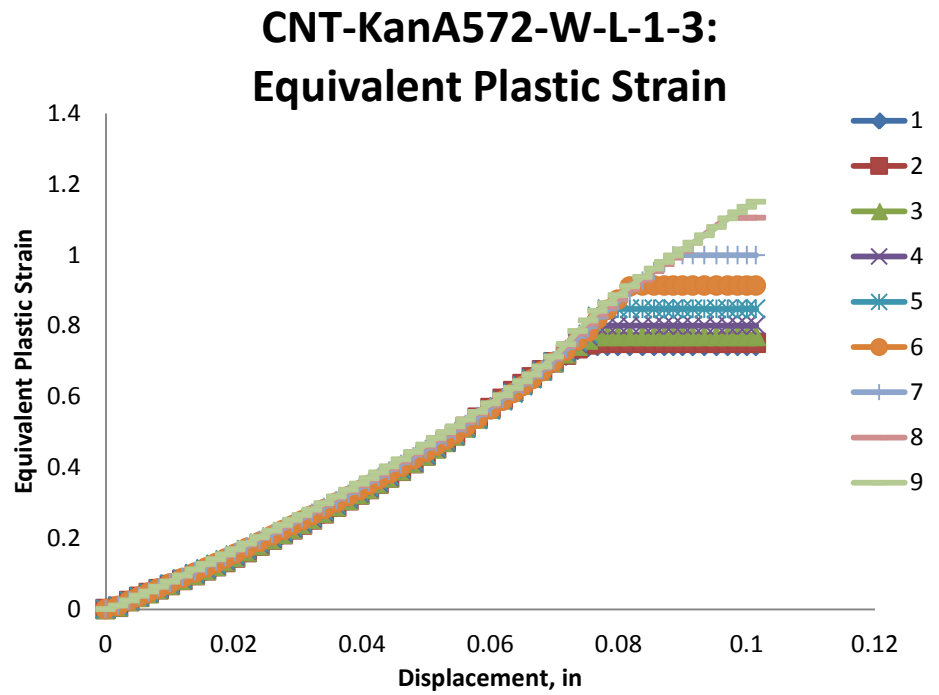

Figure B. 43: Variation of equivalent plastic strain with displacement for different elements laid out through the thickness of simulation of CNT-KanA572-W-L-1-3 specimens

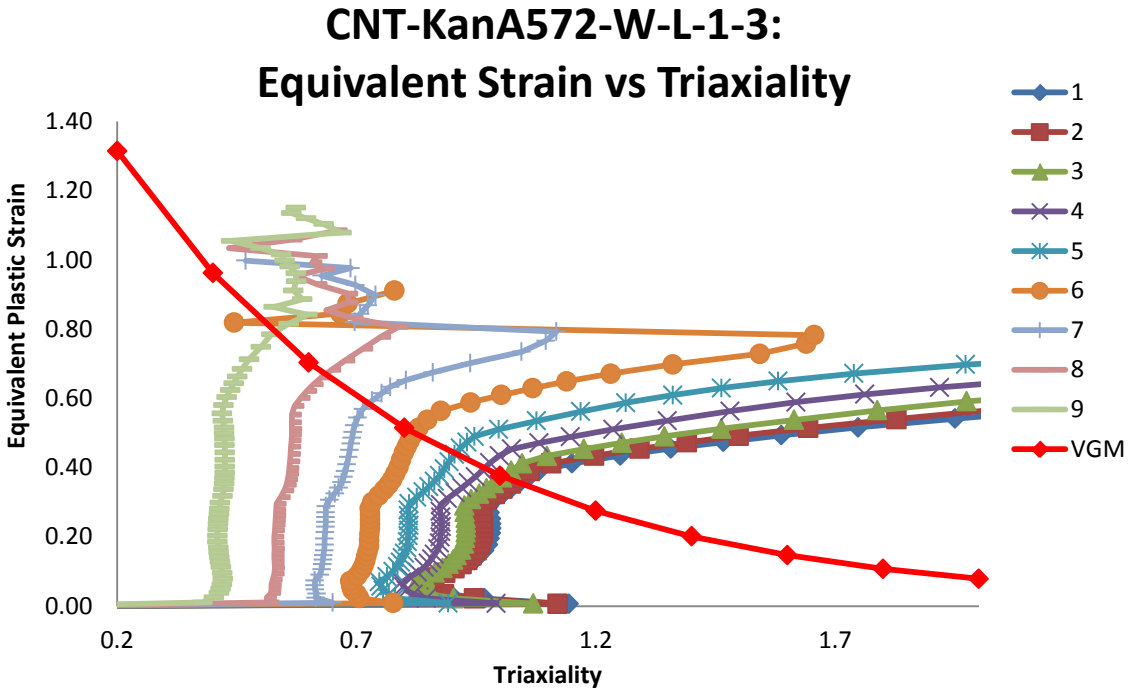

Figure B. 44: Variation of equivalent plastic strain versus triaxiality for different elements laid out through the thickness of simulation of CNT-KanA572-W-L-1-3 specimens

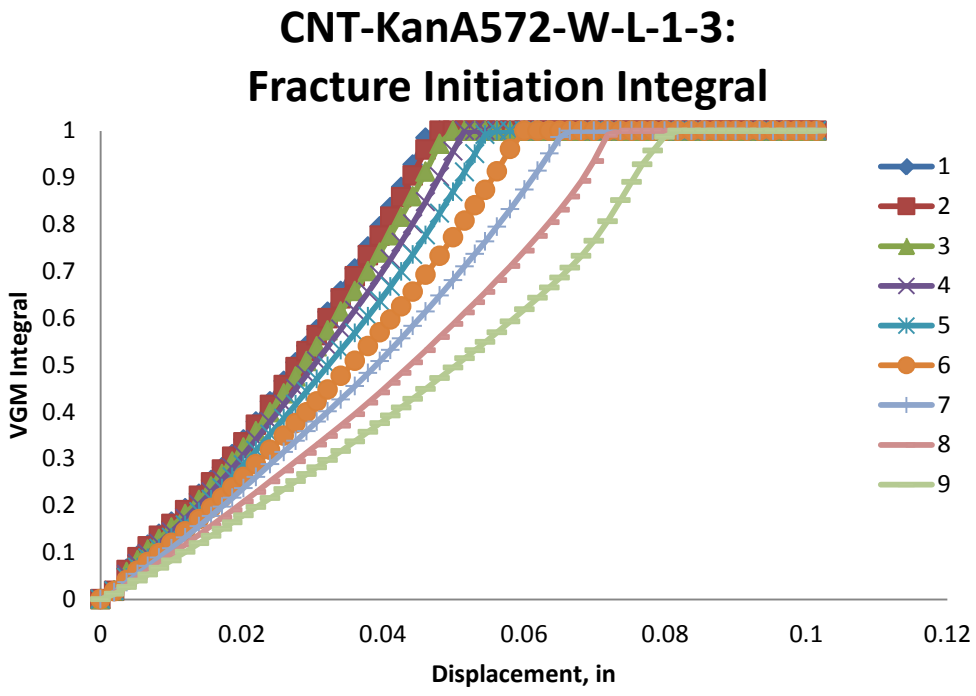

Figure B. 45: Value of fracture initiation integral for different elements laid out through the thickness of simulation of CNT-KanA572-W-L-1-3 specimens

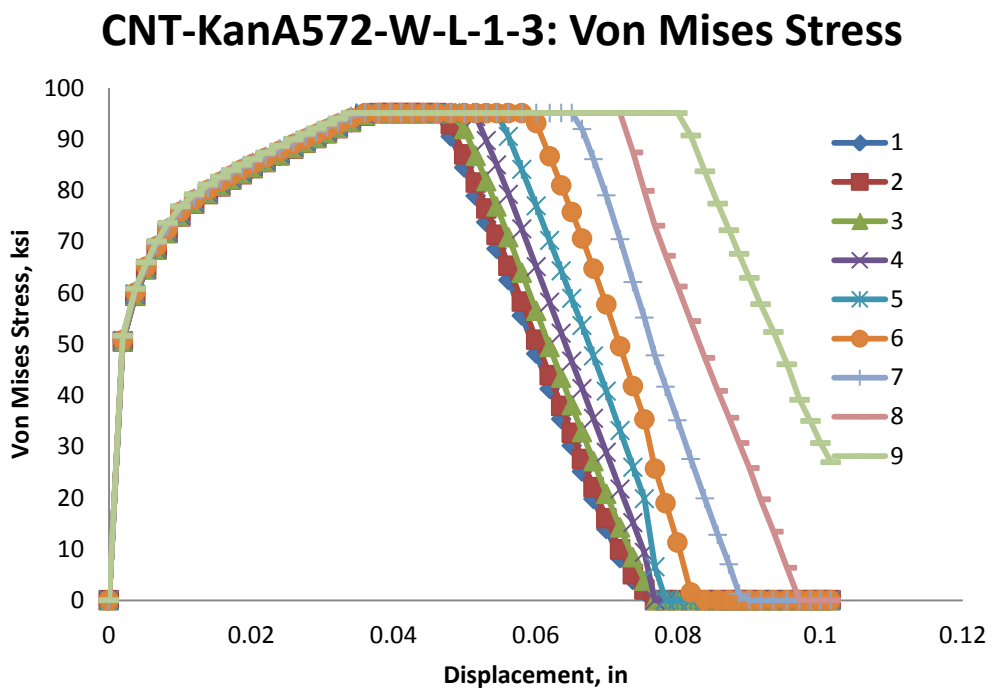

Figure B. 46: Variation of von Mises stress versus displacement for different elements laid out through the thickness of simulation of CNT-KanA572-W-L-1-3 specimens

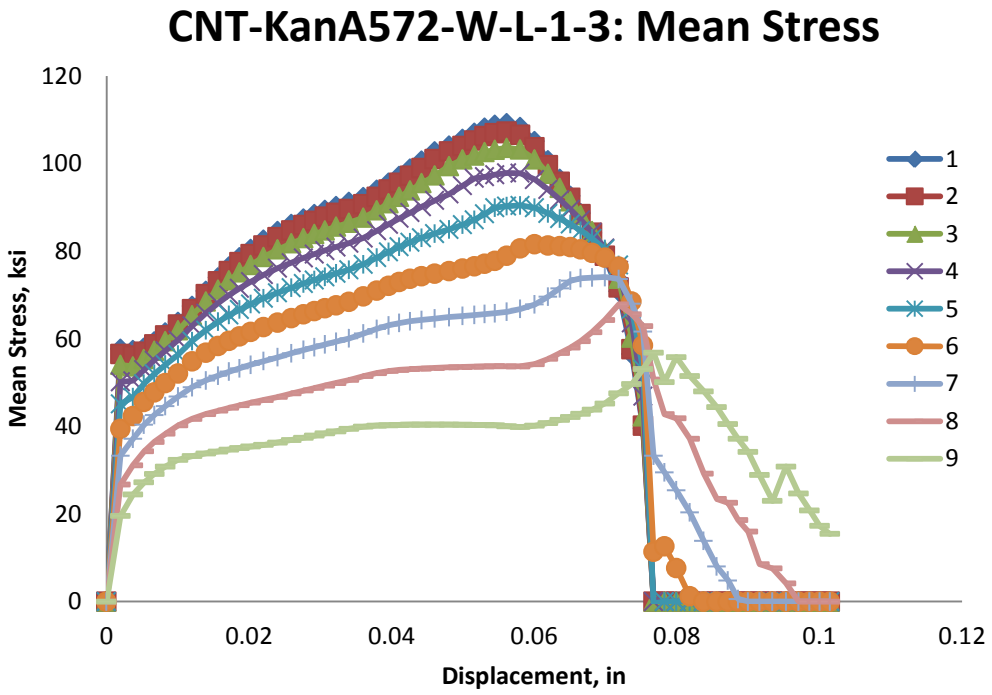

Figure B. 47: Variation of mean stress versus displacement for different elements laid out through the thickness of simulation of CNT-KanA572-W-L-1-3 specimens

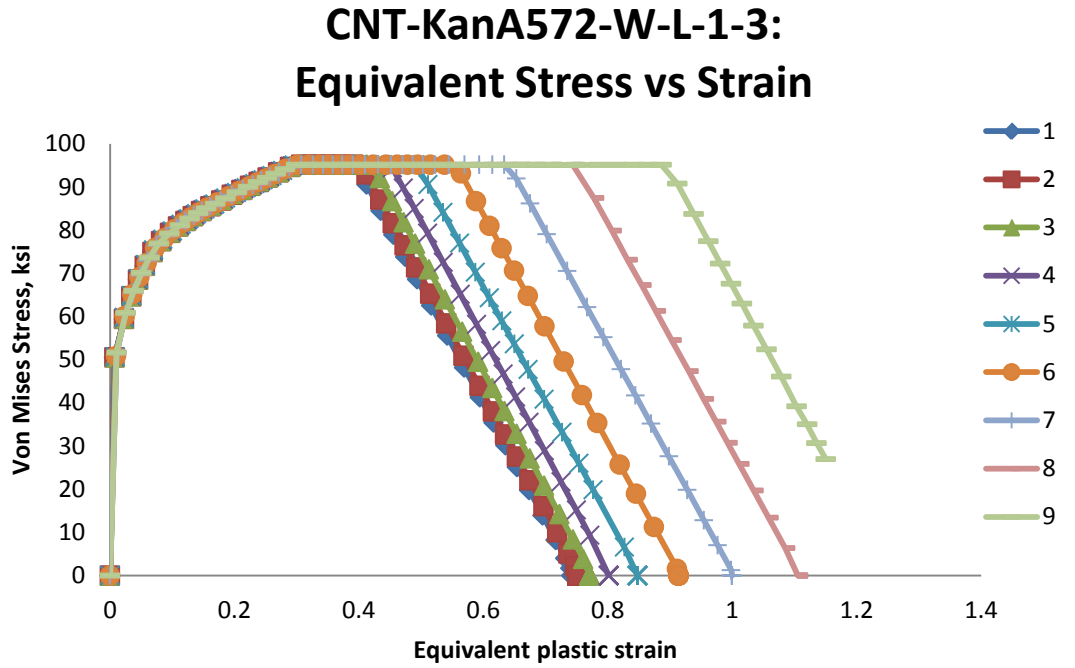

Figure B. 48: Variation of von Mises stress versus equivalent plastic strain for different elements laid out through the thickness of simulation of CNT-KanA572-W-L-1-3 specimens

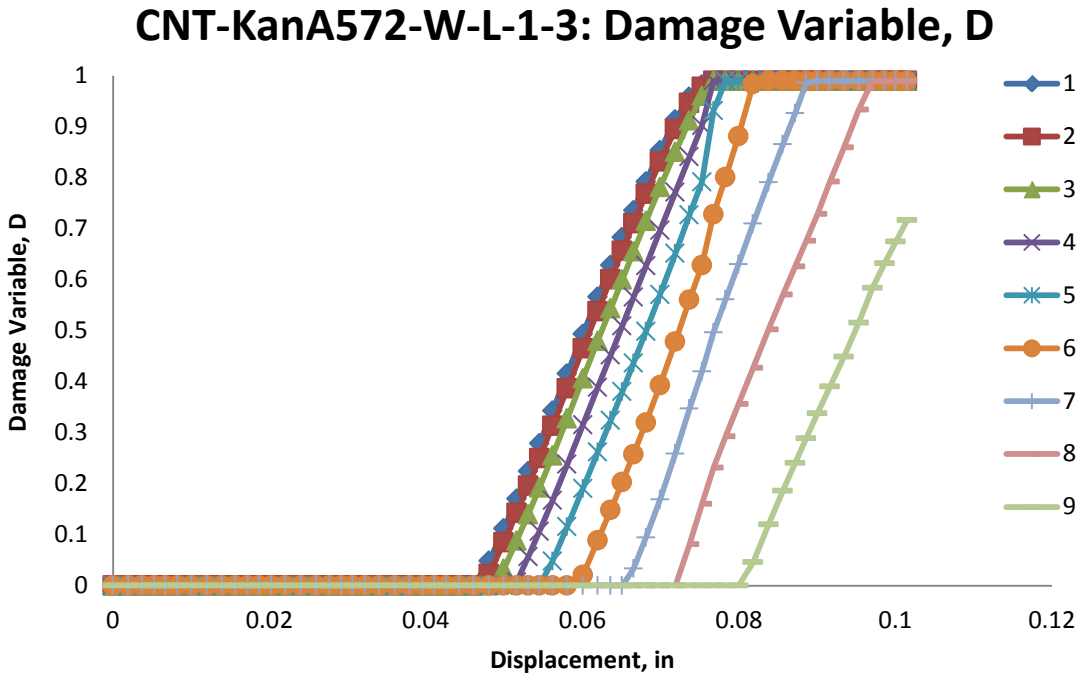

Figure B. 49: Variation of damage variable with displacement for different elements laid out through the thickness of simulation of CNT-KanA572-W-L-1-3 specimens

B.5 CNT-KanHPS70W-P-A

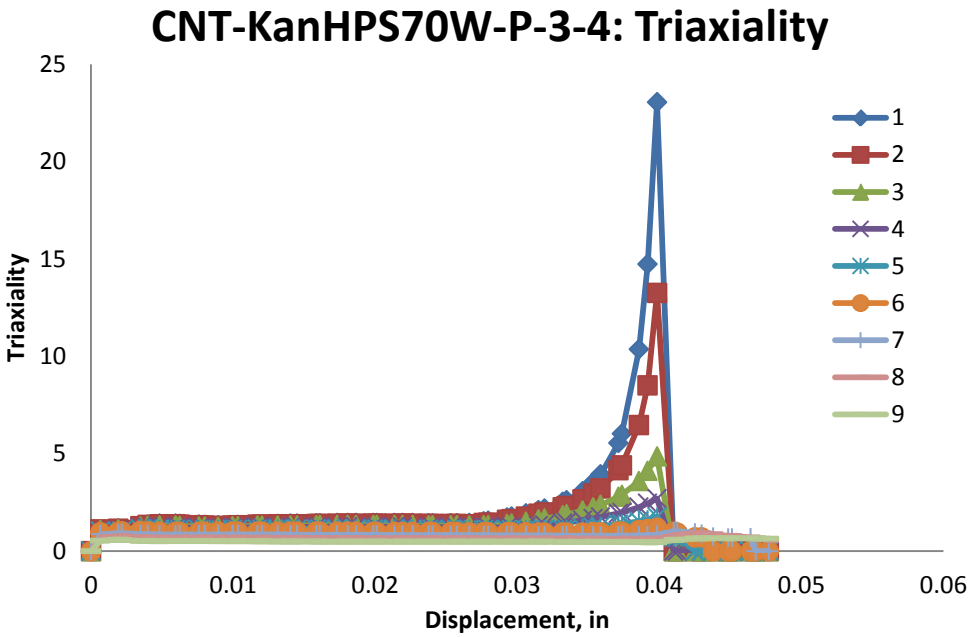

Figure B. 50: Variation of triaxiality with displacement for different elements laid out through the thickness of simulation of CNT-KanHPS70W-P-3-4 specimens

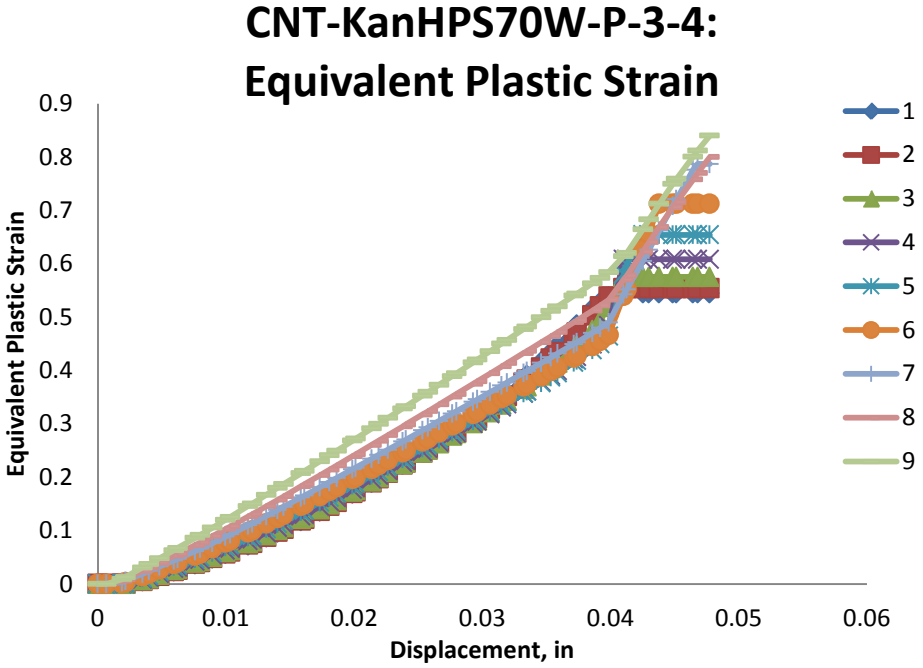

Figure B. 51: Variation of equivalent plastic strain with displacement for different elements laid out through the thickness of simulation of CNT-KanHPS70W-P-3-4 specimens

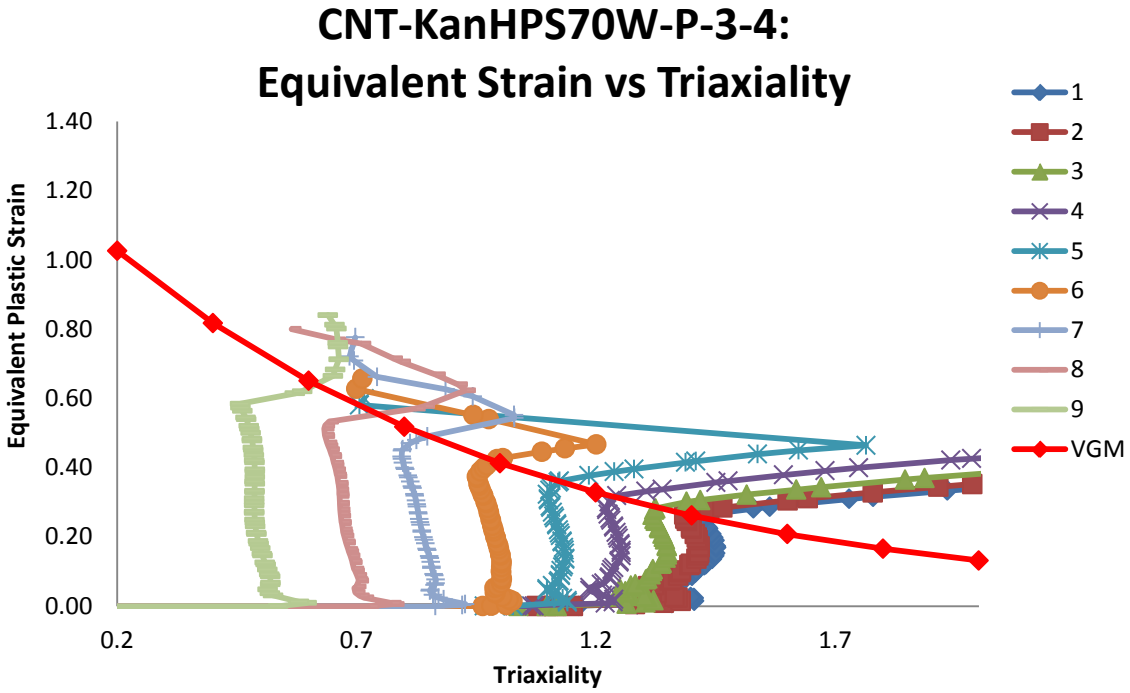

Figure B. 52: Variation of equivalent plastic strain versus triaxiality for different elements laid out through the thickness of simulation of CNT-KanHPS70W-P-3-4 specimens

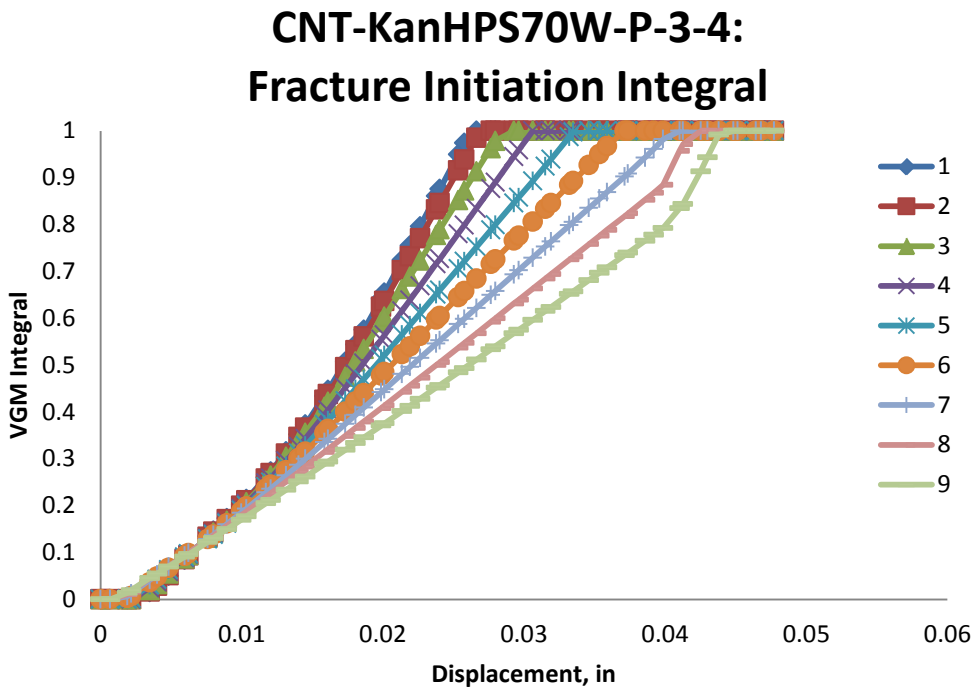

Figure B. 53: Value of fracture initiation integral for different elements laid out through the thickness of simulation of CNT-KanHPS70W-P-3-4 specimens

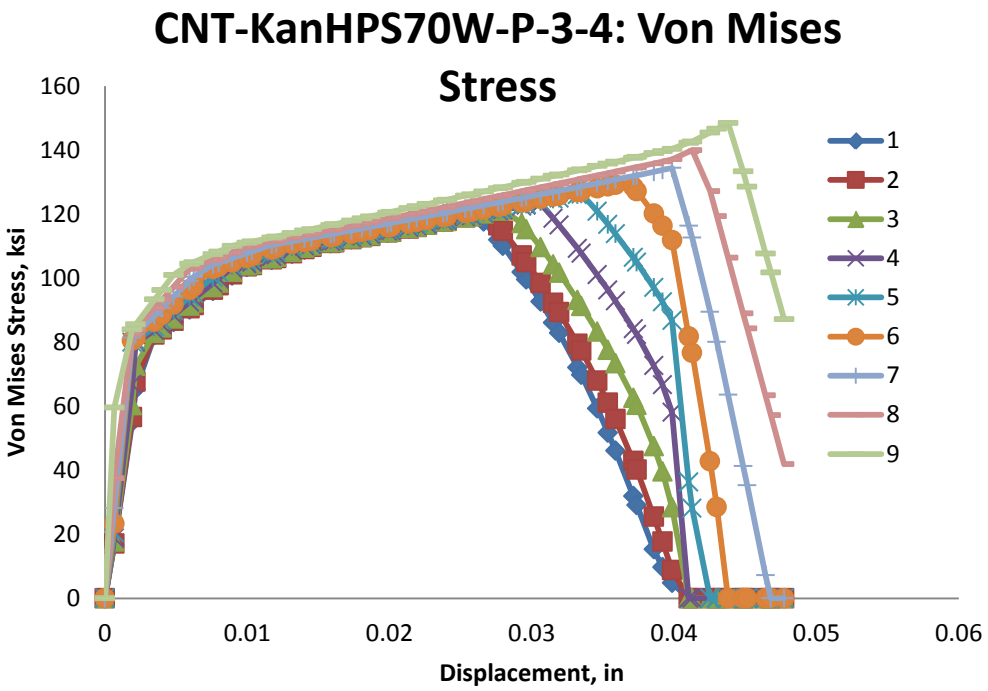

Figure B. 54: Variation of von Mises stress versus displacement for different elements laid out through the thickness of simulation of CNT-KanHPS70W-P-3-4 specimens

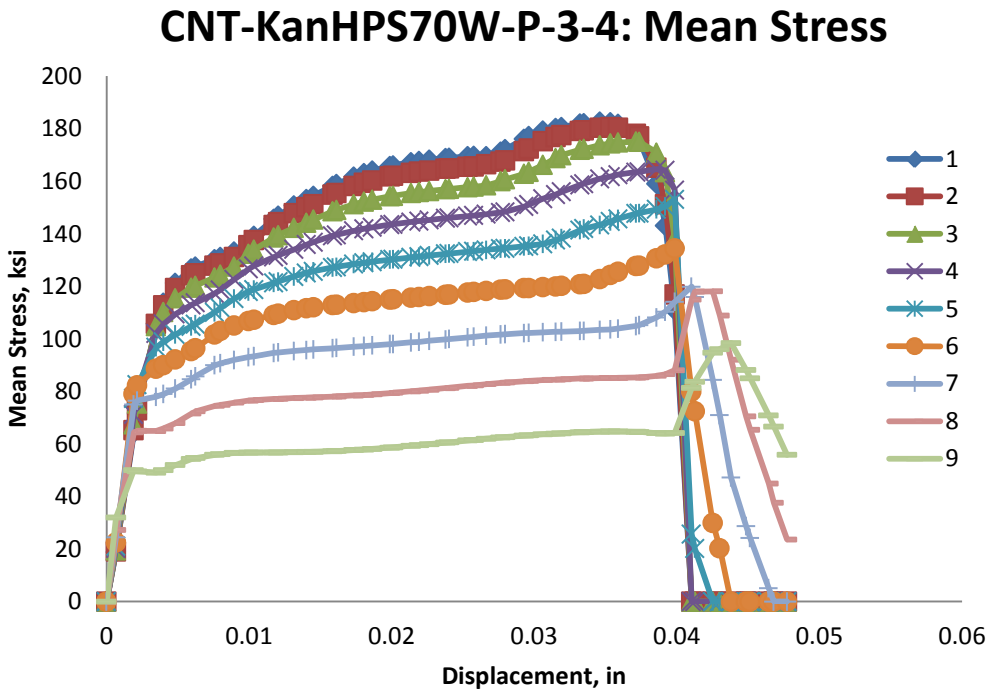

Figure B. 55: Variation of mean stress versus displacement for different elements laid out through the thickness of simulation of CNT-KanHPS70W-P-3-4 specimens

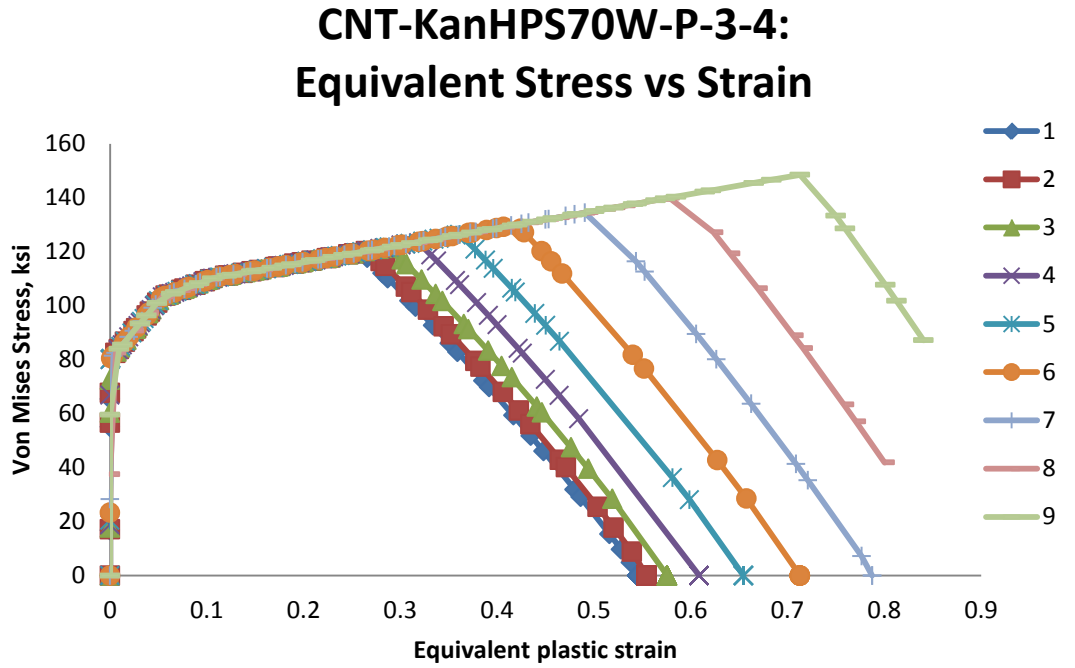

Figure B. 56: Variation of von Mises stress versus equivalent plastic strain for different elements laid out through the thickness of simulation of CNT-KanHPS70W-P-3-4 specimens

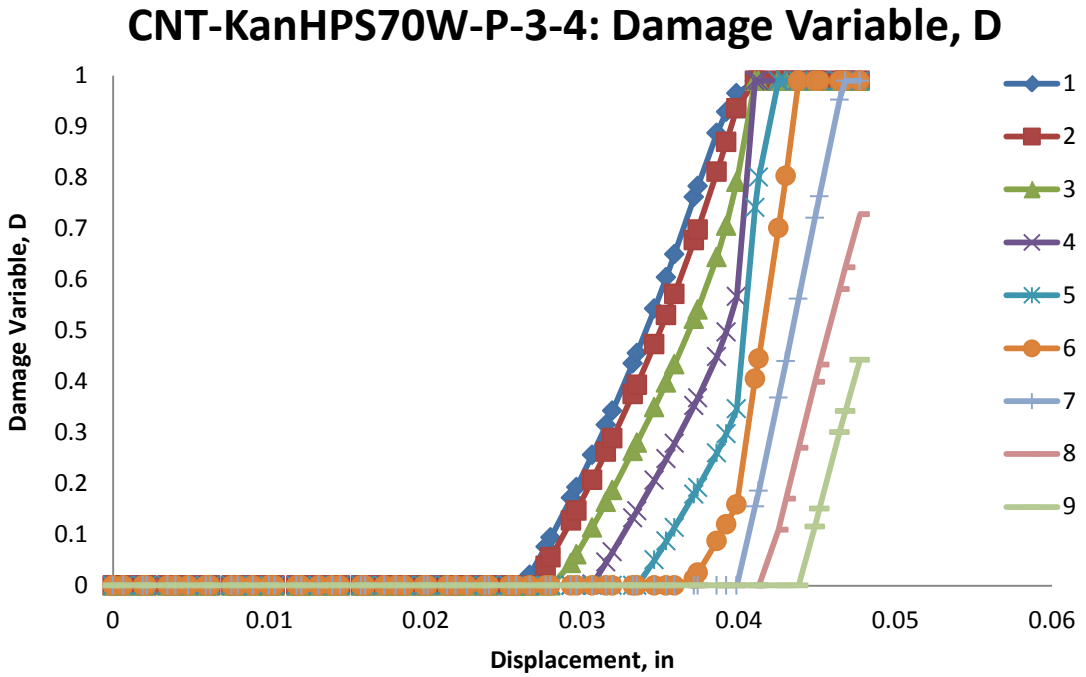

Figure B. 57: Variation of damage variable with displacement for different elements laid out through the thickness of simulation of CNT-KanHPS70W-P-3-4 specimens

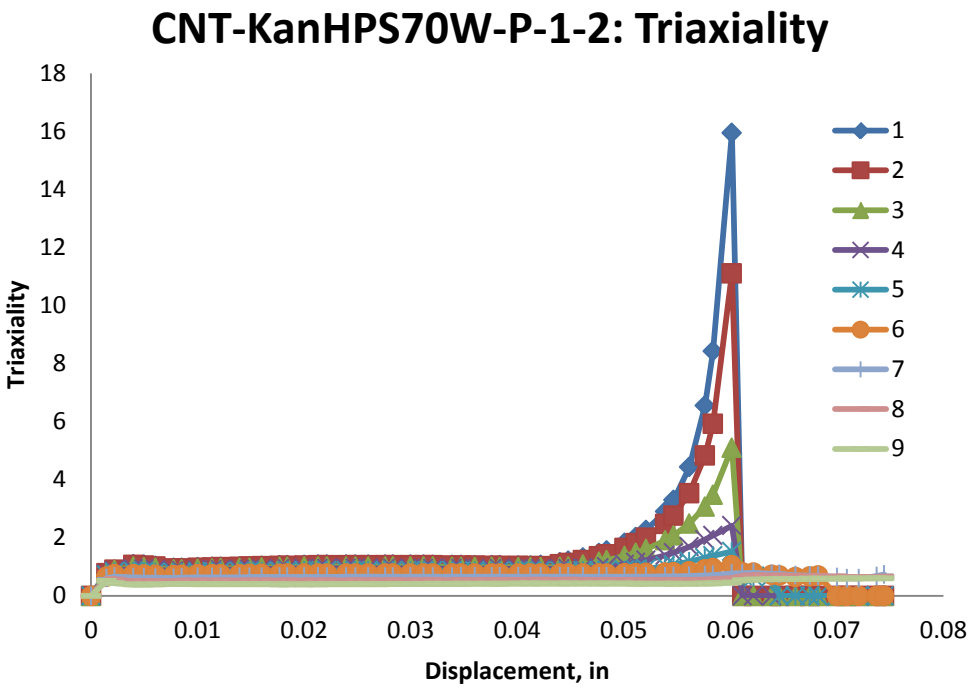

Figure B. 58: Variation of triaxiality with displacement for different elements laid out through the thickness of simulation of CNT-KanHPS70W-P-1-2 specimens

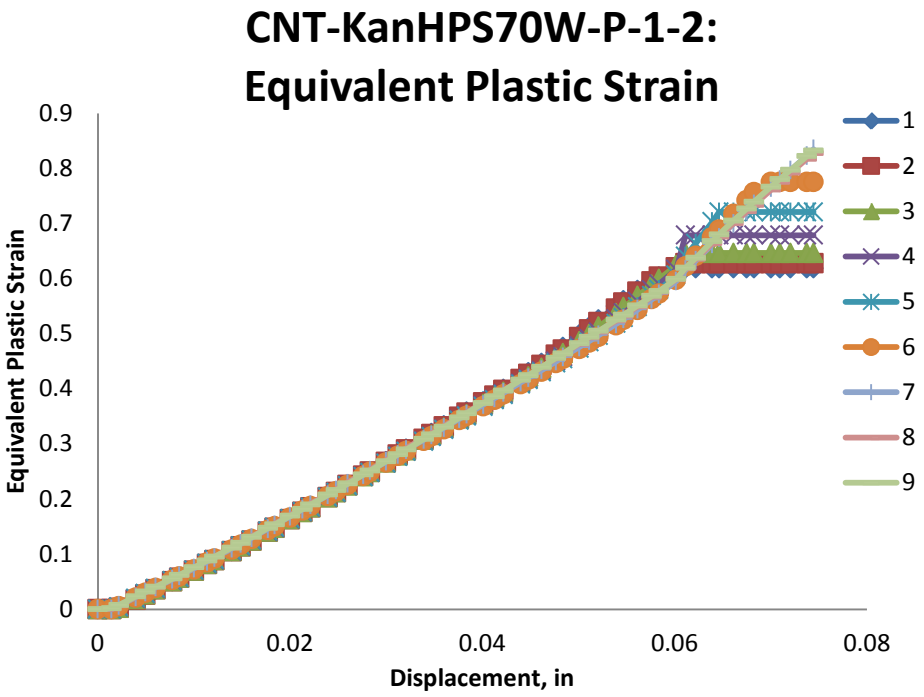

Figure B. 59: Variation of equivalent plastic strain with displacement for different elements laid out through the thickness of simulation of CNT-KanHPS70W-P-1-2 specimens

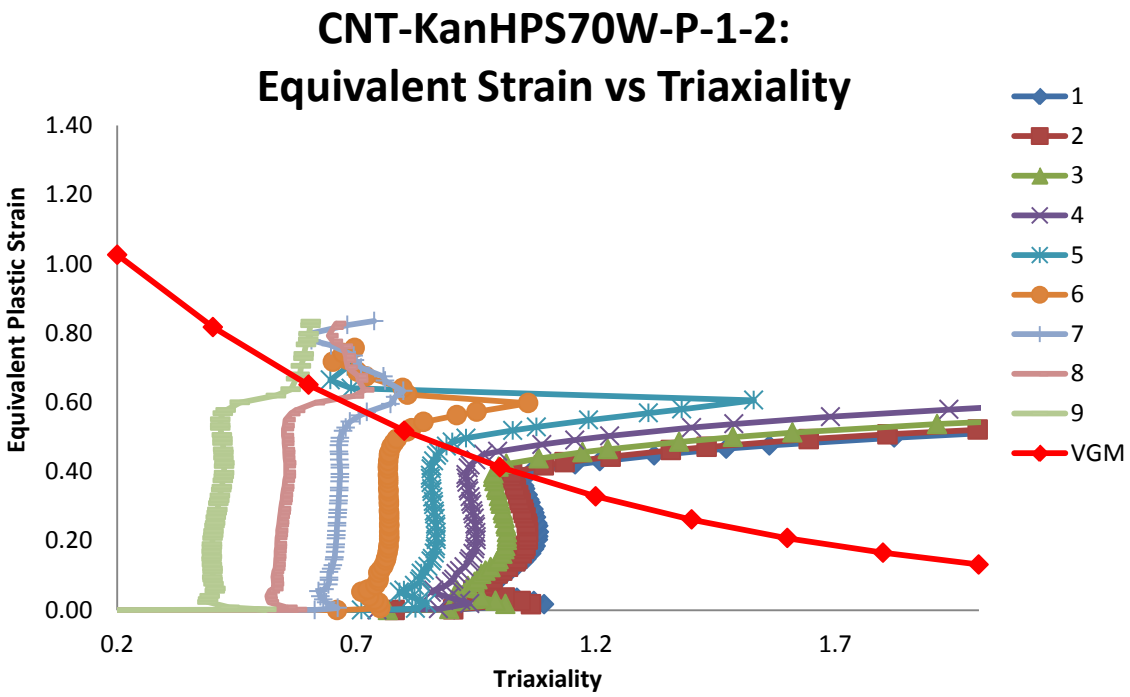

Figure B. 60: Variation of equivalent plastic strain versus triaxiality for different elements laid out through the thickness of simulation of CNT-KanHPS70W-P-1-2 specimens

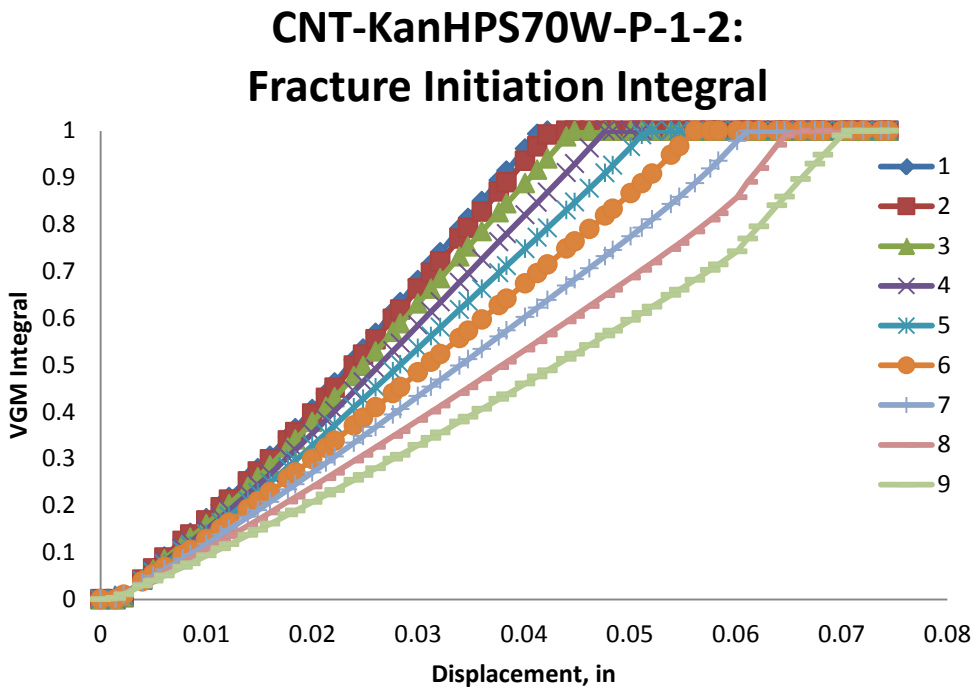

Figure B. 61: Value of fracture initiation integral for different elements laid out through the thickness of simulation of CNT-KanHPS70W-P-1-2 specimens

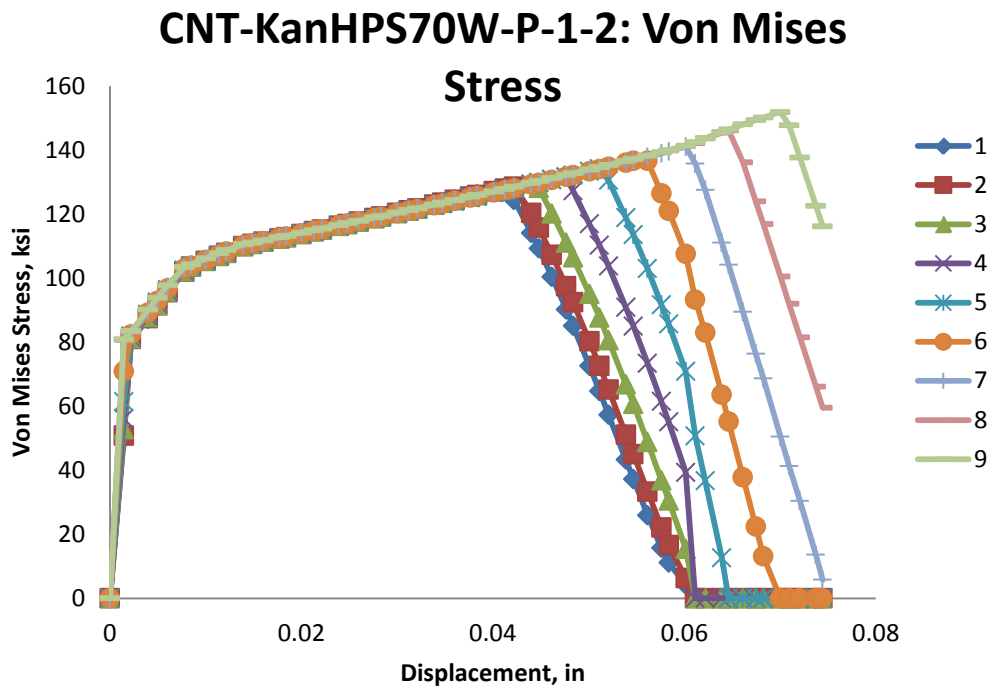

Figure B. 62: Variation of von Mises stress versus displacement for different elements laid out through the thickness of simulation of CNT-KanHPS70W-P-1-2 specimens

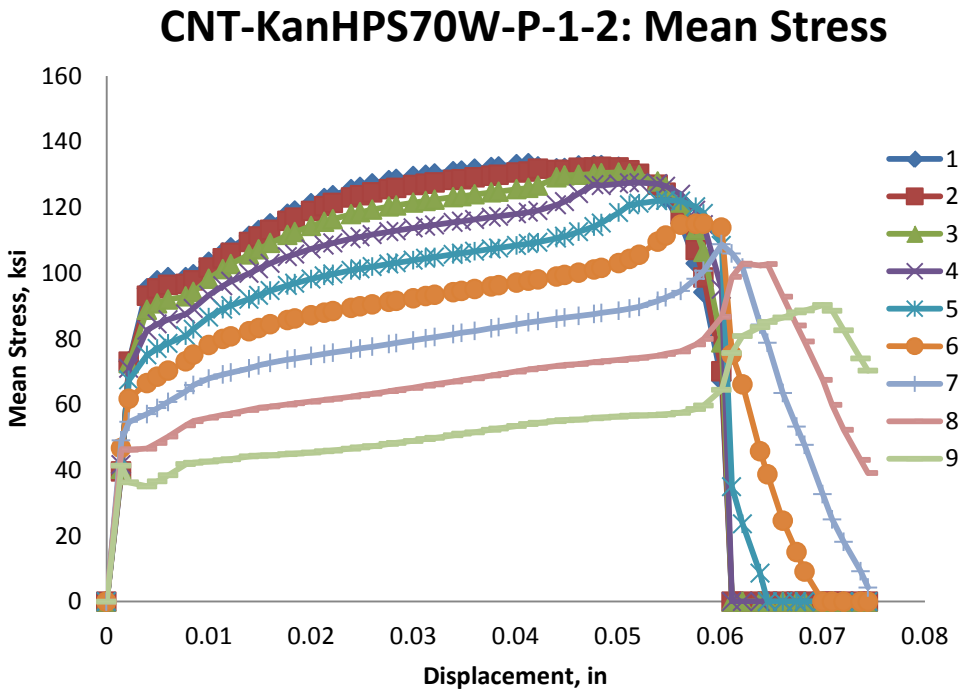

Figure B. 63: Variation of mean stress versus displacement for different elements laid out through the thickness of simulation of CNT-KanHPS70W-P-1-2 specimens

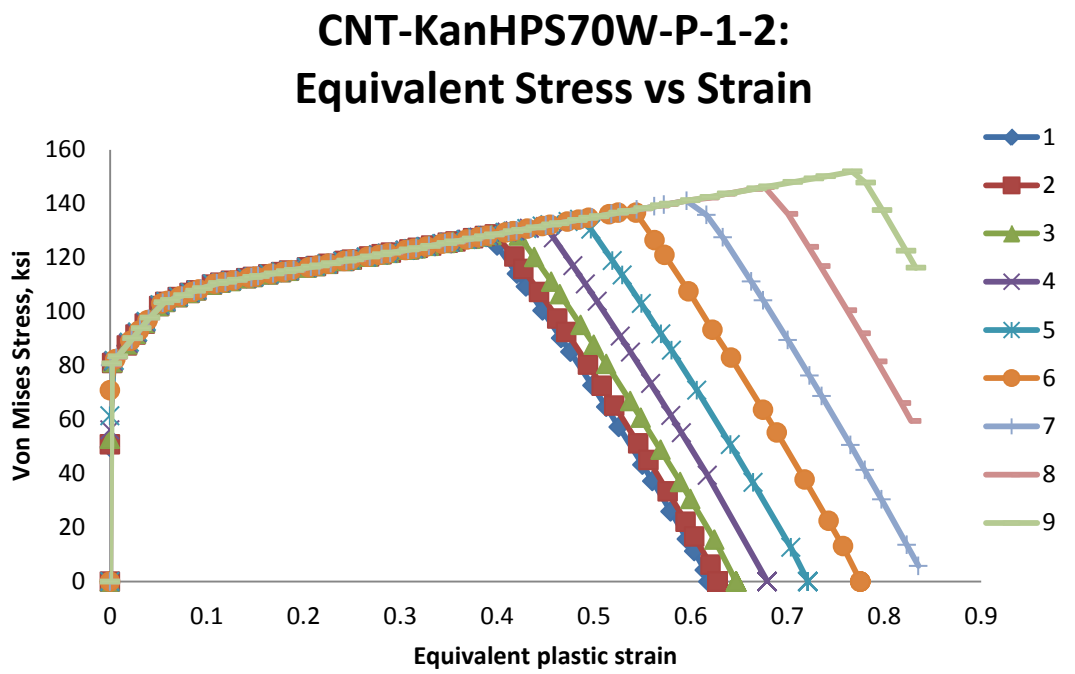

Figure B. 64: Variation of von Mises stress versus equivalent plastic strain for different elements laid out through the thickness of simulation of CNT-KanHPS70W-P-1-2 specimens

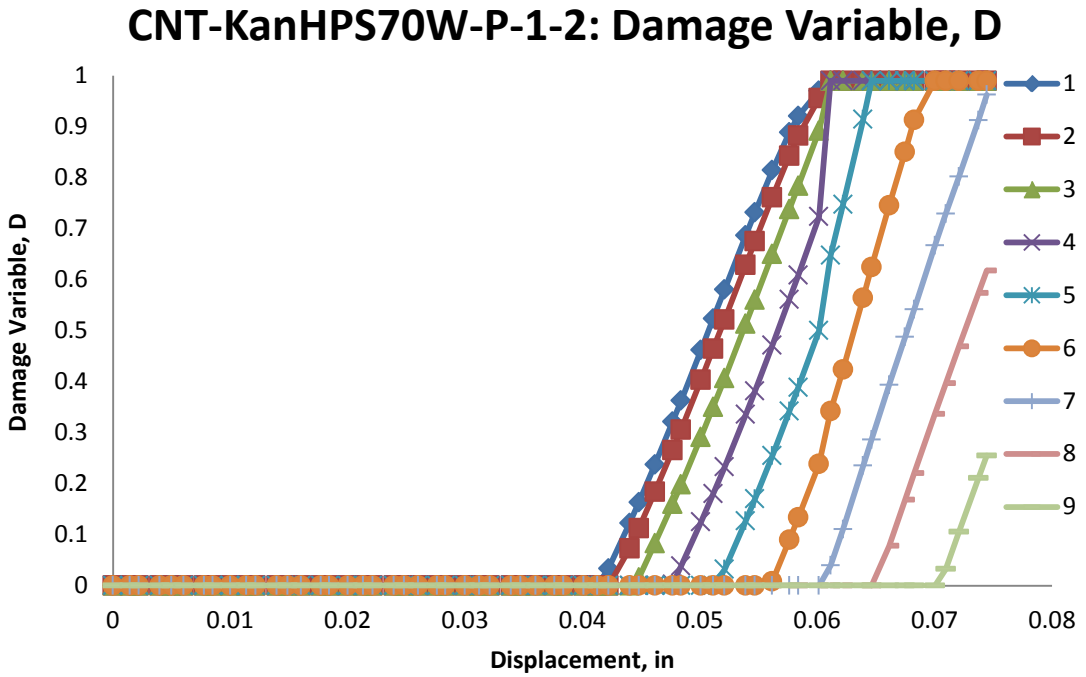

Figure B. 65: Variation of damage variable with displacement for different elements laid out through the thickness of simulation of CNT-KanHPS70W-P-1-2 specimens

B.6 CNT-KanA514-P-A

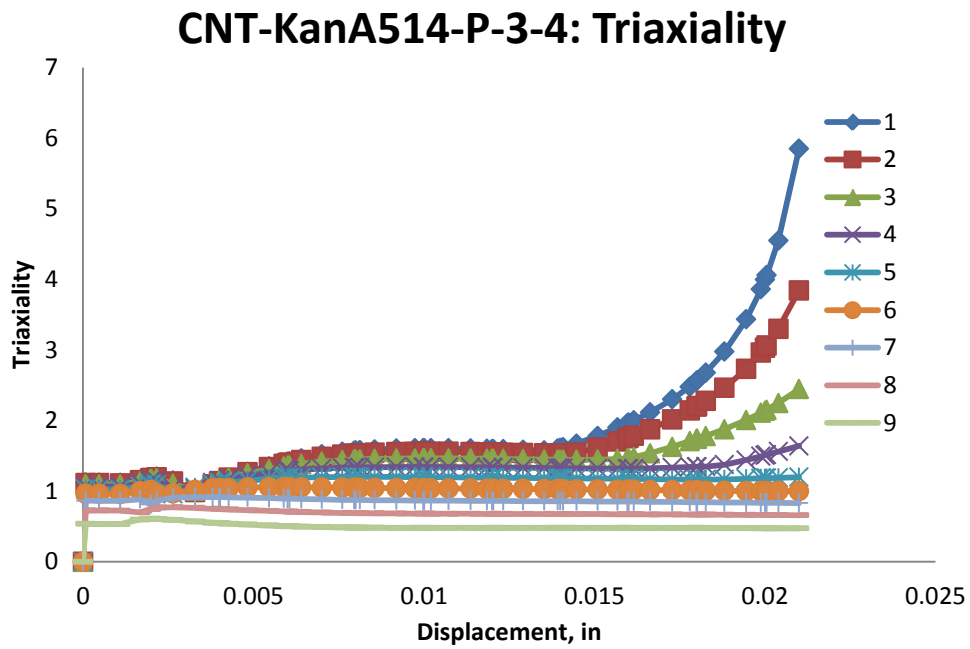

Figure B. 66: Variation of triaxiality with displacement for different elements laid out through the thickness of simulation of CNT-KanA514-P-3-4 specimens

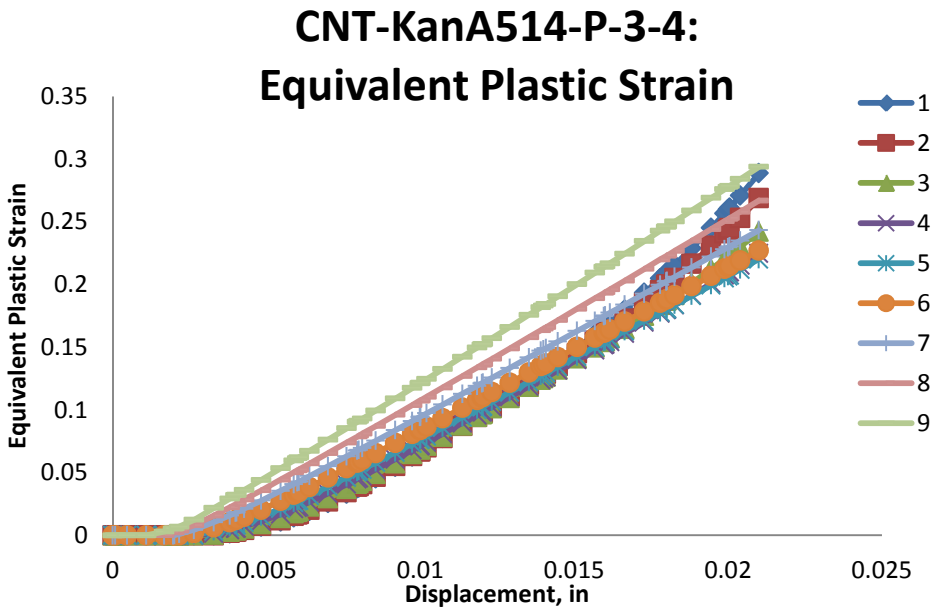

Figure B. 67: Variation of equivalent plastic strain with displacement for different elements laid out through the thickness of simulation of CNT-KanA514-P-3-4 specimens

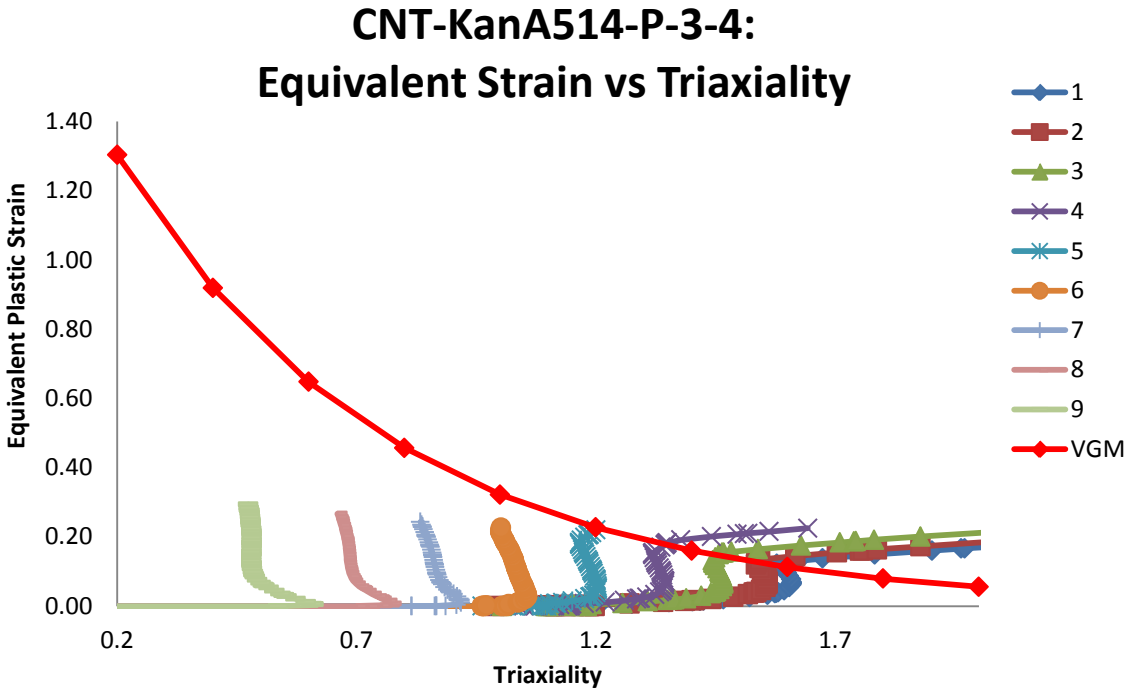

Figure B. 68: Variation of equivalent plastic strain versus triaxiality for different elements laid out through the thickness of simulation of CNT-KanA514-P-3-4 specimens

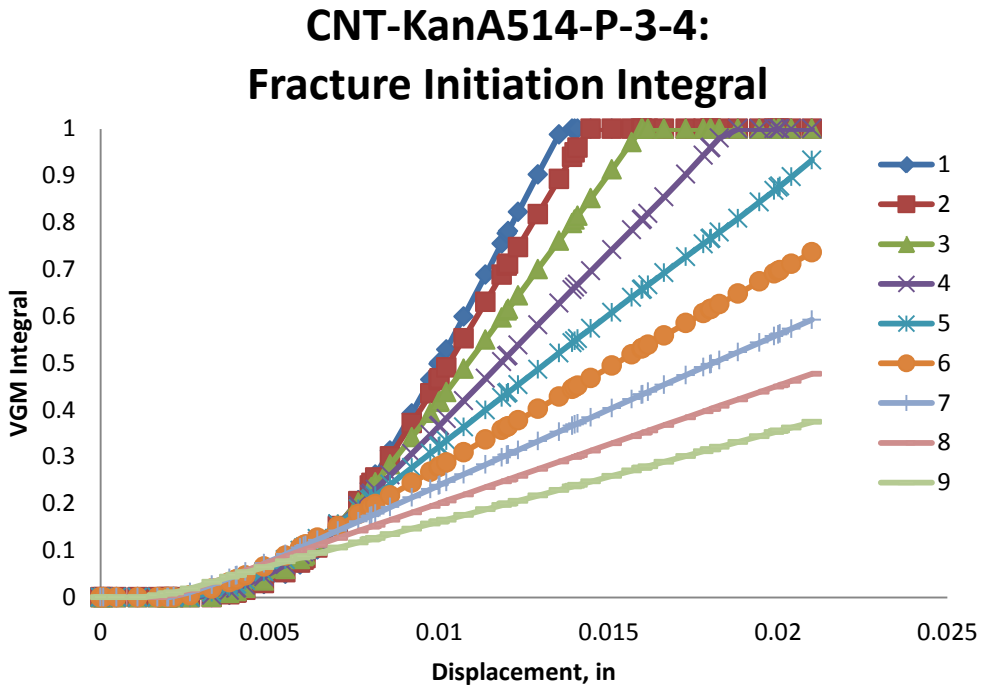

Figure B. 69: Value of fracture initiation integral for different elements laid out through the thickness of simulation of CNT-KanA514-P-3-4 specimens

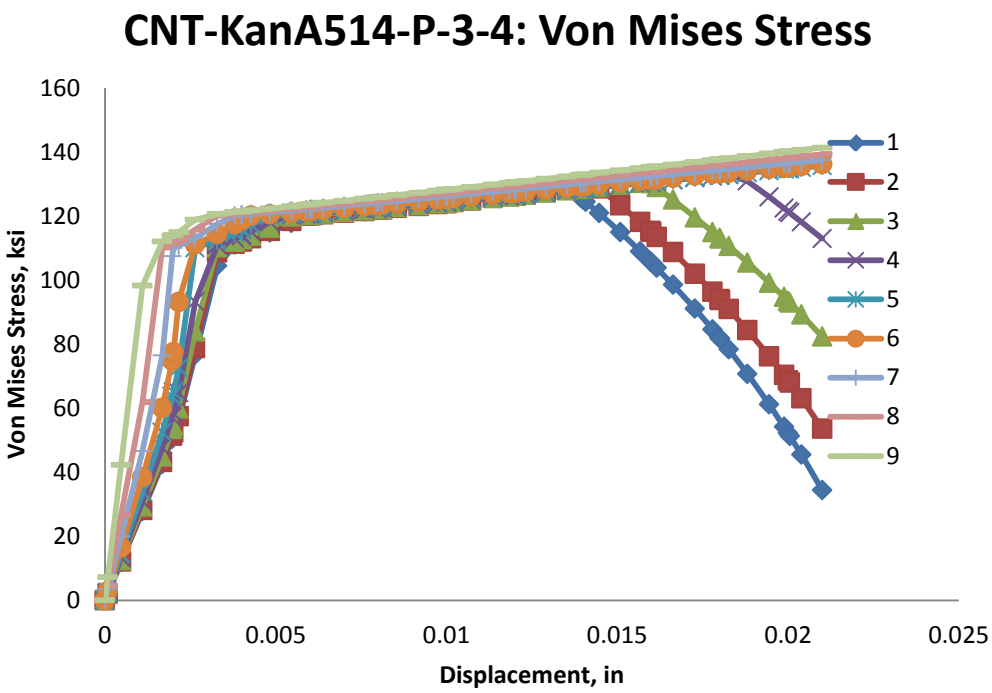

Figure B. 70: Variation of von Mises stress versus displacement for different elements laid out through the thickness of simulation of CNT-KanA514-P-3-4 specimens

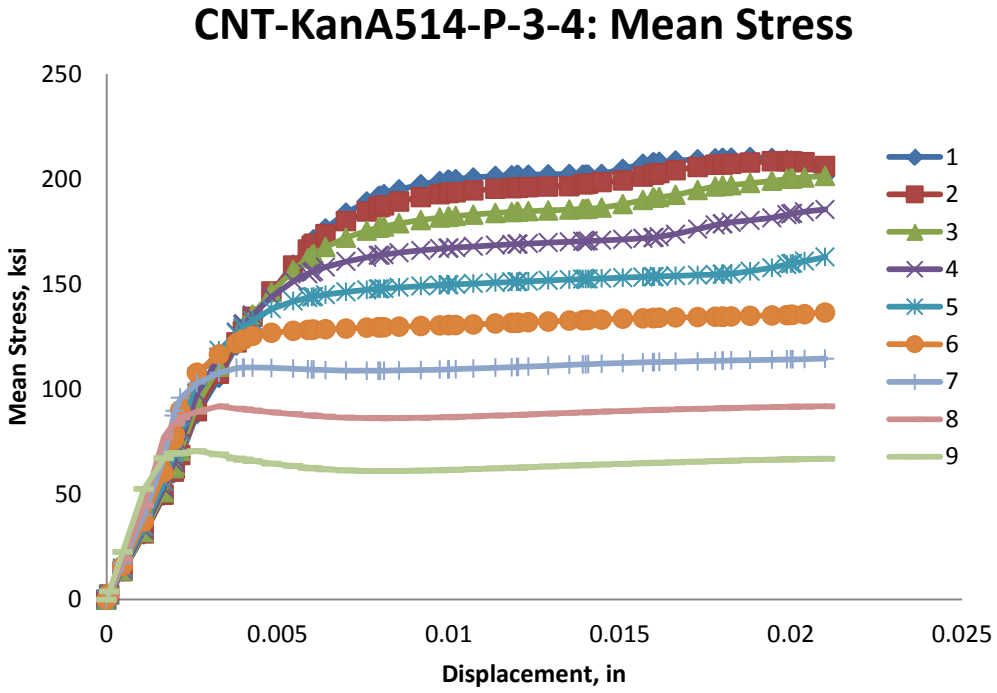

Figure B. 71: Variation of mean stress versus displacement for different elements laid out through the thickness of simulation of CNT-KanA514-P-3-4 specimens

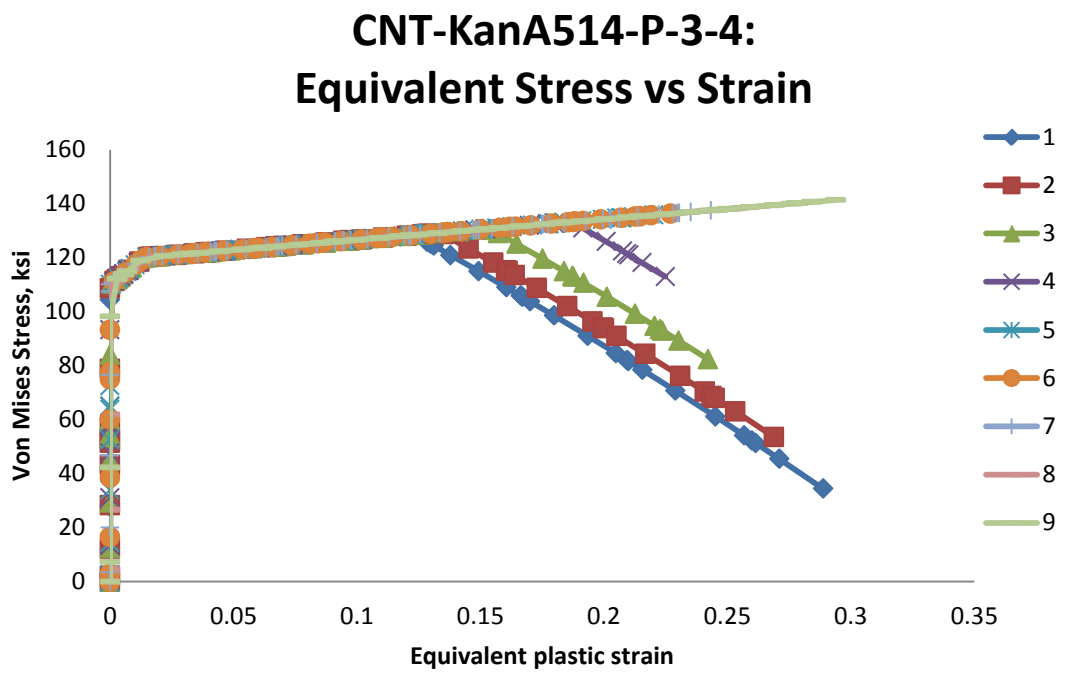

Figure B. 72: Variation of von Mises stress versus equivalent plastic strain for different elements laid out through the thickness of simulation of CNT-KanA514-P-3-4 specimens

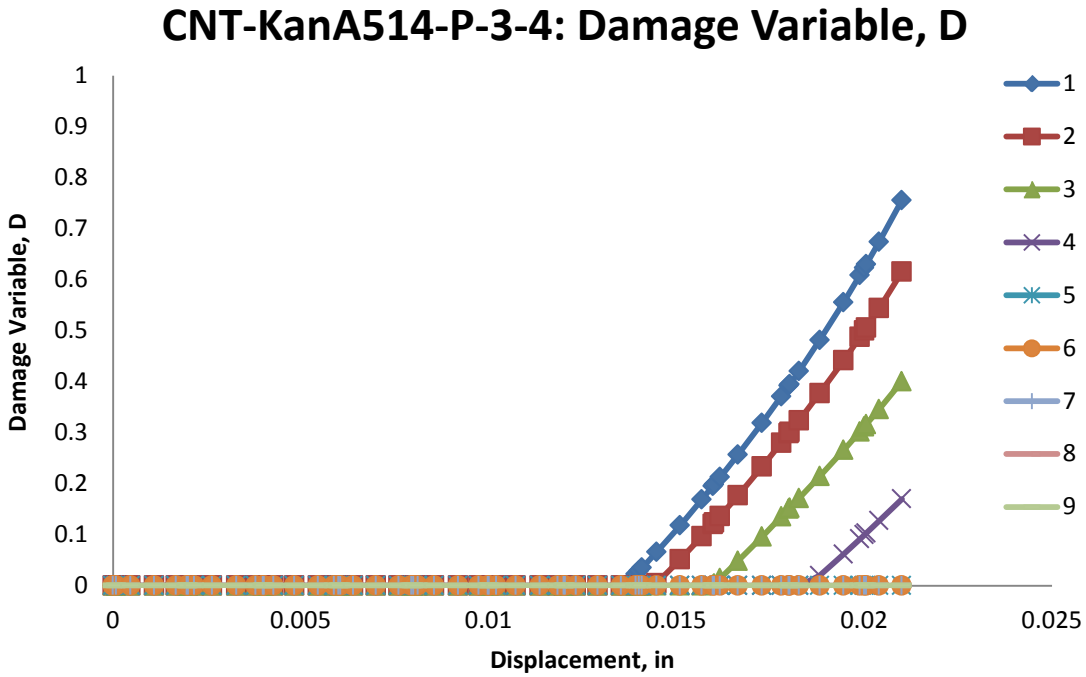

Figure B. 73: Variation of damage variable with displacement for different elements laid out through the thickness of simulation of CNT-KanA514-P-3-4 specimens

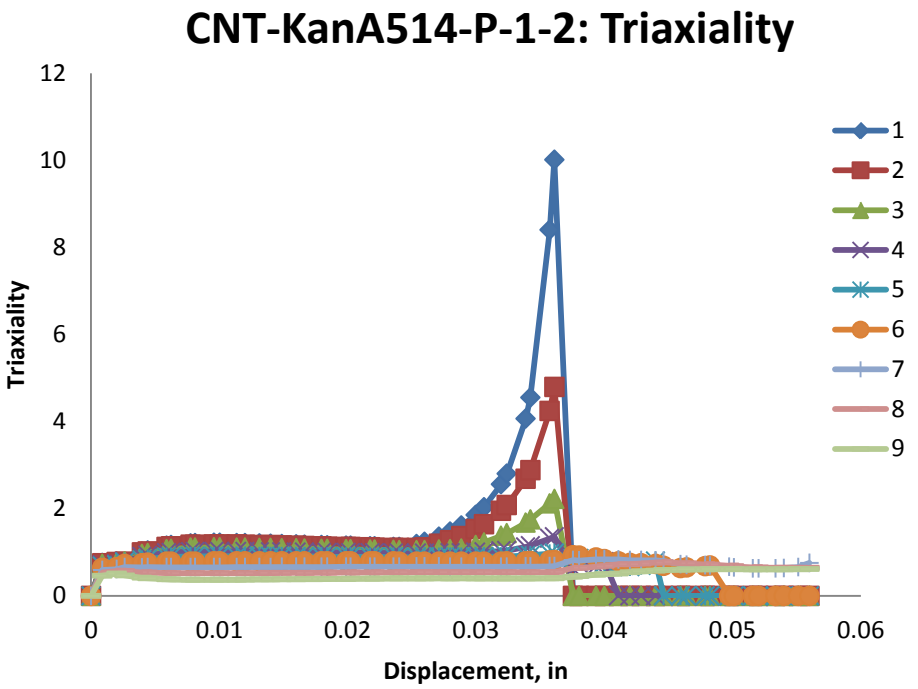

Figure B. 74: Variation of triaxiality with displacement for different elements laid out through the thickness of simulation of CNT-KanA514-P-1-2 specimens

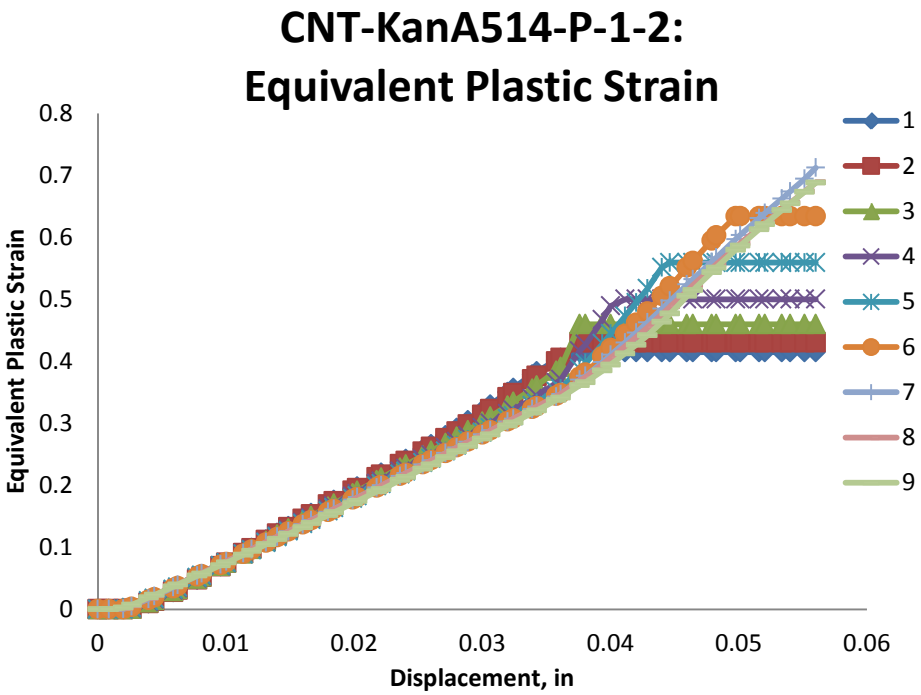

Figure B. 75: Variation of equivalent plastic strain with displacement for different elements laid out through the thickness of simulation of CNT-KanA514-P-1-2 specimens

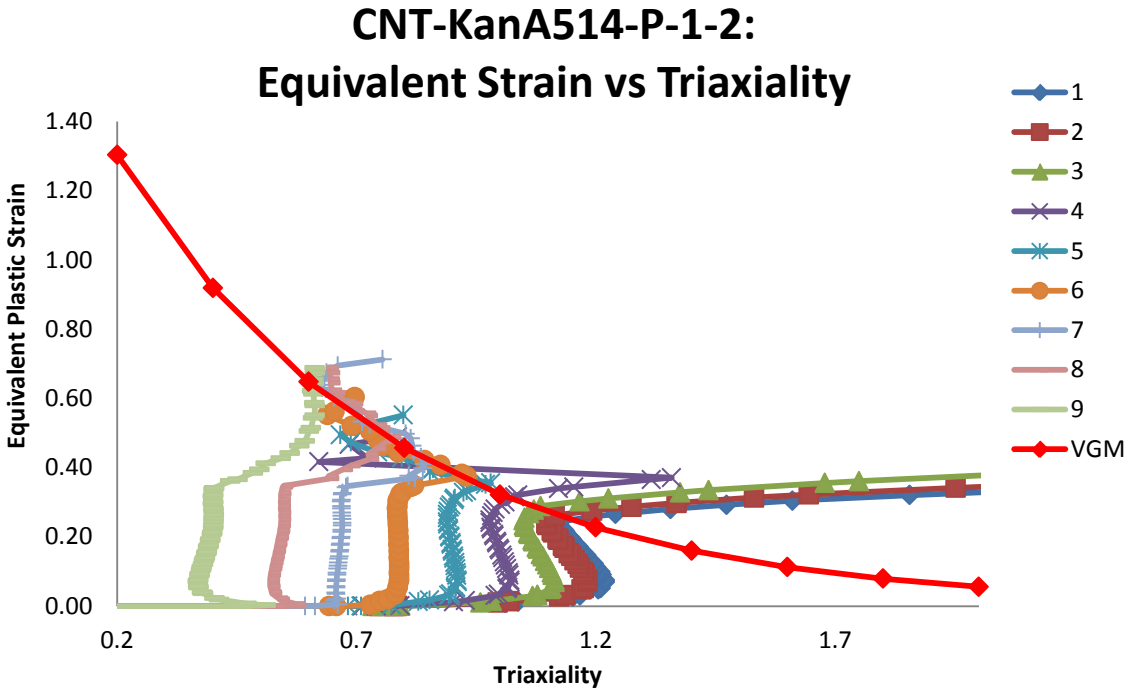

Figure B. 76: Variation of equivalent plastic strain versus triaxiality for different elements laid out through the thickness of simulation of CNT-KanA514-P-1-2 specimens

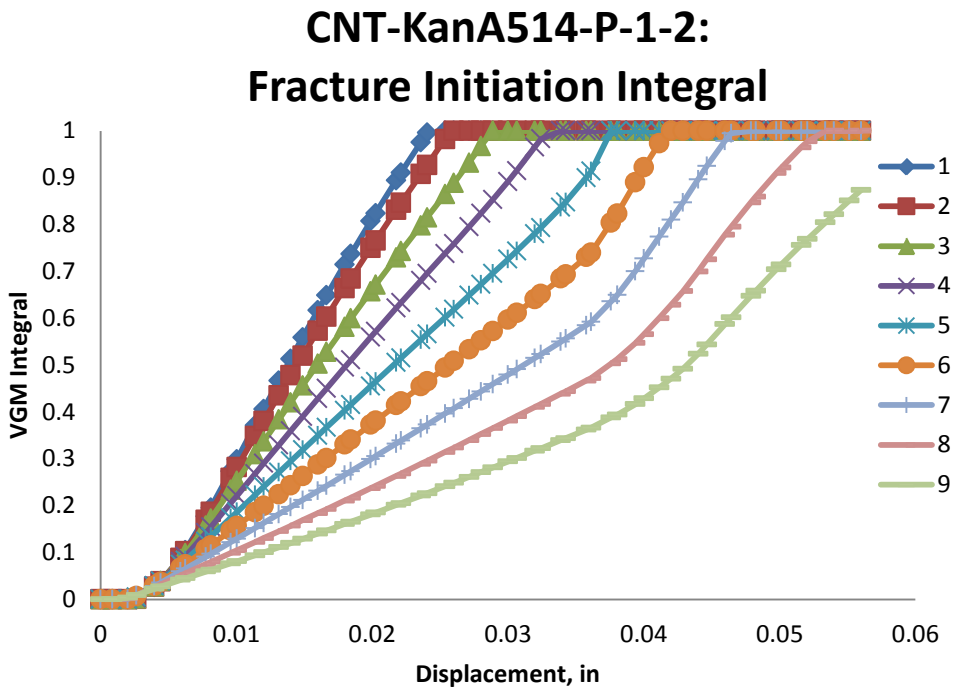

Figure B. 77: Value of fracture initiation integral for different elements laid out through the thickness of simulation of CNT-KanA514-P-1-2 specimens

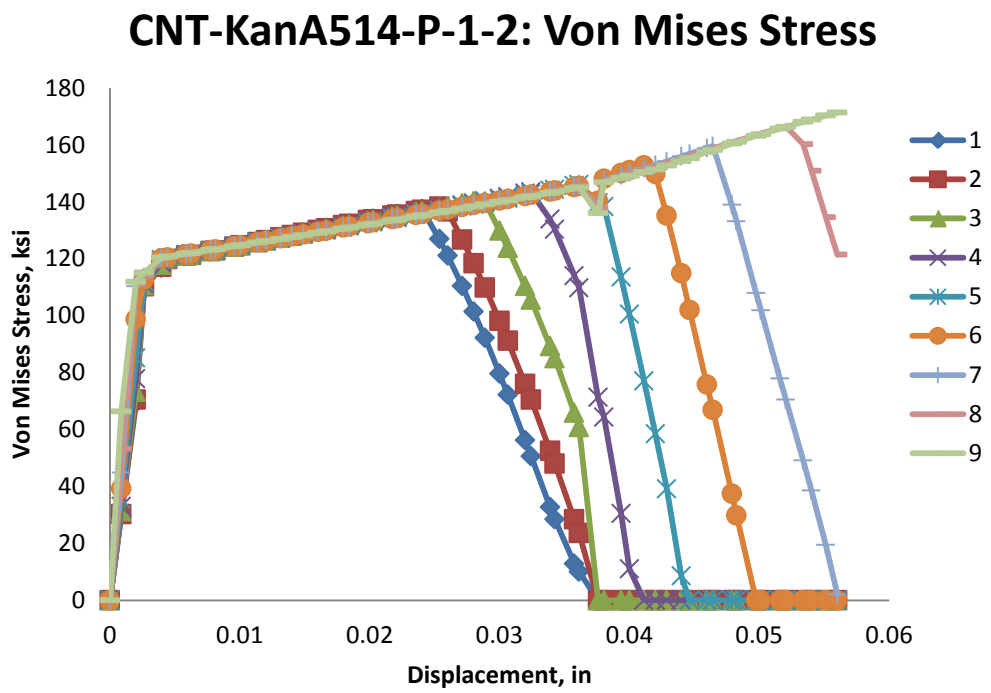

Figure B. 78: Variation of von Mises stress versus displacement for different elements laid out through the thickness of simulation of CNT-KanA514-P-1-2 specimens

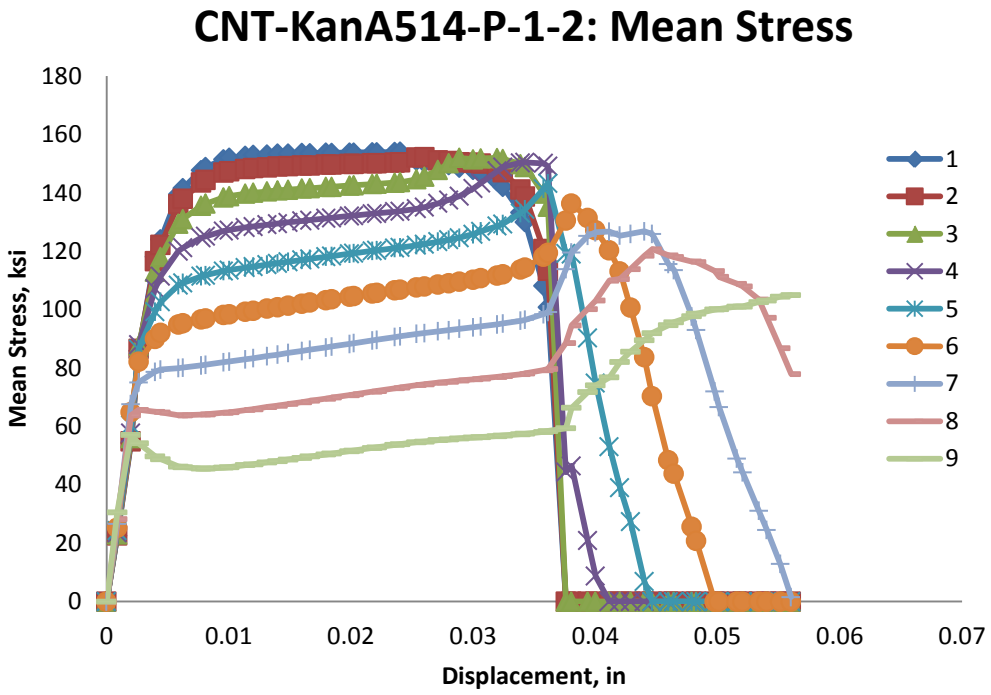

Figure B. 79: Variation of mean stress versus displacement for different elements laid out through the thickness of simulation of CNT-KanA514-P-1-2 specimens

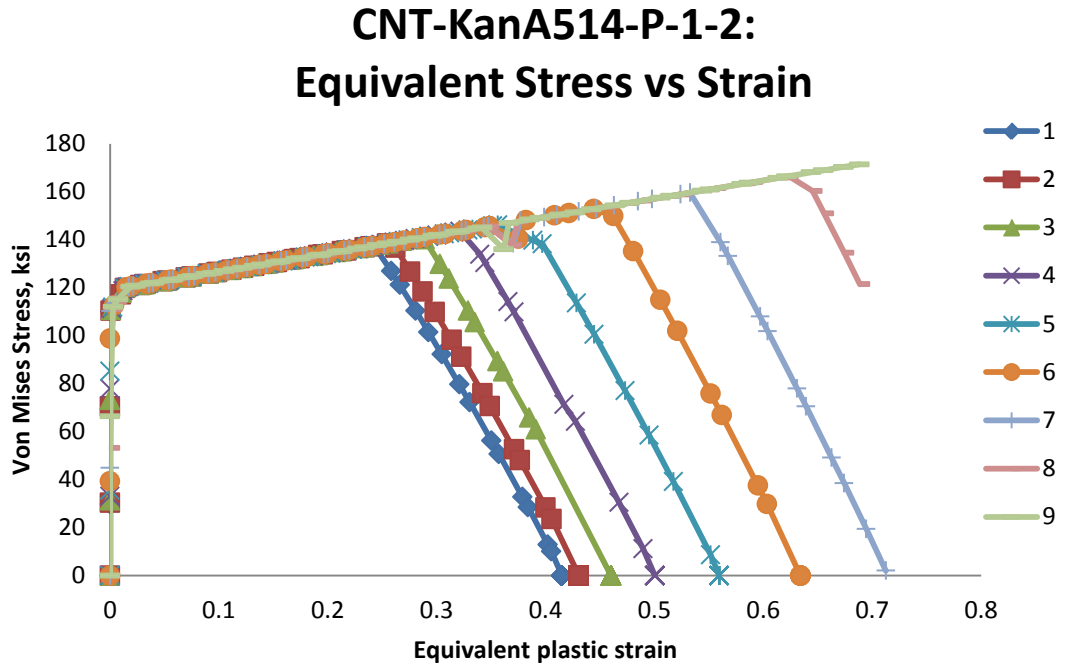

Figure B. 80: Variation of von Mises stress versus equivalent plastic strain for different elements laid out through the thickness of simulation of CNT-KanA514-P-1-2 specimens

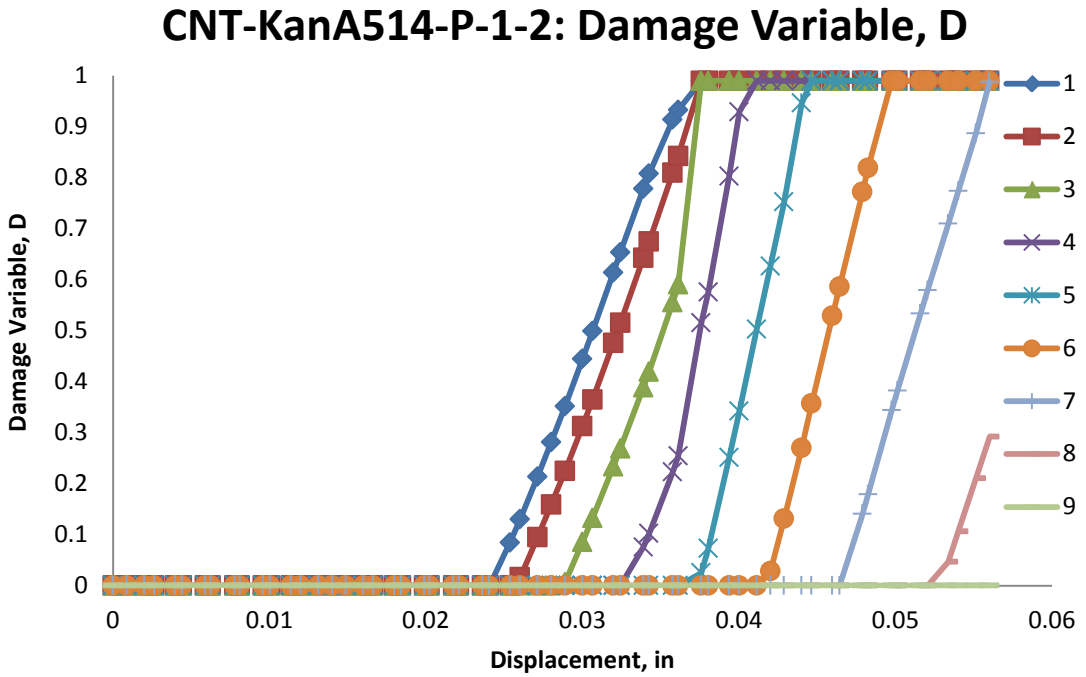

Figure B. 81: Variation of damage variable with displacement for different elements laid out through the thickness of simulation of CNT-KanA514-P-1-2 specimens

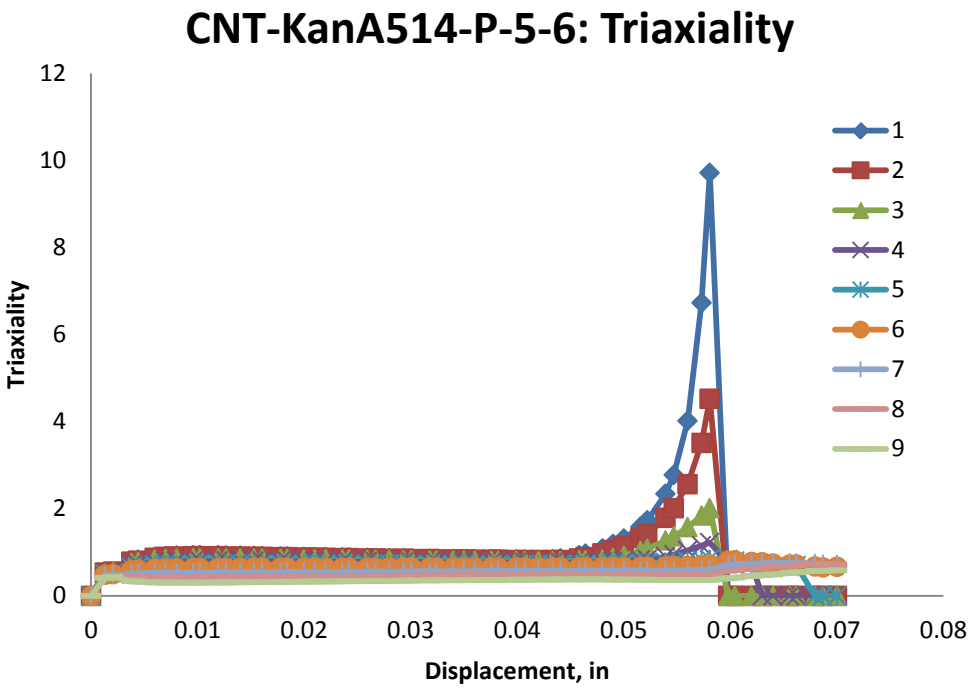

Figure B. 82: Variation of triaxiality with displacement for different elements laid out through the thickness of simulation of CNT-KanA514-P-5-6 specimens

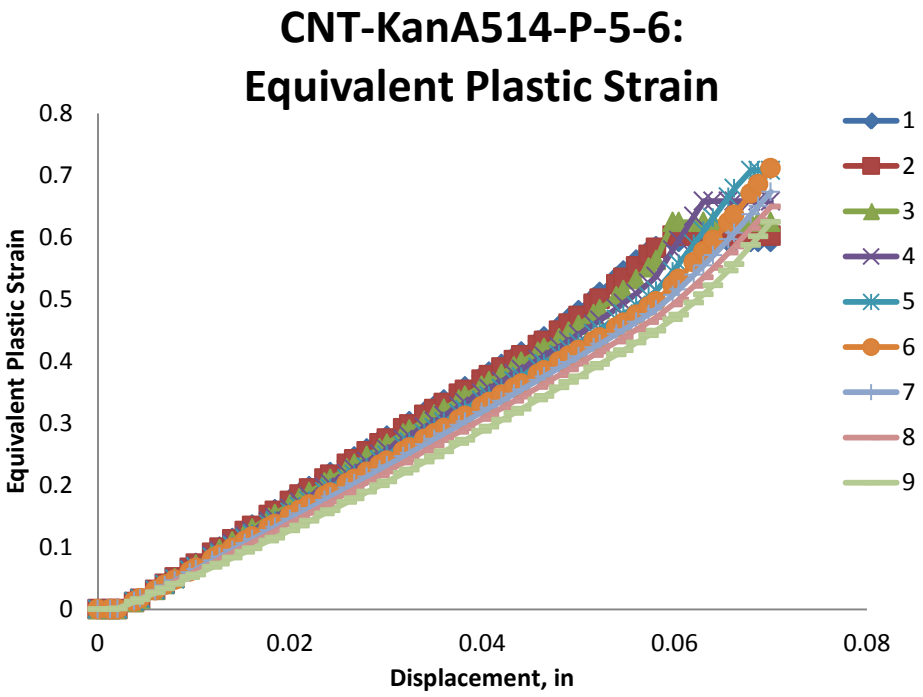

Figure B. 83: Variation of equivalent plastic strain with displacement for different elements laid out through the thickness of simulation of CNT-KanA514-P-5-6 specimens

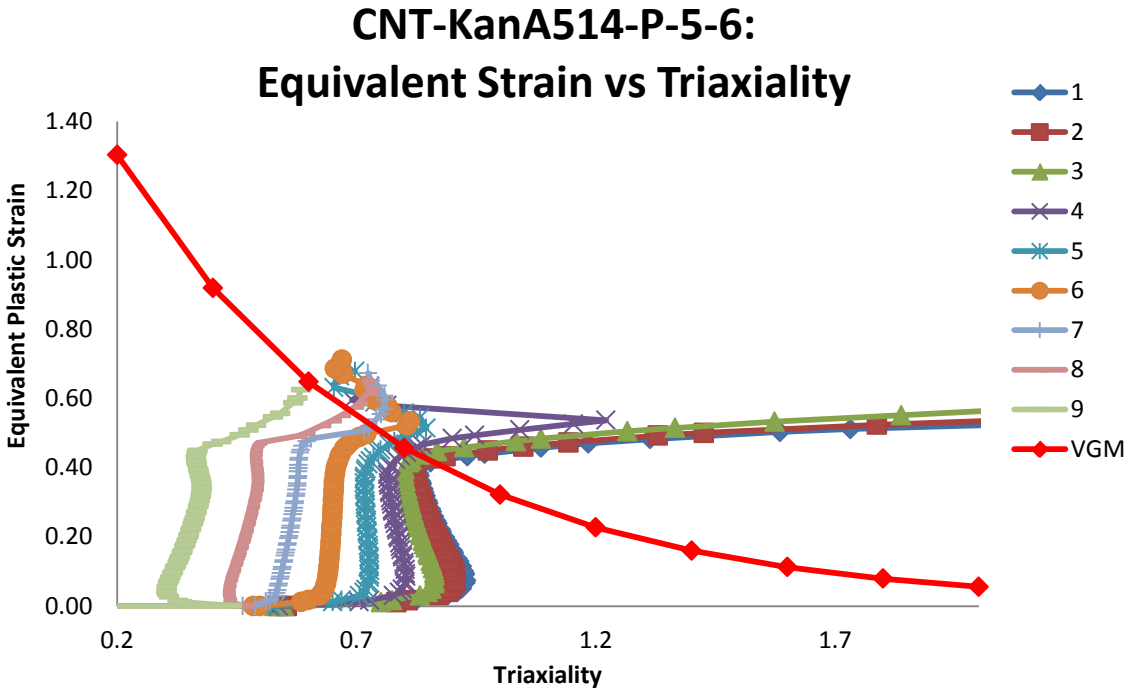

Figure B. 84: Variation of equivalent plastic strain versus triaxiality for different elements laid out through the thickness of simulation of CNT-KanA514-P-5-6 specimens

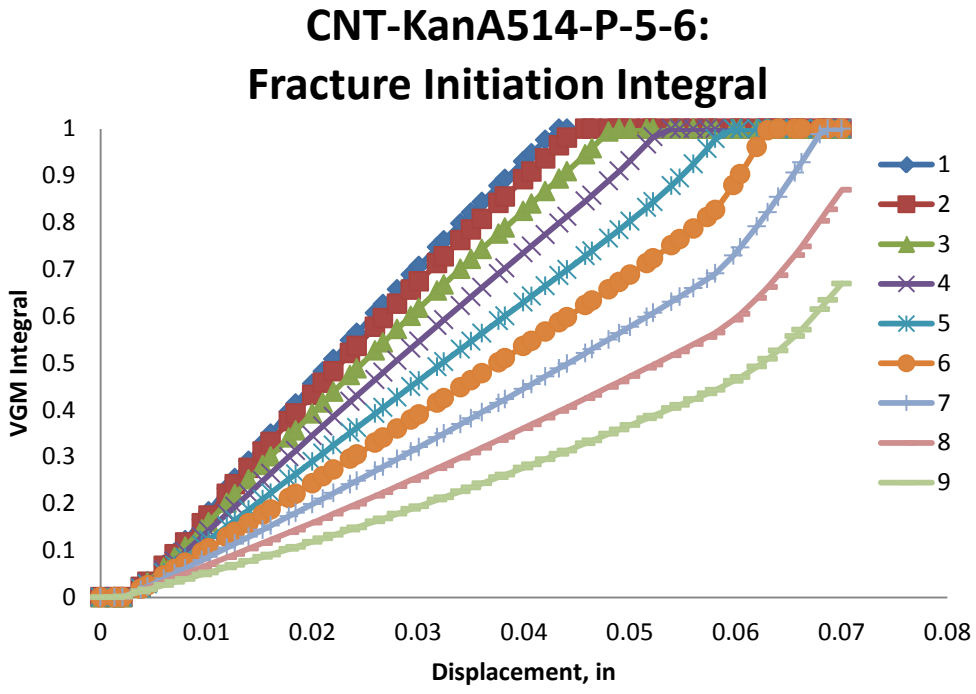

Figure B. 85: Value of fracture initiation integral for different elements laid out through the thickness of simulation of CNT-KanA514-P-5-6 specimens

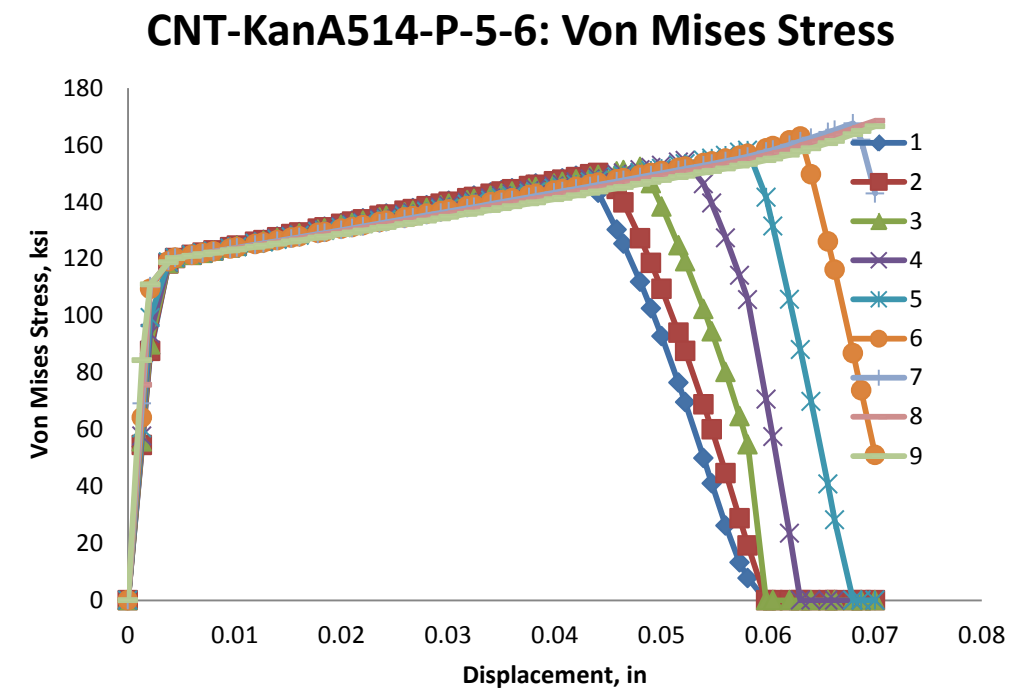

Figure B. 86: Variation of von Mises stress versus displacement for different elements laid out through the thickness of simulation of CNT-KanA514-P-5-6 specimens

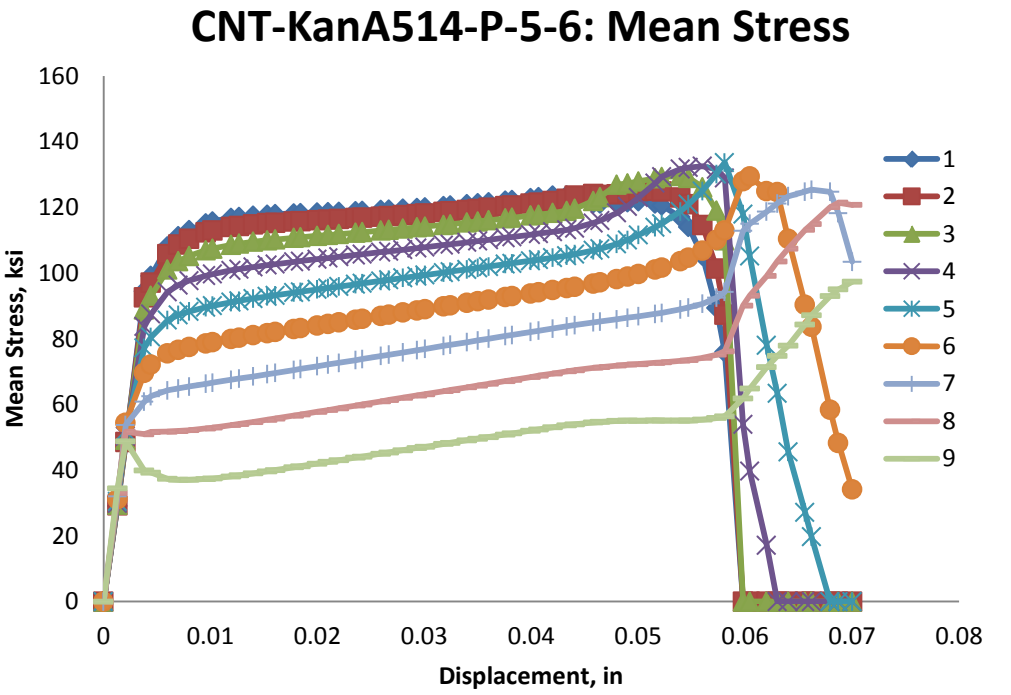

Figure B. 87: Variation of mean stress versus displacement for different elements laid out through the thickness of simulation of CNT-KanA514-P-5-6 specimens

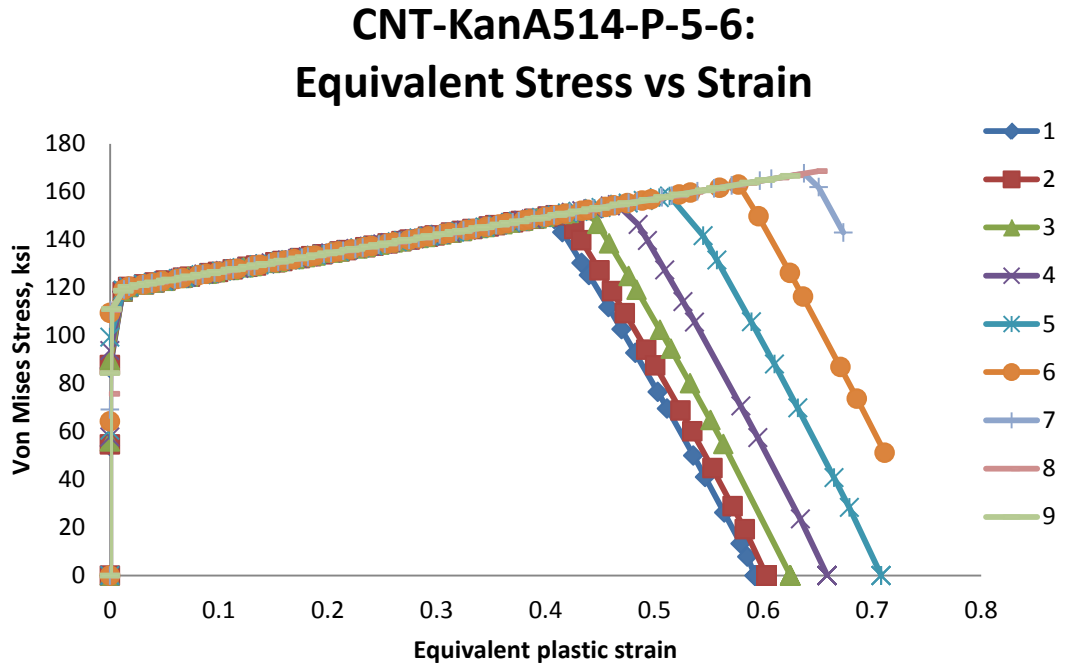

Figure B. 88: Variation of von Mises stress versus equivalent plastic strain for different elements laid out through the thickness of simulation of CNT-KanA514-P-5-6 specimens

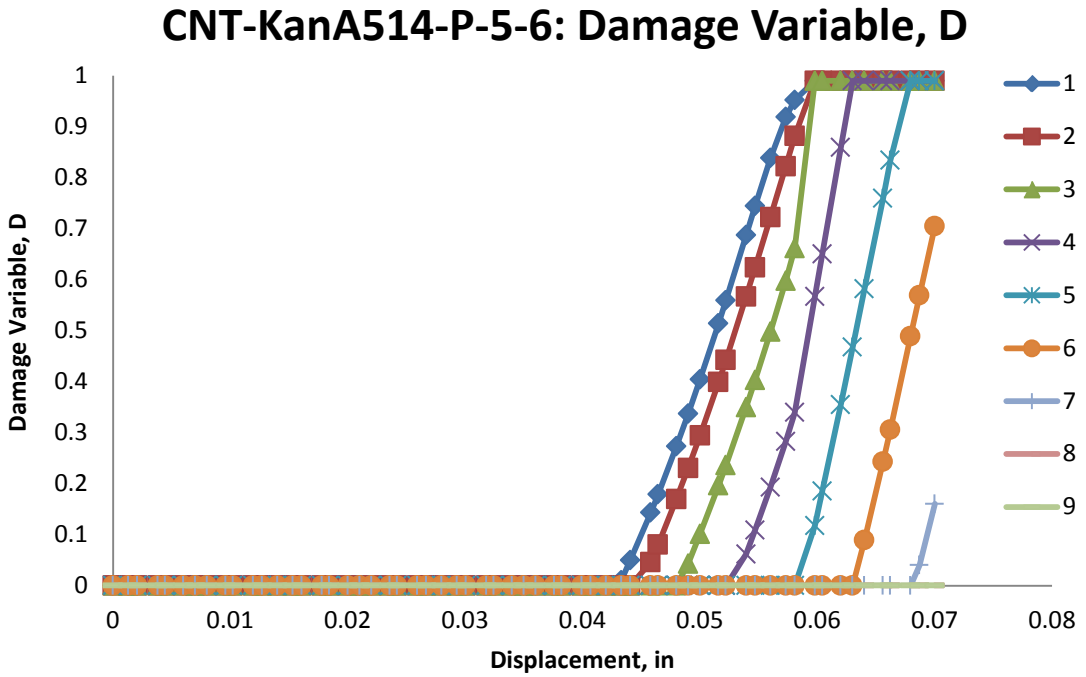

Figure B. 89: Variation of damage variable with displacement for different elements laid out through the thickness of simulation of CNT-KanA514-P-5-6 specimens

B.7 CNT-KanSN490B-P-A

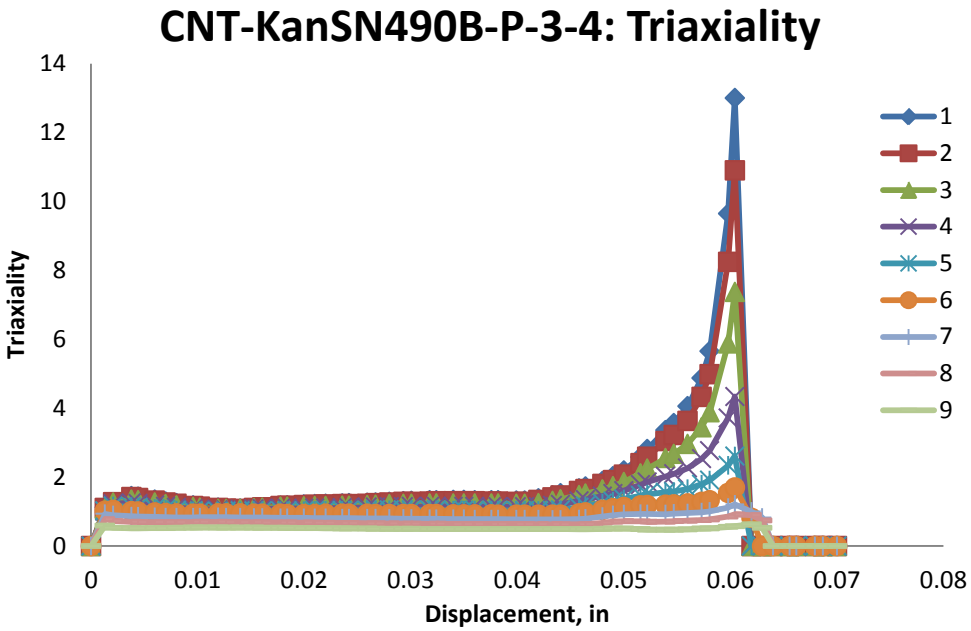

Figure B. 90: Variation of triaxiality with displacement for different elements laid out through the thickness of simulation of CNT-KanSN490B-P-3-4 specimens

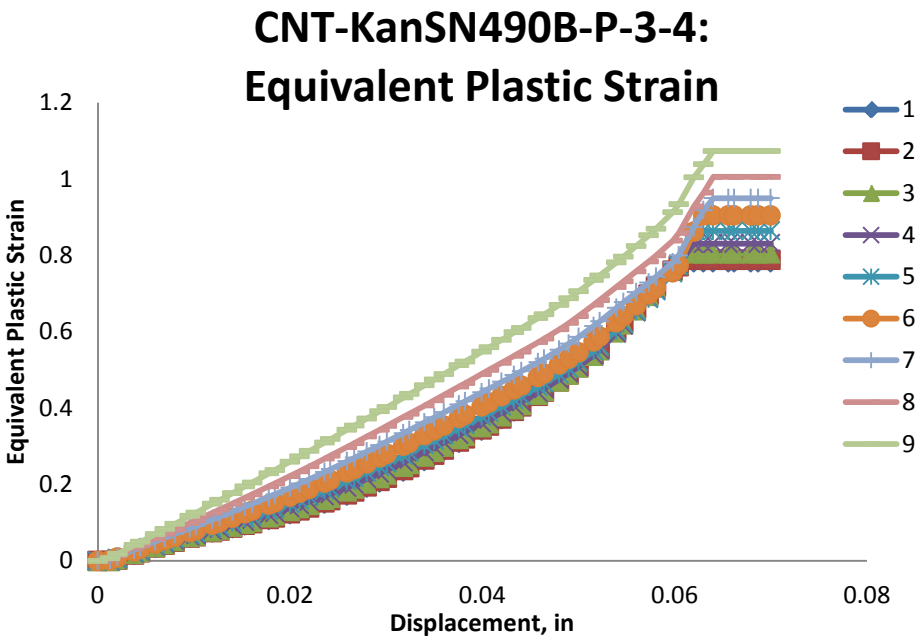

Figure B. 91: Variation of equivalent plastic strain with displacement for different elements laid out through the thickness of simulation of CNT-KanSN490B-P-3-4 specimens

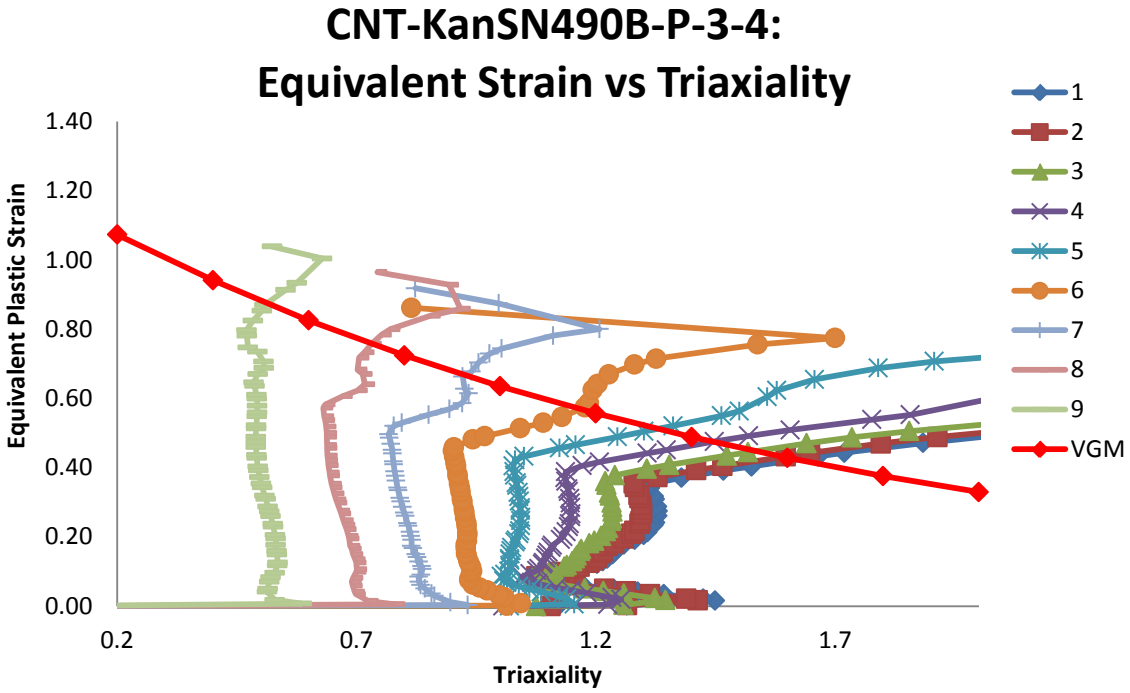

Figure B. 92: Variation of equivalent plastic strain versus triaxiality for different elements laid out through the thickness of simulation of CNT-KanSN490B-P-3-4 specimens

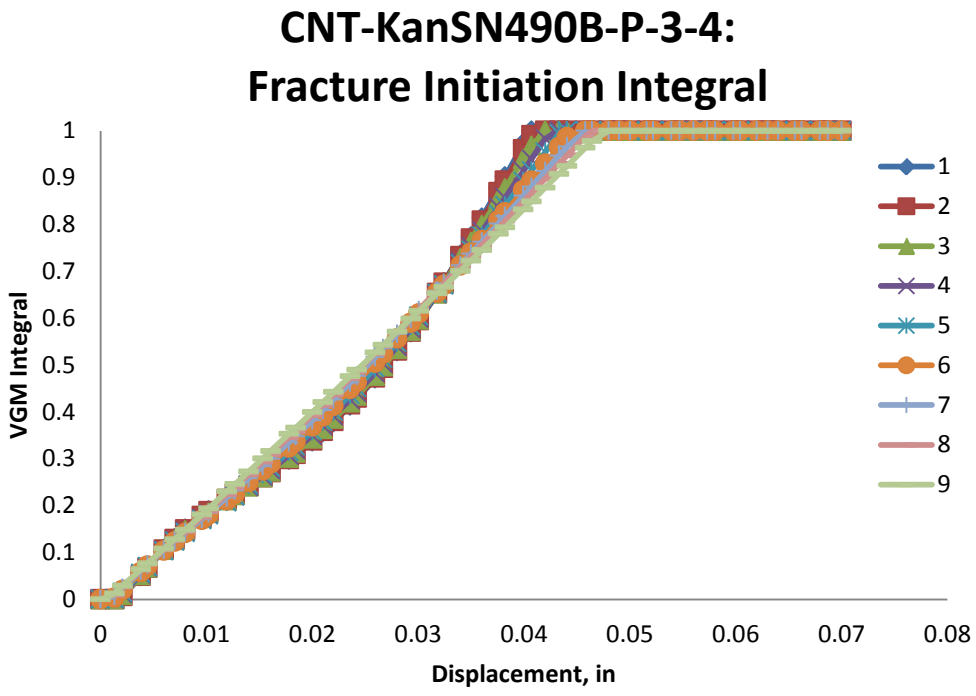

Figure B. 93: Value of fracture initiation integral for different elements laid out through the thickness of simulation of CNT-KanSN490B-P-3-4 specimens

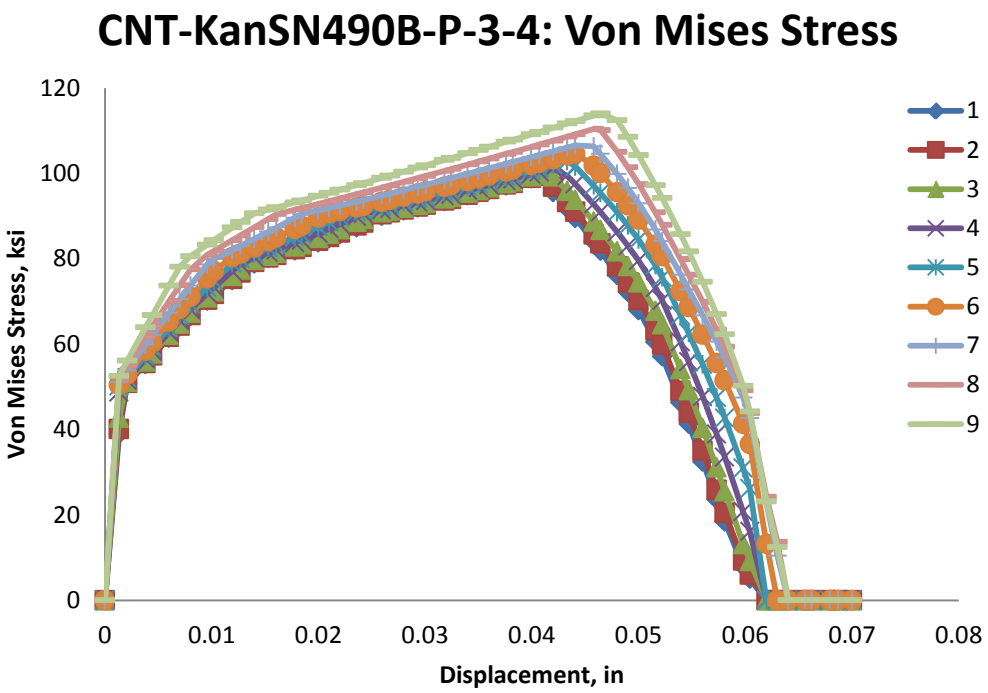

Figure B. 94: Variation of von Mises stress versus displacement for different elements laid out through the thickness of simulation of CNT-KanSN490B-P-3-4 specimens

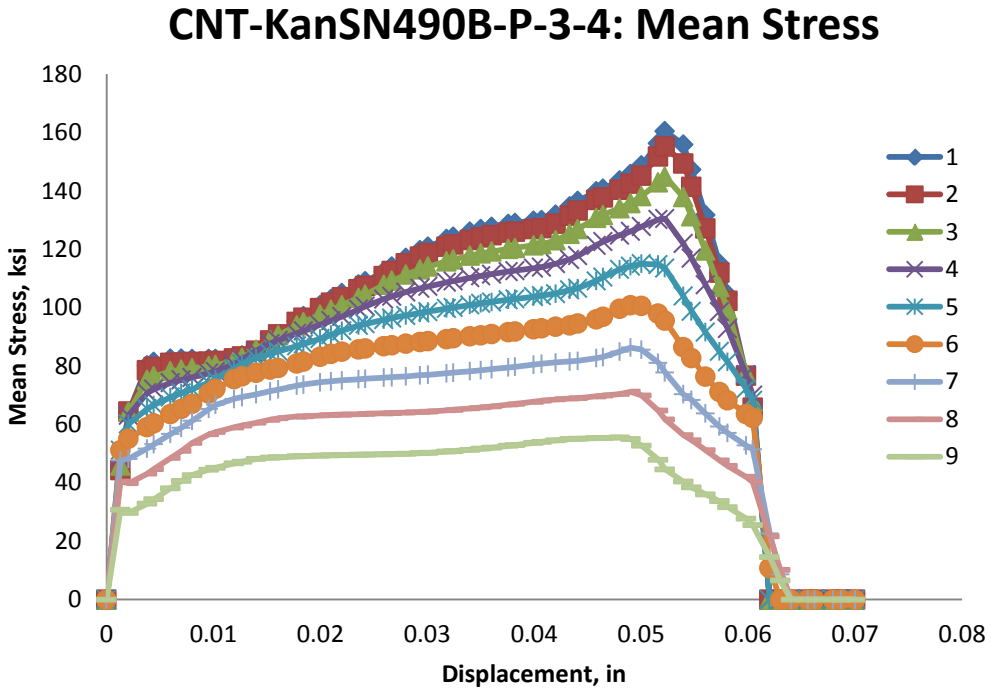

Figure B. 95: Variation of mean stress versus displacement for different elements laid out through the thickness of simulation of CNT-KanSN490B-P-3-4 specimens

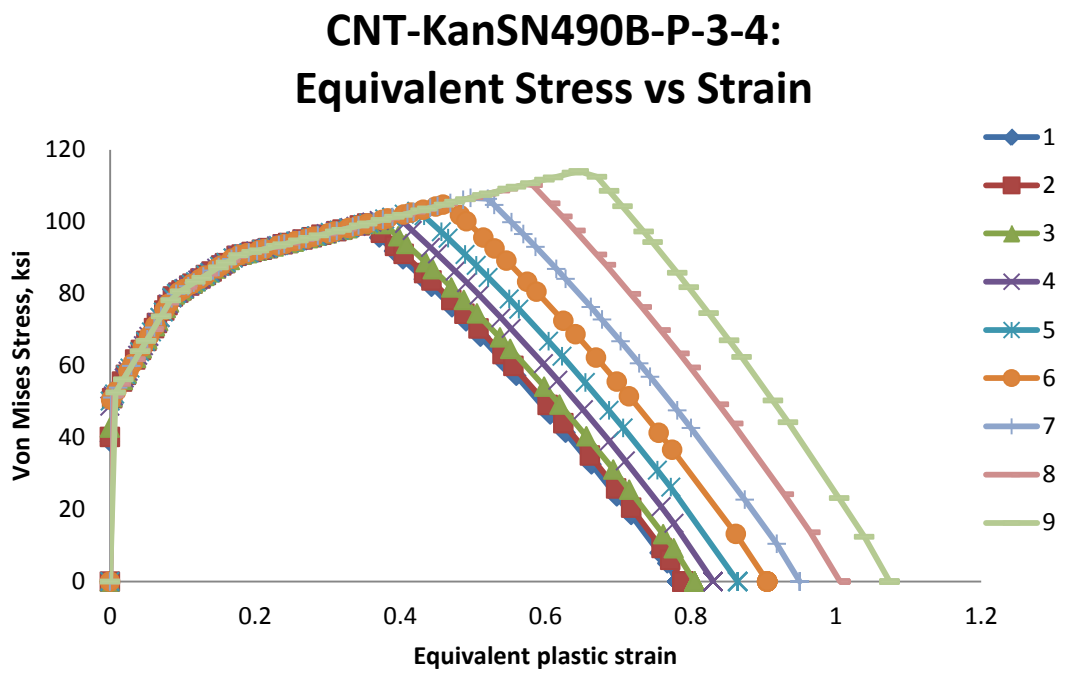

Figure B. 96: Variation of von Mises stress versus equivalent plastic strain for different elements laid out through the thickness of simulation of CNT-KanSN490B-P-3-4 specimens

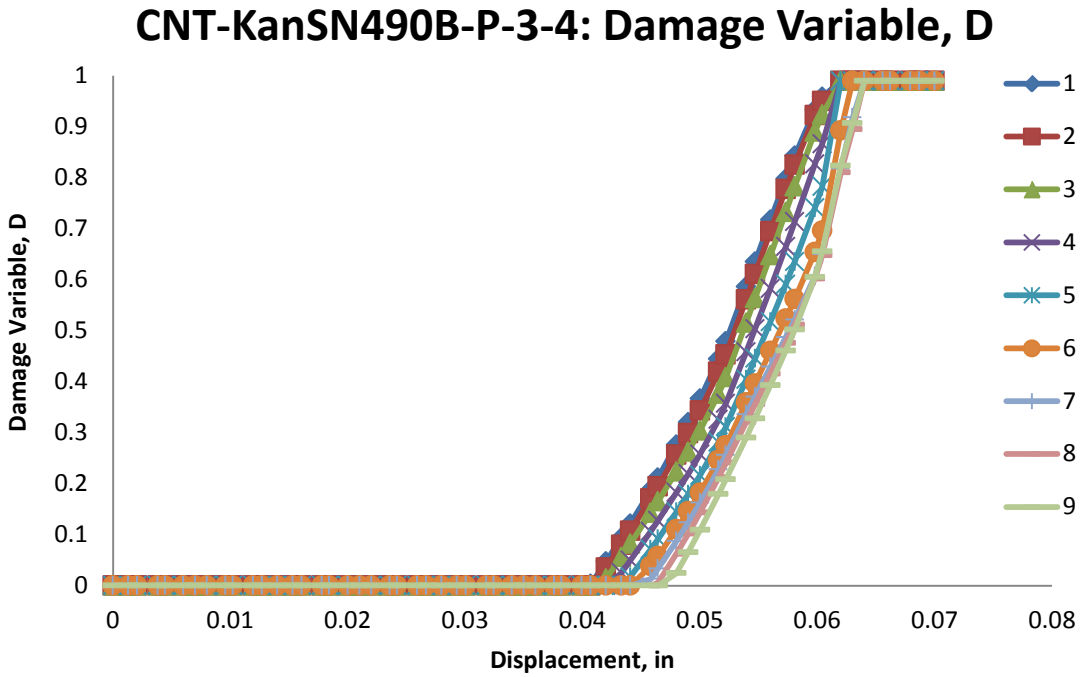

Figure B. 97: Variation of damage variable with displacement for different elements laid out through the thickness of simulation of CNT-KanSN490B-P-3-4 specimens

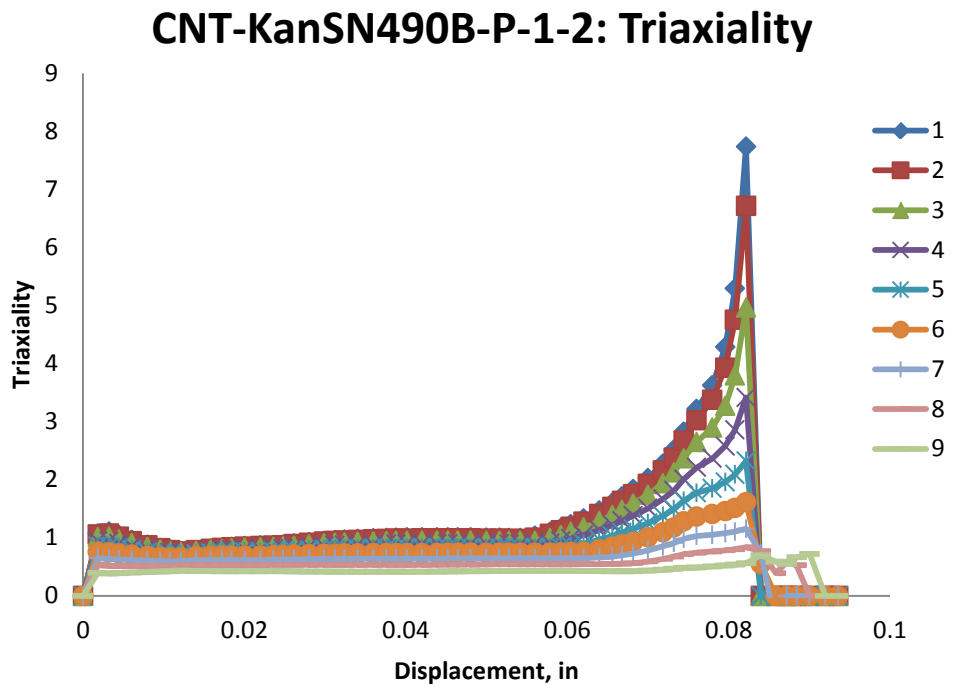

Figure B. 98: Variation of triaxiality with displacement for different elements laid out through the thickness of simulation of CNT-KanSN490B-P-1-2 specimens

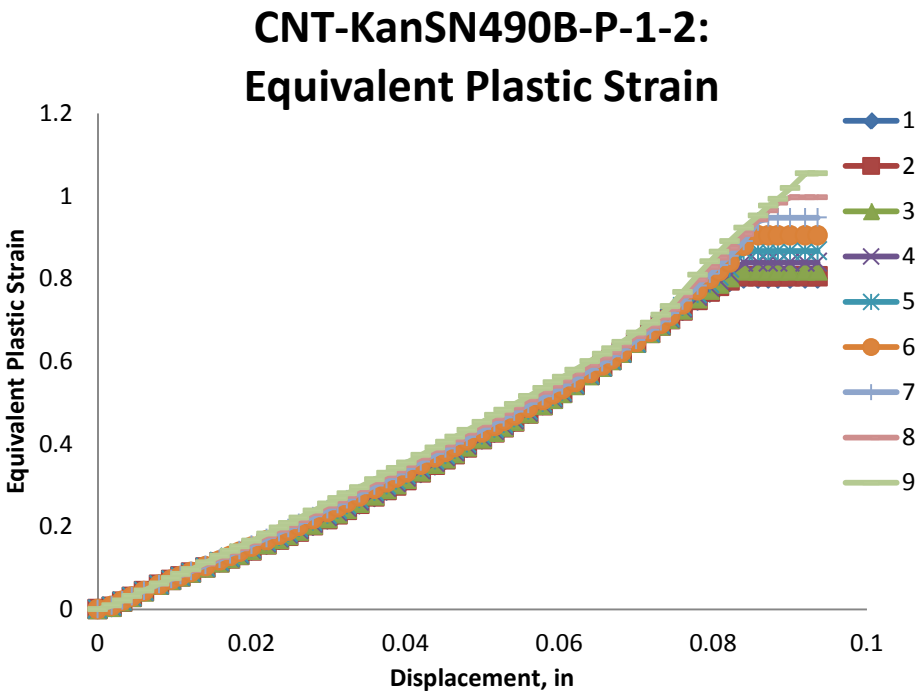

Figure B. 99: Variation of equivalent plastic strain with displacement for different elements laid out through the thickness of simulation of CNT-KanSN490B-P-1-2 specimens

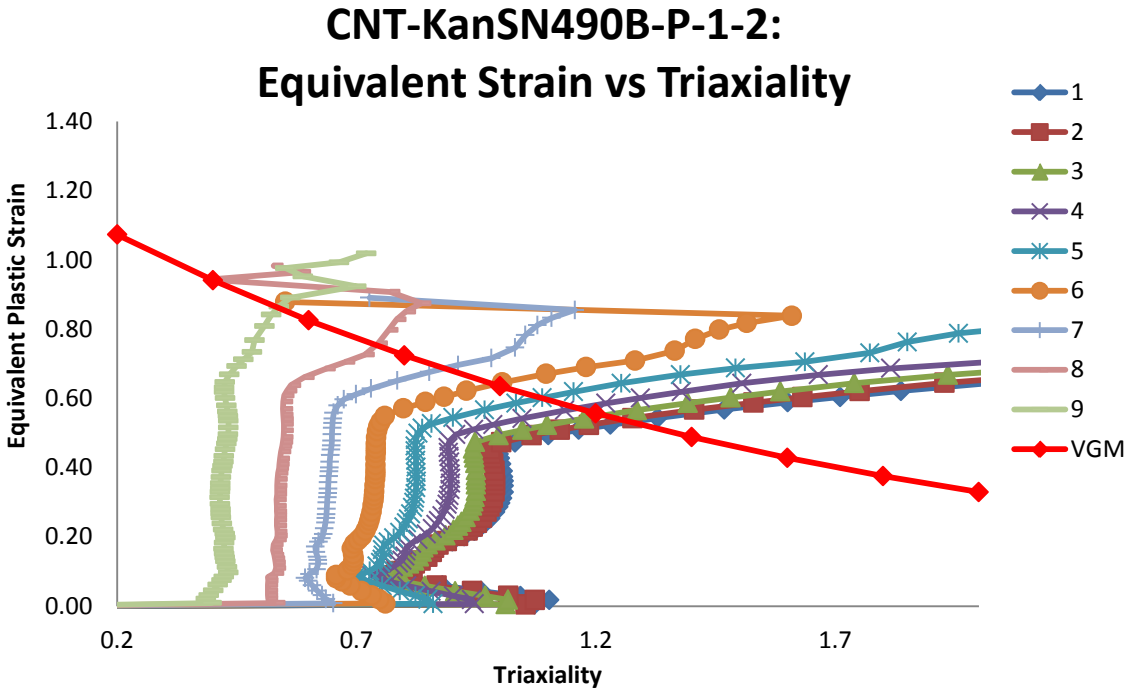

Figure B. 100: Variation of equivalent plastic strain versus triaxiality for different elements laid out through the thickness of simulation of CNT-KanSN490B-P-1-2 specimens

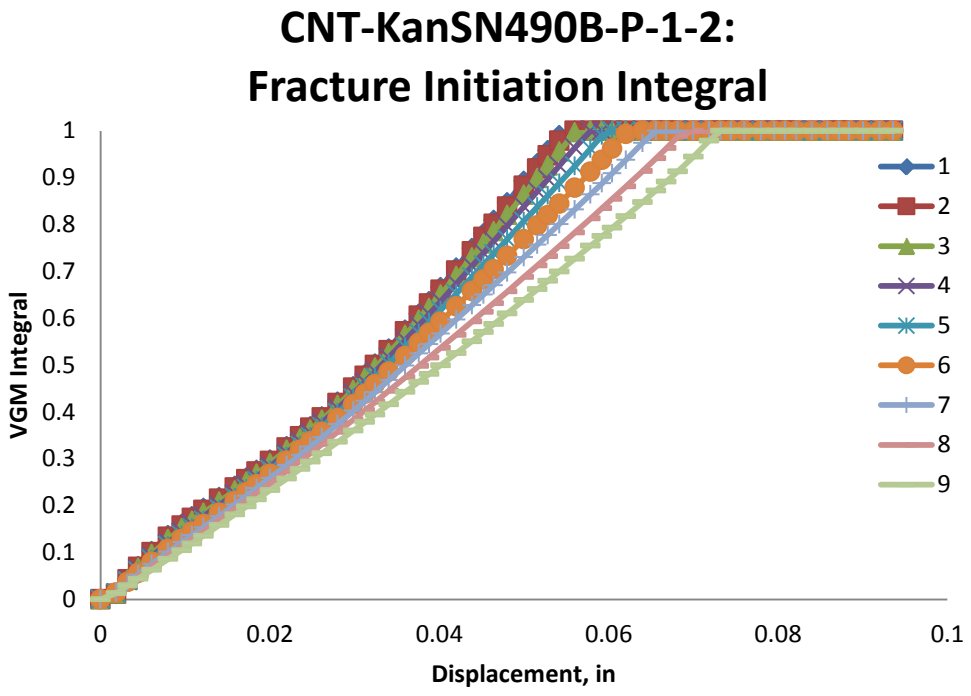

Figure B. 101: Value of fracture initiation integral for different elements laid out through the thickness of simulation of CNT-KanSN490B-P-1-2 specimens

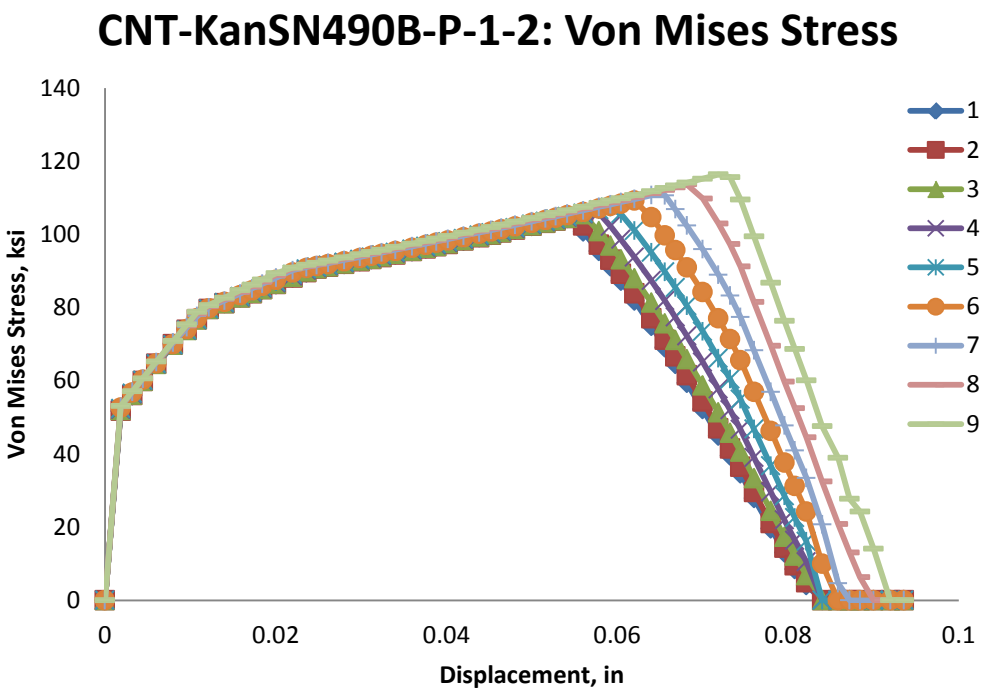

Figure B. 102: Variation of von Mises stress versus displacement for different elements laid out through the thickness of simulation of CNT-KanSN490B-P-1-2 specimens

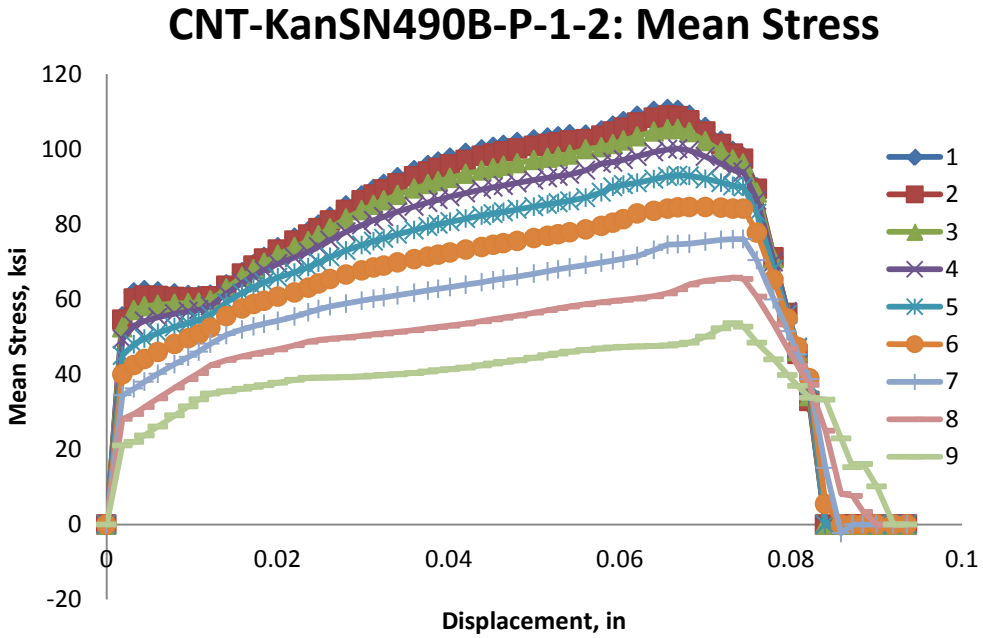

Figure B. 103: Variation of mean stress versus displacement for different elements laid out through the thickness of simulation of CNT-KanSN490B-P-1-2 specimens

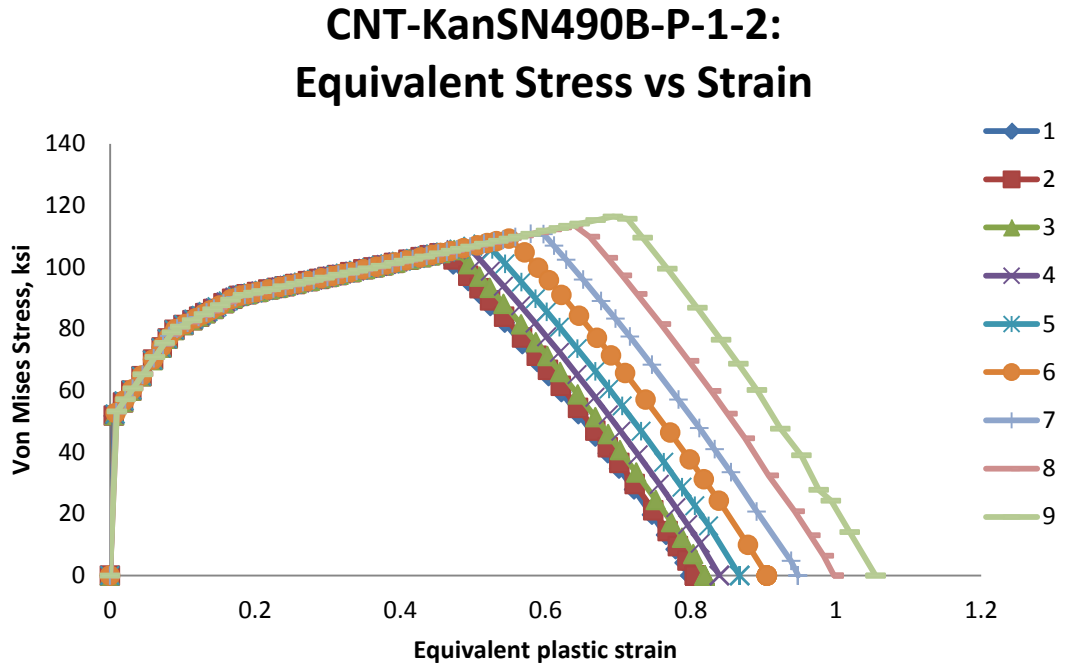

Figure B. 104: Variation of von Mises stress versus equivalent plastic strain for different elements laid out through the thickness of simulation of CNT-KanSN490B-P-1-2 specimens

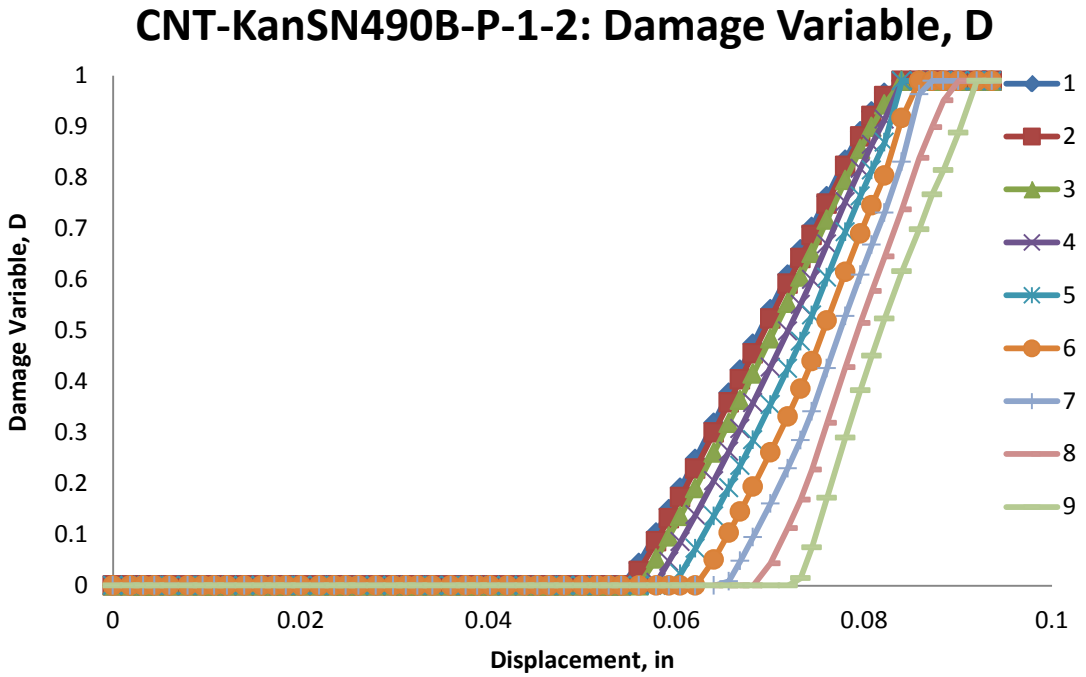

Figure B. 105: Variation of damage variable with displacement for different elements laid out through the thickness of simulation of CNT-KanSN490B-P-1-2 specimens

B.8 CNT-KanSM490YBTM-P-A

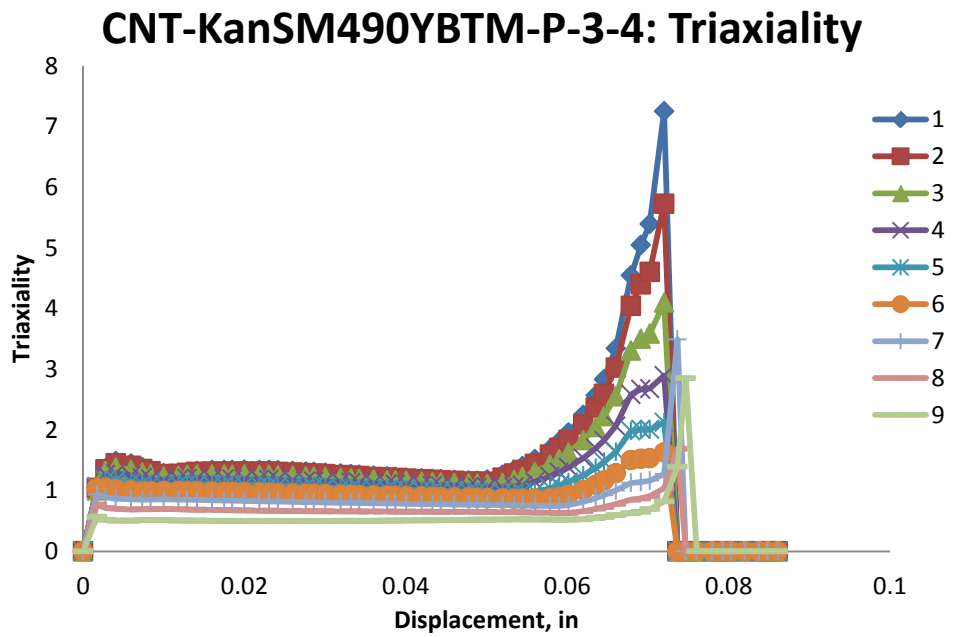

Figure B. 106: Variation of triaxiality with displacement for different elements laid out through the thickness of simulation of CNT-KanSM490YBTM-P-3-4 specimens

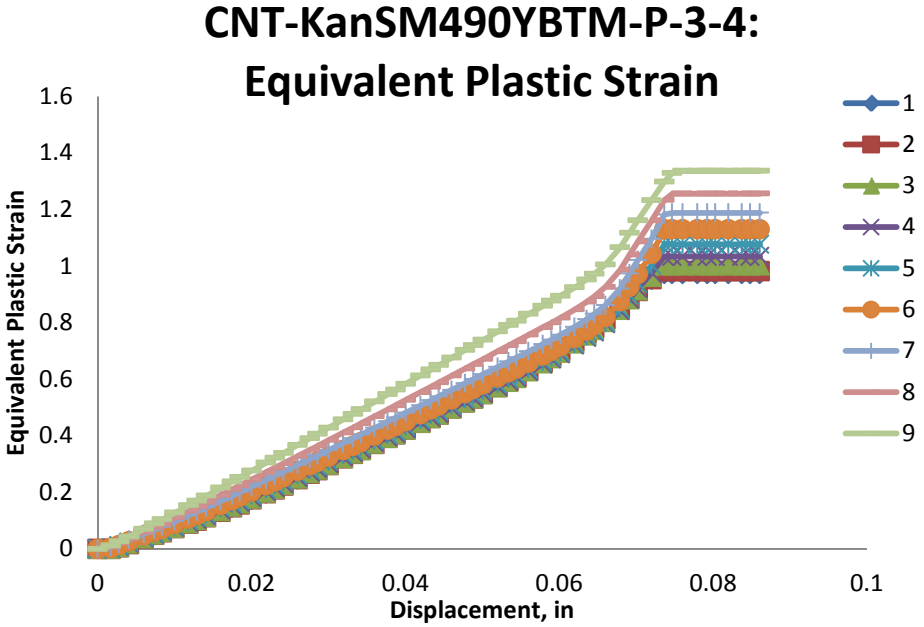

Figure B. 107: Variation of equivalent plastic strain with displacement for different elements laid out through the thickness of simulation of CNT-KanSM490YBTM-P-3-4 specimens

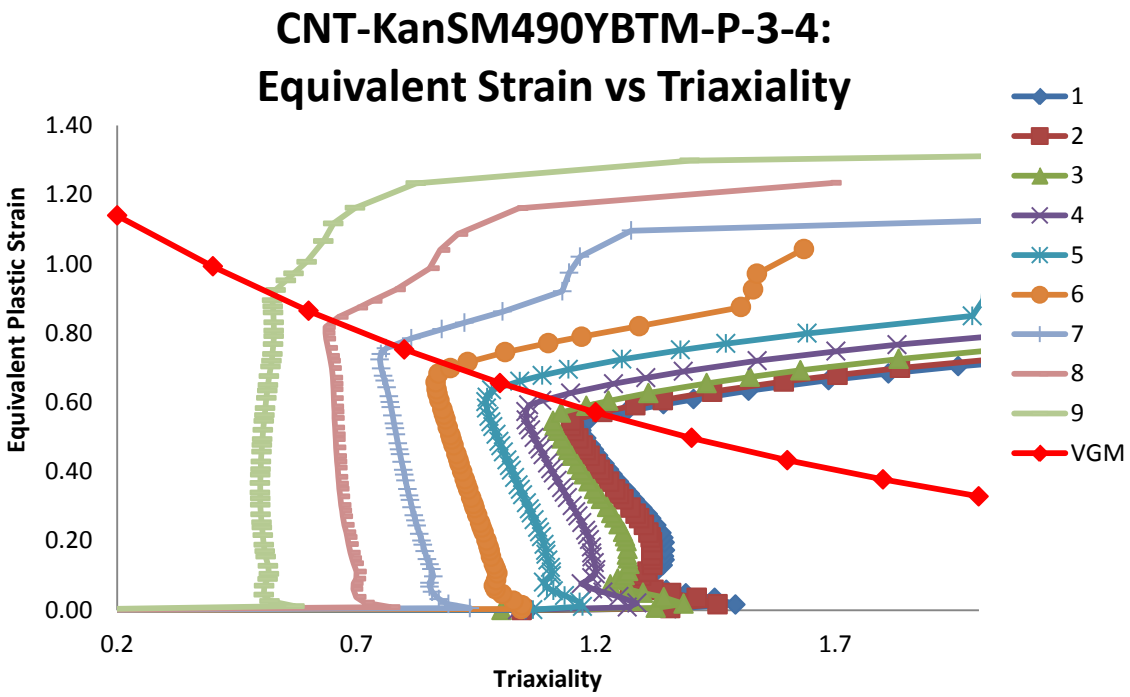

Figure B. 108: Variation of equivalent plastic strain versus triaxiality for different elements laid out through the thickness of simulation of CNT-KanSM490YBTM-P-3-4 specimens

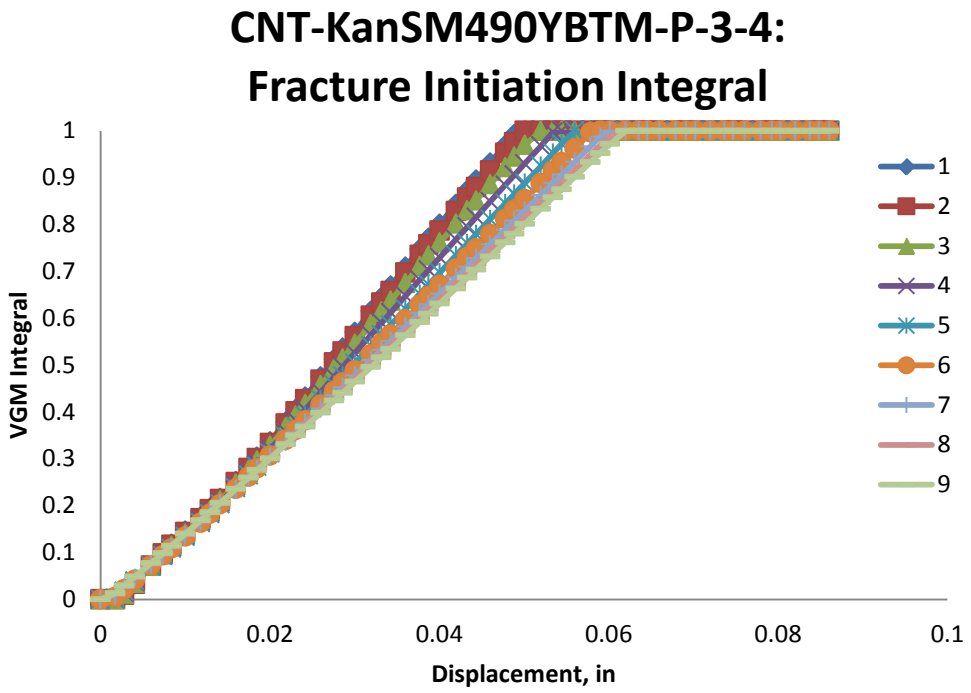

Figure B. 109: Value of fracture initiation integral for different elements laid out through the thickness of simulation of CNT-KanSM490YBTM-P-3-4 specimens

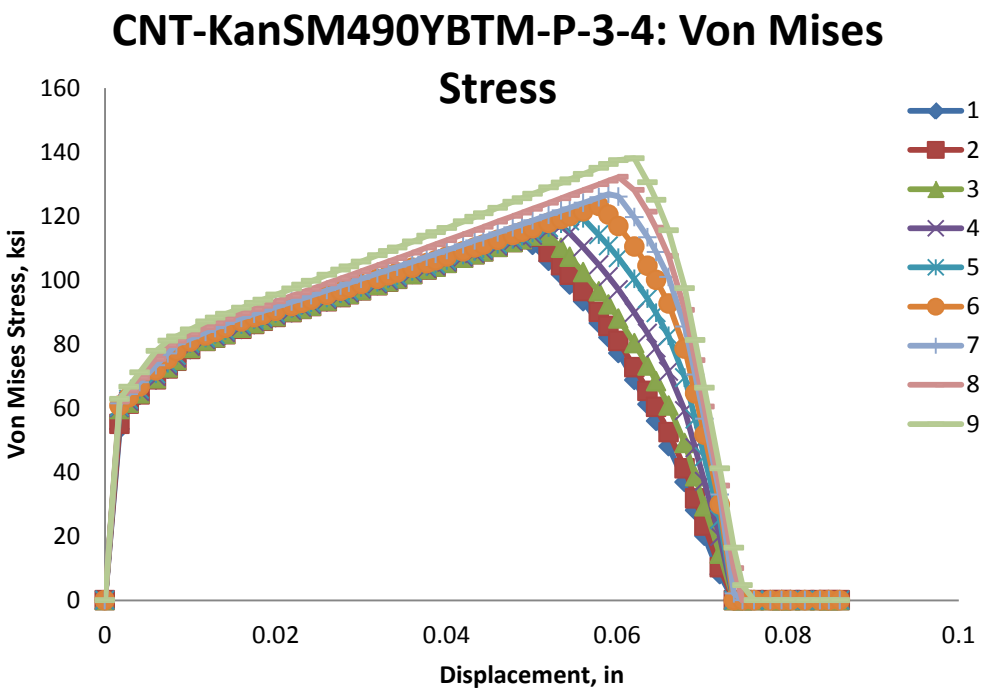

Figure B. 110: Variation of von Mises stress versus displacement for different elements laid out through the thickness of simulation of CNT-KanSM490YBTM-P-3-4 specimens

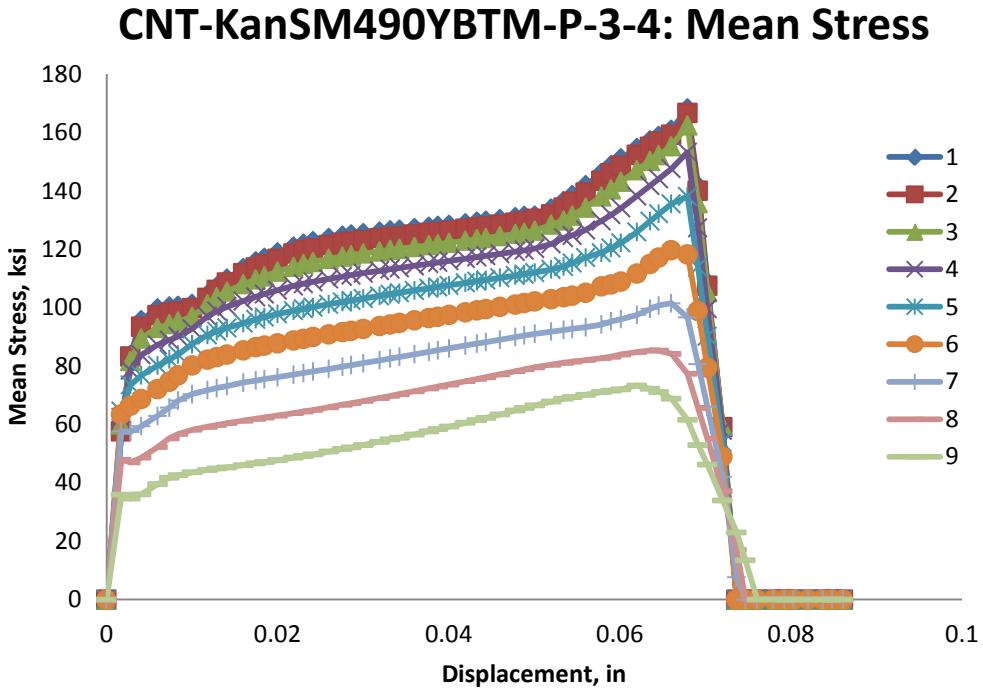

Figure B. 111: Variation of mean stress versus displacement for different elements laid out through the thickness of simulation of CNT-KanSM490YBTM-P-3-4 specimens

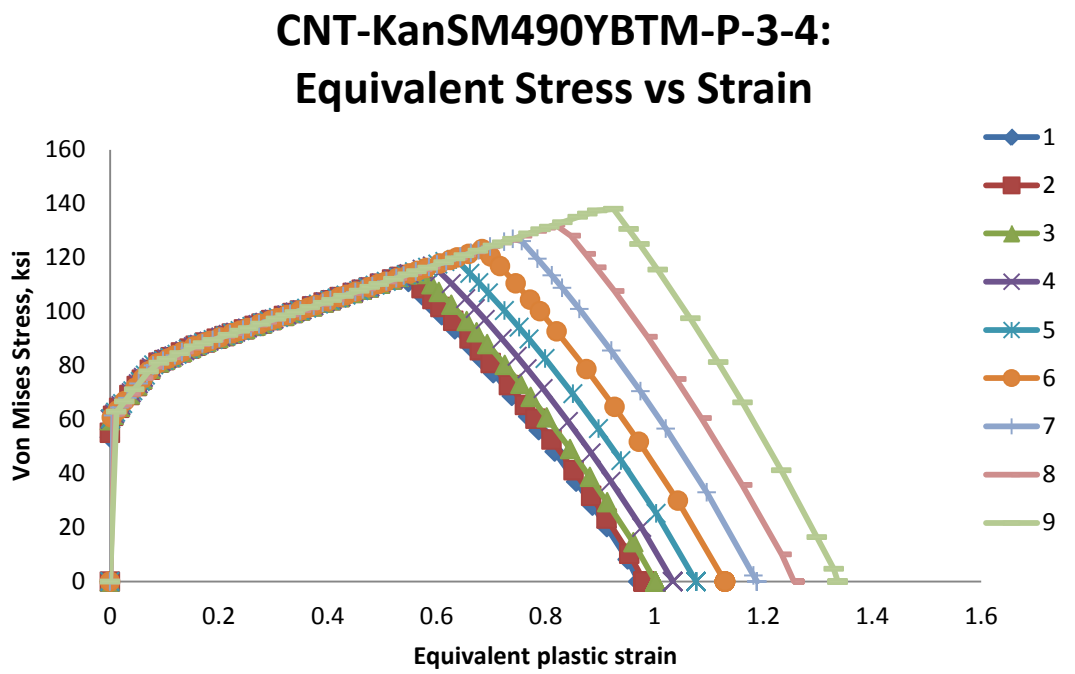

Figure B. 112: Variation of von Mises stress versus equivalent plastic strain for different elements laid out through the thickness of simulation of CNT-KanSM490YBTM-P-3-4 specimens

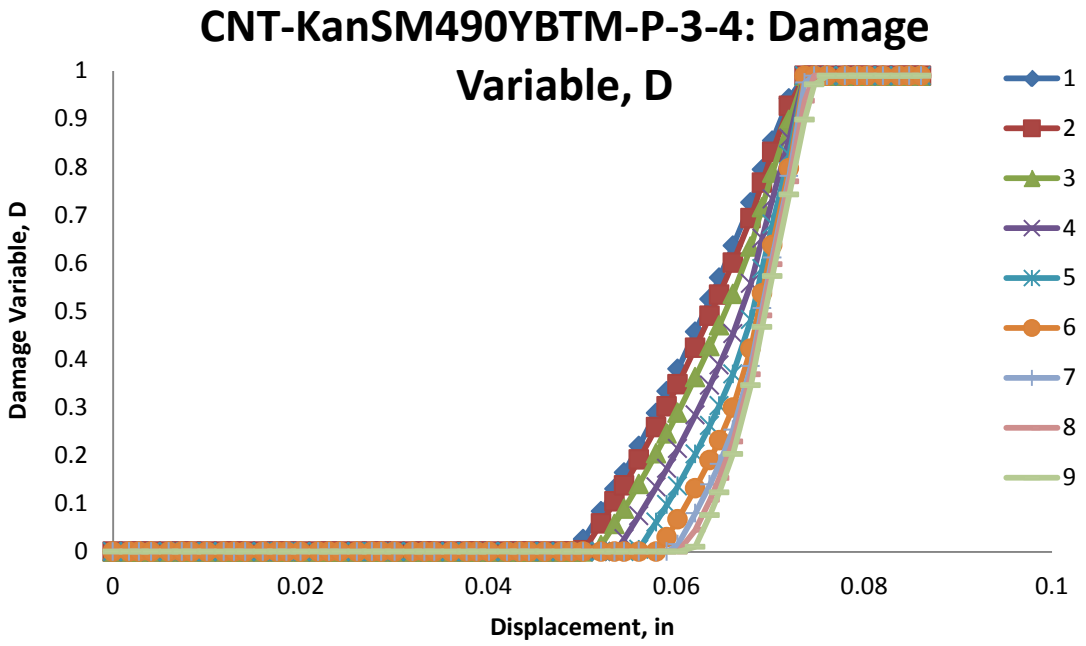

Figure B. 113: Variation of damage variable with displacement for different elements laid out through the thickness of simulation of CNT-KanSM490YBTM-P-3-4 specimens

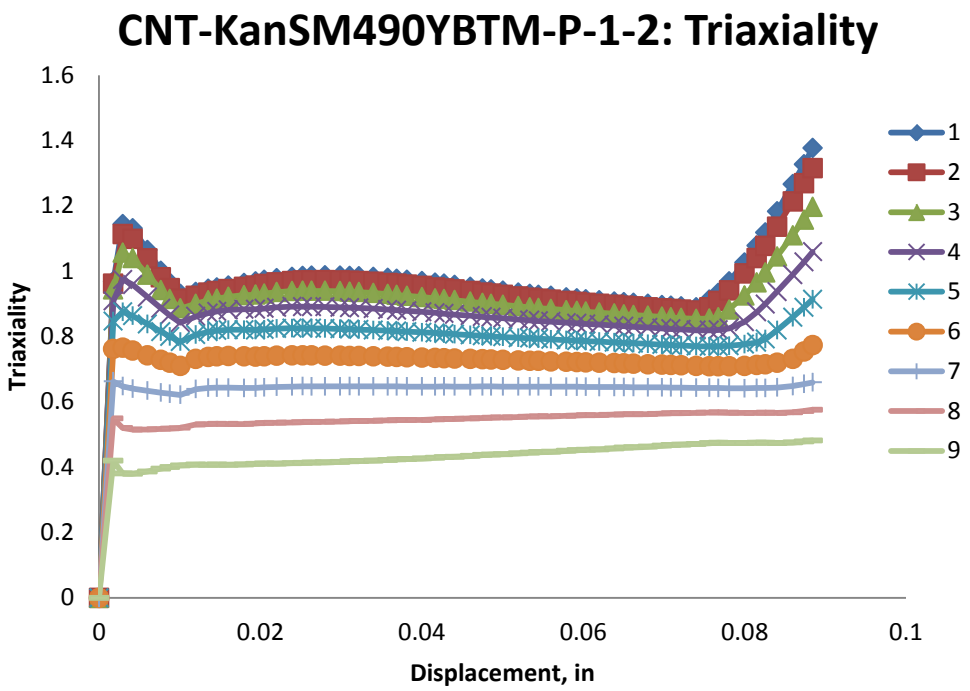

Figure B. 114: Variation of triaxiality with displacement for different elements laid out through the thickness of simulation of CNT-KanSM490YBTM-P-1-2 specimens

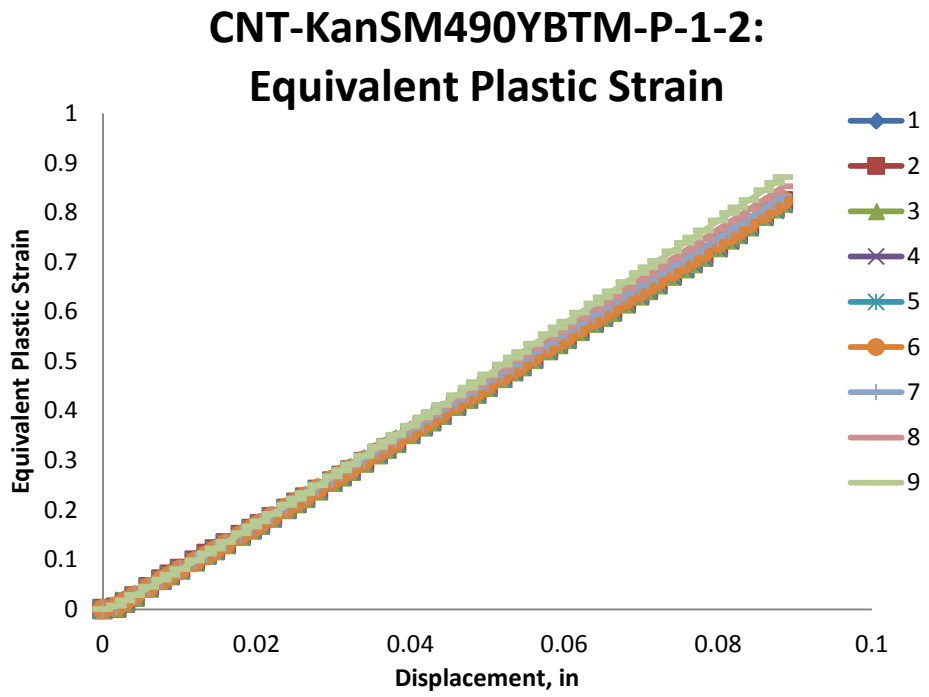

Figure B. 115: Variation of equivalent plastic strain with displacement for different elements laid out through the thickness of simulation of CNT-KanSM490YBTM-P-1-2 specimens

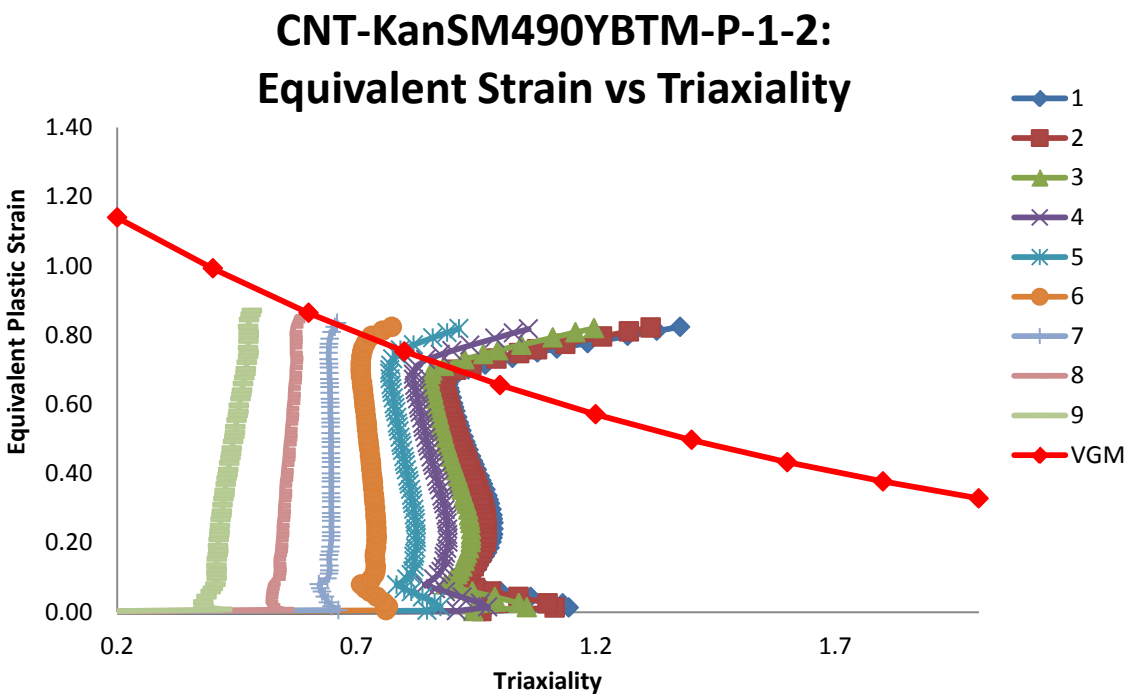

Figure B. 116: Variation of equivalent plastic strain versus triaxiality for different elements laid out through the thickness of simulation of CNT-KanSM490YBTM-P-1-2 specimens

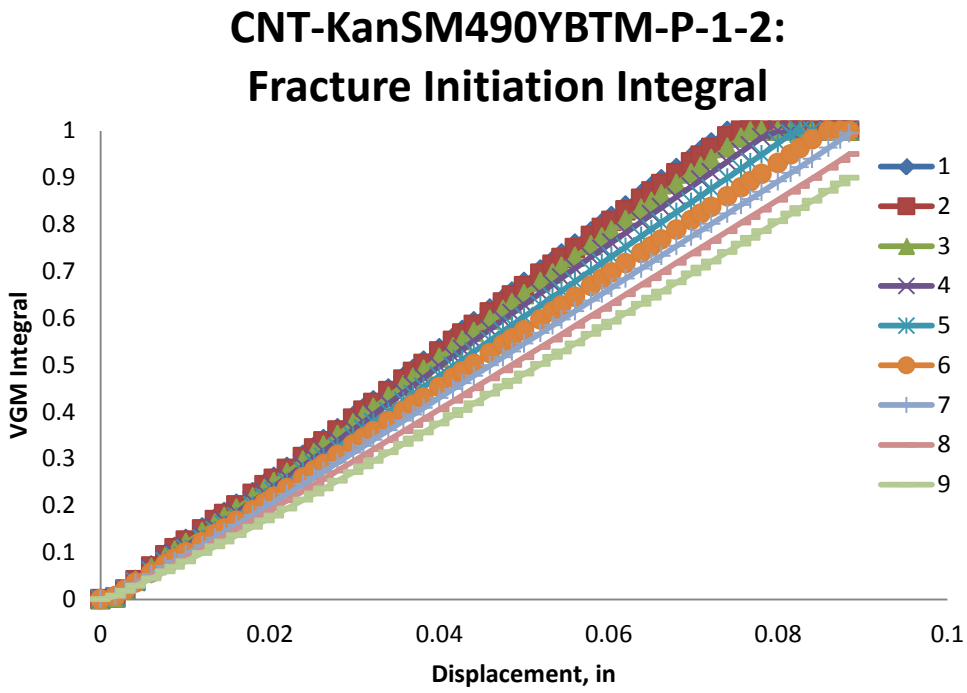

Figure B. 117: Value of fracture initiation integral for different elements laid out through the thickness of simulation of CNT-KanSM490YBTM-P-1-2 specimens

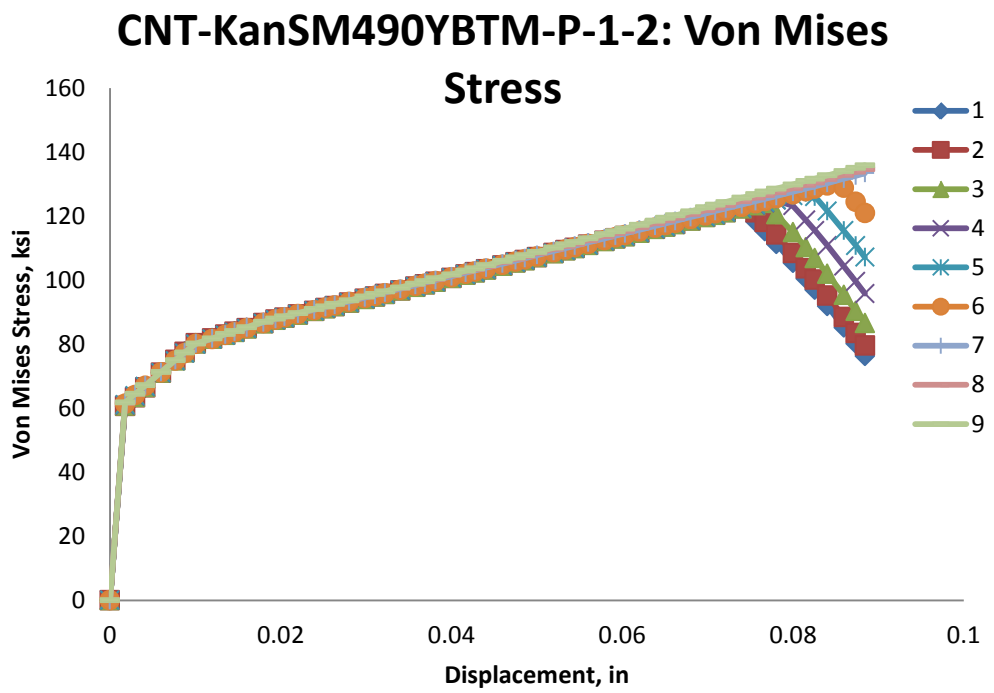

Figure B. 118: Variation of von Mises stress versus displacement for different elements laid out through the thickness of simulation of CNT-KanSM490YBTM-P-1-2 specimens

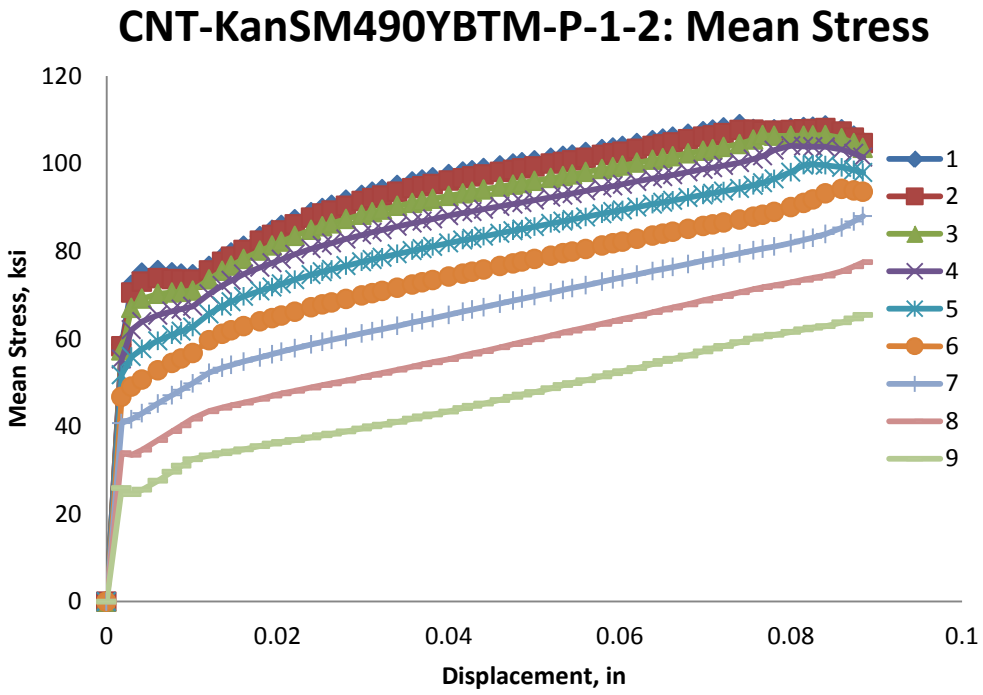

Figure B. 119: Variation of mean stress versus displacement for different elements laid out through the thickness of simulation of CNT-KanSM490YBTM-P-1-2 specimens

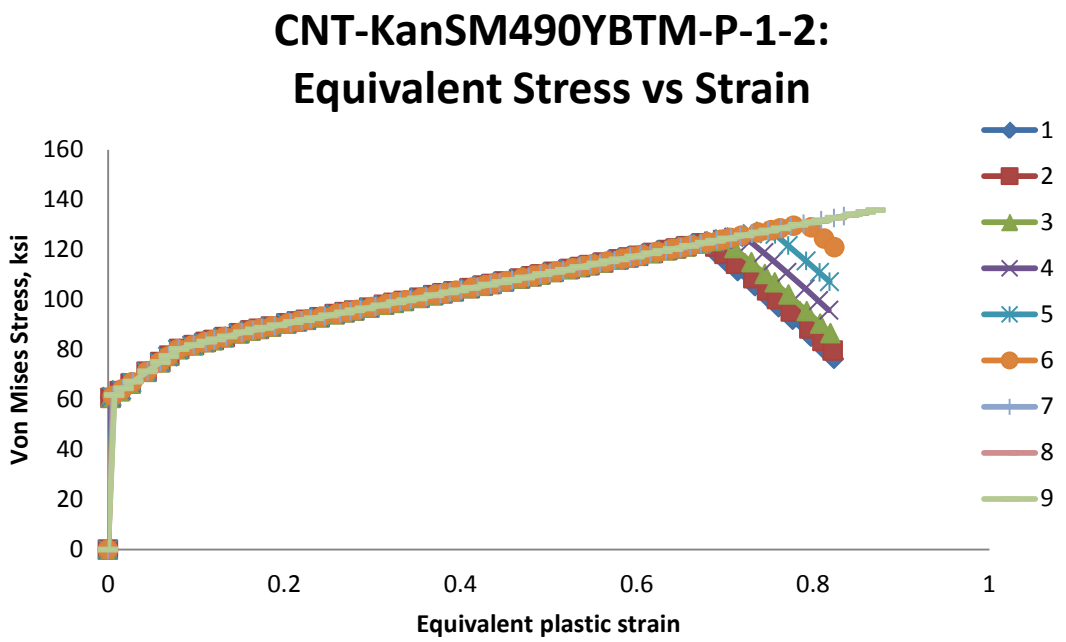

Figure B. 120: Variation of von Mises stress versus equivalent plastic strain for different elements laid out through the thickness of simulation of CNT-KanSM490YBTM-P-1-2 specimens

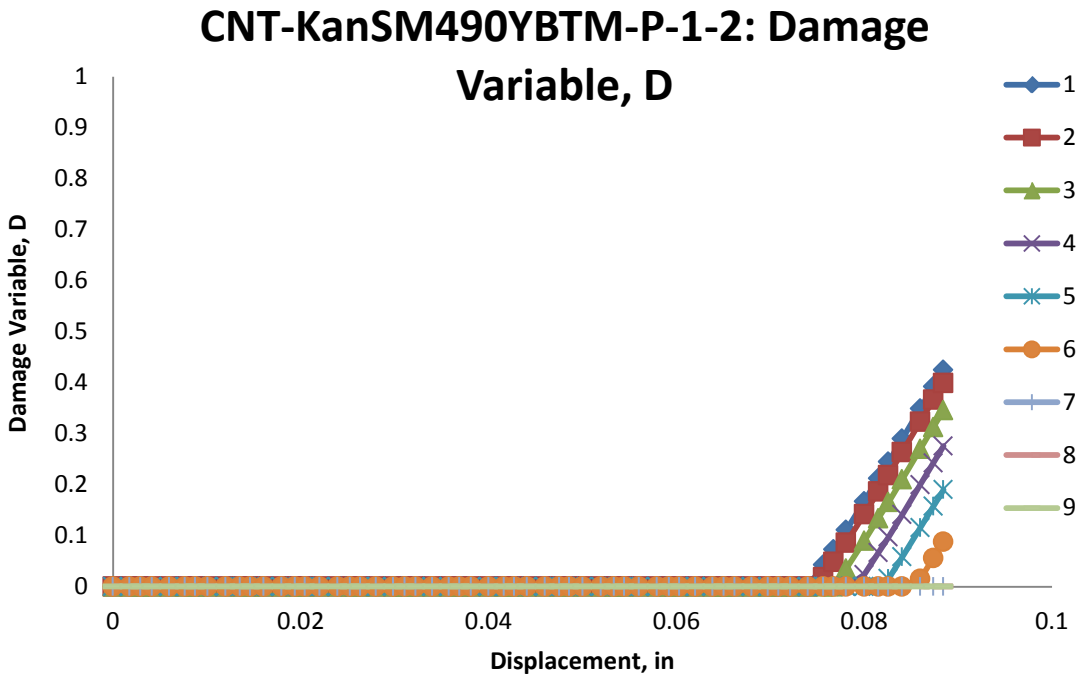

Figure B. 121: Variation of damage variable with displacement for different elements laid out through the thickness of simulation of CNT-KanSM490YBTM-P-1-2 specimens

B.9 CNT-KanSN490B-W-L-A

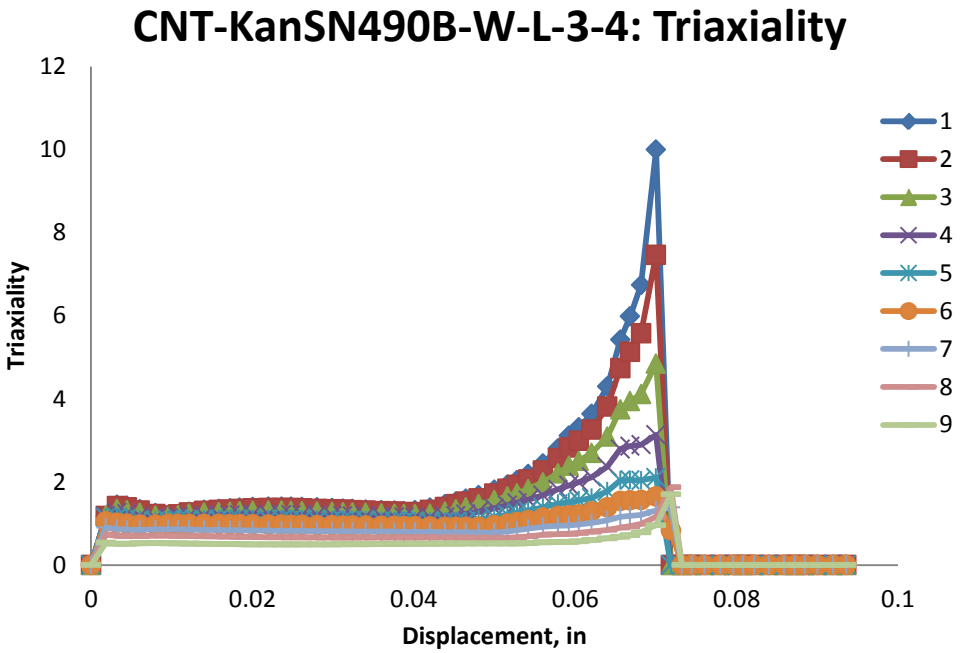

Figure B. 122: Variation of triaxiality with displacement for different elements laid out through the thickness of simulation of CNT-KanSN490B-W-L-3-4 specimens

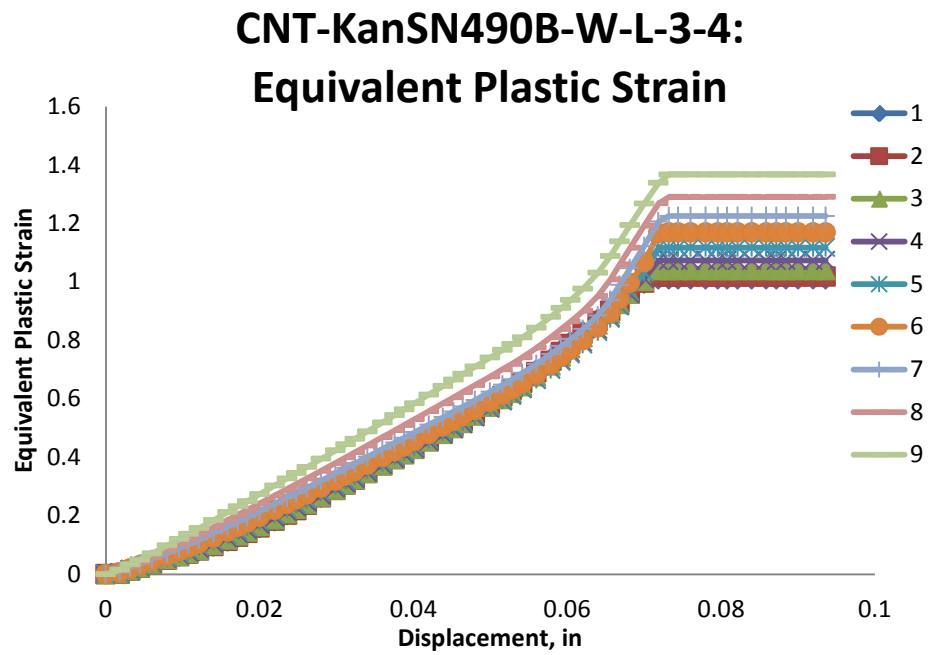

Figure B. 123: Variation of equivalent plastic strain with displacement for different elements laid out through the thickness of simulation of CNT-KanSN490B-W-L-3-4 specimens

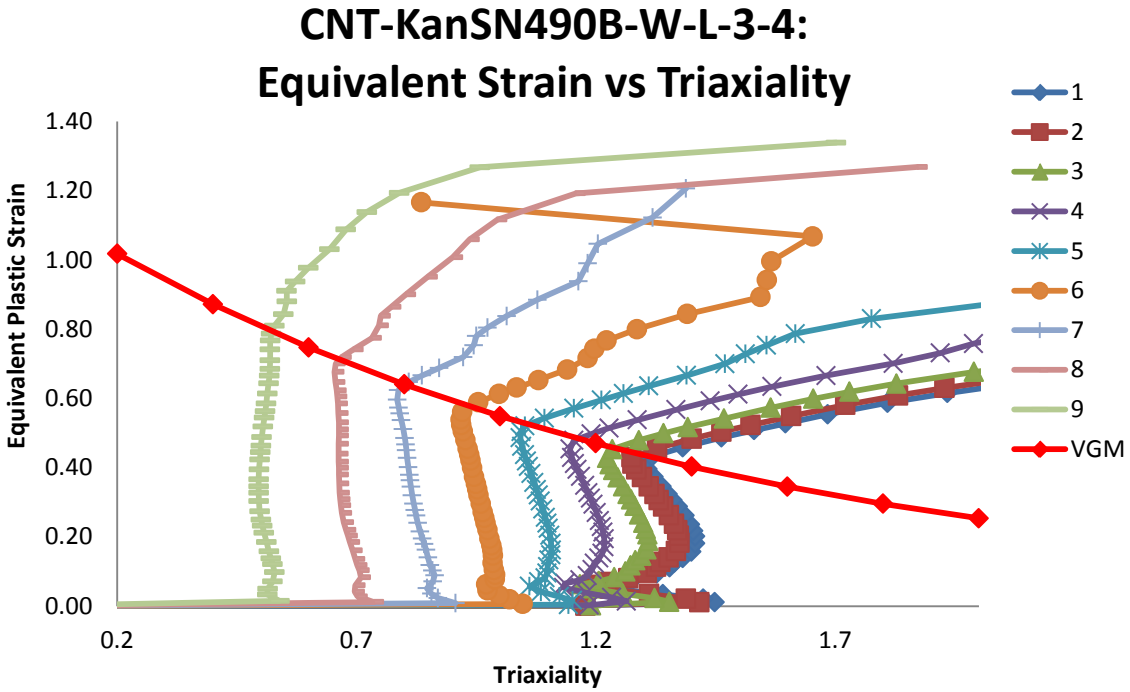

Figure B. 124: Variation of equivalent plastic strain versus triaxiality for different elements laid out through the thickness of simulation of CNT-KanSN490B-W-L-3-4 specimens

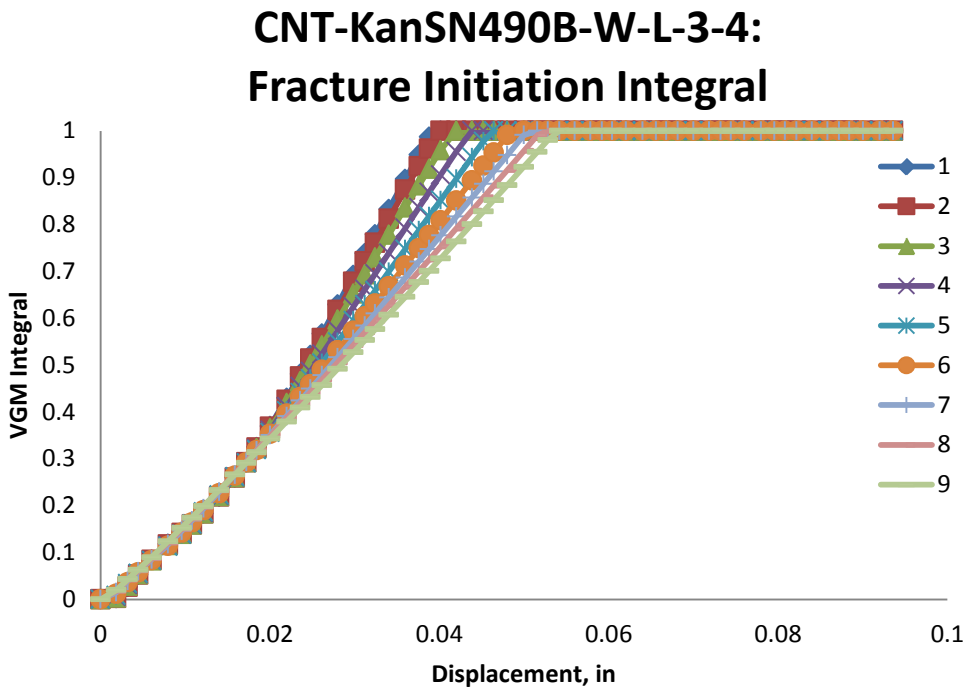

Figure B. 125: Value of fracture initiation integral for different elements laid out through the thickness of simulation of CNT-KanSN490B-W-L-3-4 specimens

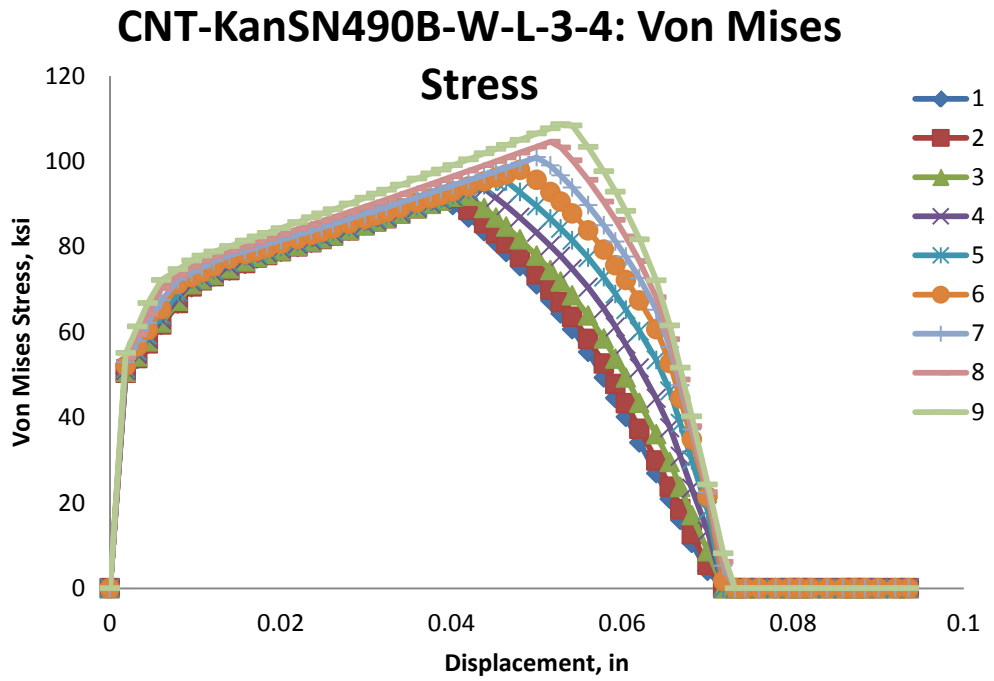

Figure B. 126: Variation of von Mises stress versus displacement for different elements laid out through the thickness of simulation of CNT-KanSN490B-W-L-3-4 specimens

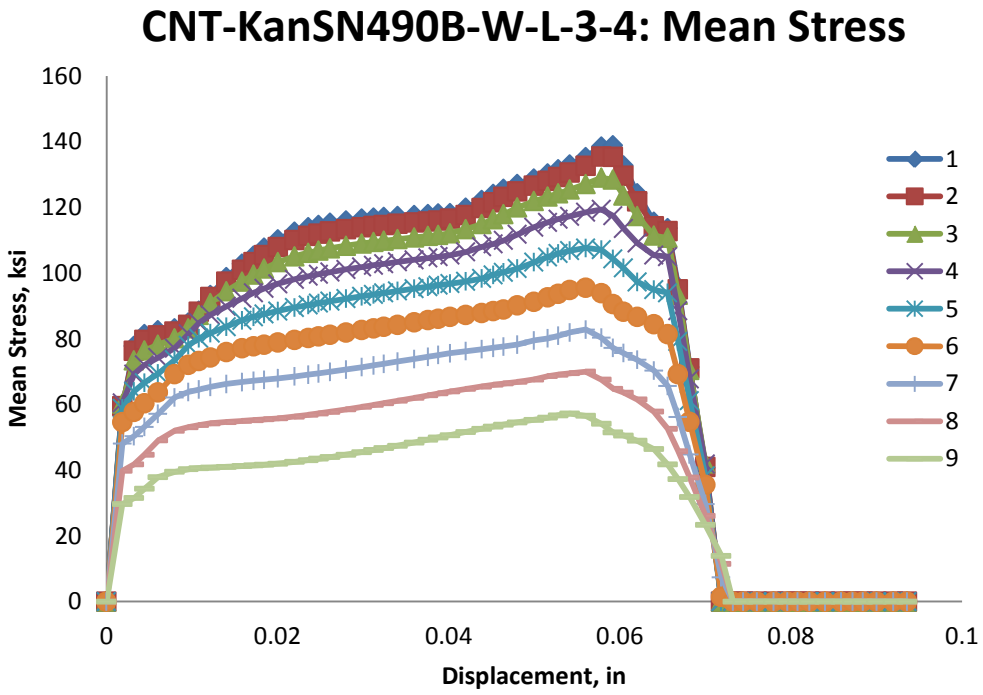

Figure B. 127: Variation of mean stress versus displacement for different elements laid out through the thickness of simulation of CNT-KanSN490B-W-L-3-4 specimens

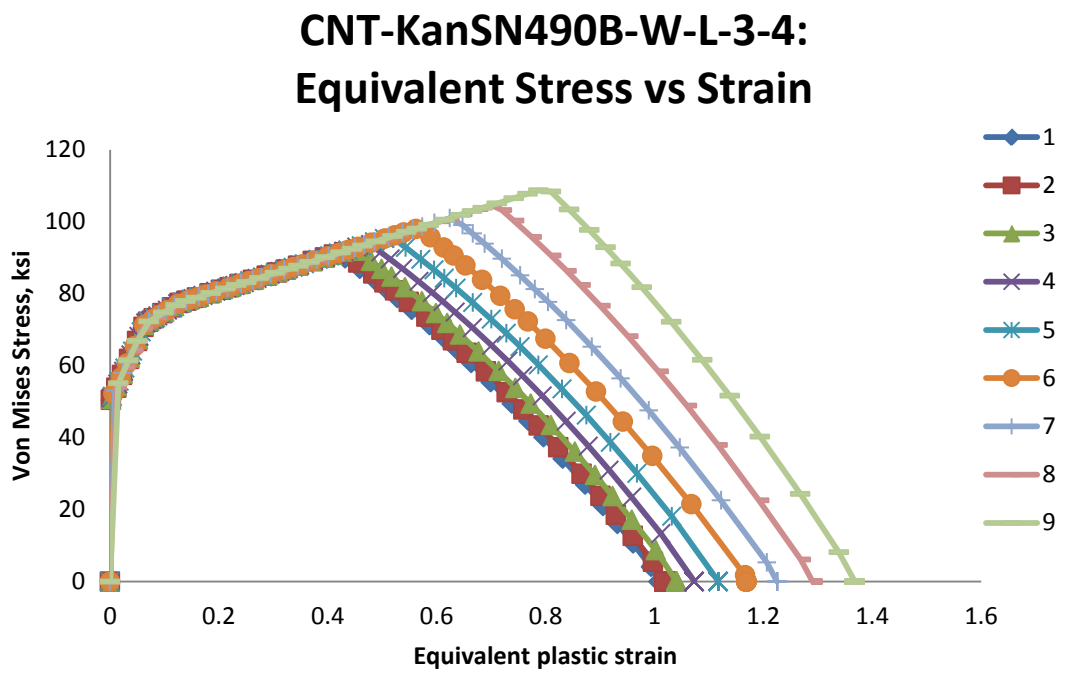

Figure B. 128: Variation of von Mises stress versus equivalent plastic strain for different elements laid out through the thickness of simulation of CNT-KanSN490B-W-L-3-4 specimens

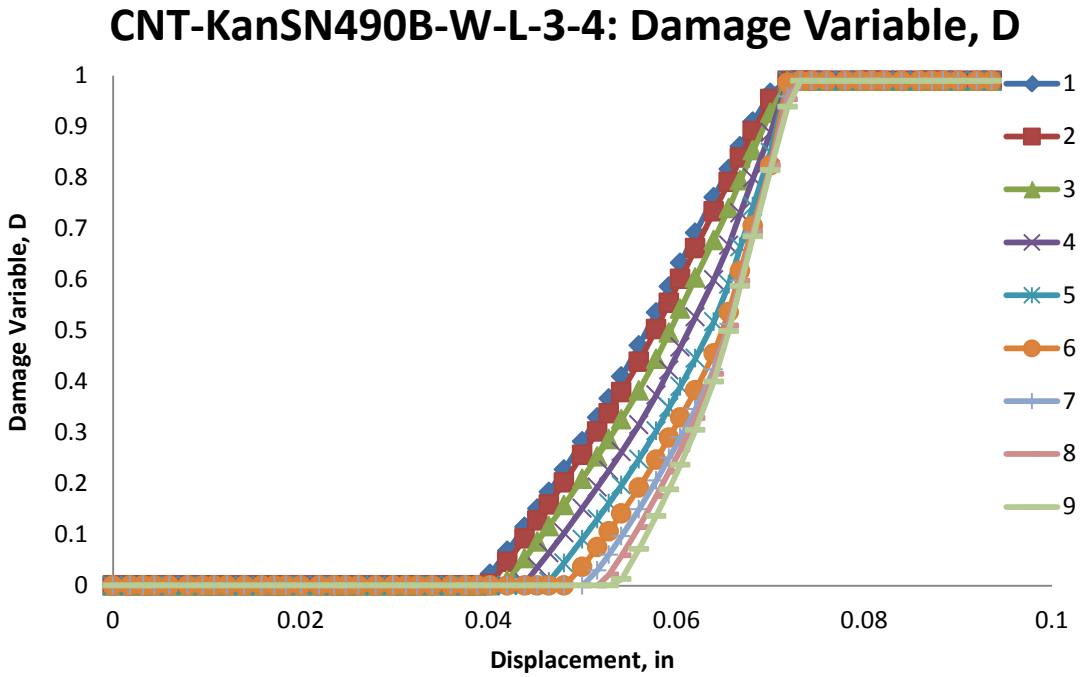

Figure B. 129: Variation of damage variable with displacement for different elements laid out through the thickness of simulation of CNT-KanSN490B-W-L-3-4 specimens

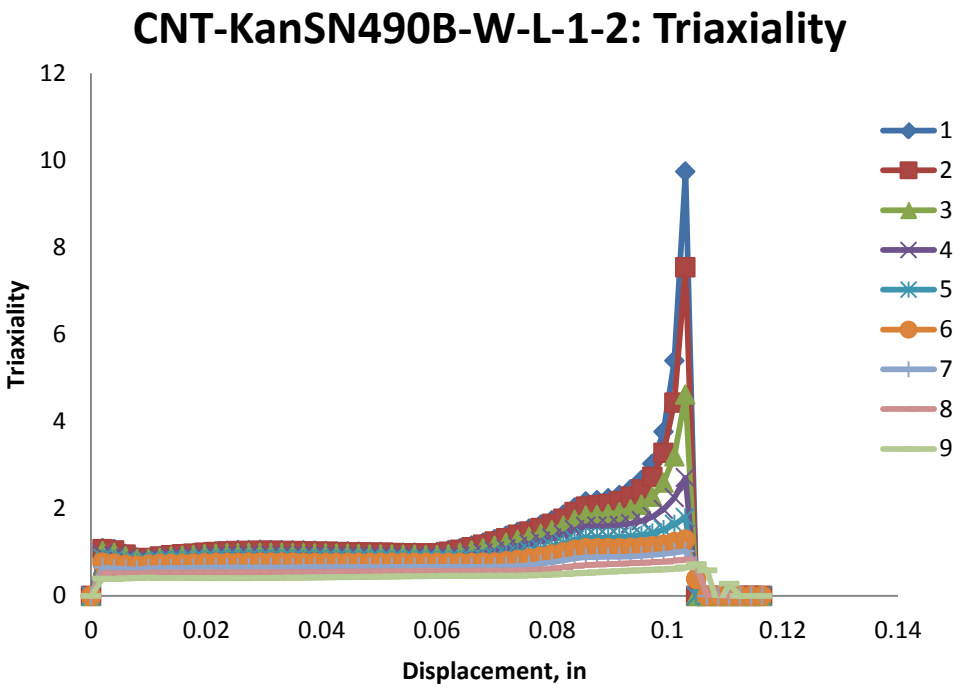

Figure B. 130: Variation of triaxiality with displacement for different elements laid out through the thickness of simulation of CNT-KanSN490B-W-L-1-2 specimens

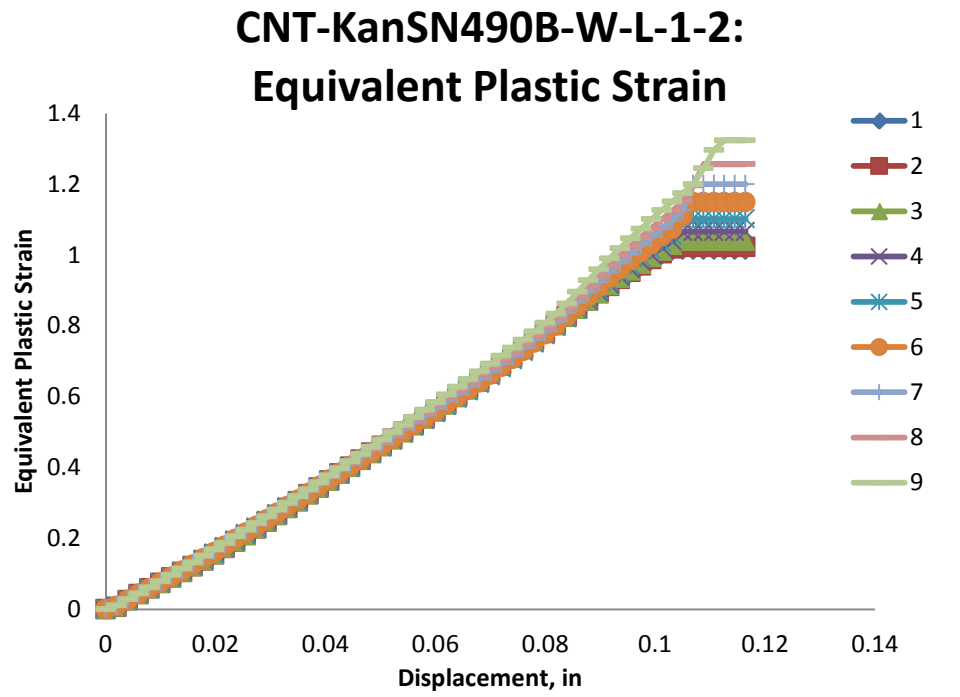

Figure B. 131: Variation of equivalent plastic strain with displacement for different elements laid out through the thickness of simulation of CNT-KanSN490B-W-L-1-2 specimens

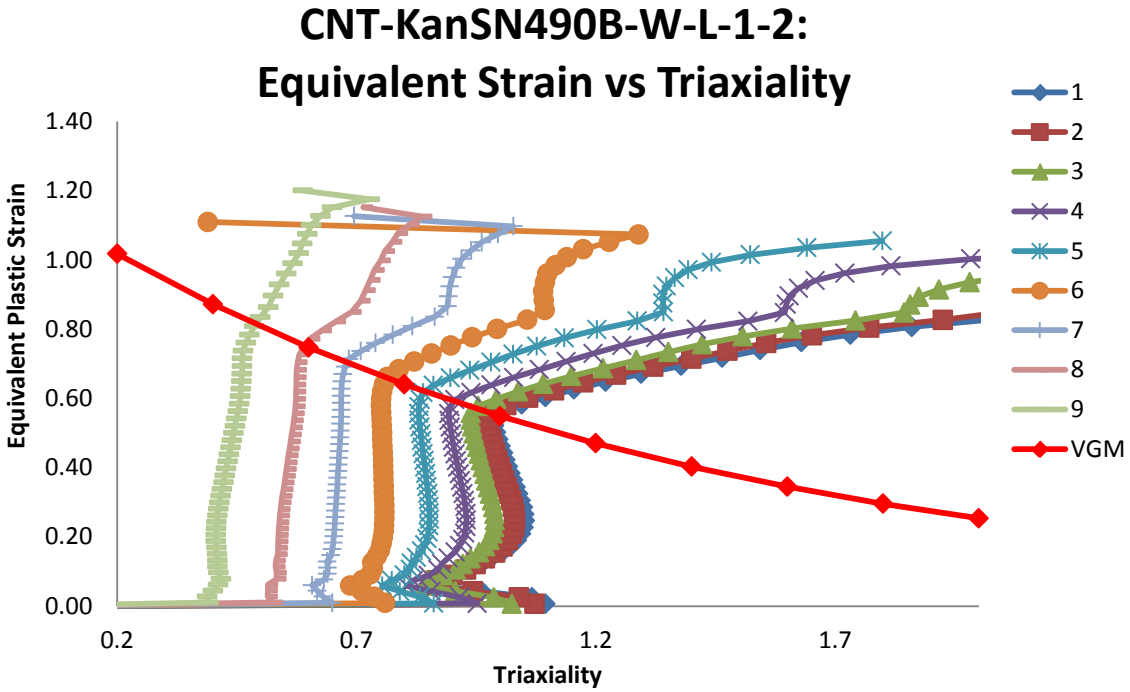

Figure B. 132: Variation of equivalent plastic strain versus triaxiality for different elements laid out through the thickness of simulation of CNT-KanSN490B-W-L-1-2 specimens

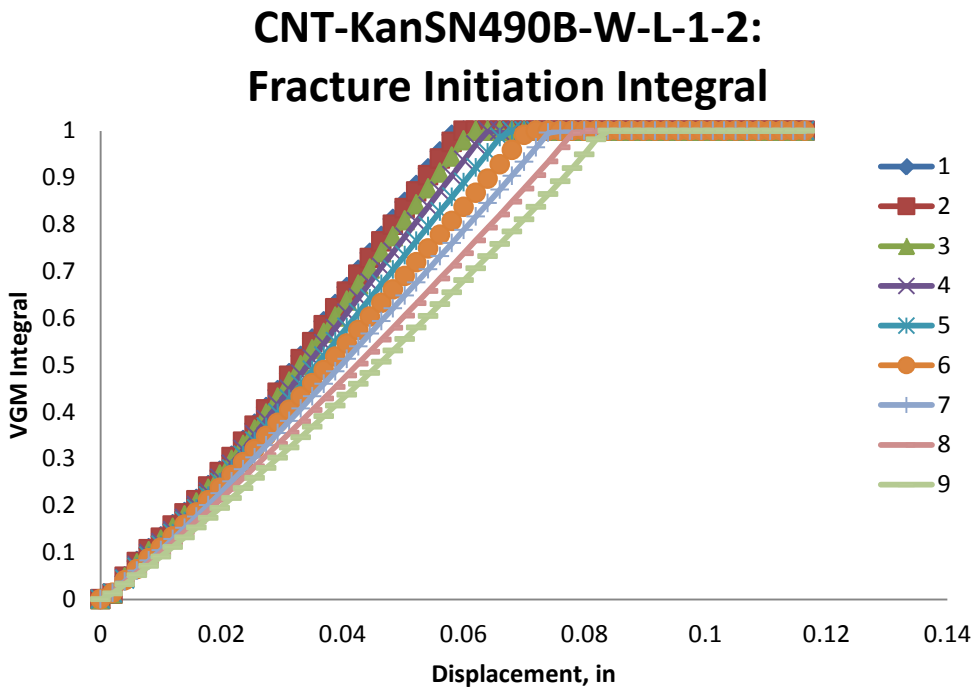

Figure B. 133: Value of fracture initiation integral for different elements laid out through the thickness of simulation of CNT-KanSN490B-W-L-1-2 specimens

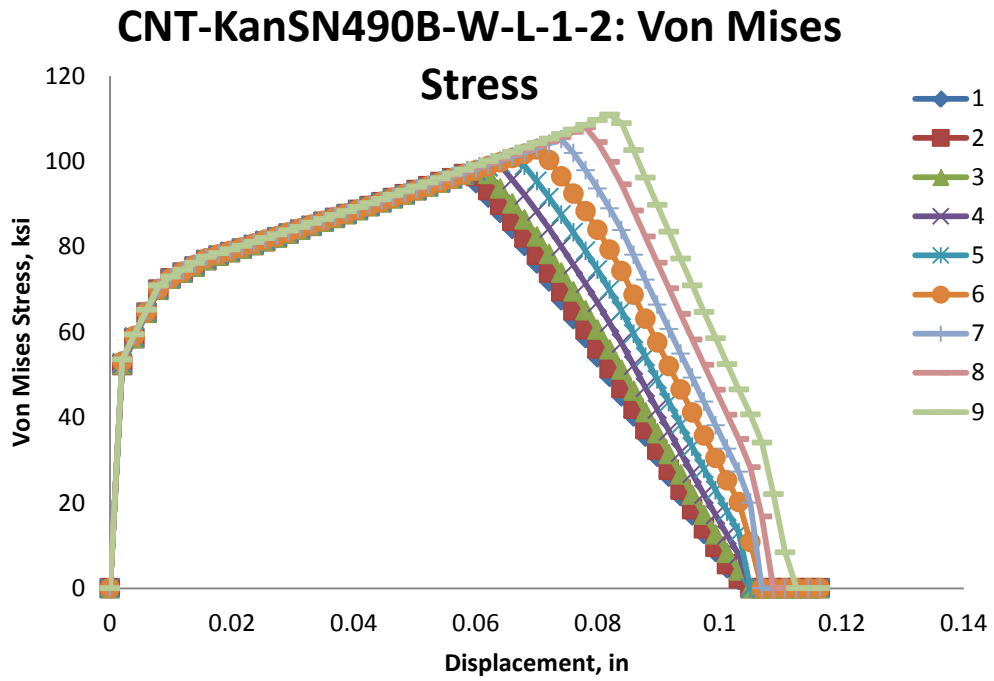

Figure B. 134: Variation of von Mises stress versus displacement for different elements laid out through the thickness of simulation of CNT-KanSN490B-W-L-1-2 specimens

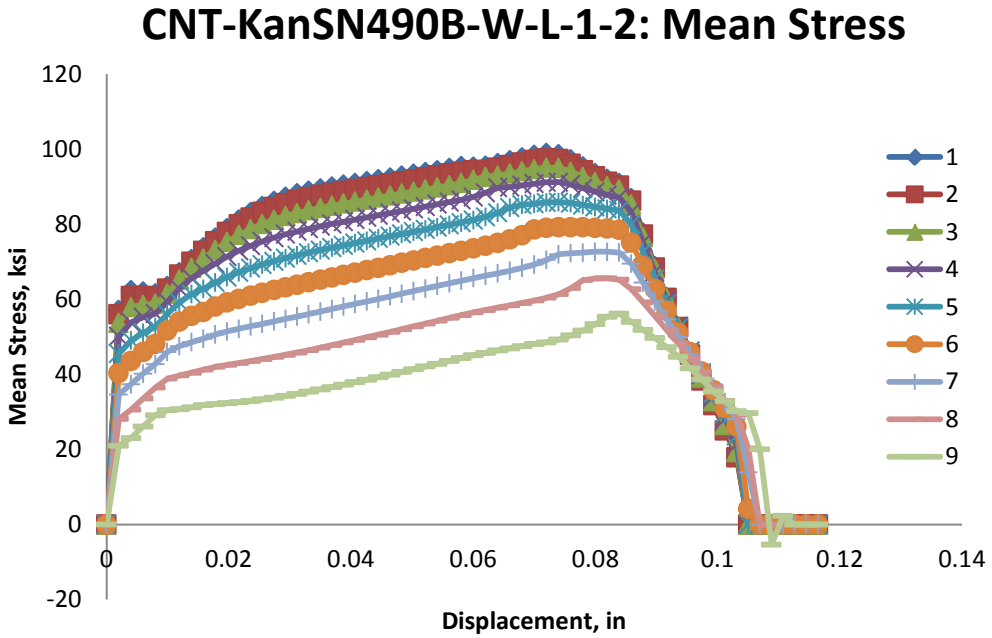

Figure B. 135: Variation of mean stress versus displacement for different elements laid out through the thickness of simulation of CNT-KanSN490B-W-L-1-2 specimens

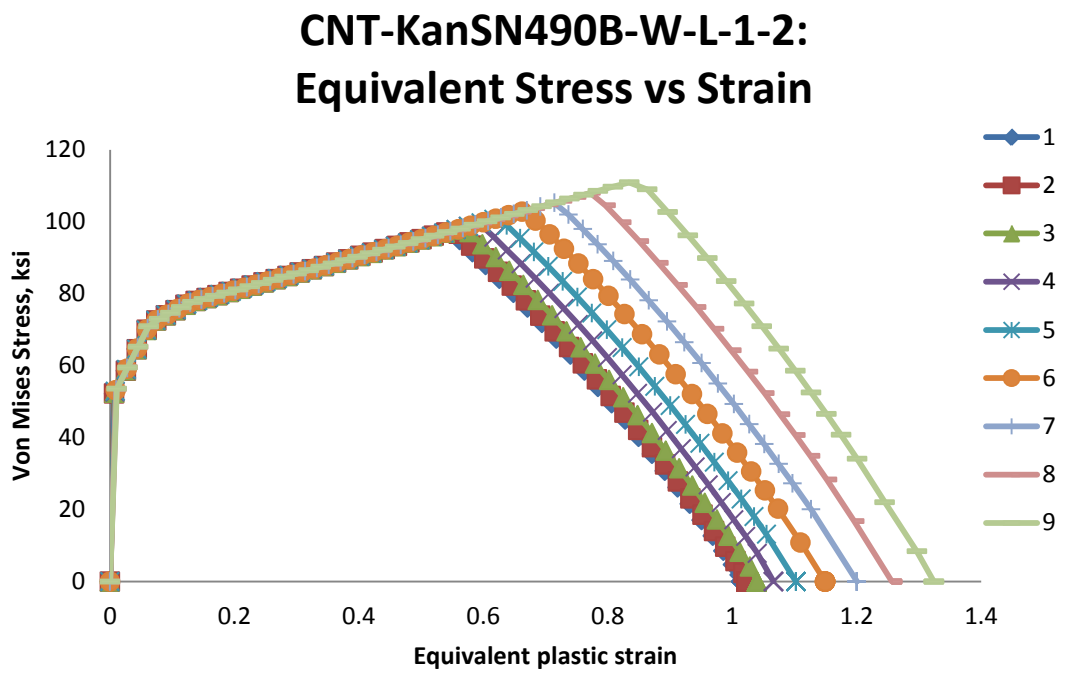

Figure B. 136: Variation of von Mises stress versus equivalent plastic strain for different elements laid out through the thickness of simulation of CNT-KanSN490B-W-L-1-2 specimens

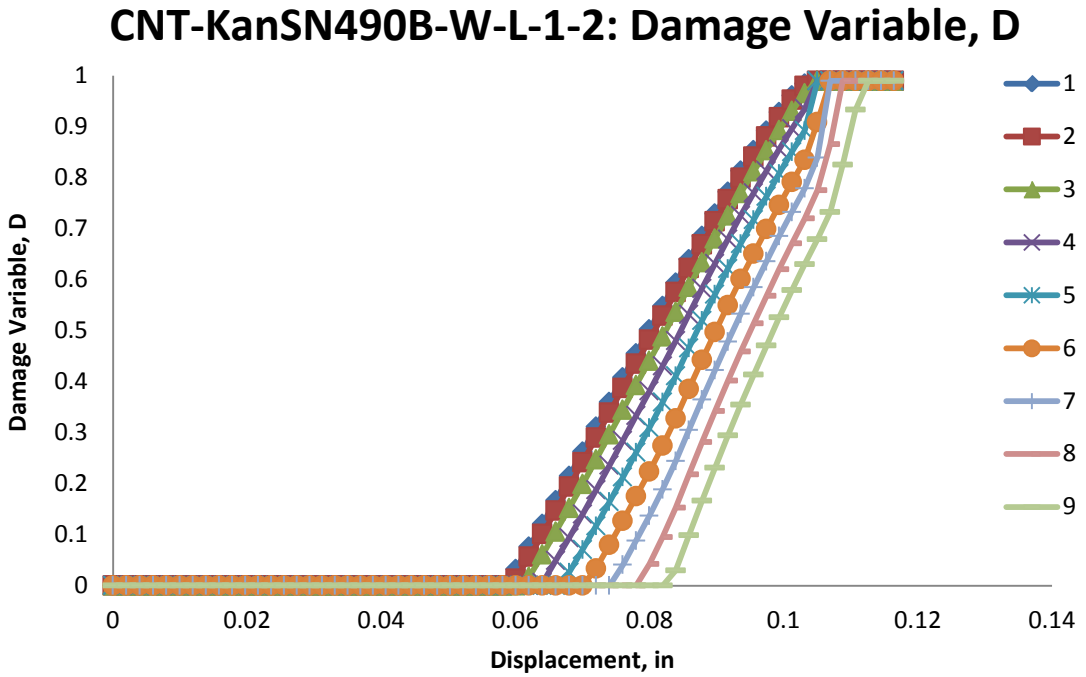

Figure B. 137: Variation of damage variable with displacement for different elements laid out through the thickness of simulation of CNT-KanSN490B-W-L-1-2 specimens

B.10 Location of Chosen Elements in Weld Calibration

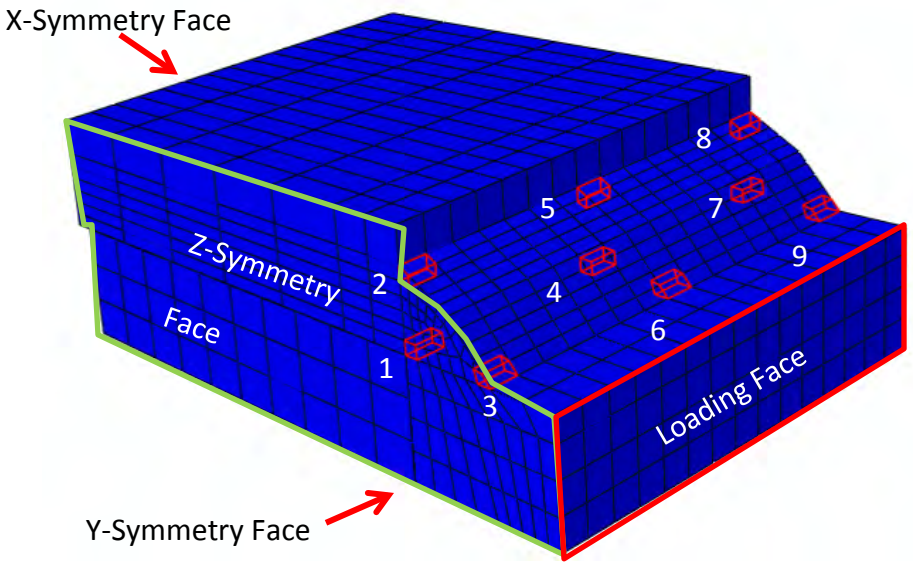

Figure B. 138: Boundary conditions and selected elements for study of fracture initiation and propagation parameters in LPT-NgE70-T4-P-6.4A, LPT-NgE70-T7-P-6.4A, LPT-NgE70T-7K2-P-6.4A, and LPT-NgE70T-8K6-P-6.4A specimens

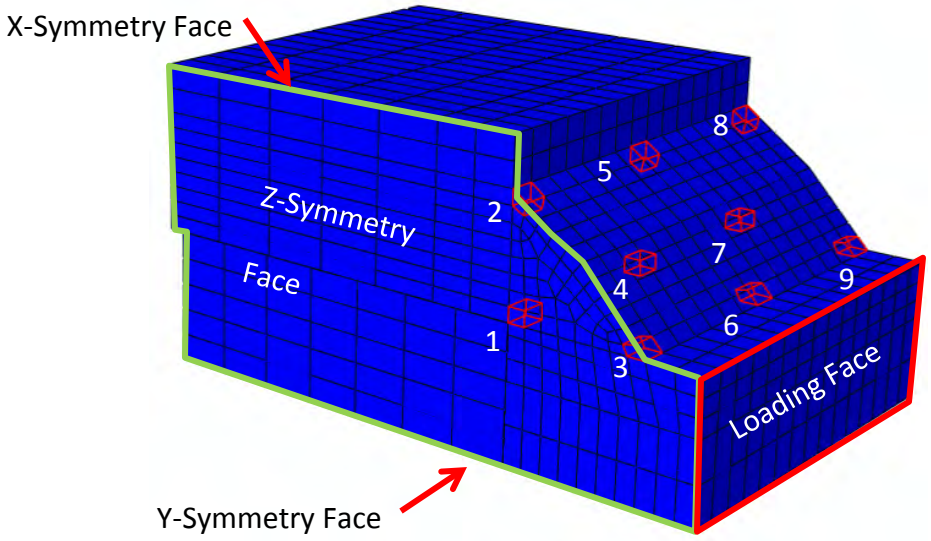

Figure B. 139: Boundary conditions and selected elements for study of fracture initiation and propagation parameters in LPT-NgE70-T4-P-12.7A, LPT-NgE70-T7-P-12.7A, LPT-NgE70T-7K2-P-12.7A, and LPT-NgE70T-8K6-P-12.7A specimens

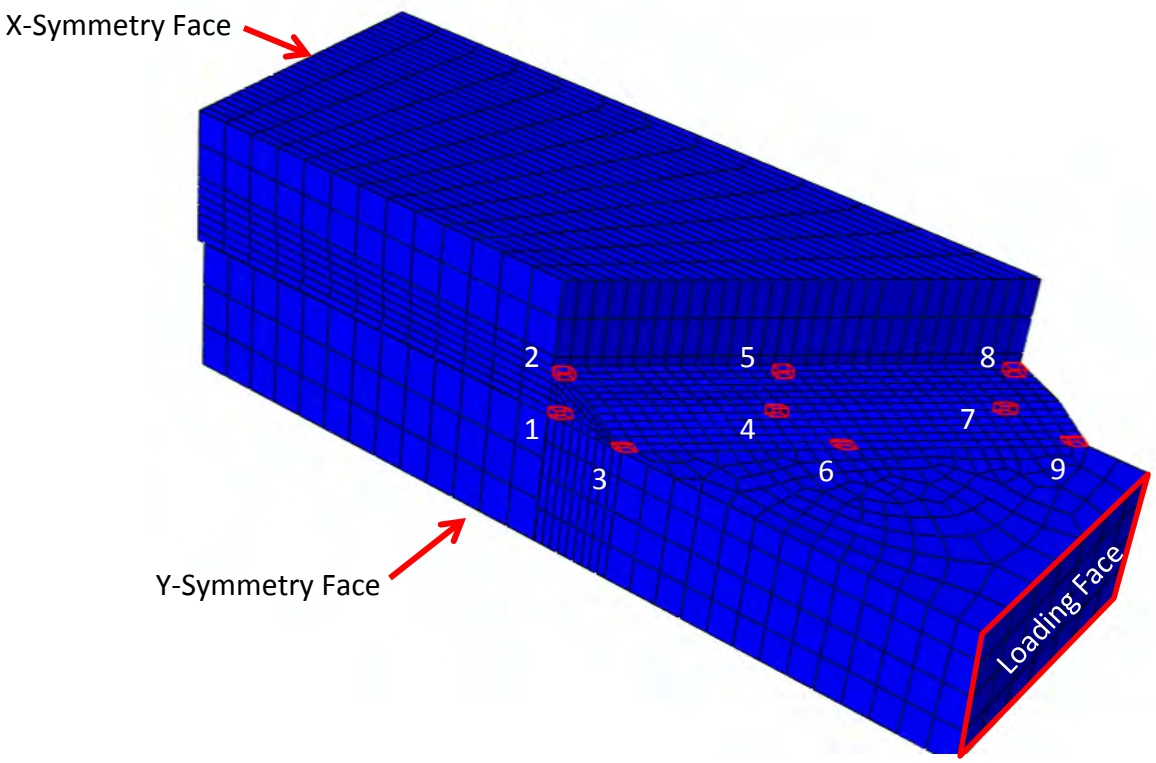

Figure B. 140: Boundary conditions and selected elements for study of fracture initiation and propagation parameters in LP45-DenE70-T4-P-12.7A, LP45-DenE70-T7-P-12.7A, and LP45-DenE70T-8K6-P-12.7A specimens

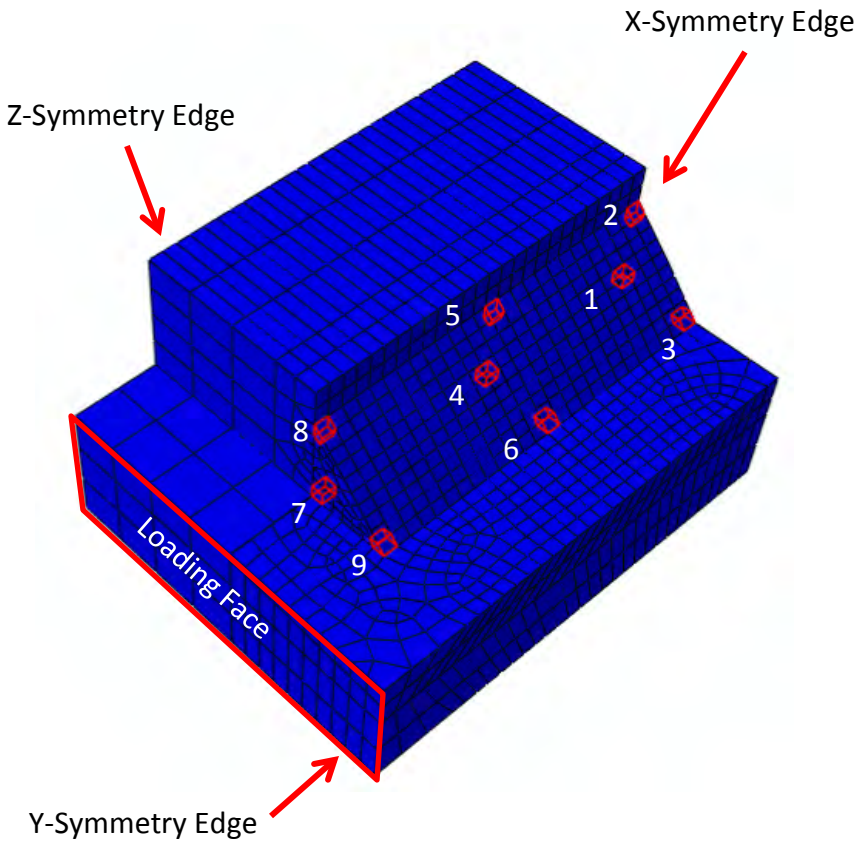

Figure B. 141: Boundary conditions and selected elements for study of fracture initiation and propagation parameters in LPL-DenE70-T4-P-12.7A, LPL-DenE70-T7-P-12.7A, and LPL-DenE70T-8K6-P-12.7A specimens

B.11 LPT-NgE70-T4-P-6.4A

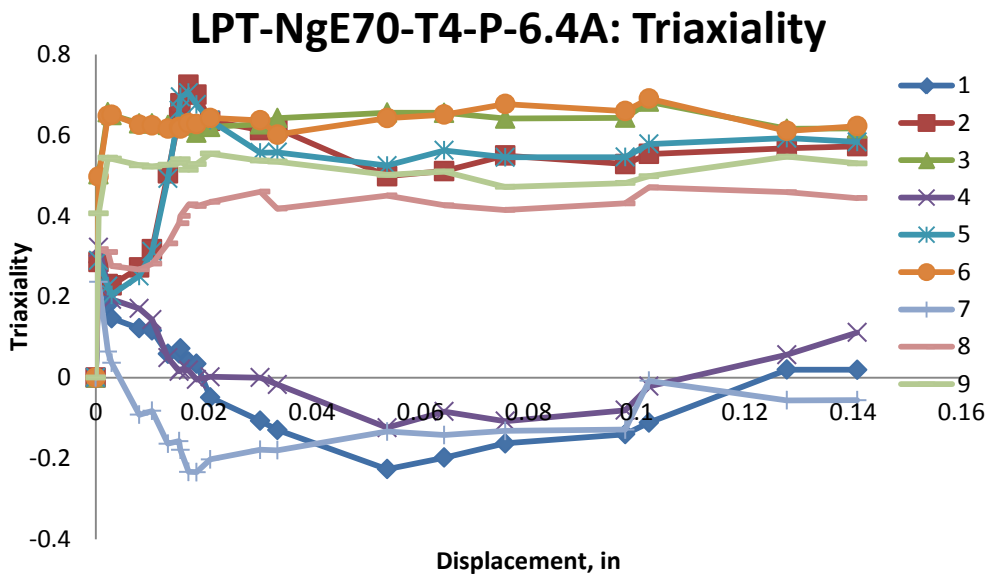

Figure B. 142: Variation of triaxiality with displacement for different elements laid out through the thickness of simulation of LPT-NgE70-T4-P-6.4A specimens

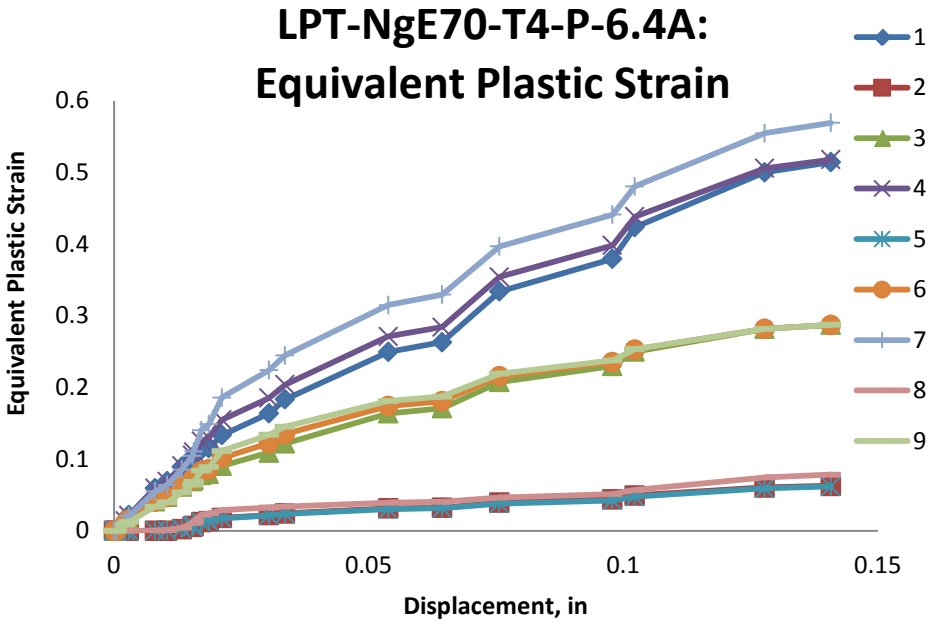

Figure B. 143: Variation of equivalent plastic strain with displacement for different elements laid out through the thickness of simulation of LPT-NgE70-T4-P-6.4A specimens

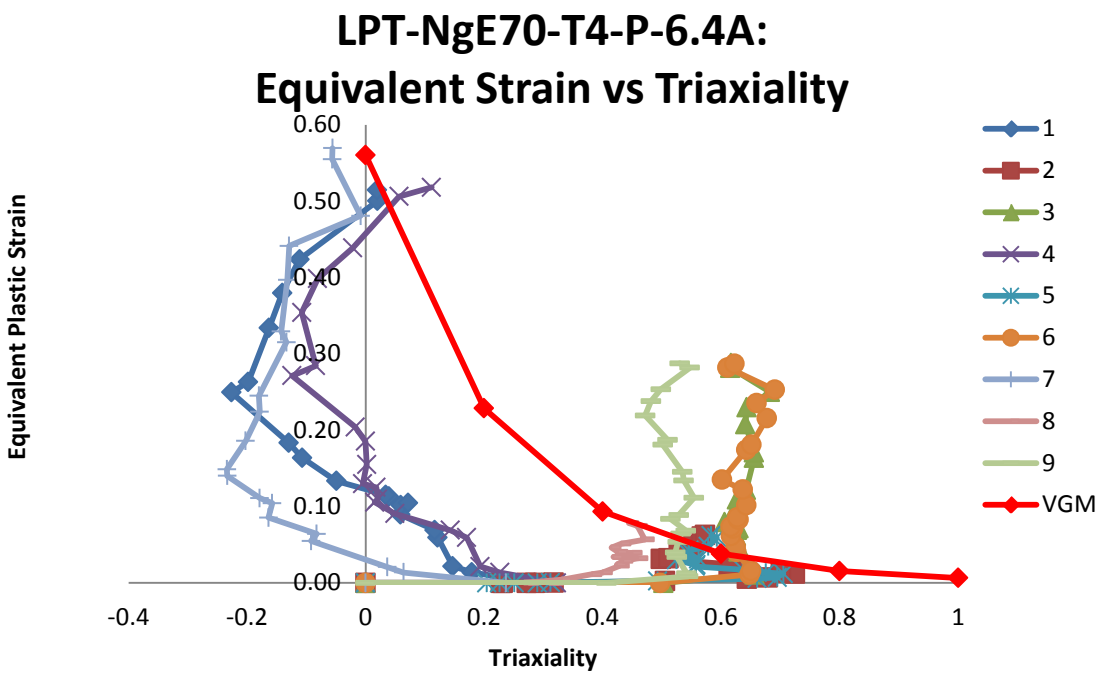

Figure B. 144: Variation of equivalent plastic strain versus triaxiality for different elements laid out through the thickness of simulation of LPT-NgE70-T4-P-6.4A specimens

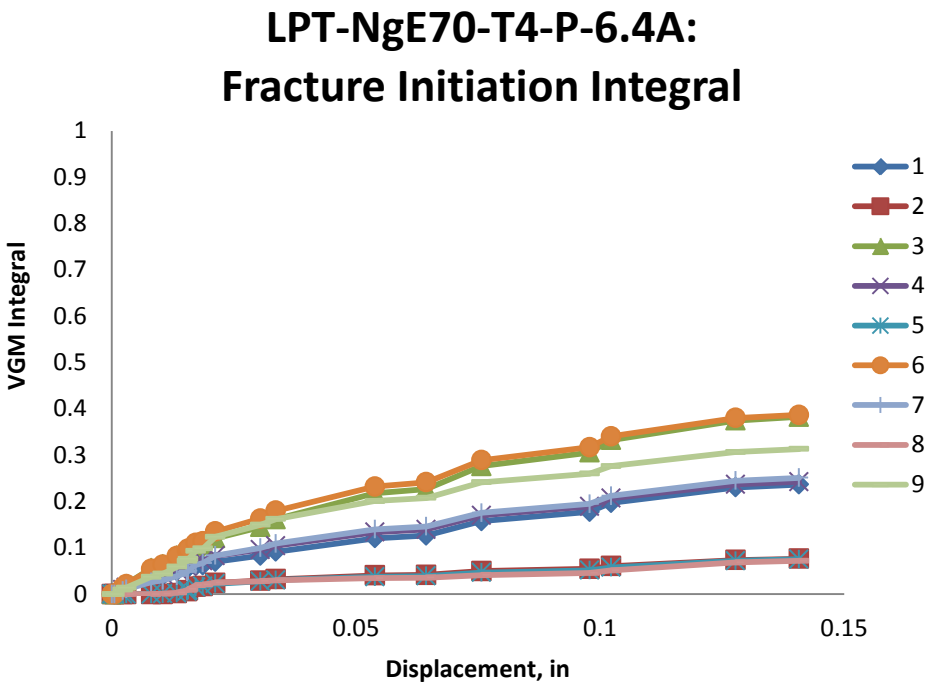

Figure B. 145: Value of fracture initiation integral for different elements laid out through the thickness of simulation of LPT-NgE70-T4-P-6.4A specimens

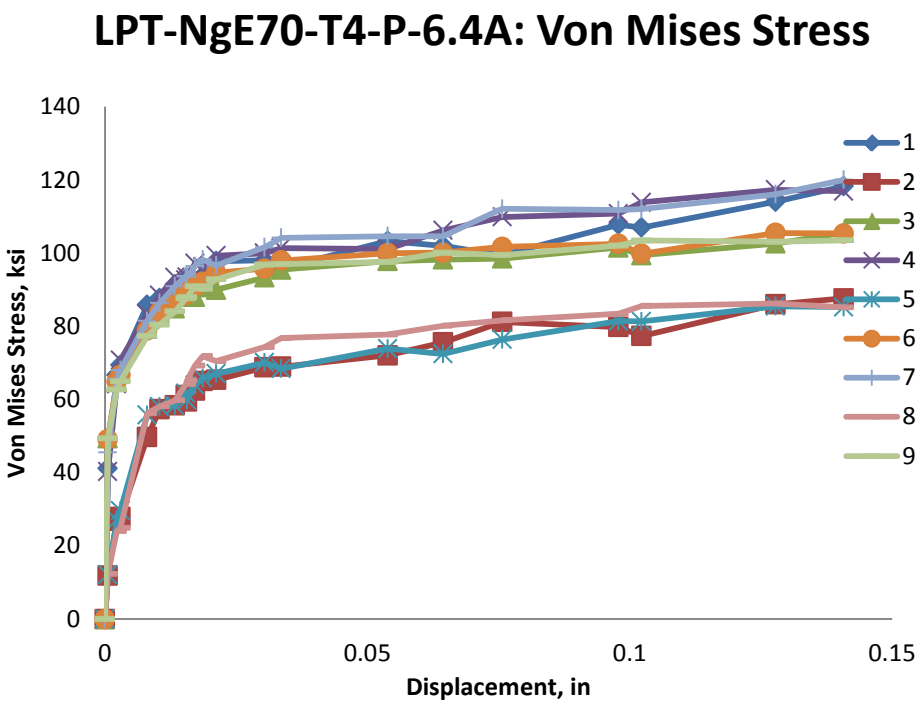

Figure B. 146: Variation of von Mises stress versus displacement for different elements laid out through the thickness of simulation of LPT-NgE70-T4-P-6.4A specimens

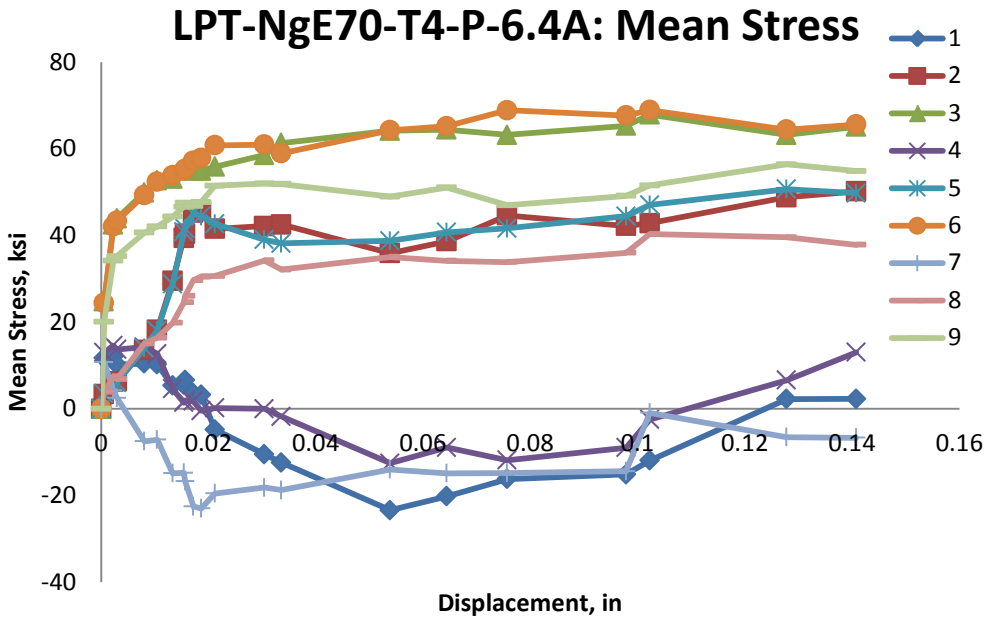

Figure B. 147: Variation of mean stress versus displacement for different elements laid out through the thickness of simulation of LPT-NgE70-T4-P-6.4A specimens

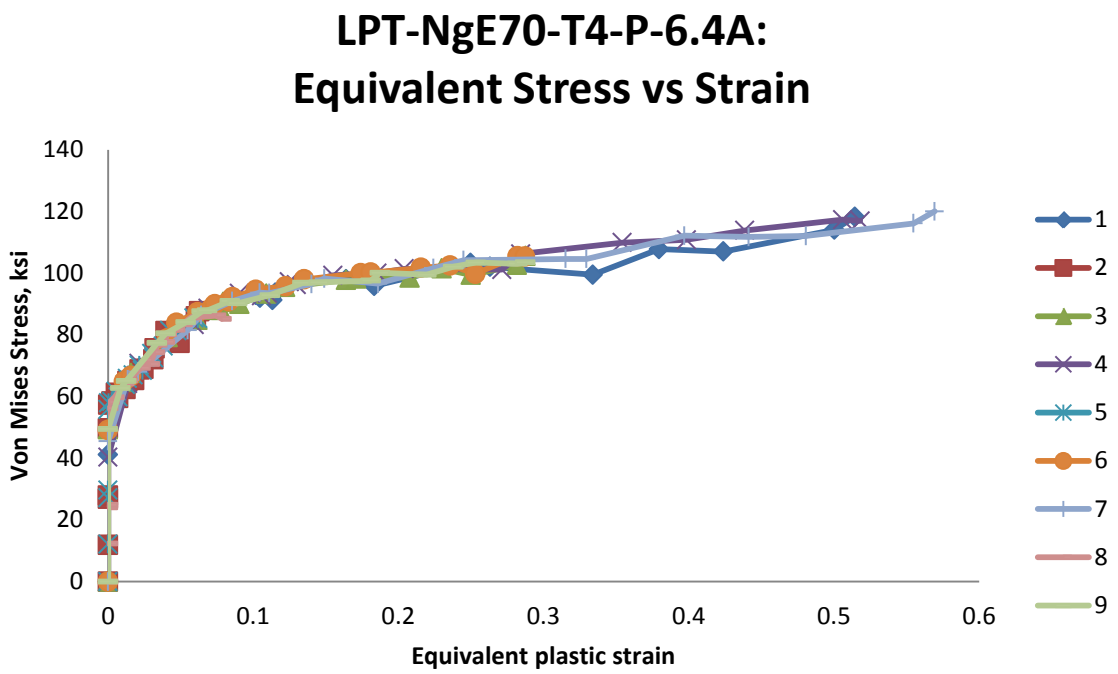

Figure B. 148: Variation of von Mises stress versus equivalent plastic strain for different elements laid out through the thickness of simulation of LPT-NgE70-T4-P-6.4A specimens

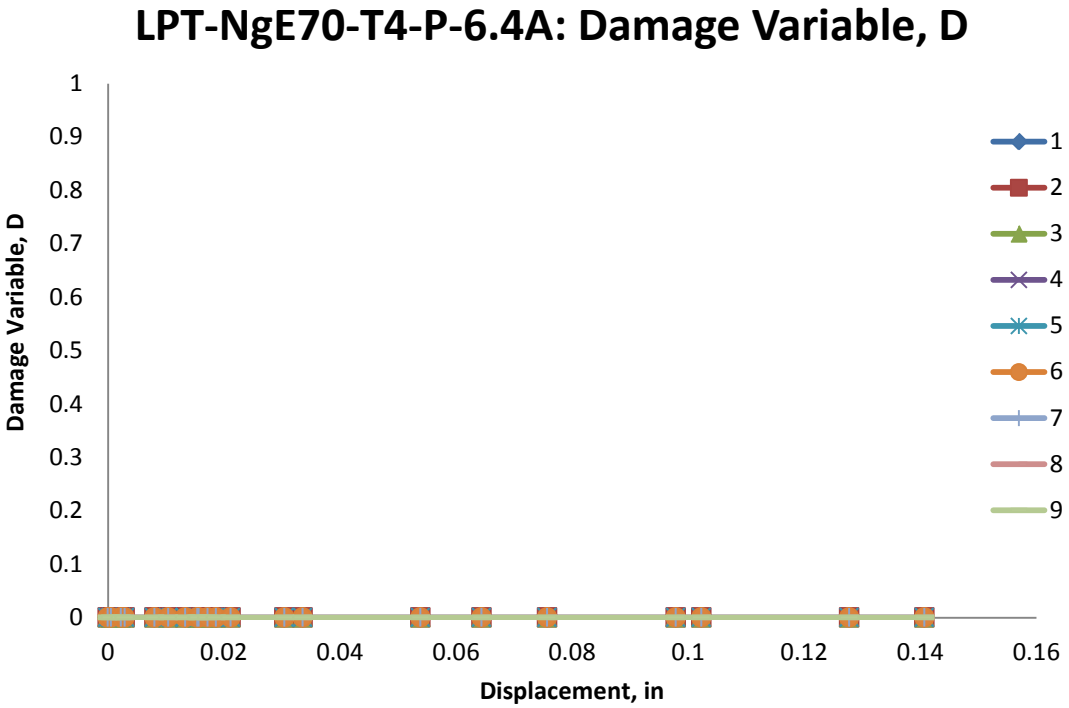

Figure B. 149: Variation of damage variable with displacement for different elements laid out through the thickness of simulation of LPT-NgE70-T4-P-6.4A specimens

B.12 LPT-NgE70-T7-P-6.4A

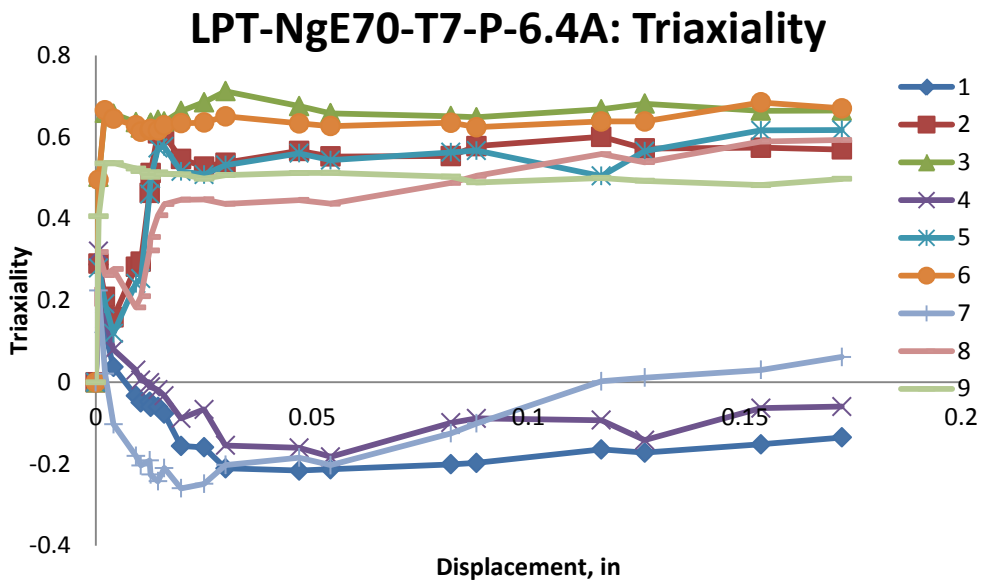

Figure B. 150: Variation of triaxiality with displacement for different elements laid out through the thickness of simulation of LPT-NgE70-T7-P-6.4A specimens

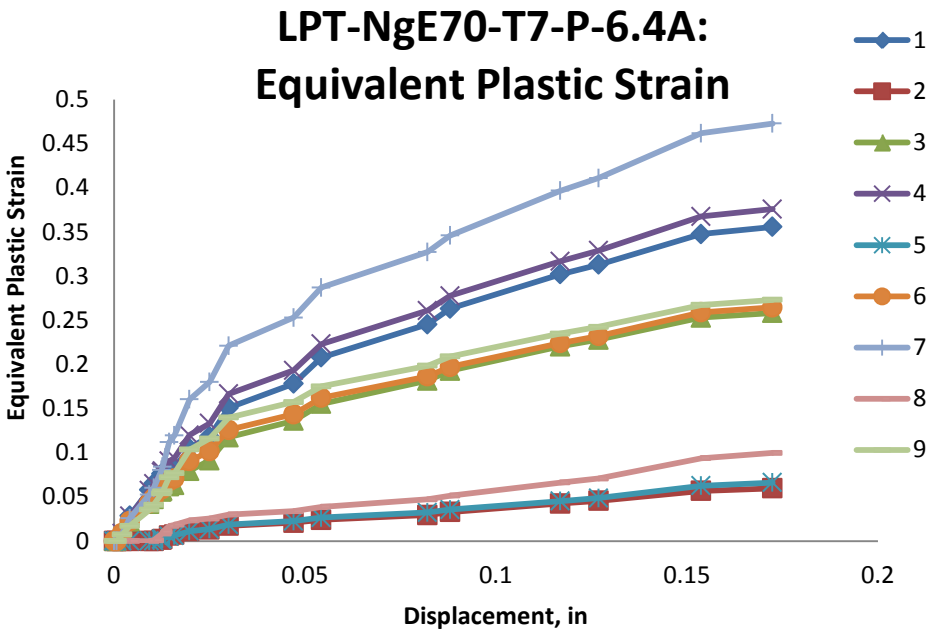

Figure B. 151: Variation of equivalent plastic strain with displacement for different elements laid out through the thickness of simulation of LPT-NgE70-T7-P-6.4A specimens

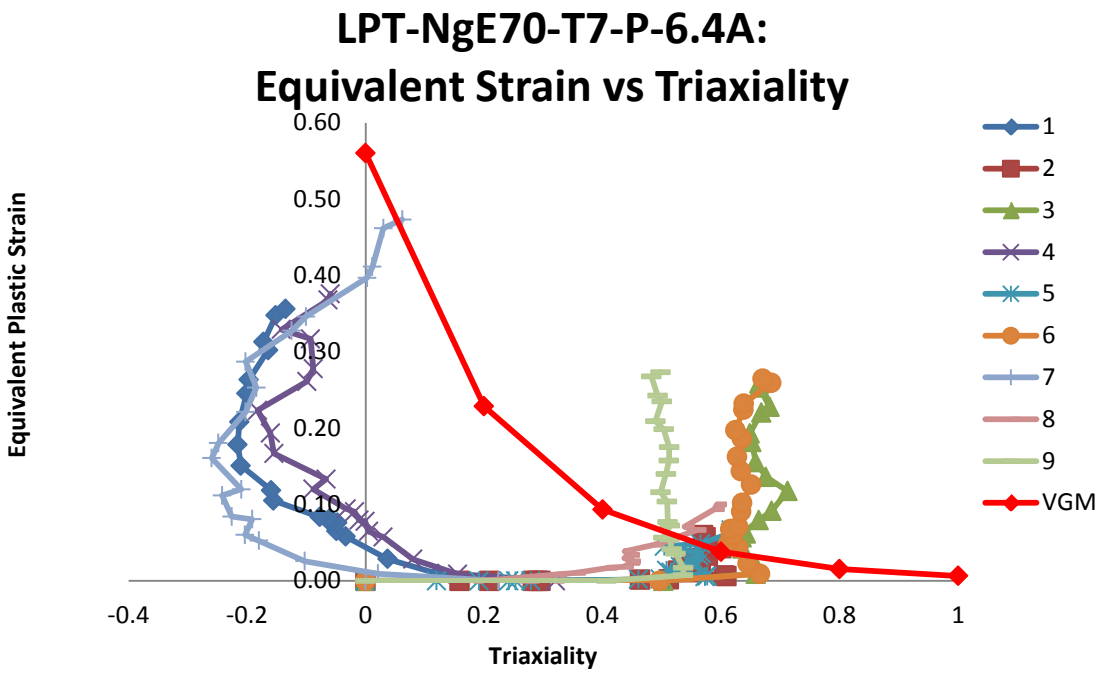

Figure B. 152: Variation of equivalent plastic strain versus triaxiality for different elements laid out through the thickness of simulation of LPT-NgE70-T7-P-6.4A specimens

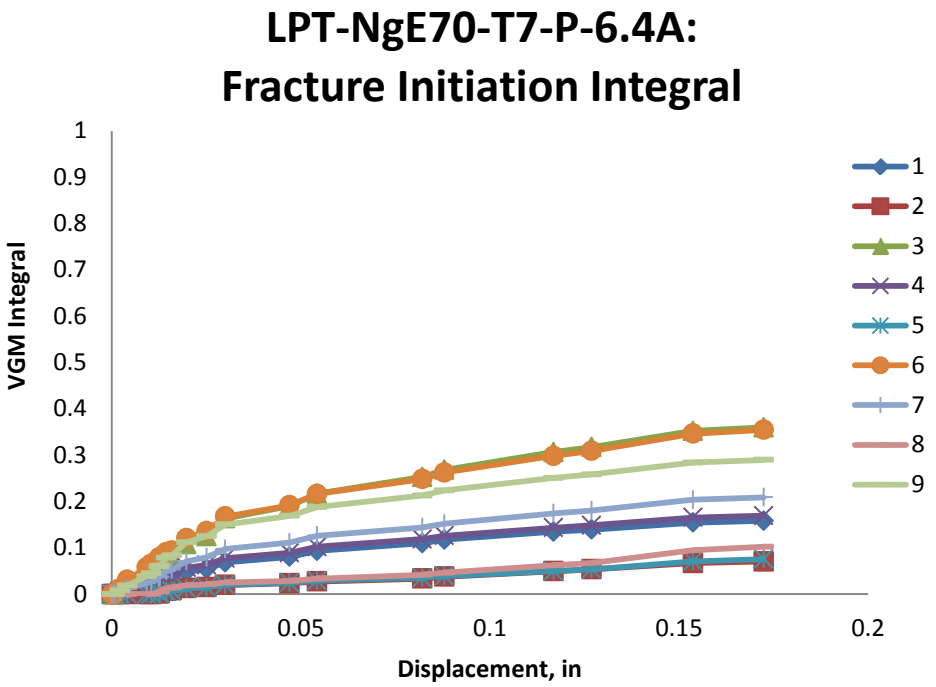

Figure B. 153: Value of fracture initiation integral for different elements laid out through the thickness of simulation of LPT-NgE70-T7-P-6.4A specimens

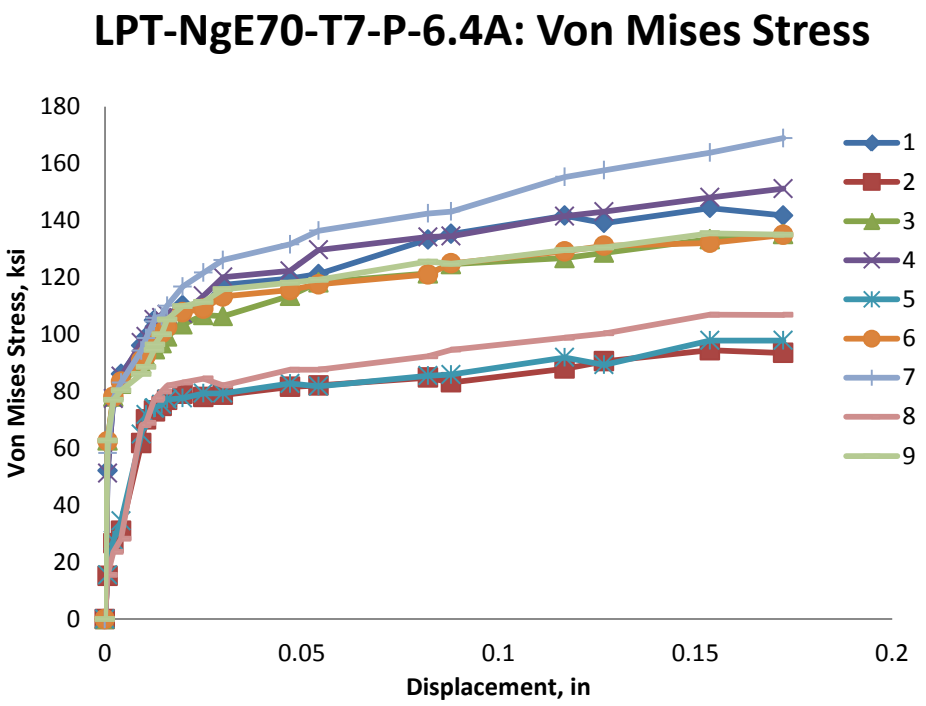

Figure B. 154: Variation of von Mises stress versus displacement for different elements laid out through the thickness of simulation of LPT-NgE70-T7-P-6.4A specimens

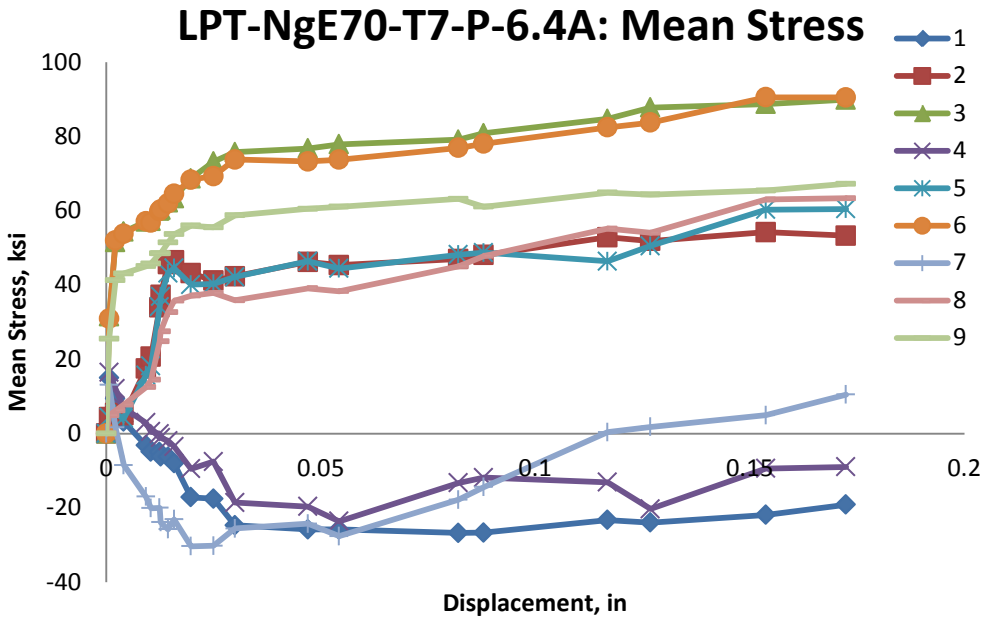

Figure B. 155: Variation of mean stress versus displacement for different elements laid out through the thickness of simulation of LPT-NgE70-T7-P-6.4A specimens

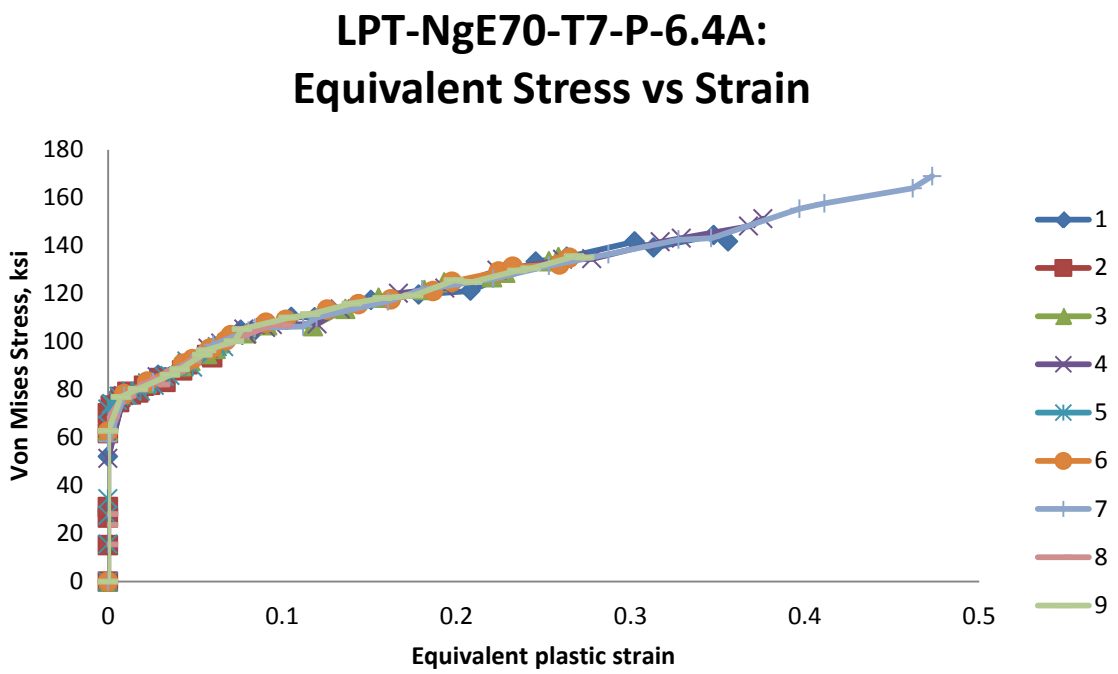

Figure B. 156: Variation of von Mises stress versus equivalent plastic strain for different elements laid out through the thickness of simulation of LPT-NgE70-T7-P-6.4A specimens

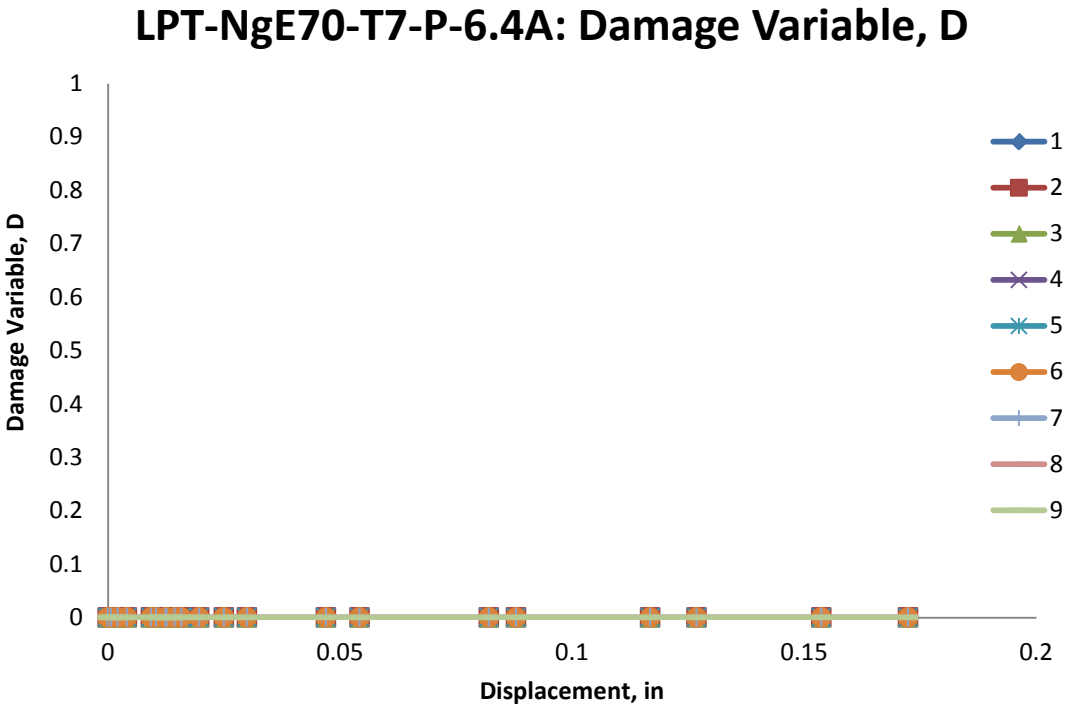

Figure B. 157: Variation of damage variable with displacement for different elements laid out through the thickness of simulation of LPT-NgE70-T7-P-6.4A specimens

B.13 LPT-NgE70T-7K2-P-6.4A

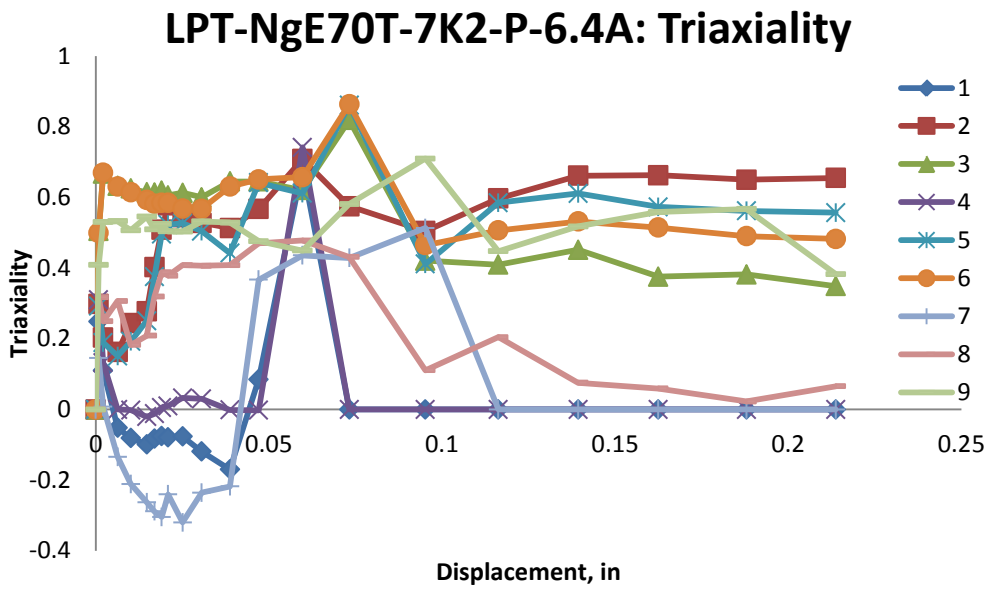

Figure B. 158: Variation of triaxiality with displacement for different elements laid out through the thickness of simulation of LPT-NgE70T-7K2-P-6.4A specimens

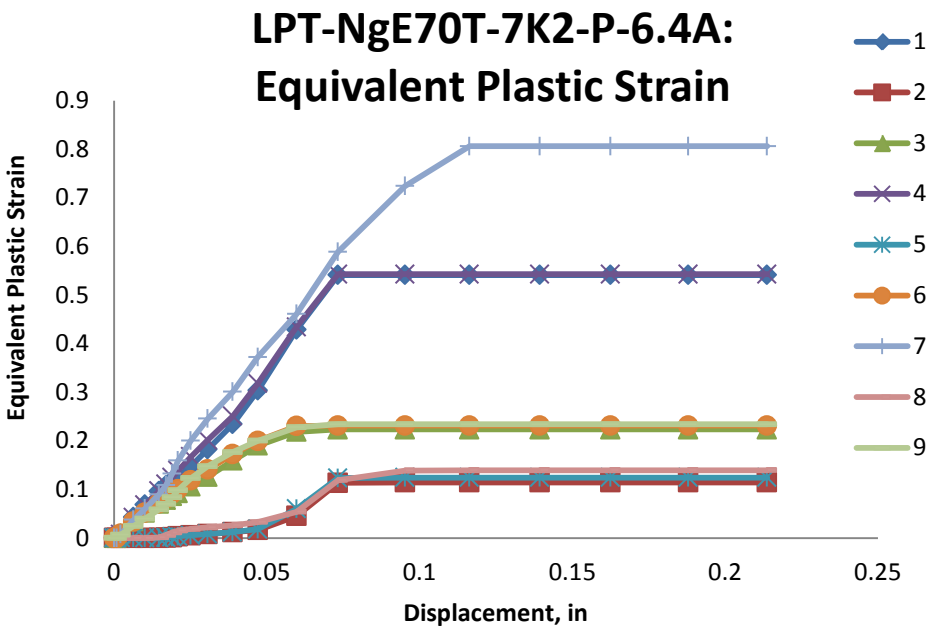

Figure B. 159: Variation of equivalent plastic strain with displacement for different elements laid out through the thickness of simulation of LPT-NgE70T-7K2-P-6.4A specimens

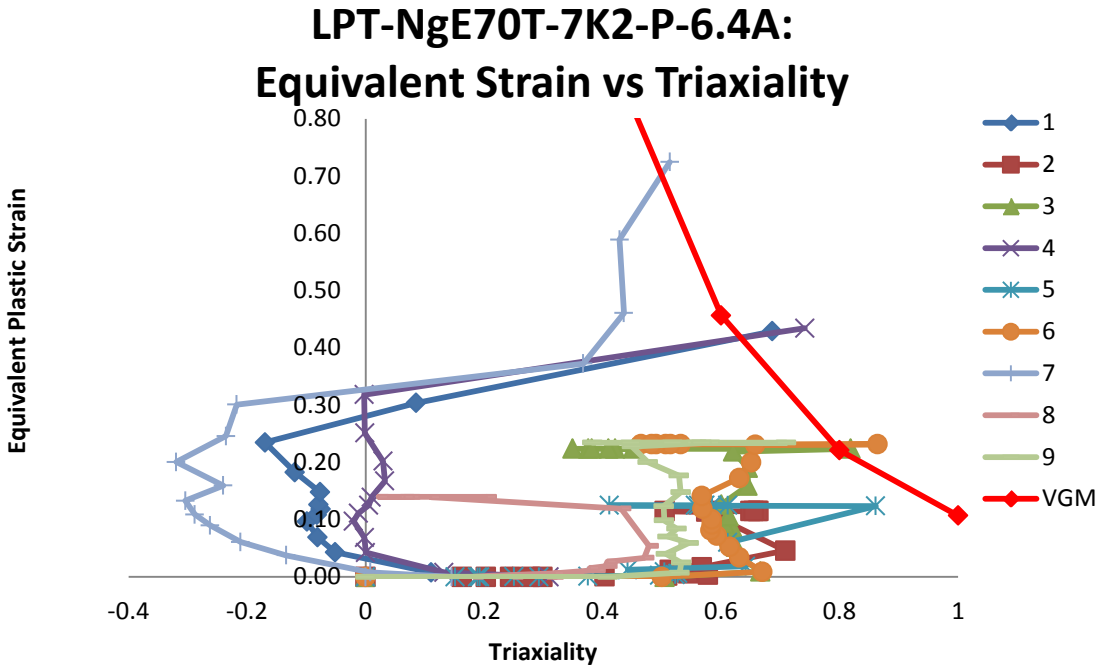

Figure B. 160: Variation of equivalent plastic strain versus triaxiality for different elements laid out through the thickness of simulation of LPT-NgE70T-7K2-P-6.4A specimens

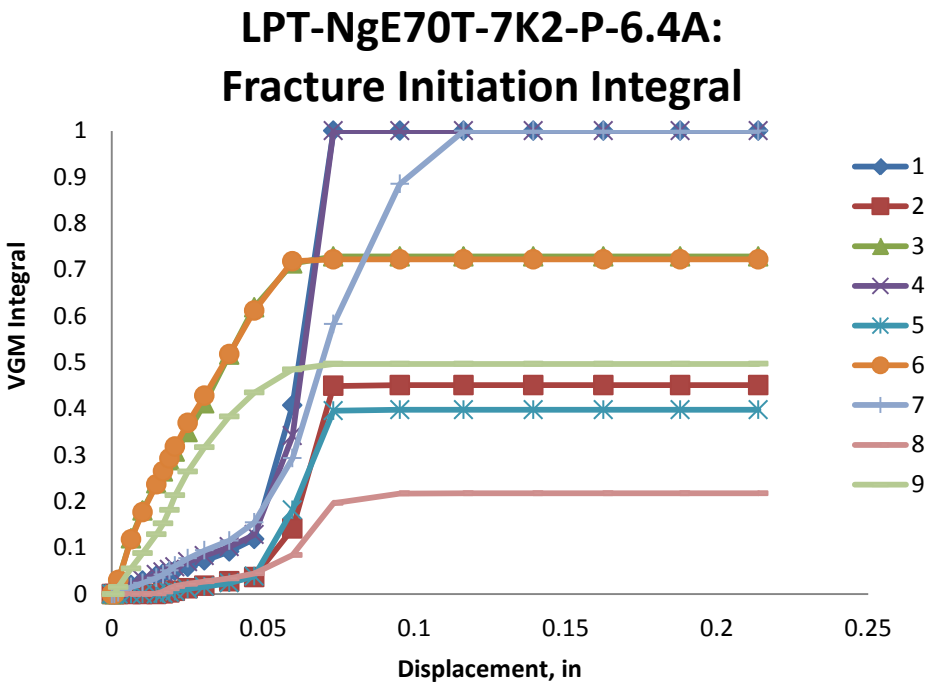

Figure B. 161: Value of fracture initiation integral for different elements laid out through the thickness of simulation of LPT-NgE70T-7K2-P-6.4A specimens

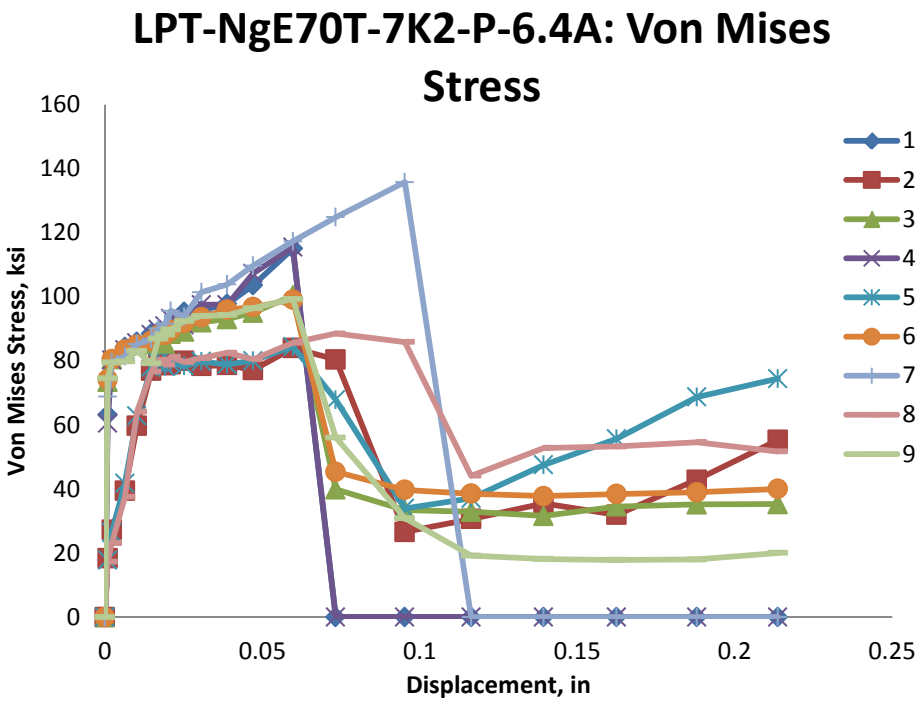

Figure B. 162: Variation of von Mises stress versus displacement for different elements laid out through the thickness of simulation of LPT-NgE70T-7K2-P-6.4A specimens

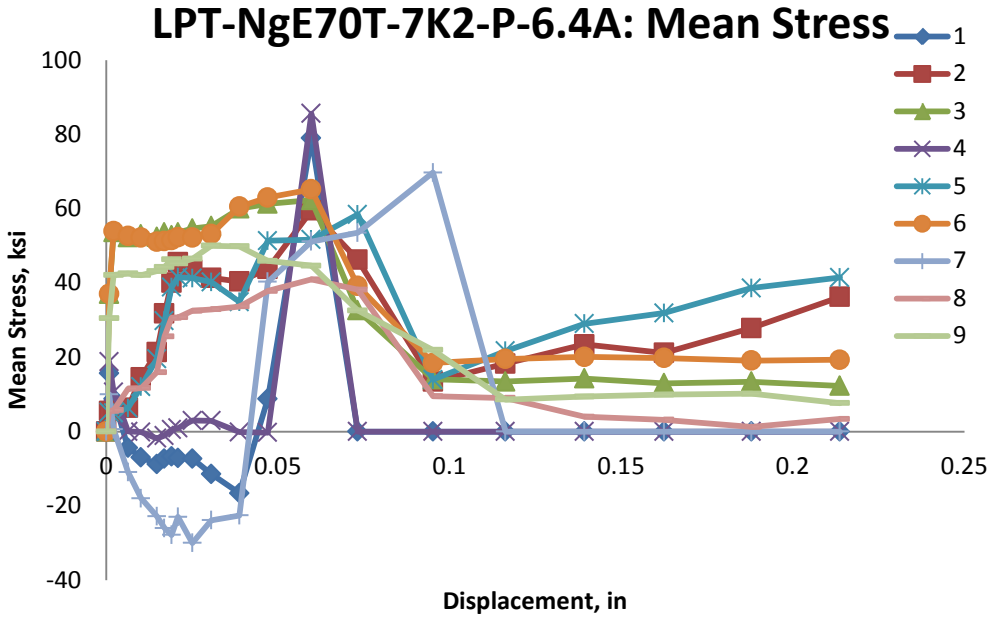

Figure B. 163: Variation of mean stress versus displacement for different elements laid out through the thickness of simulation of LPT-NgE70T-7K2-P-6.4A specimens

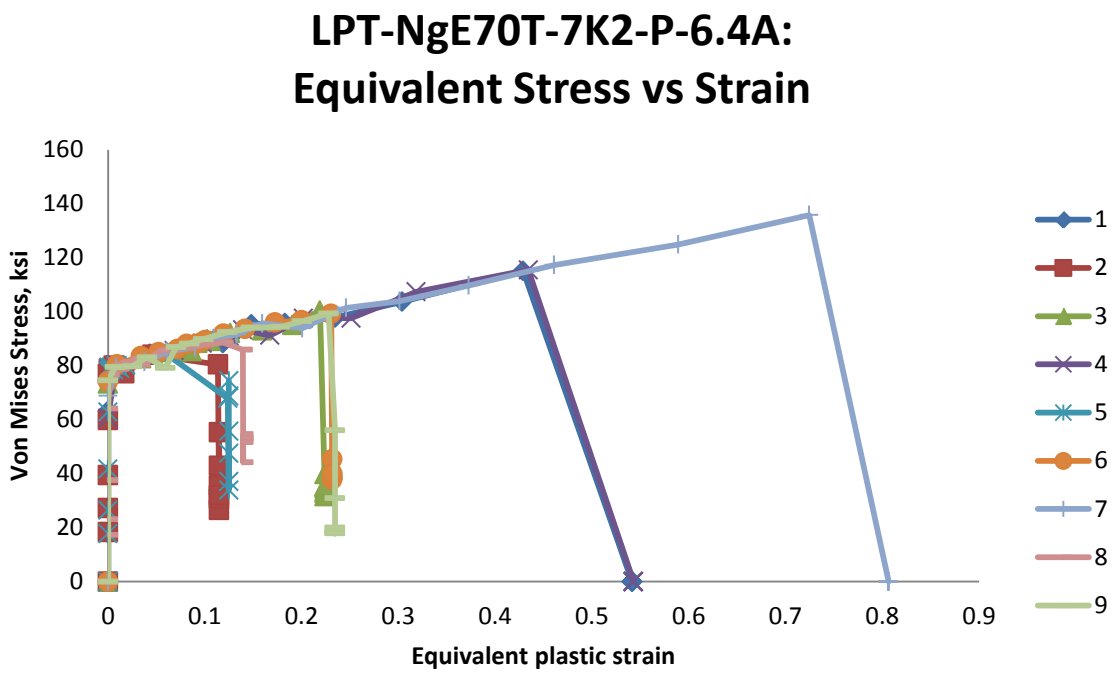

Figure B. 164: Variation of von Mises stress versus equivalent plastic strain for different elements laid out through the thickness of simulation of LPT-NgE70T-7K2-P-6.4A specimens

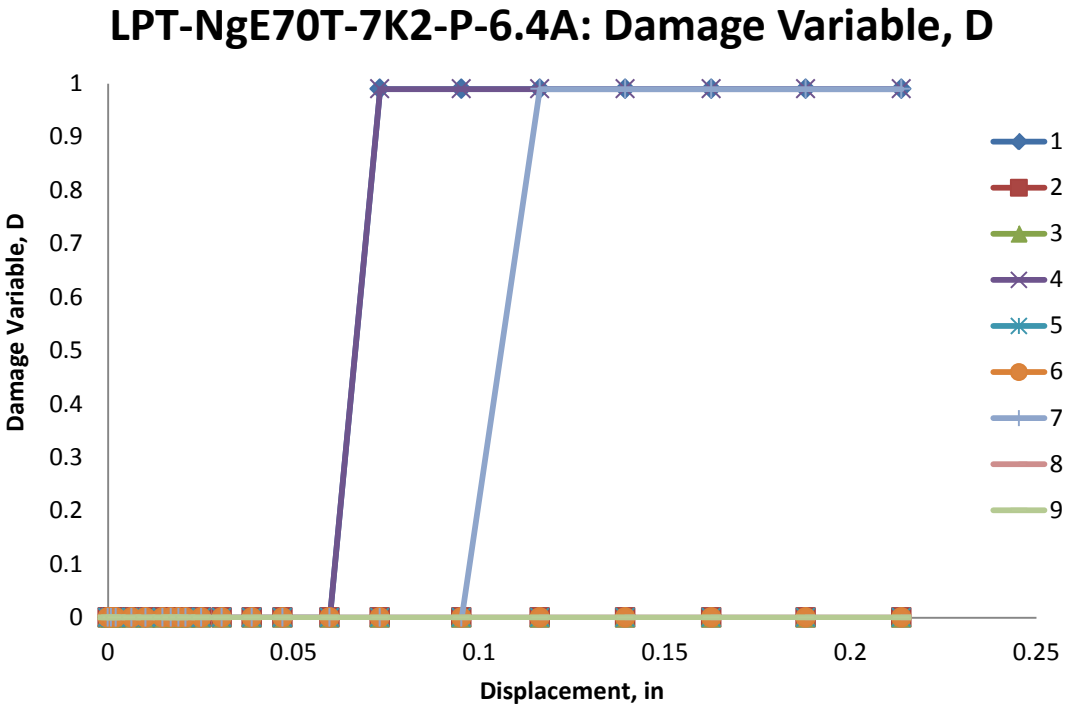

Figure B. 165: Variation of damage variable with displacement for different elements laid out through the thickness of simulation of LPT-NgE70T-7K2-P-6.4A specimens

B.14 LPT-NgE70T-8K6-P-6.4A

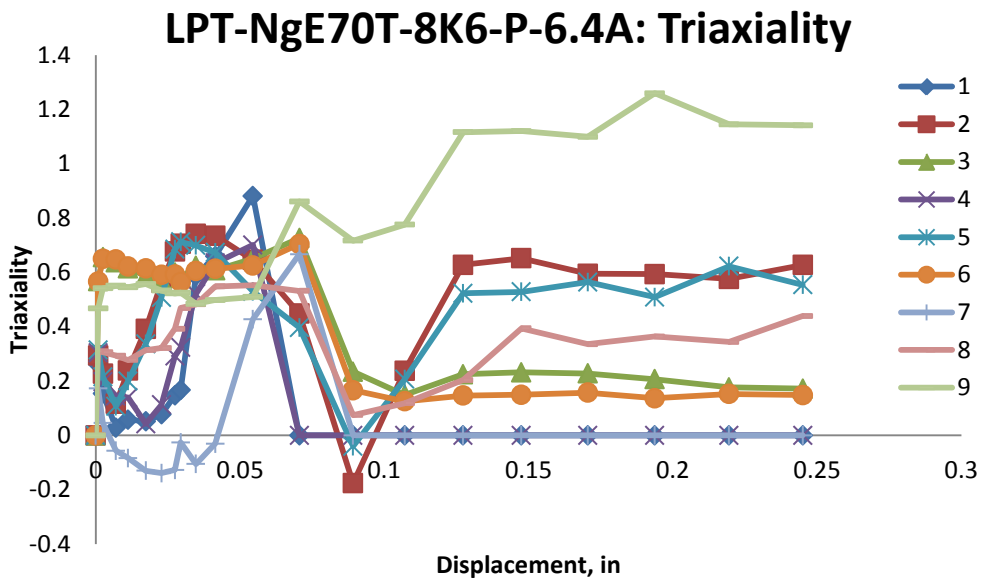

Figure B. 166: Variation of triaxiality with displacement for different elements laid out through the thickness of simulation of LPT-NgE70T-8K6-P-6.4A specimens

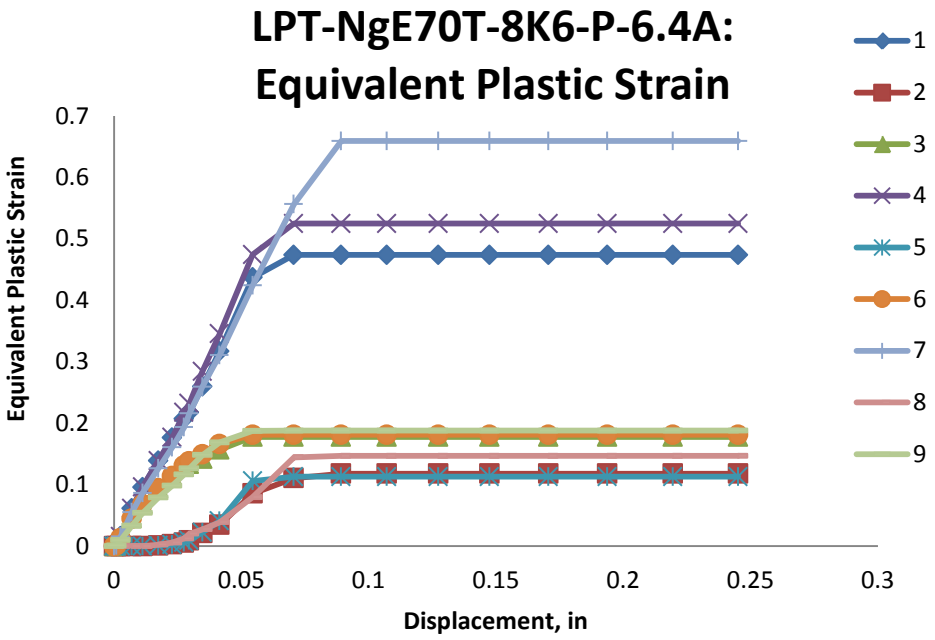

Figure B. 167: Variation of equivalent plastic strain with displacement for different elements laid out through the thickness of simulation of LPT-NgE70T-8K6-P-6.4A specimens

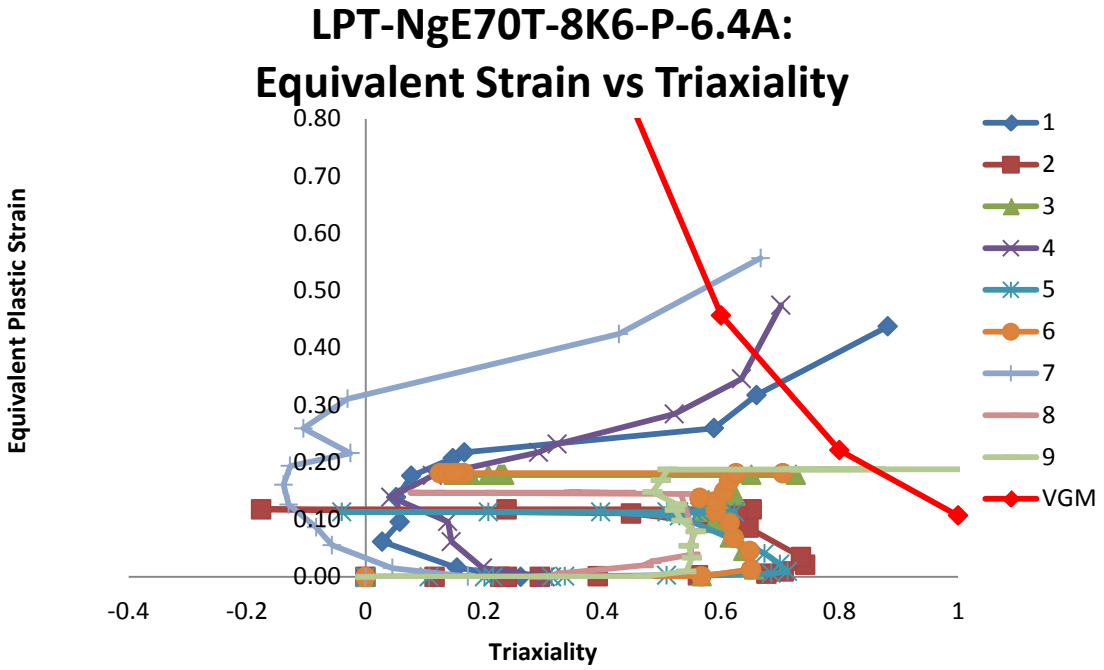

Figure B. 168: Variation of equivalent plastic strain versus triaxiality for different elements laid out through the thickness of simulation of LPT-NgE70T-8K6-P-6.4A specimens

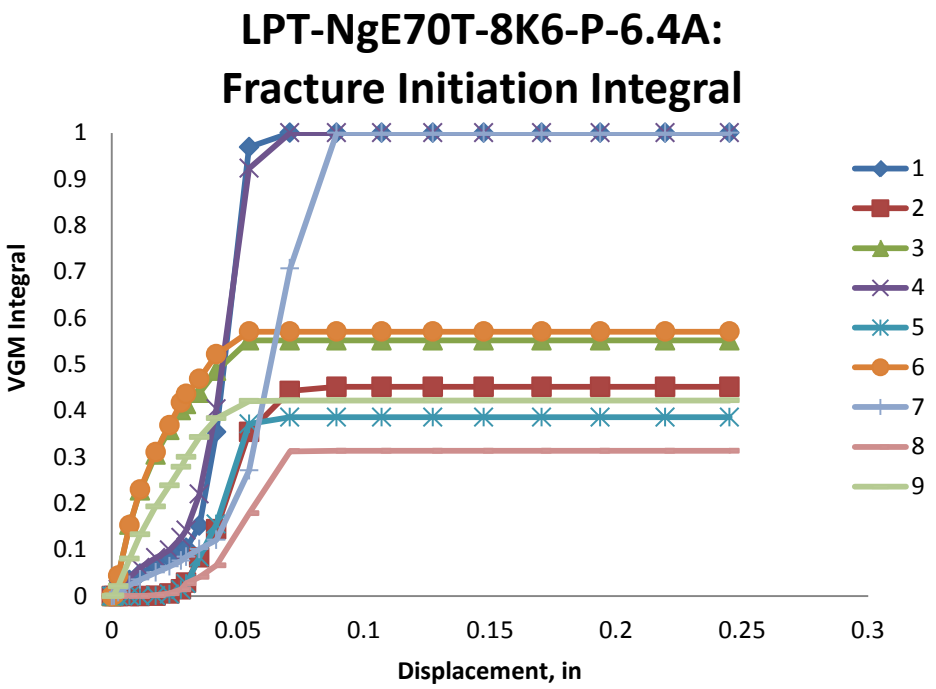

Figure B. 169: Value of fracture initiation integral for different elements laid out through the thickness of simulation of LPT-NgE70T-8K6-P-6.4A specimens

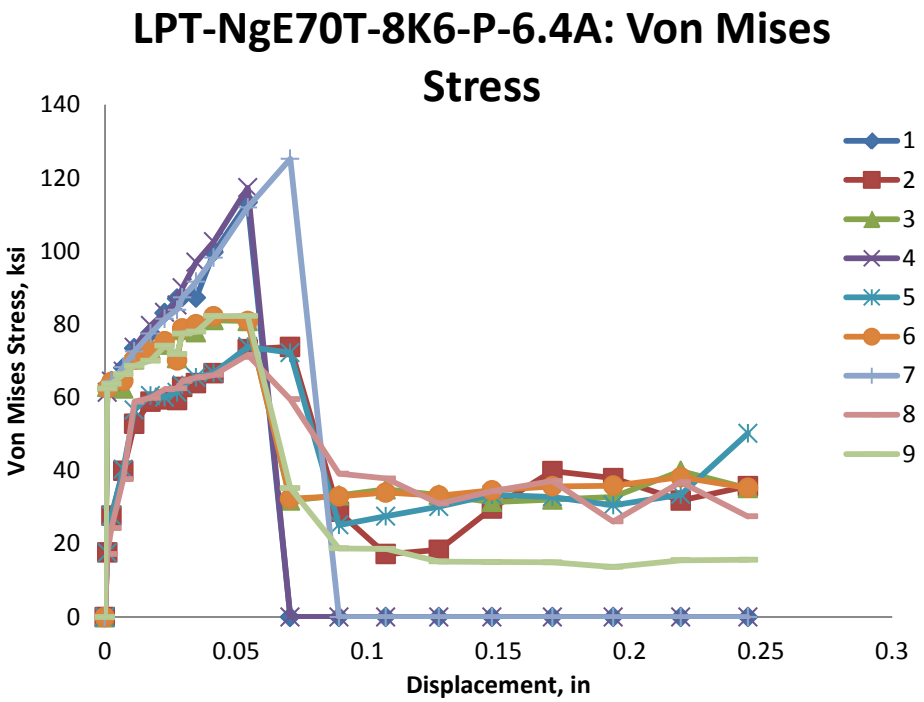

Figure B. 170: Variation of von Mises stress versus displacement for different elements laid out through the thickness of simulation of LPT-NgE70T-8K6-P-6.4A specimens

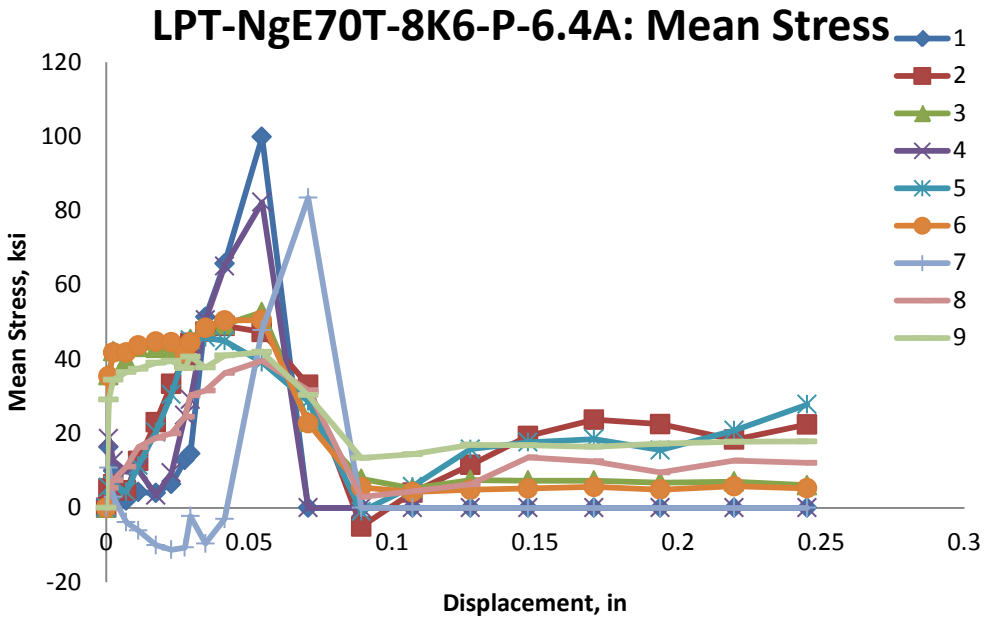

Figure B. 171: Variation of mean stress versus displacement for different elements laid out through the thickness of simulation of LPT-NgE70T-8K6-P-6.4A specimens

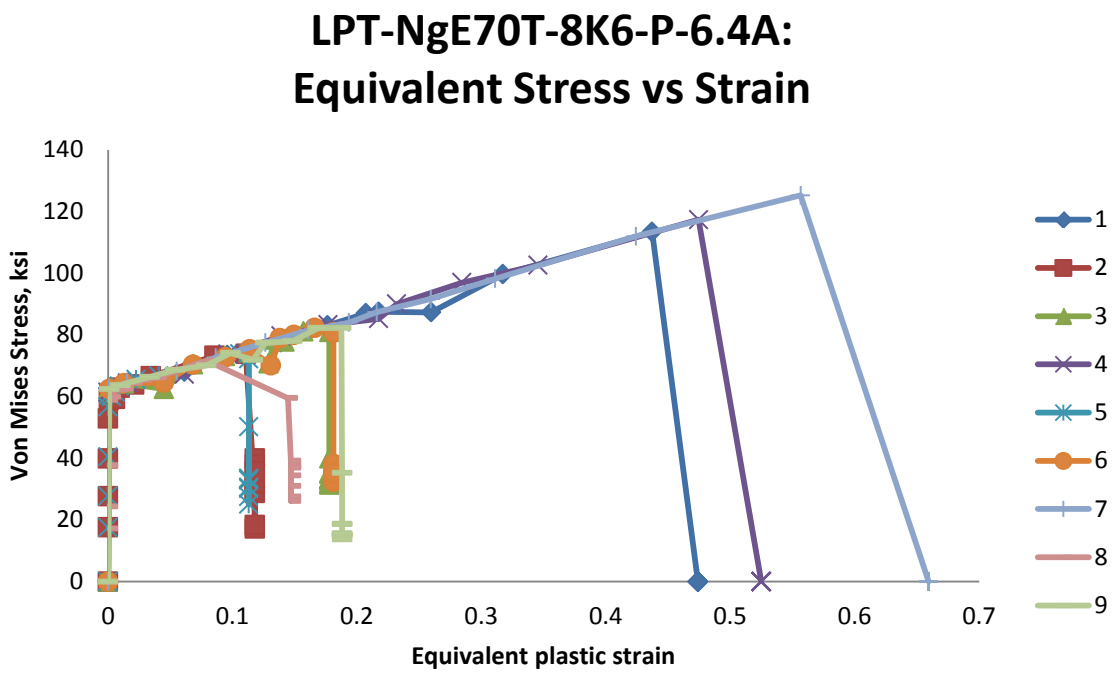

Figure B. 172: Variation of von Mises stress versus equivalent plastic strain for different elements laid out through the thickness of simulation of LPT-NgE70T-8K6-P-6.4A specimens

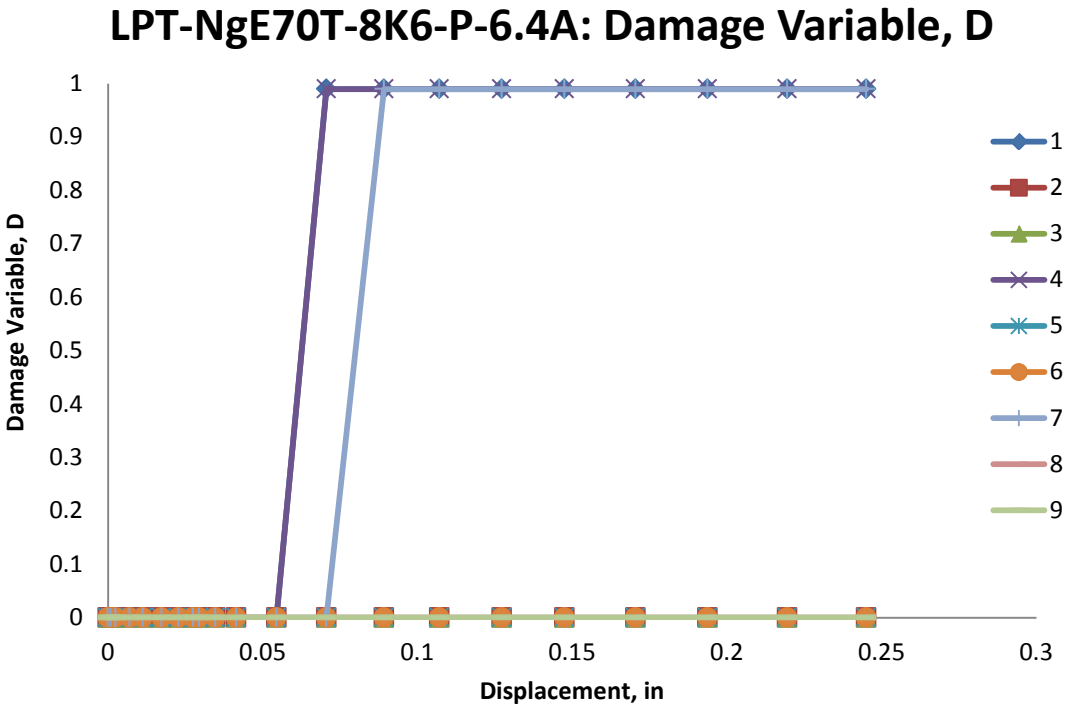

Figure B. 173: Variation of damage variable with displacement for different elements laid out through the thickness of simulation of LPT-NgE70T-8K6-P-6.4A specimens

B.15 LPT-NgE70-T4-P-12.7A

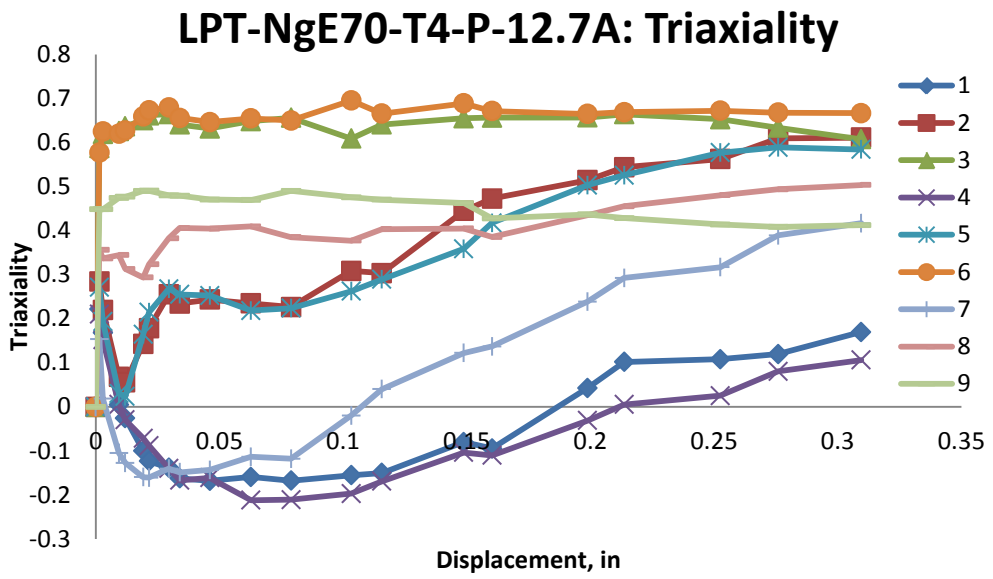

Figure B. 174: Variation of triaxiality with displacement for different elements laid out through the thickness of simulation of LPT-NgE70-T4-P-12.7A specimens

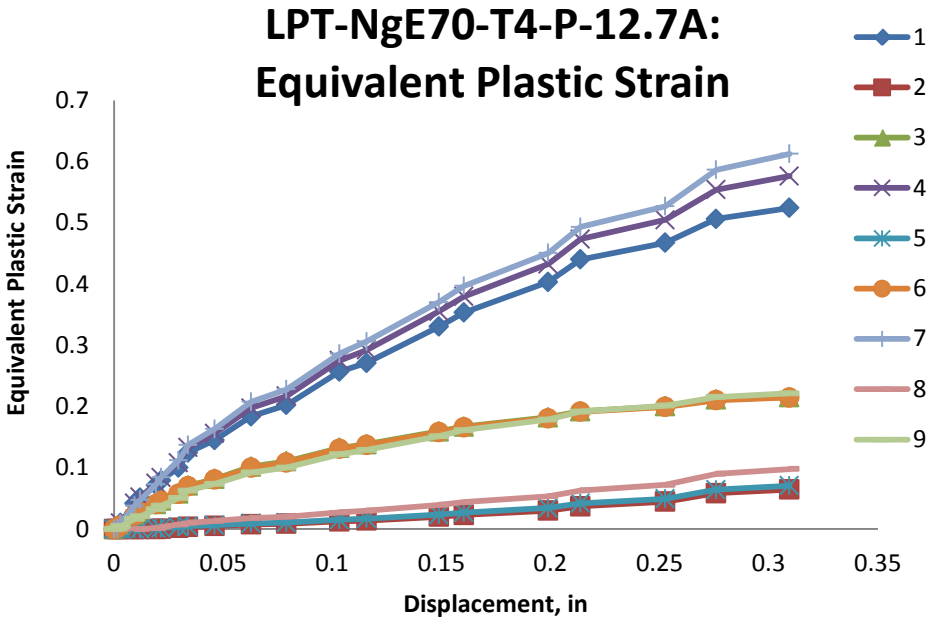

Figure B. 175: Variation of equivalent plastic strain with displacement for different elements laid out through the thickness of simulation of LPT-NgE70-T4-P-12.7A specimens

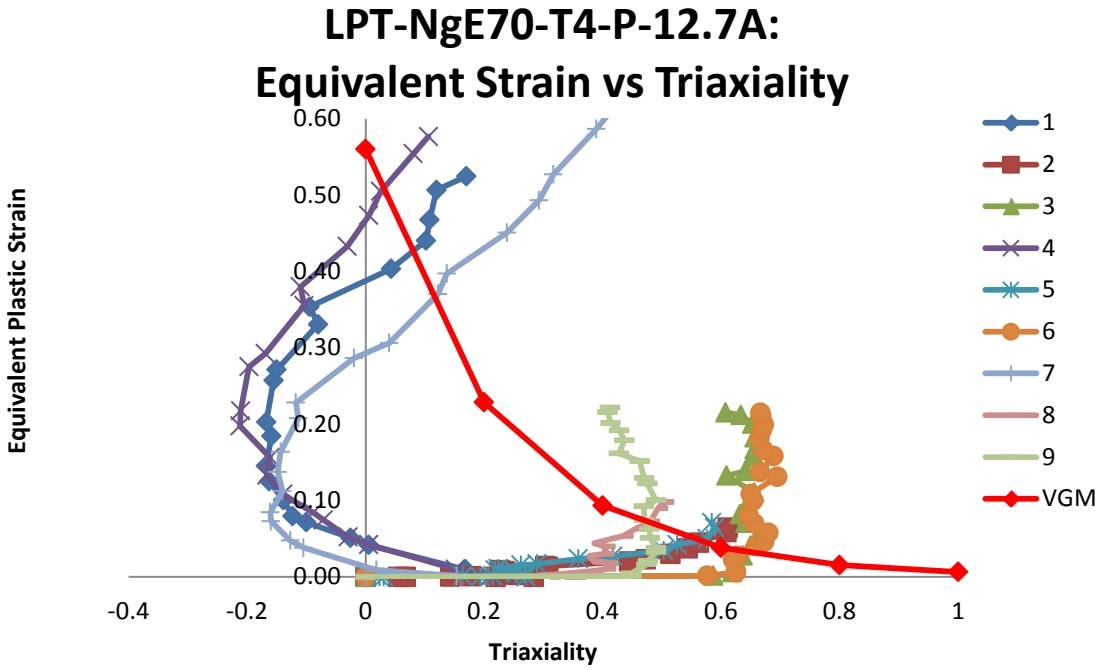

Figure B. 176: Variation of equivalent plastic strain versus triaxiality for different elements laid out through the thickness of simulation of LPT-NgE70-T4-P-12.7A specimens

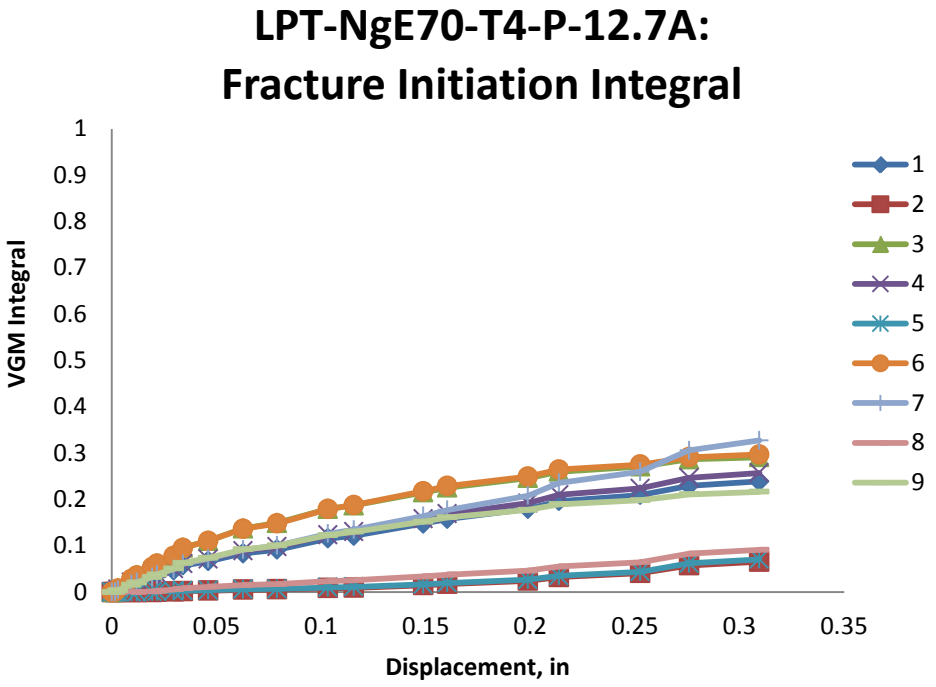

Figure B. 177: Value of fracture initiation integral for different elements laid out through the thickness of simulation of LPT-NgE70-T4-P-12.7A specimens

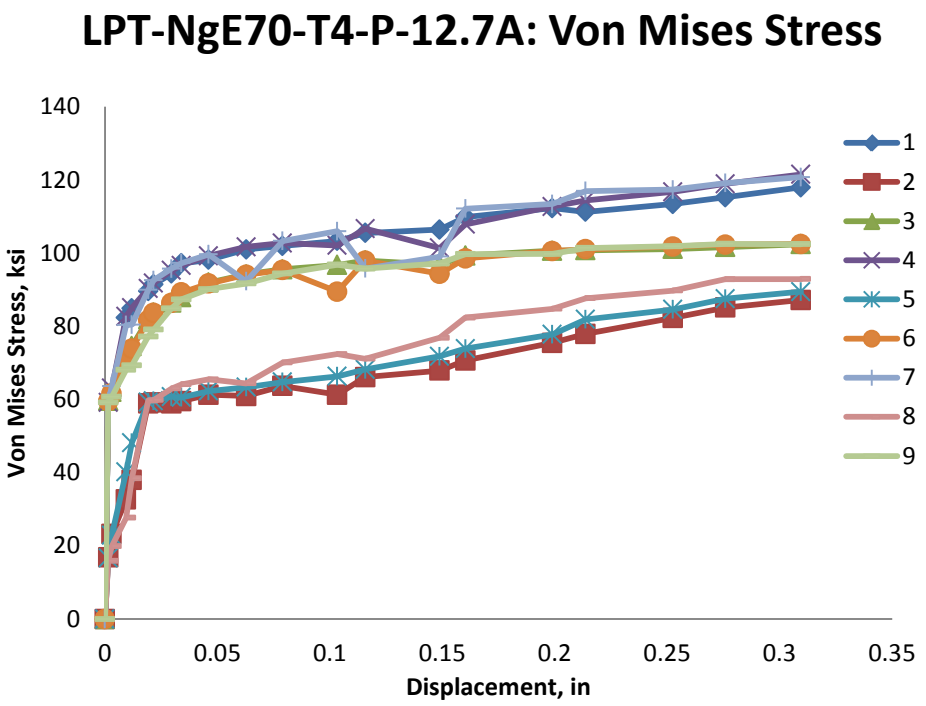

Figure B. 178: Variation of von Mises stress versus displacement for different elements laid out through the thickness of simulation of LPT-NgE70-T4-P-12.7A specimens

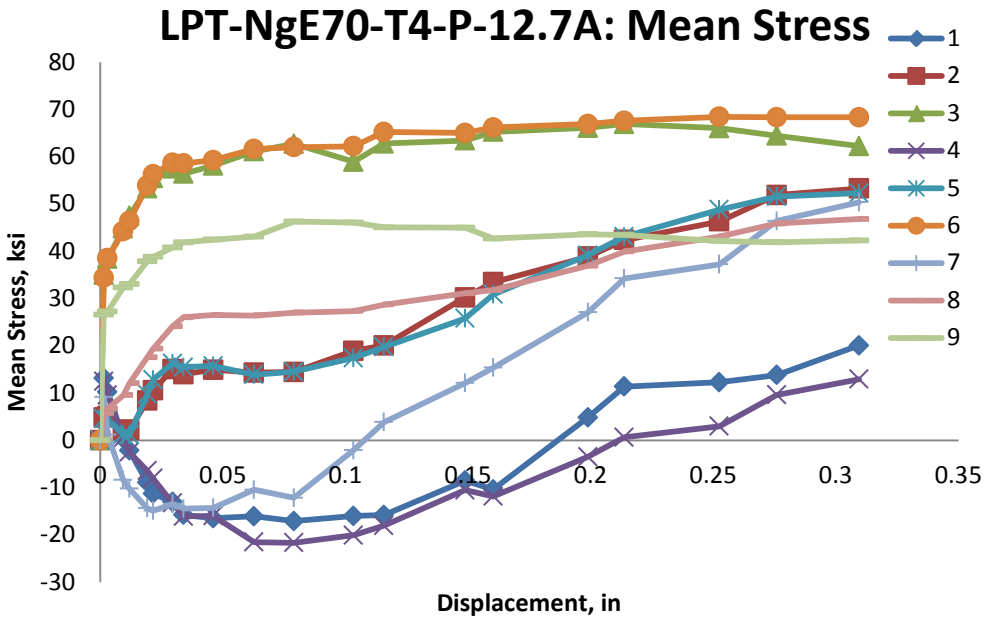

Figure B. 179: Variation of mean stress versus displacement for different elements laid out through the thickness of simulation of LPT-NgE70-T4-P-12.7A specimens

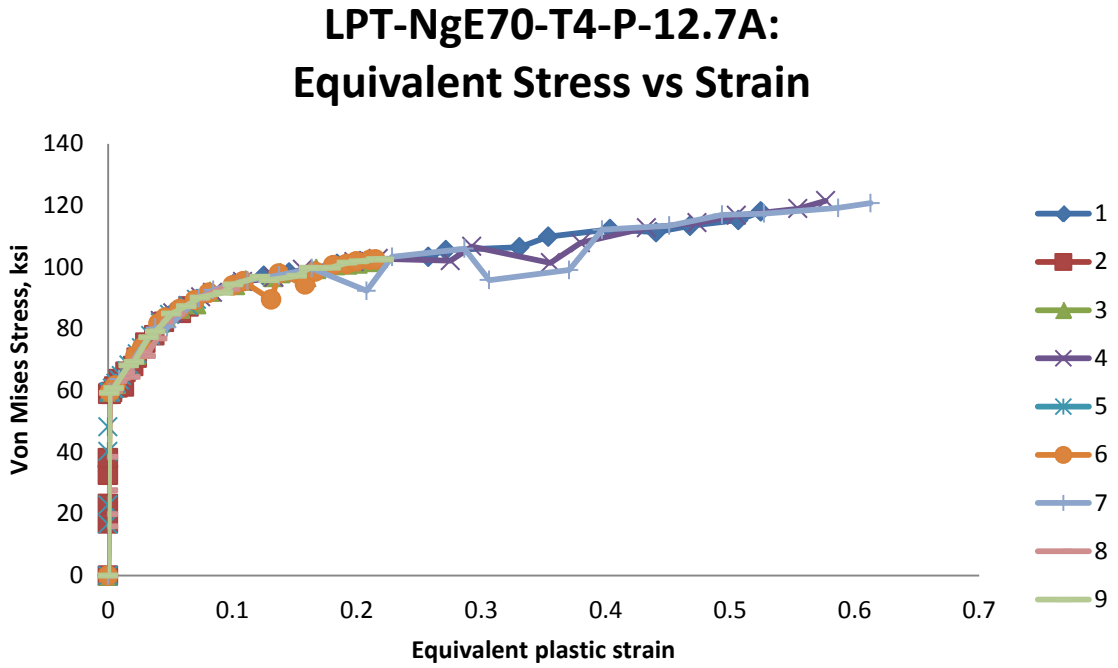

Figure B. 180: Variation of von Mises stress versus equivalent plastic strain for different elements laid out through the thickness of simulation of LPT-NgE70-T4-P-12.7A specimens

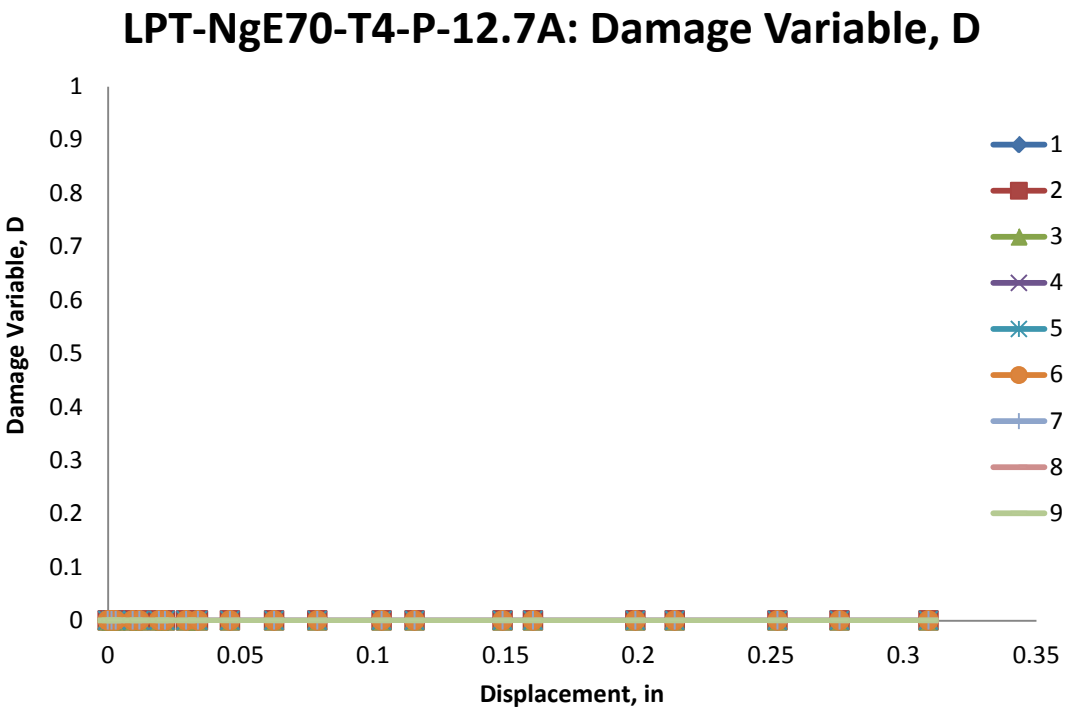

Figure B. 181: Variation of damage variable with displacement for different elements laid out through the thickness of simulation of LPT-NgE70-T4-P-12.7A specimens

B.16 LPT-NgE70-T7-P-12.7A

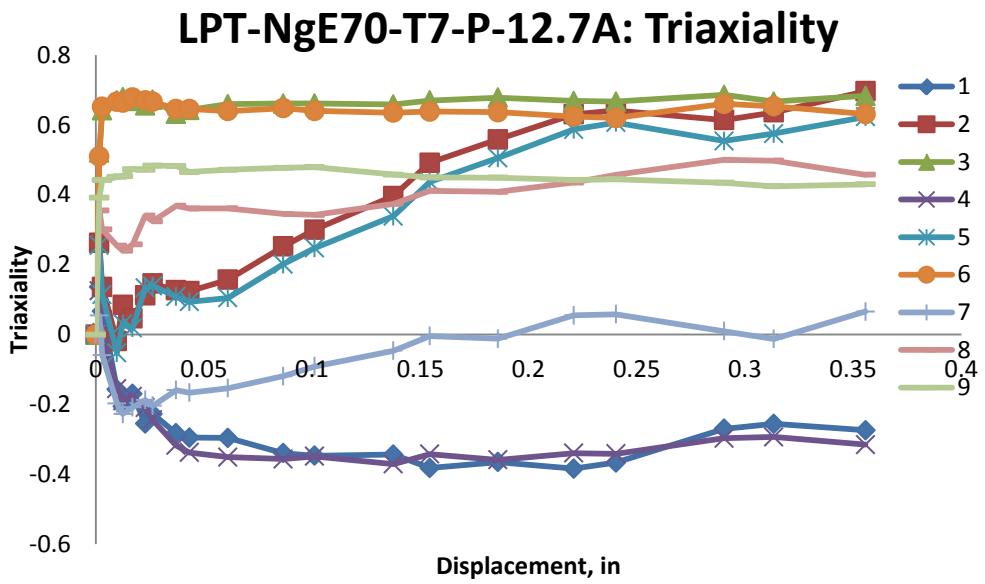

Figure B. 182: Variation of triaxiality with displacement for different elements laid out through the thickness of simulation of LPT-NgE70-T7-P-12.7A specimens

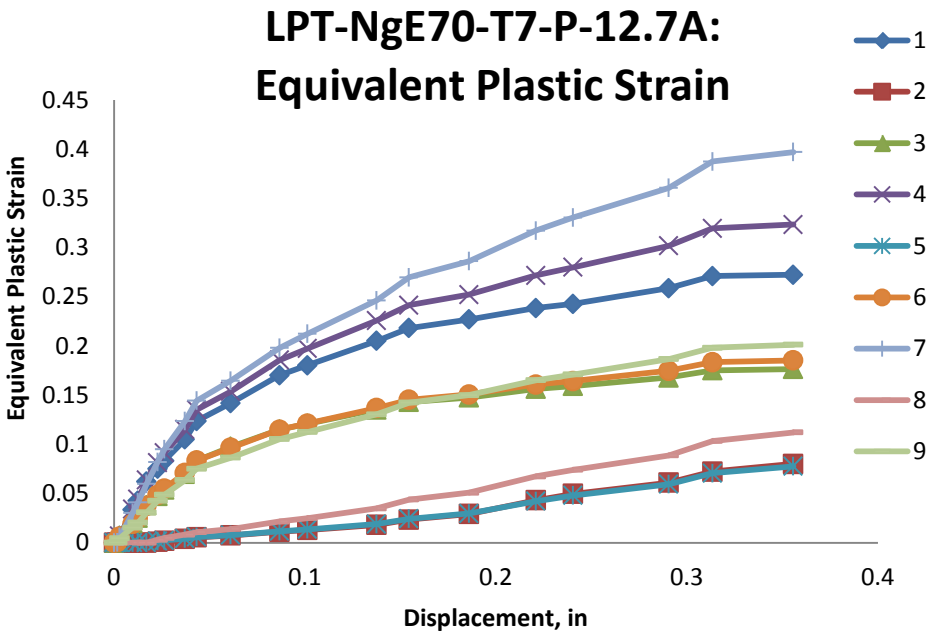

Figure B. 183: Variation of equivalent plastic strain with displacement for different elements laid out through the thickness of simulation of LPT-NgE70-T7-P-12.7A specimens

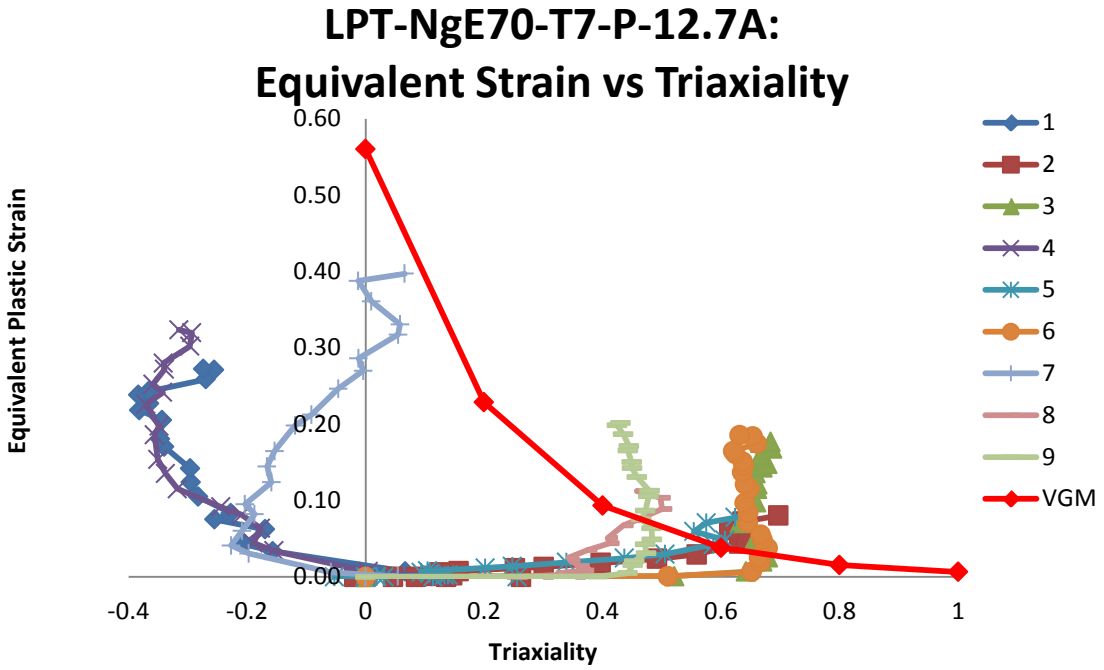

Figure B. 184: Variation of equivalent plastic strain versus triaxiality for different elements laid out through the thickness of simulation of LPT-NgE70-T7-P-12.7A specimens

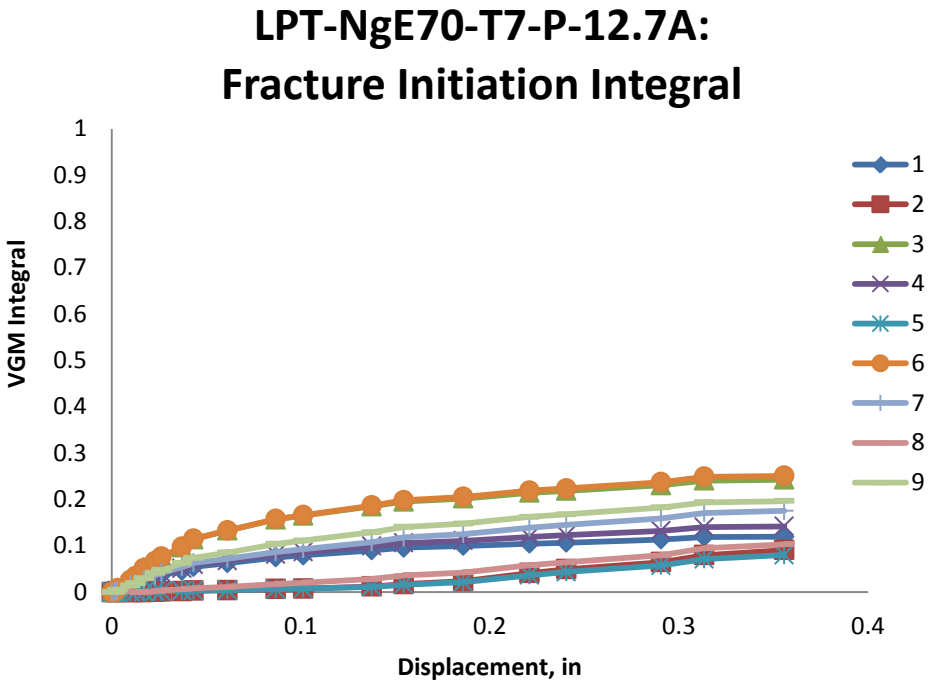

Figure B. 185: Value of fracture initiation integral for different elements laid out through the thickness of simulation of LPT-NgE70-T7-P-12.7A specimens

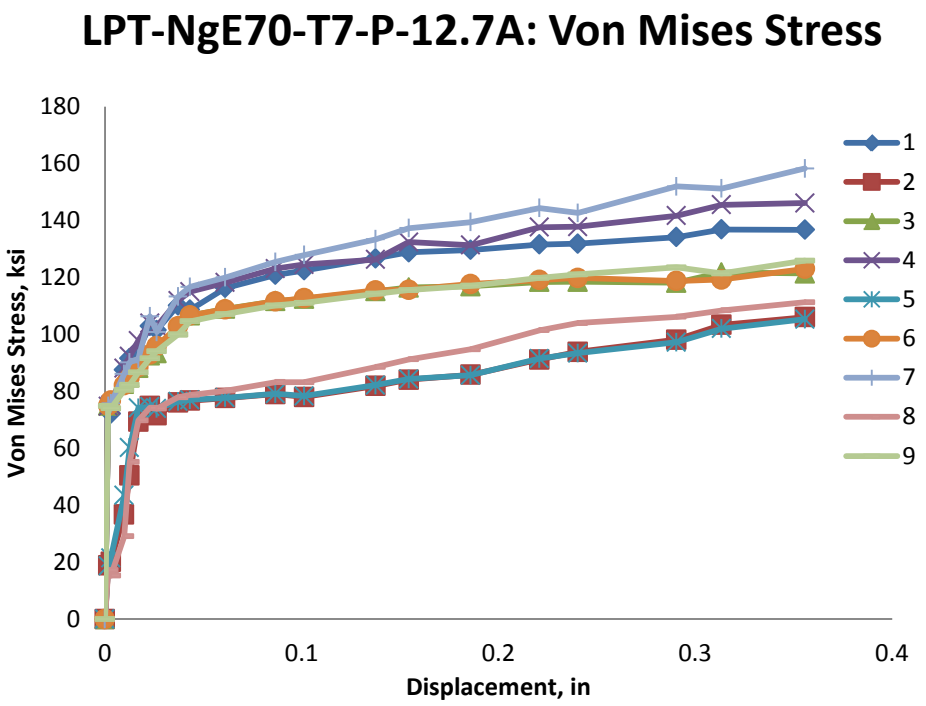

Figure B. 186: Variation of von Mises stress versus displacement for different elements laid out through the thickness of simulation of LPT-NgE70-T7-P-12.7A specimens

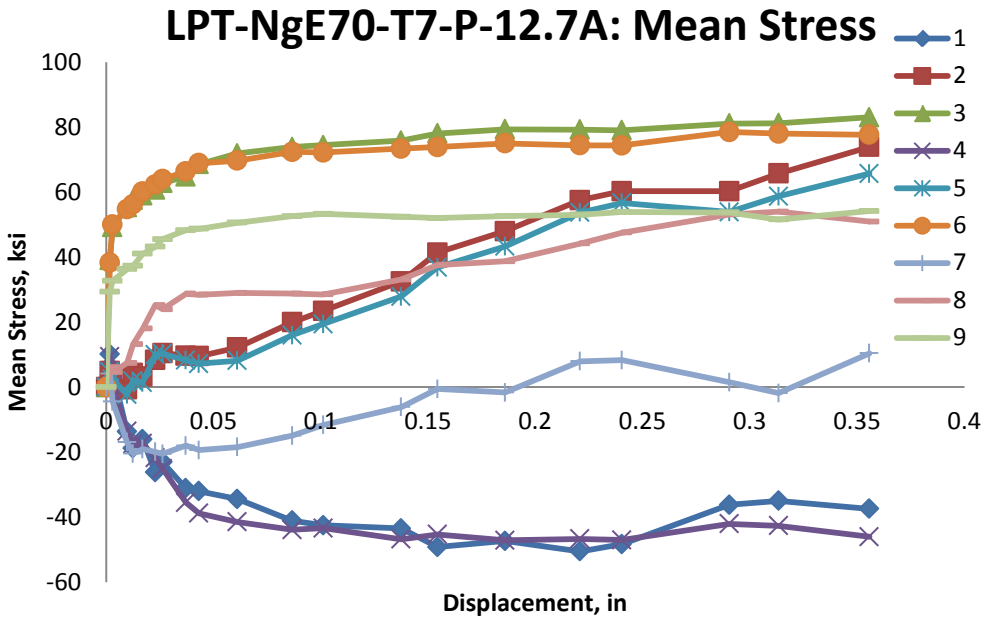

Figure B. 187: Variation of mean stress versus displacement for different elements laid out through the thickness of simulation of LPT-NgE70-T7-P-12.7A specimens

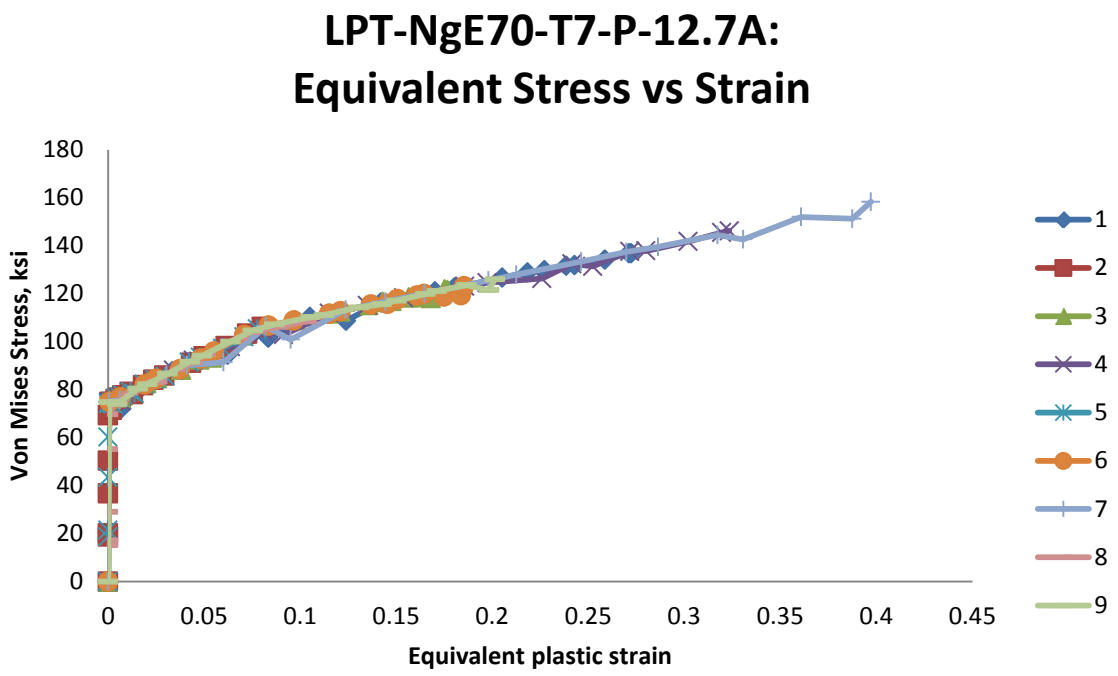

Figure B. 188: Variation of von Mises stress versus equivalent plastic strain for different elements laid out through the thickness of simulation of LPT-NgE70-T7-P-12.7A specimens

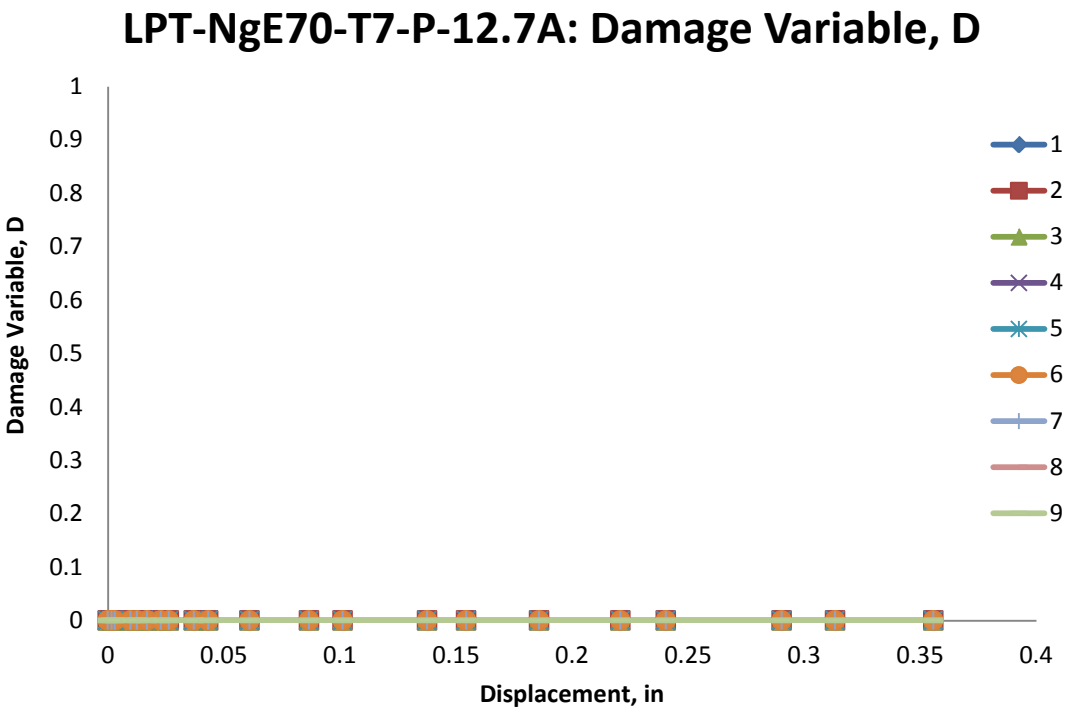

Figure B. 189: Variation of damage variable with displacement for different elements laid out through the thickness of simulation of LPT-NgE70-T7-P-12.7A specimens

B.17 LPT-NgE70T-7K2-P-12.7A

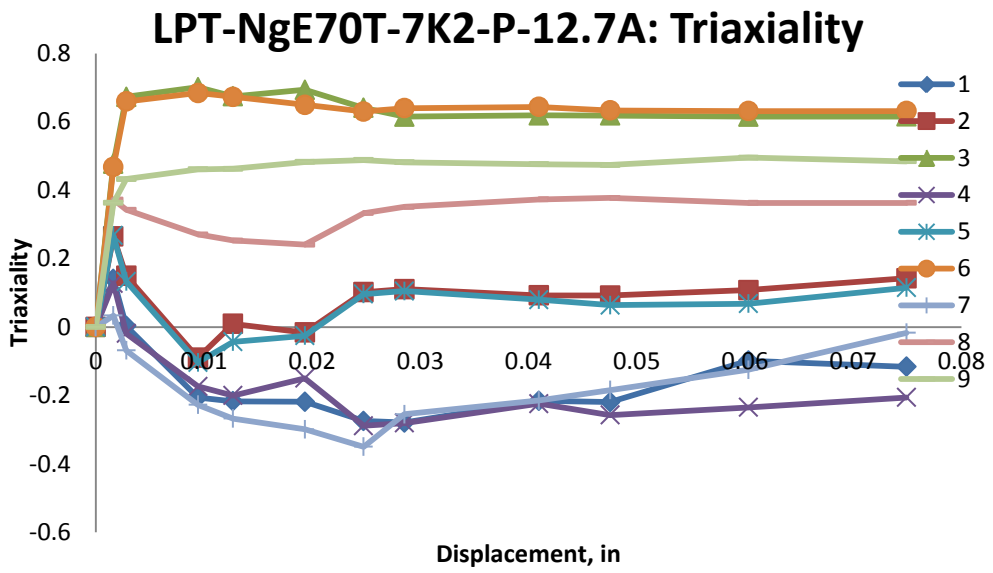

Figure B. 190: Variation of triaxiality with displacement for different elements laid out through the thickness of simulation of LPT-NgE70T-7K2-P-12.7A specimens

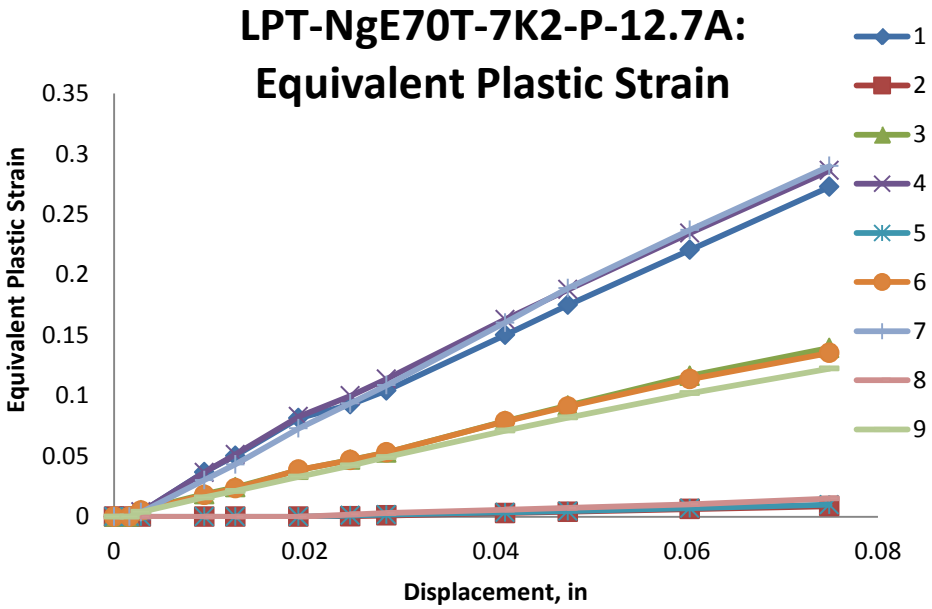

Figure B. 191: Variation of equivalent plastic strain with displacement for different elements laid out through the thickness of simulation of LPT-NgE70T-7K2-P-12.7A specimens

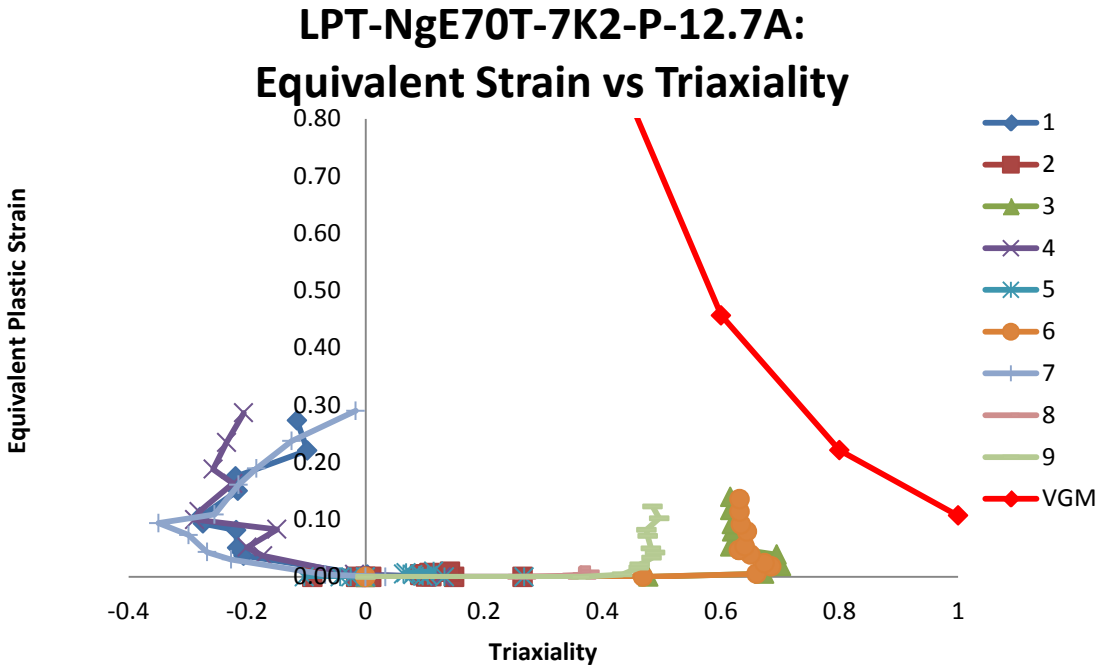

Figure B. 192: Variation of equivalent plastic strain versus triaxiality for different elements laid out through the thickness of simulation of LPT-NgE70T-7K2-P-12.7A specimens

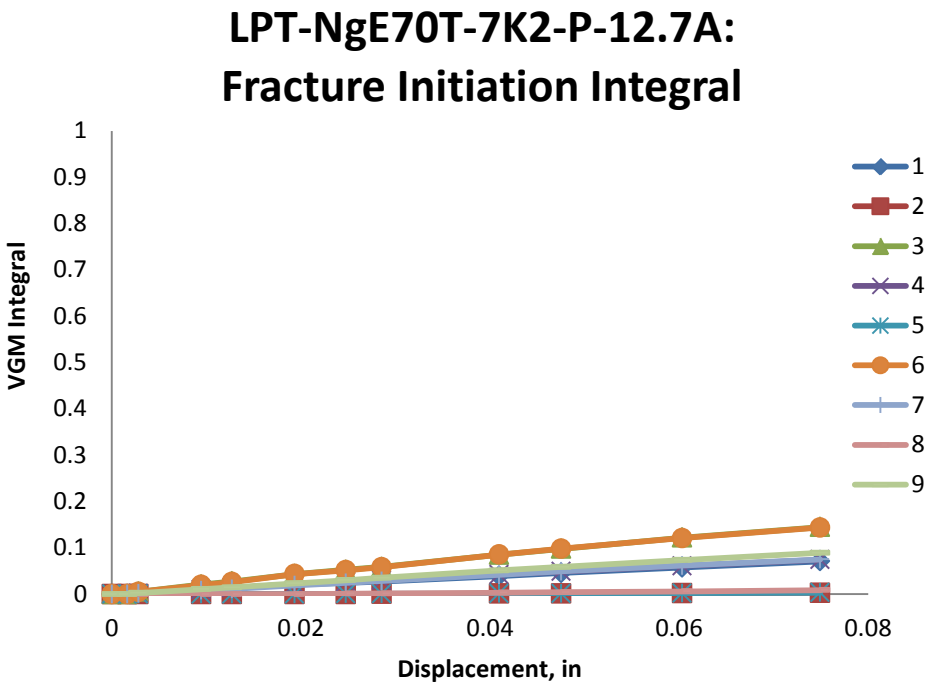

Figure B. 193: Value of fracture initiation integral for different elements laid out through the thickness of simulation of LPT-NgE70T-7K2-P-12.7A specimens

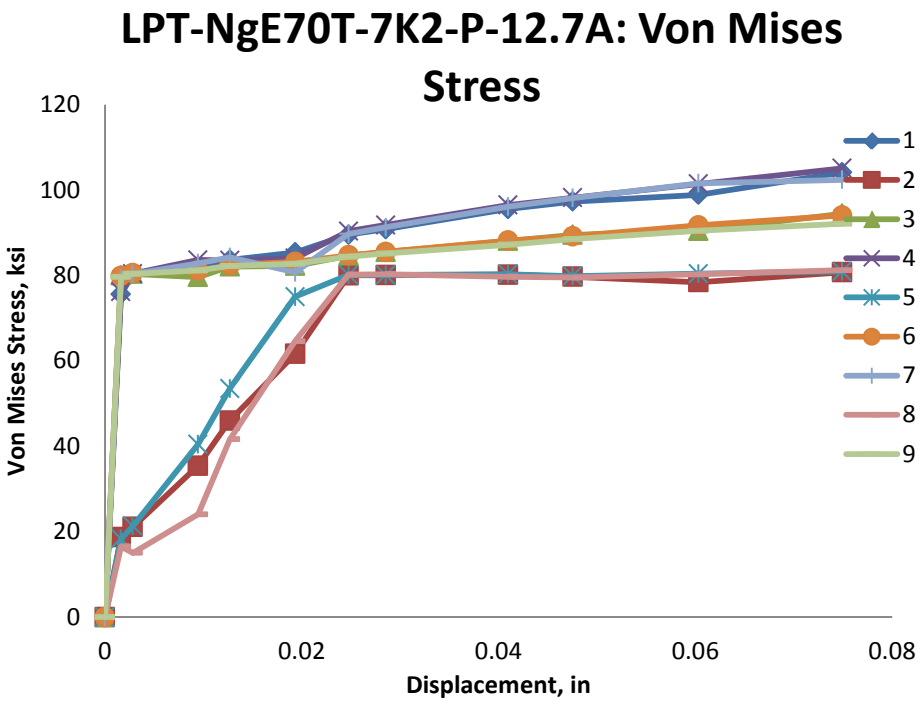

Figure B. 194: Variation of von Mises stress versus displacement for different elements laid out through the thickness of simulation of LPT-NgE70T-7K2-P-12.7A specimens

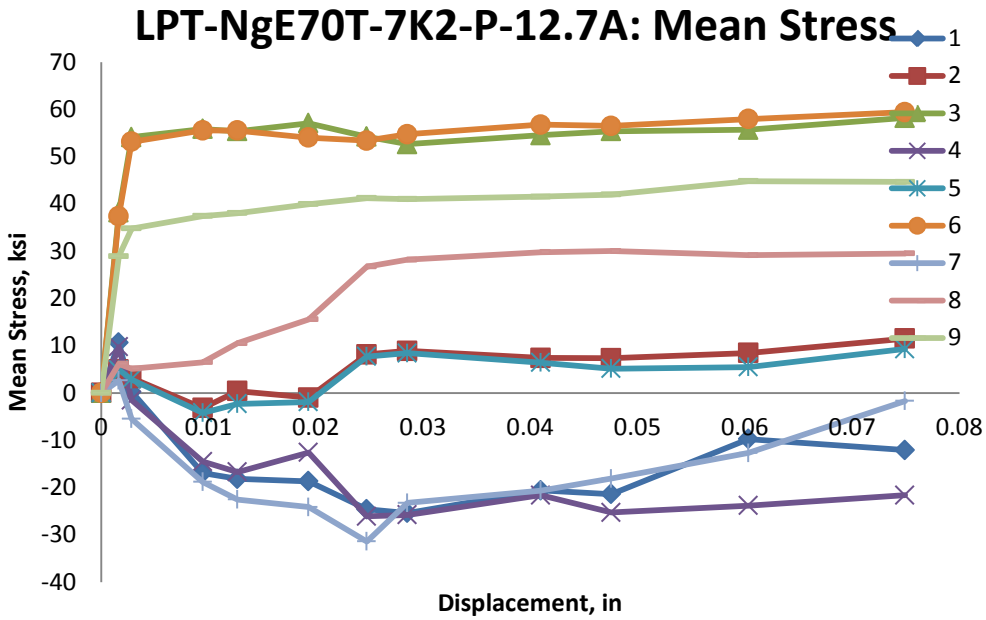

Figure B. 195: Variation of mean stress versus displacement for different elements laid out through the thickness of simulation of LPT-NgE70T-7K2-P-12.7A specimens

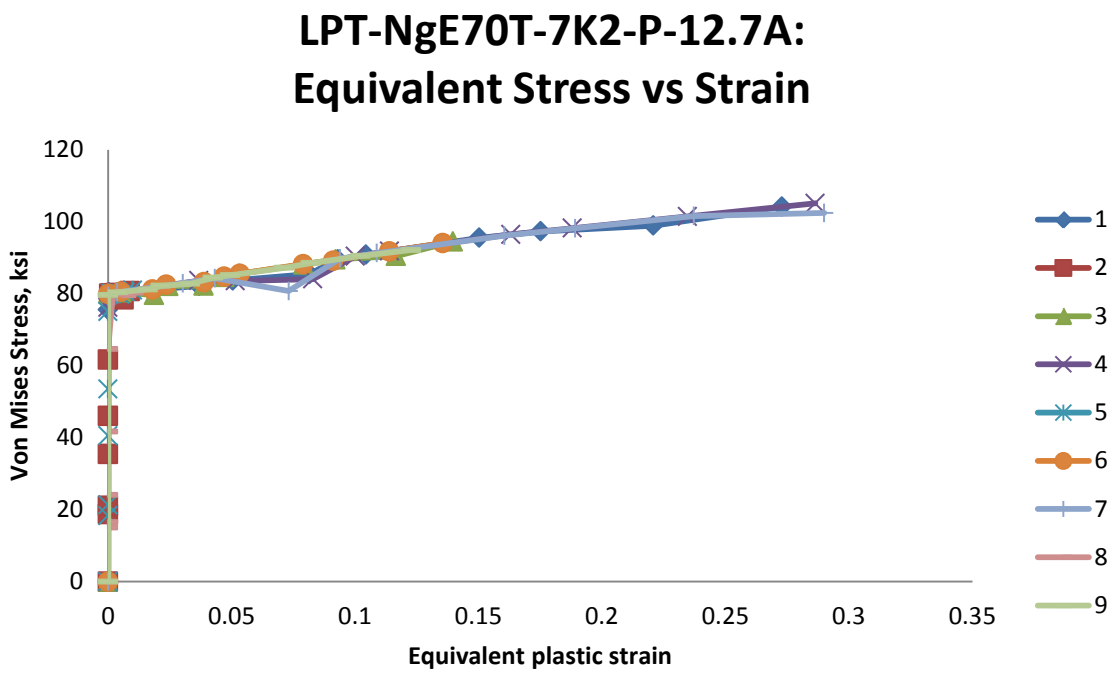

Figure B. 196: Variation of von Mises stress versus equivalent plastic strain for different elements laid out through the thickness of simulation of LPT-NgE70T-7K2-P-12.7A specimens

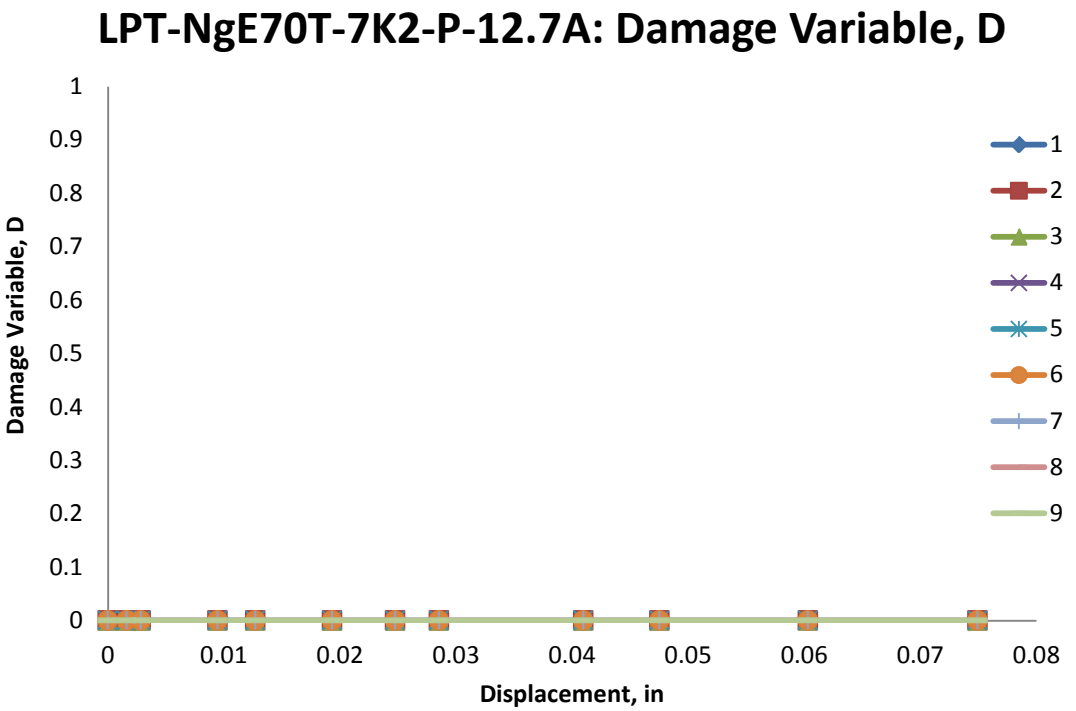

Figure B. 197: Variation of damage variable with displacement for different elements laid out through the thickness of simulation of LPT-NgE70T-7K2-P-12.7A specimens

B.18 LPT-NgE70T-8K6-P-12.7A

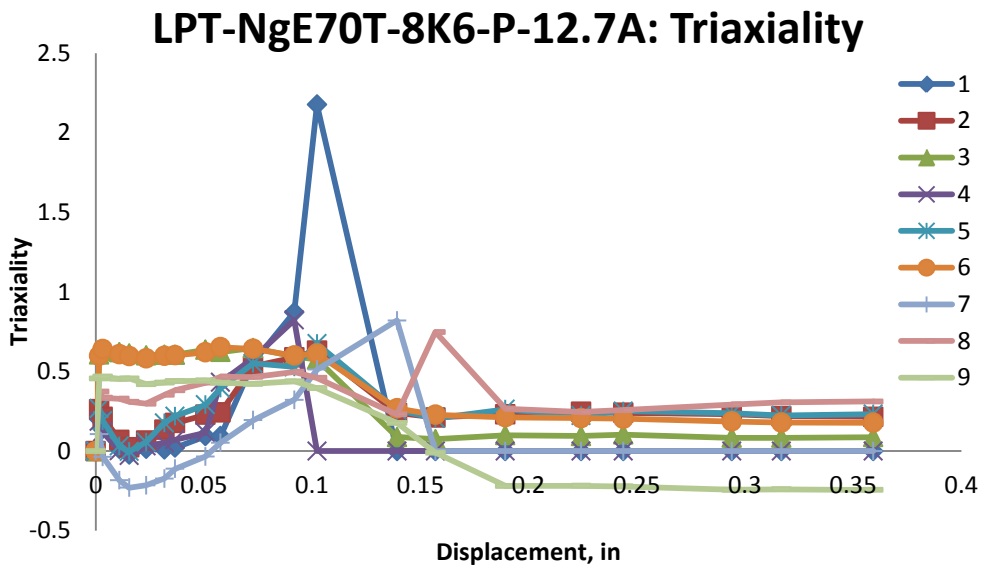

Figure B. 198: Variation of triaxiality with displacement for different elements laid out through the thickness of simulation of LPT-NgE70T-8K6-P-12.7A specimens

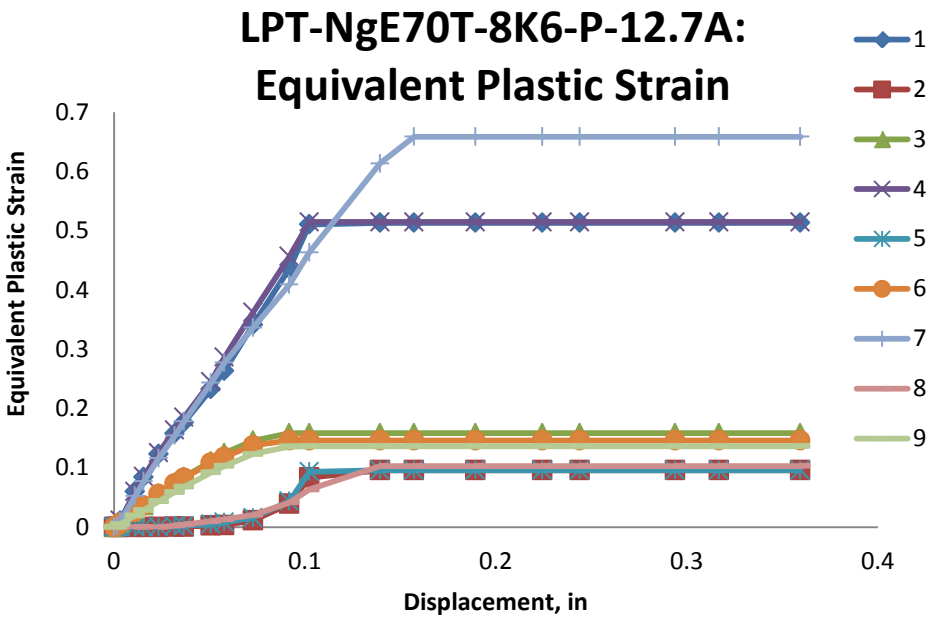

Figure B. 199: Variation of equivalent plastic strain with displacement for different elements laid out through the thickness of simulation of LPT-NgE70T-8K6-P-12.7A specimens

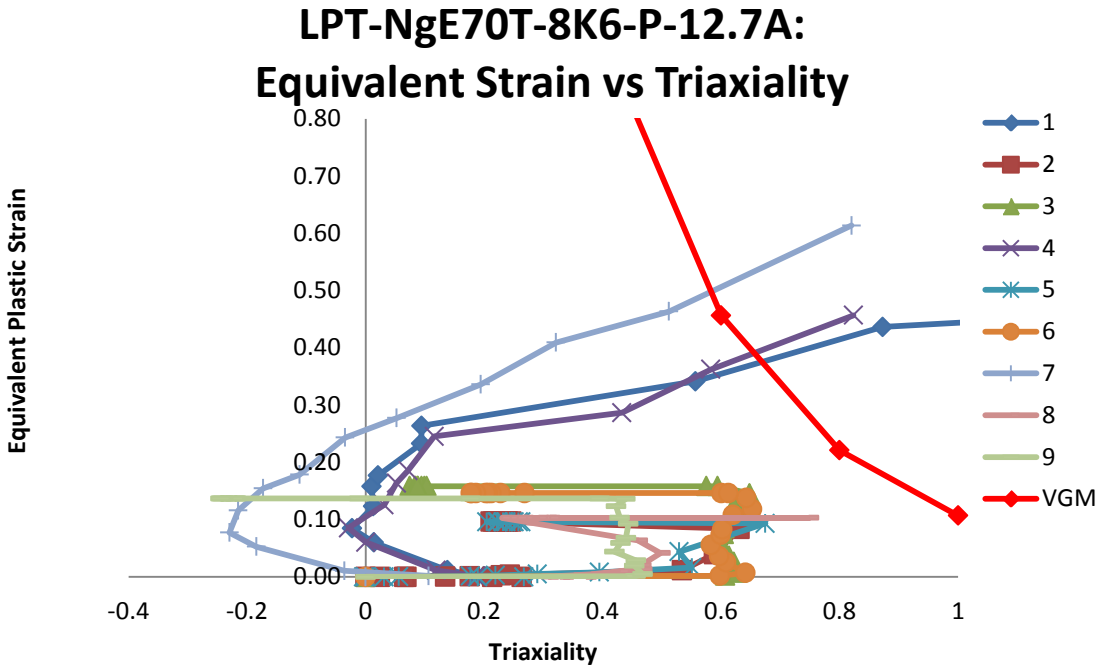

Figure B. 200: Variation of equivalent plastic strain versus triaxiality for different elements laid out through the thickness of simulation of LPT-NgE70T-8K6-P-12.7A specimens

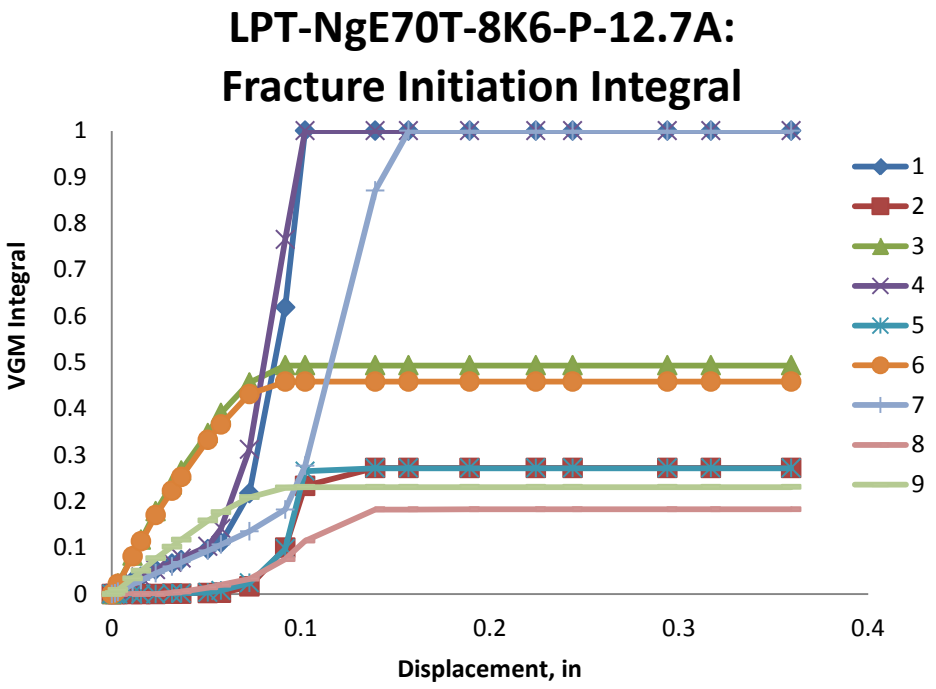

Figure B. 201: Value of fracture initiation integral for different elements laid out through the thickness of simulation of LPT-NgE70T-8K6-P-12.7A specimens

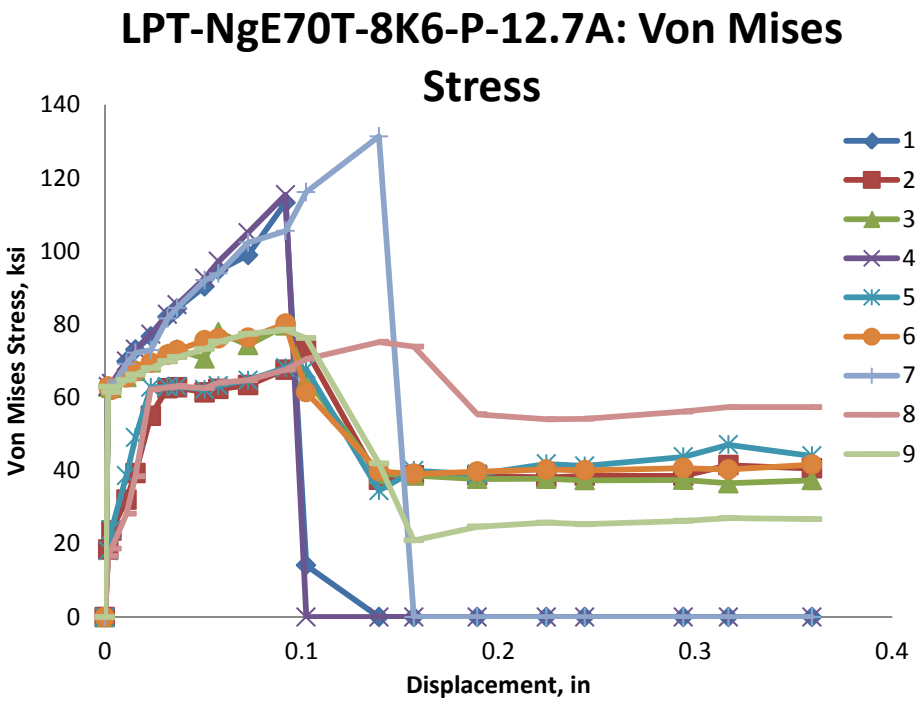

Figure B. 202: Variation of von Mises stress versus displacement for different elements laid out through the thickness of simulation of LPT-NgE70T-8K6-P-12.7A specimens

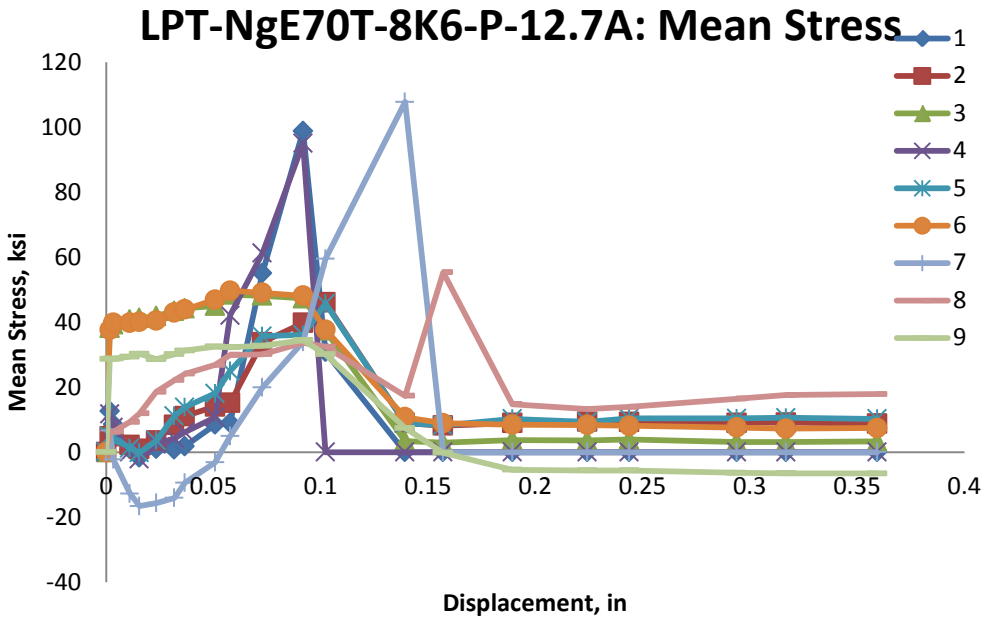

Figure B. 203: Variation of mean stress versus displacement for different elements laid out through the thickness of simulation of LPT-NgE70T-8K6-P-12.7A specimens

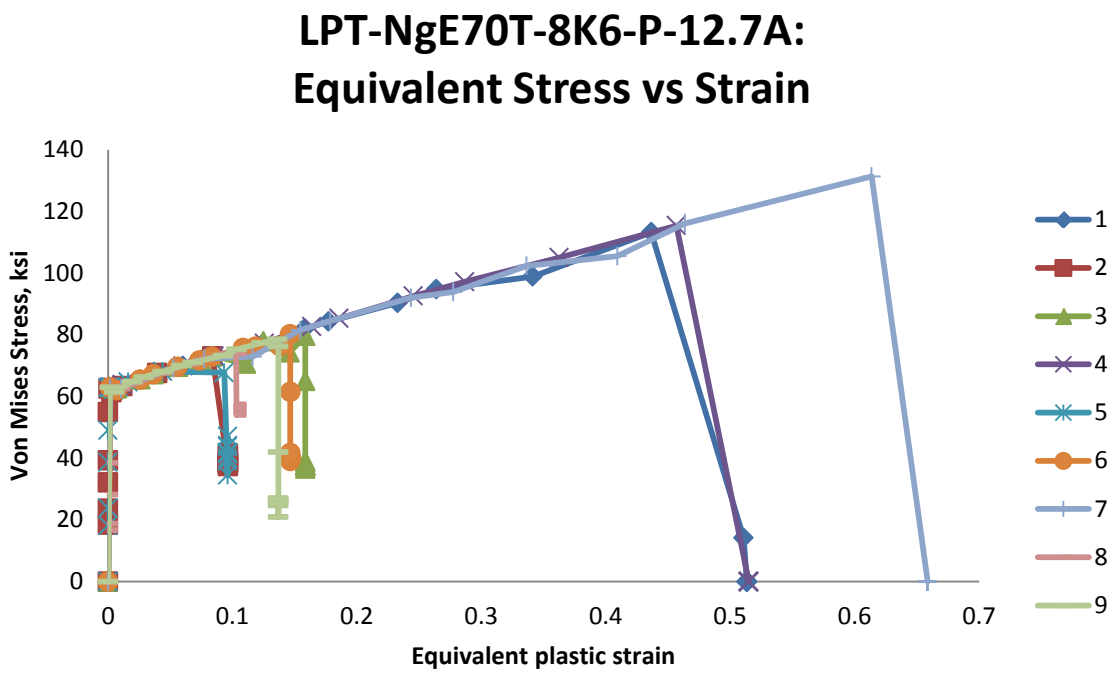

Figure B. 204: Variation of von Mises stress versus equivalent plastic strain for different elements laid out through the thickness of simulation of LPT-NgE70T-8K6-P-12.7A specimens

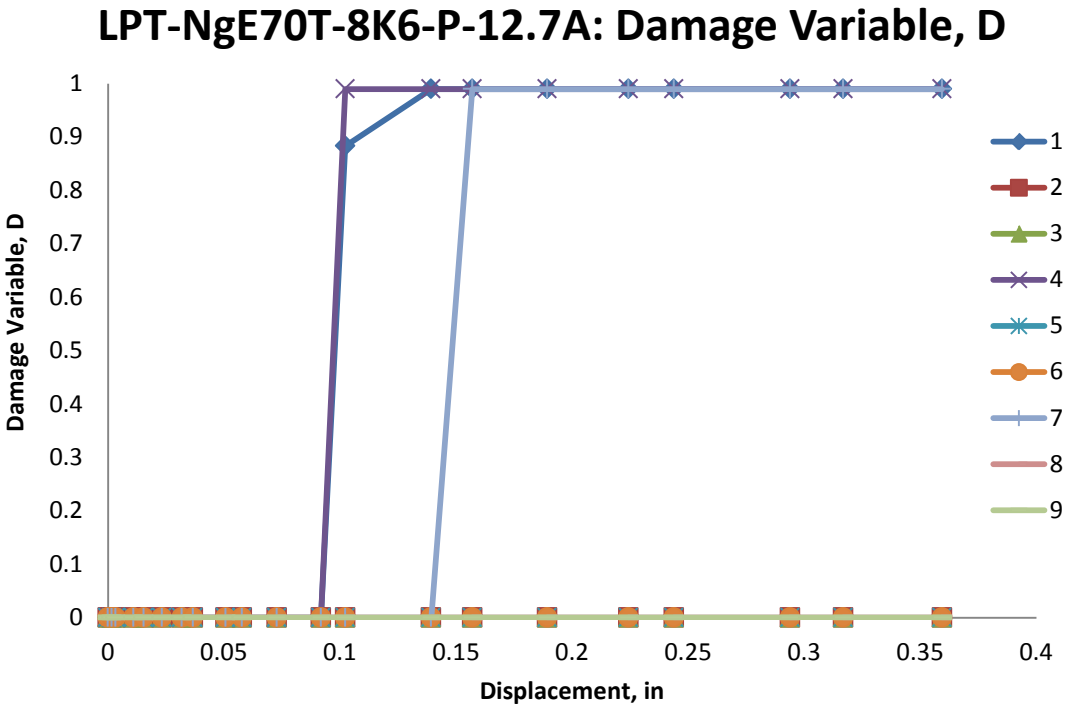

Figure B. 205: Variation of damage variable with displacement for different elements laid out through the thickness of simulation of LPT-NgE70T-8K6-P-12.7A specimens

B.19 LP45-DenE70-T4-P-12.7A

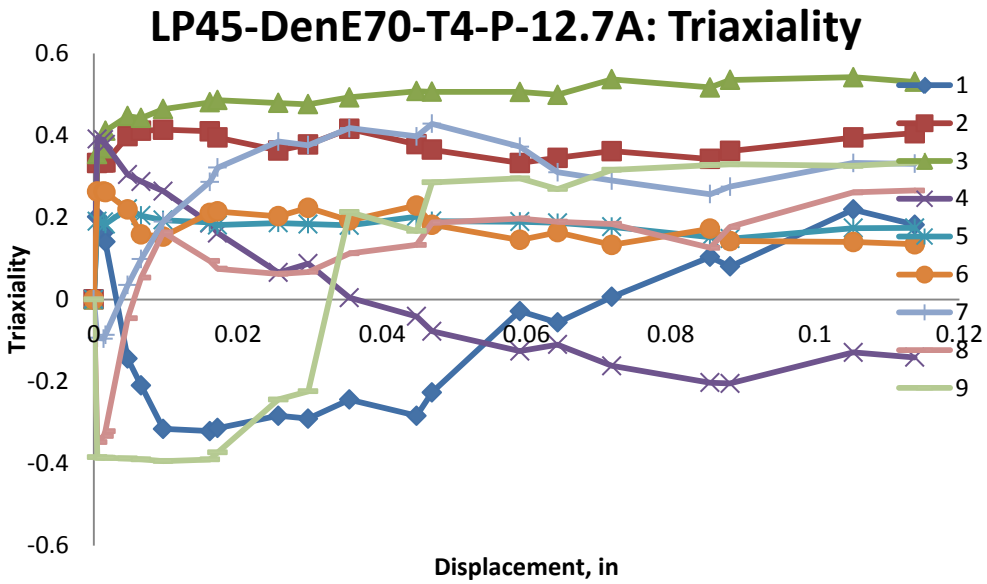

Figure B. 206: Variation of triaxiality with displacement for different elements laid out through the thickness of simulation of LP45-DenE70-T4-P-12.7A specimens

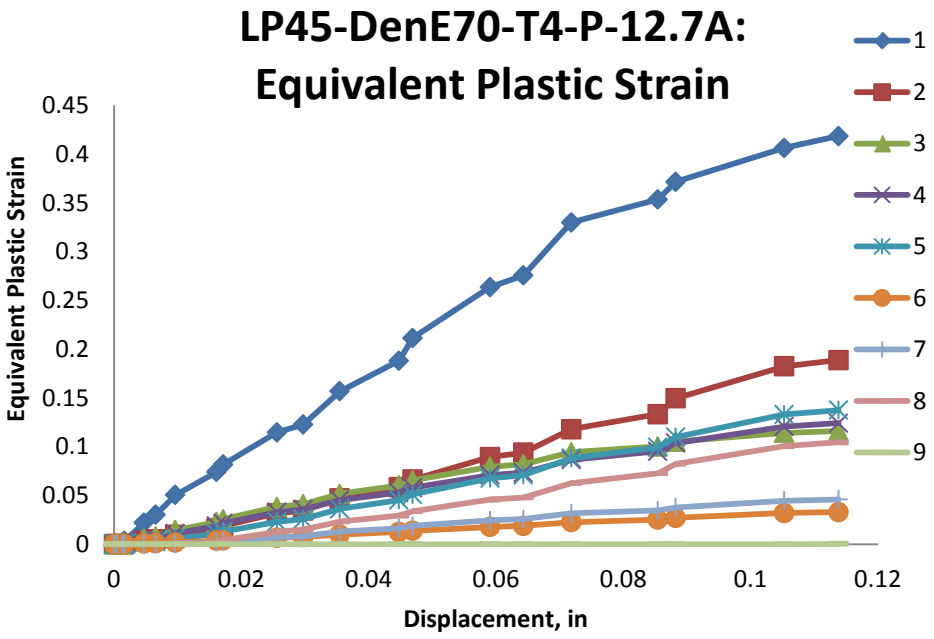

Figure B. 207: Variation of equivalent plastic strain with displacement for different elements laid out through the thickness of simulation of LP45-DenE70-T4-P-12.7A specimens

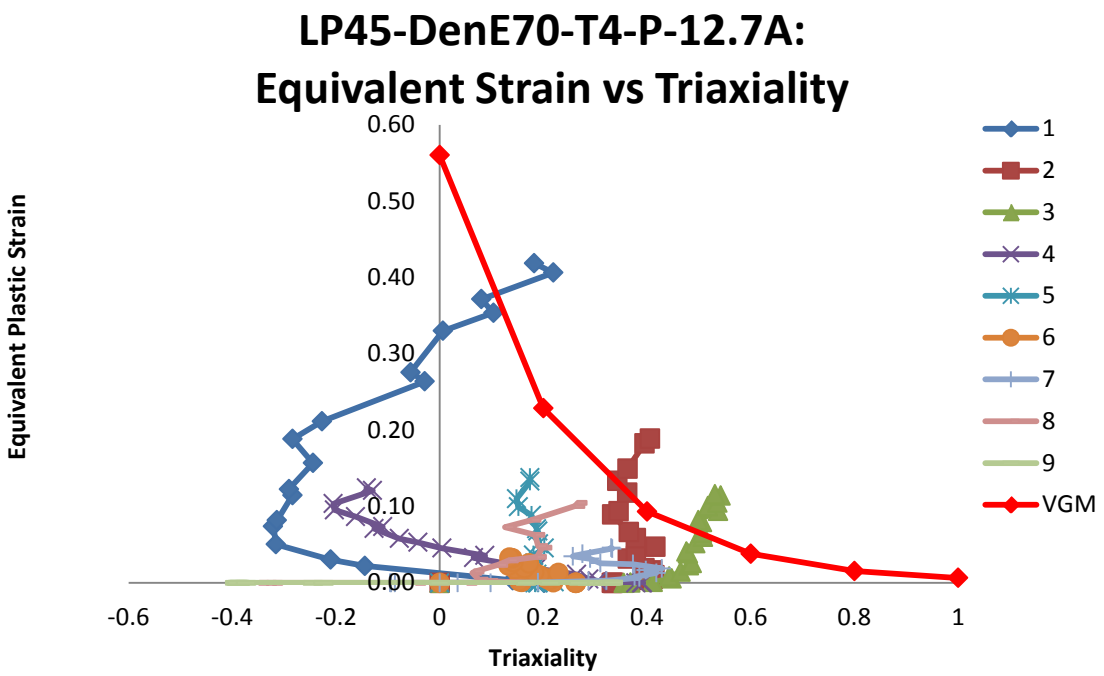

Figure B. 208: Variation of equivalent plastic strain versus triaxiality for different elements laid out through the thickness of simulation of LP45-DenE70-T4-P-12.7A specimens

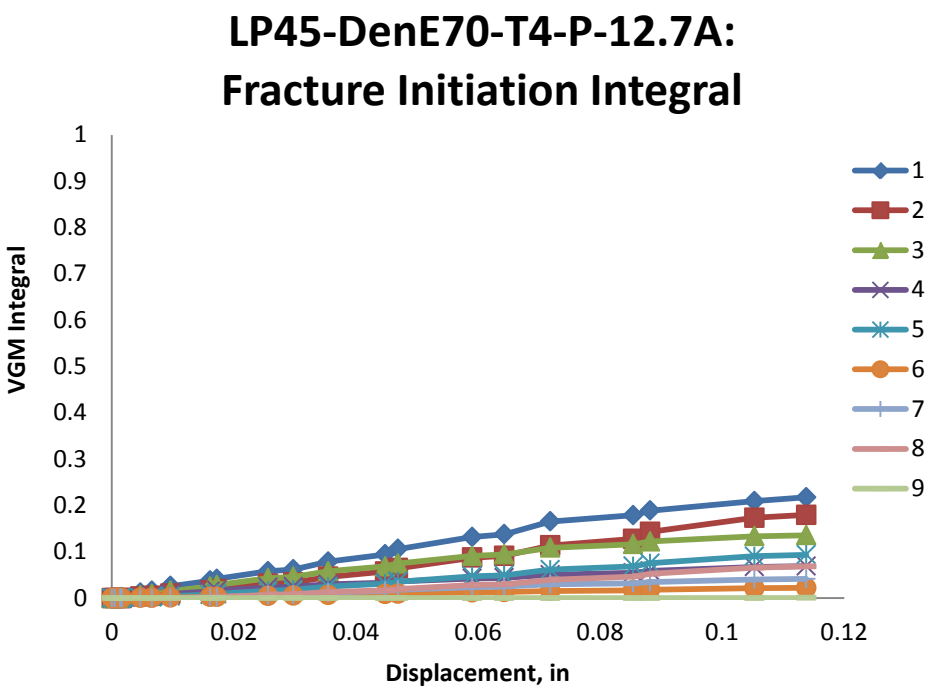

Figure B. 209: Value of fracture initiation integral for different elements laid out through the thickness of simulation of LP45-DenE70-T4-P-12.7A specimens

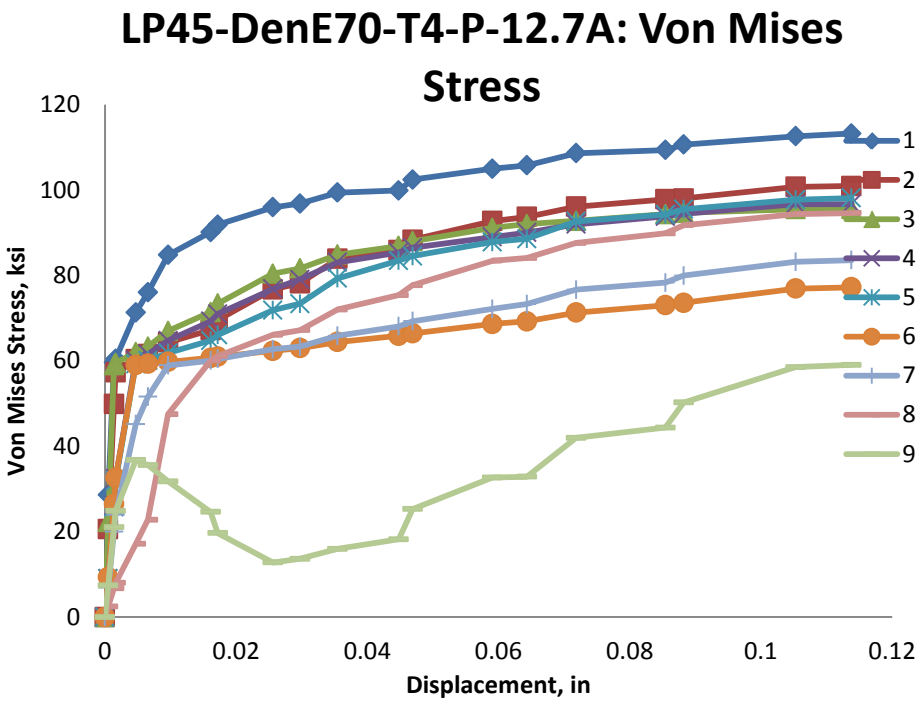

Figure B. 210: Variation of von Mises stress versus displacement for different elements laid out through the thickness of simulation of LP45-DenE70-T4-P-12.7A specimens

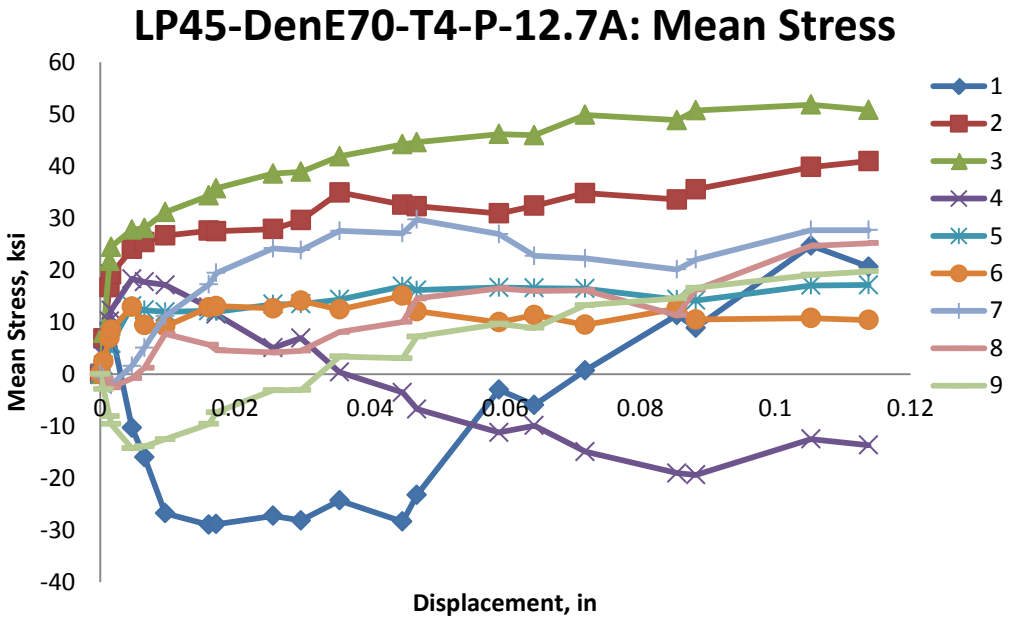

Figure B. 211: Variation of mean stress versus displacement for different elements laid out through the thickness of simulation of LP45-DenE70-T4-P-12.7A specimens

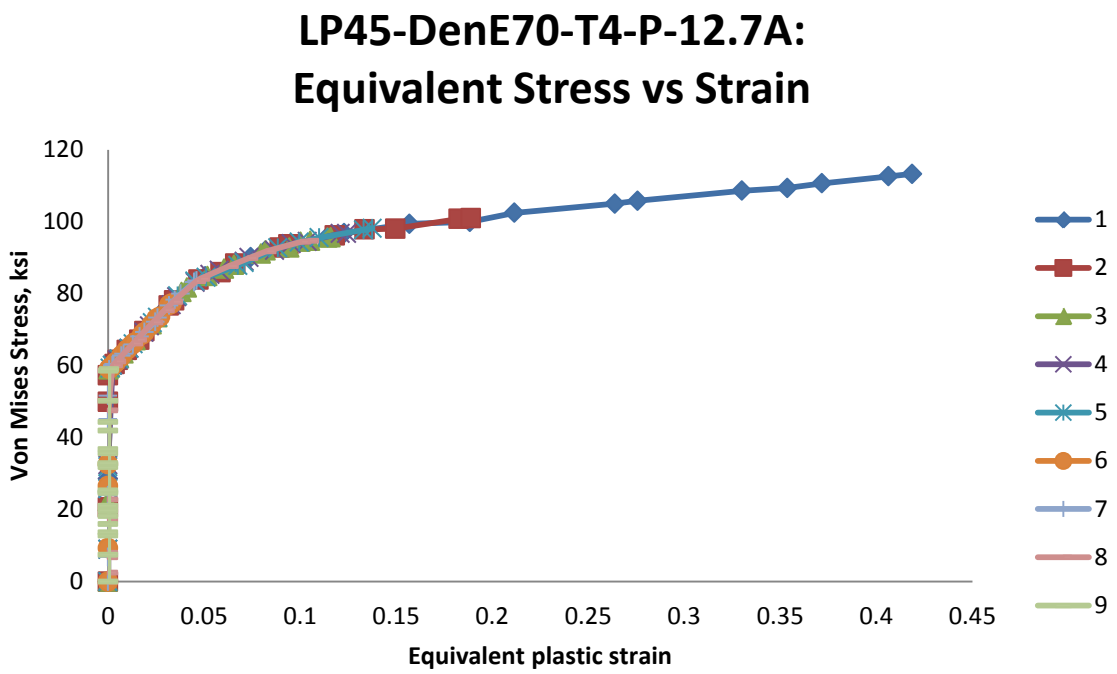

Figure B. 212: Variation of von Mises stress versus equivalent plastic strain for different elements laid out through the thickness of simulation of LP45-DenE70-T4-P-12.7A specimens

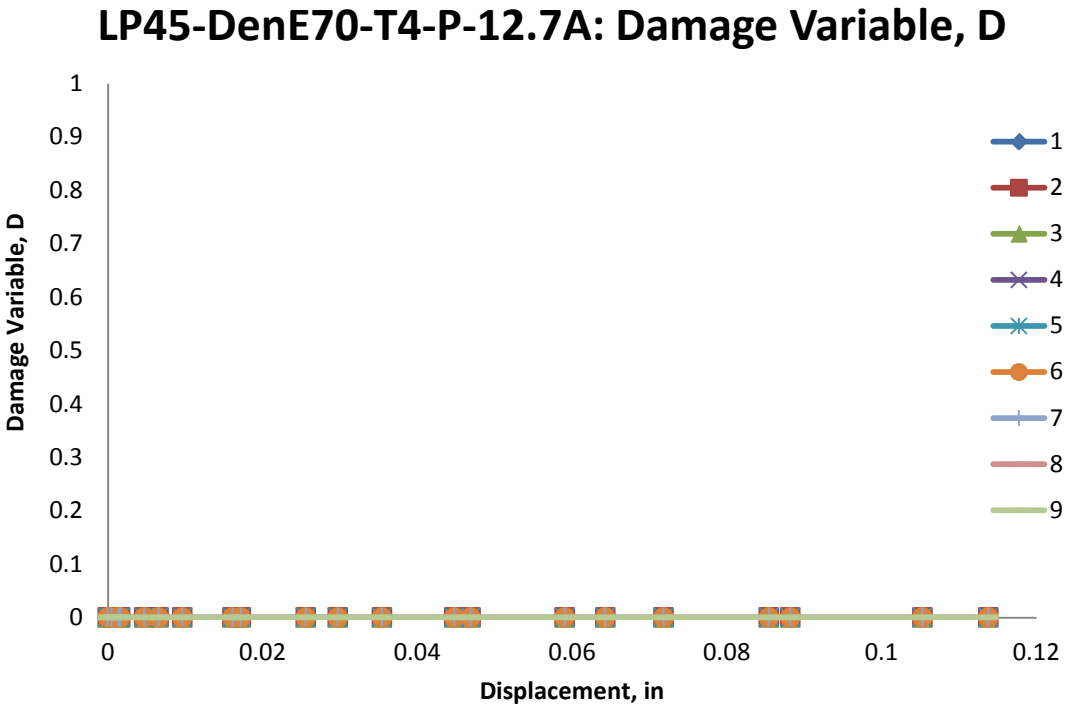

Figure B. 213: Variation of damage variable with displacement for different elements laid out through the thickness of simulation of LP45-DenE70-T4-P-12.7A specimens

B.20 LP45-DenE70-T7-P-12.7A

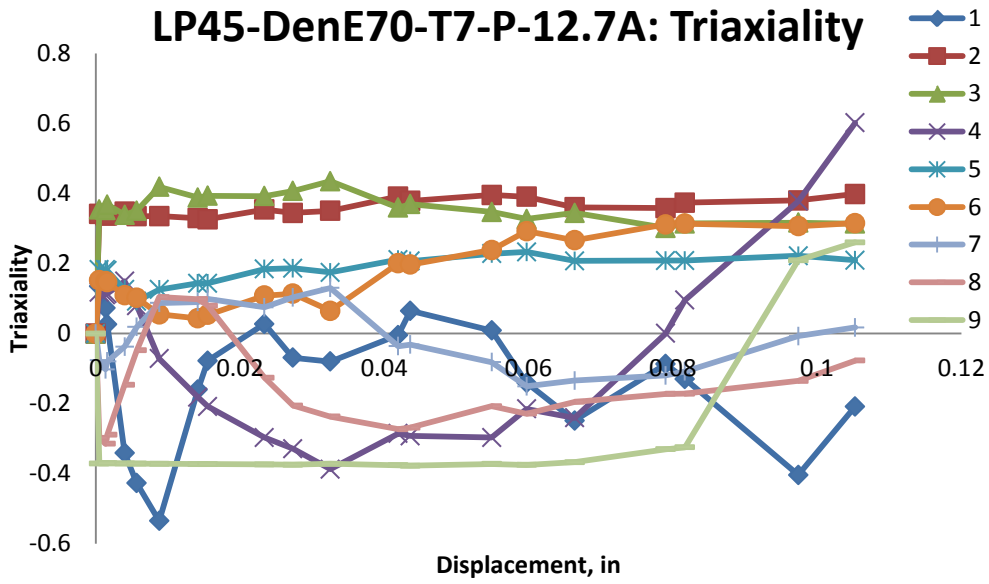

Figure B. 214: Variation of triaxiality with displacement for different elements laid out through the thickness of simulation of LP45-DenE70-T7-P-12.7A specimens

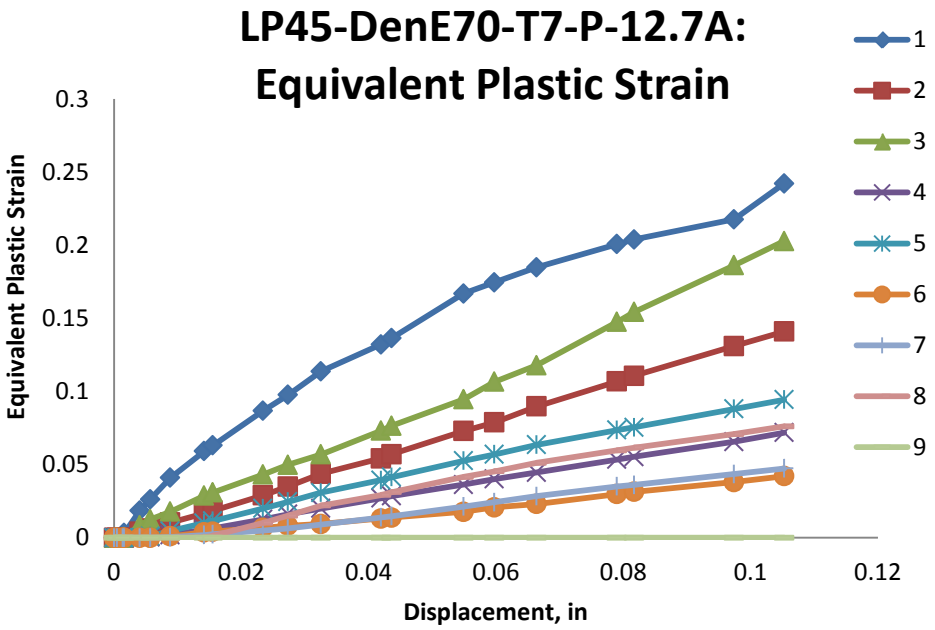

Figure B. 215: Variation of equivalent plastic strain with displacement for different elements laid out through the thickness of simulation of LP45-DenE70-T7-P-12.7A specimens

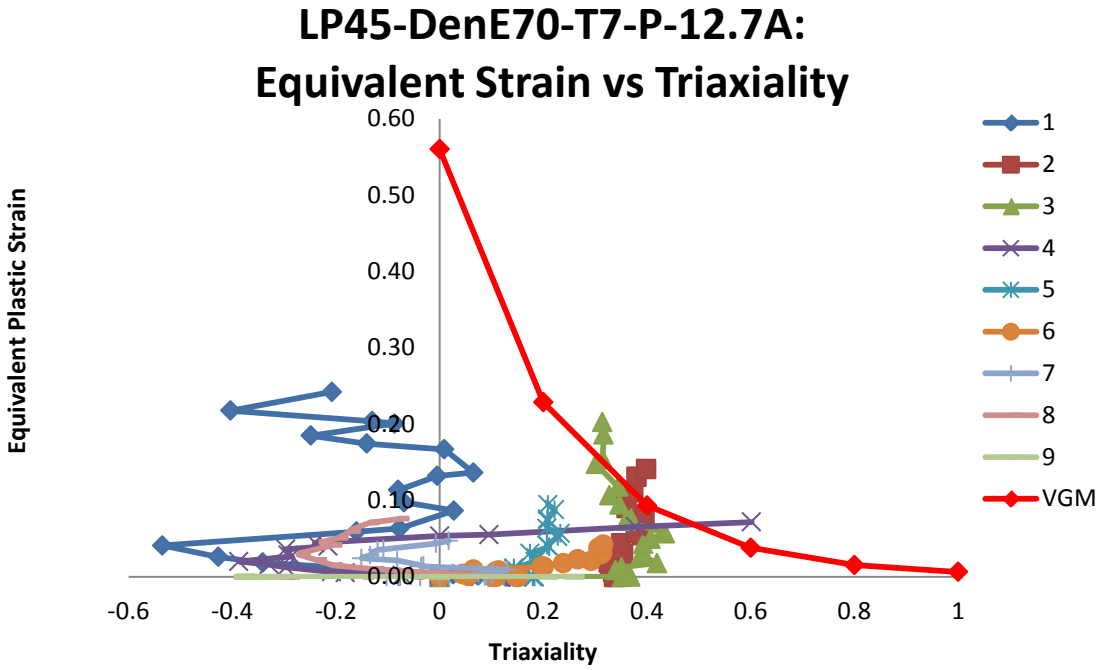

Figure B. 216: Variation of equivalent plastic strain versus triaxiality for different elements laid out through the thickness of simulation of LP45-DenE70-T7-P-12.7A specimens

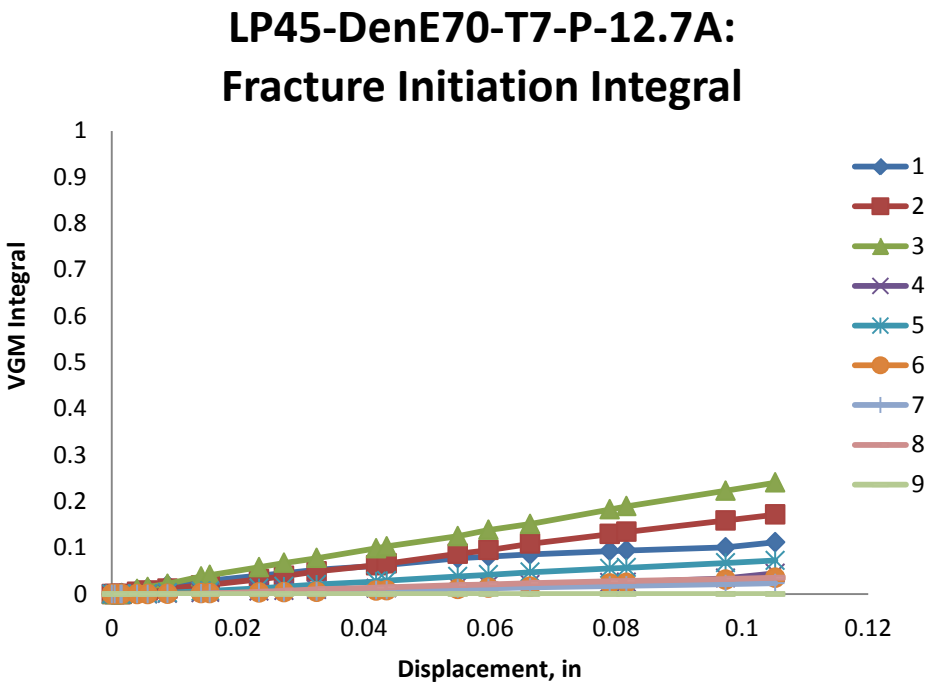

Figure B. 217: Value of fracture initiation integral for different elements laid out through the thickness of simulation of LP45-DenE70-T7-P-12.7A specimens

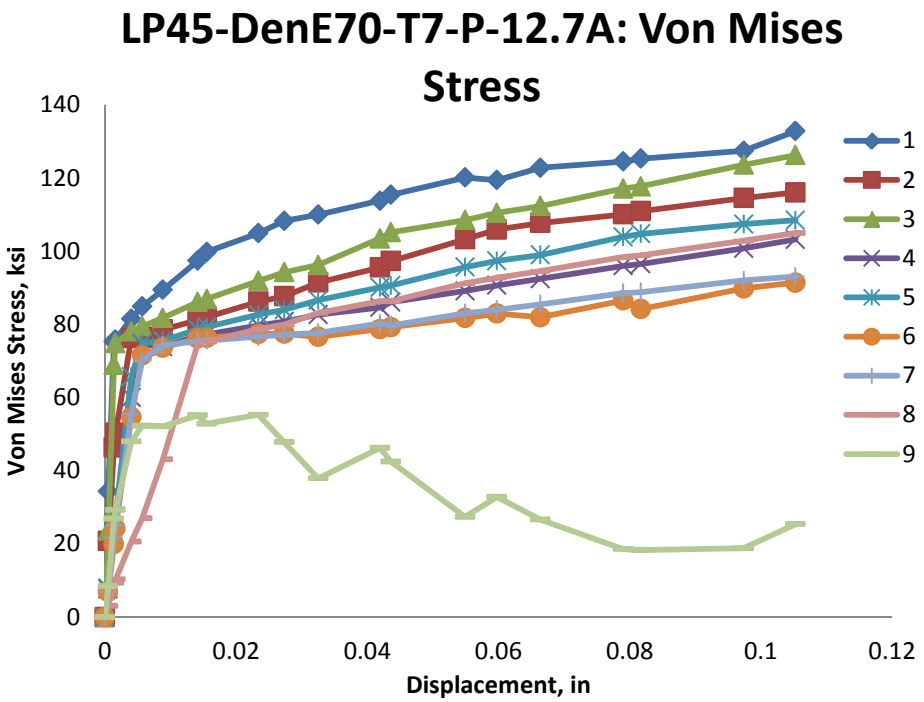

Figure B. 218: Variation of von Mises stress versus displacement for different elements laid out through the thickness of simulation of LP45-DenE70-T7-P-12.7A specimens

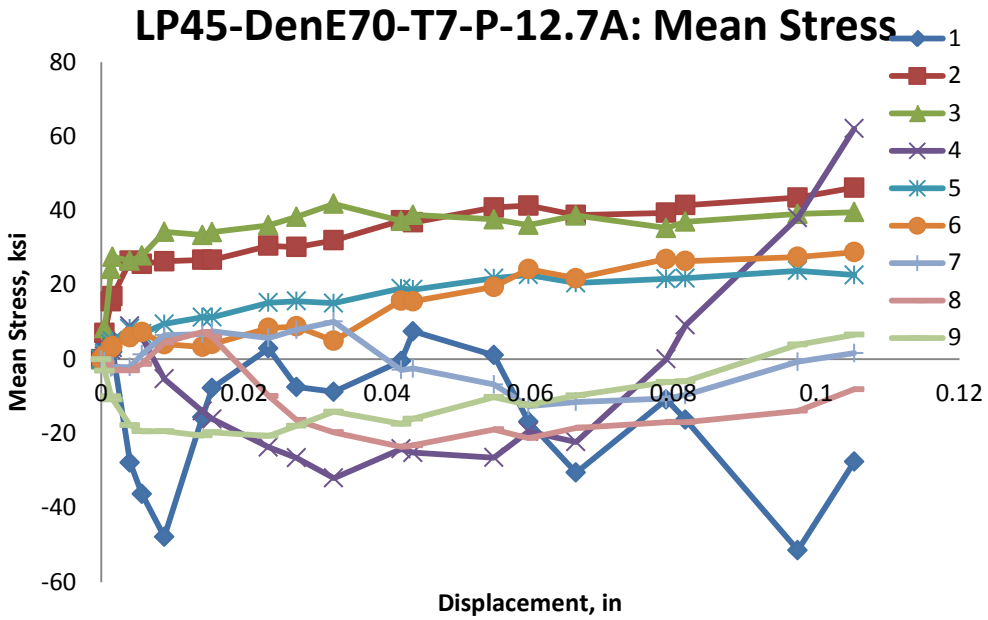

Figure B. 219: Variation of mean stress versus displacement for different elements laid out through the thickness of simulation of LP45-DenE70-T7-P-12.7A specimens

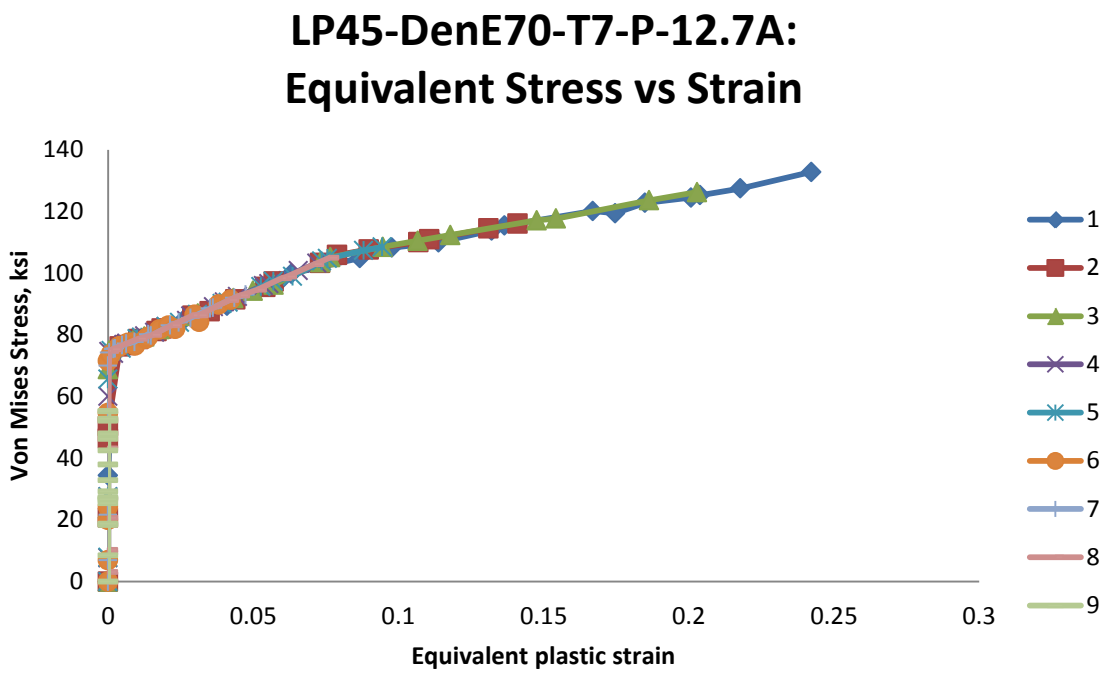

Figure B. 220: Variation of von Mises stress versus equivalent plastic strain for different elements laid out through the thickness of simulation of LP45-DenE70-T7-P-12.7A specimens

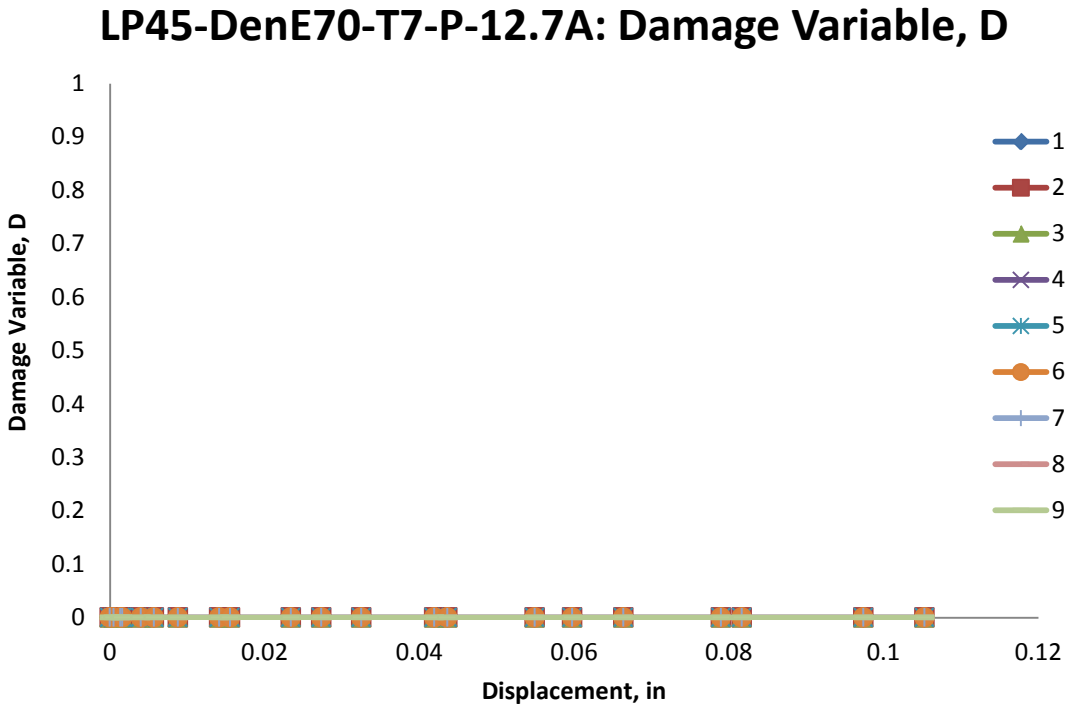

Figure B. 221: Variation of damage variable with displacement for different elements laid out through the thickness of simulation of LP45-DenE70-T7-P-12.7A specimens

B.21 LP45-DenE70T-8K6-P-12.7A

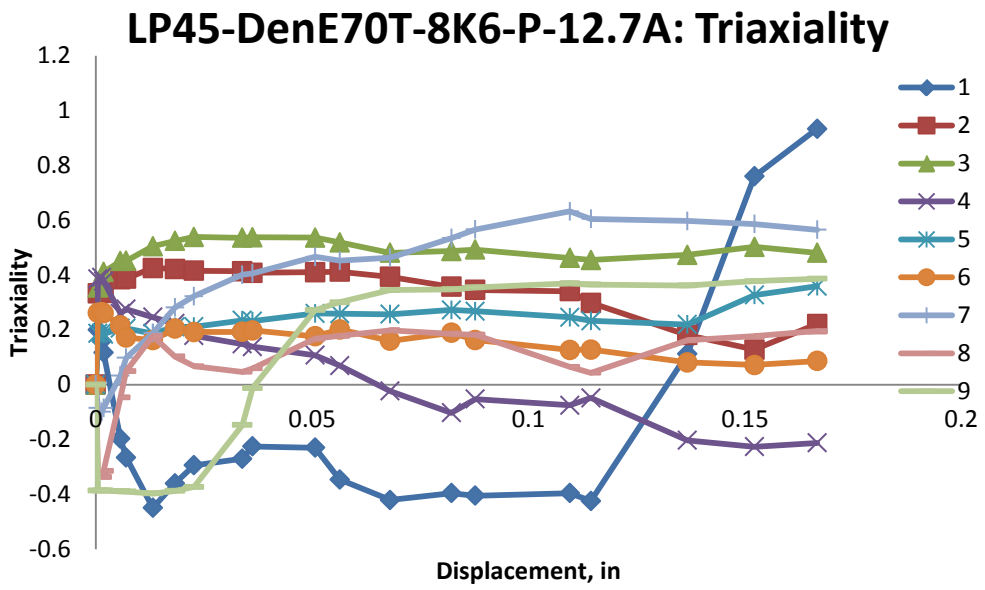

Figure B. 222: Variation of triaxiality with displacement for different elements laid out through the thickness of simulation of LP45-DenE70T-8K6-P-12.7A specimens

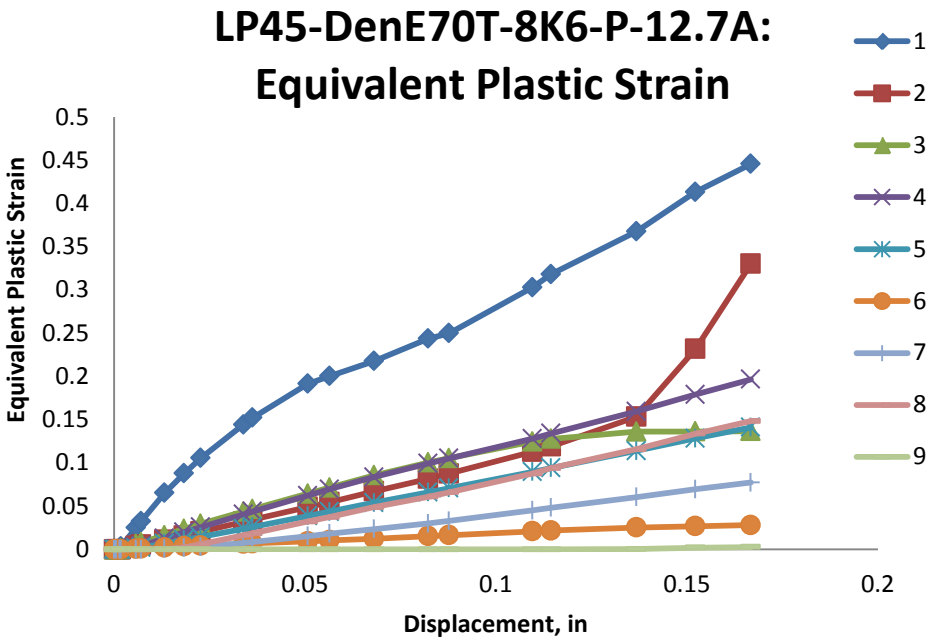

Figure B. 223: Variation of equivalent plastic strain with displacement for different elements laid out through the thickness of simulation of LP45-DenE70T-8K6-P-12.7A specimens

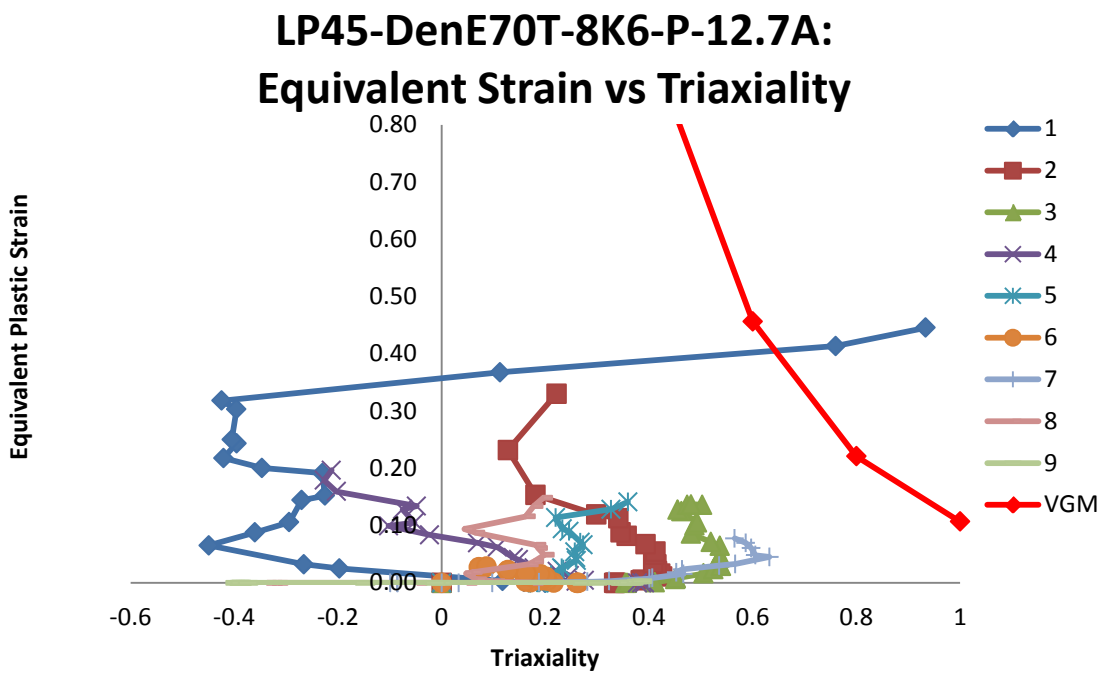

Figure B. 224: Variation of equivalent plastic strain versus triaxiality for different elements laid out through the thickness of simulation of LP45-DenE70T-8K6-P-12.7A specimens

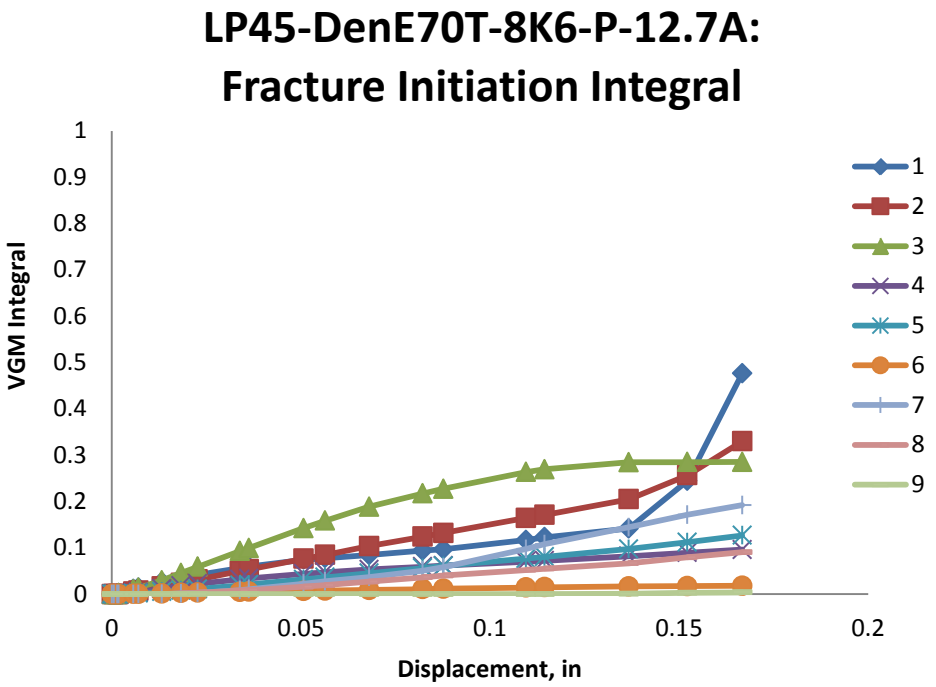

Figure B. 225: Value of fracture initiation integral for different elements laid out through the thickness of simulation of LP45-DenE70T-8K6-P-12.7A specimens

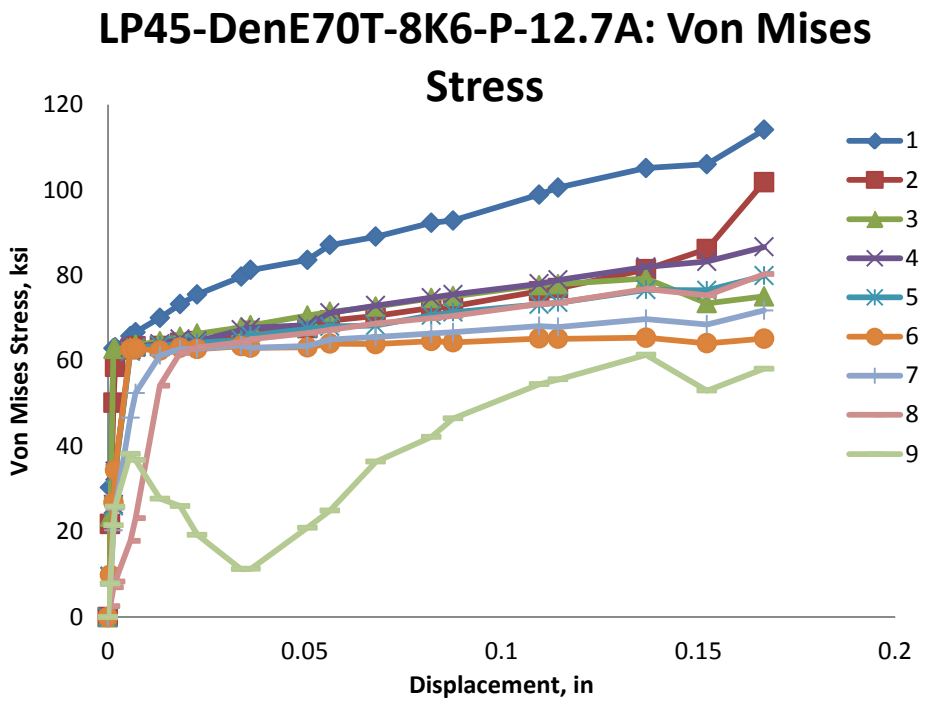

Figure B. 226: Variation of von Mises stress versus displacement for different elements laid out through the thickness of simulation of LP45-DenE70T-8K6-P-12.7A specimens

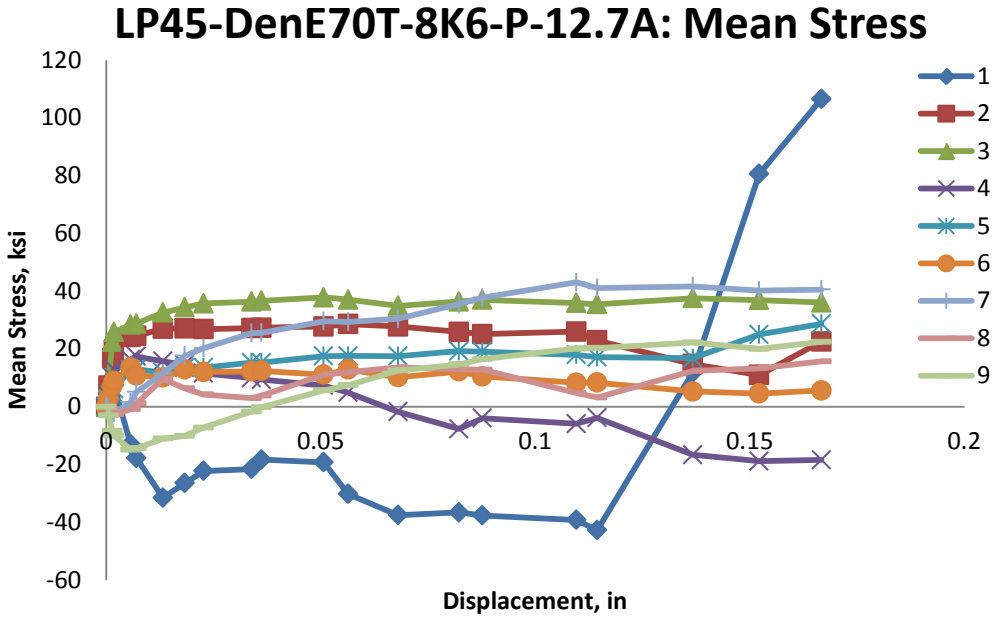

Figure B. 227: Variation of mean stress versus displacement for different elements laid out through the thickness of simulation of LP45-DenE70T-8K6-P-12.7A specimens

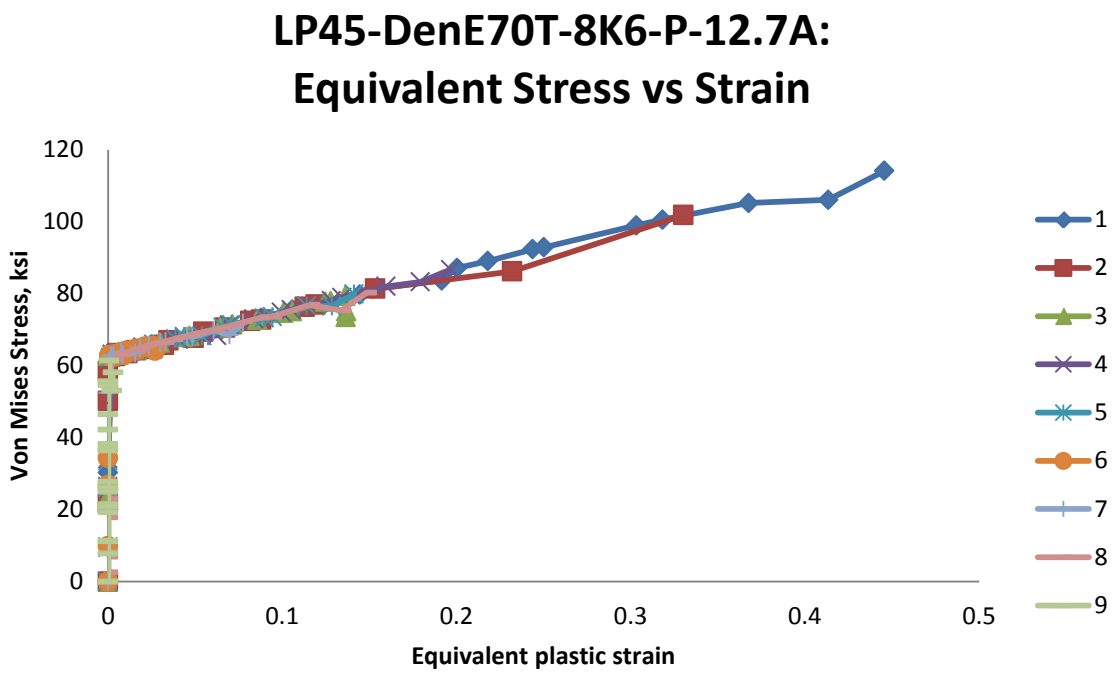

Figure B. 228: Variation of von Mises stress versus equivalent plastic strain for different elements laid out through the thickness of simulation of LP45-DenE70T-8K6-P-12.7A specimens

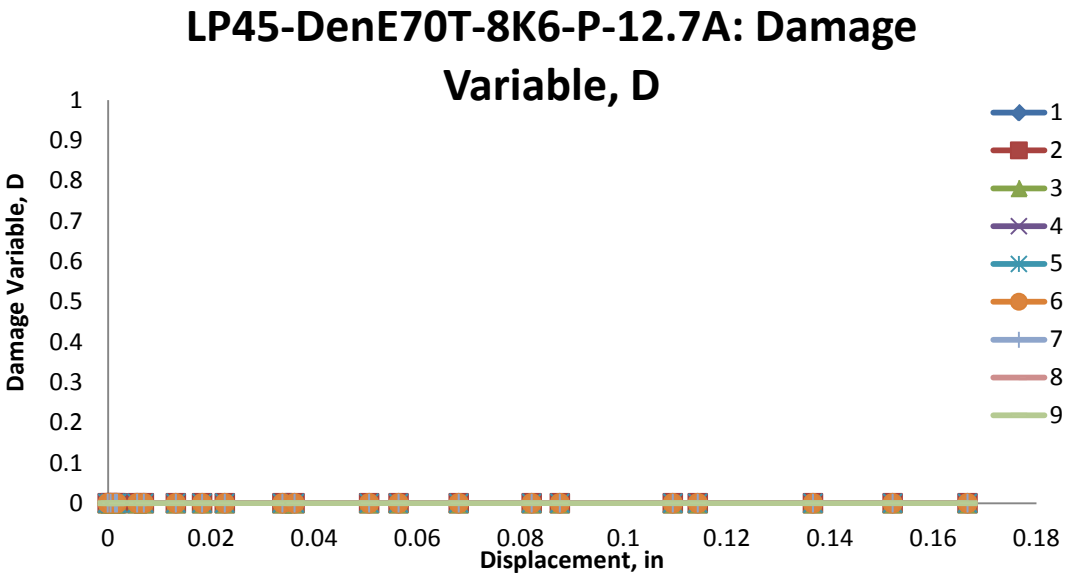

Figure B. 229: Variation of damage variable with displacement for different elements laid out through the thickness of simulation of LP45-DenE70T-8K6-P-12.7A specimens

B.22 LPL-DenE70-T4-P-12.7A

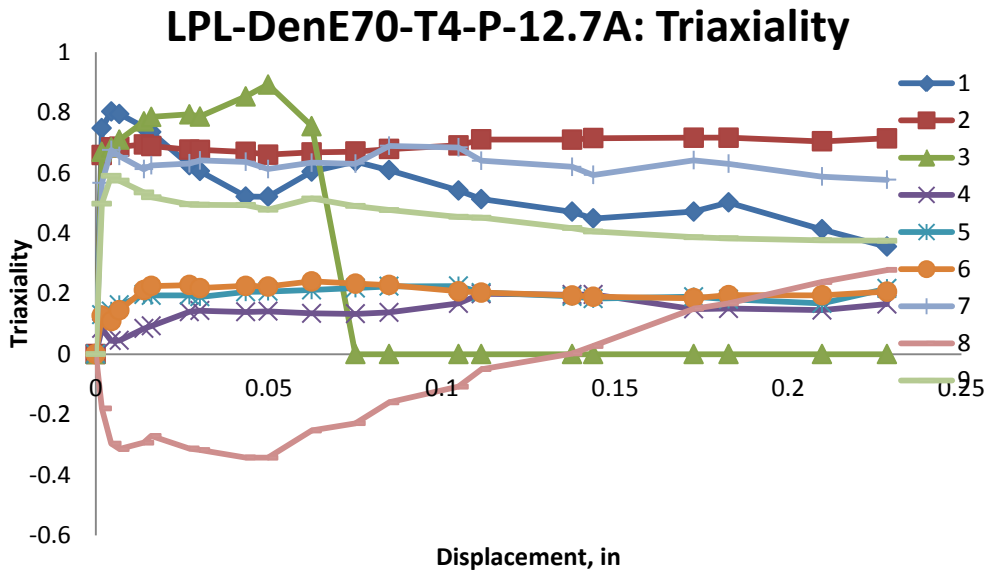

Figure B. 230: Variation of triaxiality with displacement for different elements laid out through the thickness of simulation of LPL-DenE70-T4-P-12.7A specimens

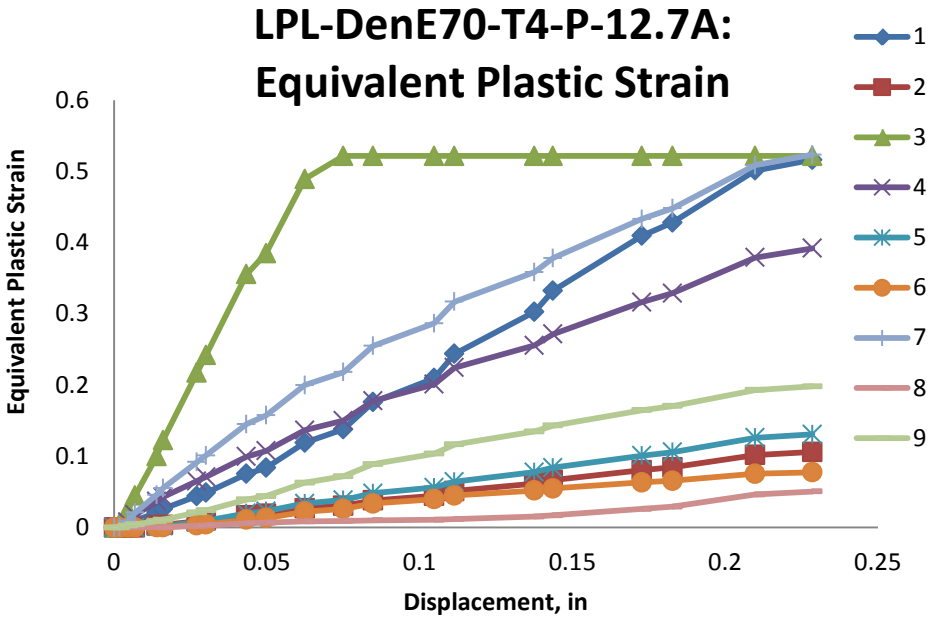

Figure B. 231: Variation of equivalent plastic strain with displacement for different elements laid out through the thickness of simulation of LPL-DenE70-T4-P-12.7A specimens

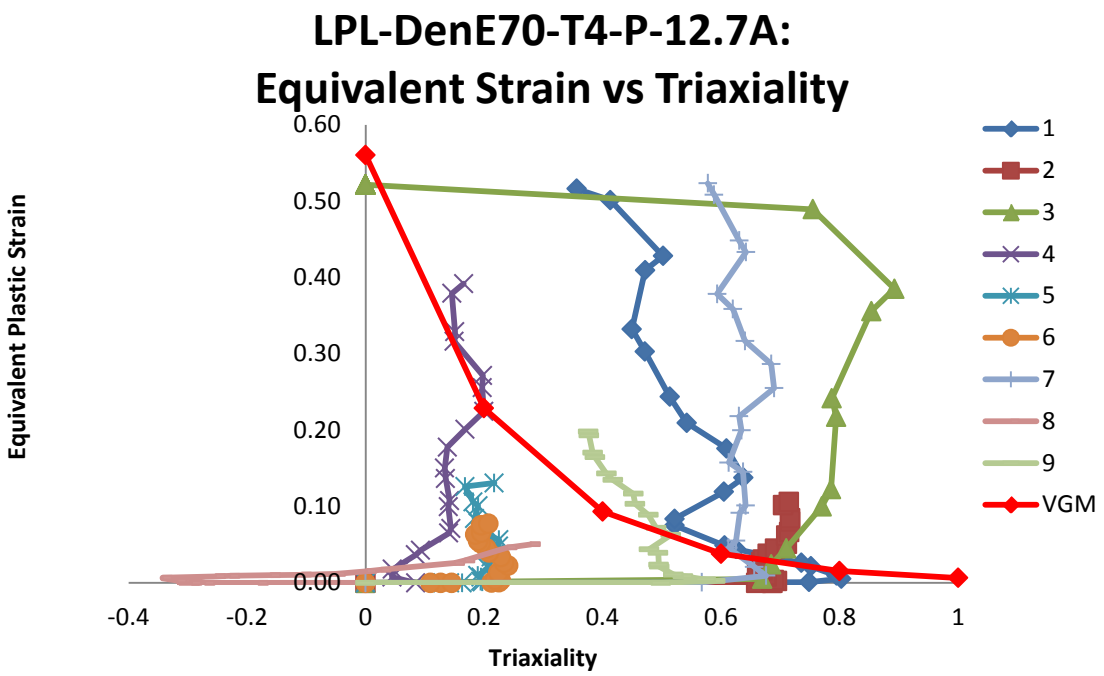

Figure B. 232: Variation of equivalent plastic strain versus triaxiality for different elements laid out through the thickness of simulation of LPL-DenE70-T4-P-12.7A specimens

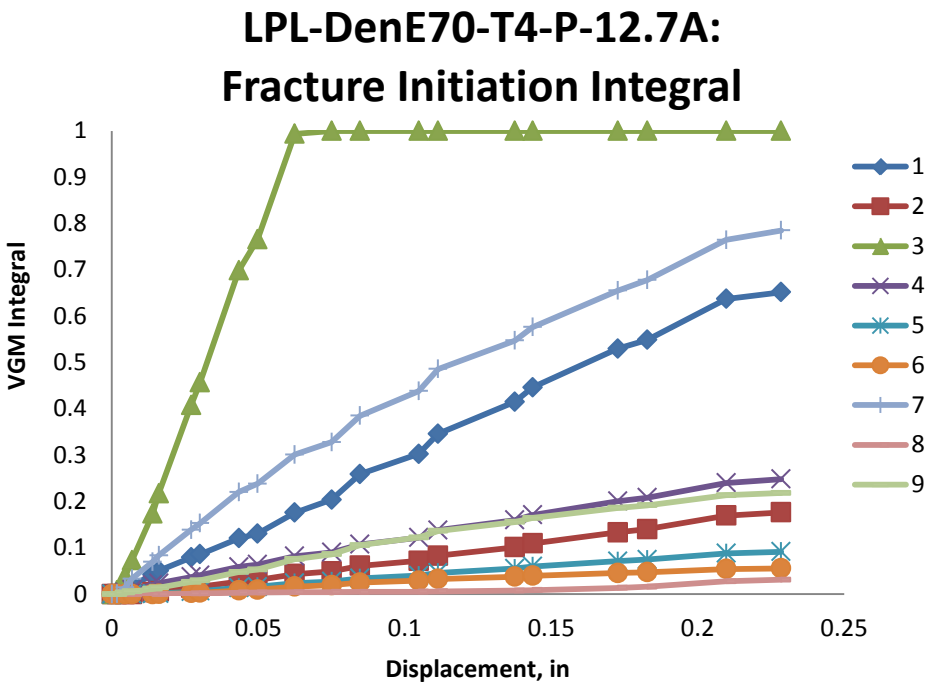

Figure B. 233: Value of fracture initiation integral for different elements laid out through the thickness of simulation of LPL-DenE70-T4-P-12.7A specimens

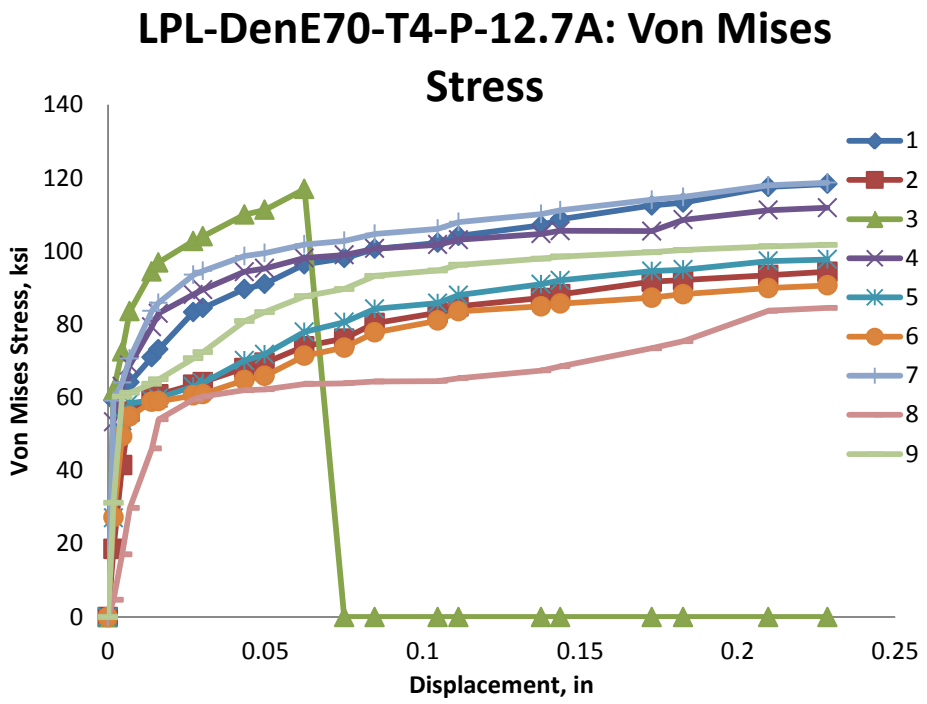

Figure B. 234: Variation of von Mises stress versus displacement for different elements laid out through the thickness of simulation of LPL-DenE70-T4-P-12.7A specimens

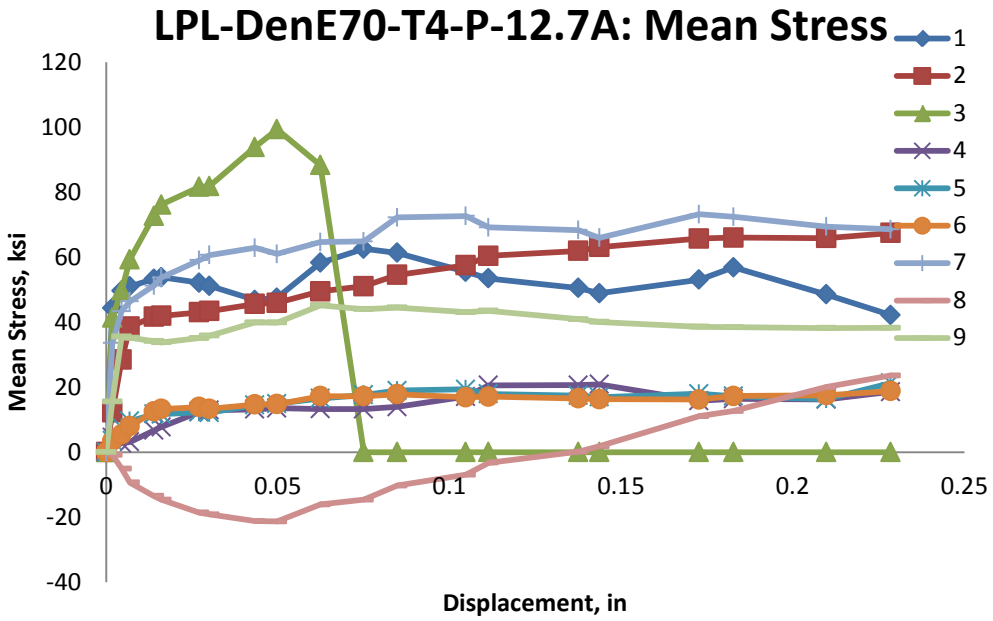

Figure B. 235: Variation of mean stress versus displacement for different elements laid out through the thickness of simulation of LPL-DenE70-T4-P-12.7A specimens

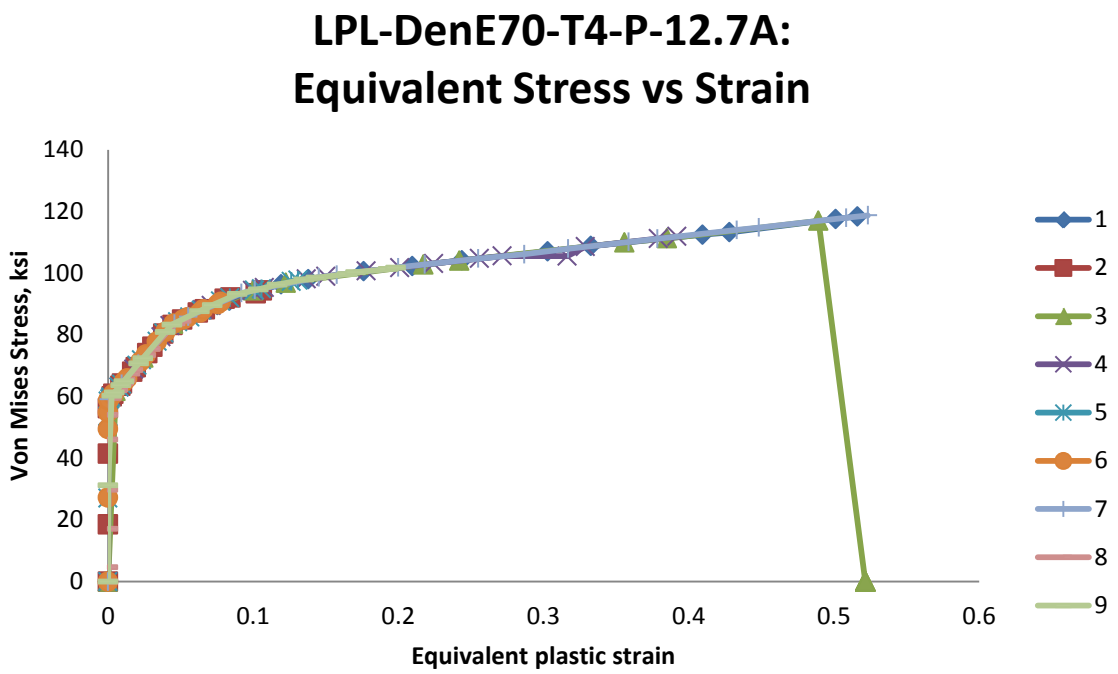

Figure B. 236: Variation of von Mises stress versus equivalent plastic strain for different elements laid out through the thickness of simulation of LPL-DenE70-T4-P-12.7A specimens

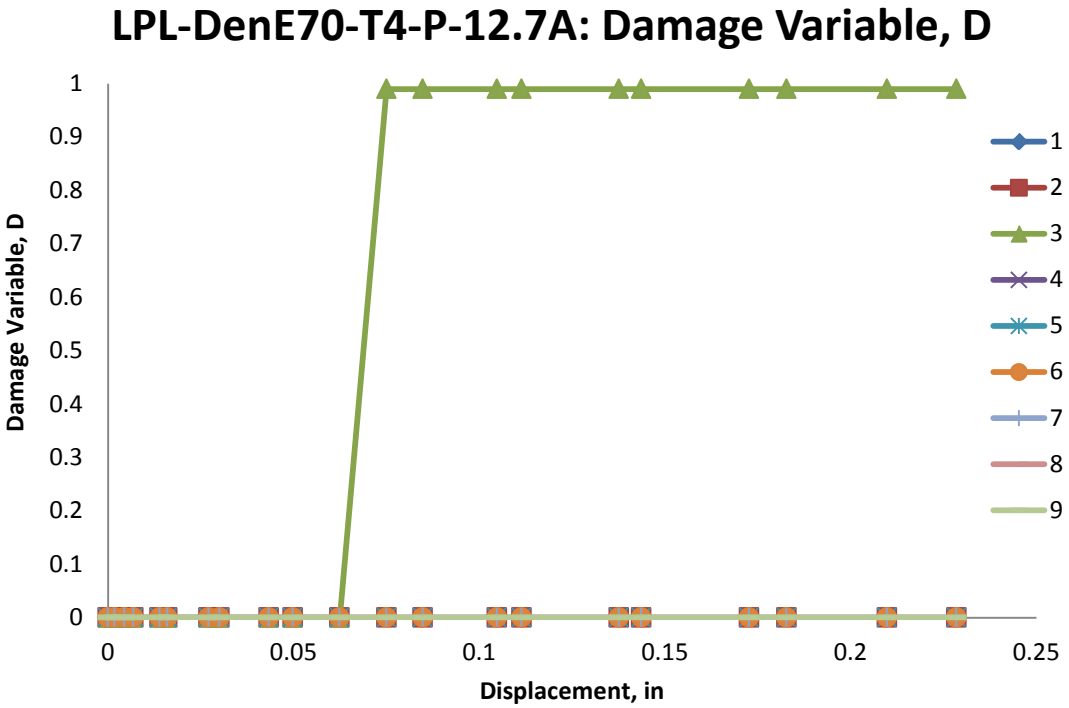

Figure B. 237: Variation of damage variable with displacement for different elements laid out through the thickness of simulation of LPL-DenE70-T4-P-12.7A specimens

B.23 LPL-DenE70-T7-P-12.7A

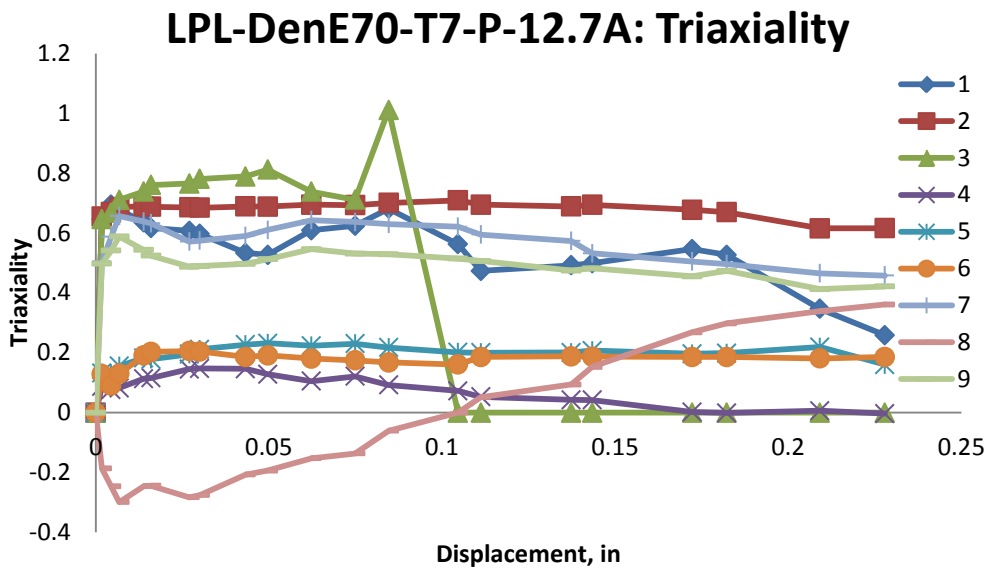

Figure B. 238: Variation of triaxiality with displacement for different elements laid out through the thickness of simulation of LPL-DenE70-T7-P-12.7A specimens

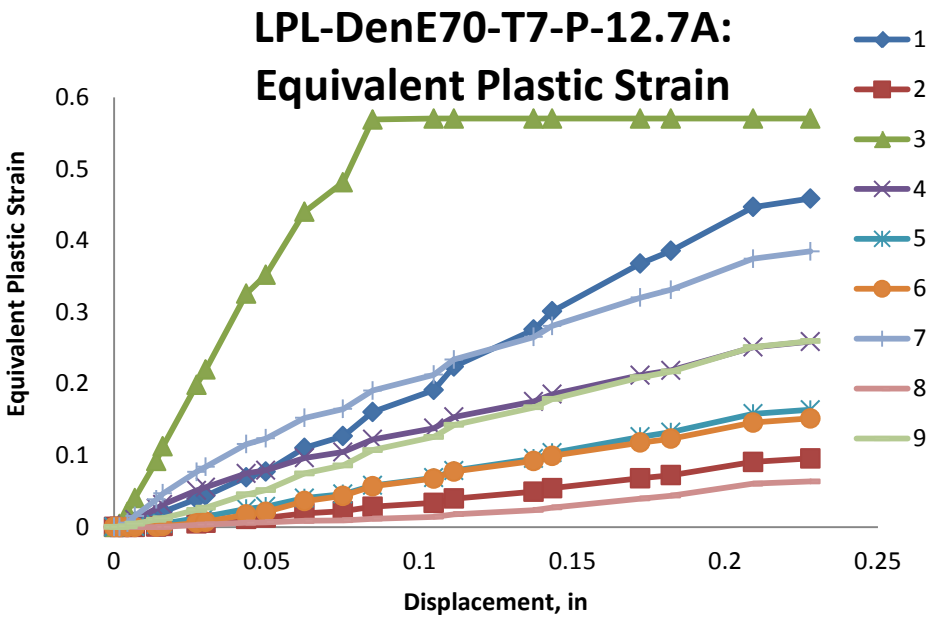

Figure B. 239: Variation of equivalent plastic strain with displacement for different elements laid out through the thickness of simulation of LPL-DenE70-T7-P-12.7A specimens

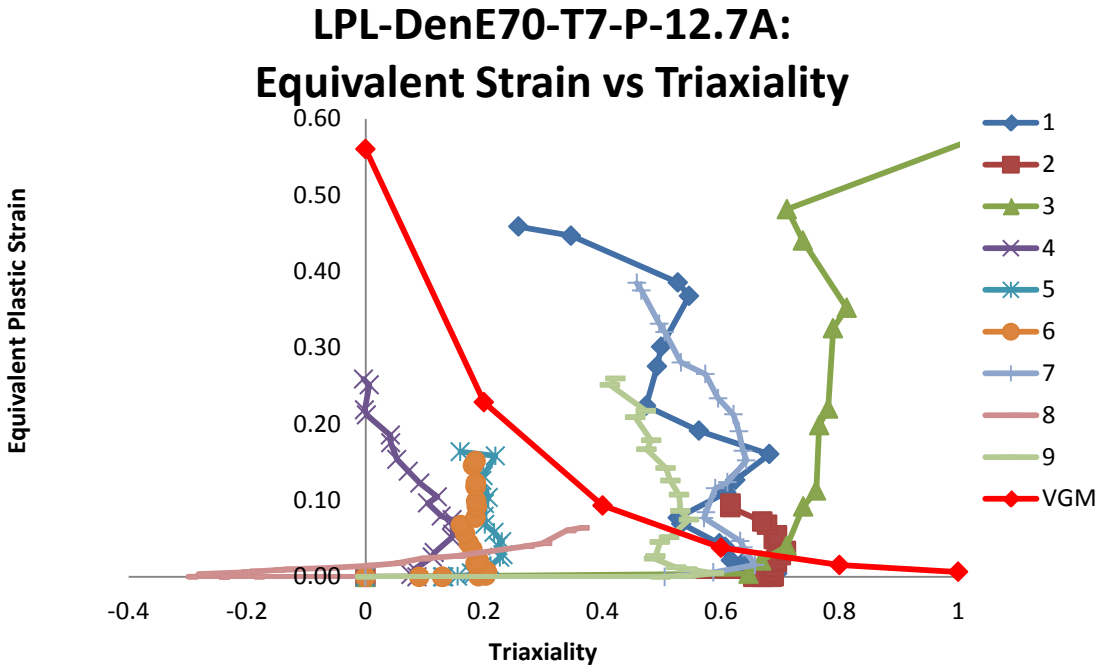

Figure B. 240: Variation of equivalent plastic strain versus triaxiality for different elements laid out through the thickness of simulation of LPL-DenE70-T7-P-12.7A specimens

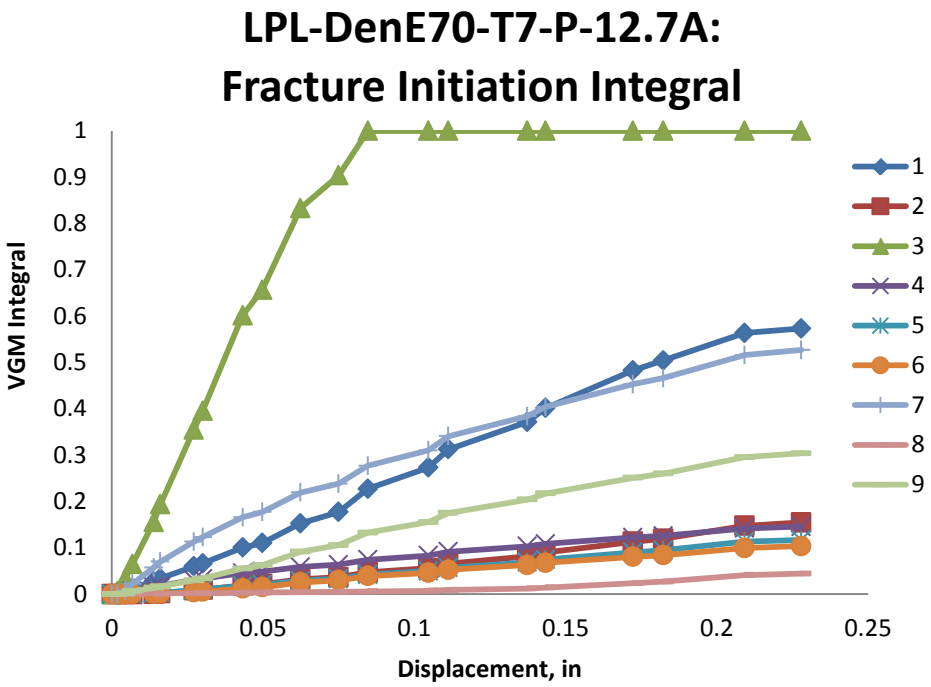

Figure B. 241: Value of fracture initiation integral for different elements laid out through the thickness of simulation of LPL-DenE70-T7-P-12.7A specimens

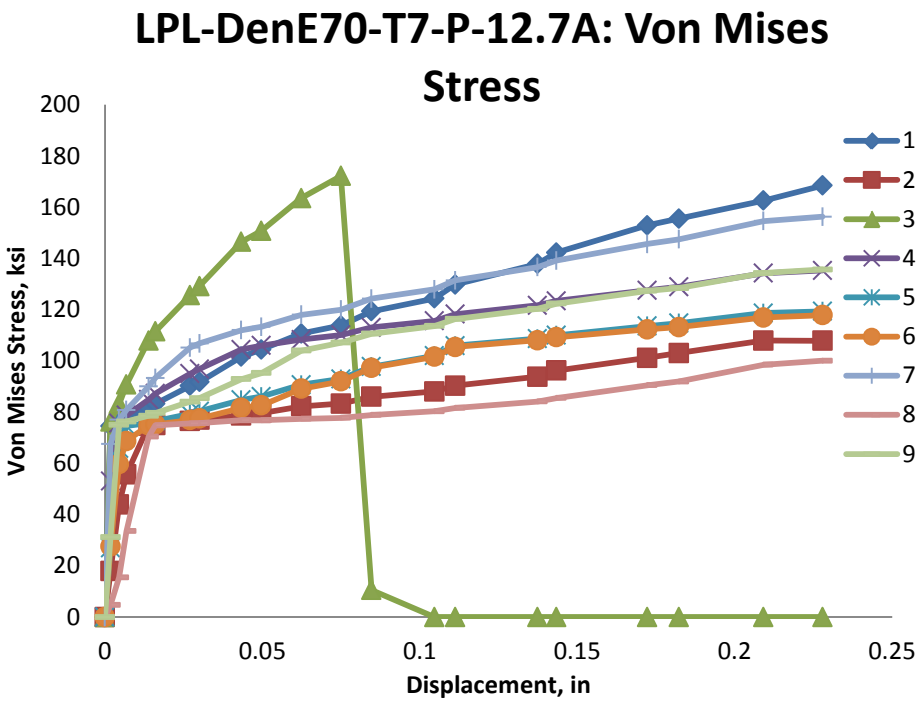

Figure B. 242: Variation of von Mises stress versus displacement for different elements laid out through the thickness of simulation of LPL-DenE70-T7-P-12.7A specimens

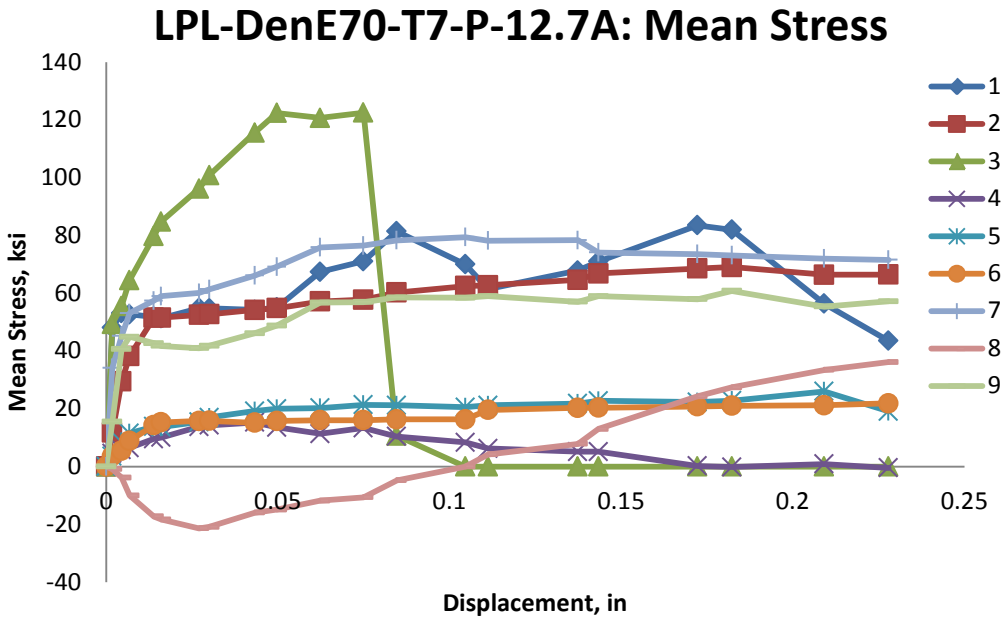

Figure B. 243: Variation of mean stress versus displacement for different elements laid out through the thickness of simulation of LPL-DenE70-T7-P-12.7A specimens

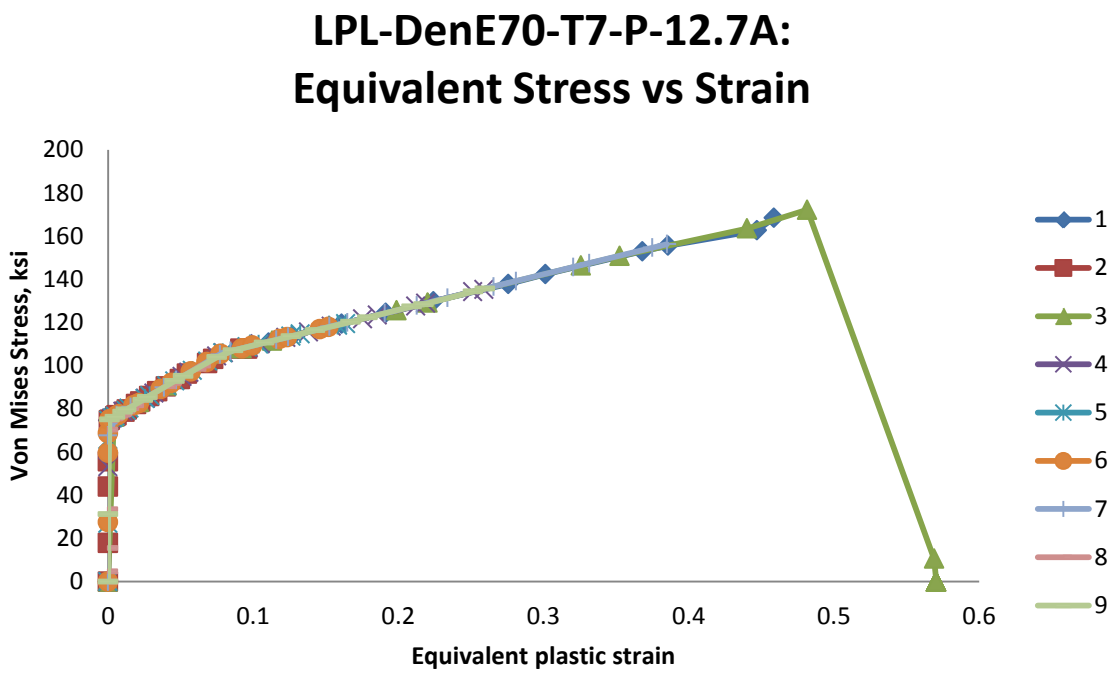

Figure B. 244: Variation of von Mises stress versus equivalent plastic strain for different elements laid out through the thickness of simulation of LPL-DenE70-T7-P-12.7A specimens

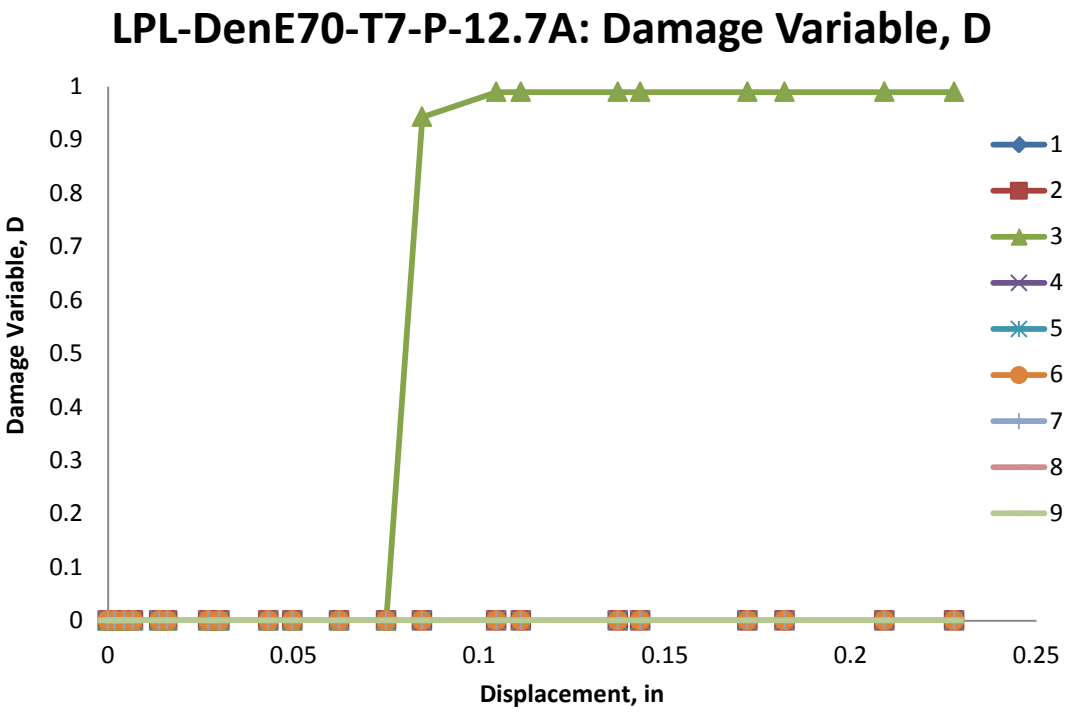

Figure B. 245: Variation of damage variable with displacement for different elements laid out through the thickness of simulation of LPL-DenE70-T7-P-12.7A specimens

B.24 LPL-DenE70T-8K6-P-12.7A

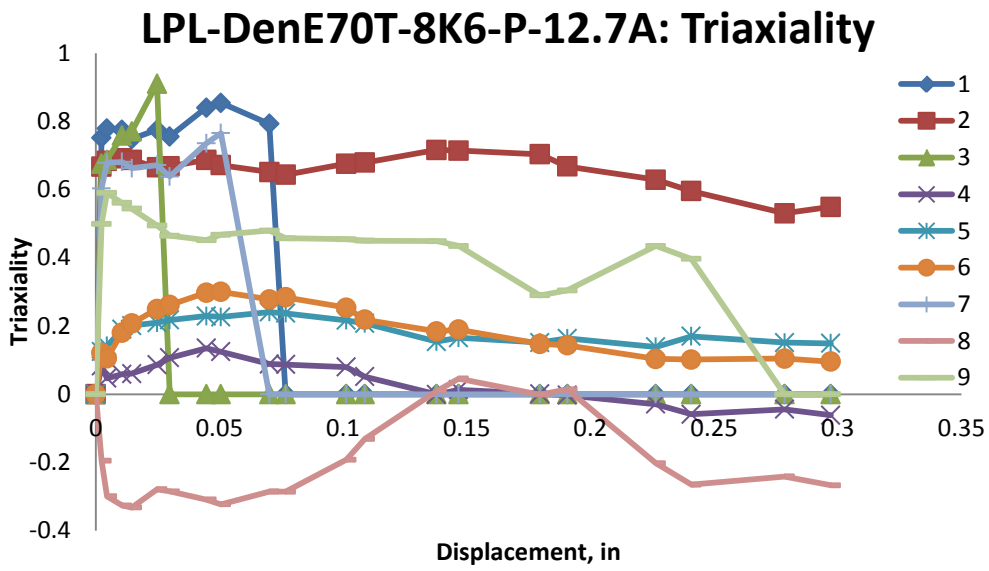

Figure B. 246: Variation of triaxiality with displacement for different elements laid out through the thickness of simulation of LPL-DenE70T-8K6-P-12.7A specimens

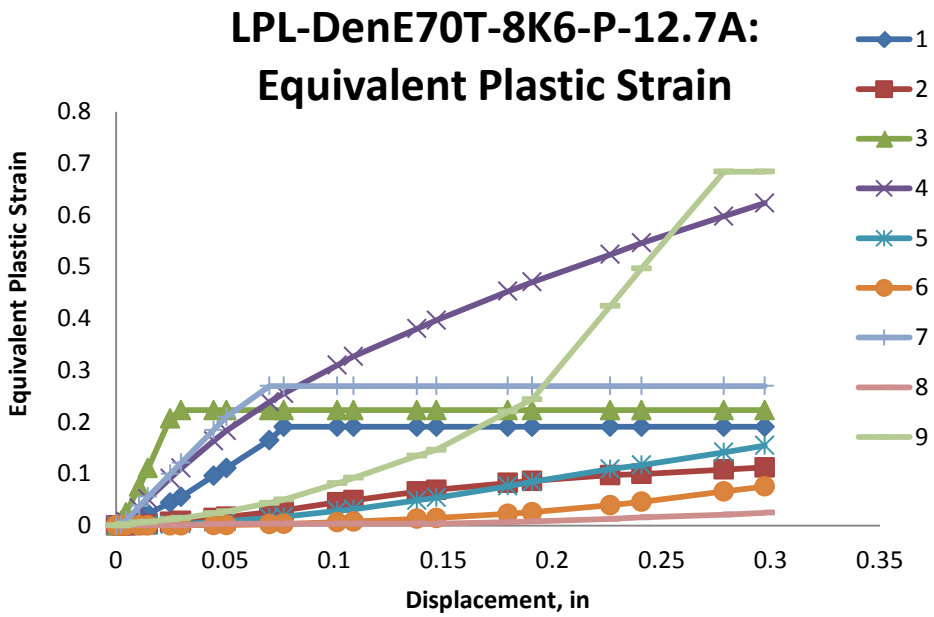

Figure B. 247: Variation of equivalent plastic strain with displacement for different elements laid out through the thickness of simulation of LPL-DenE70T-8K6-P-12.7A specimens

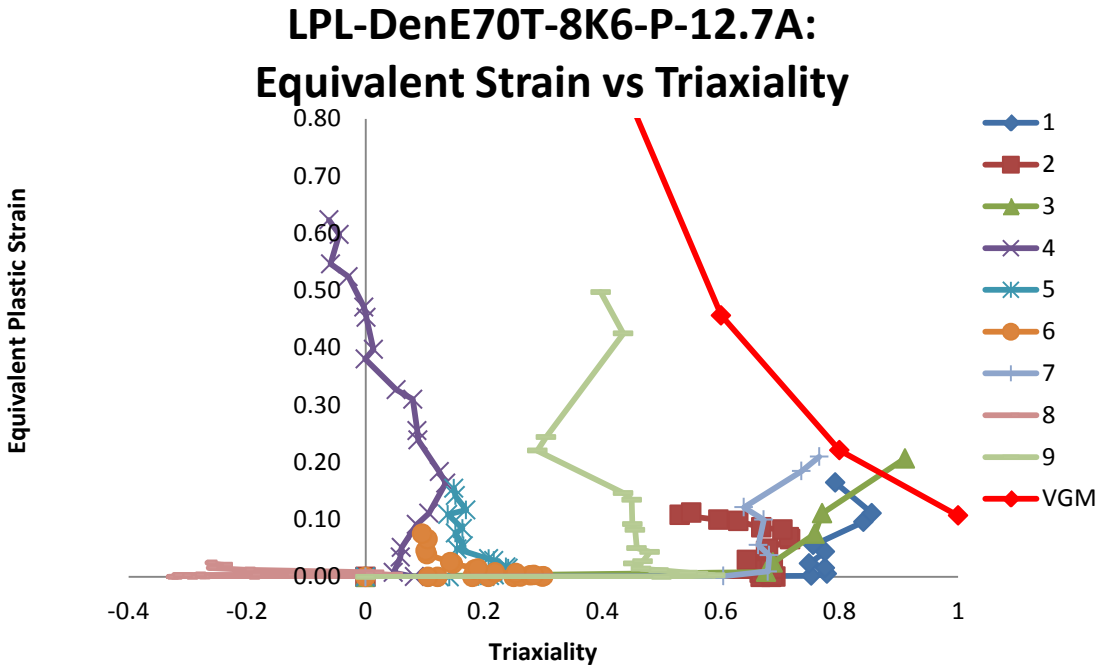

Figure B. 248: Variation of equivalent plastic strain versus triaxiality for different elements laid out through the thickness of simulation of LPL-DenE70T-8K6-P-12.7A specimens

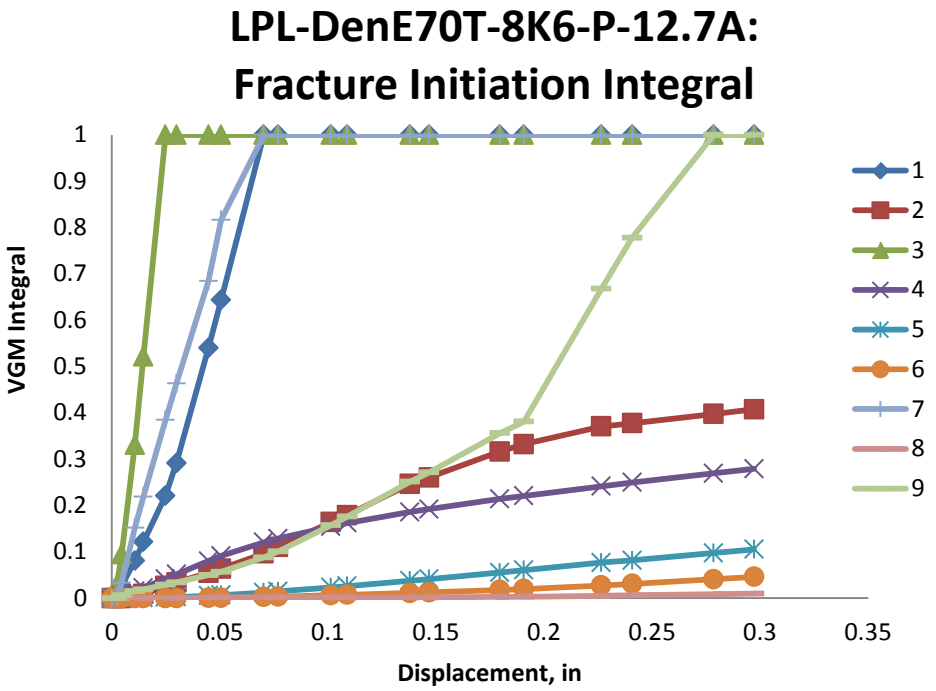

Figure B. 249: Value of fracture initiation integral for different elements laid out through the thickness of simulation of LPL-DenE70T-8K6-P-12.7A specimens

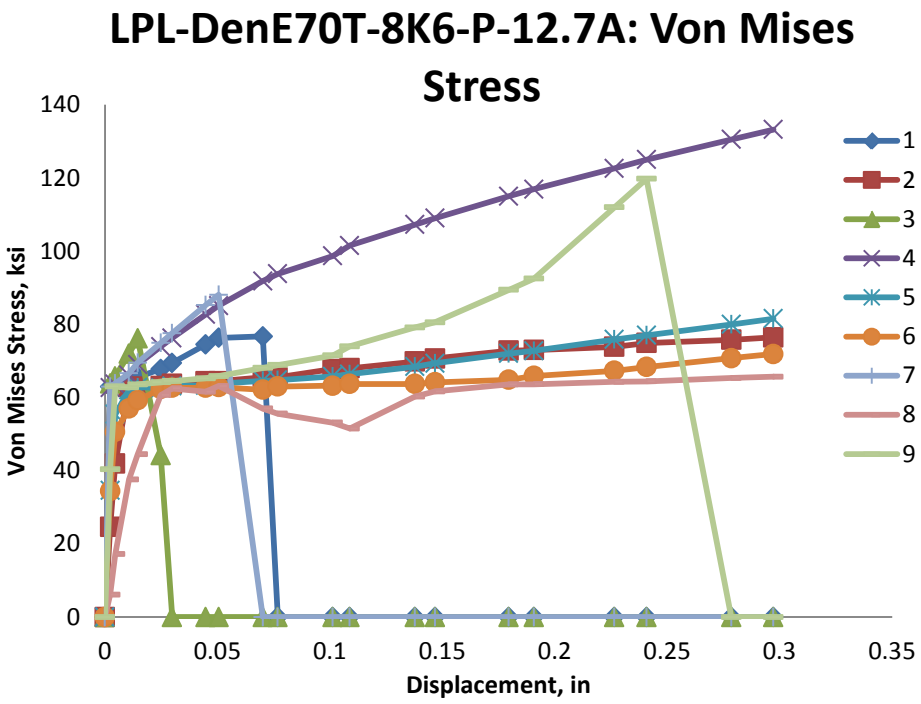

Figure B. 250: Variation of von Mises stress versus displacement for different elements laid out through the thickness of simulation of LPL-DenE70T-8K6-P-12.7A specimens

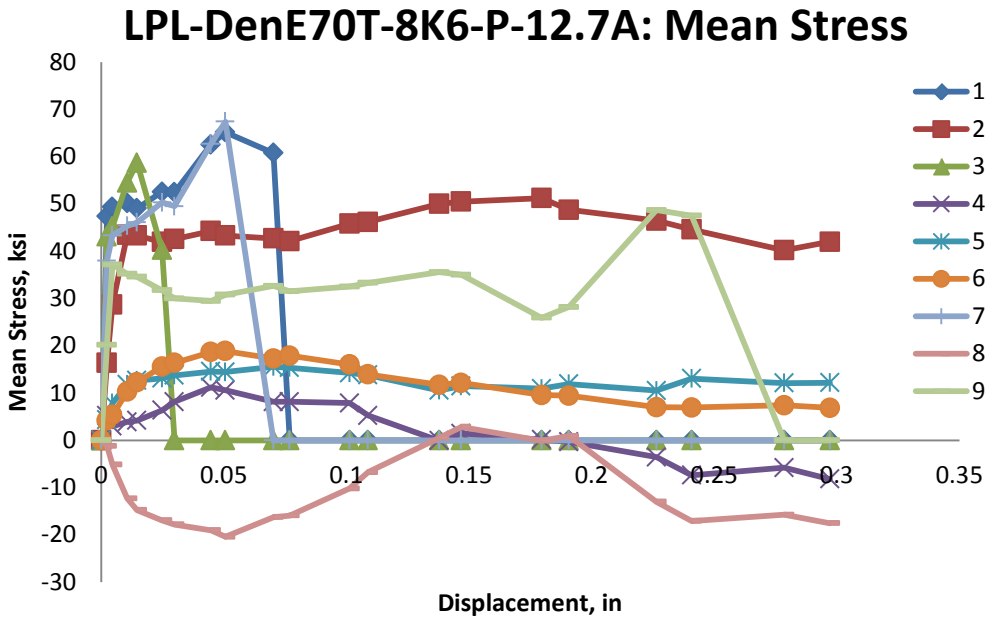

Figure B. 251: Variation of mean stress versus displacement for different elements laid out through the thickness of simulation of LPL-DenE70T-8K6-P-12.7A specimens

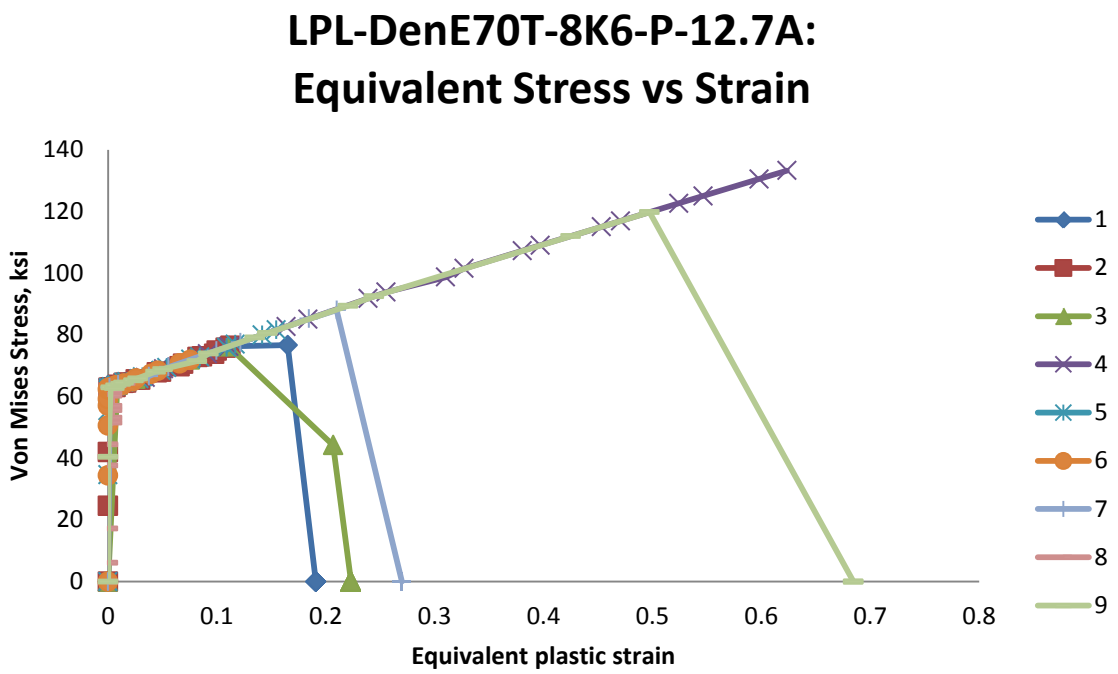

Figure B. 252: Variation of von Mises stress versus equivalent plastic strain for different elements laid out through the thickness of simulation of LPL-DenE70T-8K6-P-12.7A specimens

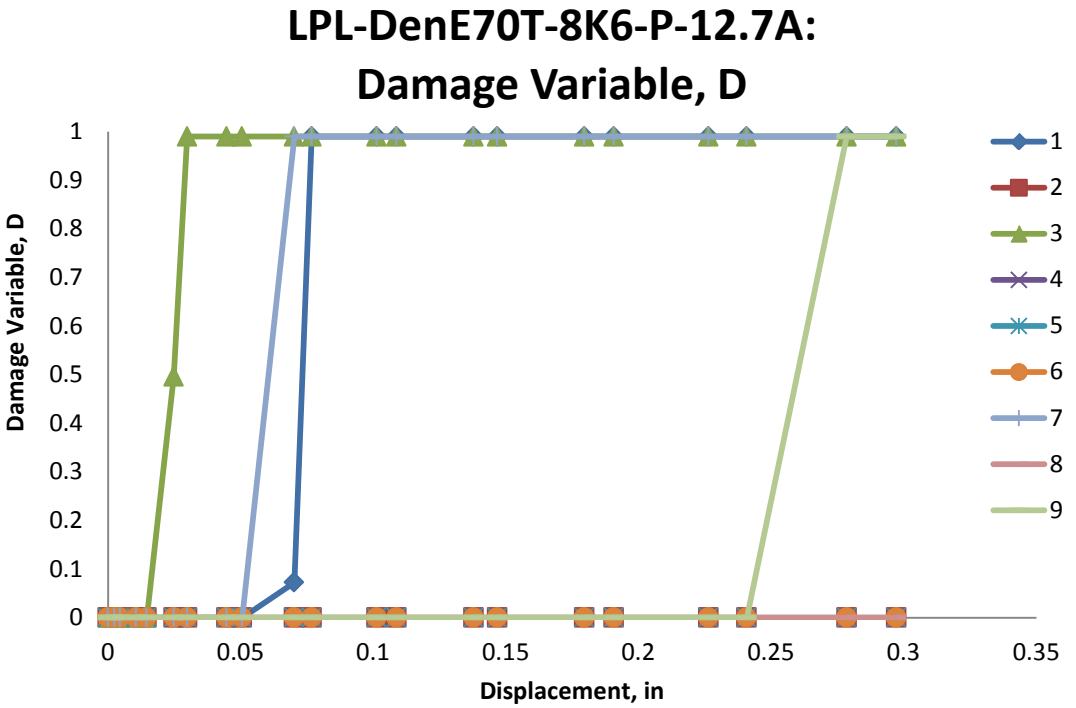

Figure B. 253: Variation of damage variable with displacement for different elements laid out through the thickness of simulation of LPL-DenE70T-8K6-P-12.7A specimens

Appendix C: Data point inputs for plasticity model

This appendix provides the data input into the isotropic hardening plasticity model that was used for all of the calibration and validation simulations. The table headings describe the material that corresponds to the nomenclature used in the tables throughout the report. The stress value is the equivalent plastic stress (von Mises) and the strain value is the equivalent plastic strain.

CNT-KanA572-W-L-A	
Stress	**Strain**
50.00	0.00000
50.00	0.00828
60.50	0.02291
69.41	0.04761
76.10	0.07238
79.50	0.09726
82.19	0.12217
84.47	0.14709
86.30	0.17202
88.28	0.19696
95.12	0.29672

CNT-KanA572-P-A	
Stress	**Strain**
50.00	0.00000
65.00	0.02000
71.00	0.03600
84.00	0.05300
90.00	0.07800
94.00	0.10300
154.00	0.81300

CNT-KanA514-P-A	
Stress	**Strain**
110.00	0.00000
114.00	0.00384
119.00	0.00546
120.00	0.01282
122.00	0.03928
180.00	0.80000
280.00	2.00000

CNT-KanHPS70W-P-A	
Stress	**Strain**
80.00	0.00000
81.50	0.00310
92.00	0.02600
96.70	0.03370
104.00	0.05600
108.00	0.08910
110.00	0.10300
191.00	1.38600

CNT-KanSN490B-P-A	
Stress	**Strain**
50.00	0.00000
56.87	0.02440
69.36	0.04830
76.95	0.07350
83.78	0.11090
90.48	0.17380
145.20	1.26900
200.20	2.26900

CNT-KanSM490YBTM-P-A	
Stress	**Strain**
60.00	0.00000
64.60	0.02556
68.00	0.03290
72.30	0.04434
76.00	0.05653
78.40	0.06657
81.40	0.08910
84.40	0.11560
86.20	0.14010
190.20	1.67000

CNT-MyeA36-B-A	
$\bar{\sigma}^{pl}$	$\bar{\varepsilon}^{pl}$
52.80	0.00000
50.33	0.00133
51.11	0.01631
53.38	0.02256
57.54	0.02748
60.45	0.03283
63.14	0.03864
65.63	0.04436
67.71	0.05029
69.31	0.05493
71.12	0.06121
72.82	0.06737
74.35	0.07371
75.63	0.07999
76.95	0.08625
78.15	0.09256
79.24	0.09894
80.31	0.10523
81.94	0.11788
82.92	0.12418
83.58	0.12876
84.09	0.13550
84.88	0.14227
85.79	0.14898
86.68	0.15578
87.32	0.16279
87.98	0.16995
88.73	0.17723
129.26	0.90926
189.34	2.00000

CNT-MyeA992-W-L-A	
$\bar{\sigma}^{pl}$	$\bar{\varepsilon}^{pl}$
53.66	0.00000
54.39	0.00800
58.45	0.01300
62.66	0.01900
65.85	0.02500
70.05	0.03400
72.08	0.03900
73.53	0.04400
74.84	0.04800
76.43	0.05400
77.89	0.05900
80.50	0.07000
81.80	0.07700
83.54	0.08700
84.70	0.09600
85.86	0.10400
86.73	0.11100
87.89	0.12000
88.47	0.12700
89.63	0.13800
90.36	0.14600
90.65	0.15300
139.96	0.82100
226.98	2.00000

CNT-MyeA992-W-T-A	
$\bar{\sigma}^{pl}$	$\bar{\varepsilon}^{pl}$
53.66	0.00000
54.39	0.00800
58.45	0.01300
62.66	0.01900
65.85	0.02500
70.05	0.03400
72.08	0.03900
73.53	0.04400
74.84	0.04800
76.43	0.05400
77.89	0.05900
80.50	0.07000
81.80	0.07700
83.54	0.08700
84.70	0.09600
85.86	0.10400
86.73	0.11100
87.89	0.12000
88.47	0.12700
89.63	0.13800
90.36	0.14600
90.65	0.15300
124.15	0.82100
183.04	2.00000

CNT-KanSN490B-W-L-A	
$\bar{\sigma}^{pl}$	$\bar{\varepsilon}^{pl}$
50.00	0.00000
53.33	0.01428
58.56	0.02420
65.47	0.04101
70.97	0.05970
75.66	0.09011
140.99	1.46800

TC-MyeE70-T6-W-T-A	
$\bar{\sigma}^{pl}$	$\bar{\varepsilon}^{pl}$
71.07	0.00000
73.82	0.00500
75.13	0.01000
77.60	0.01700
79.05	0.02400
81.66	0.03300
84.41	0.04400
85.43	0.05300
87.17	0.06100
89.05	0.06900
89.78	0.07800
91.52	0.08700
91.81	0.09400
93.11	0.10200
137.79	0.82000
211.32	2.00000

TC-MyeE70-T6-W-L-A	
$\bar{\sigma}^{pl}$	$\bar{\varepsilon}^{pl}$
69.58	0.00000
73.06	0.00500
75.10	0.01000
77.60	0.01700
79.07	0.02400
81.63	0.03300
85.18	0.04400
86.26	0.05300
88.09	0.06100
89.98	0.06900
90.64	0.07800
92.37	0.08700
92.69	0.09400
94.04	0.10200
130.00	0.82000
189.10	2.00000

TC-SadA992-W-W-A	
$\bar{\sigma}^{pl}$	$\bar{\varepsilon}^{pl}$
66.00	0.00000
69.00	0.02000
78.00	0.05000
83.00	0.07000
92.00	0.14000
96.00	0.20000
100.00	0.26000
216.00	2.00000

TC-SadA992-Col-F-A	
$\bar{\sigma}^{pl}$	$\bar{\varepsilon}^{pl}$
55.00	0.00000
57.00	0.02000
69.00	0.05000
73.00	0.07000
83.00	0.14000
88.00	0.20000
90.00	0.26000
148.00	2.00000

Bolt-SadA490-B-A	
$\bar{\sigma}^{pl}$	$\bar{\varepsilon}^{pl}$
109.17	0.00000
112.83	0.02000
116.35	0.04000
120.16	0.06000
123.60	0.08000
127.11	0.11000
131.37	0.13000
134.81	0.15000
137.13	0.17000
139.16	0.20000
141.33	0.22000
144.10	0.25000
146.27	0.27000
148.74	0.29000
149.35	0.30000
150.03	0.32000
151.24	0.35000
152.30	0.37000
153.73	0.41000
155.02	0.44000
156.30	0.46000
157.36	0.49000
158.42	0.52000
159.10	0.53000
160.00	0.55000
162.27	0.60000
164.54	0.65000
166.81	0.70000
169.08	0.75000
171.35	0.80000
173.62	0.85000
175.89	0.90000
178.16	0.95000
180.43	1.00000

TC-NgE70-T4-P-A	
$\bar{\sigma}^{pl}$	$\bar{\varepsilon}^{pl}$
58.83	0.00000
63.89	0.00951
69.44	0.01647
75.85	0.02632
82.48	0.04090
87.34	0.05668
92.00	0.07873
94.49	0.09893
98.68	0.13902
185.38	1.80000

TC-NgE70-T7-P-A	
$\bar{\sigma}^{pl}$	$\bar{\varepsilon}^{pl}$
74.70	0.00000
76.38	0.00436
81.36	0.01208
86.87	0.01879
95.06	0.03253
101.50	0.05207
389.36	1.80000

TC-NgE70T-7K2-P-A	
$\bar{\sigma}^{pl}$	$\bar{\varepsilon}^{pl}$
80.01	0.00000
80.47	0.00958
82.49	0.01434
84.29	0.02262
86.32	0.03044
87.44	0.03781
88.12	0.04358
211.16	1.80000

TC-NgE70T-8K6-P-A	
$\bar{\sigma}^{pl}$	$\bar{\varepsilon}^{pl}$
62.79	0.00000
63.02	0.00958
64.13	0.01355
65.92	0.01830
67.03	0.02263
69.04	0.02811
70.16	0.03395
259.22	1.80000

DAC-BirG40.21-W-1	
$\bar{\sigma}^{pl}$	$\bar{\varepsilon}^{pl}$
51.40	0
58.72	0.02
66.46	0.036
76.32	0.053
82.61	0.078
86.97	0.103
138.97	0.813
221.82	2

Northeastern

Department of Civil and Environmental Engineering Reports

Northeastern University

REPORT NO.	AUTHORS	TITLE	DATE
NEU-CEE-2014-02	Saykin, V. V.; Song, J.; Hajjar, J. F.	A Validated Approach to Modeling Collapse of Steel Structures	September 2014
NEU-CEE-2013-02	Denavit, M. D.; Hajjar, J. F.	Description of Geometric Nonlinearity for Beam-Column Analysis in OpenSees	September 2013
NEU-CEE-2013-01	Hajjar, J. F.; Sesen, A. H.; Jampole, E.; Wetherbee, A.	A Synopsis of Sustainable Structural Systems with Rocking, Self-Centering, and Articulated Energy-Dissipating Fuses	June 2013
NEU-CEE-2011-01	Hajjar, J. F.; Guldur, B.; and Sesen, A. H.	Laboratory for Structural Testing of Resilient and Sustainable Systems (STReSS Laboratory)	September 2011